NATIONAL TECHNICAL UNIVERSITY OF ATHENS
SCHOOL OF CIVIL ENGINEERING
DEPARTMENT OF GEOTECHNICAL ENGINEERING

ΕΘΝΙΚΟ ΜΕΤΣΟΒΙΟ ΠΟΛΥΤΕΧΝΕΙΟ
ΣΧΟΛΗ ΠΟΛΙΤΙΚΩΝ ΜΗΧΑΝΙΚΩΝ
ΤΟΜΕΑΣ ΓΕΩΤΕΧΝΙΚΗΣ

CONSTITUTIVE MODELING OF THE MONOTONIC AND CYCLIC RESPONSE OF GRANULAR SOILS WITH APPLICATIONS IN SEISMIC LIQUEFACTION

ΚΑΤΑΣΤΑΤΙΚΗ ΠΡΟΣΟΜΟΙΩΣΗ ΤΗΣ ΜΟΝΟΤΟΝΙΚΗΣ ΚΑΙ ΑΝΑΚΥΚΛΙΚΗΣ ΑΠΟΚΡΙΣΗΣ ΚΟΚΚΩΔΩΝ ΕΔΑΦΩΝ ΜΕ ΕΦΑΡΜΟΓΕΣ ΣΤΗ ΣΕΙΣΜΙΚΗ ΡΕΥΣΤΟΠΟΙΗΣΗ

DOCTORAL THESIS
of
TAXIARCHOULA G. LIMNAIOU
Diploma of Civil Engineering, National Technical University of Athens
M.Sc. National Technical University of Athens

ΔΙΔΑΚΤΟΡΙΚΗ ΔΙΑΤΡΙΒΗ
της
ΤΑΞΙΑΡΧΟΥΛΑΣ Γ. ΛΗΜΝΑΙΟΥ
Διπλ. Πολιτικός Μηχανικός Εθνικού Μετσόβιου Πολυτεχνείου
M.Sc. Εθνικό Μετσόβιο Πολυτεχνείο

Supervisor:
ACHILLEAS G. PAPADIMITRIOU
Associate Professor, National Technical University of Athens

Επιβλέπων:
ΑΧΙΛΛΕΑΣ Γ. ΠΑΠΑΔΗΜΗΤΡΙΟΥ
Αναπληρωτής Καθηγητής Εθνικού Μετσόβιου Πολυτεχνείου

Athens, July 2022

Αθήνα, Ιούλιος 2022

NATIONAL TECHNICAL UNIVERSITY OF ATHENS
SCHOOL OF CIVIL ENGINEERING
DEPARTMENT OF GEOTECHNICAL ENGINEERING

ΕΘΝΙΚΟ ΜΕΤΣΟΒΙΟ ΠΟΛΥΤΕΧΝΕΙΟ
ΣΧΟΛΗ ΠΟΛΙΤΙΚΩΝ ΜΗΧΑΝΙΚΩΝ
ΤΟΜΕΑΣ ΓΕΩΤΕΧΝΙΚΗΣ

ΚΑΤΑΣΤΑΤΙΚΗ ΠΡΟΣΟΜΟΙΩΣΗ ΤΗΣ ΜΟΝΟΤΟΝΙΚΗΣ ΚΑΙ ΑΝΑΚΥΚΛΙΚΗΣ ΑΠΟΚΡΙΣΗΣ ΚΟΚΚΩΔΩΝ ΕΔΑΦΩΝ ΜΕ ΕΦΑΡΜΟΓΕΣ ΣΤΗ ΣΕΙΣΜΙΚΗ ΡΕΥΣΤΟΠΟΙΗΣΗ

ΔΙΔΑΚΤΟΡΙΚΗ ΔΙΑΤΡΙΒΗ

της

ΤΑΞΙΑΡΧΟΥΛΑΣ Γ. ΛΗΜΝΑΙΟΥ

Διπλωματούχου Πολιτικού Μηχανικού Ε.Μ.Π, M.Sc.

Η διατριβή υποβλήθηκε στη Σχολή Πολιτικών Μηχανικών του Εθνικού Μετσόβιου Πολυτεχνείου προς εκπλήρωση των προϋποθέσεων του τίτλου της Διδάκτορος Μηχανικού.

ΤΡΙΜΕΛΗΣ ΣΥΜΒΟΥΛΕΥΤΙΚΗ ΕΠΙΤΡΟΠΗ:

1. ΑΧ. ΠΑΠΑΔΗΜΗΤΡΙΟΥ,
   Αναπλ. Καθηγητής, Ε.Μ.Π. (Επιβλέπων)
2. Μ. ΚΑΒΒΑΔΑΣ,
   Ομότιμος Καθηγητής, Ε.Μ.Π.
3. Γ. ΜΠΟΥΚΟΒΑΛΑΣ,
   Καθηγητής, Ε.Μ.Π.

ΕΠΤΑΜΕΛΗΣ ΕΞΕΤΑΣΤΙΚΗ ΕΠΙΤΡΟΠΗ:

1. ΑΧ. ΠΑΠΑΔΗΜΗΤΡΙΟΥ,
   Αναπλ. Καθηγητής, Ε.Μ.Π. (Επιβλέπων)
2. Μ. ΚΑΒΒΑΔΑΣ,
   Ομότιμος Καθηγητής, Ε.Μ.Π.
3. Γ. ΜΠΟΥΚΟΒΑΛΑΣ,
   Καθηγητής, Ε.Μ.Π.
4. Β. ΓΕΩΡΓΙΑΝΝΟΥ,
   Καθηγήτρια, Ε.Μ.Π.
5. Ν. ΓΕΡΟΛΥΜΟΣ,
   Αναπλ. Καθηγητής, Ε.Μ.Π.
6. Π. ΝΤΑΚΟΥΛΑΣ,
   Καθηγητής, Πανεπιστημίου Θεσσαλίας
7. Δ. ΚΑΡΑΜΗΤΡΟΣ,
   Senior Lecturer, University of Bristol, UK

Αθήνα, Ιούλιος 2022

NATIONAL TECHNICAL UNIVERSITY OF ATHENS
SCHOOL OF CIVIL ENGINEERING
DEPARTMENT OF GEOTECHNICAL ENGINEERING

ΕΘΝΙΚΟ ΜΕΤΣΟΒΙΟ ΠΟΛΥΤΕΧΝΕΙΟ
ΣΧΟΛΗ ΠΟΛΙΤΙΚΩΝ ΜΗΧΑΝΙΚΩΝ
ΤΟΜΕΑΣ ΓΕΩΤΕΧΝΙΚΗΣ

CONSTITUTIVE MODELING OF THE MONOTONIC AND CYCLIC RESPONSE OF GRANULAR SOILS WITH APPLICATIONS IN SEISMIC LIQUEFACTION

DOCTORAL THESIS

of

TAXIARCHOULA G. LIMNAIOU

Diploma of Civil Engineering, NTUA, M.Sc.

The thesis is submitted to the School of Civil Engineering of the National Technical University of Athens in fulfilment of the requirements for the Degree of Doctor of Philosophy

ADVISORY COMMITTEE:

1. A. PAPADIMITRIOU,
   Associate Professor, N.T.U.A (Supervisor)
2. M. KAVVADAS,
   Emeritus Professor, N.T.U.A
3. G. BOUCKOVALAS,
   Professor, N.T.U.A

EXAMINATION COMMITTEE:

1. A. PAPADIMITRIOU,
   Associate Professor, N.T.U.A (Supervisor)
2. M. KAVVADAS,
   Emeritus Professor, N.T.U.A
3. G. BOUCKOVALAS,,
   Professor, N.T.U.A
4. V. GEORGIANNOU,
   Professor, N.T.U.A
5. N. GEROLYMOS,
   Associate Professor, N.T.U.A
6. P. DAKOULAS,
   Professor, University of Thessaly
7. D. KARAMITROS,
   Senior Lecturer, University of Bristol, UK

Athens, July 2022

Ευχαριστήριο σημείωμα

Η πορεία της εκπόνησης μιας Διδακτορικής Διατριβής είναι αδιαμφισβήτητα πορεία μοναχική. Μια διαρκής εσωτερική διεργασία, όπου ο εαυτός σου είναι συνεργάτης, συνάδελφος, σύμβουλος, συνομιλητής, φίλος και συχνά αντίπαλος. Είναι όμως μαγικό, το πώς αυτή η ίδια συνθήκη σε δένει με ανθρώπους γύρω σου τόσο στενά, που πλέον τώρα που κάνω τον απολογισμό, κάθε επιτυχία, δυσκολία και αποτυχία σε όλη αυτή τη διαδρομή είναι στο μυαλό μου συνδεμένες με πρόσωπα που τις συντρόφευσαν. Αυτούς τους ανθρώπους θα ήθελα, εδώ, να ευχαριστήσω.

Το πρώτο «ευχαριστώ» ανήκει στον Επιβλέποντα Καθηγητή μου, κ. Αχιλλέα Παπαδημητρίου, Αναπληρωτή Καθηγητή ΕΜΠ. Τον ευχαριστώ που με εμπιστεύτηκε για το συγκεκριμένο αντικείμενο έρευνας, το οποίο πόσο σπουδαίο είναι το ανακάλυπτα μέρα με τη μέρα, που με πήρε από το χέρι και με οδήγησε στα «βαθιά νερά» της καταστατικής προσομοίωσης και που μου μετέφερε απλόχερα όλη τη γνώση και την εμπειρία του. Τον ευχαριστώ, ακόμη, για την υπομονή και την κατανόηση που έδειχνε σε όλα τα άγχη και τις ανησυχίες μου επί του ερευνητικού, για την πίστη του στις δυνάμεις μου και αλλά και για την ευκαιρία που μου έδωσε να τις ανακαλύψω κι εγώ η ίδια. Ο τρόπος σκέψης, η μεθοδικότητα, η συστηματικότητα, η διορατικότητα, η διακριτικότητα, η ευγένεια και οι αρχές του αποτελούν για μένα φωτεινό παράδειγμα ζωής. Κύριε Παπαδημητρίου, ήταν τύχη και τιμή να είμαι φοιτήτριά σας και θα είμαι παντοτινά ευγνώμων.

Ευχαριστώ, επίσης, θερμά τα άλλα δύο μέλη της Τριμελούς Συμβουλευτικής Επιτροπής της διδακτορικής μου διατριβής, τον κ. Γεώργιο Μπουκοβάλα, Καθηγητή ΕΜΠ και τον κ. Μιχαήλ Καββαδά, Ομότιμο Καθηγητή ΕΜΠ. Οφείλω να αναφερθώ ιδιαιτέρως στον κ. Γ. Μπουκοβάλα, ο οποίος είχα επίσης την τύχη να είναι επιβλέπων της διπλωματικής, αλλά και της μεταπτυχιακής μου εργασίας και που ήταν επίσης εκείνος, που κέντρισε το ενδιαφέρον μου για τη Γεωτεχνική Μηχανική, ήδη από το τρίτο έτος των σπουδών μου. Η σφαιρική σκέψη και ο πρακτικός τρόπος αντιμετώπισης κάθε προβλήματος (επιστημονικού ή μη), αλλά και ο ενθουσιασμός του για το αντικείμενο έρευνάς του είναι για μένα πηγή έμπνευσης. Τον ευχαριστώ για την στήριξη, τις συμβουλές, τις καρποφόρες συζητήσεις και τις παρεμβάσεις του επί του διδακτορικού, αλλά και για όλη τη συνεργασία μας.

Οφείλω επίσης να ευχαριστήσω θερμά και τα υπόλοιπα μέλη της Επταμελούς Εξεταστικής Επιτροπής για τις καίριες υποδείξεις και τις εύστοχες παρατηρήσεις τους. Πρόκειται για τους κα Βασιλική Γεωργιάννου, Καθηγήτρια ΕΜΠ, κύριο Παναγιώτη Ντακούλα, Καθηγητή Πανεπιστημίου Θεσσαλίας, κύριο Νικόλαο Γερόλυμο, Αναπλ. Καθηγητή ΕΜΠ και κύριο Δημήτριο Καραμήτρο, Ανωτ. Λέκτορα Πανεπιστημίου Bristol.

Ένα προσωπικό ευχαριστώ οφείλω, επίσης, στο Διδάκτορα (και οσονούπω Επίκ. Καθηγητή ΑΠΘ) Γιάννη Χαλούλο. Άλλο ένα φωτεινό παράδειγμα σκέψης, τρόπου δουλειάς και ήθους, που μου πρόσφερε τη γνώση του απλόχερα ήδη από τα χρόνια των φοιτητικών μου χρόνων, ως συνεπιβλέπων της διπλωματικής και της μεταπτυχιακής μου εργασίας, στη συνέχεια σε διάφορα καίρια στάδια του διδακτορικού και, τώρα πια, ως συνάδελφος. Είναι πάντα εκεί, πρόθυμος να συζητήσει κάθε ανησυχία και να προτείνει λύση ως «γενικός ειδικός», με ανιδιοτέλεια και ταπεινότητα. Γιάννη, σε ευχαριστώ για όλα. Θα είσαι ένας σπουδαίος Καθηγητής.

Ευχαριστώ ακόμη το Διδάκτορα Ιωάννη Τσιάπα για όλη την στήριξη και τη βοήθεια. Πάντα πρόθυμος να μοιραστεί γνώση και εμπειρίες, να βοηθήσει σε κάθε πρόβλημα της καθημερινότητας, να συζητήσει και να ακούσει κάθε προβληματισμό, να με καθησυχάσει και να με εμψυχώσει.

Θέλω ακόμη να ευχαριστήσω το Διδάκτορα Αλέξανδρο Βαλσαμή για τις συζητήσεις μας επί του επιστημονικού κατά τη διάρκεια αυτών των χρόνων, αλλά και για τη συνεργασία μας στο πλαίσιο των ερευνητικών προγραμμάτων.

Ένα ευχαριστώ (και μια αγκαλιά) δίνω και στα τρία κορίτσια με τα οποία συνεργαστήκαμε στο πλαίσιο των διπλωματικών τους εργασιών, στη Μαντώ Κυμπούρη, στη Δήμητρα Δελαβίνια και στην Αναστασία Παυλοπούλου. Η συνεργασία μας μου έδινε την ευκαιρία να δραπετεύω για λίγο από το αντικείμενο του διδακτορικού και σίγουρα με έκανε πιο πλούσια επιστημονικά.

Θα ήθελα ακόμη να ευχαριστήσω όλους τους αξιόλογους μηχανικούς της εταιρείας «GR8-GEO», της οποίας τους τελευταίους μήνες έχω την τύχη να είμαι κι εγώ μέλος. Συγκεκριμένα τους Jacob Chacko, Αμαλία Γιαννακού, Βασίλη Δρόσο, Τάκη Γεωργαράκο, Σπύρο Γιαννακό, Παναγιώτα Τασιοπούλου, Γιάννη Χαλούλο, Αντωνία Μάκρα, Μπάμπη Τσιφή και Κωνσταντίνο Τζιβάκο. Τους ευχαριστώ για την ευκαιρία που μου έδωσαν να ασχοληθώ ουσιαστικά με το αντικείμενο των σπουδών μου και να αρχίσω να γεφυρώνω στέρεα τη θεωρία με την πράξη.

Ευχαριστώ, επίσης, τους φίλους μου εκτός Τομέα Γεωτεχνικής, για τη φιλία τους και τις όμορφες στιγμές που έχουμε περάσει μαζί όλα αυτά τα χρόνια. Ευχαριστώ την Κατερίνα Δελιαλή, τη Δέσποινα Σουλάκη, το Μανόλη Ελένα, το Μανόλη Κατσίμπαλη, την Κωνσταντίνα Βασιλοπούλου, το Θωμά Βαζούκη, το Θανάση Λαμπρακόπουλο, τη Σωτηρία Καλύβα, το Γιώργο Αντωνακόπουλο, τη Μαριέττα Καφαράκη και το Νίκο Γιάνναρη. Τους ευχαριστώ που είναι «εκεί» όλα αυτά τα χρόνια, και κυρίως που παρέμειναν «εδώ» τα τελευταία πέντε, όταν εγώ η ίδια πολλές φορές ήμουν σώματι μεν μαζί τους, χαμένη δε στις σκέψεις του διδακτορικού.

Ωστόσο, τίποτα δε θα ήταν ίδιο και σίγουρα δε θα είχε το ίδιο νόημα, χωρίς τους συναδέλφους Υποψήφιους Διδάκτορες, μα πρωτίστως φίλους, από τον Τομέα Γεωτεχνικής. Ευχαριστώ, λοιπόν, τους Κωνσταντίνο Μπαζαίο, Ελένη Παυλοπούλου, Βασίλη Καλλιμογιάννη, Φίλιππο Χόρτη, Χαρά Ανδρικοπούλου (αν και δικηγόρος, επίτιμο μέλος του Τομέα), Κατερίνα Λεοντάρη και Δημήτρη Λίτσα. Οι ατέλειωτες ώρες στο γραφείο, έμοιαζαν πιο όμορφες επειδή υπήρχατε εσείς. Χωρίς την παρέα σας, την στήριξη, τις συμβουλές και τη βοήθειά σας, το ταξίδι δε θα ήταν το ίδιο όμορφο και σίγουρα εγώ δε θα ένιωθα το ίδιο γεμάτη. Νιώθω απίστευτα τυχερή που είχα εσάς για συνταξιδιώτες.

Οι λέξεις ακούγονται ελάχιστες, όταν έρχεται η στιγμή να ευχαριστήσω τον Μπάμπη Τσιφή. Είναι ο άνθρωπος που έζησε μαζί μου κάθε νίκη, κάθε ήττα, κάθε χαρά, κάθε λύπη, κάθε ενθουσιασμό, κάθε απογοήτευση, κάθε ανασφάλεια και άγχος κατά τη διάρκεια αυτών των χρόνων. Στάθηκε στο πλάι μου από την αρχή ως το τέλος του ταξιδιού με αγάπη, σεβασμό, στήριξη και κατανόηση. Σε ευχαριστώ Μπάμπη για όλα όσα μου πρόσφερες απλόχερα και που είσαι μέρος της ζωής μου.

Το τελευταίο, μα πιο μεγάλο ευχαριστώ το φυλάω για την οικογένειά μου. Ευχαριστώ από τα βάθη της καρδιάς μου τους γονείς μου Γρηγόρη και Χρυσάνθη, τον αδερφό μου Γιάννη και τη γιαγιά μου Ευαγγελία. Εξασφάλισαν με ανιδιοτέλεια τις απαραίτητες συνθήκες για να ακολουθήσω τα όνειρά μου από μικρή και είναι πάντα οι πιο ένθερμοι υποστηρικτές μου. Μου δίνουν διαρκώς δύναμη και κουράγιο και αποτελούν τη βασική κινητήριο δύναμη για κάθε τι που πετυχαίνω. Νιώθω περηφάνια για εκείνους και χωρίς αυτούς, σίγουρα, δε θα ήμουν ο ίδιος άνθρωπος.

Είναι ο χρόνος που ξόδεψες για το τριαντάφυλλό σου
που το κάνει τόσο σημαντικό…
(Antoine de Saint-Exupéry, Ο μικρός πρίγκηπας)

Ταξιαρχούλα Γ. Λημναίου

Αθήνα, Ιούλιος 2022

Η παρούσα έρευνα έχει χρηματοδοτηθεί από το Πρόγραμμα Υποτροφιών του Ιδρύματος Ωνάση, με κωδικό υποτροφίας G ZO 013-1/2018-2019. Ο συγγραφέας αισθάνεται την ανάγκη να ευχαριστήσει θερμά το Ίδρυμα Ωνάση για την υποστήριξή του.

ΕΘΝΙΚΟ ΜΕΤΣΟΒΙΟ ΠΟΛΥΤΕΧΝΕΙΟ
ΣΧΟΛΗ ΠΟΛΙΤΙΚΩΝ ΜΗΧΑΝΙΚΩΝ
ΤΟΜΕΑΣ ΓΕΩΤΕΧΝΙΚΗΣ

ΠΕΡΙΛΗΨΗ

της Διδακτορικής Διατριβής

της Ταξιαρχούλας Λημναίου

Η ακρίβεια των αριθμητικών αναλύσεων προβλημάτων συνοριακών τιμών που αφορούν σε έργα Γεωτεχνικού Μηχανικού βασίζονται σημαντικά στην αξιοπιστία και στη σωστή βαθμονόμηση του κατάλληλου καταστατικού προσομοιώματος, ανάλογα με το γεωυλικό και τον τύπο φόρτισης κάθε περίπτωσης. Για κοκκώδη εδάφη (όπως οι άμμοι και οι χάλικες) αποτελεί κοινή πρακτική η στοχευμένη χρήση διαφορετικών καταστατικών προσομοιωμάτων ή/και διαφορετικών βαθμονομήσεων του ίδιου προσομοιώματος, ανάλογα με τον εξεταζόμενο τύπο φόρτισης (π.χ. μονοτονική ή ανακυκλική, υπό στραγγιζόμενες ή αστράγγιστες συνθήκες, σύντομη και έντονη σεισμική διέγερση ή ήπια ανακυκλική φόρτιση πολλών κύκλων) ή/και ανάλογα με τις αρχικές συνθήκες (π.χ. σχετική πυκνότητα, επίπεδο τάσεων). Ειδικότερα, η προσομοίωση της ανακυκλικής φόρτισης κοκκωδών εδαφών, δεδομένης της πολυπλοκότητάς της, έχει προσελκύσει διαχρονικά μεγάλο ενδιαφέρον στη διεθνή βιβλιογραφία, με πληθώρα δημοσιεύσεων να αφορούν σε σχετικά καταστατικά προσομοιώματα. Ωστόσο, πολύ συχνά, οι σχετικές δημοσιεύσεις προσομοιωμάτων εμπεριέχουν επαρκείς συγκρίσεις με πειραματικά δεδομένα για την προσομοίωση της μονοτονικής συμπεριφοράς, ταυτόχρονα με συγκριτικά λίγες, προσεκτικά επιλεγμένες, ανακυκλικές δοκιμές με έμφαση στη ρευστοποίηση. Όμως, σε επίπεδο ανακυκλικής φόρτισης, μια τέτοια διακρίβωση αξιοπιστίας δεν μπορεί να θεωρείται επαρκής. Αντίθετα, για να θεωρηθεί επαρκής, θα πρέπει να καλύπτει ένα ευρύ φάσμα απόκρισης για όλες τις *περιοχές* παραμορφώσεων, ήτοι: α) *μικρές* παραμορφώσεις, όπου κυριαρχεί η οιονεί ελαστική απόκριση και έχει εξέχουσα σημασία η βαθμονόμηση με τις πραγματικές ελαστικές παραμέτρους (π.χ., από γεωφυσικές δοκιμές στο πεδίο), β) *μεσαίες παραμορφώσεις*, όπου η συμπεριφορά είναι μη-γραμμική υστερητική και παρατηρείται συσσώρευση παραμενουσών παραμορφώσεων με τον αριθμό των

επιβαλλόμενων κύκλων φόρτισης, και γ) *μεγάλες* παραμορφώσεις, με έμφαση στις παραμορφώσεις που εκδηλώνονται κατά τη ρευστοποίηση, καθώς και στη συσσώρευση παραμορφώσεων μετά την εκδήλωση αυτής. Έτσι, παρόλο που στη βιβλιογραφία υπάρχει πληθώρα πολύ αξιόλογων εξειδικευμένων καταστατικών προσομοιωμάτων, υπάρχουν ελάχιστες δημοσιεύσεις που να παρουσιάζουν λεπτομερή διακρίβωση της αξιοπιστίας τους σε όλο το φάσμα ανακυκλικής απόκρισης, σύμφωνα με την ανωτέρω συλλογιστική. Παράλληλα, έχει παρατηρηθεί πως αρκετά από τα προσομοιώματα που επιδεικνύουν ακριβή συμπεριφορά κατά την ανακυκλική φόρτιση δεν είναι εξίσου ακριβή κατά τη μονοτονική φόρτιση, ή χρειάζονται αναβαθμονόμηση για τον σκοπό αυτό. Σύμφωνα με τα παραπάνω, αναδύεται η ανάγκη για ένα καταστατικό προσομοίωμα για κοκκώδη εδάφη, το οποίο θα είναι ικανό να προσομοιώνει τόσο τη μονοτονική συμπεριφορά (μέχρι την Κρίσιμη Κατάσταση), όσο και την ανακυκλική συμπεριφορά (για οποιοδήποτε επίπεδο παραμόρφωσης) με ενιαία και μοναδική βαθμονόμηση των παραμέτρων του ανά γεωυλικό, ανεξάρτητα από τη σχετική πυκνότητα και το επίπεδο τάσης, και κυρίως ανεξάρτητα από τον τύπο φόρτισης. Αυτός είναι και ο στόχος του προσομοιώματος που αναπτύχθηκε στο πλαίσιο της παρούσας Διατριβής.

Συγκεκριμένα, καταστρώνεται ένα νέο ελαστο-πλαστικό προσομοίωμα το οποίο βασίζεται στη Θεωρία Κρίσιμης Κατάστασης, ανήκει στην οικογένεια των προσομοιωμάτων οριακής επιφάνειας SANISAND και δανείζεται στοιχεία τόσο από αυτά, όσο και από το προσομοίωμα NTUA-SAND (Andrianopoulos et al. 2010), μετά από κατάλληλες τροποποιήσεις. Βασικό χαρακτηριστικό του είναι η χρήση της τελευταίας αντιστροφής φόρτισης για τον ορισμό τόσο των ελαστικών όσο και των πλαστικών παραμορφώσεων. Η έμφαση δίνεται στον ορθό ορισμό του σημείου αντιστροφής φόρτισης ώστε να μην υπερακοντίζεται η σχέση τάσης-παραμόρφωσης. Χρησιμοποιεί μια συνάρτηση επίδρασης της δομής που ποσοτικοποιεί το πλαστικό μέτρο κράτυνσης με στόχο τον ορθό ρυθμό συσσώρευσης παραμενουσών παραμορφώσεων και μια συνάρτηση που ποσοτικοποιεί τον συντελεστή διαστολικότητας με στόχο την ορθή απόκριση μετά την αρχική ρευστοποίηση. Το προσομοίωμα έχει συνολικά 14 παραμέτρους, 12 από τις οποίες βαθμονομούνται πρώτα και αφορούν στη μονοτονική φόρτιση και στο τέλος βαθμονομούνται ακόμη 2 που αφορούν στην ανακυκλική φόρτιση. Από τις παραμέτρους αυτές, 9 βαθμονομούνται άμεσα επί τη βάση πειραματικών αποτελεσμάτων και μετά

βαθμονομούνται οι υπόλοιπες 5 (3 για μονοτονική και 2 για ανακυκλική φόρτιση) μέσω επαναληπτικής διαδικασίας.

Η κατάστρωση έγινε σε επίπεδο μοναδιαίου στοιχείου και παρουσιάζεται βαθμονόμηση για πέντε (5) άμμους της βιβλιογραφίας (Nevada, Toyoura, Ottawa, M31, Monterey), αλλά και δύο (2) χάλικες, που ως σύνολο καλύπτουν ένα εύρος τιμών μέσης διαμέτρου κόκκων D_{50} από 0.1 έως 9 mm. Έγιναν συγκρίσεις με πειραματικά δεδομένα με τεράστιο εύρος αρχικών συνθηκών και τύπων φόρτισης (συνολικό εύρος σχετικής πυκνότητας D_r = 2 – 90% και αρχικής μέσης ενεργού τάσης p_o = 33.33 – 2000 kPa). Όταν δεν υπάρχουν διαθέσιμα εξειδικευμένα πειραματικά αποτελέσματα για κάποιο γεωυλικό, χρησιμοποιούνται εμπειρικές σχέσεις από τη βιβλιογραφία. Μέσω της ενδελεχούς αυτής διερεύνησης καλύπτεται όλο το εύρος των ανακυκλικών παραμορφώσεων, όπως συζητήθηκε ανωτέρω, αλλά και η μονοτονική φόρτιση, με ενιαίο σετ παραμέτρων ανά κοκκώδες έδαφος, τουλάχιστον όσον αφορά στις άμμους. Από την άλλη, όσον αφορά στους χάλικες, η απενεργοποίηση της λειτουργίας των συναρτήσεων συσσώρευσης της δομής κατά τη μονοτονική φόρτιση (θέτοντας την παράμετρο N_o = 0) αποδεικνύεται επαρκής ώστε να μην απαιτείται περαιτέρω τροποποίηση της βαθμονόμησης. Η διερεύνηση αυτή αποτυπώνει ότι το προτεινόμενο καταστατικό προσομοίωμα για κοκκώδη εδάφη είναι, με βάση το σχεδιασμό του, ένα προσομοίωμα γενικής χρήσης, το οποίο παρέχει στο χρήστη τη δυνατότητα για μία ικανοποιητική προσομοίωση, χωρίς να απαιτείται αναβαθμονόμηση για το ίδιο γεωυλικό, ανεξάρτητα από το αν το εξεταζόμενο πρόβλημα είναι στατικό, δυναμικό ή ανακυκλικό.

Προκειμένου να καταστεί δυνατή η χρήση του σε προβλήματα συνοριακών τιμών, το νέο προσομοίωμα ενσωματώνεται στους κώδικες πεπερασμένων διαφορών *FLAC* και *FLAC*^{3D} για αναλύσεις σε 2 και 3 διαστάσεις, αντίστοιχα. Οι κώδικες αυτοί μπορούν να χρησιμοποιηθούν σε πλήρως-συζευγμένες μη-γραμμικές στατικές και δυναμικές αναλύσεις ρεαλιστικών προβλημάτων από το μελετητή μηχανικό. Αρχικά, οι εξισώσεις του προσομοιώματος προγραμματίζονται σε γλώσσα C++ και στη συνέχεια ενσωματώνονται στο λογισμικό ως υπό-ρουτίνα χρήστη (User-Defined-Model routine). Η ενσωμάτωση υλοποιείται με χρήση εμπρός-τασικής ολοκλήρωσης Euler με αυτόματο έλεγχο λάθους, η οποία έχει αποδειχθεί αξιόπιστη για προβλήματα δυναμικής φόρτισης εδαφών σε καθεστώς ρευστοποίησης.

Στο τελευταίο στάδιο της διατριβής αξιολογείται εκτενώς η ικανότητα του βαθμονομημένου προσομοιώματος να προβλέψει την απόκριση του εδάφους σε επίπεδο προβλημάτων συνοριακών τιμών μεγάλης κλίμακας. Για τον σκοπό αυτό, λόγω της πολυπλοκότητάς τους, επιλέχθηκαν προβλήματα δυναμικής φόρτισης με εκδήλωση ρευστοποίησης. Για τη διακρίβωση του προσομοιώματος γίνεται χρήση αποτελεσμάτων πειραματικών δοκιμών φυγοκεντριστή της βιβλιογραφίας σε άμμο Nevada. Συνολικά, έγινε προσομοίωση εννιά (9) προβλημάτων που εντάσσονται σε τέσσερις (4) διαφορετικές κατηγορίες:

(α) σεισμική απόκριση οριζόντιας ρευστοποιήσιμης εδαφικής στρώσης,

(β) πλευρική εξάπλωση ελαφρώς κεκλιμένης ρευστοποιήσιμης εδαφικής στρώσης,

(γ) σεισμική απόκριση συστήματος αβαθούς θεμελίου - ρευστοποιήσιμου εδάφους με διαφορετικές στρωματογραφίες και υπό διαφορετικές διεγέρσεις,

(δ) σεισμική απόκριση ομάδας πασσάλων υπό πλευρική εξάπλωση ελαφρώς κεκλιμένης ρευστοποιήσιμης εδαφικής στρώσης.

Τα προβλήματα (α), (β) και (γ) διερευνήθηκαν στο διδιάστατο χώρο (2Δ) με χρήση του λογισμικού *FLAC*, ενώ το (δ) στον τριδιάστατο χώρο (3Δ) με χρήση του *FLAC*^{3D}. Καθώς το ρευστοποιήσιμο αμμώδες έδαφος είναι κοινό και στις εννιά (9) δοκιμές φυγοκεντριστή (άμμος Nevada διαφορετικών τιμών σχετικής πυκνότητας D_r = 40 – 85%), υιοθετήθηκε επιπλέον: (i) κοινή βαθμονόμηση του προσομοιώματος (βασισμένη σε εργαστηριακές δοκιμές σε επίπεδο μοναδιαίου στοιχείου) και (ii) κοινή αριθμητική μεθοδολογία ανάλυσης (σε όρους συντελεστή διαπερατότητας, αριθμητικής απόσβεσης κ.α.). Έτσι, αποτυπώνεται αμιγώς η ικανότητα του προσομοιώματος να προβλέπει αποτελεσματικά την απόκριση του ίδιου εδάφους, ανεξάρτητα από το εξεταζόμενο πρόβλημα, χωρίς η αποτύπωση αυτή να επηρεάζεται από την αριθμητική μεθοδολογία ανάλυσης. Η αξιολόγηση αυτή δείχνει ικανοποιητική προσομοίωση, χωρίς ανάγκη αναβαθμονόμησης για το ίδιο κοκκώδες έδαφος, ανεξάρτητα από το εξεταζόμενο πρόβλημα συνοριακών τιμών.

Τέλος, εκτελέστηκαν παραμετρικές αναλύσεις κάποιων εξ αυτών των προβλημάτων συνοριακών τιμών με στόχο την αποτύπωση της ευαισθησίας των αποτελεσμάτων της προσομοίωσης σε δύο (2) από τα πρωτότυπα χαρακτηριστικά του προσομοιώματος, ήτοι τη μεθοδολογία ορθού ορισμού του σημείου αντιστροφής φόρτισης (ώστε να μην

«*υπερακοντίζεται*» η σχέση τάσης-παραμόρφωσης) και τη συνάρτηση που μεταβάλλει το συντελεστή διαστολικότητας με στόχο την ορθή απόκριση μετά την αρχική ρευστοποίηση. Οι αναλύσεις αυτές υπογραμμίζουν ότι τα εν λόγω καταστατικά χαρακτηριστικά είναι χρήσιμα, μα δεν μπορούν να θεωρηθούν κρίσιμα, τουλάχιστον για τα εξετασμένα προβλήματα συνοριακών τιμών.

NATIONAL TECHNICAL UNIVERSITY OF ATHENS
SCHOOL OF CIVIL ENGINEERING
DEPARTMENT OF GEOTECHNICAL ENGINEERING

ABSTRACT

of PhD Thesis

of Taxiarchoula Limnaiou

The accuracy of numerical analyses of boundary value problems (BVPs) in Geotechnical Engineering depends significantly on the reliability and the proper calibration of the employed constitutive model, depending on the soil type and the loading conditions. For granular soils (like sands and gravels), different constitutive models and/or different calibrations of the same model are usually adopted, depending on the loading conditions (e.g., monotonic vs. cyclic, under drained vs. undrained conditions, short and intense seismic excitation vs. sustained cyclic loading of many cycles of small to medium intensity). Historically, given its complexity, the simulation of cyclic response of granular soils has attracted great interest in the literature, with a multitude of publications presenting relevant constitutive models. Very often, however, publications that present relevant models exhibit accurate numerical simulation of the monotonic response and include only a few, hand-picked, cyclic tests with emphasis on liquefaction. Such a validation procedure can hardly be considered sufficient for cyclic loading, in general. On the contrary, model validation should cover the whole range of cyclic response in each discrete *strain regime*. Namely, the validation process should focus distinctly on: a) *small* strains, where the soil response is "*quasi-elastic*" and the use of the true elastic parameters (e.g., measured from field tests) is crucial for an accurate simulation, b) *medium* strains, where the response is non-linear hysteretic and accumulation of strains with the number of applied cycles is observed and, finally, on c) *large* strains, where of importance are the deformations due to liquefaction and the post-liquefaction strain accumulation. Hence, despite the plethora of very remarkable specialized constitutive models in published literature, there are very few publications that present model validations against the whole foregoing strain range. Concurrently, it has been observed that some of the models that have exhibited a

satisfactory performance for cyclic loading may not be as accurate when it comes to monotonic loading, or need to be recalibrated for that type of loading. Based on the above, there is a need for a constitutive model for granular soils, which will be able to capture accurately both the monotonic response (until the critical state) and the cyclic response (for any shear strain level) with a single set of soil - specific parameters for any relative density and stress level. This is the main purpose of the constitutive model developed in the context of this Thesis.

The new elasto-plastic constitutive model is based on Critical State Theory, it belongs to the family of SANISAND bounding surface models and it inherits concepts from the NTUA-SAND model, albeit modified. Its basic characteristic is the use of the last load reversal point to define both the elastic and the plastic strain rates. Special attention is given to the proper definition of the last load reversal point, so as to mitigate stress-strain overshooting. The model incorporates a macroscopic cumulative fabric function scaling the plastic modulus and targeting an accurate rate of strain accumulation with loading cycles. Post-liquefaction strains are also in focus with an appropriate modification of the dilatancy function. The constitutive model has a total of 14 parameters requiring calibration, 12 of which target the monotonic response and should be calibrated first, i.e., before the remaining 2 that refer solely to cyclic loading. Of these 14 parameters, 9 are calibrated first and directly on the basis of experimental data, while the remaining 5 parameters (3 for monotonic and 2 for cyclic loading) require trial-and-error runs.

The constitutive equations are developed at element level and the calibration of model parameters is presented for five (5) sands from the literature (Nevada, Toyoura, Ottawa - F65, M31 and Monterey) and two (2) gravels. As a whole, the selected soils for calibration purposes cover a range of mean diameter of grains (D_{50}) from 0.1 to 9 mm. The validation includes comparisons to element test data for different types of loading and drainage conditions, corresponding to a very large range of initial conditions (whole range of relative density D_r = 2 – 90% and initial mean effective stress p_o = 33.33 - 2000 kPa). When experimental data for a specific soil are lacking, empirical relationships from the literature are employed. This thorough investigation focuses on all levels of induced cyclic deformations on the basis of the rationale discussed above, but also satisfies the requirement for a unique set of soil-specific model parameters, regardless of the loading

conditions. The validation process proves that the proposed constitutive model is, by design, a general-purpose model that provides satisfactory accuracy without a need for recalibration regardless of whether the problem is static, cyclic or dynamic, at least when it comes to sands. When it comes to gravels, the de-activation of fabric-related functions (via simply nullifying the respective N_o model parameter) in monotonic simulations proves sufficient, without changing any other model parameter.

For its possible use in the numerical analyses of BVPs, the new constitutive model is implemented in finite difference numerical codes *FLAC* and *FLAC*^{3D}. These codes can be used in fully-coupled nonlinear numerical analyses of both static and dynamic boundary value problems of geostructures. The constitutive equations are initially written in C++ programming language, and then are implemented into the numerical codes as a User Defined Model (UDM) routine. For the implementation, a second order Euler integration scheme with automatic error control and a sub-stepping technique are adopted.

At the final stage of the Thesis, the ability of the calibrated constitutive model to simulate sand response at system level is evaluated. For this purpose and due to their complexity, dynamic BVPs including liquefaction are selected. The validation is performed against experimental results from nine (9) dynamic centrifuge tests on Nevada sand, grouped in four (4) different categories:

(a) the seismic response of a horizontal liquefiable sand layer,

(b) the lateral spreading of a mildly sloping liquefiable sand layer,

(c) the seismic response of shallow foundation systems in liquefiable sand profiles with different stratigraphies subjected to different seismic excitations,

(d) the seismic response of a pile group subjected to the lateral spreading of a mildly sloping liquefiable sand layer.

Categories (a), (b) and (c) are analyzed in the two-dimensional (2D) space using numerical code *FLAC*, while category (d) is analyzed in the three-dimensional (3D) space using numerical code *FLAC*^{3D}. Since the employed liquefiable sand is the same in all the above centrifuge tests (Nevada sand in different relative densities, D_r = 40 – 85%), the following additional modeling approaches are adopted: (i) a common calibration of the constitutive model, based on laboratory test results at element level and (ii) a common analysis methodology (in terms of adopted permeability coefficient, numerical damping,

etc.). In this way, the comparison of simulations to data reflects purely the satisfactory ability of the model to simulate the response of a specific sand material, regardless of the problem at hand and without any need for recalibration.

Finally, some of the aforementioned BVPs are studied parametrically in order to evaluate the sensitivity of the numerical results to the use of two (2) of the novel constitutive ingredients. The focus is on the adopted methodology for the mitigation of stress-strain overshooting and on the incorporated factor affecting the dilatancy coefficient targeting post-liquefaction shear strain accumulation. The results of the sensitivity analyses underline that these constitutive features are useful, but possibly not crucial for accuracy, at least for the examined BVPs.

Εκτενής περίληψη

Ι. ΕΙΣΑΓΩΓΗ – ΣΤΟΧΟΣ

Κύρια προϋπόθεση για ακριβείς αριθμητικές αναλύσεις προβλημάτων συνοριακών τιμών που αφορούν σε έργα Γεωτεχνικού Μηχανικού αποτελεί η χρήση ενός σωστά βαθμονομημένου καταστατικού προσομοιώματος, κατάλληλου για το γεωυλικό και τον τύπο φόρτισης κάθε περίπτωσης. Για κοκκώδη εδάφη, όπως οι άμμοι, αποτελεί κοινή πρακτική η στοχευμένη χρήση διαφορετικών καταστατικών προσομοιωμάτων ή/και διαφορετικών βαθμονομήσεων του ίδιου προσομοιώματος, ανάλογα με τον εξεταζόμενο τύπο φόρτισης (π.χ. μονοτονική ή ανακυκλική, υπό στραγγιζόμενες ή αστράγγιστες συνθήκες, σύντομη και έντονη σεισμική διέγερση ή ήπια ανακυκλική φόρτιση πολλών κύκλων) ή/και ανάλογα με τις αρχικές συνθήκες (π.χ. πυκνότητα, επίπεδο τάσεων). Ειδικότερα, η προσομοίωση της ανακυκλικής φόρτισης κοκκωδών υλικών, δεδομένης της πολυπλοκότητάς της, έχει προσελκύσει διαχρονικά μεγάλο ενδιαφέρον στη διεθνή βιβλιογραφία, με πληθώρα δημοσιεύσεων που αφορούν σε σχετικά καταστατικά προσομοιώματα. Αρκετά από τα εν λόγω προσομοιώματα θεμελιώνουν το καταστατικό τους πλαίσιο στην καλά εδραιωμένη Θεωρία Κρίσιμης Κατάστασης (Critical State Theory, Schofield and Wroth, 1968), ενώ τελευταία, ένα μεγάλο ποσοστό εξ αυτών ανήκει στην κατηγορία προσομοιωμάτων SANISAND. Πρόκειται για προσομοιώματα τα οποία στο γενικευμένο χώρο των τάσεων, πέραν της Επιφάνειας Κρίσιμης Κατάστασης, διαθέτουν επιπρόσθετα μία Οριακή Επιφάνεια (Bounding Surface) και μια Επιφάνεια Διαστολικότητας (Dilatancy Surface). Οι δύο αυτές επιφάνειες, οι οποίες ορίζουν τη μέγιστη τιμή του αποκλίνοντα λόγου των τάσεων και την τιμή του στην αλλαγή φάσης αντίστοιχα, συσχετίζονται άμεσα με την Παράμετρο Κατάστασης, ψ (Been and Jefferies, 1985) και την Επιφάνεια Κρίσιμης Κατάστασης με την οποία είναι ομόλογες. Ιστορικά, τα πρώτα προσομοιώματα αυτής της κατηγορίας είναι των Manzari and Dafalias (1997) και Li and Dafalias (2000), με τον όρο SANISAND να έχει εισαχθεί μεταγενέστερα (Taiebat and Dafalias, 2008).

Πολύ συχνά, στις δημοσιεύσεις που παρουσιάζουν καταστατικά προσομοιώματα για την ανακυκλική φόρτιση κοκκωδών εδαφών, ενώ περιλαμβάνεται επαρκής σύγκριση με

πειραματικά δεδομένα για την προσομοίωση της μονοτονικής συμπεριφοράς, αυτή συνοδεύεται από συγκριτικά λίγες ανακυκλικές δοκιμές, με αυτές συνήθως να επικεντρώνονται στην εκδήλωση ρευστοποίησης. Μία τέτοιου είδους διακρίβωση αξιοπιστίας, αν και επαρκής για τη μονοτονική φόρτιση, δε θεωρείται απαραίτητα επαρκής για την ανακυκλική, της οποίας τα χαρακτηριστικά εξαρτώνται σε μεγάλο βαθμό από το μέγεθος της επιβαλλόμενης ανακυκλικής διατμητικής παραμόρφωσης (Vucetic, 1994). Ως εκ τούτου, προκειμένου να θεωρηθεί πλήρης η επαλήθευση ενός προσομοιώματος έναντι ανακυκλικής φόρτισης, θα πρέπει να καλύπτει ένα ευρύ φάσμα απόκρισης μεταξύ των «*περιοχών*»: α) *μικρών παραμορφώσεων*, όπου κυριαρχεί η οιονεί ελαστική απόκριση και εξέχουσα σημασία έχει η βαθμονόμηση με τις πραγματικές ελαστικές παραμέτρους (π.χ., από γεωφυσικές δοκιμές στο πεδίο), β) *μεσαίων παραμορφώσεων*, όπου η συμπεριφορά είναι μη-γραμμική υστερητική και παρατηρείται συσσώρευση παραμενουσών παραμορφώσεων με τον αριθμό των επιβαλλόμενων κύκλων φόρτισης, και γ) *μεγάλων παραμορφώσεων*, δίνοντας έμφαση στις παραμορφώσεις που εκδηλώνονται κατά τη ρευστοποίηση και στη συσσώρευση παραμορφώσεων μετά την εκδήλωση αυτής.

Η σημασία κάθε διακριτής «*περιοχής*» παραμόρφωσης στη σωστή συνολική προσομοίωση έχει αρχίσει τελευταία να προσελκύει την προσοχή στη διεθνή βιβλιογραφία, όπως παρουσιάζεται με λεπτομέρεια στο **Κεφάλαιο 2** της διατριβής. Για παράδειγμα, οι McAllister et al. (2015) απέδειξαν πως εάν, κατά τη χρήση ενός προσομοιώματος τύπου SANISAND, η βαθμονόμηση των ελαστικών παραμέτρων του, που καθορίζουν την οιονεί ελαστική απόκριση, γίνει επί τη βάση μονοτονικών δοκιμών και όχι δυναμικών, υποεκτιμάται σημαντικά η επί τόπου ταχύτητα διάδοσης διατμητικών κυμάτων και προβλέπεται λανθασμένα η σεισμική απόκριση του εδάφους (π.χ., λάθος θεμελιώδης ιδιοπερίοδος ταλάντωσης εδάφους). Αντίστοιχα, πρόσφατα έχουν αναπτυχθεί προσομοιώματα (π.χ., Liu et al., 2019) που εξειδικεύονται στην ορθή προσομοίωση της συσσώρευσης παραμορφώσεων ύστερα από μεγάλο αριθμό κύκλων φόρτισης μεσαίου μεγέθους επιβαλλόμενης ανακυκλικής παραμόρφωσης (π.χ., για την ανάλυση θεμελίωσης θαλάσσιων κατασκευών), ένα ζήτημα που σπάνια θίγεται σε δημοσιεύσεις προσομοιωμάτων που στοχεύουν γενικά στην ανακυκλική φόρτιση. Τέλος, αρκετές πρόσφατες δημοσιεύσεις προσομοιωμάτων σχετίζονται με τη συσσώρευση παραμορφώσεων μετά την εκδήλωση της ρευστοποίησης (π.χ. Barrero et al., 2020.

Tasiopoulou et al., 2020), υπογραμμίζοντας την κρισιμότητά της για την ακριβή πρόβλεψη της απόκρισης κατασκευών που εδράζονται σε έδαφος υπό καθεστώς ρευστοποίησης. Παρ' όλο, λοιπόν, που στη βιβλιογραφία υπάρχει πληθώρα πολύ αξιόλογων εξειδικευμένων καταστατικών προσομοιωμάτων, ωστόσο, υπάρχουν ελάχιστες δημοσιεύσεις που να παρουσιάζουν λεπτομερή διακρίβωση της αξιοπιστίας τους σε όλο το φάσμα ανακυκλικής απόκρισης, σύμφωνα με την ανωτέρω συλλογιστική (π.χ. Papadimitriou and Bouckovalas 2002, Andrianopoulos et al., 2010a, Boulanger and Ziotopoulou, 2013, Cheng and Detournay, 2021). Παράλληλα, έχει παρατηρηθεί πως αρκετά από τα προσομοιώματα που επιδεικνύουν ακριβή συμπεριφορά κατά την ανακυκλική φόρτιση δεν είναι εξίσου ακριβή κατά τη μονοτονική. Για παράδειγμα, το προσομοίωμα NTUA-SAND (Andrianopoulos et al., 2010a) απαιτεί την αλλαγή των τιμών 2 εκ των 13 παραμέτρων του, ώστε να αποτυπώσει επαρκώς τη μονοτονική συμπεριφορά.

Από την άλλη, κάποια υποσχόμενα προσομοιώματα (π.χ., Papadimitriou and Bouckovalas, 2002) δεν ενσωματώθηκαν ποτέ σε αριθμητικούς κώδικες επίλυσης προβλημάτων συνοριακών τιμών. Η τελευταία αυτή διαπίστωση έχει σημασία, καθώς έχει αποδειχθεί πως στοχευμένη επαλήθευση μπορεί να επιτευχθεί εξίσου ικανοποιητικά μέσω της εκτεταμένης χρήσης ενός προσομοιώματος σε αναλύσεις προβλημάτων συνοριακών τιμών, οι οποίες μάλιστα ίσως να θεωρούνται και προτιμότερες σε σχέση με τις συγκρίσεις δοκιμών σε επίπεδο μοναδαίου στοιχείου (π.χ., Manzari and el Ghoraiby, 2021). Υπό αυτό το πρίσμα, προσομοιώματα που έχουν χρησιμοποιηθεί με επιτυχία σε προβλήματα συνοριακών τιμών (π.χ., Dafalias and Manzari, 2004, Andrianopoulos et al., 2010a, Boulanger and Ziotopoulou, 2013) θα πρέπει να αναγνωρίζονται και να θεωρούνται επαρκώς ακριβή, τουλάχιστον για προβλήματα στα οποία έχουν χρησιμοποιηθεί εκτενώς. Σε αυτό το σημείο, θα πρέπει να καταστεί σαφές, πως η παραπάνω διαπίστωση δεν υπονοεί πως εξελιγμένα προσομοιώματα, των οποίων η διακρίβωση μέσω των σχετικών δημοσιεύσεών τους δεν καλύπτει όλο το προαναφερθέν εύρος απόκρισης, δεν είναι ακριβή. Σημαίνει μόνο πως η χρήση τους εκτός του διακριβωμένου εύρους απόκρισης θα πρέπει να γίνεται με προσοχή.

Σύμφωνα με την παραπάνω συλλογιστική, προκύπτει η ανάγκη για ένα καταστατικό προσομοίωμα για κοκκώδη εδάφη, το οποίο θα είναι ικανό να προβλέπει ικανοποιητικά τόσο τη μονοτονική, όσο και την ανακυκλική συμπεριφορά (για όλο το φάσμα απόκρισης)

με ενιαία και μοναδική βαθμονόμηση των παραμέτρων του ανά γεωυλικό, ανεξάρτητα από τη σχετική πυκνότητα και το επίπεδο τάσης, και κυρίως ανεξάρτητα από τον τύπο φόρτισης (π.χ. μονοτονική ή ανακυκλική, υπό στραγγιζόμενες ή αστράγγιστες συνθήκες, σύντομη και έντονη σεισμική διέγερση ή ήπια ανακυκλική φόρτιση πολλών κύκλων). Αυτός είναι ο στόχος του προσομοιώματος τύπου SANISAND που παρουσιάζεται σε αυτή τη διατριβή. Το προσομοίωμα αυτό θα πρέπει να επαληθεύεται με επιτυχία για πολλά κοκκώδη εδάφη, και όχι μόνον σε επίπεδο μοναδιαίου στοιχείου επί τη βάση πειραματικών δοκιμών και εμπειρικών σχέσεων της βιβλιογραφίας, αλλά, και σε προβλήματα συνοριακών τιμών που αφορούν καθεστώς ρευστοποίησης, δηλαδή την πλέον κρίσιμη και πολύπλοκη φόρτιση που αντιμετωπίζουν τα εδάφη αυτά.

Σε αυτό το σημείο, θα πρέπει να διευκρινιστεί εξ' αρχής, πως το προτεινόμενο καταστατικό προσομοίωμα για κοκκώδη εδάφη είναι, με βάση το σχεδιασμό του, ένα προσομοίωμα γενικής χρήσης. Αυτό σημαίνει πως, διατηρώντας σταθερή τη βαθμονόμησή του ανά γεωυλικό σε όλα τα προβλήματα συνοριακών τιμών, η ακρίβειά του ενδέχεται να μην είναι πάντα αντίστοιχη με αυτήν εξειδικευμένων προσομοιωμάτων ανά κατηγορία προβλήματος. Ωστόσο, στόχος του είναι να αποτελέσει ένα χρήσιμο αριθμητικό εργαλείο, το οποίο να μπορεί να βαθμονομηθεί σε επίπεδο δοκιμών μοναδιαίου στοιχείου και, στη συνέχεια, να παρέχει στο χρήστη τη δυνατότητα για μία επιτυχή προσομοίωση διαφορετικών τύπων προβλημάτων χωρίς αναβαθμονόμηση (για το ίδιο γεωυλικό), ανεξάρτητα αν το εξεταζόμενο πρόβλημα είναι στατικό, δυναμικό ή ανακυκλικό.

ΙΙ. ΚΑΤΑΣΤΑΤΙΚΗ ΔΙΑΤΥΠΩΣΗ

Στον **Πίνακα 1** παρουσιάζονται συνοπτικά εκείνες οι καταστατικές εξισώσεις του προσομοιώματος που έχουν γενική χρήση και αποτελούν, λίγο έως πολύ, κοινό καταστατικό πλαίσιο της οικογένειας των προσομοιωμάτων τύπου SANISAND, αλλά και του προσομοιώματος NTUA-SAND (Andrianopoulos et al., 2010a) από το οποίο υιοθετεί κάποια επιπλέον στοιχεία.

Όλες οι καταστατικές εξισώσεις είναι διατυπωμένες στο γενικευμένο τασικό χώρο και γράφονται σε τανυστική μορφή. Οι τανυστές δεύτερης τάξης γράφονται με έντονους χαρακτήρες, ώστε να διαχωρίζονται από τα βαθμωτά μεγέθη, ενώ όλες οι ορθές τάσεις θεωρούνται ενεργές (π.χ. ο τανυστής των ενεργών τάσεων συμβολίζεται ως $\boldsymbol{\sigma}$).

Πίνακας 1: *Καταστατικό πλαίσιο ελαστοπλαστικού προσομοιώματος*

Περιγραφή	**Καταστατική εξίσωση**	**Αριθ. Εξίσ.**	**Σημειώσεις**
Ογκομετρική συνιστώσα της μεταβολής της παραμόρφωσης	$\dot{\varepsilon}_{\mathrm{vol}} = \dot{\varepsilon}^{\mathrm{e}}_{\mathrm{vol}} + \dot{\varepsilon}^{\mathrm{p}}_{\mathrm{vol}}$	(3.1)	Συνιστώσες: e : ελαστική, p : πλαστική
Αποκλίνουσα συνιστώσα της μεταβολής της παραμόρφωσης	$\dot{\boldsymbol{e}} = \dot{\boldsymbol{e}}^{\mathrm{e}} + \dot{\boldsymbol{e}}^{\mathrm{p}}$	(3.2)	
Ελαστική συνιστώσα της μεταβολής της παραμόρφωσης για δεδομένη μεταβολή της τάσης	$\dot{\boldsymbol{\varepsilon}}^{\mathrm{e}} = \dot{\boldsymbol{e}}^{\mathrm{e}} + \frac{\varepsilon^{\mathrm{e}}_{\mathrm{vol}}}{3}\boldsymbol{I} = \frac{1}{2G_{\mathrm{t}}}\dot{\boldsymbol{s}} + \frac{1}{3K_{\mathrm{t}}}\dot{p}\boldsymbol{I}$	(3.3)	G_{t} και K_{t} : εφαπτομενικά ελαστικά μέτρα διάτμησης και ογκομετρικής παραμόρφωσης
Πλαστική συνιστώσα της μεταβολής της παραμόρφωσης	$\dot{\boldsymbol{\varepsilon}}^{\mathrm{p}} = \dot{\boldsymbol{e}}^{\mathrm{p}} + \frac{\dot{\varepsilon}^{\mathrm{p}}_{\mathrm{vol}}}{3}\boldsymbol{I} = \langle \Lambda \rangle \boldsymbol{R}$	(3.4)	
Νόμος πλαστικής ροής	$\boldsymbol{R} = \boldsymbol{n} + (D/3)\boldsymbol{I}$	(3.5)	D : συνάρτηση διαστολικότητας
Δείκτης φόρτισης για δεδομένη μεταβολή της τάσης	$\Lambda = \frac{1}{K_{\mathrm{p}}}\boldsymbol{L} : \dot{\boldsymbol{\sigma}} = \frac{1}{K_{\mathrm{p}}}\boldsymbol{n} : p\dot{\boldsymbol{r}}$	(3.6)	K_p : πλαστικό μέτρο κράτυνσης
Διεύθυνση φόρτισης	$\boldsymbol{L} = \boldsymbol{n} - \frac{(\boldsymbol{n}:\boldsymbol{r})}{3}\boldsymbol{I}$	(3.7)	$\boldsymbol{n}$: αποκλίνουσα συνιστώσα διεύθυνση φόρτισης
Μεταβολή της τάσης για δεδομένη μεταβολή της παραμόρφωσης	$\dot{\boldsymbol{\sigma}} = 2G_{\mathrm{t}}\dot{\boldsymbol{e}} + K_{\mathrm{t}}\dot{\varepsilon}_{\mathrm{vol}}\boldsymbol{I} - \langle \Lambda \rangle (2G_{\mathrm{t}}\boldsymbol{n} + K_{\mathrm{t}}D\boldsymbol{I})$	(3.8)	
Δείκτης φόρτισης για δεδομένη μεταβολή της παραμόρφωσης	$\Lambda = \frac{2G_{\mathrm{t}}\boldsymbol{n}:\dot{\boldsymbol{e}} - (\boldsymbol{n}:\boldsymbol{r})K_{\mathrm{t}}\dot{\varepsilon}_{\mathrm{vol}}}{K_{\mathrm{p}} + 2G_{\mathrm{t}} - (\boldsymbol{n}:\boldsymbol{r})K_{\mathrm{t}}D}$	(3.9)	
Αποκλίνων λόγος των τάσεων στην Οριακή Επιφάνεια	$M^{\mathrm{b}}_{\mathrm{c}} = M^{\mathrm{c}}_{\mathrm{c}}\ exp\left(n^{\mathrm{b}}\langle -\psi \rangle\right)$	(3.10)	$M^{\mathrm{c}}_{\mathrm{c}}$, n^{b} : παράμετροι βαθμονόμησης
Αποκλίνων λόγος των τάσεων στην Επιφάνεια Διαστολικότητας	$M^{\mathrm{d}}_{\mathrm{c}} = M^{\mathrm{c}}_{\mathrm{c}}\ exp\left(n^{\mathrm{d}}\psi\right)$	(3.11)	n^{d} : παράμετρος βαθμονόμησης
Επιφάνεια Κρίσιμης Κατάστασης στο χώρο Δείκτη πόρων *e* - *p*	$e_{\mathrm{cs}} = e_{\mathrm{ref}} - \lambda\left(p/p_{\mathrm{atm}}\right)^{\xi}$	(3.12)	e_{ref}, ξ, λ : παράμετροι βαθμονόμησης
Παράμετρος κατάστασης	$\psi = e - e_{\mathrm{cs}}$	(3.13)	
Γωνία Lode θ της διεύθυνσης φόρτισης	$\cos(3\theta) = \sqrt{6}\,\mathrm{tr}\left(\boldsymbol{n}^3\right) = 3\sqrt{6}\,\det\boldsymbol{n}$	(3.14)	
Μορφή επιφανειών του προσομοιώματος στο αποκλίνον επίπεδο-π	$g(\theta,c) = 2^{\mu}\ c\Big/\left[1 + c^{1/\mu} - \left(1 - c^{1/\mu}\right)\cos(3\theta)\right]^{\mu}$	(3.15)	c : παράμετρος βαθμονόμησης μ = 0.16
Μέγιστη και εφαπτομενική τιμή του ελαστικού μέτρου διάτμησης	$G_{\max} = G_{\mathrm{o}}\ p_{\mathrm{atm}}\left[1\Big/\left(0.3 + 0.7e^2\right)\right]\sqrt{p/p_{\mathrm{atm}}}$ $G_{\mathrm{t}} = G_{\max}/T$	(3.16)	G_o : παράμετρος βαθμονόμησης
Μη-γραμμική σχέση απομείωσης ελαστικού μέτρου διάτμησης	$T = 1 + 2\left(1/a_1 - 1\right)\frac{\sqrt{0.5(\boldsymbol{r}-\boldsymbol{r}_{\mathrm{ini}}):(\boldsymbol{r}-\boldsymbol{r}_{\mathrm{ini}})}}{a_1\left(G_{\max}/p\right)\gamma_1}$	(3.17)	a_1 = 0.85, γ_1 = 0.0003

Η υπερτιθέμενη κουκκίδα είτε στα βαθμωτά, είτε στα τανυστικά μεγέθη υποδηλώνει την πρώτη παράγωγο ή αλλιώς την επαύξηση του αντίστοιχου μεγέθους. Το σύμβολο **:** μεταξύ δύο τανυστών συμβολίζει το διπλό εσωτερικό τους γινόμενο ή ισοδύναμα το ίχνος (*tr*) του γινομένου τους. Ο τανυστής της παραμόρφωσης συμβολίζεται ως $\boldsymbol{\varepsilon}$ και αποτελείται από τη (βαθμωτή) ογκομετρική του συνιστώσα $\varepsilon_{vol} = \mathrm{tr}\boldsymbol{\varepsilon}$ και την (τανυστική) αποκλίνουσά του συνιστώσα $\boldsymbol{e} = \boldsymbol{\varepsilon} - (\varepsilon_{vol}/3)\boldsymbol{I}$, όπου $\boldsymbol{I}$ ο μοναδιαίος τανυστής. Καθοριστικής σημασίας για την καταστατική διατύπωση είναι ο τανυστής του αποκλίνοντα λόγου των τάσεων $\boldsymbol{r} = \boldsymbol{s}/p$, όπου ο τανυστής $\boldsymbol{s}$ αποτελεί την αποκλίνουσα συνιστώσα του τανυστή ενεργών τάσεων $\boldsymbol{\sigma}$, ενώ ως p ορίζεται η μέση ενεργός τάση και συνεπώς $\boldsymbol{\sigma} = \boldsymbol{s} + p\boldsymbol{I}$. Τα σύμβολα $< >$ είναι οι αγκύλες Macauley, που δίνουν $< x > = x$ για κάθε βαθμωτό μέγεθος $x > 0$ και $< x > = 0$ αν $x \leq 0$. Η εξάρτηση των καταστατικών εξισώσεων από το λόγο $\boldsymbol{r}$ υπονοεί πως πρόκειται για ένα προσομοίωμα καθοριστικά εξαρτώμενο από τη μεταβολή του λόγου των τάσεων. Ουσιαστικά δηλαδή, μια μη-μηδενική μεταβολή του αποκλίνοντα λόγου των τάσεων είναι αναγκαία, ωστόσο όχι ικανή - (Εξ. 6), συνθήκη για την πρόβλεψη μεταβολής της πλαστικής παραμόρφωσης από το συγκεκριμένο προσομοίωμα.

Καθώς ανήκει στην οικογένεια προσομοιωμάτων SANISAND, το προσομοίωμα διαθέτει 3 επιφάνειες στο χώρο των τάσεων και συγκεκριμένα, την Οριακή Επιφάνεια, την Επιφάνεια Διαστολικότητας και την Επιφάνεια Κρίσιμης Κατάστασης. Και οι τρεις αυτές επιφάνειες έχουν τη μορφή ομοιόθετων ανοιχτών κωνικών επιφανειών (ανοίγματος σύμφωνα με τις Εξ. 10 και 11) με την κορυφή τους να βρίσκεται στην αρχή των αξόνων του τασικού χώρου. Μία σχηματική απεικόνισή τους επί του επιπέδου-π του χώρου του αποκλίνοντα λόγου των τάσεων παρουσιάζεται στο **Σχήμα 1**. Το άνοιγμά τους εξαρτάται από την τρέχουσα γωνία Lode, θ (Εξ. 14 και 15) και από την τρέχουσα παράμετρο κατάστασης, ψ (Εξ. 12 και 13, κατά Been and Jefferies, 1985), όπως αρχικά προτάθηκε από τους Manzari and Dafalias (1997) και τους Li and Dafalias (2000). Στην ενδεικτική απεικόνισή τους στο **Σχήμα 1**, το σχετικό τους μέγεθος αντιστοιχεί σε μία κατάσταση πυκνότερη από την κρίσιμη ($e < e_{cs}$ και $\psi < 0$). Ο νόμος προβολής της τρέχουσας κατάστασης επί των επιφανειών αυτών ορίζεται μέσω του τανυστή $\boldsymbol{r}_{ini}$, ο οποίος ανανεώνει τις τιμές του σε αυτές του τανυστή $\boldsymbol{r}$ ακριβώς κατά την αντιστροφή φόρτισης, δηλαδή όταν ξεκινά μια νέα τασική όδευση. Η αντιστροφή φόρτισης ορίζεται όταν προκύπτει $\Lambda < 0$, αλλά το συγκεκριμένο προσομοίωμα ενσωματώνει διαδικασία προσαρμογής της τιμής του

$\boldsymbol{r}_{ini}$ για την αποφυγή υπερακόντισης (overshooting) της σχέσης τάσης-παραμόρφωσης, όπως περιγράφεται παρακάτω. Σε κάθε περίπτωση, ο συγκεκριμένος τανυστής $\boldsymbol{r}_{ini}$ χρησιμοποιείται σε πληθώρα καταστατικών εξισώσεων του προσομοιώματος, όπως επίσης εξηγείται παρακάτω. Στο **Σχήμα 1** φαίνεται ο πρωταρχικός του ρόλος για τον καθορισμό του νόμου προβολής (της τρέχουσας κατάστασης $\boldsymbol{r}$) επί της Οριακής Επιφάνειας, σύμφωνα με τον οποίο προσδιορίζεται η θέση του συζυγούς λόγου των τάσεων $\boldsymbol{r}^b$. Αυτός ο συζυγής λόγος τάσεων ορίζει τον αποκλίνοντα τανυστή $\boldsymbol{n}$ που καθορίζει τη διεύθυνση της φόρτισης $\boldsymbol{L}$ (Εξ. 7), τη γωνία Lode θ της διεύθυνσης φόρτισης (Εξ. 14) και τους συζυγείς λόγους των τάσεων επί των Επιφανειών Διαστολικότητας $\boldsymbol{r}^d$ και Κρίσιμης Κατάστασης $\boldsymbol{r}^c$.

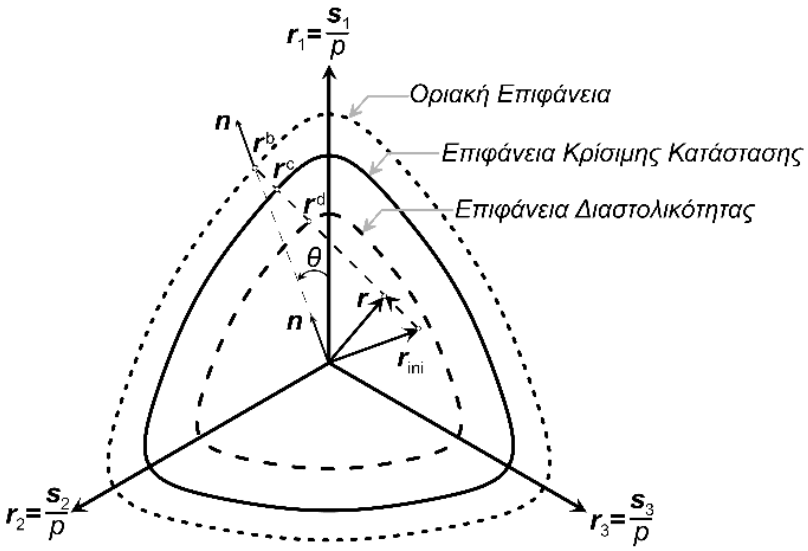

***Σχήμα 1**: Επιφάνειες προσομοιώματος επί του επιπέδου-π του αποκλίνοντα λόγου των τάσεων και νόμος προβολής (παρουσίαση για μ=0.16 και c=0.712, Εξ. (15) - Πίνακας 1).*

Το προτεινόμενο προσομοίωμα δε διαθέτει επιφάνεια διαρροής, οπότε κάθε επαυξητικό βήμα είναι εν δυνάμει ελαστο-πλαστικό, εκτός αν $< \Lambda > = 0$ στην Εξ. 8. Το ελαστικό μέτρο διάτμησης G_t ακολουθεί μια μη-γραμμική υστερητική απομείωση τύπου Ramberg-Osgood (Εξ. 17) (Ramberg and Osgood, 1943). Αυτό το καταστατικό στοιχείο υιοθετήθηκε από το προσομοίωμα NTUA-SAND (Andrianopoulos et al., 2010a), αλλά εδώ θεωρήθηκε απλουστευτικά ότι οι τιμές για τα α_1 και γ_1 είναι σταθερές και ίσες με τα άνω όρια της μεταβολής τους σύμφωνα με τους Papadimitriou et al. (2001). Αντίστοιχα, η μέγιστη τιμή του μέτρου διάτμησης G_{max} σε κάθε αντιστροφή της φόρτισης ακολουθεί μια υπο-ελαστική σχέση (Εξ. 16) (Hardin, 1978). Το ελαστικό μέτρο ογκομετρικής

παραμόρφωσης K_t σχετίζεται με το απομειωμένο G_t μέσω μιας σταθερής τιμής του λόγου του Poisson ν (= παράμετρος βαθμονόμησης).

Στη συνέχεια περιγράφονται οι καταστατικές εξισώσεις που χαρακτηρίζουν το προτεινόμενο προσομοίωμα, καθώς και ο τρόπος λειτουργίας τους. Αναγκαστικά, η περιγραφή του τρόπου λειτουργίας τους στην Περίληψη αυτή είναι **αδρή**, ενώ η αναλυτική τους περιγραφή παρατίθεται στο **Κεφάλαιο 3** της διατριβής.

Α. Πλαστικό μέτρο κράτυνσης (K_p)

Καθώς η επιβαλλόμενη παραμόρφωση αυξάνει, η ελαστο-πλαστική συμπεριφορά κυριαρχεί και σημαντικό ρόλο για την απόκριση έχει το πλαστικό μέτρο κράτυνσης K_p. Πρόκειται για ένα βαθμωτό μέγεθος, του οποίου η συνοπτική διατύπωση έχει τη μορφή:

$$K_p = h_o \; h_f \; f_A\left(p, e, \theta\right) \frac{(\boldsymbol{r}^b - \boldsymbol{r}) : \boldsymbol{n}}{(\boldsymbol{r} - \boldsymbol{r}_{ini}) : \boldsymbol{n}} \tag{3.18}$$

όπου h_o είναι μια παράμετρος βαθμονόμησης που μπορεί να λάβει μόνο μη-αρνητικές τιμές, h_f μια μη-αρνητική συνάρτηση που περιγράφεται αναλυτικά στη συνέχεια και f_A η συνοπτική διατύπωση ενός γινόμενου συναρτήσεων που αφορούν την επίδραση της μέσης ενεργού τάσης p, του λόγου των κενών e και της γωνίας Lode θ. Σύμφωνα με την Εξ. 18, το μέτρο K_p ορίζεται μέσω της απόστασης του τρέχοντα αποκλίνοντα λόγου των τάσεων $\boldsymbol{r}$ από τον συζυγή του επί της Οριακής Επιφάνειας $\boldsymbol{r}^b$. Η επιπρόσθετη συσχέτιση με την αντίστοιχη απόσταση από τον λόγο $\boldsymbol{r}_{ini}$ (ως προβολή της επί του $\boldsymbol{n}$) διασφαλίζει μηδενική μεταβολή της πλαστικής παραμόρφωσης στο αρχικό στάδιο της επικείμενης νέας φόρτισης μετά από μία αντιστροφή φόρτισης (όπου τότε ο τανυστής $\boldsymbol{r}_{ini}$ ανανεώνει την τιμή του στην τιμή του τρέχοντος τανυστή $\boldsymbol{r}$). Εδώ θα πρέπει να σημειωθεί πως στην περίπτωση μονοτονικής φόρτισης, όπου δεν υπάρχει αντιστροφή, ο δείκτης ini σηματοδοτεί την αρχική τιμή του μεγέθους στο οποίο αναφέρεται (π.χ. $\boldsymbol{r}_{ini} = \boldsymbol{r}$ σε συνθήκες γεωστατικών τάσεων). Υιοθετώντας την ιδέα των Papadimitriou and Bouckovalas (2002) και αργότερα των Andrianopoulos et al. (2010a), η βαθμωτή συνάρτηση h_f περιγράφει μακροσκοπικά την επίδραση της εξέλιξης της δομής του κοκκώδους εδάφους στην τιμή του K_p, αλλά εδώ έχει την εξής διαφοροποιημένη διατύπωση:

$$h_{\mathrm{f}} = \frac{1+\left\langle f_{\mathrm{p}} - c_{\mathrm{f}} \right\rangle^{2}}{1+\left\langle \boldsymbol{f}_{\mathrm{ini}} : \boldsymbol{n} \right\rangle} \tag{3.19}$$

Ο αριθμητής της συνάρτησης h_{f} είναι μία τετραγωνική συνάρτηση του βαθμωτού μεγέθους f_{p} εντός αγκυλών Macauley. Ο παρονομαστής είναι μια γραμμική συνάρτηση του διπλού εσωτερικού γινομένου μεταξύ του αποκλίνοντα τανυστή $\boldsymbol{n}$ της διεύθυνσης της φόρτισης και του μακροσκοπικά εξελισσόμενου (αποκλίνοντα) τανυστή δομής $\boldsymbol{f}$, κατά την στιγμή αντιστροφής της φόρτισης, η οποία επίσης περικλείεται από αγκύλες Macauley. Τόσο το μέγεθος f_{p}, όσο και ο τανυστής δομής $\boldsymbol{f}$ έχουν μηδενική τιμή στην αρχική (π.χ., γεωστατική) κατάσταση και εξελίσσονται συνεχώς και με ανεξάρτητο τρόπο, συναρτήσει της μεταβολής της πλαστικής ογκομετρικής παραμόρφωσης $\dot{\varepsilon}_{\mathrm{vol}}^{\mathrm{p}}$ σύμφωνα με:

$$\dot{f}_{\mathrm{p}} = \left(2-a\right) N(N_{\mathrm{o}}, e_{\mathrm{o}}, \psi_{\mathrm{o}}) f_{\mathrm{B}}(p_{\mathrm{o}})\, \dot{\varepsilon}_{\mathrm{vol}}^{\mathrm{p}} \tag{3.20}$$

$$\dot{\boldsymbol{f}} = -N(N_{\mathrm{o}}, e_{\mathrm{o}}, p_{\mathrm{o}}) h_{\text{post-liq}} \left[\boldsymbol{f} + f_{max}^{\left(1+a\right)} \boldsymbol{n} \right] \left\langle -\dot{\varepsilon}_{\mathrm{vol}}^{\mathrm{p}} \right\rangle \tag{3.21}$$

Εδώ, θα πρέπει να σημειωθεί πως ενώ το μέγεθος f_{p} εξελίσσεται καθ' όλη τη διάρκεια της φόρτισης, ο τανυστής δομής $\boldsymbol{f}$ εξελίσσεται μόνο κατά τη φάση της διαστολής του υλικού (βλ. χρήση αγκυλών Macauley στο $-\dot{\varepsilon}_{\mathrm{vol}}^{\mathrm{p}}$). Η μη-αρνητική συνάρτηση N εκφράζει το κοινό ρυθμό εξέλιξης των f_{p} και $\boldsymbol{f}$ και εξαρτάται από τη μη-αρνητική παράμετρο βαθμονόμησης N_{o} και από την αρχική κατάσταση σε όρους δείκτη πόρων (e_{o}) και παραμέτρου κατάστασης (ψ_{o}). Στην εξέλιξη του f_{p} συμμετέχει επιπλέον η συνάρτηση $f_{\mathrm{B}}(p_{\mathrm{o}})$, η οποία εισάγει την επίδραση της αρχικής μέσης ενεργού τάσης p_{o}, ενώ στην εξέλιξη του $\boldsymbol{f}$ συμμετέχει και η συνάρτηση $h_{\text{post-liq}}$, η οποία ενεργοποιείται (και παίρνει τιμές $h_{\text{post-liq}} > 1$) μετά την εκδήλωση της αρχικής ρευστοποίησης (initial liquefaction), αν και εφόσον αυτή υπάρξει ως αποτέλεσμα της φόρτισης. Σε όλες τις υπόλοιπες περιπτώσεις η συνάρτηση $h_{\text{post-liq}}$ παραμένει ανενεργή και η τιμή της είναι ίση με 1. Επισημαίνεται ότι η αρχική ρευστοποίηση ορίζεται ως η *πρώτη φορά* που η τρέχουσα p γίνεται μικρότερη της τιμής p_{l} που ισούται με το 5% της p_{o}, με την τιμή της p_{l} να είναι μικρότερη ή ίση των 10kPa. Η μορφή της συνάρτηση $h_{\text{post-liq}}$ συζητείται παρακάτω. Η συνεχής και σταδιακή αύξηση του

αριθμητή της Εξ. 19 όταν η πλαστική ογκομετρική παραμόρφωση είναι θετική, εξασφαλίζει μία συνεχή αύξηση του πλαστικού μέτρου κράτυνσης K_p, και επομένως μείωση του ρυθμού συσσώρευσης πλαστικών παραμορφώσεων. Αυτό συμβαίνει κατά τη διάρκεια διαδοχικών κύκλων φόρτισης-αποφόρτισης-επαναφόρτισης (σχετικά) μικρού πλάτους παραμόρφωσης. Αντίθετα, η σταδιακή αύξηση του παρονομαστή, όταν η πλαστική ογκομετρική παραμόρφωση είναι αρνητική, βοηθάει στην προσομοίωση της έντονης μείωσης της στιβαρότητας και της συσσώρευσης μεγάλων πλαστικών παραμορφώσεων, που ακολουθούν έναν κύκλο φόρτισης μεγάλου πλάτους υπό αστράγγιστες συνθήκες, καθώς και εντέλει την εκδήλωση αρχικής ρευστοποίησης. Στην Εξ. 19, η σταθερά $c_f = 1$. Έτσι, ορίζεται ένα κατώφλι, κάτω από το οποίο η επίδραση του μεγέθους f_p στο μέτρο κράτυνσης K_p δεν είναι εμφανής, με στόχο να αποτραπεί η μη-ρεαλιστική αύξηση της στιβαρότητας στα αρχικά στάδια μιας μονοτονικής φόρτισης.

Η σταδιακή αύξηση της στιβαρότητας κατά την ανακυκλική φόρτιση παρατηρείται τόσο καθ' όλη τη διάρκεια της φόρτισης υπό στραγγιζόμενες συνθήκες, όσο και κατά το αρχικό στάδιο της φόρτισης υπό αστράγγιστες συνθήκες. Γι' αυτόν ακριβώς το λόγο, η συνάρτηση h_f έχει επιλεχθεί, κατ' αρχήν, να συναρτάται με την πλαστική συνιστώσα των ογκομετρικών παραμορφώσεων και όχι με το ολικό τους μέγεθος. Ωστόσο, αυτό δημιουργεί μία εγγενή ποσοτική διαφοροποίηση της εξέλιξης της συνάρτησης h_f για διαφορετικές συνθήκες στράγγισης. Για παράδειγμα, υπό στραγγιζόμενες συνθήκες (είτε πλήρως, είτε μερικώς), η μεταβολή του δείκτη πόρων e επηρεάζει άμεσα το μέτρο K_p (μέσω της συνάρτησης f_A), και κατά συνέπεια τις αναπτυσσόμενες πλαστικές ογκομετρικές παραμορφώσεις, που υπεισέρχονται στις Εξ. 20 και 21.

Επιπλέον, ενώ η τάση του παρονομαστή της συνάρτησης h_f να απομειώνει τη στιβαρότητα μιας φόρτισης που ακολουθεί πρωτύτερη εκδήλωση διαστολής είναι απόλυτα κατάλληλη για να προσομοιώνει την έντονη αύξηση υπερπιέσεων στην περιοχή μικρών ενεργών τάσεων και την εκδήλωση αρχικής ρευστοποίησης υπό αστράγγιστες συνθήκες, παραμένει ασαφές πως επιδρά για την ίδια μεγάλου πλάτους φόρτιση υπό στραγγιζόμενες συνθήκες. Η διερεύνηση αυτού γίνεται στα **Σχήματα 2α** και **2β** όπου παρουσιάζονται οι σχέσεις διατμητικής τάσης τ – διατμητικής παραμόρφωσης γ_{SS} και ογκομετρικής παραμόρφωσης ε_{vol} – γ_{SS}, για 30 κύκλους ανακυκλικής δοκιμής απλής διάτμησης, όπου το ημι-εύρος της επιβαλλόμενης διατμητικής παραμόρφωσης είναι επαρκώς μεγάλο ώστε να

οδηγήσει την τασική όδευση σε συνθήκες διαστολής λόγω αύξησης της στιβαρότητας. Συγκεκριμένα, θεωρώντας $a = 1$ στις Εξ. 20 και 21, η ήπια αύξηση του αριθμητή της συνάρτησης h_f, σε συνδυασμό με την παράλληλη έντονη αύξηση του παρονομαστή της, οδηγούν σε μη ρεαλιστική απόκριση (π.χ., μη-μονότονη μεταβολή του ρυθμού συσσώρευσης της ογκομετρικής παραμόρφωσης στο **Σχήμα 2β**).

Για να διορθωθεί αυτή η μη-ρεαλιστική πρόβλεψη, στο παρόν προσομοίωμα, οι Εξ. 20 και 21εξελίσσονται μεν σύμφωνα με την πλαστική ογκομετρική παραμόρφωση, ωστόσο ο ρυθμός αυτής της εξέλιξης θεωρείται ότι εξαρτάται ποσοτικά από τον συντελεστή a που συσχετίζει τις απόλυτες τιμές της συσσωρευμένης πλαστικής και της ολικής ογκομετρικής παραμόρφωσης από την αρχή της φόρτισης (π.χ., ξεκινώντας από γεωστατικές συνθήκες):

$$0 \le a = -2\left(\frac{\left|\int \dot{\varepsilon}_{\mathrm{vol}}\right|}{\left|\int \dot{\varepsilon}^{\mathrm{p}}_{\mathrm{vol}}\right|} - 1\right) \le 1 \tag{3.22}$$

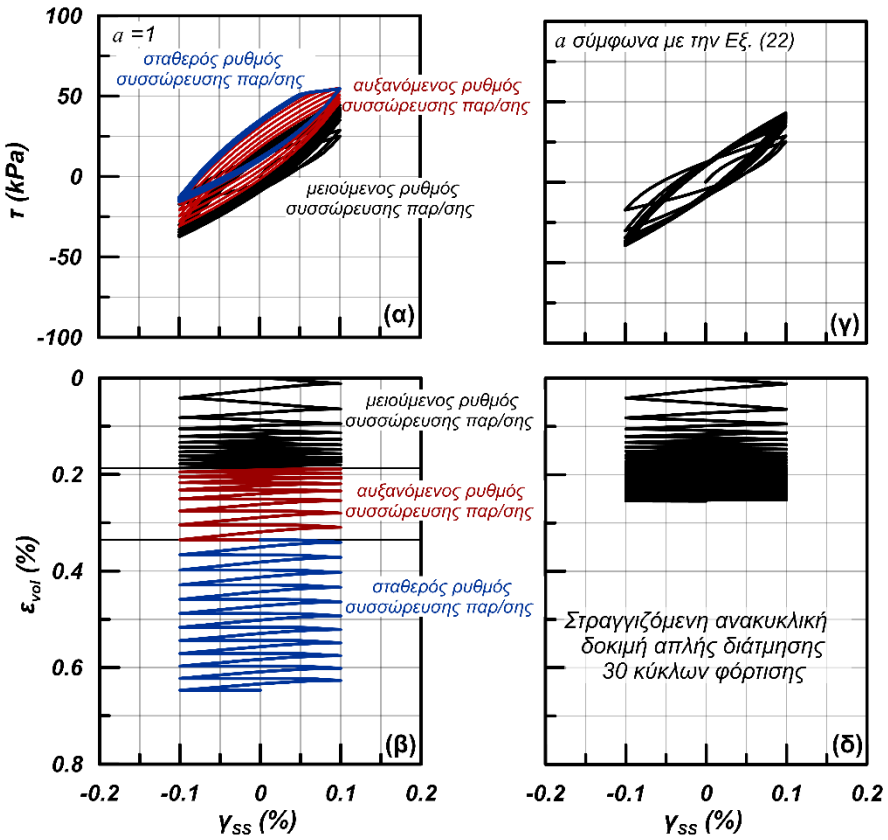

***Σχήμα 2**: Επίδραση του συντελεστή a στη σχέση τάσης – διατμητικής παραμόρφωσης (τ – γss) και διατμητικής – ογκομετρικής παραμόρφωσης (εvol – γss) μιας στραγγιζόμενης δοκιμής απλής διάτμησης, όταν: (α), (β) a =1,και (γ), (δ) το α εξελίσσεται σύμφωνα με την Εξ. (22).*

Σύμφωνα με την Εξ. 22, ο συντελεστής a παίρνει τιμές μεταξύ 0 και 1. Έτσι, όταν η ολική ογκομετρική παραμόρφωση είναι μηδενική (π.χ. στην ακραία περίπτωση των πλήρως αστράγγιστων συνθηκών), τότε ο συντελεστής $a = 1$. Από την άλλη, όταν έχει συσσωρευθεί σημαντική ογκομετρική παραμόρφωση (π.χ., σε πλήρως στραγγιζόμενες συνθήκες, οδηγώντας σε σημαντική μεταβολή του e), τότε $a = 0$. Στην ουσία, ο ρόλος του συντελεστή a είναι να ενισχύει ή να εξασθενεί την επίδραση των επιμέρους συνιστωσών εξέλιξης της δομής επί του K_p στις Εξ. 20 και 21. Αποτέλεσμα της λειτουργίας του συντελεστή a είναι η βελτίωση της απόκρισης, όπως φαίνεται στα **Σχήματα 2γ** και **2δ** για το παράδειγμα των πλήρως στραγγιζόμενων συνθηκών, συγκριτικά με την εικόνα στα **Σχήματα 2α** και **2β**.

Β. Συνάρτηση Διαστολικότητας (D)

Το παρόν προσομοίωμα υιοθετεί μη-συσχετισμένο νόμο πλαστικής ροής για την εκτίμηση της πλαστικής παραμόρφωσης, η ογκομετρική συνιστώσα του οποίου ορίζεται μέσω της βαθμωτής συνάρτησης διαστολικότητας D. Η συνάρτηση D εκφράζεται μέσω διαφορετικών σχέσεων για συνθήκες συστολής ή διαστολής αντίστοιχα, αλλά και στις δύο περιπτώσεις ισχύει $D = 0$ όταν η τρέχουσα κατάσταση βρίσκεται επί της Επιφάνειας Διαστολικότητας ($\boldsymbol{r} = \boldsymbol{r}^{\mathrm{d}}$ στο **Σχήμα 1**).

Σε συνθήκες συστολής, η συνάρτηση D (> 0) ορίζεται ως:

$$D=A_{\mathrm{o}}\frac{f_{\mathrm{C}}\left((\boldsymbol{r}-\boldsymbol{r}_{\mathrm{ini}}):\boldsymbol{n}\right)}{f_{\mathrm{D}}\left(p\right)}\left((\boldsymbol{r}^{\mathrm{d}}-\boldsymbol{r}):\boldsymbol{n}\right) \tag{3.23}$$

όπου A_{o} είναι μια μη-αρνητική παράμετρος βαθμονόμησης του προσομοιώματος, η μη-αρνητική συνάρτηση f_{D} σχετίζεται με την επίδραση της μέσης ενεργού τάσης p και η συνάρτηση f_{C} κυρίως με την απόσταση $(\boldsymbol{r}-\boldsymbol{r}_{\mathrm{ini}}):\boldsymbol{n}$, μια συνάρτηση που παίρνει μικρές τιμές σε κάθε αντιστροφή φόρτισης. Η Εξ. 23, ενώ βασίζεται στην αρχή της Θεωρίας Διαστολικότητας του Rowe (1962), διαφέρει σημαντικά από αυτήν, καθώς, πέρα από την απόσταση του λόγου $\boldsymbol{r}$ από τον συζυγή του $\boldsymbol{r}^{\mathrm{d}}$ επί της Επιφάνειας Διαστολικότητας, εξαρτάται και από την ιστορία διατμητικής φόρτισης μέσω της απόστασης $(\boldsymbol{r}-\boldsymbol{r}_{\mathrm{ini}}):\boldsymbol{n}$ που υπεισέρχεται στη συνάρτηση f_{C}.

Από την άλλη, σε συνθήκες διαστολής, η συνάρτηση D (< 0) ορίζεται ως:

$$D=A_o \frac{f_E(\theta)}{h_{post\text{-}liq}\, h_{fd}}\left((\boldsymbol{r}^d-\boldsymbol{r}):\boldsymbol{n}\right) \tag{3.24}$$

όπου η παράμετρος A_o είναι ίδια όπως και στην Εξ. 23, και η f_E είναι μια μη-αρνητική συνάρτηση της γωνίας Lode θ. Εδώ, αξίζει να σημειωθεί πως η Εξ. 24 υιοθετεί άμεσα την αρχή της Θεωρίας Διαστολικότητας του Rowe (1962), ορίζοντας μια γραμμική σχέση μεταξύ του D και της απόστασης μεταξύ της τρέχουσας κατάστασης $\boldsymbol{r}$ και της Επιφάνειας Διαστολικότητας (μέσω του συζυγούς της λόγου $\boldsymbol{r}^d$). Επιπλέον, η συνάρτηση h_{fd} εισάγει μια επίδραση της εξέλιξης της δομής των κόκκων στη συνάρτηση D, ως εξής:

$$h_{fd}=1+\left\langle f_{pd}-c_{fd}\right\rangle \tag{3.25}$$

Η συνάρτηση h_{fd} βασίζεται στον συσσωρευτικής φύσης δείκτη f_{pd}, ο οποίος - ξεκινώντας από $f_{pd} = 0$ στην αρχή της φόρτισης (π.χ. σε γεωστατικές συνθήκες) - αυξάνεται σταδιακά για θετική μεταβολή της πλαστικής ογκομετρικής παραμόρφωσης (δηλ. μόνο κατά τη διάρκεια της συστολής). Αυτή η αύξηση της h_{fd} έχει ως αποτέλεσμα μια σταδιακά μειούμενη προ-διάθεση για διαστολή, ειδικά μάλιστα όταν η ολική μεταβολή του όγκου είναι σημαντική (π.χ. υπό πλήρως στραγγιζόμενες συνθήκες). Στην Εξ. 25, η σταθερά c_{fd} = 3, υπονοώντας πως η f_{pd} θα πρέπει να αυξηθεί σημαντικά, ώστε η επίδρασή της επί της D να καταστεί εμφανής. Τέλος, η συνάρτηση $h_{post\text{-}liq}$, όπως και στην Εξ. 21, ενεργοποιείται μετά την εκδήλωση της αρχικής ρευστοποίησης (όταν $p \le p_l$ για πρώτη φορά) και μόνο τότε αρχίζει να συμμετέχει, όπως συζητείται εκτενώς στην επόμενη παράγραφο.

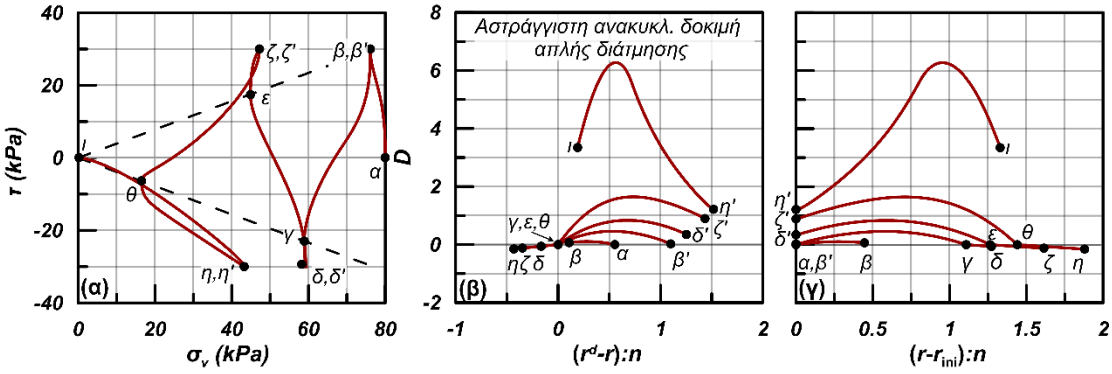

***Σχήμα 3**: (α) Ενδεικτική τασική όδευση αστράγγιστης ανακυκλικής δοκιμής και εξέλιξη της διαστολικότητας D ως συνάρτηση (β) της απόστασης (**$\boldsymbol{r}^d$-$\boldsymbol{r}$):$\boldsymbol{n}$ και (γ) της απόστασης (**$\boldsymbol{r}$-$\boldsymbol{r}_{ini}$):$\boldsymbol{n}$.*

Για να γίνει κατανοητό πως οι Εξ. 23 και 24 λειτουργούν κατά τη διάρκεια μιας ανακυκλικής φόρτισης, στο **Σχήμα 3** παρουσιάζεται η τασική όδευση κατά τη διάρκεια μιας δοκιμής απλής διάτμησης υπό αστράγγιστες συνθήκες (**Σχήμα 3α**), σε συνδυασμό με την εξέλιξη της διαστολικότητας D ως συνάρτηση της απόστασης $(\boldsymbol{r}^{d} - \boldsymbol{r}):\boldsymbol{n}$ (**Σχήμα 3β**) και της απόστασης $(\boldsymbol{r} - \boldsymbol{r}_{ini}):\boldsymbol{n}$ (**Σχήμα 3γ**). Τα σημεία a – i αναφέρονται σε κοινά σημεία στα επιμέρους διαγράμματα, ώστε να γίνεται εύκολα η αντιστοίχιση, ενώ οι διακεκομμένες γραμμές στο **Σχήμα 3α** είναι η προβολή της Επιφάνειας Διαστολικότητας επί του συγκεκριμένου τασικού χώρου. Σε όσα σημεία προκύπτει αντιστροφή φόρτισης, το ίδιο σημείο στο χώρο των τάσεων εμφανίζεται με τόνο (π.χ. β και β') πριν και μετά από αυτή.

Κατά την αρχική φόρτιση από το σημείο a έως το σημείο β η διαστολικότητα D, σύμφωνα με την Εξ. 23, ξεκινάει από μηδενική τιμή (λόγω του μηδενικού όρου $(\boldsymbol{r} - \boldsymbol{r}_{ini}):\boldsymbol{n}$), παρόλο που ο όρος $(\boldsymbol{r}^{d} - \boldsymbol{r}):\boldsymbol{n}$ είναι μη-μηδενικός. Στη συνέχεια, εξελίσσεται ανάλογα με το γινόμενο των όρων $[(\boldsymbol{r} - \boldsymbol{r}_{ini}):\boldsymbol{n}]\,[(\boldsymbol{r}^{d} - \boldsymbol{r}):\boldsymbol{n}]$. Συγκεκριμένα, καθώς αυτοί οι όροι δρουν πρακτικώς αντίθετα, η D στο αρχικό στάδιο της φόρτισης επηρεάζεται περισσότερο από τον γρήγορα αυξανόμενο όρο $(\boldsymbol{r} - \boldsymbol{r}_{ini}):\boldsymbol{n}$ και ως εκ τούτου αυξάνεται, ενώ στη συνέχεια η μείωση του όρου $(\boldsymbol{r}^{d} - \boldsymbol{r}):\boldsymbol{n}$ επικρατεί, ώσπου η D μειώνεται τελικά και η ίδια. Στην περίπτωση που η τασική όδευση φθάσει επί της Επιφάνειας Διαστολικότητας και συνεπώς $(\boldsymbol{r}^{d} - \boldsymbol{r}):\boldsymbol{n} = 0$, η D επίσης μηδενίζεται (π.χ. σημείο γ). Αν η φόρτιση συνεχίσει πέρα από το σημείο αυτό, εκτός της Επιφάνειας Διαστολικότητας (π.χ. από γ έως δ), τότε η φόρτιση τελεί υπό καθεστώς διαστολής και η απόκριση περιγράφεται πλέον από την Εξ. 24, σύμφωνα με την οποία η σχέση μεταξύ D και $(\boldsymbol{r}^{d} - \boldsymbol{r}):\boldsymbol{n}$ είναι γραμμική. Τέλος, θα πρέπει να σημειωθεί πως στην περίπτωση που η αντιστροφή της φόρτισης γίνει εκτός της Επιφάνειας Διαστολικότητας (π.χ., στο σημείο δ', αφού είχε προηγηθεί διαστολή κατά τη φόρτιση γ-δ και $(\boldsymbol{r}^{d} - \boldsymbol{r}):\boldsymbol{n} < 0$), τότε στην αρχή της επικείμενης φόρτισης η διαστολικότητα D είναι θετική (και όχι μηδενική), καθώς η συνάρτηση f_C που υπεισέρχεται στην Εξ. 23 ισούται με την απόλυτη τιμή του όρου $(\boldsymbol{r}^{d} - \boldsymbol{r}):\boldsymbol{n} < 0$ στο σημείο αντιστροφής της φόρτισης (π.χ., στο σημείο δ). Με βάση τα παραπάνω, προκύπτει ότι η συγκεκριμένη διμερής μορφή της συνάρτησης διαστολικότητας D διασφαλίζει πως για ανακυκλική φόρτιση μικρού πλάτους, η τάση για μεταβολή του όγκου είναι μικρή είτε υπό στραγγιζόμενες, είτε υπό αστράγγιστες συνθήκες, όπως προκύπτει από τα πειραματικά αποτελέσματα στη βιβλιογραφία.

Γ. Συσσώρευση διατμητικών παραμορφώσεων μετά την αρχική ρευστοποίηση

Η εκδήλωση ρευστοποίησης (π.χ. λόγω ανακυκλικής φόρτισης υπό αστράγγιστες συνθήκες) αποτελεί μια χαρακτηριστική πτυχή της απόκρισης των κοκκωδών εδαφών, όπως οι άμμοι, και η καταστατική προσομοίωσή της αποτελεί διαχρονικά ένα από τα πιο απαιτητικά θέματα. Σε αυτό το πλαίσιο, τα τελευταία χρόνια το ερευνητικό ενδιαφέρον της καταστατικής προσομοίωσης ρευστοποιήσιμων εδαφών έχει στραφεί και προς την ορθή πρόβλεψη της συσσώρευσης παραμορφώσεων μετά την εκδήλωση αρχικής ρευστοποίησης (Barrero et al., 2020, Boulanger and Ziotopoulou, 2013, Elgamal et al., 2003, Tasiopoulou and Gerolymos, 2016, Zhang and Wang, 2012). Εδώ, αυτή η απόκριση προσομοιώνεται μέσω της συνάρτησης $h_{\text{post-liq}}$, που επιδρά κυρίως στην Εξ. 24 για τη συνάρτηση διαστολικότητας D σε φάση διαστολής, αλλά και στην Εξ. 21 για την εξέλιξη του τανυστή δομής $\boldsymbol{f}$ που υπεισέρχεται στο πλαστικό μέτρο κράτυνσης K_{p}. Στόχος της $h_{\text{post-liq}}$ είναι να επιτρέψει τη σταδιακή συσσώρευση διατμητικής παραμόρφωσης μετά την αρχική ρευστοποίηση, μειώνοντας κυρίως την τάση του υλικού για διαστολή. Η συνάρτηση $h_{\text{post-liq}}$ δίνεται ως:

$$h_{\text{post-liq}} = 1 + \left(2^{f_{\text{G}}(p)} - 1\right) f_{\text{l}} \tag{3.26}$$

όπου f_{l} είναι ένας μη-αρνητικός συσσωρευτικός δείκτης, όπου $f_{\text{l}} = 0$ μέχρι την αρχική ρευστοποίηση (αντιστοιχώντας σε $h_{\text{post-liq}} = 1$), ενώ $f_{\text{l}} > 0$ αυξανόμενο ως συνάρτηση του μέτρου της πλαστικής ογκομετρικής παραμόρφωσης από εκεί και πέρα, με ρυθμό αύξησης που καθορίζεται από την παράμετρο βαθμονόμησης L_{o}. Επιπλέον, ο όρος $f_{\text{G}}(p)$, είναι μια μη-αρνητική συνάρτηση του p με άνω όριο ίσο με 1 (όταν η μέση ενεργός τάση $p \approx 0$, ή ακριβέστερα όταν $p < p_{\text{l}}$) και κάτω όριο το 0 (όταν το p έχει αυξηθεί αρκετά, απομακρυνόμενο από την περιοχή $p \approx 0$). Έτσι, όταν προκύπτει στερεοποίηση μετά τη ρευστοποίηση, το προσομοίωμα θεωρεί $h_{\text{post-liq}} = 1$ ξανά, ανεξάρτητα από την τιμή του f_{l}.

Με άλλα λόγια, η απομειωτική επίδραση της συνάρτησης $h_{\text{post-liq}}$ επί της συνάρτησης διαστολικότητας D κατά τη διαστολή είναι εμφανής μόνο όταν η τρέχουσα κατάσταση βρίσκεται εντός της ευρύτερης περιοχής ρευστοποίησης σε όρους ενεργών τάσεων. Ο ορισμός της $h_{\text{post-liq}}$ θυμίζει αντίστοιχη πρόταση των Barrero et al. (2020), οι οποίοι όρισαν και την ευρύτερη περιοχή ρευστοποίησης ως ημι-ρευστοποιημένη περιοχή. Ο τρόπος λειτουργίας της συνάρτησης $h_{\text{post-liq}}$ παρουσιάζεται στο **Σχήμα 4**, μέσω μιας ανακυκλικής

δοκιμής απλής διάτμησης υπό αστράγγιστες συνθήκες. Και εδώ τα σημεία *α* έως *μ* αναφέρονται σε κοινά σημεία στα επιμέρους διαγράμματα, ώστε να γίνεται εύκολα η αντιστοίχιση. Οι 3 επικαλυπτόμενοι κύκλοι φόρτισης σε όρους τασικής όδευσης (**Σχήμα 4α**) αντιστοιχούν σε 3 μη επικαλυπτόμενους κύκλους τάσης–παραμόρφωσης διαρκώς αυξανόμενου εύρους (**Σχήμα 4β**), λόγω εξέλιξης της συνάρτησης $h_{\text{post-liq}}$ κατά τη διάρκεια αυτών των 3 κύκλων, με βάση όσα αναφέρθηκαν παραπάνω (**Σχήμα 4γ**).

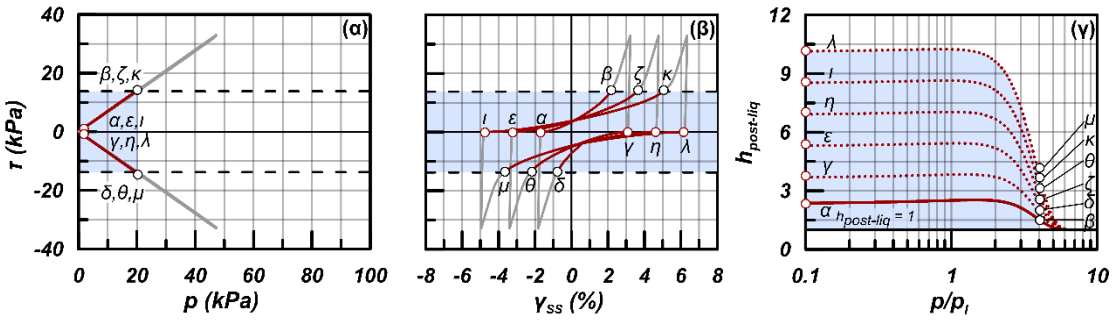

Σχήμα 4: *(α) Ενδεικτική παρουσίαση επικαλυπτόμενων κύκλων της τασικής όδευσης αστράγγιστης ανακυκλικής δοκιμής μετά την αρχική εκδήλωση ρευστοποίησης, (β) αντίστοιχοι κύκλοι τάσης–παραμόρφωσης και σταδιακή συσσώρευση παραμόρφωσης και (γ) εξέλιξη της συνάρτησης* $h_{post\text{-}liq}$ *με το λόγο* p/p_l.

Δ. Αντιμετώπιση «*υπερακόντισης*» (*overshooting*) της σχέσης τάσης–παραμόρφωσης

Σύμφωνα με όσα έχουν αναφερθεί, ο τανυστής $\boldsymbol{r}_{\text{ini}}$ εισάγεται σε πληθώρα καταστατικών εξισώσεων του προσομοιώματος, όπως στο νόμο προβολής και στη διεύθυνση φόρτισης (**Σχήμα 1**), στον υπολογισμό των μέτρων ελαστικότητας (μέσω της σχέσης απομείωσης τύπου Ramberg – Osgood, Εξ. 17), στο πλαστικό μέτρο κράτυνσης K_p (Εξ. 18) και στη συνάρτηση διαστολικότητας D κατά τη συστολή (Εξ. 23). Κατά συνέπεια, το παρόν προσομοίωμα, όπως και πολλά άλλα της βιβλιογραφίας (βλ. Duque et al. 2021), είναι ιδιαίτερα ευάλωτο στο πρόβλημα της «*υπερακόντισης*» (*overshooting*) της σχέσης τάσης–παραμόρφωσης ύστερα από αποφόρτιση και άμεση επαναφόρτιση. Συγκεκριμένα, το πρόβλημα έγκειται στο ότι η καμπύλη τάσης–παραμόρφωσης «*υπερακοντίζεται*» πέραν της προδιαγεγραμμένης της πορείας, λόγω της παρεμβολής μιας μικρής διαδρομής αποφόρτισης–επαναφόρτισης και, ως εκ τούτου, της («*αχρείαστης*») ανανέωσης του τανυστή $\boldsymbol{r}_{\text{ini}}$. Πρόκειται για ένα γνωστό πρόβλημα των προσομοιωμάτων με επιφάνειες αντιστροφής φόρτισης (stress reversal surfaces, π.χ. Mroz et al. 1979), ή απλούστερα

προσομοιωμάτων που χρησιμοποιούν τον τανυστή $\boldsymbol{r}_{\text{ini}}$ στο καταστατικό τους πλαίσιο και διορθώνεται προσαρμόζοντας την τιμή του $\boldsymbol{r}_{\text{ini}}$ ανάλογα με την ιστορία φόρτισης.

Στο προτεινόμενο προσομοίωμα η αντιμετώπιση αυτού του προβλήματος γίνεται σε 2 βήματα. Κατά το πρώτο βήμα, όταν εντοπίζεται μια αντιστροφή φόρτισης (σημείο όπου $\Lambda < 0$), αυτή ορίζεται ως «*κατ' αρχήν αποδεκτή*» ή «*κατ' αρχήν μη αποδεκτή*». Με άλλα λόγια, μόλις εντοπιστεί κάποια αντιστροφή φόρτισης (όταν $\boldsymbol{r} = \boldsymbol{r}^{(\text{m})}$, όπου m η τρέχουσα διαδρομή φόρτισης) που σηματοδοτεί την έναρξη μιας νέας επικείμενης διαδρομής φόρτισης (m+1), τότε αυτή θεωρείται «*κατ'αρχήν μη αποδεκτή*» και ο τανυστής $\boldsymbol{r}_{\text{ini}}$ προσωρινά δεν ανανεώνεται. Αυτό εξακολουθεί να ισχύει όσο η απόσταση του αποκλίνοντα λόγου των τάσεων $\boldsymbol{r}$ από την θέση που σηματοδοτήθηκε η («*κατ'αρχήν μη αποδεκτή*») αντιστροφή φόρτισης (στο σημείο $\boldsymbol{r}^{(\text{m})}$) παραμένει μικρότερη από μια προδιαγεγραμμένη (μικρή) τιμή (ίση με 0.01 σε αυτό το προσομοίωμα). Αυτό ποσοτικοποιείται μέσω του ακόλουθου κριτηρίου:

$$\sqrt{(2/3)\left(\boldsymbol{r}-\boldsymbol{r}^{(\text{m})}\right):\left(\boldsymbol{r}-\boldsymbol{r}^{(\text{m})}\right)} \le r_{\text{tol}} \tag{3.27}$$

Όταν η παραπάνω ανίσωση πάψει να είναι αληθής, τότε η απόσταση του $\boldsymbol{r}$ από το $\boldsymbol{r}^{(\text{m})}$ γίνεται επαρκώς μεγάλη και η αμφισβητούμενη αντιστροφή φόρτισης θεωρείται πια «*κατ' αρχήν αποδεκτή*», οπότε ενεργοποιείται το δεύτερο βήμα, κατά το οποίο η κατάλληλη τιμή του $\boldsymbol{r}_{\text{ini}}^{(\text{m+1})}$ που αφορά την επικείμενη διαδρομή φόρτισης (m+1) εκτιμάται με βάση το προτεινόμενο από τους Dafalias and Taiebat (2016) κριτήριο, σύμφωνα με το οποίο:

$$\boldsymbol{r}_{\text{ini}}^{(\text{m+1})} = k\,\boldsymbol{r}_{\text{ini}}^{(\text{m-1})} + (1-k)\,\boldsymbol{r}^{(\text{m})} \tag{3.28}$$

όπου $\boldsymbol{r}_{\text{ini}}^{(\text{m-1})}$ είναι ο τανυστής $\boldsymbol{r}_{\text{ini}}$ της προηγούμενης διαδρομής φόρτισης (m-1) που έχει διατηρηθεί στη μνήμη, και k είναι ένας παράγοντας στάθμισης (με τιμή μεταξύ 0 και 1) της τιμής του $\boldsymbol{r}_{\text{ini}}^{(\text{m+1})}$ που κυμαίνεται μεταξύ των τιμών $\boldsymbol{r}_{\text{ini}}^{(\text{m-1})}$ και $\boldsymbol{r}^{(\text{m})}$. Η στάθμιση αυτή γίνεται ως συνάρτηση της πλαστικής αποκλίνουσας παραμόρφωσης που αναπτύχθηκε κατά τη διαδρομή φόρτισης (m) σε σύγκριση με μια προκαθορισμένη (μικρή) οριακή τιμή (ίση με 10^{-4} εδώ). Πρακτικά αυτό σημαίνει ότι αν η διαδρομή φόρτισης (m) είναι «*μικρή*», τότε k=1 και $\boldsymbol{r}_{\text{ini}}^{(\text{m+1})} = \boldsymbol{r}_{\text{ini}}^{(\text{m-1})}$ πρακτικώς αγνοώντας την αντιστροφή φόρτισης στο σημείο $\boldsymbol{r}^{(\text{m})}$. Αντίθετα, αν η διαδρομή φόρτισης (m) είναι «*μεγάλη*», τότε k=0 και $\boldsymbol{r}_{\text{ini}}^{(\text{m+1})} = \boldsymbol{r}_{\text{ini}}^{(\text{m})}$ πρακτικώς διαγράφοντας από τη μνήμη την παλαιά $\boldsymbol{r}_{\text{ini}}^{(\text{m-1})}$, ενώ για ενδιάμεσου μήκους

διαδρομές ισχύει $0 < k < 1$.

Ένα παράδειγμα του προβλήματος «*υπερακόντισης*» της σχέσης τάσης-παραμόρφωσης παρουσιάζεται στο **Σχήμα 5β**, όπου η μη-αντιμετώπιση οδηγεί σε υπερεκτίμηση της αποκλίνουσας τάσης q έως και 100%. Στην περίπτωση αυτή, επιβάλλεται ένας «*μικρός*» κύκλος αποφόρτισης-επαναφόρτισης ($\Delta\varepsilon_a$ = 0.005%) και η χρήση της διαδικασίας 2 βημάτων δεν κρίνεται αναγκαία, καθώς αρκεί η Εξ. 28, σύμφωνα με τη βιβλιογραφία. Όμως, αν υπάρξουν πολλοί διαδοχικοί «*μικροί*» κύκλοι αποφόρτισης-επαναφόρτισης (**Σχήμα 5γ**), τότε προκύπτει ότι η αντιμετώπιση σε 2 βήματα (Εξ. 27 & 28) αποδεικνύεται πιο αποτελεσματική. Τέλος, από το **Σχήμα 5α** προκύπτει ότι αν ο κύκλος αποφόρτισης-επαναφόρτισης είναι «*μεγάλος*» ($\Delta\varepsilon_a$ = 0.1%), τότε η φόρτιση ορθώς παύει να είναι μονοτονική, και αυτό προβλέπεται ισότιμα είτε η αντιμετώπιση γίνεται σε 2 βήματα, είτε σε 1 βήμα (Εξ. 28).

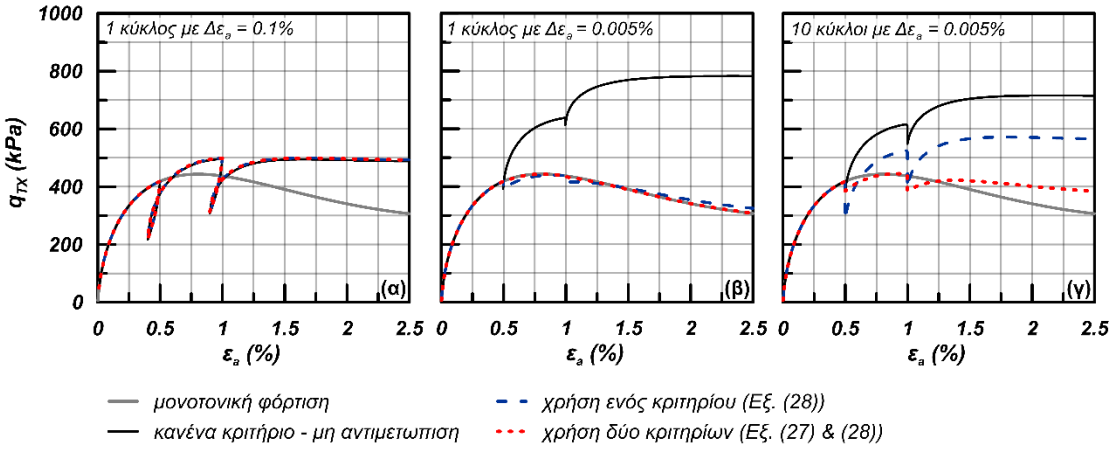

Σχήμα 5: *Διαφορετικοί τρόποι αντιμετώπισης της «υπερακόντισης» (overshooting) της σχέσης τάσης - παραμόρφωσης, στις 3 διαφορετικές περιπτώσεις τεχνητά επιβαλλόμενων εμβόλιμων κύκλων αποφόρτισης – επαναφόρτισης όταν ε_a = 0.5% και 1.0%: (α) ένας κύκλος πλάτους $\Delta\varepsilon_a$ = 0.1%, (β) ένας κύκλος πλάτους $\Delta\varepsilon_a$ = 0.005% και (γ) 10 διαδοχικοί κύκλοι πλάτους $\Delta\varepsilon_a$ = 0.005%.*

ΙΙΙ. ΑΞΙΟΛΟΓΗΣΗ ΑΠΟΚΡΙΣΗΣ ΠΡΟΣΟΜΟΙΩΜΑΤΟΣ ΣΕ ΕΠΙΠΕΔΟ ΜΟΝΑΔΙΑΙΟΥ ΣΤΟΙΧΕΙΟΥ

Το νέο προσομοίωμα έχει 14 παραμέτρους, 12 από τις οποίες αφορούν στη μονοτονική φόρτιση και 2 (N_o και L_o) στην ανακυκλική φόρτιση. Από τις συνολικά 14 παραμέτρους, οι 9 βαθμονομούνται απευθείας, ενώ οι υπόλοιπες 5 (h_o, c_h, A_o, N_o, L_o) βαθμονομούνται

τελευταίες με επαναληπτική διαδικασία: αρχικά βαθμονομούνται οι 3 πρώτες (h_o, c_h, A_o) με βάση μονοτονικές δοκιμές, και μετά οι υπόλοιπες 2 (N_o και L_o) με βάση ανακυκλικές δοκιμές. Η μεθοδολογία βαθμονόμησης βασίζεται σε εργαστηριακές δοκιμές σε επίπεδο μοναδιαίου στοιχείου ή/και εμπειρικές σχέσεις (όταν λείπουν πειραματικά δεδομένα) και περιγράφεται αναλυτικά στο **Κεφάλαιο 5** της Διατριβής. Συνολικά, στην παρούσα Διατριβή, το νέο προσομοίωμα έχει βαθμονομηθεί για 7 κοκκώδη εδάφη της βιβλιογραφίας, ήτοι 5 άμμους και 2 χάλικες (βλ. **Σχήμα 6**).

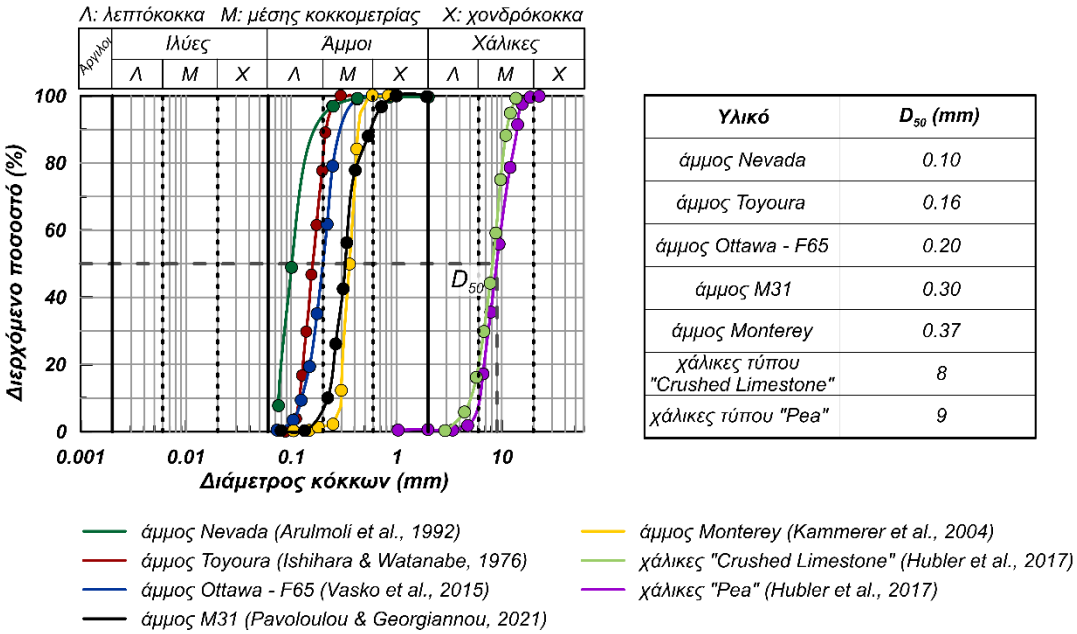

Υλικό	D_{50} (mm)
άμμος Nevada	0.10
άμμος Toyoura	0.16
άμμος Ottawa - F65	0.20
άμμος M31	0.30
άμμος Monterey	0.37
χάλικες τύπου "Crushed Limestone"	8
χάλικες τύπου "Pea"	9

Σχήμα 6: *Καμπύλες κοκκομετρικής διαβάθμισης κοκκωδών εδαφών για τα οποία έχει βαθμονομηθεί το παρόν προσομοίωμα στο πλαίσιο της παρούσας Διατριβής.*

Αντίστοιχα, στον **Πίνακα 2** παρουσιάζονται συγκεντρωτικά οι βαθμονομήσεις των 14 παραμέτρων του προσομοιώματος και για τα 7 κοκκώδη εδάφη. Η κοκκομετρία των υλικών καλύπτει συνολικά, σε όρους μέσης διαμέτρου D_{50}, ένα εύρος από 0.10 έως 9 mm. Για τις άμμους επιτυγχάνεται ο στόχος του μοναδικού σετ παραμέτρων για μονοτονική και ανακυκλική φόρτιση, αλλά για τους (συγκεκριμένους έστω) χάλικες προκύπτει διαφοροποίηση στην τιμή της παραμέτρου N_o που σχετίζεται με την εξέλιξη της δομής, η οποία απλά «*απενεργοποιείται*» ($N_o = 0$) κατά τη μονοτονική φόρτιση.

Στη συνέχεια, στο πλαίσιο αξιολόγησης του προσομοιώματος σε επίπεδο μοναδιαίου στοιχείου, παρουσιάζονται ενδεικτικά αντιπροσωπευτικές συγκρίσεις της απόκρισής του με πειραματικά δεδομένα ή/και εμπειρικές σχέσεις, όχι ανά κοκκώδες έδαφος αλλά ανά

είδος φόρτισης. Οι πλήρεις συγκρίσεις ανά κοκκώδες έδαφος παρουσιάζονται σε ξεχωριστές παραγράφους στο **Κεφάλαιο 5** της Διατριβής.

Πίνακας 2: *Βαθμονόμηση παραμέτρων προσομοιώματος για διαφορετικά κοκκώδη εδάφη.*

Λειτουργία	**Παράμετρος**	**Τιμές ανά κοκκώδες έδαφος**						
		άμμος Toyoura	**άμμος Ottawa-F65**	**άμμος Nevada**	**άμμος Monterey**	**άμμος M31**	**χάλικες "Pea"**	**χάλικες "Crushed Limestone"**
Ελαστικότητα	G_o	650	400	500	400	450	580	660
	ν	0.15	0.15	0.15	0.15	0.05	0.05	0.05
Κρίσιμη Κατάσταση	e_{ref}	0.934	0.81	0.875	0.934	0.786	0.72	0.825
	λ	0.019	0.02	0.079	0.019	0.013	0.019	0.003
	ξ	0.70	0.75	0.19	0.70	0.61	2	1.5
	M_c^c	1.25	1.38	1.25	1.25	1.25	1.1	1.3
	c	0.712	0.74	0.74	0.72	0.712	0.74	0.712
Μέτρο πλαστικής κράτυνσης	n^b	1.1	0.7	1.1	1.1	1	0.05	0.01
	h_o	60	29	235	200	200	300	200
	c_h	12	8	4	7	4	0.5	0.5
Συνάρτηση διαστολικότητας	n^d	2	2	1.2	0.5	2.6	1.25	1.3
	A_o	1.5	2.4	2.6	2	1.3	1.5	0.6
Εξέλιξη της δομής	N_o	1550	600	4400	1800	3400	0 (μονοτονική) 7250 (ανακυκλική)	0 (μονοτονική) 11700 (ανακυκλική)
Συσσώρευση παρ/σεων μετά την εκδήλωση ρευστοποίησης (εφόσον υπάρξει)	L_o	2500	5000	750	200	200	100	50

Α. Μονοτονική φόρτιση υπό στραγγιζόμενες συνθήκες

Στο **Σχήμα 7** προσομοιώνεται η απόκριση της άμμου Toyoura υπό μονοτονική φόρτιση σε στραγγιζόμενες συνθήκες. Οι συγκρίσεις των **Σχημάτων 7α** και **7β** αναφέρονται στις δοκιμές τριαξονικής θλίψης των Verdugo and Ishihara (1996) σε ισότροπα στερεοποιημένα δοκίμια σε τάση στερεοποίησης p_o = 500 kPa και αρχικούς δείκτες πόρων e_o = 0.810 - 0.960 (D_r = 43% - 3%). Η σύγκριση γίνεται σε όρους (τριαξονικής) αποκλίνουσας τάσης $q_{TX} = \sigma_a - \sigma_r$ έναντι αξονικής παραμόρφωσης ε_a (**Σχήμα 7α**) και ογκομετρικής παραμόρφωσης ε_{vol} έναντι αξονικής παραμόρφωσης ε_a (**Σχήμα 7β**). Οι δείκτες a και r δηλώνουν την αξονική και την ακτινική διεύθυνση επί του τριαξονικού δοκιμίου, αντίστοιχα. Από την άλλη, τα **Σχήματα 7γ** και **7δ** αναφέρονται σε δοκιμές στρεπτικής διάτμησης των Pradhan et al. (1988) σε δοκίμια στερεοποιημένα υπό συνθήκες K_o, με επιβολή σταθερής κατακόρυφης τάσης $\sigma_{a,o}$ (100 έως 200 kPa) καθ' όλη τη διάρκεια της δοκιμής. Οι αρχικοί δείκτες πόρων κυμαίνονται από 0.674 έως 0.798 (D_r = 48% - 81%) και

η σύγκριση γίνεται σε όρους λόγου τάσεων, τ/σ_a, έναντι διατμητικής παραμόρφωσης, $\gamma = \varepsilon_1 - \varepsilon_3$ (**Σχήμα 7γ**), και ε_{vol} έναντι γ (**Σχήμα 7δ**), όπου οι δείκτες 1 και 3 δηλώνουν τη μέγιστη και ελάχιστη τιμή των κύριων τιμών του εκάστοτε τανυστή.

Και για τους δύο τύπους μονοτονικών δοκιμών, το προσομοίωμα προβλέπει αρκετά ικανοποιητικά την απόκριση, δεδομένου του εύρους των μέσων ενεργών τάσεων (< 100 έως 500 kPa) και των σχετικών πυκνοτήτων (3% – 81%).

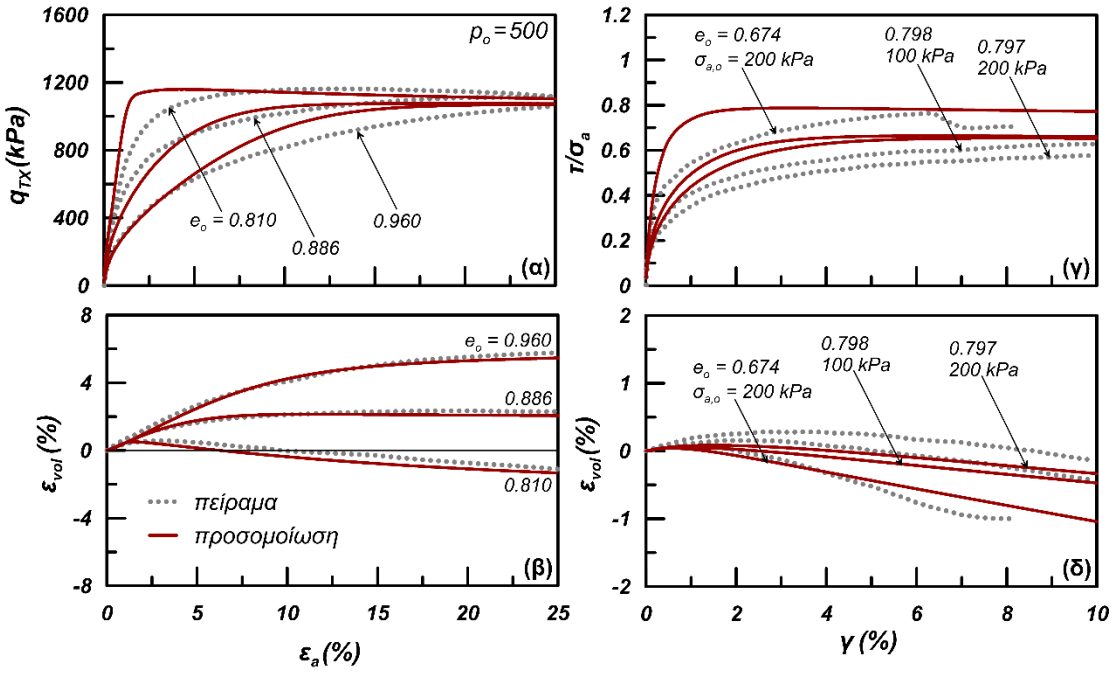

Σχήμα 7: *Σύγκριση αριθμητικών αποτελεσμάτων και πειραματικών δεδομένων μονοτονικής φόρτισης υπό στραγγιζόμενες συνθήκες σε: (α), (β) δοκιμή τριαξονικής θλίψης - πειραματικά δεδομένα Verdugo and Ishihara (1996) και (γ), (δ) δοκιμή στρεπτικής διάτμησης - πειραματικά δεδομένα Pradhan et al. (1988).*

Β. Μονοτονική φόρτιση υπό αστράγγιστες συνθήκες

Στη συνέχεια, στο **Σχήμα 8** προσομοιώνεται η απόκριση της άμμου Toyoura υπό μονοτονική φόρτιση σε αστράγγιστες, αυτή τη φορά, συνθήκες. Οι συγκρίσεις των **Σχημάτων 8α** και **8β** αναφέρονται στις δοκιμές τριαξονικής θλίψης των Verdugo and Ishihara (1996) σε ισότροπα στερεοποιημένα δοκίμια με αρχική τάση στερεοποίησης p_o = 100 - 1000 kPa και δείκτες πόρων e = 0.735 - 0.833 (D_r = 37% - 63%). Η σύγκριση γίνεται σε όρους q_{TX} έναντι ε_a (**Σχήμα 8α**) και q_{TX} έναντι μέσης ενεργού τάσης p (**Σχήμα 8β**). Αντίστοιχα, οι συγκρίσεις των **Σχημάτων 8γ** και **8δ** αναφέρονται στις δοκιμές απλής

διάτμησης των Yoshimine et al. (1998) σε ισότροπα στερεοποιημένα δοκίμια με αρχική τάση στερεοποίησης p_o = 100 kPa. Οι δείκτες πόρων κυμαίνονται από 0.804 έως 0.888 (D_r = 22% έως 45%) και η σύγκριση γίνεται σε όρους αποκλίνουσας τάσης $q = \sigma_1 - \sigma_3$ έναντι γ (**Σχήμα 8γ**) και q έναντι p (**Σχήμα 8δ**).

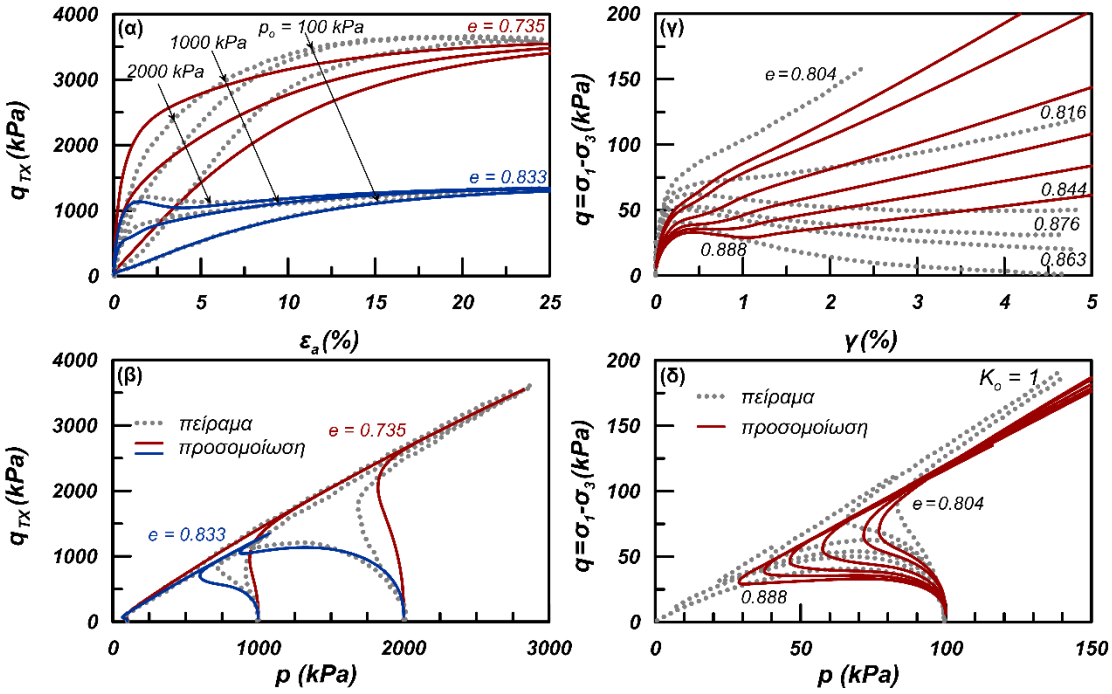

Σχήμα 8: *Σύγκριση αριθμητικών αποτελεσμάτων και πειραματικών δεδομένων μονοτονικής φόρτισης υπό αστράγγιστες συνθήκες σε: (α), (β) δοκιμή τριαξονικής θλίψης - πειραματικά δεδομένα Verdugo and Ishihara (1996) και (γ), (δ) δοκιμή απλής διάτμησης - πειραματικά δεδομένα Yoshimine et al. (1998).*

Οι προβλέψεις του προσομοιώματος για τις τριαξονικές συνθήκες φόρτισης είναι συνολικά ικανοποιητικές σε σύγκριση με τα πειραματικά δεδομένα, ειδικά εάν ληφθεί υπόψη το πολύ μεγάλο εύρος της αρχικής μέσης ενεργού τάσης p_o (= 100 – 1000 kPa). Όσον αφορά στις συνθήκες απλής διάτμησης, και πάλι η σύγκριση θεωρείται αποδεκτή, με τις προβλέψεις ωστόσο να υποεκτιμούν την έντονα συστολική συμπεριφορά των δοκιμίων με μεγαλύτερο δείκτη πόρων για μεγάλες παραμορφώσεις (γ <1%). Ωστόσο, εκτιμάται ότι και οι συγκεκριμένες προβλέψεις θα μπορούσαν να βελτιωθούν αν η έμφαση της βαθμονόμησης είχε δοθεί στο σαφώς πιο περιορισμένο εύρος τιμών δείκτη πόρων e (= 0.804 – 0.888) των δοκιμών και όχι στο πολύ μεγάλο εύρος που στοχεύθηκε για την εφ' άπαξ βαθμονόμηση της άμμου Toyoura (e = 0.674 έως 0.996, D_r <3% - 81%).

Γ. Ανακυκλική φόρτιση υπό αστράγγιστες συνθήκες

Με χρήση των ίδιων τιμών για τις παραμέτρους βαθμονόμησης ανά άμμο, όπως χρησιμοποιήθηκαν για την πρόβλεψη της μονοτονικής συμπεριφοράς, στο **Σχήμα 9** παρουσιάζονται συγκρίσεις μεταξύ προβλεπόμενης απόκρισης και πειραματικών δεδομένων για ανακυκλική φόρτιση υπό αστράγγιστες συνθήκες. Συγκεκριμένα, οι συγκρίσεις των **Σχημάτων 9α** έως **9δ** αναφέρονται στην προσομοίωση δοκιμής ανακυκλικής τριαξονικής φόρτισης των El Ghoraiby et al. (2018) σε άμμο Ottawa - F65. Για την εν λόγω δοκιμή, πραγματοποιήθηκε ισότροπη στερεοποίηση του δοκιμίου σε αρχική τάση p_o = 100 kPa και δείκτη πόρων e = 0.585 (D_r = 62%), ενώ κατά τη δοκιμή επιβλήθηκε ανακυκλική αποκλίνουσα τάση σταθερού μονού πλάτους $q_{TX,cyc}$ = 34 kPa. Η σύγκριση γίνεται σε όρους q_{TX} έναντι σ_r (**9α** και **9β**) και q_{TX} έναντι ε_a (**9γ** και **9δ**). Αντίστοιχα, οι συγκρίσεις των **9ε** έως **9θ** αναφέρονται στην προσομοίωση ανακυκλικής δοκιμής στρεπτικής διάτμησης του Zhang (1997) σε άμμο Toyoura. Για την εν λόγω δοκιμή, πραγματοποιήθηκε ισότροπη στερεοποίηση του δοκιμίου σε αρχική τάση p_o = 100 kPa και δείκτη πόρων e = 0.736 (D_r = 70%), ενώ κατά τη δοκιμή επιβλήθηκε ανακυκλική διατμητική τάση σταθερού μονού πλάτους τ_{cyc} = 33 kPa. Η σύγκριση γίνεται σε όρους τ έναντι p (**9ε** και **9ζ**) και τ έναντι γ_{SS} (**9η** και **9θ**).

Οι συγκρίσεις και για τις δύο δοκιμές είναι αρκετά ικανοποιητικές, τόσο σε όρους διαδρομής τάσεων, όσο και σε όρους τάσης-παραμόρφωσης. Όσον αφορά στις υπερπιέσεις πόρων, κατά την τριαξονική δοκιμή (**Σχήματα 9α** έως **9δ**) προσομοιώνεται ορθά ο αρχικά μειούμενος ρυθμός ανάπτυξής τους πριν αυτός μεγαλώσει ραγδαία οδηγώντας στην αρχική ρευστοποίηση, όπως παρουσιάζουν συστηματικά τα πειραματικά δεδομένα για κοκκώδη εδάφη. Ωστόσο, λόγω της διαφορετικής διατμητικής αντοχής μεταξύ θλίψης και εφελκυσμού, παρατηρείται μια τάση για «*μη-συμμετρική*» συσσώρευση των παραμορφώσεων με τους κύκλους, η οποία πολλές φορές υπερεκτιμάται στις καταστατικές προσομοιώσεις (βλ. Duque et al. 2021), αλλά εδώ εμφανίζεται αρκετά μειωμένη, κυρίως λόγω του όρου $h_{post-liq}$ που αφορά σε συσσώρευση παραμορφώσεων μετά την αρχική ρευστοποίηση. Από την άλλη, κατά τη «*συμμετρική*» δοκιμή απλής διάτμησης (**Σχήματα 9ε** έως **9θ**) το προσομοίωμα προβλέπει ορθά την εξελισσόμενη συσσώρευση παραμορφώσεων με τον αριθμό των κύκλων μετά την εκδήλωση της αρχικής ρευστοποίησης.

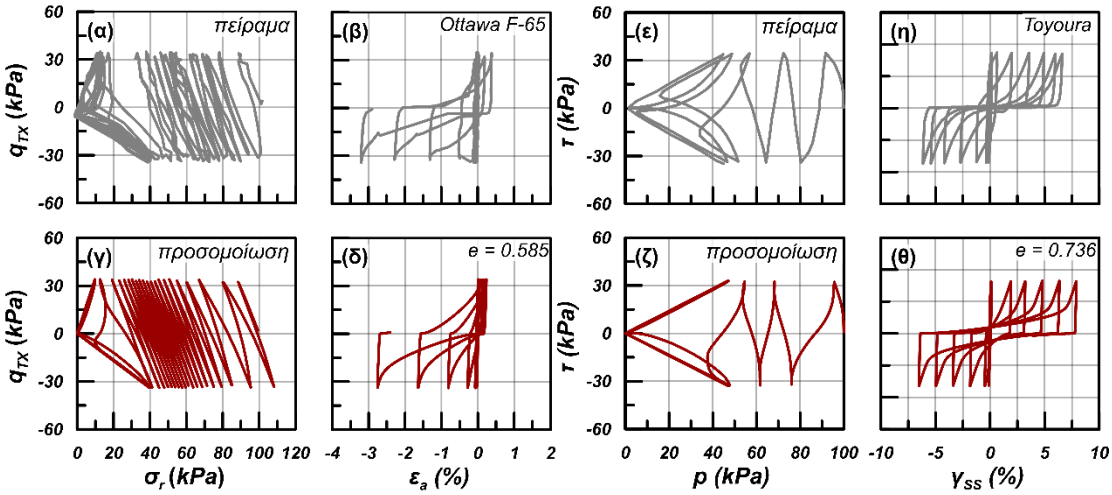

Σχήμα 9: *Σύγκριση αριθμητικών αποτελεσμάτων και πειραματικών δεδομένων ανακυκλικής φόρτισης υπό αστράγγιστες συνθήκες σε: (α)-(δ) τριαξονική δοκιμή – δεδομένα από El Ghoraiby et al. (2018) και (ε)-(θ) δοκιμή απλής διάτμησης – δεδομένα από Zhang (1997).*

Πέρα από την αναλυτική σύγκριση επιμέρους δοκιμών (όπως στο **Σχήμα 9**), για την αξιολόγηση του προσομοιώματος ως προς την ορθή πρόβλεψη της αντοχής σε ρευστοποίηση, στο **Σχήμα 10** γίνεται σύγκριση πειραματικών και προβλεπόμενων καμπυλών αντοχής σε ρευστοποίησης για διάφορες άμμους. Συγκεκριμένα, στο **Σχήμα 10α** έχει γίνει επιλογή ενδεικτικών τέτοιων καμπυλών για την άμμο Toyoura, από την πληθώρα της βιβλιογραφίας. Όλες οι επιλεχθείσες καμπύλες στηρίζονται σε πειραματικά αποτελέσματα από ανακυκλικές τριαξονικές δοκιμές υπό αστράγγιστες συνθήκες, σε δοκίμια που έχουν παρασκευαστεί με τη μέθοδο ξηράς απόθεσης (*air – pluviation*) και έχουν στερεοποιηθεί ισότροπα σε αρχική ενεργό τάση στερεοποίησης ίση με 100 kPa. Η ταξινόμησή τους έχει γίνει ανάλογα με τη σχετική πυκνότητα D_r των επιμέρους δοκιμίων, σε τρεις ομάδες με D_r = 45%, 60% και 75 - 80%. Η σύγκριση γίνεται σε όρους ανακυκλικού λόγου τάσεων *CSR* (= $q_{TX,cyc}/2p_o$) έναντι N_l, όπου N_l ο αριθμός των απαιτούμενων κύκλων φόρτισης ώστε να αναπτυχθεί παραμόρφωση διπλού πλάτους ίση με 5%. Σε γενικές γραμμές, οι καμπύλες ρευστοποίησης που προβλέπονται από το προσομοίωμα βρίσκονται εντός του εύρους των πειραματικών ανά τιμή D_r, παρόλο που παρουσιάζουν ελαφρώς πιο έντονη κλίση. Ωστόσο, είναι εμφανές ότι το προσομοίωμα δεν προβλέπει ρευστοποίηση ($N_l \rightarrow \infty$) για πολύ μικρές τιμές του λόγου *CSR*, σε συμφωνία με τα πειραματικά δεδομένα.

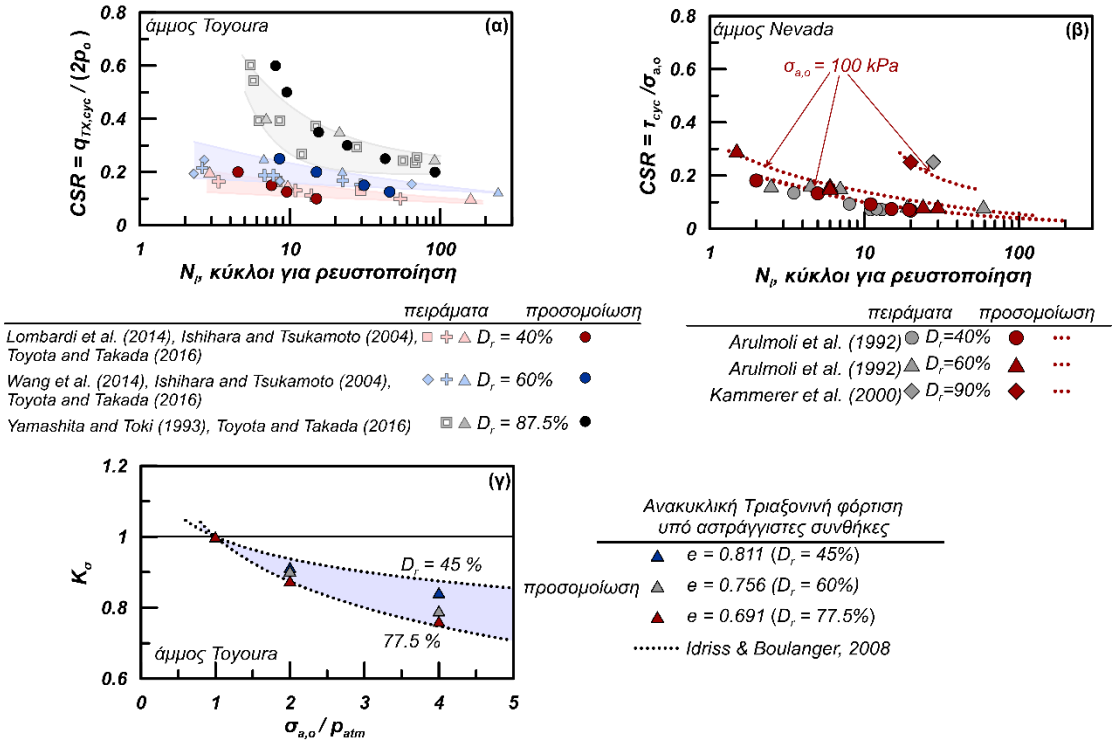

Σχήμα 10: *Σύγκριση αριθμητικών και πειραματικών καμπυλών αντοχής σε ρευστοποίηση, υπό (α) τριαξονική φόρτιση και (β) απλή διάτμησης - (γ) σύγκριση αριθμητικά προβλεπόμενου συντελεστή K_σ με εμπειρική σχέση Idriss and Boulanger (2008).*

Αντίστοιχα, στο **Σχήμα 10β** συγκρίνονται οι καμπύλες αντοχής σε ρευστοποίηση της άμμου Nevada υπό φόρτιση απλής διάτμησης, όπως έχουν μετρηθεί πειραματικά από τους Arulmoli et al. (1992) και Kammerer et al. (2000) και όπως προβλέπονται από το προσομοίωμα. Οι συγκεκριμένες δοκιμές έχουν πραγματοποιηθεί για ένα εύρος ενεργών αξονικών τάσεων στερεοποίησης από 40 έως 160 kPa. Μιας και για τη συγκεκριμένη σύγκριση συνδυάζονται δεδομένα από διαφορετικές έρευνες, οι τιμές του N_l για τις σχετικές πυκνότητες 40% και 60% (Arulmoli et al., 1992) αναφέρονται στην αρχική ρευστοποίηση ($p \approx 0$), ενώ η τιμή του N_l για D_r = 90% (Kammerer et al., 2000) αναφέρεται σε παραμόρφωση διπλού πλάτους ίση με 3%. Παράλληλα, έχουν προστεθεί οι αριθμητικές καμπύλες ρευστοποίησης που έχουν προκύψει για αξονική τάση ίση με 100 kPa, ως μια μέση τιμή των πειραματικών τιμών. Και για την άμμο αυτή προκύπτει ικανοποιητική ακρίβεια του προσομοιώματος στην πρόβλεψη της αντοχής σε ρευστοποίηση για το σημαντικό εύρος τιμών D_r που παρουσιάζεται.

Τέλος, στο **Σχήμα 10γ** αξιολογείται η ικανότητα του προσομοιώματος να προβλέπει ορθά τον συντελεστή διόρθωσης της αντοχής σε ρευστοποίηση λόγω υπερκείμενου

φορτίου μεγαλύτερου της 1 atm, για διάφορες τιμές της σχετικής πυκνότητας D_r (γνωστό στη βιβλιογραφία ως K_σ). Οι τιμές του προβλεπόμενου K_σ για άμμο Toyoura έχουν προκύψει συγκρίνοντας τους λόγους αντοχής σε ρευστοποίηση, *CRR*, που αντιστοιχούν σε 15 κύκλους φόρτισης για αρχικές αξονικές τάσεις $\sigma_{a,o}$ = 100, 200, 400 kPa. Οι συνθήκες φόρτισης, καθώς και οι εξεταζόμενες σχετικές πυκνότητες είναι όμοιες με αυτές που παρουσιάστηκαν στο **Σχήμα 10α**. Η αξιολόγηση γίνεται επί τη βάση των εμπειρικών σχέσεων των Idriss and Boulanger (2008) και η σύγκριση θεωρείται πολύ ικανοποιητική.

Δ. Ανακυκλική φόρτιση υπό στραγγιζόμενες συνθήκες

Στο **Σχήμα 11α** συγκρίνονται οι τιμές του ελαστικού μέτρου διάτμησης της άμμου Nevada (G_{max}) μετρούμενες σε μικρές παραμορφώσεις με τις αντίστοιχες προβλεπόμενες από το παρόν προσομοίωμα για σχετικές πυκνότητες D_r = 40% και 60% και για τάσεις στερεοποίησης από 40 έως 320 kPa. Τα πειραματικά αποτελέσματα αναφέρονται στις δοκιμές συντονισμού στήλης των Arulmoli et al. (1992). Η διαγώνιος ορίζει το γεωμετρικό τόπο των σημείων, όπου υπάρχει απόλυτη συμφωνία μεταξύ πειραματικών και προβλεπόμενων τιμών και ως φαίνεται η σύγκριση είναι εξαιρετική, όπως ήταν βέβαια αναμενόμενο καθώς το παρόν προσομοίωμα προτείνεται να βαθμονομείται με αυτόν τον τρόπο.

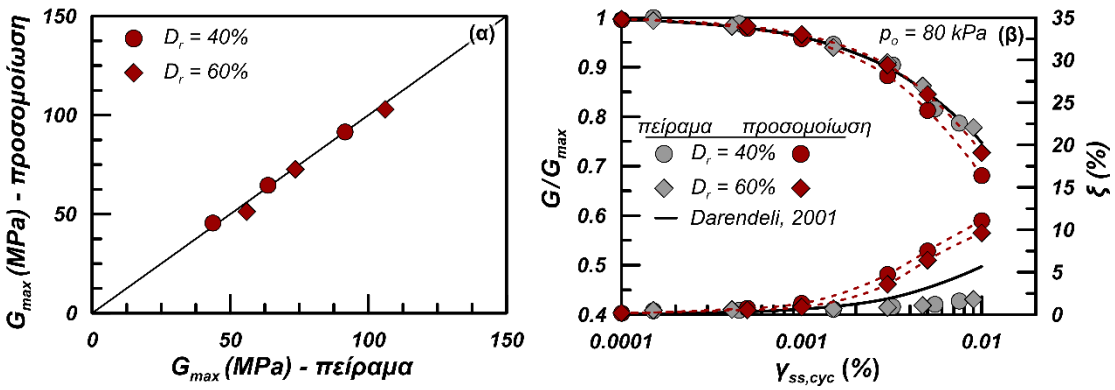

***Σχήμα 11**: Σύγκριση (α) τιμής G_{max} και (β) καμπυλών απομείωσης εφαπτομενικού μέτρου διάτμησης και αντίστοιχης αύξησης λόγου απόσβεσης με πειραματικές μετρήσεις των Arulmoli et al. (1992) και εμπειρικές σχέσεις του Darendeli (2001).*

Από την άλλη, στο **Σχήμα 11β** συγκρίνεται η απομείωση του κανονικοποιημένου μέτρου διάτμησης (G/G_{max}) και η αντίστοιχη αύξηση του λόγου απόσβεσης ξ συναρτήσει της επιβαλλόμενης διατμητικής παραμόρφωσης, όπως αυτές έχουν μετρηθεί πειραματικά και όπως προβλέπονται αριθμητικά. Σε αυτή τη σύγκριση συμπεριλαμβάνονται και οι εμπειρικές καμπύλες του Darendeli (2001). Σε όρους απομείωσης του μέτρου διάτμησης G/G_{max} η σύγκριση είναι αρκετά ικανοποιητική τόσο με τα πειραματικά, όσο και με τα εμπειρικά δεδομένα. Από την άλλη, σε όρους λόγου απόσβεσης ξ, η σύγκριση παύει να είναι ικανοποιητική όσο μεγαλώνει η διατμητική παραμόρφωση, καθώς το προσομοίωμα την υπερεκτιμά. Πρόκειται για ένα σύνηθες μειονέκτημα των προσομοιωμάτων που υιοθετούν τους νόμους του Masing κατά την αποφόρτιση, όπως συζητείται με λεπτομέρεια στο **Κεφάλαιο 5** της Διατριβής.

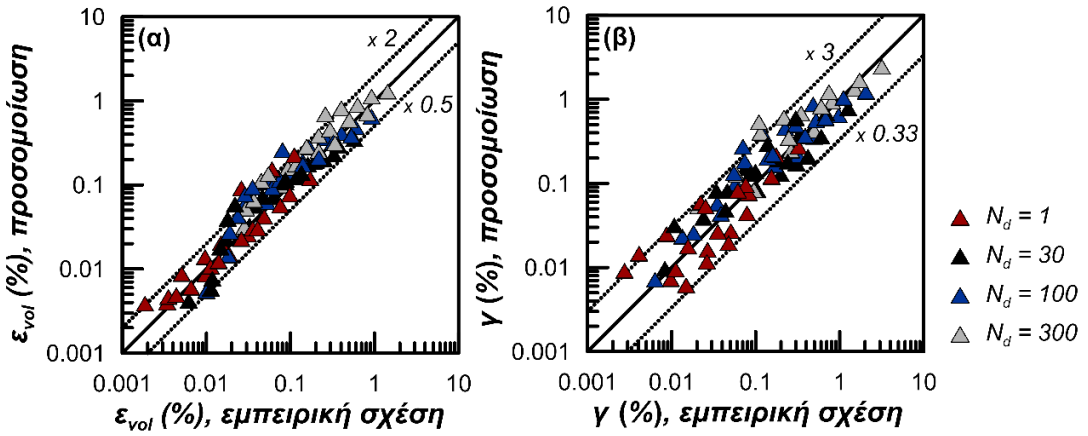

***Σχήμα 12**: Σύγκριση συσσωρευόμενων (α) ογκομετρικών ε_{vol} και (β) διατμητικών γ παραμορφώσεων μετά από N_d = 1, 30, 100 και 300 κύκλους στραγγιζόμενης τριαξονικής φόρτισης. Προσομοίωμα με παραμέτρους για άμμο Toyoura, p_o = 200 kPa και D_r = 40 – 80% και εμπειρικές σχέσεις Bouckovalas et al. (1984) και Stamatopoulos et al. (1991).*

Τέλος, στο **Σχήμα 12** παρουσιάζονται συγκεντρωτικά οι ογκομετρικές (**Σχήμα 12α**) και διατμητικές (**Σχήμα 12β**) παραμορφώσεις που συσσωρεύονται κατά τη διάρκεια ανακυκλικών στραγγιζόμενων τριαξονικών δοκιμών, όπως προβλέπονται από το προσομοίωμα συγκριτικά με τις τιμές που υπολογίζονται από τις εμπειρικές σχέσεις των Bouckovalas et al. (1984) και των Stamatopoulos et al. (1991). Η συσσώρευση μετράται μετά από N_d = 1, 30, 100 και 300 κύκλους φόρτισης. Οι προβλέψεις του προσομοιώματος προκύπτουν με βαθμονόμηση για άμμο Toyoura και αντιστοιχούν σε D_r = 40%, 60% και

80%, θεωρώντας ανισότροπες συνθήκες στερεοποίησης σε μέση ενεργό τάση p_o = 200 kPa και κατάλληλο συνδυασμό αξονικής και ακτινικής τάσης ώστε να προκύπτουν αρχικοί λόγοι τάσεων κατά την στερεοποίηση $q_{TX,o}/p_o$ = 0.35 και 0.75. Αξίζει διευκρίνησης ότι στις δοκιμές αυτές υπάρχει ταυτόχρονη συσσώρευση ογκομετρικών και διατμητικών παραμορφώσεων λόγω της ανισότροπης στερεοποίησης των δοκιμίων. Σε αντίθετη περίπτωση, δηλαδή αν η στερεοποίηση ήταν ισότροπη, θα υπήρχε μόνο ογκομετρική παραμόρφωση.

Στα δύο υπο-σχήματα, η διαγώνιος υποδεικνύει την απόλυτη πρόβλεψη, ενώ οι διακεκομμένες γραμμές δείχνουν το εύρος της υπερεκτίμησης ή υποεκτίμησης. Όσον αφορά στη συσσώρευση ογκομετρικών παραμορφώσεων (**Σχήμα 12α**), η σύγκριση κρίνεται συνολικά ικανοποιητική, καθώς ο λόγος των προβλεπόμενων τιμών από το προσομοίωμα προς τις αντίστοιχες εμπειρικές κυμαίνεται μεταξύ 0.5 και 2. Σε όρους διατμητικών παραμορφώσεων, η σύγκριση είναι λιγότερο καλή, παραμένει ωστόσο ικανοποιητική καθώς κυμαίνεται μεταξύ 1/3 και 3, δεδομένου και του μεγάλου εύρους αριθμού κύκλων (έως 300).

IV. ΑΞΙΟΛΟΓΗΣΗ ΑΠΟΚΡΙΣΗΣ ΣΕ ΔΥΝΑΜΙΚΑ ΠΡΟΒΛΗΜΑΤΑ ΣΥΝΟΡΙΑΚΩΝ ΤΙΜΩΝ

Προκειμένου να καταστεί δυνατή η χρήση του σε προβλήματα συνοριακών τιμών, το νέο προσομοίωμα ενσωματώθηκε στους κώδικες πεπερασμένων διαφορών FLAC (Itasca Consulting Group Inc., 2011) και FLAC^{3D} (Itasca Consulting Group Inc., 2012), μέσω της λειτουργίας ενσωμάτωσης προσομοιωμάτων που παρέχουν οι εν λόγω κώδικες στους ίδιους τους χρήστες (User Defined Models – UDMs) με προγραμματισμό σε γλώσσα C++. Η διαδικασία ενσωμάτωσης περιγράφεται αναλυτικά στο **Κεφάλαιο 4** της Διατριβής, και πραγματοποιήθηκε μέσω επέκτασης του αλγορίθμου (μη-πεπλεγμένης) εμπρός-τασικής ολοκλήρωσης Euler με τη μέθοδο των υποβημάτων και αυτόματο έλεγχο λάθους, που είχαν προτείνει για το προσομοίωμα NTUA-SAND οι Andrianopoulos et al. (2010b).

Επομένως στη συνέχεια, πραγματοποιείται το δεύτερο στάδιο αξιολόγησης του προσομοιώματος, σε επίπεδο πλέον προβλημάτων συνοριακών τιμών μεγάλης κλίμακας. Για τον σκοπό αυτό, επιλέχθηκαν προβλήματα δυναμικής φόρτισης με εκδήλωση ρευστοποίησης που είναι από τα πλέον περίπλοκα για το μελετητή μηχανικό. Όπως

παρουσιάζεται με κάθε λεπτομέρεια στο **Κεφάλαιο 6** της Διατριβής, για τη διακρίβωση του προσομοιώματος σε αυτό το επίπεδο έγινε χρήση αποτελεσμάτων δυναμικών δοκιμών φυγοκεντριστή της βιβλιογραφίας σε άμμο Nevada. Συνολικά, έγινε προσομοίωση εννιά (9) προβλημάτων που εντάσσονται σε τέσσερις (4) διαφορετικές κατηγορίες:

(α) σεισμική απόκριση οριζόντιας ρευστοποιήσιμης εδαφικής στρώσης,

(β) πλευρική εξάπλωση ελαφρώς κεκλιμένης ρευστοποιήσιμης εδαφικής στρώσης,

(γ) σεισμική απόκριση συστήματος αβαθούς θεμελίου – ρευστοποιήσιμου εδάφους με διαφορετικές στρωματογραφίες και υπό διαφορετικές διεγέρσεις

(δ) σεισμική απόκριση ομάδας πασσάλων υπό πλευρική εξάπλωση ελαφρώς κεκλιμένης ρευστοποιήσιμης εδαφικής στρώσης.

Τα προβλήματα (α), (β) και (γ) διερευνήθηκαν στον διδιάστατο χώρο (2Δ) με χρήση του λογισμικού *FLAC*, ενώ το πρόβλημα (δ) διερευνήθηκε στον τριδιάστατο χώρο (3Δ) με χρήση του *FLAC*^{3D}. Στον **Πίνακα 3** συνοψίζονται τα προβλήματα συνοριακών τιμών που χρησιμοποιήθηκαν προς αξιολόγηση του νέου προσομοιώματος στην παρούσα Διατριβή.

Καθώς το κύριο ρευστοποιήσιμο έδαφος που χρησιμοποιείται σε όλα τα παραπάνω προβλήματα είναι κοινό (άμμος Nevada σε διαφορετικές τιμές της D_r), σε όλα τα προβλήματα υιοθετήθηκε: (i) κοινή βαθμονόμηση του προσομοιώματος, βασισμένη σε αποτελέσματα εργαστηριακών δοκιμών σε επίπεδο μοναδιαίου στοιχείου (βλ. **Πίνακα 2**), (ii) κοινή αριθμητική μεθοδολογία ανάλυσης (π.χ., συνοριακές συνθήκες, συντελεστής διαπερατότητας εδαφών ανάλογα με την τιμή D_r της άμμου, επιπλέον μικρή αριθμητική απόσβεση), όπως παρουσιάζεται με λεπτομέρεια μόνο στο πρώτο από τα προβλήματα συνοριακών τιμών. Με τον τρόπο αυτό αποτυπώνεται αμιγώς η ικανότητα του προσομοιώματος για γενικευμένη χρήση, να προβλέπει δηλαδή αποτελεσματικά την απόκριση του ίδιου εδάφους, ανεξάρτητα από το εξεταζόμενο πρόβλημα, χωρίς η αποτύπωση αυτή να επηρεάζεται από τη μεθοδολογία ανάλυσης.

Παράλληλα, η επίδραση συγκεκριμένων καταστατικών λειτουργιών του προσομοιώματος, όπως η συσσώρευση διατμητικών παραμορφώσεων μετά την εκδήλωση ρευστοποίησης και η αντιμετώπιση της αριθμητικής «*υπερακόντισης*» της σχέσης τάσης – παραμόρφωσης (*stress – strain overshooting*), που παρουσιάστηκε σε επίπεδο μοναδιαίου στοιχείου στην προηγούμενη ενότητα, εξετάζεται τώρα στοχευμένα σε επίπεδο προβλημά-

των συνοριακών τιμών.

Πίνακας 3: *Προβλήματα συνοριακών τιμών για την αξιολόγηση του νέου προσομοιώματος.*

Κατηγορία προβλήματος	**Πείραμα φυγοκεντριστή**	**Αμμώδη εδάφη**	**Σύνολο αναλύσεων**	**Πρόσθετες αναλύσεις**
Σεισμική απόκριση οριζόντιας ρευστοποιήσιμης εδαφικής στρώσης	Taboada and Dobry (1994a)	άμμος Nevada - D_r = 40%	1	επίδραση τιμής διαπερατότητας
Πλευρική εξάπλωση ελαφρώς κεκλιμένης ρευστοποιήσιμης εδαφικής στρώσης	Taboada and Dobry (1994b)	άμμος Nevada - D_r = 40%	1	επίδραση παραμέτρου L_o
Σεισμική απόκριση συστήματος αβαθούς θεμελίου - ρευστοποιήσιμου εδάφους	Carnevale and Elgamal (1994) Dashti et al. (2009, 2010b) Farrel and Kutter (1994)	άμμος Nevada - D_r = 50%, 60%, 85% - 90% άμμος Monterey - D_r = 85%	6	επίδραση μεθόδου αντιμετώπισης *overshooting*
Σεισμική απόκριση ομάδας πασσάλων υπό πλευρική εξάπλωση ελαφρώς κεκλιμένης ρευστοποιήσιμης εδαφικής στρώσης	Pamuk et al. (2007)	άμμος Nevada - D_r = 40%	1	-

Α. Σεισμική απόκριση οριζόντιας ρευστοποιήσιμης εδαφικής στρώσης

Για την αξιολόγηση του προσομοιώματος στη συγκεκριμένη κατηγορία προβλήματος, έγινε χρήση των πειραματικών αποτελεσμάτων της δοκιμής φυγοκεντριστή No. 1 του προγράμματος VELACS (Taboada and Dobry, 1994). Σε διαστάσεις πρωτοτύπου, στη συγκεκριμένη δοκιμή εξετάστηκε η απόκριση μιας ομοιόμορφης στρώσης ρευστοποιήσιμης άμμου Nevada πάχους 10 m και σχετικής πυκνότητας D_r = 40%. Για τη διάταξη έγινε χρήση εύκαμπτου δοχείου (*laminar box*) πλάτους πρωτοτύπου 22.86 m, ενώ ο υδροφόρος ορίζοντας τοποθετήθηκε 1m πάνω από την στρώση της άμμου. Στο **Σχήμα 13α** παρουσιάζεται ο κάνναβος πεπερασμένων διαφορών που χρησιμοποιήθηκε κατά την ανάλυση, καθώς και η διάταξη των χρησιμοποιούμενων κατά το πείραμα οργάνων μέτρησης πιέσεων πόρων, επιταχύνσεων και μετακινήσεων. Για τον κορεσμό του εδαφικού υλικού χρησιμοποιήθηκε νερό και η διάταξη επιβλήθηκε σε φυγοκεντρική επιτάχυνση μεγέθους 50 g. Η σεισμική διέγερση που επιβλήθηκε στη βάση του δοχείου, σε μονάδες πρωτοτύπου, παρουσιάζεται στο **Σχήμα 13β.**

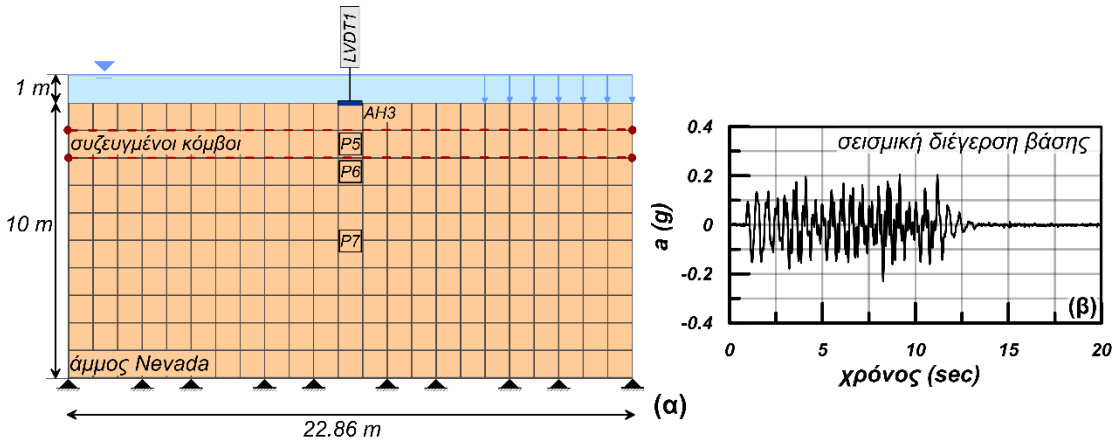

***Σχήμα 13**: (α) Διάταξη της δοκιμής φυγοκεντριστή No. 1 του προγράμματος VELACS (Taboada and Dobry, 1994) και (β) χρονοϊστορία σεισμικής διέγερσης βάσης.*

Λόγω του εύκαμπτου δοχείου, οι μετακινησιακές συνοριακές συνθήκες προσομοιώθηκαν αριθμητικά με τη μέθοδο των συζευγμένων κόμβων, κατά την οποία επιβάλλεται κοινή ταχύτητα στους κόμβους των πλευρικών συνόρων του καννάβου που βρίσκονται στο ίδιο υψόμετρο, ώστε να κινούνται με τον ίδιο τρόπο σαν να ήταν συζευγμένοι. Η στήλη νερού ύψους 1 m πάνω από την εδαφική στρώση προσομοιώθηκε με μια ομοιόμορφη ορθή τάση μεγέθους 9.81 kPa επί της επιφάνειας, ενώ στην ίδια τιμή αρχικοποιήθηκε σε αυτό το σημείο και η πίεση των πόρων. Αρχικά επιτεύχθηκε γεωστατικό πεδίο τάσεων με συντελεστή ουδέτερης ώθησης γαιών K_o = 0.50 και στη συνέχεια ακολούθησε η δυναμική ανάλυση υπό πλήρως συζευγμένες υδρομηχανικά συνθήκες. Κατά τη δυναμική ανάλυση έγινε χρήση μικρής πρόσθετης απόσβεσης τοπικής φύσης (*local damping*) ίσης με 2%, η οποία δρα συμπληρωματικά με την απόσβεση του προσομοιώματος και εξασφαλίζει μη-μηδενική τιμή για μικρές παραμορφώσεις. Ο συντελεστής διαπερατότητας του εδαφικού υλικού, που υιοθετήθηκε, προέκυψε από τον πειραματικά μετρούμενο συντελεστή διαπερατότητας k = $6.5 \cdot 10^{-5}$ - $6.6 \cdot 10^{-5}$ m/sec της άμμου Nevada με D_r = 40% υπό συνθήκες 1 g (Arulmoli et al., 1992), αφού έγινε κατάλληλη προσαρμογή της ώστε να ληφθούν υπόψιν οι περιορισμοί στη ροή του υγρού των πόρων κατά τη διάρκεια της φυγοκέντρισης (Dashti and Bray, 2013, Liu and Dobry, 1997, Tan and Scott, 1985). Συγκεκριμένα, ο τελικά χρησιμοποιούμενος συντελεστής διαπερατότητας είχε τιμή ίση με k' = (50/4) k = $8.25 \cdot 10^{-4}$ m/sec.

Επιπρόσθετα, πέραν της ανάλυσης με σταθερή τιμή συντελεστή διαπερατότητας *k'* (ανάλυση αναφοράς), εξετάστηκε και μία δεύτερη περίπτωση κατά την οποία ο συντελεστής διαπερατότητας *k* δεν παραμένει σταθερός κατά τη διάρκεια της ανάλυσης, αλλά μεταβάλλεται συναρτήσει του χρόνου: $k' = f(t)$. Η τακτική αυτή απαντάται συχνά στη βιβλιογραφία κατά την αριθμητική προσομοίωση του συγκεκριμένου προβλήματος (Andrianopoulos et al., 2010a; Manzari and Arulanandan, 1994) και σχετίζεται με την αύξηση της διαπερατότητας του υλικού με την αύξηση της υπερπίεσης των πόρων, ειδικά όταν φτάνει σε αρχική ρευστοποίηση. Εδώ εξετάζεται ενδεικτικά η περίπτωση κατά την οποία ο συντελεστής διαπερατότητας με αρχική τιμή $k' = 8.25 \cdot 10^{-4}$ m/sec αυξάνεται γραμμικά με το χρόνο έως και 6.7 φορές την στιγμή της αρχικής ρευστοποίησης (t = 1.8 sec) και στη συνέχεια μειώνεται και πάλι γραμμικά έως την αρχική τιμή της *k'* (t = 7.8 sec).

Στο **Σχήμα 14** γίνεται η αξιολόγηση της αριθμητικής μεθοδολογίας μέσω διαφορετικών συγκρίσεων με τα πειραματικά δεδομένα. Συγκεκριμένα, στα **Σχήματα 14α** και **14β** συγκρίνεται η πειραματικά μετρούμενη χρονοϊστορία ανάπτυξης λόγου υπερπιέσεων πόρων $r_u = \Delta u/\sigma_{v,o}$ με την αριθμητικά προβλεπόμενη από το προσομοίωμα. Η ποσότητα Δu συμβολίζει τις αναπτυσσόμενες υπερπιέσεις, ενώ η ποσότητα $\sigma_{v,o}$ την κατακόρυφη αρχική ενεργή γεωστατική τάση πριν την επιβολή της δυναμικής φόρτισης. Συγκρίσεις παρουσιάζονται ενδεικτικά για τις δύο θέσεις των μετρητών πιέσεων πόρων P5 (**Σχήμα 14α**) και P7 (**Σχήμα 14β**), που είναι τοποθετημένα σε βάθη $z \approx$ -1.5 m and -5.0 m, αντίστοιχα, από την επιφάνεια του εδάφους, επί του άξονα συμμετρίας της διάταξης. Οι κόκκινες γραμμές αντιστοιχούν στα αποτελέσματα από την ανάλυση αναφοράς με σταθερή τιμή συντελεστή διαπερατότητας *k'* καθ' όλη τη διάρκεια της ανάλυσης, ενώ οι μπλε γραμμές στην περίπτωση μεταβλητού συντελεστή διαπερατότητας με το χρόνο $k' = f(t)$. Στην περίπτωση του σταθερού συντελεστή διαπερατότητας *k'*, η σύγκριση θεωρείται αρκετά ικανοποιητική και για τα δύο εξεταζόμενα βάθη με τα αριθμητικά αποτελέσματα να προβλέπουν ελαφρώς πιο έντονη ανάπτυξη υπερπίεσης πόρων κατά το πρώτο στάδιο της φόρτισης μέχρι την αρχική ρευστοποίηση. Ωστόσο, ο ρυθμός αποτόνωσής τους δείχνει να προβλέπεται αρκετά ικανοποιητικά από το προσομοίωμα. Αντίστοιχα, τα αποτελέσματα της ανάλυσης όπου $k' = f(t)$ είναι παραπλήσια, με μόνη διαφορά την καθυστέρηση της ανάπτυξης υπερπιέσεων στο πρώτο στάδιο της φόρτισης. Αυτό οφείλεται στην αυξημένη

τιμή του συντελεστή διαπερατότητας, η οποία επιτρέπει μια - έστω μικρή - παράλληλη στράγγιση κατά τη διάρκεια της φόρτισης και επομένως, παρεμποδίζει την ανάπτυξη μεγάλων λόγων r_u, ειδικά στα μεγαλύτερα βάθη.

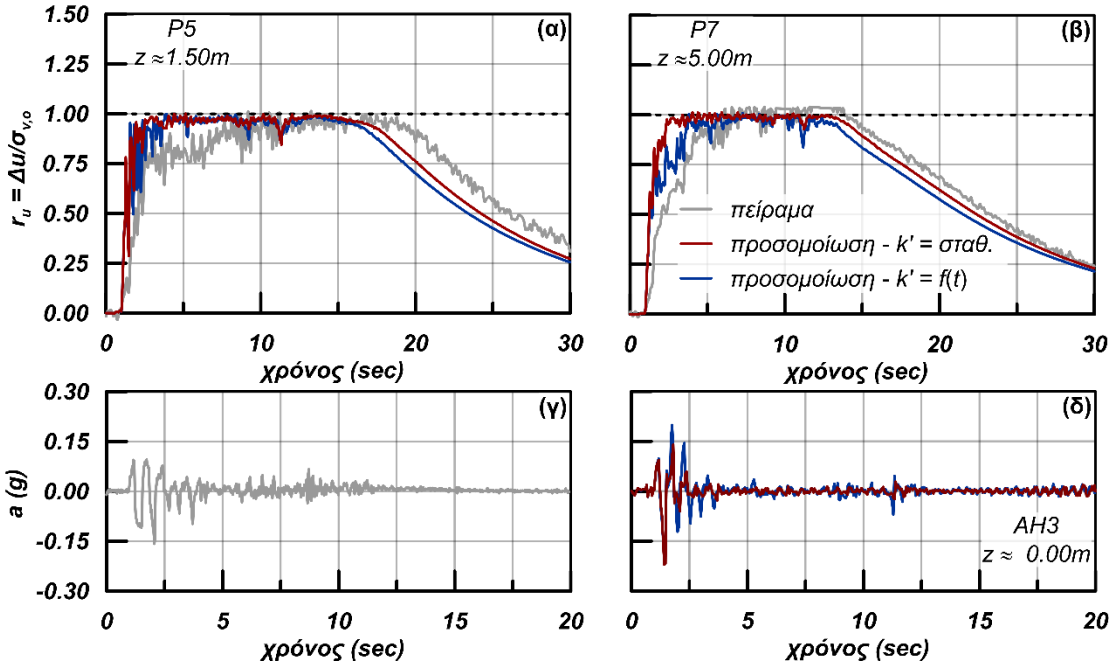

***Σχήμα 14**: Σύγκριση πειραματικών δεδομένων και αριθμητικής προσομοίωσης του πειράματος φυγοκεντριστή No. 1 του προγράμματος VELACS σε όρους: (α), (β) χρονοϊστορίας αναπτυσσόμενου λόγου υπερπιέσεων r_u και (γ), (δ) χρονοϊστορίας οριζόντιας επιτάχυνσης. Πειραματικά δεδομένα από τους Taboada and Dobry (1994).*

Στη συνέχεια, στα **Σχήματα 14γ** και **14δ** γίνεται σύγκριση μεταξύ της πειραματικά μετρούμενης (**Σχήμα 14γ**) και της αριθμητικά προβλεπόμενης (**Σχήμα 14δ**) χρονοϊστορίας οριζόντιας επιτάχυνσης στην επιφάνεια του εδάφους και συγκεκριμένα στη θέση του επιταχυνσιογράφου AH3 στον άξονα συμμετρίας της διάταξης. Και πάλι, η κόκκινη γραμμή στο **Σχήμα 14δ** αντιστοιχεί στην περίπτωση σταθερού *k'*, ενώ η μπλε γραμμή στην περίπτωση μεταβαλλόμενου χρονικά *k' = f(t)*. Με αυτή τη σύγκριση γίνεται φανερό πως τόσο η πειραματική μέτρηση της οριζόντιας επιτάχυνσης, όσο και η αριθμητική πρόβλεψή της δείχνουν εξασθένηση της μετά τη ρευστοποίηση ($r_u \approx 1$). Ωστόσο, σε συμφωνία με τα **Σχήματα 14α** και **14β**, η εξασθένιση αυτή ξεκινάει λίγο νωρίτερα στην αριθμητική ανάλυση απ' ότι στο πείραμα και είναι εντονότερη ειδικά για την περίπτωση του σταθερού συντελεστή διαπερατότητας, λόγω των μεγαλύτερων τιμών r_u κατά τα πρώτα δευτερόλεπτα.

Συνολικά, με βάση τις παραπάνω συγκρίσεις, μπορεί να θεωρηθεί πως το νέο προσομοίωμα προβλέπει αρκετά ικανοποιητικά τη σεισμική απόκριση οριζόντιας ρευστοποιήσιμης εδαφικής στρώσης, χωρίς να χρειάζεται υιοθέτηση μιας χρονικά μεταβαλλόμενης τιμής του συντελεστή διαπερατότητας. Ωστόσο, σε αυτό το σημείο, για λόγους πληρότητας, θα πρέπει να σημειωθεί πως η πρόβλεψη δεν είναι τόσο ικανοποιητική σε αυτή την κατηγορία προβλημάτων, όταν το μέγεθος ενδιαφέροντος είναι η καθίζηση της ελεύθερης επιφάνειας. Αυτό γίνεται κατανοητό, αν κανείς αναλογιστεί πως η καθίζηση του ελεύθερου πεδίου, σε ένα πρόβλημα σαν κι αυτό, δεν προέρχεται λόγω αναπτυσσόμενης διάτμησης, αλλά σχεδόν αποκλειστικά λόγω συσσώρευσης πλαστικών ογκομετρικών παραμορφώσεων κατά τη διάρκεια της στερεοποίησης μετά την εκδήλωση ρευστοποίησης. Η συγκεκριμένη φόρτιση εμπίπτει στην κατηγορία των φορτίσεων που δεν προκαλούν ουσιαστική μεταβολή του αποκλίνοντα λόγου των τάσεων $\boldsymbol{r}$. Συνεπώς, προσομοιώματα τύπου SANISAND (όπως το παρόν) των οποίων το καταστατικό πλαίσιο βασίζεται σε αυτή τη μεταβολή για την πρόβλεψη πλαστικών παραμορφώσεων, υποεκτιμούν σημαντικά (π.χ., κατά 3 φορές) την ανάπτυξη καθιζήσεων στο ελεύθερο πεδίο λόγω στερεοποίησης.

Β. Πλευρική εξάπλωση ελαφρώς κεκλιμένης ρευστοποιήσιμης εδαφικής στρώσης

Για την επαλήθευση του προσομοιώματος στη συγκεκριμένη κατηγορία προβλήματος, έγινε χρήση των πειραματικών αποτελεσμάτων της δοκιμής φυγοκεντριστή No. 2 του προγράμματος VELACS (Taboada and Dobry, 1994b). Η πειραματική διάταξη παρουσιάζει μεγάλη ομοιότητα με αυτήν της δοκιμής No. 1, με μόνη διαφορά πως είναι στραμμένη ωρολογιακά κατά 2^o, ώστε να προσομοιωθεί ως κεκλιμένη. Στο **Σχήμα 15α** παρουσιάζεται ο κάνναβος πεπερασμένων διαφορών που χρησιμοποιήθηκε κατά την ανάλυση, καθώς και η διάταξη επιλεγμένων οργάνων μέτρησης πιέσεων πόρων, επιταχύνσεων και μετακινήσεων που χρησιμοποιήθηκαν κατά το πείραμα. Επιπλέον, στο **Σχήμα 15β** παρουσιάζεται η χρονοϊστορία σεισμικής διέγερσης που επιβλήθηκε στη βάση του δοχείου, σε μονάδες πρωτοτύπου.

Η αριθμητική μεθοδολογία που ακολουθήθηκε είναι ακριβώς όμοια με αυτήν που περιγράφηκε στην **Παράγραφο ΙΙΙ.Α** για την οριζόντια εδαφική στρώση. Η μόνη διαφοροποίηση έγκειται στην προσομοίωση της κεκλιμένης στρώσης και του αντίστοιχου

τασικού πεδίου. Για τον σκοπό αυτό, εφαρμόστηκε στον κάνναβο στραμμένο διάνυσμα βαρυτικής επιτάχυνσης κατά 2° ως προς την κατακόρυφο, με την οριζόντια συνιστώσα του να έχει κατεύθυνση προς τα κατάντη της κεκλιμένης στρώσης.

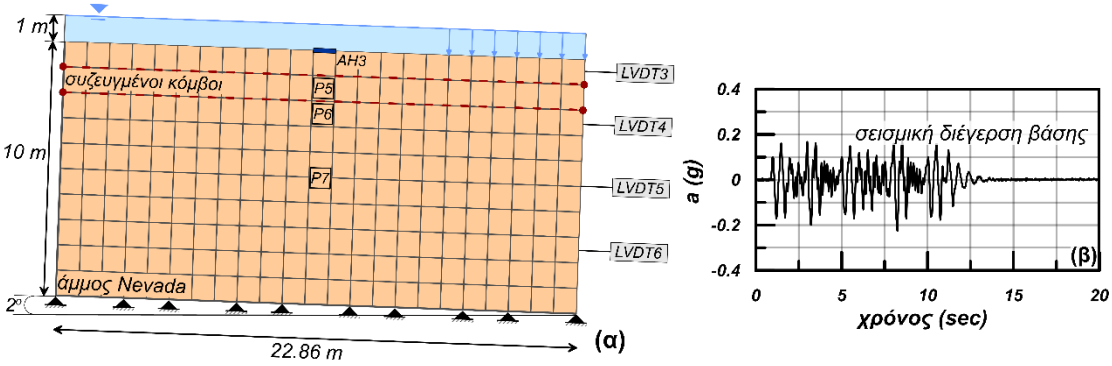

***Σχήμα 15**: (α) Διάταξη της δοκιμής φυγοκεντριστή No. 2 του προγράμματος VELACS (Taboada and Dobry, 1994b) και (β) χρονοϊστορία σεισμικής διέγερσης βάσης.*

Επιπρόσθετα, πέραν της ανάλυσης με τις τιμές των παραμέτρων προσομοιώματος του **Πίνακα 2** (ανάλυση αναφοράς), εξετάστηκε και μία δεύτερη περίπτωση κατά την οποία υπερεκτιμάται καταστατικά η συσσώρευση διατμητικών παραμορφώσεων μετά την αρχική ρευστοποίηση. Αυτό γίνεται μέσω της μεταβολής της τιμής της παραμέτρου L_o, που καθορίζει το ρυθμό εξέλιξης της συνάρτησης f_l και κατά συνέπεια και τη συσσωρευμένη τιμή της που υπεισέρχεται στην Εξ. (26). Συγκεκριμένα, όσο η τιμή της παραμέτρου L_o αυξάνει, τόσο αυξάνεται και η μέγιστη τιμή της συνάρτησης $h_{post\text{-}liq}$, άρα και η μείωση της τάσης για διαστολή μετά τη ρευστοποίηση, κι έτσι κατά συνέπεια αναμένεται μεγαλύτερη συσσώρευση παραμορφώσεων. Έτσι, στην ανάλυση αναφοράς, για την άμμο Nevada υιοθετείται η τιμή του L_o = 750, όπως προέκυψε με βάση τη βαθμονόμηση του προσομοιώματος σε επίπεδο μοναδιαίου στοιχείου (**Πίνακας 2**), ενώ στη δεύτερη ανάλυση θεωρήθηκε η πολύ μεγαλύτερη τιμή για την παράμετρο L_o ίση με 75000 (100 φορές μεγαλύτερη). Έτσι, εξετάζεται ο ρόλος και η σημασία της συγκεκριμένης καταστατικής λειτουργίας, σε επίπεδο πλέον προσομοίωσης προβλήματος μεγάλης κλίμακας, και όχι σε επίπεδο μοναδιαίου στοιχείου.

Στο **Σχήμα 16** γίνεται η αξιολόγηση της αριθμητικής μεθοδολογίας μέσω διαφορετικών συγκρίσεων με τα πειραματικά δεδομένα. Συγκεκριμένα, στα **Σχήματα 16α** και **16β** συγκρίνεται η πειραματικά μετρούμενη χρονοϊστορία ανάπτυξης λόγου

υπερπιέσεων πόρων $r_u = \Delta u/\sigma_{v,o}$ με την αριθμητικά προβλεπόμενη από το προσομοίωμα. Συγκρίσεις παρουσιάζονται ενδεικτικά για τις δύο θέσεις των μετρητών πιέσεων πόρων P5 (**Σχήμα 16α**) και P7 (**Σχήμα 16β**), που είναι τοποθετημένα σε βάθη z ≈ -1.5 m and -5.0 m αντίστοιχα από την επιφάνεια του εδάφους, επί του άξονα συμμετρίας της διάταξης. Οι κόκκινες γραμμές αντιστοιχούν στα αποτελέσματα από την ανάλυση με L_o = 750, όπως έχει προκύψει από τη βαθμονόμηση, ενώ οι μπλε γραμμές αντιστοιχούν στην πολύ μεγαλύτερη τιμή του L_o = 75000. Σε γενικές γραμμές οι συγκρίσεις είναι αρκετά ικανοποιητικές και τα αριθμητικά αποτελέσματα για τις δύο διαφορετικές τιμές του L_o δε διαφέρουν σημαντικά. Συγκεκριμένα, παρόλο που οι αριθμητικές προβλέψεις παρουσιάζουν εντονότερη ανάπτυξη λόγου υπερπιέσεων πόρων στο αρχικό στάδιο της διέγερσης, τόσο οι πειραματικές, όσο και οι αριθμητικές μετρήσεις φθάνουν σε τιμές λόγου $r_u \geq 0.95$ ήδη από τα πρώτα δευτερόλεπτα της διέγερσης και διατηρούνται σε υψηλές (μέγιστες) τιμές μέχρι και τα 14 sec. Εξίσου ικανοποιητικά προβλέπεται και ο ρυθμός αποτόνωσης των υπερπιέσεων μετά το πέρας της δυναμικής φόρτισης, ειδικά για την περίπτωση όπου L_o = 750. Επιπλέον, είναι εμφανές πως σε αυτή την κατηγορία προβλήματος η προσομοίωση παρουσιάζει συχνότερες και εντονότερες αιχμές διαστολικότητας στην χρονοϊστορία του r_u, ιδιαίτερα για την περίπτωση όπου L_o = 75000 όπως θα συζητηθεί παρακάτω.

Στη συνέχεια, στα **Σχήματα 16γ** και **16δ** γίνεται σύγκριση μεταξύ της πειραματικά μετρούμενης (**Σχήμα 16γ**) και της αριθμητικά προβλεπόμενης (**Σχήμα 16δ**) χρονοϊστορίας οριζόντιας επιτάχυνσης στην επιφάνεια του εδάφους και συγκεκριμένα στη θέση του επιταχυνσιογράφου AH3 στον άξονα συμμετρίας της διάταξης. Και πάλι, η κόκκινη γραμμή στο **Σχήμα 16δ** αντιστοιχεί στην περίπτωση της βαθμονομημένης τιμής του L_o = 750, ενώ η μπλε γραμμή στην περίπτωση του L_o = 75000. Σε γενικές γραμμές, η σύγκριση πειραματικών και αριθμητικών αποτελεσμάτων είναι ικανοποιητική και για τις δύο τιμές της παραμέτρου L_o. Ειδικότερα, τόσο τα πειραματικά αποτελέσματα, όσο και η αριθμητική προσομοίωση δεν καταλήγουν σε πλήρη απόσβεση της επιτάχυνσης μετά τη ρευστοποίηση. Το γεγονός αυτό οφείλεται στην ύπαρξη αιχμών διαστολικότητας, που οδηγούν σε μικρότερες μέσες τιμές του λόγου r_u, συγκριτικά με το πρόβλημα της οριζόντιας στρώσης που παρουσιάστηκε στην **Παράγραφο ΙΙΙ.Α**, με τις αιχμές να είναι

μεγαλύτερες για την ανάλυση με L_o = 75000. Αυτό έχει ως αποτέλεσμα την πρόβλεψη αιχμών με μεγαλύτερες τιμές επιτάχυνσης για την ανάλυση με L_o = 75000.

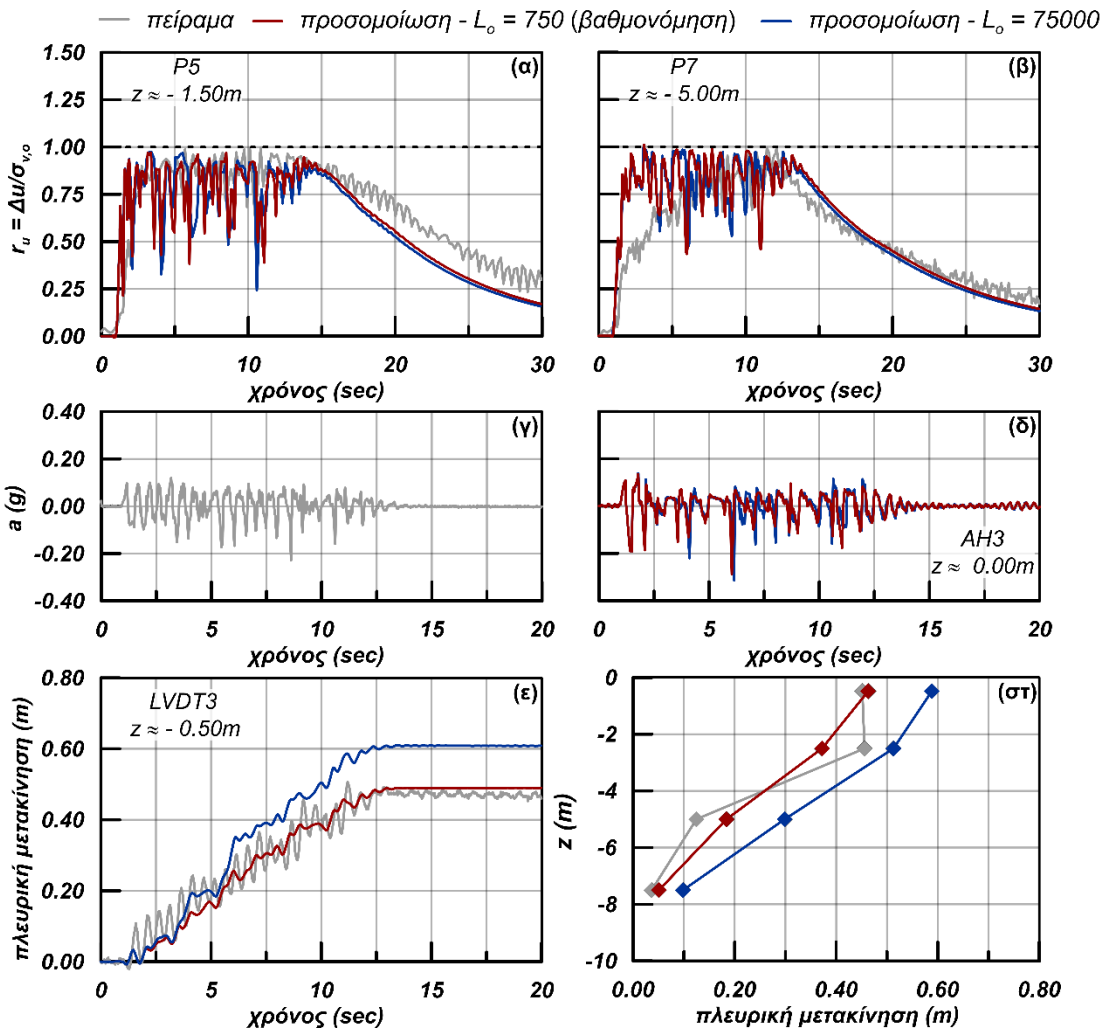

***Σχήμα 16**: Σύγκριση πειραματικών δεδομένων και αριθμητικής προσομοίωσης του πειράματος φυγοκεντριστή No. 2 του προγράμματοος VELACS σε όρους: (α), (β) χρονοϊστορίας αναπτυσσόμενου λόγου υπερπιέσεων r_u, (γ), (δ) χρονοϊστορίας οριζόντιας επιτάχυνσης και (ε), (στ) χρονοϊστορίας και τελικών τιμών πλευρικών μετακινήσεων. Πειραματικά δεδομένα από τους Taboada and Dobry (1994b).*

Τέλος, στα **Σχήματα 16ε** και **16στ** γίνεται σύγκριση πειραματικών και αριθμητικών αποτελεσμάτων σε όρους αναπτυσσόμενης πλευρικής μετακίνησης της κεκλιμένης στρώσης. Συγκεκριμένα, στο **Σχήμα 16ε** παρουσιάζεται η χρονοϊστορία της πλευρικής μετακίνησης σημείου στο κατάντη σύνορο του καννάβου επί της εδαφικής επιφάνειας, όπως καταγράφηκε από το μετρητή μετατόπισης LVDT3 και όπως προβλέπεται από τις

αριθμητικές αναλύσεις. Σε αντιστοιχία με την έως τώρα παρουσίαση, η κόκκινη γραμμή αντιστοιχεί στην περίπτωση της βαθμονομημένης τιμής του $L_o = 750$, ενώ η μπλε γραμμή στην περίπτωση όπου $L_o = 75000$. Η συσσώρευση πλευρικής μετατόπισης είναι πρακτικά γραμμική με το χρόνο με βάση τόσο τα πειραματικά, όσο και τα αριθμητικά αποτελέσματα. Στην περίπτωση του ορθά βαθμονομημένου L_o, η σύγκριση είναι ιδιαίτερα ικανοποιητική. Αντίθετα, στην περίπτωση όπου $L_o = 75000$, υπάρχει μια σαφής υπερεκτίμηση της μετακίνησης. Η υπερεκτίμηση αυτή προέρχεται από την εντονότερη συσσώρευση διατμητικών παραμορφώσεων μετά την αρχική ρευστοποίηση λόγω της μεγαλύτερης τιμής του L_o. Ενδιαφέρον, ακόμη, παρουσιάζει το γεγονός πως, σύμφωνα με τις χρονοϊστορίες του λόγου r_u και της επιτάχυνσης, η διαφοροποίηση στην απόκριση μεταξύ των δύο αυτών αναλύσεων ξεκινά να γίνεται εμφανής από τη χρονική στιγμή των $t \approx 2$ sec και έπειτα, όταν δηλαδή σύμφωνα με τα **Σχήματα 16α** και **16β** εκδηλώθηκε η αρχική ρευστοποίηση. Συμπληρωματική για την επαλήθευση της μεθοδολογίας είναι και η λειτουργία του **Σχήματος 16στ**, όπου η σύγκριση της αναπτυσσόμενης μετακίνησης περιορίζεται σε ένα στιγμιότυπο της χρονοϊστορίας και συγκεκριμένα στη χρονική στιγμή των $t = 12$ sec, όταν η επιβαλλόμενη σεισμική φόρτιση έχει πλέον εξασθενίσει. Μέσω αυτής της παρουσίασης, σύγκριση δε γίνεται μόνο στο σημείο κοντά στην επιφάνεια του εδάφους, αλλά σε ολόκληρη την εδαφική στρώση (σε βάθη z = -0.50, -2.50, -5.00, -7.50 m). Και εδώ, φαίνεται πως για την περίπτωση του βαθμονομημένου $L_o = 750$, η σύγκριση πειραματικών και αριθμητικών αποτελεσμάτων είναι ικανοποιητική με τις αριθμητικές τιμές να ακολουθούν μια πιο γραμμική κατανομή με το βάθος σε σχέση με τις πειραματικές, ενώ όταν $L_o = 75000$ υπάρχει υπερεκτίμηση των μετατοπίσεων σε όλα τα βάθη.

Με βάση τις παραπάνω συγκρίσεις προκύπτει, ότι η ορθή βαθμονόμηση της παραμέτρου L_o είναι αναγκαία για την ακριβή προσομοίωση της εδαφικής απόκρισης, όταν η διέγερση οδηγεί σε ρευστοποίηση, και μάλιστα νωρίς. Από την άλλη, γίνεται σαφές ότι η μεγάλη υπερ-εκτίμηση (κατά 100 φορές) της παραμέτρου L_o οδηγεί σε συγκριτικά σαφώς μικρότερη υπερεκτίμηση των μετατοπίσεων, ή των αιχμών διαστολικότητας και επιτάχυνσης. Συνεπώς, η προσομοίωση της συσσώρευσης παραμορφώσεων μετά την αρχική ρευστοποίηση είναι μια χρήσιμη καταστατική ιδέα, αλλά δεν θεωρείται κρίσιμη σε προβλήματα συνοριακών τιμών, αυτής της κατηγορίας τουλάχιστον.

Γ. Σεισμική απόκριση συστήματος αβαθούς θεμελίου – ρευστοποιήσιμου εδάφους

Σε αυτή την παράγραφο αξιολογείται η ικανότητα του προσομοιώματος να προβλέπει την σεισμική απόκριση συστήματος αβαθούς θεμελίωσης – ρευστοποιήσιμου εδάφους. Για τον σκοπό αυτό αξιοποιήθηκαν τα δεδομένα από τα πειράματα φυγοκεντριστή της δοκιμής No. 12 του προγράμματος VELACS (Carnevale and Elgamal, 1994; Farrel and Kutter, 1994; Krstelj and Prevost, 1994), καθώς και αυτά από αντίστοιχα πειράματα από τους Dashti et al. (2010a; b). Και στις δύο σειρές πειραμάτων χρησιμοποιήθηκε ως ρευστοποιήσιμο έδαφος η άμμος Nevada, ενώ η ειδοποιός διαφορά τους έγκειται στο ότι ενώ στη πειραματική διάταξη του VELACS το θεμέλιο εδράζεται επί ομοιόμορφης ρευστοποιήσιμης στρώσης, στη διάταξη των Dashti et al. (2010a; b) το εδαφικό προφίλ κάτω από το θεμέλιο αποτελείται από δύο στρώσεις της άμμου Nevada σε διαφορετικές ωστόσο τιμές σχετικής πυκνότητας D_r που ανάλογα το καθιστούν ρευστοποιήσιμο ή μη.

Γ1. Θεμέλιο επί ομοιόμορφης ρευστοποιήσιμης εδαφικής στρώσης

Αρχικά, αξιολογείται η απόκριση του προσομοιώματος συγκριτικά με τα πειραματικά αποτελέσματα της δοκιμής No. 12 του προγράμματος VELACS. Η διάταξη της δοκιμής και της οργανομέτρησης παρουσιάζονται στο **Σχήμα 17α**. Πρόκειται για μια στρώση άμμου Nevada πάχους 6 m, σε διαστάσεις πρωτοτύπου, με σχετική πυκνότητα D_r = 60%, η οποία επικαλύπτεται από μια στρώση ιλύος Bonnie πάχους 1 m. Ο υδροφόρος ορίζοντας βρίσκεται σε απόσταση 1 m πάνω από την στρώση της ιλύος. Μια άκαμπτη κατασκευή τετραγωνικής κάτοψης, με ύψος ίσο με 4 m και πλάτος 3 m βρίσκεται θεμελιωμένη σε βάθος 0.50 m κάτω από τη διεπιφάνεια των στρώσεων άμμου και ιλύος, επιβάλλοντας μια τάση έδρασης ίση με 150 kPa. Για τη διάταξη της δοκιμής χρησιμοποιήθηκε δοχείο άκαμπτων τοιχωμάτων (*rigid box*) και επιβλήθηκε φυγοκεντρική επιτάχυνση 100 g. Για τον κορεσμό των εδαφικών υλικών χρησιμοποιήθηκε νερό. Καθώς η συγκεκριμένη δοκιμή εκτελέστηκε από τρία διαφορετικά πανεπιστημιακά εργαστήρια (Carnevale and Elgamal, 1994; Farrel and Kutter, 1994; Krstelj and Prevost, 1994) παρουσιάστηκαν διαφοροποιήσεις στη σεισμική διέγερση βάσης που εφαρμόστηκε σε κάθε μια από αυτές. Για την παρούσα αριθμητική προσομοίωση επιλέχθηκε να εφαρμοσθεί η διέγερση βάσης

της δοκιμής στο Πανεπιστήμιο του RPI (Carnevale and Elgamal, 1994) και η οποία παρουσιάζεται στο **Σχήμα 17β**.

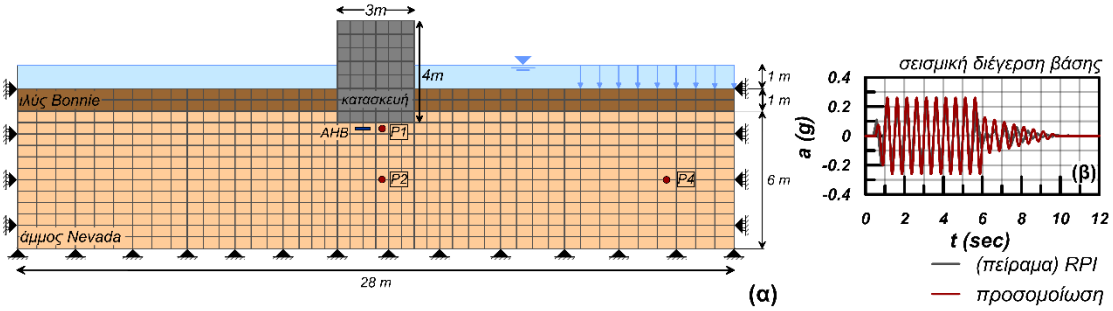

***Σχήμα 17**: (α) Διάταξη της δοκιμής φυγοκεντριστή No. 12 του προγράμματος VELACS και (β) χρονοϊστορία σεισμικής διέγερσης βάσης - RPI (Carnevale and Elgamal, 1994).*

Για την προσομοίωση των μετακινησιακών συνθηκών που επέβαλε το άκαμπτο δοχείο, επιβλήθηκε η χρονοϊστορία της σεισμικής διέγερσης τόσο στο οριζόντιο κάτω σύνορο, όσο και στα πλευρικά κατακόρυφα σύνορα του καννάβου. Καθώς η επιφανειακή στρώση ιλύος δεν αποτελεί ρευστοποιήσιμο υλικό, για την προσομοίωσή της μη-γραμμικής υστερητικής απόκρισής της, χρησιμοποιήθηκε το απλουστευμένο καταστατικό προσομοίωμα Ramberg - Osgood (Ramberg and Osgood, 1943) θεωρώντας γι' αυτή την στρώση ταχύτητα διάδοσης διατμητικών κυμάτων ίση με 60 m/sec για τη βαθμονόμηση του ελαστικού μέτρου διάτμησης και βαθμονομώντας τις υπόλοιπες παραμέτρους του σύμφωνα με τις καμπύλες απομείωσης του μέτρου ελαστικότητας των Vucetic and Dobry (1991) για ένα δείκτη πλαστιμότητας PI = 15%.

Η κατασκευή προσομοιώθηκε ως άκαμπτο ελαστικό στερεό σώμα, όπως φαίνεται στο **Σχήμα 17α**, θεωρώντας τις ελαστικές παραμέτρους του αλουμινίου (ελαστικό μέτρο διάτμησης ίσο με $29 \cdot 10^6$ kPa και ελαστικό μέτρο ογκομετρικής παραμόρφωσης ίσο με $39 \cdot 10^6$ kPa). Από την στιγμή που η αριθμητική ανάλυση πραγματοποιήθηκε στο διδιάστατο χώρο (2Δ), ουσιαστικά υπό συνθήκες επίπεδης παραμόρφωσης, έγινε κατάλληλη προσαρμογή της επιβαλλόμενης τάσης στο έδαφος από το θεμέλιο, ώστε να ληφθεί υπόψιν η τριδιάστατη κατανομή (3Δ) του πραγματικού προβλήματος. Ακολουθώντας την πρόταση των Popescu and Prevost (1993), η οποία έχει εφαρμοσθεί ξανά στη βιβλιογραφία για την προσομοίωση του συγκεκριμένου προβλήματος από τους Andrianopoulos et al. (2010a), και εφαρμόζοντας τη θεωρία των Janbu et al. (1956) για προσαρμογή φορτίου θεμελίου σε

ισοδύναμο φορτίο θεμελιολωρίδας, υπολογίστηκε ισοδύναμη επιβαλλόμενη τάση ίση με 120 kPa. Όσον αφορά την υιοθετούμενη τιμή συντελεστή διαπερατότητας, ακολουθήθηκε η ίδια συλλογιστική όπως περιγράφηκε στην **Παράγραφο ΙΙΙ.Α**, θεωρώντας όμως τιμή $k = 5 \cdot 10^{-5}$ - $5.5 \cdot 10^{-5}$ m/sec για άμμο Nevada με $D_r = 60\%$ υπό συνθήκες 1 g. Επομένως, η τελική τιμή της αμμώδους στρώσης, έπειτα από προσαρμογή για τις συνθήκες φυγοκέντρισης (100 g), προέκυψε ίση με $1.25 \cdot 10^{-3}$ m/sec. Κατά τ' άλλα, ακολουθήθηκε ακριβώς η ίδια αριθμητική μεθοδολογία, όπως περιγράφηκε για τα δύο προηγούμενα προβλήματα συνοριακών τιμών.

Επιπρόσθετα, πέραν της ανάλυσης με τη μεθοδολογία αντιμετώπισης της «*υπερακόντισης*» (overshooting) της σχέσης τάσης-παραμόρφωσης (ανάλυση αναφοράς, με Εξ. 27 και 28), εξετάστηκε και μία δεύτερη περίπτωση κατά την οποία η συγκεκριμένη μεθοδολογία δεν είναι ενεργοποιημένη. Έτσι, στο **Σχήμα 18** γίνεται η αξιολόγηση της αριθμητικής μεθοδολογίας μέσω συγκρίσεων με τα πειραματικά δεδομένα. Συγκεκριμένα, στα **Σχήματα 18α** και **18β** συγκρίνεται η πειραματικά μετρούμενη χρονοϊστορία ανάπτυξης λόγου υπερπιέσεων πόρων $r_u = \Delta u/\sigma_{v,o}$ με την αριθμητικά προβλεπόμενη από το προσομοίωμα. Συγκρίσεις παρουσιάζονται ενδεικτικά για τις δύο θέσεις των μετρητών πιέσεων πόρων P2 (**Σχήμα 18α**) και P4 (**Σχήμα 18β**), που είναι τοποθετημένοι σε βάθος $z \approx -4.0$ m από την επιφάνεια του εδάφους, επί του άξονα συμμετρίας της θεμελίωσης και στο ελεύθερο πεδίο αντίστοιχα. Με κόκκινες γραμμές παρουσιάζονται τα αποτελέσματα της αριθμητικής ανάλυσης με ενσωματωμένη την προαναφερθείσα καταστατική μεθοδολογία, ενώ με μπλε γραμμές παρουσιάζονται τα αποτελέσματα της ανάλυσης όταν αυτή είναι απενεργοποιημένη. Οι συγκρίσεις περιλαμβάνουν πειραματικά αποτελέσματα μόνο από τις δοκιμές φυγοκεντριστή στις οποίες εφαρμόστηκε αντίστοιχη σεισμική διέγερση με αυτή της αριθμητικής ανάλυσης, και συγκεκριμένα αυτά της δοκιμής του RPI (Carnevale and Elgamal, 1994) και της δοκιμής No. 3 του UCD (Farrel and Kutter, 1994). Η σύγκριση των πειραματικών αποτελεσμάτων και αυτών της ανάλυσης αναφοράς είναι αρκετά ικανοποιητική. Συγκεκριμένα, για τη θέση του μετρητή πιέσεων πόρων P2 (**Σχήμα 18α**) προβλέπεται χαμηλή μέγιστη τιμή λόγου $r_u = 0.25 – 0.30$, τόσο κατά τη δοκιμή όσο και ορθά από την αριθμητική ανάλυση. Αντίθετα, στη θέση του μετρητή πιέσεων πόρων P4 (**Σχήμα 18β**) προβλέπεται υψηλότερη μέγιστη τιμή λόγου r_u τόσο κατά τη δοκιμή, όσο και ορθά από την αριθμητική ανάλυση. Η σχεδόν αρμονική διακύμανση του λόγου r_u

συναρτήσει του χρόνου σε αυτή τη θέση, όπως προβλέπεται από την αριθμητική ανάλυση, θεωρείται ότι προέρχεται από τις συγκεκριμένες συνοριακές συνθήκες που έχουν επιβληθεί στα πλευρικά σύνορα του καννάβου για να προσομοιώσουν το άκαμπτο δοχείο.

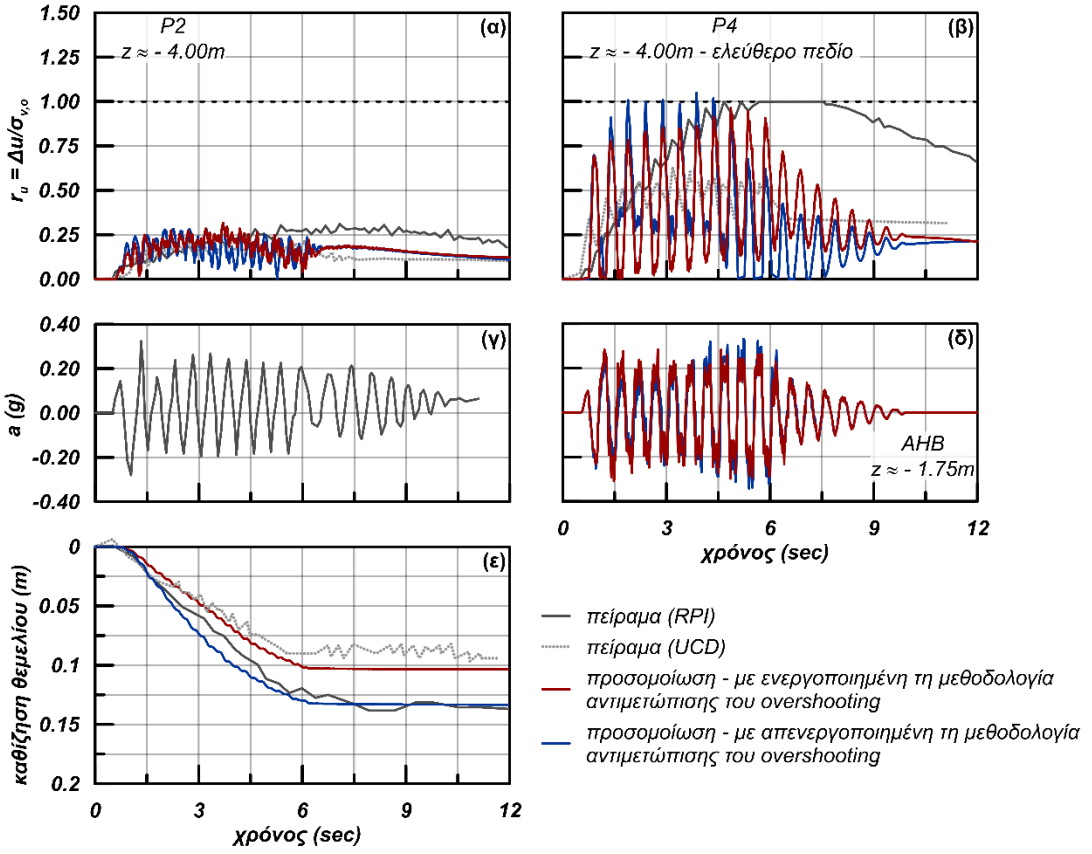

***Σχήμα 18**: Σύγκριση πειραματικών δεδομένων και αριθμητικής προσομοίωσης του πειράματος φυγοκεντριστή No. 12 του προγράμματος VELACS σε όρους: (α), (β) χρονοϊστορίας αναπτυσσόμενου λόγου υπερπιέσεων r_u, (γ), (δ) χρονοϊστορίας οριζόντιας επιτάχυνσης και (ε) χρονοϊστορίας καθίζησης της κατασκευής. Πειραματικά δεδομένα από τους Carnevale and Elgamal (1994) και Farrel and Kutter (1994).*

Επιπλέον, σύγκριση γίνεται και ανάμεσα στις δύο αριθμητικές αναλύσεις - με και χωρίς ενσωμάτωση της μεθοδολογίας για την αντιμετώπιση της «*υπερακόντισης*» της σχέσης τάσης-παραμόρφωσης. Σε γενικές γραμμές, οι διαφορές στα αποτελέσματα των δύο αναλύσεων σε όρους r_u (**Σχήματα 18α** και **18β**) δεν είναι μεγάλες. Ωστόσο, στα πρώτα δευτερόλεπτα της διέγερσης (π.χ., έως t = 3 sec) η ανάλυση χωρίς την ενσωμάτωση της συγκεκριμένης μεθοδολογίας (μπλε γραμμή) προβλέπει ελαφρώς μεγαλύτερες τιμές r_u. Αυτή η τάση μπορεί να αποδοθεί στο ότι οι συνεχείς (μη αναμενόμενες) αντιστροφές φορτίου και συνεπακόλουθες ανανεώσεις του τανυστή r_{ini} όταν η μεθοδολογία είναι

απενεργοποιημένη, δεν επιτρέπουν την απομείωση του ελαστικού μέτρου διάτμησης μέσω της μη-γραμμικότητας που παρέχει η σχέση του Ramberg-Osgood (Ramberg and Osgood, 1943) στην οποία υπεισέρχεται ο όρος $\boldsymbol{r}_{\text{ini}}$, με αποτέλεσμα και τη μη-απομείωση του ελαστικού μέτρου ισότροπης συμπίεσης K_{t}. Αντίθετα, σε μεταγενέστερη φάση της διέγερσης (για $t > 3$ sec) ο λόγος υπερπίεσης των πόρων r_{u} όταν η μεθοδολογία αυτή είναι ανενεργή, παρουσιάζει σταδιακή πτώση, γεγονός που συσχετίζεται με την αυξημένη διαστολικότητα που παρουσιάζεται στο πρόβλημα, όπως συζητείται στη συνέχεια.

Στα **Σχήματα 18γ** και **18δ** γίνεται σύγκριση μεταξύ της πειραματικά μετρούμενης (**Σχήμα 18γ**) και της αριθμητικά προβλεπόμενης (**Σχήμα 18δ**) χρονοϊστορίας οριζόντιας επιτάχυνσης στην περιοχή κάτω από το θεμέλιο και συγκεκριμένα στη θέση του επιταχυνσιογράφου ΑΗΒ στον άξονα συμμετρίας του θεμελίου. Και πάλι, η κόκκινη γραμμή στο **Σχήμα 18δ** αντιστοιχεί στην περίπτωση που η μεθοδολογία για την αντιμετώπιση της «*υπερακόντισης*» της σχέσης τάσης-παραμόρφωσης είναι ενεργοποιημένη, ενώ η μπλε γραμμή στην περίπτωση που είναι ανενεργή. Τα πειραματικά αποτελέσματα στο **Σχήμα 18γ** προέρχονται από τη δοκιμή του πανεπιστημίου RPI (Carnevale and Elgamal, 1994), καθώς είναι τα μόνα διαθέσιμα σε όρους επιτάχυνσης. Μετά από σύγκριση, είναι φανερό πώς τόσο τα πειραματικά, όσο και τα αριθμητικά αποτελέσματα δεν παρουσιάζουν απόσβεση της επιτάχυνσης κάτω από την κατασκευή, γεγονός που αποδίδεται στη μη-ρευστοποίηση του εδάφους. Οι μέγιστες τιμές (των αιχμών) στη χρονοϊστορία της επιτάχυνσης, όπως έχουν καταγραφεί πειραματικά, προβλέπονται από την αριθμητική ανάλυση αρκετά ικανοποιητικά. Και πάλι, παρατηρεί κανείς πως, κατά τη δεύτερη φάση της διέγερσης ($t > 3$ sec), η ανάλυση με την απενεργοποιημένη μεθοδολογία αντιμετώπισης της «*υπερακόντισης*» οδηγεί σε ελαφρώς μεγαλύτερες τιμές επιτάχυνσης, σε συμφωνία με όσα συζητήθηκαν παραπάνω.

Τέλος, στο **Σχήμα 18ε** γίνεται σύγκριση πειραματικών και αριθμητικών αποτελεσμάτων σε όρους αναπτυσσόμενης καθίζησης της κατασκευής κατά τη διάρκεια της διέγερσης. Αριθμητικά αποτελέσματα παρουσιάζονται με και χωρίς την ενσωμάτωση της προαναφερθείσας μεθοδολογίας, τηρώντας τη γνωστή έως τώρα χρωματική διαφοροποίηση. Και για αυτή τη σύγκριση, τα πειραματικά αποτελέσματα προέρχονται μόνο από τις δοκιμές φυγοκεντριστή στις οποίες εφαρμόστηκε αντίστοιχη σεισμική διέγερση με αυτή που εφαρμόστηκε στην αριθμητική ανάλυση, και συγκεκριμένα αυτά της

δοκιμής του RPI (Carnevale and Elgamal, 1994) και της δοκιμής No. 3 του UCD (Farrel and Kutter, 1994), κατ' αντιστοιχία με τα **Σχήματα 18α** και **18β**. Η σύγκριση είναι, γενικά, ικανοποιητική και σε συμφωνία με τα εν λόγω Σχήματα. Συγκρίνοντας αμιγώς τα αριθμητικά αποτελέσματα μεταξύ τους, προκύπτει πως όταν δεν εφαρμόζεται η μεθοδολογία αντιμετώπισης της «*υπερακόντισης*» της σχέσης τάσης-παραμόρφωσης (μπλε καμπύλη) ο ρυθμός συσσώρευσης της καθίζησης υπερεκτιμάται κατά τη διάρκεια της ισχυρής φάσης της διέγερσης, με αποτέλεσμα ελαφρώς μεγαλύτερη τελική τιμή καθίζησης. Η τάση αυτή παρουσιάζεται πιο έντονη στην πρώτη φάση της διέγερσης ($t < 3$ sec), όπου, σύμφωνα με τα **Σχήματα 18α και 18β**, επικρατούν και συγκριτικά υψηλότεροι λόγοι r_u, ενώ στη συνέχεια ο ρυθμός συσσώρευσης μειώνεται σημαντικά. Αποτέλεσμα αυτής της αυξημένης τάσης για καθίζηση και της μεγαλύτερης τελικής τιμής της, είναι η αυξημένη διαστολικότητα στην περιοχή κάτω από την κατασκευή και η αντιστοιχούσα μειωμένη τιμή του λόγου υπερπίεσης των πόρων στα **Σχήματα 18α και 18β**.

Γ2. Θεμέλιο επί δίστρωτου εδάφους με ρευστοποιήσιμη στρώση

Στη συνέχεια, αξιολογείται η απόκριση του προσομοιώματος συγκριτικά με τα αποτελέσματα δοκιμής φυγοκεντριστή T3-50 από τη σειρά πειραμάτων των Dashti et al. (2010a; b). Συγκεκριμένα, επιλέχθηκε η διάταξη που απεικονίζεται στο **Σχήμα 19α**. Πρόκειται για ένα εδαφικό σχηματισμό που, σε διαστάσεις πρωτοτύπου, αποτελείται από μία στρώση μέσης πυκνότητας ($D_r \approx 50\%$) άμμου Nevada πάχους 3 m, η οποία υπέρκειται μιας στρώσης πολύ πυκνής άμμου Nevada ($D_r \approx 85$ - 90%) πάχους 21 m. Η στρώση μέσης πυκνότητας 3 m, επικαλύπτεται από μία στρώση πυκνής άμμου Monterey ($D_r \approx 85\%$) πάχους 2 m, ενώ ο υδροφόρος ορίζοντας βρίσκεται σε βάθος 1 m από την επιφάνεια του εδάφους. Η εν λόγω δοκιμή περιλαμβάνει 3 τύπους μεταλλικών και αλουμινένιων κατασκευών διαφορετικών διαστάσεων και επιβαλλόμενων τάσεων έδρασης στο έδαφος, τοποθετημένων επί άκαμπτων πλακών θεμελίωσης και σε επαρκώς μεγάλες αποστάσεις μεταξύ τους, ώστε να μην αλληλεπιδρούν και να μπορούν να προσομοιωθούν αριθμητικά ανεξάρτητα (Dashti and Bray, 2013).

Εδώ, η αριθμητική προσομοίωση επικεντρώνεται στην κατασκευή BL. Η συγκεκριμένη κατασκευή προσεγγίζει την απόκριση ενός μονοβάθμιου ταλαντωτή ύψους 5 m, θεμελιωμένου επί πλάκας θεμελίωσης πλάτους $B = 6$ m και μήκους $L = 9$ m, η οποία

είναι εγκιβωτισμένη σε βάθος 1 m από την επιφάνεια εντός της άμμου Monterey και επιβάλλει στο έδαφος τάση έδρασης 80 kPa. Για τη διάταξη χρησιμοποιήθηκε εύκαμπτο δοχείο (*laminar box*) και επιβλήθηκε φυγοκεντρική επιτάχυνση μεγέθους 55 g. Για τον κορεσμό του εδαφικού υλικού χρησιμοποιήθηκε κατάλληλο υγρό με ιξώδες 22 φορές μεγαλύτερο από αυτό του νερού. Οι μετρήσεις του πειράματος έγιναν με σειρά οργάνων τοποθετημένων εντός της διάταξης, κάποια από τα οποία παρουσιάζονται στο **Σχήμα 19α**. Η επιβαλλόμενη χρονοϊστορία σεισμικής διέγερσης (**Σχήμα 19β**) στη βάση της διάταξης αποτελεί μία κλιμακωμένη εκδοχή της συνιστώσας στη διεύθυνση Βορρά–Νότου σε βάθος 83 m από την καταγραφή στο νησί Kobe της Ιαπωνίας, κατά το σεισμό του Kobe το 1995, με μέγιστη επιτάχυνση 0.15g.

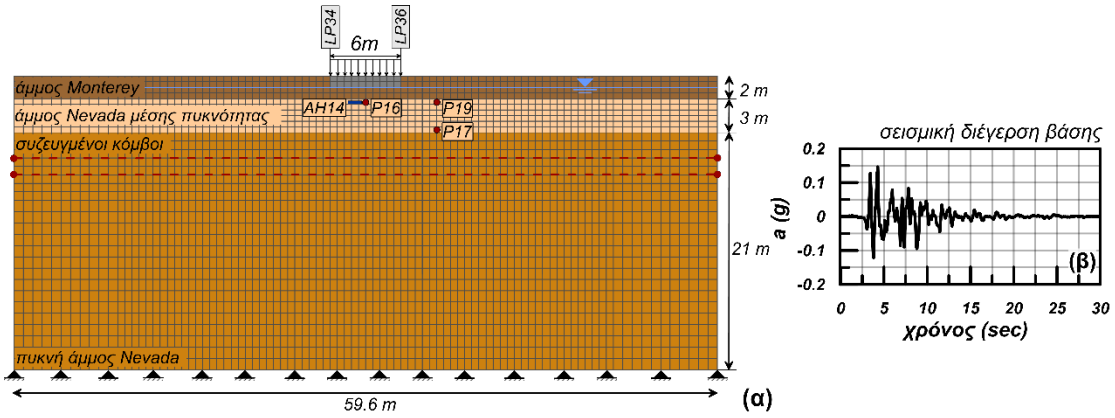

***Σχήμα 19**: (α) Διάταξη του καννάβου πεπερασμένων διαφορών και (β) χρονοϊστορία σεισμικής διέγερσης βάσης (Dashti et al., 2010a; b; Dashti and Bray, 2013).*

Η βάση του αριθμητικού καννάβου ακολουθεί την επιβαλλόμενη σεισμική διέγερση, ενώ στα πλευρικά σύνορα εφαρμόστηκε η συνοριακή συνθήκη των συζευγμένων κόμβων, ώστε να προσομοιωθούν οι μετακινησιακοί περιορισμοί του εύκαμπτου δοχείου. Η πλάκα θεμελίωσης προσομοιώθηκε ως άκαμπτο ελαστικό στερεό σώμα, υιοθετώντας τα μέτρα ελαστικότητας του αλουμινίου. Η επιβαλλόμενη τάση επί του εδάφους από την υπερκείμενη κατασκευή επιβλήθηκε μέσω ομοιόμορφης τάσης επί της πλάκας. Η προσομοίωση αυτή, αν και απλουστευτική, θεωρείται πως δεν επηρεάζει ουσιαστικά την απόκριση δεδομένης της σχετικά μικρής λυγηρότητας της κατασκευής (π.χ. Bullock et al., 2019; Dashti et al., 2009; Karimi et al., 2018) και της μικρής επίδρασης της αλληλεπίδρασης εδάφους-κατασκευής σε προβλήματα ρευστοποίησης (π.χ. Karamitros et

al., 2013). Επιπλέον, εξετάστηκε η πιθανή ανάγκη για απομείωση της επιβαλλόμενης τάσης λόγω προσομοίωσης ενός τριδιάστατου προβλήματος (3Δ) ως διδιάστατο (2Δ). Με βάση τη μεθοδολογία των Janbu et al. (1956) που χρησιμοποιήθηκε και στο πρόβλημα της **Παραγράφου ΙΙΙ.Γ1**, πέρα από τις διαστάσεις της κατασκευής, στον υπολογισμό του απομειωτικού συντελεστή υπεισέρχεται και το πάχος της συμπιεστής στρώσης κάτω από το θεμέλιο, όπου αναμένονται να εκδηλωθούν οι καθιζήσεις κατά τη φόρτιση. Στο παρόν πρόβλημα, κάτω από το θεμέλιο βρίσκεται μία στρώση ρευστοποιήσιμης άμμου μέσης πυκνότητας ($D_r \approx 50\%$) και από κει και κάτω μια στρώση πολύ πυκνής άμμου ($D_r \approx 85$ - 90%) που δεν αναμένεται να ρευστοποιηθεί (βλ. διαφορά στην αντοχή στο **Σχήμα 10β**). Δεδομένου του μικρού πάχους (μισό από το πλάτος του θεμελίου) της ρευστοποιήσιμης στρώσης, που αποτελεί και τη συμπιεστή στρώση όπου αναμένεται να αναπτυχθεί το συντριπτικά μεγαλύτερο ποσοστό των καθιζήσεων, η ως άνω μεθοδολογία υποδεικνύει πως δεν απαιτείται πρακτικά απομείωση του επιβαλλόμενου φορτίου. Επισημαίνεται επίσης ότι η άμμος Monterey προσομοιώθηκε και αυτή με το νέο προσομοίωμα, το οποίο βαθμονομήθηκε με βάση τα εργαστηριακά αποτελέσματα ανακυκλικής φόρτισης των Wu et al. (2004), και οι παράμετροι που χρησιμοποιήθηκαν φαίνονται στον **Πίνακα 2**. Όσον αφορά στην τιμή του συντελεστή διαπερατότητας που χρησιμοποιήθηκε κατά την αριθμητική ανάλυση, ακολουθήθηκε η ίδια συλλογιστική όπως και στα προηγούμενα προβλήματα λαμβάνοντας υπόψιν τη διαπερατότητα των εδαφών μετρούμενη σε συνθήκες 1 g ($k = 6 \cdot 10^{-5}$ m/sec για τη μέσης πυκνότητας άμμος Nevada, $k = 2.25 \cdot 10^{-5}$ m/sec για την πυκνή άμμος Nevada, $k = 5.29 \cdot 10^{-4}$ m/sec – για την πυκνή άμμο Monterey) και τη φυγοκεντρική επιτάχυνση (55 g). Επιπλέον αυτών, στο συγκεκριμένο πρόβλημα λήφθηκε υπόψιν και το αυξημένο, κατά 22 φορές, ιξώδες του υγρού των πόρων σε σχέση με αυτό του νερού. Επομένως, οι τελικές τιμές του συντελεστή διαπερατότητας για τα επιμέρους υλικά προέκυψαν πολλαπλασιάζοντας τις μετρημένες τιμές σε συνθήκες 1 g επί έναν συντελεστή ίσο με (55/22) και στη συνέχεια διαιρώντας δια 4, ώστε να ληφθούν υπόψιν οι περιορισμοί στη ροή του υγρού των πόρων κατά τη διάρκεια της φυγοκέντρισης. Πέραν αυτών, ακολουθήθηκε η ίδια αριθμητική μεθοδολογία, όπως περιγράφηκε για όλα τα προηγούμενα προβλήματα συνοριακών τιμών.

Στο **Σχήμα 20** γίνεται αξιολόγηση της αριθμητικής μεθοδολογίας μέσω συγκρίσεων με τα πειραματικά δεδομένα. Συγκεκριμένα, στα **Σχήματα 20α** και **20β** συγκρίνεται η

πειραματικά μετρούμενη χρονοϊστορία λόγου υπερπιέσεων πόρων $r_u = \Delta u/\sigma_{v,o}$ με την αριθμητικά προβλεπόμενη από το προσομοίωμα. Συγκρίσεις παρουσιάζονται ενδεικτικά για τις δύο θέσεις των μετρητών πιέσεων πόρων P16 (**Σχήμα 20α**) και P17 (**Σχήμα 20β**), που είναι τοποθετημένοι στο άνω όριο της ρευστοποιήσιμης άμμου Nevada κάτω από το θεμέλιο και στο κάτω όριο της ρευστοποιήσιμης άμμου Nevada στο ελεύθερο πεδίο, αντίστοιχα. Σε γενικές γραμμές η σύγκριση είναι ικανοποιητική, με το προσομοίωμα να προβλέπει σωστά τη μη-εκδήλωση ρευστοποίησης στην περιοχή κάτω από το θεμέλιο (P16), καθώς και την ανάπτυξη και, στη συνέχεια, την αποτόνωση του λόγου υπερπιέσεων r_u στο ελεύθερο πεδίο (P17). Έπειτα, γίνεται σύγκριση μεταξύ της πειραματικά μετρούμενης (**Σχήμα 20γ**) και της αριθμητικά προβλεπόμενης (**Σχήμα 20δ**) χρονοϊστορίας οριζόντιας επιτάχυνσης στην περιοχή κάτω από την κατασκευή και συγκεκριμένα στη θέση του επιταχυσνιογράφου AH14 στον άξονα συμμετρίας του θεμελίου, εντός της μέσης πυκνότητας άμμου Nevada. Και εδώ η σύγκριση είναι αρκετά καλή, με το προσομοίωμα ορθά να μην προβλέπει πλήρη απόσβεση της επιτάχυνσης, καθώς δεν έχει εκδηλωθεί πλήρης ρευστοποίηση. Αντίστοιχα, στο **Σχήμα 20ε** συγκρίνεται η πειραματικά μετρούμενη και η αριθμητικά προβλεπόμενη χρονοϊστορία καθίζησης της κατασκευής κατά τη διάρκεια της διέγερσης. Τα αριθμητικά αποτελέσματα συγκρίνονται ικανοποιητικά με τα πειραματικά, ειδικά κατά τη φάση της ισχυρής διέγερσης (έως t = 10 sec), με το προσομοίωμα ωστόσο να υποεκτιμά ελαφρώς την τελική καθίζηση. Τέλος, στο **Σχήμα 20στ** παρουσιάζεται ο μηχανισμός παραμόρφωσης του εδάφους μέσω του παραμορφωμένου καννάβου με επίθεση ισοκαμπυλών συσσωρευμένης διατμητικής παραμόρφωσης, όπως προέκυψε από την ανάλυση μετά το τέλος της διέγερσης.

Ο μηχανισμός παραμόρφωσης είναι διατμητικού τύπου, με την κατασκευή να εισχωρεί εντός της μέσης πυκνότητας στρώσης άμμου με μειωμένη αντοχή. Επιπλέον, φαίνεται καθαρά πως ο μηχανισμός και η αναπτυσσόμενη παραμόρφωση περιορίζονται σχεδόν αποκλειστικά εντός της στρώσης αυτής, στην οποία αναπτύχθηκαν κάποιες υπερπιέσεις πόρων που αύξησαν περαιτέρω τη συμπιεστότητά της σε σχέση με την υποκείμενη πυκνή στρώση. Επιπλέον, η εικόνα αυτή επιβεβαιώνει την παραδοχή που έγινε κατά την κατάστρωση της αριθμητικής ανάλυσης, για το ότι η συμπιεστή στρώση είναι πρακτικώς μόνο η στρώση της μέσης πυκνότητας, γεγονός που υπαγόρεψε τη μη-αναγκαιότητα απομείωσης του φορτίου του θεμελίου κατά τη μετάβαση από τις

πραγματικές τριδιάστατες (3Δ) συνθήκες του προβλήματος σε διδιάστατες (2Δ) συνθήκες προσομοίωσης.

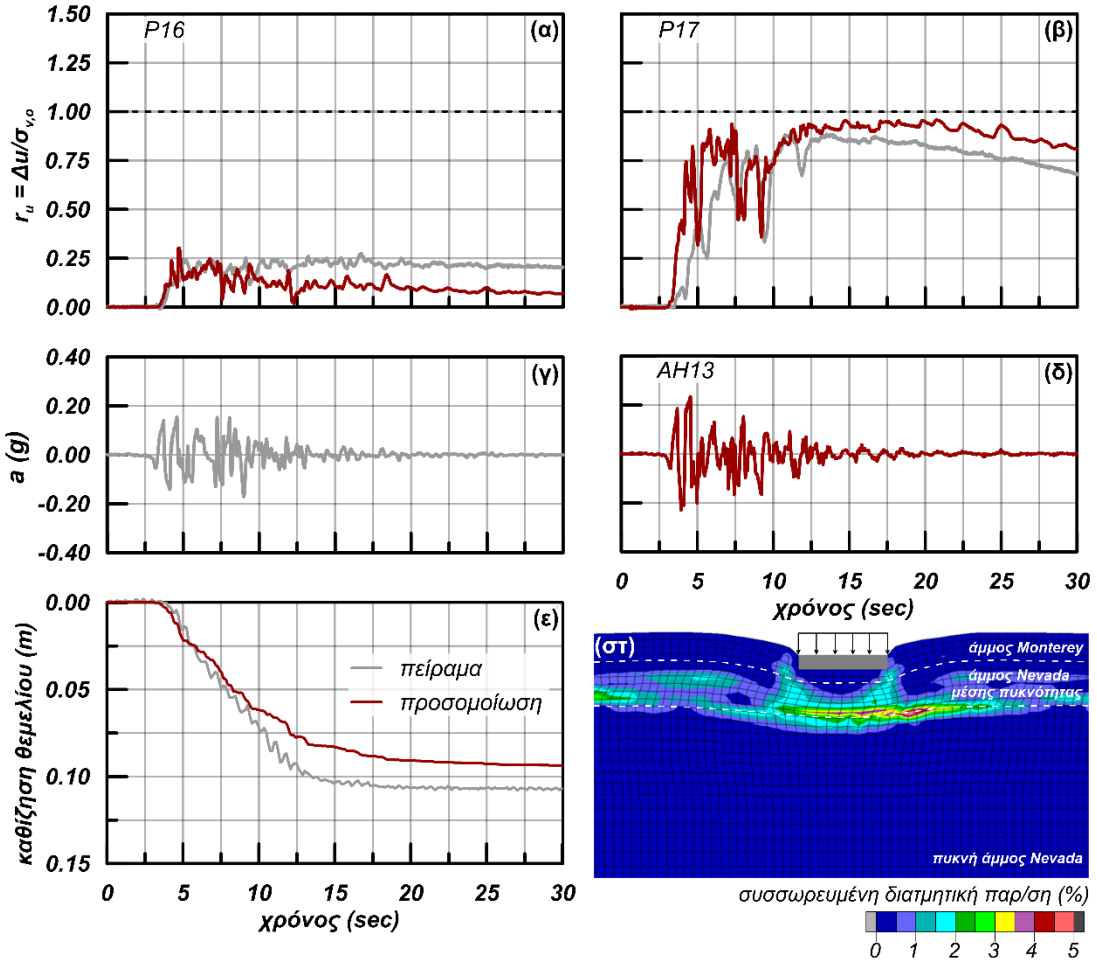

Σχήμα 20*: Σύγκριση πειραματικών δεδομένων και αριθμητικής προσομοίωσης του πειράματος φυγοκεντριστή των Dashti et al. (2010b) σε όρους: (α), (β) χρονοϊστορίας αναπτυσσόμενου λόγου υπερπιέσεων* r_u*, (γ), (δ) χρονοϊστορίας οριζόντιας επιτάχυνσης και (ε) χρονοϊστορίας καθίζησης της κατασκευής. (στ) Ισοκαμπύλες συσσωρευμένης διατμητικής παραμόρφωσης και παραμορφωμένος κάνναβος στο τέλος της αριθμητικής ανάλυσης.*

Γ3. Σύνοψη αναλύσεων για αβαθή θεμέλια επί εδάφους με ρευστοποιήσιμη στρώση

Συμπληρωματικά, για κάθε μια από τις κατηγορίες προβλημάτων που περιγράφηκαν στις **Παραγράφους ΙΙΙ.Γ1** και **ΙΙΙ.Γ2,** εκτελέστηκαν παραμετρικές αναλύσεις με στόχο την αξιολόγηση της ακρίβειας του προσομοιώματος (με την ίδια βαθμονόμηση και αριθμητική μεθοδολογία) να αποτυπώνει την επίδραση παραμέτρων, όπως το μέγεθος της επιβαλλόμενης σεισμικής διέγερσης και το πάχος της ρευστοποιήσιμης στρώσης. Η

αξιολόγηση έγινε ως προς την καθίζηση του θεμελίου, δηλαδή το πλέον σημαντικό μέγεθος από απόψεως επιτελεστικού σχεδιασμού γεωκατασκευών (performance-based design). Οι παραμετρικές αναλύσεις δεν έγιναν τυφλά, αλλά ορίσθηκαν με βάση δοκιμές φυγοκεντριστή που είχαν εκτελεστεί από τους ίδιους ερευνητές ως παραλλαγές των δοκιμών που παρουσιάστηκαν στις προηγούμενες 2 παραγράφους. Συγκεκριμένα, για τη δοκιμή φυγοκεντριστή No. 12 του προγράμματος VELACS (**Παράγραφος ΙΙΙ.Γ1**) εξετάστηκαν για την ίδια διάταξη σεισμικές διεγέρσεις 12 κύριων κύκλων φόρτισης (αντί για 10) και μέγιστης επιτάχυνσης a_{max} ίσης με 0.32 g και 0.37 g (αντί για 0.26 g), ενώ η συχνότητα παρέμεινε ίση με 2 Hz. Τα αποτελέσματα της καθίζησης από τις αναλύσεις συγκρίθηκαν με αυτά των Carnevale and Elgamal (1994) και Farrel and Kutter (1994) για αντίστοιχες διεγέρσεις. Επιπλέον, για τη δοκιμή φυγοκεντριστή των Dashti et al. (2010b) εκτελέστηκαν επίσης 2 συμπληρωματικές δοκιμές. Η μία αναφέρεται στην ίδια ακριβώς διάταξη με αυτήν που παρουσιάστηκε στην **Παράγραφο ΙΙΙ.Γ2**, μόνο που η κλιμάκωση της επιβαλλόμενης σεισμική διέγερσης είναι τέτοια που να αντιστοιχεί σε μέγιστη επιτάχυνση a_{max} ίση με 0.38 g (αντί για 0.15 g), ενώ η δεύτερη ανάλυση διατηρεί τη σεισμική διέγερση του **Σχήματος 19β**, αναφέρεται όμως σε στρωματογραφία όπου το πάχος της ρευστοποιήσιμης στρώσης H_{liq} είναι πλέον 6 m (αντί για 3 m). Τα αποτελέσματα αυτών των αναλύσεων σε όρους καθίζησης θεμελίου συγκρίθηκαν με τα σχετικά πειράματα των Dashti et al. (2010b).

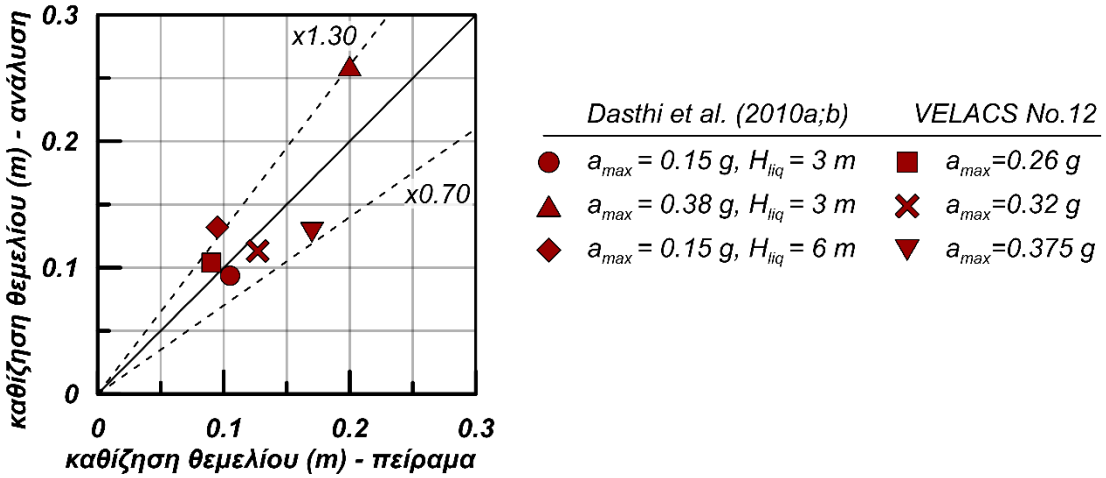

***Σχήμα 21**: Σύγκριση πειραματικών δεδομένων από δοκιμές φυγοκεντριστή και αριθμητικών αποτελεσμάτων καθιζήσεων (αβαθών) θεμελίων πλάτους B = 3 και 6 m επί ρευστοποιήσιμης άμμου Nevada μέσης σχετικής πυκνότητας (D_r = 40 - 85%) και πάχους H_{liq} = 3 και 6 m, υπό σεισμικές διεγέρσεις με μέγιστη επιτάχυνση a_{max} = 0.15 έως 0.38 g .*

Επομένως, στο **Σχήμα 21** παρουσιάζεται συγκεντρωτικά μια σύγκριση όλων των αριθμητικών αποτελεσμάτων σε όρους καθίζησης θεμελίων με τα αντίστοιχα πειραματικά αποτελέσματα από 6 δοκιμές φυγοκεντριστή. Η σύγκριση δείχνει ικανοποιητική ακρίβεια (± 30%) στην εκτίμηση της καθίζησης θεμελίων σε καθεστώς ρευστοποίησης.

Δ. Σεισμική απόκριση ομάδας πασσάλων υπό πλευρική εξάπλωση ελαφρώς κεκλιμένης ρευστοποιήσιμης εδαφικής στρώσης

Σε αυτή την παράγραφο αξιολογείται η ικανότητα του προσομοιώματος να προβλέπει την σεισμική απόκριση ομάδας πασσάλων που βρίσκεται σε περιβάλλον πλευρικής εξάπλωσης μιας ελαφρώς κεκλιμένης ρευστοποιήσιμης εδαφικής στρώσης. Στην ουσία, πρόκειται για μια σαφώς πιο σύνθετη εκδοχή του προβλήματος που παρουσιάστηκε στην **Παράγραφο ΙΙΙ.Β**, καθώς δεν επικρατούν πλέον συνθήκες ελεύθερου πεδίου λόγω της ύπαρξης των πασσάλων εντός του εδάφους. Για την αξιολόγηση χρησιμοποιήθηκαν τα αποτελέσματα του πειράματος φυγοκέντρισης των Pamuk et al. (2007).

Συγκεκριμένα, πρόκειται για έναν εδαφικό σχηματισμό που, σε διαστάσεις πρωτοτύπου, αποτελείται από μία στρώση χαλαρής ($D_r \approx 40\%$) άμμου Nevada πάχους 6 m, η οποία βρίσκεται ανάμεσα σε δύο στρώσεις ελαφρώς σιμεντοποιημένης άμμου, πάχους 2 m η κάθε μία. Ο υδροφόρος ορίζοντας βρίσκεται επί της εδαφικής επιφάνειας και για τον κορεσμό χρησιμοποιήθηκε νερό. Για τη διάταξη χρησιμοποιήθηκε εύκαμπτο δοχείο (*laminar box*) μήκους 35.5 m και πλάτους 17.5 m, σε διαστάσεις πρωτοτύπου. Στο κέντρο της διάταξης βρίσκεται τοποθετημένη ομάδα τεσσάρων πασσάλων από πλαστικό, διαμέτρου D = 0.60 m και ακαμψίας EI = 8100 kNm^2 ο καθένας, συνδεδεμένων με κεφαλόδεσμο (αγνώστου υλικού) διαστάσεων 3 m x 3 m x 0.70 m στην κορυφή τους. Οι πάσσαλοι είναι διατεταγμένοι σε κάθετες αποστάσεις 3D μεταξύ τους και D από τα σύνορα του κεφαλόδεσμου.

Η διάταξη, αντίστοιχα με αυτήν της **Παραγράφου ΙΙΙ.Β**, είναι στραμμένη ωρολογιακά κατά 2^o, ώστε να είναι ελαφρώς κεκλιμένη και υποβλήθηκε σε φυγοκεντρική επιτάχυνση μεγέθους 50 g. Δεδομένης της συμμετρίας του προβλήματος (τέσσερις πάσσαλοι με κεφαλόδεσμο τοποθετημένοι κεντρικά στο δοχείο και επιβαλλόμενη σεισμική διέγερση βάσης σε μία διεύθυνση), επιλέχθηκε να προσομοιωθεί το μισό πρόβλημα στο *FLAC*^{3D}.

Στα **Σχήματα 22α** έως **22γ** παρουσιάζεται η εν λόγω (μισή) διάταξη. Στη βάση της επιβλήθηκε ημιτονοειδής οριζόντια διέγερση με μέγιστη τιμή επιτάχυνσης ίση με 0.20 g, συχνότητας 2 Hz, 29 κύριων κύκλων φόρτισης και 2 κύκλων συναρμογής στην αρχή και στο τέλος.

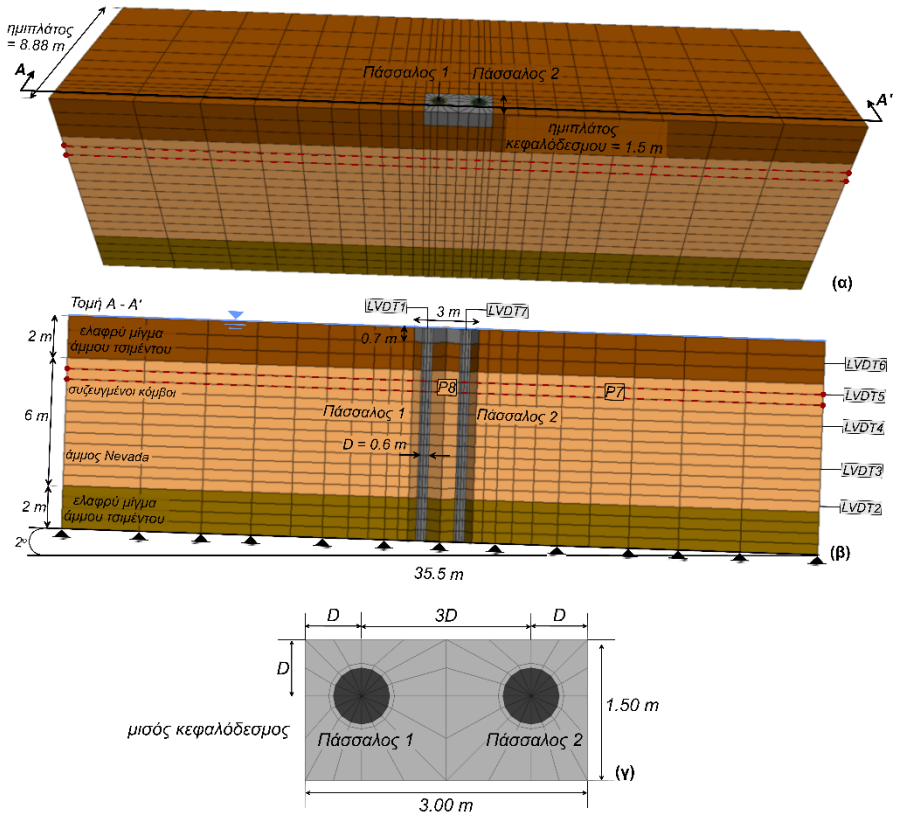

Σχήμα 22*: Διάταξη της δοκιμής φυγοκεντριστή των Pamuk et al. (2007): (α) Προοπτική άποψη, (β) κατακόρυφη τομή, (γ) λεπτομέρεια κεφαλόδεσμου*

Σε γενικές γραμμές ακολουθήθηκε ακριβώς η ίδια αριθμητική μεθοδολογία, όπως περιγράφηκε για τα προηγούμενα προβλήματα συνοριακών τιμών και βάση αναφοράς της προσομοίωσης αποτέλεσαν οι διπλωματικές εργασίες των Tiptiris (2017) και Pavlopoulou (2021). Θα πρέπει εξ' αρχής να αναφερθεί πως στο συγκεκριμένο πρόβλημα οι πληροφορίες για τις σιμεντοποιημένες αμμώδεις στρώσεις και τα δομικά στοιχεία είναι σχετικά ελλιπείς, επομένως οι ιδιότητές τους, καθώς και η προσομοίωσή τους επιλέχθηκαν με βάση λογικές παραδοχές, δεδομένης της συνολικής εικόνας των πειραματικών αποτελεσμάτων.

Συγκεκριμένα, τόσο για τη σιμεντοποιημένη αμμώδη στρώση βάσης, όσο και για την επιφανειακή σιμεντοποιημένη αμμώδη στρώση χρησιμοποιήθηκε ελαστικό προσομοίωμα. Ύστερα από αναλύσεις ευαισθησίας με γνώμονα τη μετακίνησή της στο τέλος της διέγερσης, για την στρώση βάσης τα ελαστικά μέτρα διάτμησης G και ογκομετρικής παραμόρφωσης K θεωρήθηκαν ίσα με 4350 kPa και 11300 kPa, αντίστοιχα, ενώ για την επιφανειακή στρώση, λόγω μειωμένων υπερκείμενων τάσεων, οι αντίστοιχες τιμές ήταν μικρότερες και ίσες με G = 1450 kPa και K = 3782 kPa, αντίστοιχα. Και για τις δύο αυτές στρώσεις η τιμή του συντελεστή διαπερατότητας κατά την ανάλυση θεωρήθηκε ίση με 10^{-8} m/sec, υπονοώντας στρώσεις συγκριτικά μη-διαπερατές λόγω της σιμεντοποίησης. Από την άλλη, όσον αφορά στη ρευστοποιήσιμη στρώση, το νέο προσομοίωμα βαθμονομήθηκε σύμφωνα με τον **Πίνακα 2** για άμμο Nevada και επιλέχθηκε τιμή συντελεστή διαπερατότητας ίση με $k = 8.25 \cdot 10^{-4}$ m/sec για D_r = 40%, σύμφωνα με τη συλλογιστική των **Παραγράφων ΙΙΙ.Α** και **ΙΙΙ.Β**.

Όσον αφορά στους πασσάλους και στον κεφαλόδεσμο, προσομοιώθηκαν κι αυτοί ελαστικά με στοιχεία συνεχούς μέσου. Συγκεκριμένα, για τα ελαστικά μέτρα διάτμησης και ογκομετρικής παραμόρφωσης των πασσάλων επιλέχθηκαν τιμές αντιπροσωπευτικές της ακαμψίας των δομικών στοιχείων του πειράματος. Υπογραμμίζεται εδώ ότι η προσομοίωση των πασσάλων με στοιχεία συνεχούς μέσου δεν ισοδυναμεί απόλυτα σε όρους δυσκαμψίας με την αντίστοιχη προσομοίωσή τους με στοιχεία δοκού. Έτσι, οι ελαστικές παράμετροι των πασσάλων της προσομοίωσης προσαρμόστηκαν έτσι ώστε να οδηγούν σε μετακίνηση πασσάλου κοινή με αυτήν που αντιστοιχεί σε προσομοίωση με στοιχεία δοκού δυσκαμψίας EI = 8000 kN/m^2 (Pamuk et al., 2007), για κοινή επιβαλλόμενη δύναμη.

Συγκεκριμένα, θεωρήθηκαν για τους πασσάλους $G = 23.56 \cdot 10^4$ kPa και $K = 31.31 \cdot 10^4$ kPa. Ακόμη, θεωρήθηκε διεπιφάνεια μεταξύ των πασσάλων και του εδάφους με γωνία τριβής ίση με 36^o. Αντίστοιχα, για τον κεφαλόδεσμο (για τον οποίο δεν υπάρχουν δεδομένα) οι παράμετροι του ελαστικού προσομοιώματος θεωρήθηκαν ίσες με $G = 70.68 \cdot 10^4$ kPa και $K = 93.93 \cdot 10^4$ kPa, ιδιότητες που εξασφαλίζουν επαρκή δυσκαμψία για το στοιχείο σε σχέση με τους πασσάλους. Επίσης, οι πάσσαλοι και ο κεφαλόδεσμος θεωρήθηκαν πρακτικά αδιαπέρατοι, ορίζοντας γι' αυτούς τιμή συντελεστή διαπερατότητας ίση με 10^{-8} m/sec. Σε αυτό το σημείο αναγνωρίζεται πως η αβεβαιότητα της προσομοίωσης

όλων των παραπάνω στοιχείων, πλην της ρευστοποιήσιμης στρώσης, είναι αυξημένη. Ωστόσο, η έμφαση στη συγκεκριμένη ανάλυση δίνεται στη ρευστοποιήσιμη στρώση και στην απόκριση του συστήματος των πασσάλων εντός αυτής, η οποία δεν αναμένεται να επηρεαστεί σημαντικά από τις αβεβαιότητες που αναφέρθηκαν παραπάνω.

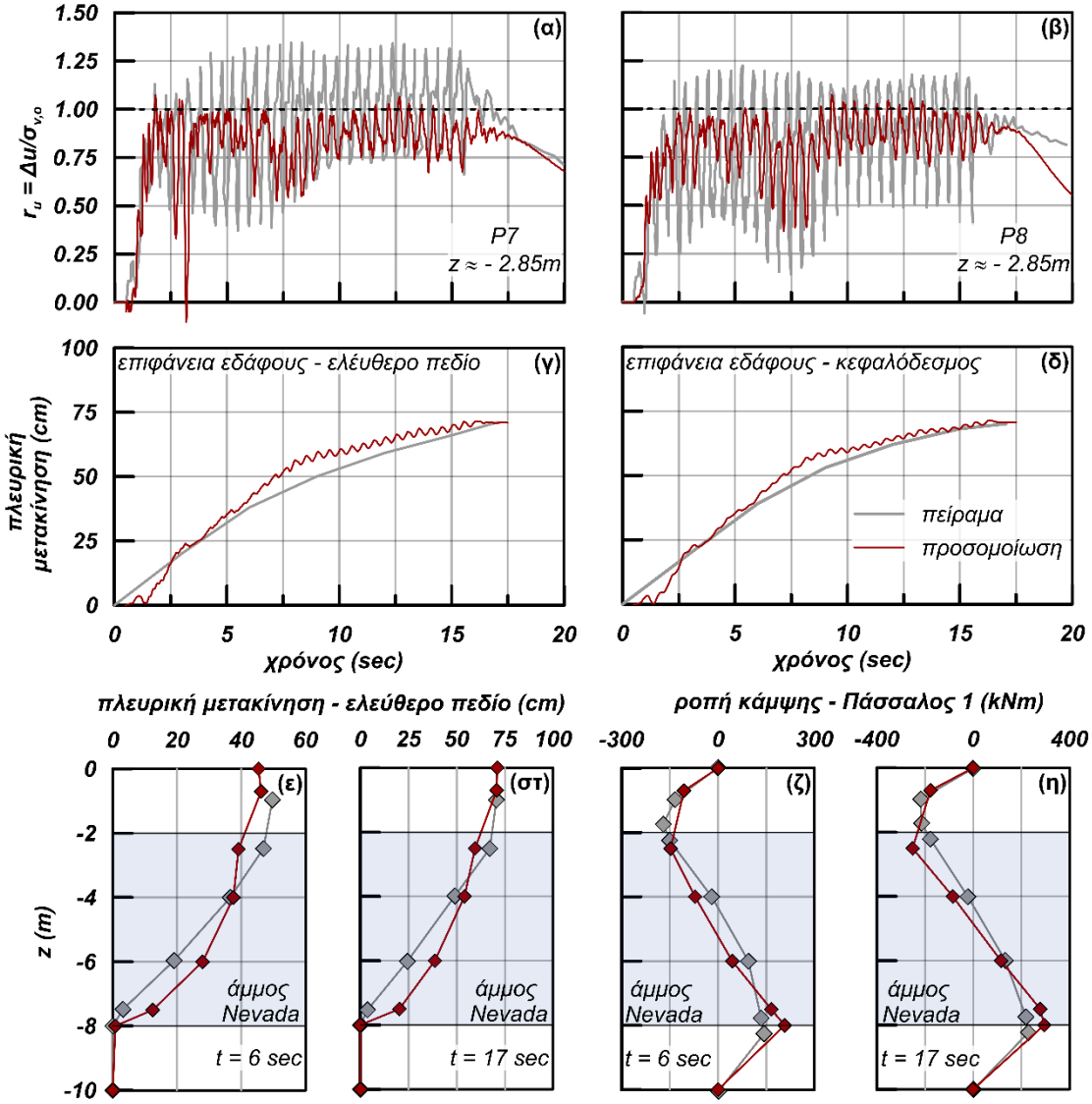

***Σχήμα 23**: Σύγκριση πειραματικών δεδομένων και αριθμητικής προσομοίωσης του πειράματος φυγοκεντριστή των Pamuk et al. (2007) σε όρους: (α) και (β) χρονοϊστορίας λόγου υπερπιέσεων r_u, (γ) και (δ) χρονοϊστορίας πλευρικής μετακίνησης, (ε) και (στ) πλευρικής μετακίνησης με το βάθος, (ζ) και (η) ροπών κάμψης του (ανάντη) Πασσάλου 1.*

Στο **Σχήμα 23** γίνεται αξιολόγηση της αριθμητικής μεθοδολογίας μέσω συγκρίσεων με τα πειραματικά δεδομένα για το πείραμα των Pamuk et al. (2007). Συγκεκριμένα, στα

Σχήματα 23α και **23β** συγκρίνεται η πειραματικά μετρούμενη χρονοϊστορία λόγου υπερπιέσεων πόρων $r_u = \Delta u/\sigma_{v,o}$ με την αριθμητικά προβλεπόμενη από την ανάλυση. Συγκρίσεις παρουσιάζονται για τις δύο θέσεις των μετρητών πιέσεων πόρων P7 (**Σχήμα 23α**) και P8 (**Σχήμα 23β**), που είναι τοποθετημένοι σε βάθος z = -2.85 m στο ελεύθερο πεδίο και ανάμεσα στους πασσάλους, αντίστοιχα (βλ. **Σχήμα 22β**). Σε γενικές γραμμές η σύγκριση είναι ικανοποιητική, με την ανάλυση να προβλέπει σωστά την εκδήλωση ρευστοποίησης τόσο στο ελεύθερο πεδίο (P7), όσο και ενδιάμεσα στους πασσάλους (P8). Έπειτα, παρουσιάζονται οι χρονοϊστορίες της πλευρικής μετακίνησης σημείων της εδαφικής επιφάνειας στο ελεύθερο πεδίο (**Σχήμα 23γ**) και επί του κεφαλόδεσμου (**Σχήμα 23δ**), όπως έχουν μετρηθεί πειραματικά και όπως προβλέπονται από την ανάλυση. Η σύγκριση είναι πολύ ικανοποιητική σε όλη τη διάρκεια της δόνησης και στα δύο σημεία. Αντίστοιχα, στα **Σχήματα 23ε** και **23στ** συγκρίνονται οι πειραματικά μετρούμενες και οι αριθμητικά προβλεπόμενες οριζόντιες μετακινήσεις ολόκληρου του εδαφικού σχηματισμού λόγω πλευρικής εξάπλωσης, ως στιγμιότυπα των χρονικών στιγμών t = 6 sec και t = 17 sec. Τα πειραματικά δεδομένα προέρχονται από τους μετρητές LVDT2 έως LVDT6 (βλ. **Σχήμα 22β**). Και εδώ η σύγκριση είναι αρκετά ικανοποιητική, τουλάχιστον όσον αφορά στις μετακινήσεις εντός της ρευστοποιήσιμης στρώσης, και για τις 2 χρονικές στιγμές.

Τέλος, στα **Σχήματα 23ζ** και **23η**, η γίνεται σύγκριση των ροπών κάμψης που αναπτύσσονται στον (ανάντη) Πάσσαλο 1 (βλ. **Σχήμα 22**) λόγω της πλευρικής εξάπλωσης του εδάφους, ενδεικτικά για τις χρονικές στιγμές t = 6 sec και t = 17 sec, όπως αυτές παρουσιάζονται στη δημοσίευση των Pamuk et al. (2007) κι όπως προκύπτουν από την αριθμητική ανάλυση. Οι συγκρίσεις δείχνουν ότι οι σημαντικές εδαφικές μετακινήσεις (βλ. **Σχήματα 23ε** και **23στ**) οδηγούν σε σημαντικές καμπτικές ροπές, ειδικά στις διεπιφάνειες της ρευστοποιήσιμης στρώσης με την άνω και κάτω σιμεντοποιημένη αμμώδη στρώση, οι οποίες προβλέπονται πολύ ικανοποιητικά από την ανάλυση στα **Σχήματα 23ζ** και **23η**.

IV. ΣΥΝΟΨΗ - ΣΥΜΠΕΡΑΣΜΑΤΑ

Στην παρούσα Διατριβή παρουσιάζεται ένα νέο ελαστο-πλαστικό προσομοίωμα το οποίο βασίζεται στη Θεωρία Κρίσιμης Κατάστασης (CST), ανήκει στην οικογένεια των προσομοιωμάτων Οριακής επιφάνειας SANISAND, και δανείζεται στοιχεία τόσο από

αυτά, όσο και από το προσομοίωμα NTUA-SAND (Andrianopoulos et al. 2010a). Βασικό χαρακτηριστικό του είναι η χρήση της τελευταίας αντιστροφής φόρτισης για τον ορισμό τόσο των ελαστικών όσο και των πλαστικών παραμορφώσεων. Η έμφαση δίνεται στον ορθό ορισμό του σημείου αντιστροφής φόρτισης ώστε να μην «*υπερακοντίζεται*» (overshooting) η σχέση τάσης-παραμόρφωσης. Χρησιμοποιεί μια συνάρτηση επίδρασης της δομής που ποσοτικοποιεί το πλαστικό μέτρο κράτυνσης με στόχο τον ορθό ρυθμό συσσώρευσης παραμενουσών παραμορφώσεων και μια συνάρτηση που ποσοτικοποιεί το συντελεστή διαστολικότητας με στόχο την ορθή απόκριση μετά την αρχική ρευστοποίηση. Το προσομοίωμα έχει συνολικά 14 παραμέτρους, 12 από τις οποίες βαθμονομούνται πρώτα και αφορούν στη μονοτονική φόρτιση και στο τέλος βαθμονομούνται ακόμη 2 που αφορούν στην ανακυκλική φόρτιση. Από τις παραμέτρους αυτές, 9 βαθμονομούνται άμεσα και 5 χρειάζονται επαναληπτική διαδικασία.

Η κατάστρωση έγινε σε επίπεδο μοναδιαίου στοιχείου, και παρουσιάζεται βαθμονόμηση για πέντε (5) άμμους της βιβλιογραφίας (Nevada, Toyoura, Ottawa, M31, Monterey), αλλά και δύο (2) χάλικες, που ως σύνολο καλύπτουν ένα εύρος τιμών μέσης διαμέτρου κόκκων D_{50} από 0.1 έως 9 mm. Στη συνέχεια έγινε διακρίβωση της αξιοπιστίας του προσομοιώματος ανά κοκκώδες έδαφος μέσω συγκρίσεων με αποτελέσματα μονοτονικών, ανακυκλικών και δυναμικών εργαστηριακών δοκιμών σε επίπεδο μοναδιαίου στοιχείου για τεράστιο εύρος αρχικών συνθηκών (συνολικό εύρος D_r = 2 – 90% και p_o = 100 - 2000 kPa) και διαφορετικές συνθήκες στράγγισης. Στο πλαίσιο της αξιολόγησης χρησιμοποιήθηκαν και εμπειρικές σχέσεις από τη βιβλιογραφία, ειδικά όταν δεν υπήρχαν τα αντίστοιχα δεδομένα για τα ελεγχόμενα κοκκώδη εδάφη (π.χ., Darendeli, 2001 για τις καμπύλες απομείωσης G/G_{max} και αύξησης ξ, Idriss and Boulanger, 2008 για τον συντελεστή διόρθωσης K_σ της αντοχής σε ρευστοποίηση λόγω υπερκείμενου φορτίου).

Μέσω της ενδελεχούς αυτής διερεύνησης καλύπτεται όλο το εύρος των ανακυκλικών παραμορφώσεων, που συζητήθηκε στην **Παράγραφο Ι**, αλλά και η μονοτονική φόρτιση έως την Κρίσιμη Κατάσταση, με ενιαίο σετ παραμέτρων ανά κοκκώδες έδαφος. Η αξιολόγηση δείχνει ότι το προτεινόμενο καταστατικό προσομοίωμα είναι, με βάση το σχεδιασμό του, ένα προσομοίωμα γενικής χρήσης, το οποίο παρέχει στο

χρήστη τη δυνατότητα για μία ικανοποιητική προσομοίωση, χωρίς να απαιτείται αναβαθμονόμηση για την ίδια άμμο, ανεξάρτητα από το αν το εξεταζόμενο πρόβλημα είναι στατικό, δυναμικό ή ανακυκλικό.

Ως περιορισμοί του προσομοιώματος θα πρέπει να αναφερθούν οι κοινοί περιορισμοί προσομοιωμάτων τύπου SANISAND, δηλαδή ότι προβλέπουν μόνο ελαστική παραμόρφωση σε διαδρομές τάσεων με μηδενική μεταβολή του αποκλίνοντα λόγου τάσεων (π.χ., 1Δ στερεοποίηση), ενώ δεν προβλέπουν με ακρίβεια τις πλαστικές παραμορφώσεις που προκαλούνται σε φορτίσεις με περιστροφή των κυρίων αξόνων των τάσεων λόγω της μη-ομοαξονικότητας (non-coaxiality) των τανυστών επαύξησης των τάσεων και των πλαστικών παραμορφώσεων. Από τη διακρίβωση αξιοπιστίας σε επίπεδο μοναδιαίου στοιχείου προέκυψε ότι σε χάλικες, αντίθετα με τις άμμους, φαίνεται να χρειάζεται απενεργοποίηση της λειτουργίας που σχετίζεται με την εξέλιξη της δομής στη μονοτονική φόρτιση (μηδενισμός μίας παραμέτρου) ώστε να επιτευχθεί ορθή προσομοίωση.

Προκειμένου να καταστεί δυνατή η χρήση του σε προβλήματα συνοριακών τιμών, το νέο προσομοίωμα ενσωματώθηκε στους κώδικες πεπερασμένων διαφορών FLAC και FLAC^{3D} για αναλύσεις σε 2 και 3 διαστάσεις, αντίστοιχα. Οι κώδικες αυτοί μπορούν να χρησιμοποιηθούν σε πλήρως-συζευγμένες μη-γραμμικές στατικές και δυναμικές αναλύσεις ρεαλιστικών προβλημάτων από το μελετητή μηχανικό. Αρχικά, οι εξισώσεις του προσομοιώματος προγραμματίστηκαν σε γλώσσα C++ και στη συνέχεια ενσωματώθηκαν στο λογισμικό ως υπό-ρουτίνα χρήστη (User-Defined-Model routine). Η ενσωμάτωση υλοποιήθηκε με χρήση εμπρός-τασικής ολοκλήρωσης Euler με αυτόματο έλεγχο λάθους, η οποία έχει αποδειχθεί αξιόπιστη για προβλήματα δυναμικής φόρτισης εδαφών σε καθεστώς ρευστοποίησης (π.χ. Andrianopoulos et al. 2010a).

Στο τελευταίο στάδιο της Διατριβής αξιολογήθηκε εκτενώς η ικανότητα του βαθμονομημένου προσομοιώματος να προβλέψει την απόκριση κοκκωδών εδαφών σε επίπεδο προβλημάτων συνοριακών τιμών μεγάλης κλίμακας. Για τον σκοπό αυτό, επιλέχθηκαν προβλήματα δυναμικής φόρτισης με εκδήλωση ρευστοποίησης που είναι από τα πλέον περίπλοκα για το μελετητή μηχανικό. Συγκεκριμένα, έγινε χρήση αποτελεσμάτων

εννιά (9) δυναμικών δοκιμών φυγοκεντριστή της βιβλιογραφίας, που εντάσσονται σε τέσσερις (4) διαφορετικές κατηγορίες:

(α) σεισμική απόκριση οριζόντιας ρευστοποιήσιμης εδαφικής στρώσης,

(β) πλευρική εξάπλωση ελαφρώς κεκλιμένης ρευστοποιήσιμης εδαφικής στρώσης,

(γ) σεισμική απόκριση συστήματος αβαθούς θεμελίου – ρευστοποιήσιμου εδάφους με διαφορετικές στρωματογραφίες και υπό διαφορετικές διεγέρσεις

(δ) σεισμική απόκριση ομάδας πασσάλων υπό πλευρική εξάπλωση ελαφρώς κεκλιμένης ρευστοποιήσιμης εδαφικής στρώσης.

Τα προβλήματα (α), (β) και (γ) διερευνήθηκαν στον διδιάστατο χώρο (2Δ) με χρήση του λογισμικού *FLAC*, ενώ το (δ) στον τριδιάστατο χώρο (3Δ) με χρήση του *FLAC*^{3D}. Καθώς το ρευστοποιήσιμο αμμώδες έδαφος είναι κοινό και στις 9 δοκιμές φυγοκεντριστή (άμμος Nevada διαφορετικών τιμών σχετικής πυκνότητας D_r), υιοθετήθηκε: (i) κοινή βαθμονόμηση του προσομοιώματος (βασισμένη σε εργαστηριακές δοκιμές σε επίπεδο μοναδιαίου στοιχείου) και (ii) κοινή αριθμητική μεθοδολογία ανάλυσης (π.χ., ίδιες συνοριακές συνθήκες, συντελεστής διαπερατότητα άμμου ανάλογα με την τιμή D_r, επιπλέον μικρή αριθμητική απόσβεση). Έτσι αποτυπώνεται αμιγώς η ικανότητα του προσομοιώματος να προβλέπει αποτελεσματικά την απόκριση του ίδιου εδάφους, ανεξάρτητα από το εξεταζόμενο πρόβλημα, χωρίς η αποτύπωση αυτή να επηρεάζεται από τη μεθοδολογία ανάλυσης. Η αξιολόγηση αυτή έδειξε ικανοποιητική προσομοίωση, χωρίς ανάγκη αναβαθμονόμησης για το ίδιο κοκκώδες έδαφος, ανεξάρτητα από το εξεταζόμενο πρόβλημα συνοριακών τιμών. Για παράδειγμα, με βάση τις δοκιμές φυγοκεντριστή που αφορούν την σεισμική απόκριση θεμελίου (πλάτους 3 και 6 m) σε ρευστοποιήσιμη στρώση (πάχους 3 - 6 m) υπό σεισμικές διεγέρσεις με μέγιστη επιτάχυνση 0.15 έως 0.38 g, οι αριθμητικές αναλύσεις προβλέπουν σωστά την τελική καθίζηση με ποσοστό λάθους μόλις ±30%. Μόνη εξαίρεση στις ακριβείς προβλέψεις είναι τα μεγέθη που σχετίζονται με τους εντοπισμένους περιορισμούς του προσομοιώματος. Για παράδειγμα, υποεκτιμάται η καθίζηση οριζόντιας ρευστοποιήσιμης εδαφικής στρώσης (πρόβλημα α), καθώς το προσομοίωμα (τύπου SANISAND) προβλέπει μόνο ελαστική παραμόρφωση υπό 1Δ στερεοποίηση.

Τέλος, εκτελέστηκαν παραμετρικές αναλύσεις κάποιων εξ αυτών των προβλημάτων συνοριακών τιμών με στόχο την αποτύπωση της ευαισθησίας των αποτελεσμάτων της προσομοίωσης σε δύο από τα πρωτότυπα χαρακτηριστικά του προσομοιώματος, ήτοι στη μεθοδολογία ορθού ορισμού του σημείου αντιστροφής φόρτισης (ώστε να μην «*υπερακοντίζεται*» η σχέση τάσης-παραμόρφωσης) και στη συνάρτηση που μεταβάλλει το συντελεστή διαστολικότητας υπό διαστολή με στόχο την ορθή απόκριση μετά την αρχική ρευστοποίηση. Οι αναλύσεις αυτές υπογραμμίζουν ότι τα εν λόγω καταστατικά χαρακτηριστικά είναι χρήσιμα, μα δεν μπορούν να θεωρηθούν κρίσιμα, τουλάχιστον για τα εξετασμένα προβλήματα συνοριακών τιμών.

Table of Contents

List of Figures

Chapter 2: Literature Survey

Chapter 4: Implementation in numerical codes *FLAC* and *FLAC^{3D}*

Chapter 5: Model Performance in Element Tests

***Figure 5.8**: Sensitivity of simulated monotonic drained triaxial response to value of model parameter c_h: (a,b) c_h = 3, (c,d) c_h = 12 - (calibrated value) and (e,f) c_h = 20. Data after Verdugo and Ishihara (1996).*

List of Tables

Chapter 3: Constitutive Formulation

Chapter 5: Model Performance in Element Tests

Appendix

Chapter 1

Introduction

1.1 Background and research objective

The accuracy of numerical analyses of boundary value problems of geotechnical structures relies significantly (but not exclusively) on the use of properly calibrated constitutive models that are appropriate for the geomaterial and the loading at hand. For granular geomaterials (e.g., sands, gravels and non-plastic silts), users of numerical codes often employ different constitutive models and/or different calibrations of the same constitutive model, depending on the target loading (e.g., monotonic versus cyclic, cyclic due to earthquakes versus cyclic due to wave action, under drained or undrained conditions). Such materials have a complex mechanical response, which becomes even more complex under cyclic loading. As such, their simulation has attracted a lot of attention in the literature, leading to multiple publications of constitutive models, with some of them incorporating the well-established framework of Critical State Soil Mechanics (Schofield and Wroth, 1968). Nowadays, a large percentage of the pertinent Critical State models is of the SANISAND type, i.e., bounding surface models (Dafalias, 1986; Dafalias and Popov, 1975) in which the peak and the dilatancy deviatoric stress ratios depend on the state parameter ψ (Been and Jefferies, 1985). Although the term SANISAND was coined in 2008 by Taiebat and Dafalias (2008), the concept was firstly proposed by Manzari and Dafalias (1997) in their two-surface model and adopted thereafter by many. The reason for its popularity is that it enables successful simulations for any relative density or stress level with the same set of model parameters.

In many cases, the papers that present models for cyclic loading of sands include accurate simulations of monotonic response, as well as of few, hand-picked, cyclic loading tests leading to liquefaction. Such a presentation, although possibly sufficient for monotonic loading, may not be adequately complete for cyclic loading, whose characteristics are highly dependent on cyclic shear strain level (Vucetic, 1994). As such, a complete model verification for cyclic loading should cover the whole range of possible cyclic shear strains, namely: a) small-strain response, where "*elasticity*" predominates and

the proper calibration of elastic parameters on the basis of dynamic measurements (e.g., geophysical tests) is of high importance, b) medium-strain response, where the response is non-linear hysteretic and strain accumulation with number of cycles is observed and finally, c) large-strain response, mainly with emphasis on resistance to liquefaction and post-liquefaction strain accumulation. The importance of these distinct cyclic shear strain regimes for proper simulations has started to attract attention in the literature lately. For example, McAllister et al. (2015) showed that if the "*elastic*" modulus stiffness of SANISAND-type models is calibrated on the basis of monotonic tests instead of in-situ or dynamic measurements, it underestimates significantly the in situ shear wave velocity leading to erroneous prediction of seismic ground response. Similarly, specialized models are being formulated for proper simulation of strain accumulation with large number of (medium-strain) cycles (e.g., Li and Liu, 2020; Liu et al., 2019), an issue rarely studied in papers presenting cyclic models in the past. Finally, a multitude of recent papers deal specifically with post-liquefaction strain accumulation (e.g., Barrero et al., 2020; Duque et al., 2021; Tasiopoulou et al., 2020), underlining its importance for accurate simulations of displacements of geostructures in a liquefaction regime. To our knowledge, in the pertinent literature, there are very few papers of models verified across the whole range of response as described above (e.g., Andrianopoulos et al., 2010a; Boulanger and Ziotopoulou, 2013; Cheng and Detournay, 2021; Papadimitriou and Bouckovalas, 2002; Tasiopoulou and Gerolymos, 2016). Of course, this does not mean that sophisticated cyclic models that are not verified in this manner are inaccurate. It only means that their users should be cautious when using them outside their verified cyclic shear strain range.

Concurrently, some of the models that have exhibited a satisfactory performance for cyclic loading may not be as accurate when it comes to monotonic loading (e.g., the NTUA-SAND model (Andrianopoulos et al., 2010a) requires a change in the values of 2 model parameters in order to capture the monotonic response, while the PM4Sand model (e.g., (Boulanger and Ziotopoulou, 2013) has not been verified against monotonic test data). In addition, some promising cyclic models were never implemented in numerical codes (e.g., Papadimitriou and Bouckovalas, 2002), while models that have been implemented in such codes have not been necessarily verified for the whole range of cyclic loading response (e.g., Zhang and Wang, 2012). It goes without saying that targeted verification may also

come from use in boundary value problems (e.g., Zhang et al., 2021), which may even be preferable from mere comparison with element test data (e.g., Manzari and El Ghoraiby, 2021). In this respect, one should acknowledge models that have been widely used throughout the years, at least for liquefaction-related problems (e.g., Andrianopoulos et al., 2010a; Boulanger and Ziotopoulou, 2013; Dafalias and Manzari, 2004; Tasiopoulou and Gerolymos, 2016). Such models should be considered as equally accurate, at least for the problems that they have been repeatedly used effectively.

Based on the above, there is a need for **a constitutive model for granular materials,** which will be able to capture accurately **both the monotonic response** (until the critical state) **and the cyclic response** (for any shear strain level) with **a single set of parameters for any relative density, stress level and loading condition**. For enhanced reliability, any such model should be thoroughly validated against laboratory results and empirical relationships from the literature for a **multitude of granular materials**. In addition, it should also be verified against measurements from a **multiple of centrifuge tests on the same geomaterial,** all with a single set of geomaterial-specific values of model parameters. Given that the focus here is on granular materials, it would be best if the centrifuge tests involved **liquefaction** that comprises the most complex response of such materials.

1.2 Scope of research

Aiming to fulfill the foregoing need, this Thesis presents the development, implementation and validation of a new constitutive model for the monotonic and cyclic response of granular soils with applications in boundary value problems related to seismic liquefaction. The target is to provide a general-purpose constitutive model with a satisfactory performance without a need for recalibration regardless of the nature of the boundary value problem at hand.

The proposed model belongs to the SANISAND family of models and incorporates stress reversal surfaces (Mroz and Zienkiewicz, 1984; Wang et al., 1990) facilitating the simulation of cyclic loading without a (small) yield surface. In this respect, it is a SANISAND-R model, a term introduced recently by Papadimitriou et al. (2019). It builds on the constitutive framework of the NTUA-SAND model (Andrianopoulos et al., 2010a), from which it inherits concepts like the small and medium strain nonlinearity and the fabric

evolution index for large strain response, albeit modified. Stress reversals are appropriately updated in order to avoid the stress-strain overshooting problem (e.g., Dafalias and Taiebat, 2016), but also to establish that strain accumulation at very small-strain cyclic loading is limited, in accordance to the literature (Vucetic, 1994). It incorporates a fabric-related cumulative function that scales the plastic modulus, targeting at an accurate rate of strain accumulation, while post-liquefaction strains are in focus with an appropriate modification of the dilatancy function. The use of the constitutive model requires the calibration of 14 parameters in total, 12 of which can be calibrated on the basis of monotonic loading tests while the other 2 can be calibrated last and refer only to cyclic loading conditions. Of its 14 parameters, 9 may be directly measured or estimated, while the other 5 (3 for monotonic and 2 for cyclic loading) require a trial-and-error procedure.

The constitutive formulation is built at the element level, while a complete calibration of model's parameters for monotonic, cyclic and dynamic loading conditions is provided for 5 sands of the literature (Toyoura, Ottawa F-65, Nevada, M31 and Monterey), but also for 2 gravels. The validation covers a wide range of initial conditions, in terms of density and stress level. Thorough comparisons were made with experimental data for a variety of initial conditions and types of loading, but also with empirical relationships from the literature when material-specific experimental data are lacking. This extensive verification procedure shed light on the simulative potential of the new model for the whole range of cyclic loading, but also for the monotonic response with a single set of model parameters per examined granular material, at least when it comes to sands. On the other hand, when it comes to gravels, the de-activation of fabric-related functions (via nullifying the model parameter N_o) in monotonic simulations has proven sufficient, without changing any other model parameter.

Since the ultimate purpose of the proposed model is to be used in numerical analyses of 2D and 3D boundary value problems, it was also implemented in the finite-difference computer codes *FLAC* (Itasca Consulting Group Inc., 2011) and *FLAC*^{3D} (Itasca Consulting Group Inc. 2012). These u-p codes can be used for fully-coupled, non-linear numerical analyses, of both static or dynamic geotechnical problems. Initially, the constitutive equations and routines were written in programming language C++ and then, they were implemented in the codes as dynamic link libraries (.dlls) using the User-Defined-Model

(UDM) option. Integration of the constitutive equations at each finite difference zone is performed via a second order modified forward Euler method, while the given strain increment is applied incrementally and an automatic error control procedure is made at each applied sub-increment.

For fully validating the new model, the Thesis also evaluates its accuracy at the system level of boundary value problems. For this purpose, and due to their complexity, dynamic problems related to seismic liquefaction are selected for simulation. The validation is made on the basis of experimental results of centrifuge tests of geostructures on Nevada sand. In total, 9 different boundary value problems were examined, that fall into 4 different categories. Specifically, the validation included the 2D seismic response of: a) horizontal free-field liquefiable sand layer, b) a mildly sloping free-field liquefiable sand layer and c) systems of shallow foundations on different soil profiles, including liquefiable sand layers, excited to different seismic motions and finally, the 3D seismic response of a pile group installed in a mildly sloping soil profile including a liquefiable sand layer. Since the utilized liquefiable sand is common in all the above boundary value problems, its calibration is unique in all the examined cases and is derived on the basis of laboratory data and comparisons at element level. In addition, the same numerical methodology (e.g., permeability estimates, numerical damping) is adopted in all cases. This validation process showed satisfactory accuracy of the model without any need of re-calibration or changes in the numerical methodology, despite the range of examined problems.

In addition, the proposed model includes dedicated constitutive ingredients aiming at complicated aspects of response, like the formulations for the post-liquefaction shear strain accumulation and the avoidance of stress-strain overshooting. Apart from the demonstration of their importance and constitutive role through comparisons at element-level, their effect is also examined in the analyses of boundary value problems. This is shown in the final section of the Thesis, by presenting parametric analyses showing the sensitivity of the results on these additional constitutive features.

1.3 Overview of Thesis contents

The Thesis comprises seven Chapters (including the Introduction as **Chapter 1**), namely:

Chapter 2 presents a review of the literature about constitutive modeling of granular materials. Emphasis is given on elastoplastic models, that share the same fundamental framework of the hereby proposed model. Focusing on distinct characteristic aspects of the response of granular materials, a rough categorization of models or constitutive frameworks is attempted.

In **Chapter 3,** the basic principles and the constitutive formulation of the model are presented in the multiaxial stress space. All the equations are given in tensorial form and their functionality is discussed in detail. Reference is made to the NTUA–SAND model of Andrianopoulos et al. (2010a), which is essentially the basis of the proposed, and how the present model improves, evolves or supplements some of its features. At the same time, all the characteristic aspects of response of granular materials that are attempted to be modeled, are clarified through references to experimental data from the literature.

In **Chapter 4,** the implementation procedure of the proposed model in numerical codes *FLAC* (Itasca Consulting Group Inc., 2011) and *FLAC*^{3D} (Itasca Consulting Group Inc., 2012) is discussed. Initially, a brief description of the basic points of the theoretical background of these codes is presented. Subsequently, the adopted Euler integration scheme of the stress-strain equation and the sub-stepping technique with automatic error control are presented in detail. Reference is made to Andrianopoulos et al. (2010b), Andrianopoulos (2006) and Karamitros (2010), where this implementation procedure was originally introduced, albeit modified in this Thesis.

Chapter 5 presents a step-by-step methodology for the calibration of model parameters. The role of each parameter in the constitutive equations is explained in detail, while the effect on the response of those that are calibrated via a trial-and-error procedure is demonstrated through sensitivity analyses. Subsequently, the performance of the new model is verified at element-level comparisons between simulations and experimental data on a multitude of granular materials including 5 sands and 2 gravels from the literature. The validation includes simulations of both monotonic and cyclic shearing tests.

In **Chapter 6** the validation process of the new model is complemented by verifying its simulative potential through comparisons with experimental data from a total of 9 dynamic centrifuge tests related to liquefaction. The same numerical methodology and modeling procedure, as well as a unique set of sand-specific model parameters are

maintained throughout the process, regardless of the 2D or 3D boundary value problem. In addition, sensitivity analyses for specific boundary value problems were performed aiming at analyzing the effects of specific novel constitutive ingredients.

Finally, in **Chapter 7**, the conclusions of the Thesis are summarized and directions for future research are proposed. The Thesis ends with the bibliography of the whole document and an Appendix that summarizes the information about all 450 laboratory tests employed in the model validation process in Chapter 5.

Chapter 2

Literature Survey

2.1 Constitutive modeling approaches for granular soils

In general, constitutive models describe the mechanical relationship between stresses and strains in continuum media. When soils are considered as continua, their mechanical response may be simulated via constitutive models. In the past decades, numerous constitutive models for soils have been developed following different constitutive approaches. They may be divided in several categories depending on: a) the soil type whose behavior they attempt to model, b) the assumptions, theories and mechanical analogues on which they are based, and c) the specific mathematical form of their constitutive equations. The majority of these constitutive models are built on the framework of elasto-plasticity, but there are also models that are based on other frameworks, like hypoplasticity (e.g., Bauer and Wu, 1993), visco-elasticity (e.g. Zhang et al., 2020), visco-plasticity (e.g., Askarinejad et al., 2021), barodesy (i.e., Kolymbas, 2012), or models that combine elasto-plasticity and thermodynamics under the framework of hyperplasticity (e.g., Houlsby and Puzrin, 2006). With regard to granular soils (e.g., sands), a breakthrough in constitutive modeling was the incorporation of Critical State Theory (Roscoe et al. 1958; Schofield and Wroth 1968), which can interpret the basic behavioral characteristics of granular materials and can be combined with any of the aforementioned frameworks.

In the following paragraphs, a rough categorization of constitutive modeling approaches for granular soils is attempted with emphasis on the elastoplastic models, since the hereby proposed model is built on this framework.

2.1.1 Framework of elasto-plasticity

Initiating from the description of metals' response, the theory of elasto-plasticity provides nowadays the constitutive framework for the majority of the existing models for geomaterials in the literature. The models adopting this framework consider the total strain rate as the summation of an elastic and a plastic component. Their basic components include:

- an elastic equation describing the evolution of elastic strains,
- a surface in stress space (which may change in size, location and shape) defining the points where yielding (i.e., non-zero plastic strain rates) appears,
- a flow rule describing the direction of plastic strain rates (e.g., as a vector perpendicular to a so-called plastic potential surface in stress space),
- a set of hardening laws for the evolution of the hardening parameters (e.g., the size, location and shape of the yield surface) and
- a consistency condition ensuring that the plastic strains are consistent with the hardening of the yield surface.

As the theory of elasto-plasticity is quite general, there is a variety of sub-categories included and derived from it and in the following, an attempt is made to refer to the most indicative of them. However, it should be noted that their differences are not always distinct and a specific model can adopt features from more than one them. Therefore, the presented categorization may be considered somewhat subjective.

A. Models of generalized plasticity

The basic characteristic of the models that belong to the framework of generalized plasticity is that there is no need to define the flow rule on the basis of a (plastic potential) surface in stress space. The term was originally introduced by Zienkiewicz and Mroz (1984) and found application in many modern elasto-plastic constitutive models, mostly in the manner introduced by Pastor et al. (1990), who proposed that the deviatoric and volumetric components of the plastic strain direction can be determined explicitly into the stress space. As a result, non-associativity of the flow rule appears as a general rule.

B. Multi-surface models

Mróz (1967) and Iwan and Yoder (1983) proposed the use of multiple nested yield surfaces (like in **Figure 2.1**) to predict elasto-plastic response during loading and unloading. Each one of them defines a locus in the stress space where the plastic modulus retains a constant value. During loading, the surface on which the current stress state lies moves until it reaches the next (larger) surface and so, surface after surface, a continuous hardening is simulated. These surfaces never intersect and it is like they constantly "*transfer the baton*"

one to another. Plastic strains, in the same way, are also well predicted upon unloading as the loading direction, and hence the surfaces, reverse in their movement in stress space. However, due to their complicated geometry and challenging numerical implementation, multi-surface models have not gained popularity in the literature. However, there are some models for granular soils adopting this feature and among them are those proposed by Elgamal et al. (2003) and Yang and Elgamal (2008).

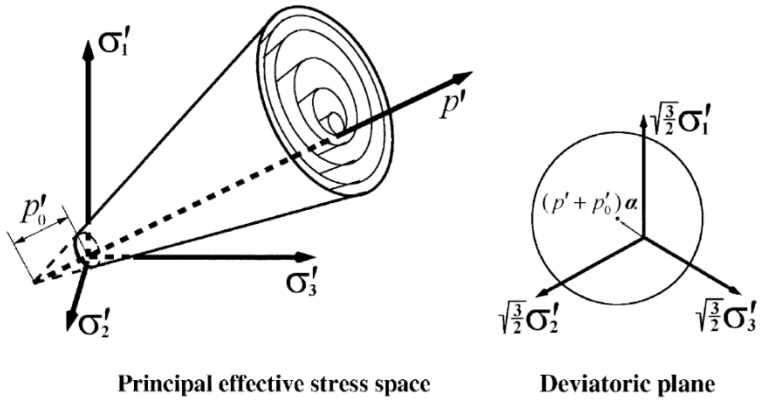

***Figure 2.1**: Surfaces of a multi-surface model in the principal stress space and deviatoric plane (figure after Elgamal et al., 2003).*

C. Bounding surface models

Models of this category were initially proposed by Dafalias and Popov (1975) and Krieg (1975) for the simulation of response of metals, but very quickly began to be widely used for soils, as well. Similarly to multi-surface models, the basic feature of such models is the existence of a second surface, apart from the yield, which bounds the feasible stress states in the stress space. This so-called "*bounding surface*" encapsulates the yield surface and can also harden, i.e., it can evolve in size, location or shape. The bounding surface is used for scaling the plastic modulus, on the basis of the distance between the stress state and its conjugate (or image) point on the bounding surface. The definition of this conjugate point is made on the basis of a so-called mapping rule of the stress state. Nowadays, a large number of models for granular soils in the literature are bounding surface models and some examples are those proposed by Manzari and Dafalias (1997) (**Figure 2.2**), Papadimitriou and Bouckovalas (2002), Dafalias and Manzari (2004), Taiebat and Dafalias (2008),

Loukidis and Salgado (2009), Andrianopoulos et al. (2010a), Boulanger and Ziotopoulou (2013), (Taborda et al. (2014) just to name a few. In addition, there are also other models that incorporate a similar reference surface, acting in a similar manner, even if their constitutive framework has some differences from the classical bounding surface plasticity framework (e.g., Tasiopoulou and Gerolymos, 2016).

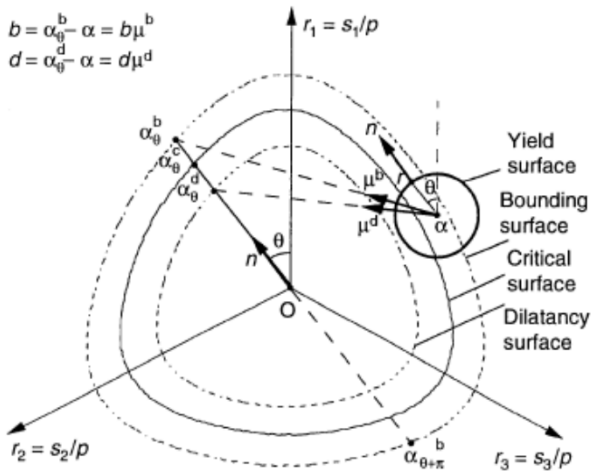

***Figure 2.2**: Surfaces of a bounding surface model in principal stress-ratio space (figure after Manzari and Dafalias 1997).*

D. Vanished yield surface models

This category can be regarded actually as a sub-category of all previous categories, in the sense that it includes models whose basic characteristic is the degeneration of the yield surface to zero-size in the stress space, as first proposed by Dafalias and Popov (1975). The main advantage of having a model with a vanished yield surface is that there is no need for a consistency condition, thus allowing for a more robust stress integration. Some examples of models incorporating a vanished yield surface are those proposed by Mróz et al. (1979), Andrianopoulos et al. (2010a) (**Figure 2.3**), Dafalias and Taiebat (2016), Tasiopoulou and Gerolymos (2016). It has to be underlined here that having a vanished elastic region does not mean that every step is necessarily elasto-plastic, since whether plastic strains appear or not depends on the definition of the loading index at each step. In other words, it is possible that purely elastic strain rates may be predicted for neutral (tangential) loading paths along implied loading surfaces, as clarified in Dafalias and Taiebat (2016).

E. Models with reversal surfaces

Concurrently with its numerical benefits, having a vanished yield surface does not allow the definition of a back-stress, namely a stress point describing its recent loading history. Such a back-stress may be used for the definition of the loading direction, or the mapping rule (in bounding surface models). One way of solving this problem is to incorporate the concept of "*reversal surfaces*", i.e., keeping in memory a stress quantity or a whole surface in stress space during the last load reversal in history. This quantity can then be used similarly to a back-stress. The concept is originally proposed by Mróz (1967), Mroz and Zienkiewicz (1984) and Wang et al. (1990) and has been adopted by a multitude of models that do not employ a yield surface in stress space, mainly bounding surface models (e.g., Andrianopoulos et al. 2010a; Papadimitriou et al. 2019). It is mentioned here that the model proposed in this Thesis is a model with reversal surfaces.

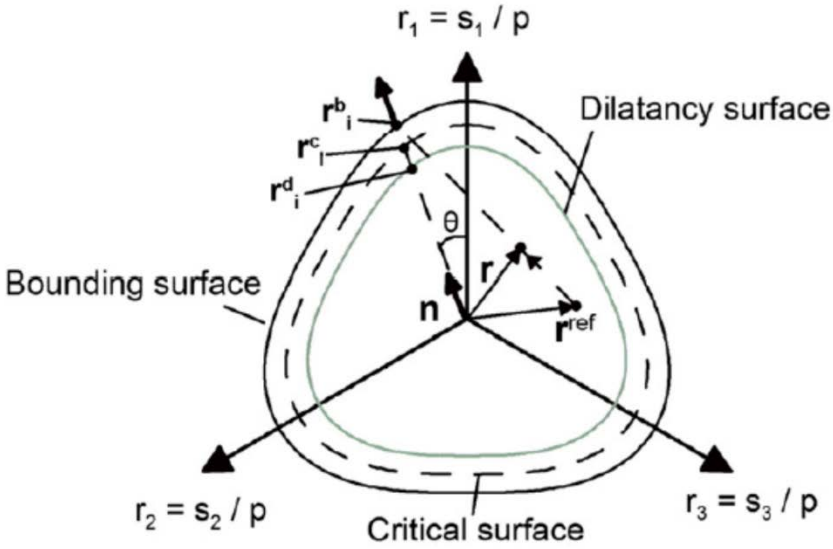

***Figure 2.3**: Bounding surface model with vanished yield surface (figure after Andrianopoulos et al., 2010a).*

F. Models with a "*cap*" surface

Given that granular soils produce plastic strains primarily when the deviatoric stress ratio changes, in many models of the literature model surfaces appear as open wedges in stress space. This poses a problem for loading paths that are characterized primarily by change in mean effective stress. On the other hand, the traditional approach of using closed yield

surfaces intersecting the mean effective stress *p* - axis, such as in the original or modified Cam-Clay models, creates the following unacceptable paradox: one can follow a neutral loading path starting at the point of intersection of the yield surface with the *p*-axis and moving tangentially along the surface, thus, changing drastically the stress ratio without inducing any plastic deformation. This may be accurate for clays, but is contrary to experimental evidence for sands. Because sand deforms primarily under stress-ratio changes, such yield surface shapes are in general unacceptable and should be avoided. One possible solution to this problem is to implement a closed kinematically hardening yield surface that allows for predicting plastic strains in constant stress-ratio paths, e.g., like the SANISAND model of Taiebat and Dafalias (2008) (**Figure 2.4**). In models with a vanished yield surface such a solution is not possible, and hence the incorporation of an extra yield surface in the stress space, intersecting the hydrostatic axis and acting like a "*cap*" to the other model surfaces has been proposed (e.g., DorMohammadi and Khoei 2008; Li and Dafalias 2002; Wang et al. 1990). Based on the above, the category outlined here is not really an independent category of models, but models included in the previous categories that are also equipped with a "*cap*" surface of some sort.

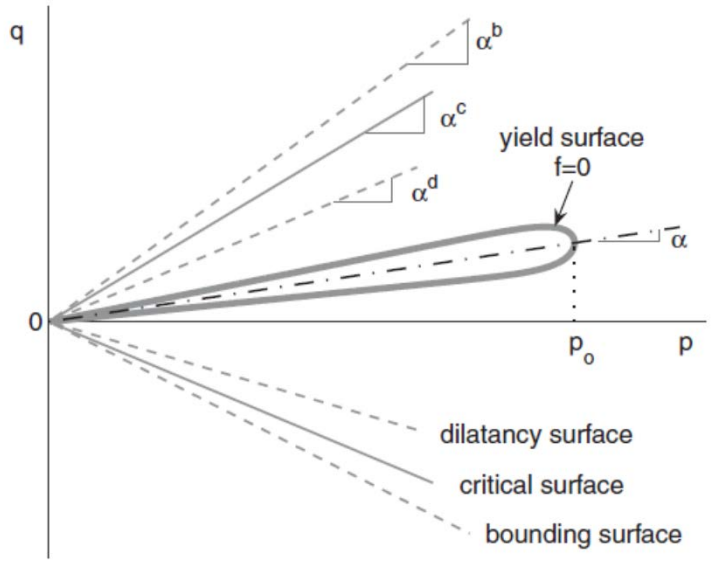

***Figure 2.4**: Surfaces of a bounding surface model in q-p space and closed-type yield surface (figure after Taiebat and Dafalias 2008).*

2.1.2 Framework of Critical State Theory

The Critical State Theory (CST) has been introduced by Roscoe et al. (1958) and Schofield and Wroth (1968) and constitutes a milestone in soil modeling, as it is the core of the majority of constitutive models for soils (e.g., for sands: Dafalias and Manzari, 2004; Manzari and Dafalias, 1997; Papadimitriou and Bouckovalas, 2002; Taiebat and Dafalias, 2008). This concept implies that the soil, if continuously sheared along a constant direction it will eventually approach a well-defined critical state. In this state, for even further shearing, the stress ratio maintains a constant soil-specific critical state value, the volumetric strain increment is zero, while deviatoric strain continues to accumulate. While in stress space there is a sand-specific value that the stress ratio reaches at CS, in the void ratio-mean effective stress space, there is also a well-defined correlation of eventual critical states that the soil may reach (**Figure 2.5**). Based on this figure, there are two conditions for attaining the CS: a) attaining a deviatoric stress ratio equal to M (i.e., being on the CSL in **Figure 2.5**a) , b) attaining a void ratio equal to the void ratio at CS (e_{cs}), which translates into being on the CSL in **Figure 2.5**b. Having these CSLs acting as soil-specific attractor states, provides a base of reference and dictates the response up to CS.

For sands in particular, of importance is the state parameter ψ that dictates the "*distance*" of the current stress ratio e from the void ratio e_{cs} (for the same p) on the CSL in the *e-p* space. Given that $\psi = e - e_{cs}$ according to Been and Jefferies (1985), values of $\psi < 0$ imply dilative response, while $\psi > 0$ depicts contractive shearing.

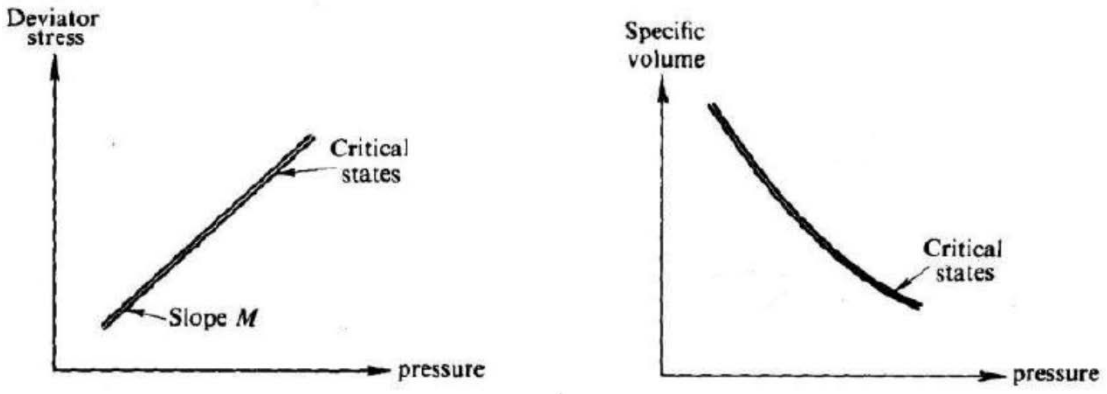

***Figure 2.5**: Critical State in stress and void ratio- mean effective stress spaces (figure after Schofield and Wroth, 1968).*

Based on the above, CST is isotropic. In an attempt to incorporate fabric effects and their evolution during loading in constitutive modeling, Li and Dafalias (2012) developed the Anisotropic Critical State Theory (ACST). The ACST enhances the traditional CST by introducing a third, fabric-related condition for the soil to reach and maintain the critical state, apart from those referred into the previous paragraph, as according to Theocharis et al. (2017), these two have been proven insufficient.

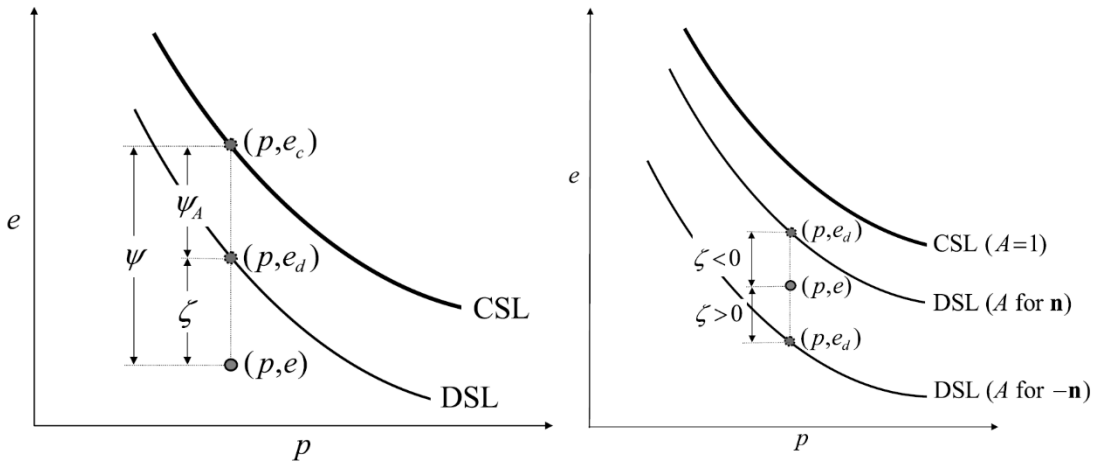

***Figure 2.6**: Anisotropic Critical State in the void ratio-mean effective stress space and introduction of a new DSL line and parameter ζ (figure after Li and Dafalias, 2012).*

This is achieved via a fabric anisotropy variable A which captures the relative orientation of the sand voids' orientation and the loading direction, as both evolve during shearing. Based on **Figure 2.6**, this parameter enables the definition of the Dilatancy State Line (DSL) in the *e-p* space (DSL), which is used for definition an anisotropic state parameter ζ, that dictates the "*distance*" of the current void ratio e from the void ratio e_d (for the same p) on the DSL in the *e-p* space. Positive and negative ζ values imply exactly the same as positive and negative ψ values, only now fabric effects are accounted for.

2.1.3 SANISAND family of models

Bardet (1986) enriched the bounding surface plasticity for sands by incorporating ingredients from CST, albeit the resulting model would still require different sets of parameters to model the behavior of a given sand at different relative densities. This drawback was later overcome by introducing in constitutive modeling of granular soils, the

state parameter ψ proposed by Been and Jefferies (1985). The incorporation of the state parameter concept into bounding surface plasticity in combination with CST, gave birth to the family of SANISAND models, the main ancestor of the constitutive model presented in this Thesis. The first model to combine the state parameter ψ with bounding surface plasticity within the CST was the two-surface model of Manzari and Dafalias (1997). Historically, it is considered the first SANISAND model, although the acronym of 'Simple ANIsotropic SAND' model was firstly introduced much later, by Taiebat and Dafalias (2008). SANISAND family of models has been growing in recent years with new members to be introduced in order to remedy specific limitations. Whenever a model of such type has the two-surface logic of the model of Manzari and Dafalias (1997), it is considered a SANISAND model (e.g., Papadimitriou and Bouckovalas 2002, Dafalias and Manzari 2004, Taiebat and Dafalias 2008). If a model of such type has a vanished yield surface and a true zero elastic range it may be considered as a SANISAND-Z model (e.g., Dafalias and Taiebat, 2016). Similarly, if a model of such type has a vanished yield surface, but also employs reversal surfaces it may be considered as a SANISAND-R model (e.g., Li and Dafalias 2000, Andrianopoulos et al. 2010a). Finally, if a SANISAND model has also a memory surface, it may be named SANISAND-MS (e.g., Liu et al., 2020)

On top of the above, if the SANISAND concept is built on the premises of the ACST and not the CST, a suffix F is added, like in the SANISAND-F (Petalas et al., 2020) and the SANISAND-FR (Papadimitriou et al., 2019) models. In other words, all these model names that have appeared in the literature may be considered as model type-specific and not constitutive model specific.

2.2 Modeling approaches of behavioral aspects of granular soils

The mechanical response of granular soils (i.e., gravels, sands, non-plastic silts) is highly determined by their particle gradation, shape (and fabric), their relative density and the applied stress level. Moreover, any given granular soil can exhibit quite different responses for different types of loading and drainage conditions, albeit initiating from the same state. Therefore, due to this complexity and behavioral diversity, there are constitutive models in the literature that introduce themselves not as generic, but as loading-type specific, since they target accuracy for specific aspects of sand response. However, while these models

offer a very precise and robust numerical tool for dedicated and specialized research and practice, their validity may not be as impressive when used for other types of loading of the same soil. On the other hand, in the literature there are also numerous models which, while in principle are capable of simulating the whole range of response, to achieve this, require different calibrated sets of their model parameters depending on the target loading conditions. This approach, while offers a flexibility in analyzing different aspects of response with the same model, presupposes highly-experienced users in model calibration.

In the following paragraphs, a review of various constitutive models for sand response is presented, with emphasis on those constructed within the framework of elasto-plasticity. The most characteristic aspects of sand response are discussed separately, since there is no model in the literature able to capture all aspects of response with the same set of model parameters.

2.2.1 Monotonic loading

Over the years and after the meticulous observation of a plethora of experimental results, it has been confirmed that the combination of void ratio and confining stress level play an essential role in determining the monotonic response of sands. Such materials experience shear induced volumetric change and this is respectively reflected upon the stress-strain response during shearing up to the critical state. The tendency of the material to either reduce its volume (contractive response) or increase it (dilative response) depends on the combination of the characteristics described above with respect to the critical state location (**Figure 2.7**). In addition, while in drained conditions the aforementioned volume change is feasible, in undrained conditions, where volume remains unchanged, this is expressed through increase or respectively, decrease of pore pressures within the sand and eventually, change of effective stresses (**Figure 2.8**). What is therefore required in order for a simulation of the monotonic behavior to be considered reliable is the verification of the stress-strain response against numerous monotonic tests for widely different initial conditions. What is important to ascertain is whether accuracy may be achieved with a unique set of model parameters irrespectively of the relative density (or void ratio), stress level, loading type and drainage conditions.

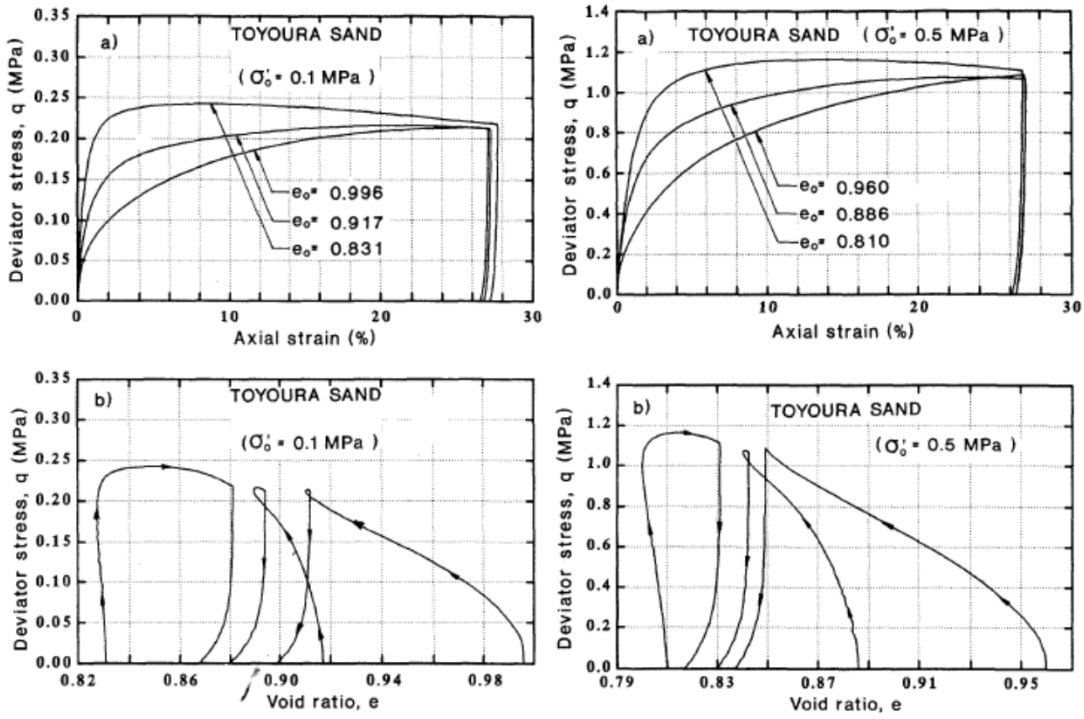

***Figure 2.7**: Drained triaxial compression tests on sand samples of various initial combinations of void ratio, e - effective stress level, p after Verdugo and Ishihara (1996) (figure after Verdugo and Ishihara, 1996).*

The constitutive model presented by Manzari and Dafalias (1997) was the first to combine bounding surface plasticity with CST utilizing the state parameter ψ introduced by Been and Jefferies (1985). This incorporation of ψ into the bounding-surface plasticity framework gives its character to the so-called SANISAND family of models. Their concept quickly gained enough ground, since it enabled successful simulations for any relative density or stress level with the same set of model parameters, while accurate monotonic response is predicted for both drained and undrained loading conditions. As the CST can be combined with any constitutive modeling approach, Gajo and Muir Wood (1999) followed also this concept by evolving the hypoplastic constitutive model originally proposed by Wood and Belkheir (1994). In a similar vein, Cubrinovski and Ishihara (1998) utilized a similar state index, proposed by Ishihara (1993) and Verdugo (1992), for their model which albeit intended to predict liquefaction, showed also satisfactory monotonic simulations. Following the same rationale, Wang et al. (2002) introduced a new state parameter and incorporated it in an evolved version of the bounding surface hypoplasticity

model originally proposed by Wang et al. (1990) to predict accurate monotonic response. Concurrently, at these early stages of advanced constitutive modeling of sands, there was a lot of research on the expression of an accurate dilatancy equation able to describe the experimentally observed response and depend on density (via void ratio) and stress level, but also on the applied stress-ratio level (e.g., Wan and Guo, 1998; Li et al., 1999; Li and Dafalias, 2000).

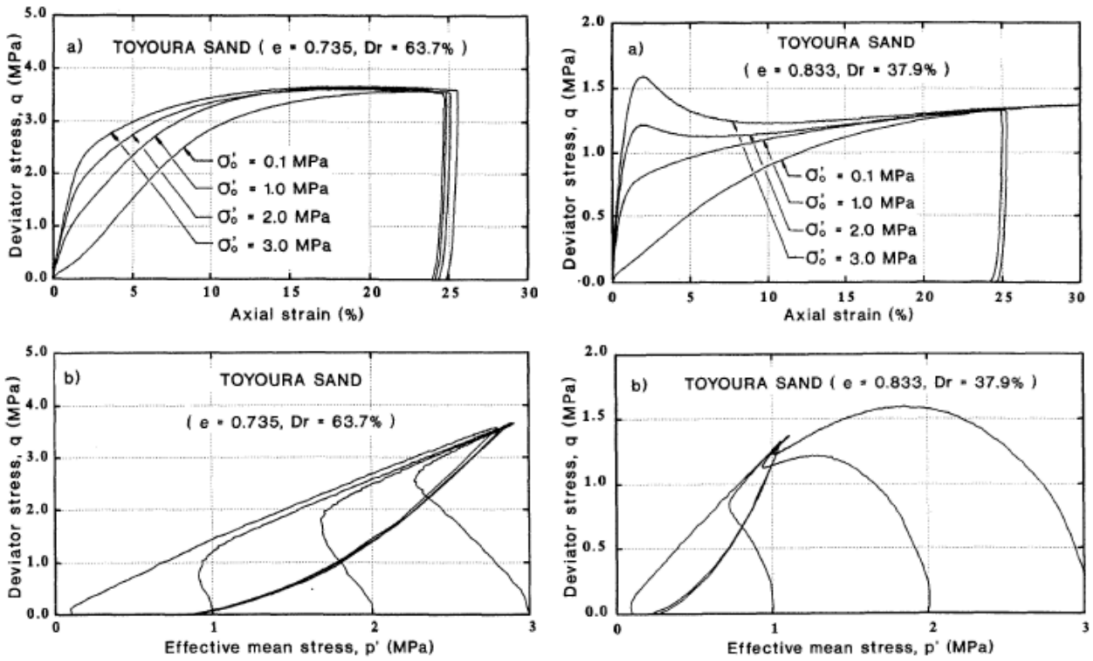

***Figure 2.8**: Undrained triaxial compression tests on sand samples of various initial combinations of void ratio, e - effective stress level, p after Verdugo and Ishihara (1996) (figure after Verdugo and Ishihara, 1996).*

Later, Papadimitriou et al. (2001) and Papadimitriou and Bouckovalas (2002) in their model, based on that of Manzari and Dafalias (1997), and trying to bridge the gap between monotonic and cyclic response, added a smooth shear induced non-linearity on the elastic moduli via a Ramberg and Osgood (1943) type of stress-strain relation and invented the concept of a macroscopic cumulative index accounting for fabric effects on the response. Later, Andrianopoulos et al. (2010a) implemented a vanished-yield surface version of this model in numerical code *FLAC*. Both models are able to predict satisfactory monotonic response, albeit they require the change of two model parameters between their monotonic and cyclic calibration. Taborda et al. (2014), presented a modification of the model of

Papadimitriou and Bouckovalas (2002) in order to enhance its predictive capabilities. Satisfactory monotonic response is predicted also by the model presented by Tasiopoulou and Gerolymos (2016), which builds on a joint plasticity framework combining perfect elasto-plasticity and Bouc-Wen hysteresis, albeit utilizing different sets of model parameters during monotonic and cyclic loading.

In the sequel, the model presented by Dafalias and Manzari (2004) is one of the most referenced constitutive models regarding the monotonic response of sands. This model builds on the previous work of Manzari and Dafalias (1997) and furtherly extends it to account for the effects of fabric changes during cyclic loading following initial liquefaction. Albeit predicting cyclic loading and liquefaction phenomena, as derived by its calibration, emphasis is given in monotonic response which is also simulated very well. In 2008, Taiebat and Dafalias (2008) introduced an evolution of this model, by adopting a closed-type yield surface, thus accounting for constant stress-ratio loadings to predict plastic strains. It was then that the term SANISAND was officially coined. Subsequently, Dafalias and Taiebat (2016) proposed a vanished yield surface version of the same model with some other modifications, including the non-dependency of strength on Lode angle.

A. Anisotropy

As soil layers are formed under a gravitational field, an anisotropic soil fabric with transverse isotropy on the bedding plane is structured, affecting the mechanical response of such formations. Oda et al. (1978) (**Figure 2.9**) and Vaid and Chern (1985) were among the first to show, through undrained triaxial tests, that the critical state strength of sand measured in extension is much lower than that in triaxial compression under otherwise identical conditions, and that the significant difference was directly associated with the soil dilatancy. In general, it was found that the sand response was far more contractive in triaxial extension than it was under triaxial compression. Unfortunately, it has been proven that the Lode angle dependency of the strength, which the majority of the previously referenced models incorporate, is not enough to replicate these effects.

Hence, this justifies why, in recent years, the majority of attempts of constitutive modeling of the monotonic response of sands focuses more and more on capturing the role of fabric and its anisotropy. Li and Dafalias (2002) proposed a relatively simple approach

to include the influence of the material-inherent anisotropy, by employing a second order constant fabric tensor ***F***, defined by micromechanics, to describe material-inherent anisotropy at the initial state and a scalar-value state variable *A* representing the material anisotropic state. The fundamentally different proposition from the premises of classical Critical State Theory is that the location of the critical-state line in the *e* - *p* plane is not unique, but it is a proper function of *A*. This work was then combined with the Dafalias and Manzari (2004) model, and resulted in the publication of Dafalias et al. (2004), which is a different version of the first, accounting for inherent fabric anisotropy in a simpler form, i.e., considering that the location of CSL into the *e* - *p* space depends on the loading-direction in the deviatoric plane via the Lode angle and the direction of loading with respect to the sand fabric. These findings were also included in the model presented by Loukidis and Salgado (2009).

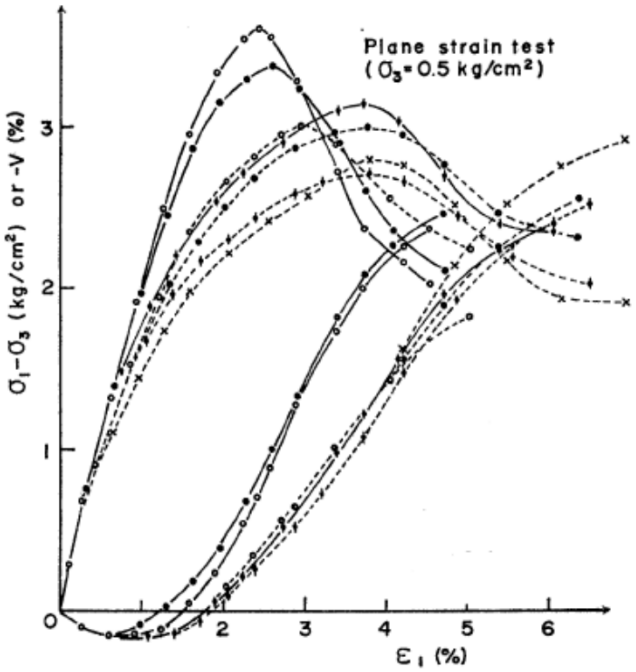

Figure 2.9*: Drained plane strain shear tests for different orientations of the shear plane with respect to the bedding plane, for initial axial σ_a=50 kPa (figure after Oda et al., 1978).*

After almost a decade and various experimental findings, Li and Dafalias (2012) proposed the Anisotropic Critical State Theory (ACST), according to which, the fabric tensor is no longer, but it evolves towards its critical value. In other words, the fabric tensor

does not only reflect initial anisotropy, but also its evolution during shearing towards its critical value. This approach resulted in the re-affirmation of the uniqueness of the CSL in the $e - p$ space. In the sequel, Papadimitriou et al. (2019) incorporated the ASCT in the framework of bounding surface plasticity and proposed the SANISAND-FR model with reversal surfaces and a vanished yield surface. The model accurately simulates a large dataset of monotonic shearing tests with very different densities, loading directions, drainage conditions and anisotropic fabric structures due to different preparation methods and deposition plane orientations, obtained over the years at several different laboratories, with a single set of model constants. Moreover, following the same rationale, Petalas et al. (2020) evolved the model proposed by Dafalias and Manzari (2004) by including the framework of ASCT and proposed the SANISAND-F model. Gao et al. (2014) proposed also an elastoplastic model capable to predict fabric evolution effects, in combination with a yield cap enclosing the bounding surfaces of their model. More recently, Wang et al. (2021) developed a plasticity model incorporating fabric evolution for monotonic and cyclic sand behavior by utilizing quantitative micromechanical information obtained through DEM numerical tests.

2.2.2 Cyclic loading

Cyclic response of granular materials cannot be regarded separately form monotonic response, albeit it is characterized by some different behavioral aspects. For example, although it can be studied within the CST framework, it cannot be fully described by it. Specifically, during undrained cyclic loading where continuous decrease of effective stresses occurs, critical state is never reached in the $e - p$ space. On the other hand, after extensive shear straining, critical state may be reached in terms of stress-ratio. It is therefore well- understood, that while in monotonic loading the critical state is well-defined by these two aforementioned conditions, in cycling loading this is not so clear. Moreover, during drained cyclic loading, experimental data (e.g. Shahnazari and Towhata, 2002 - **Figure 2.10**) imply that the material exhibits pure contractive behavior, even for large cyclic shear strain amplitudes, albeit under monotonic loading up to that applied stain level dilation would occur. These contradicting mechanisms make the constitutive modeling of sands, via a common approach for both monotonic and cyclic loading, extremely challenging.

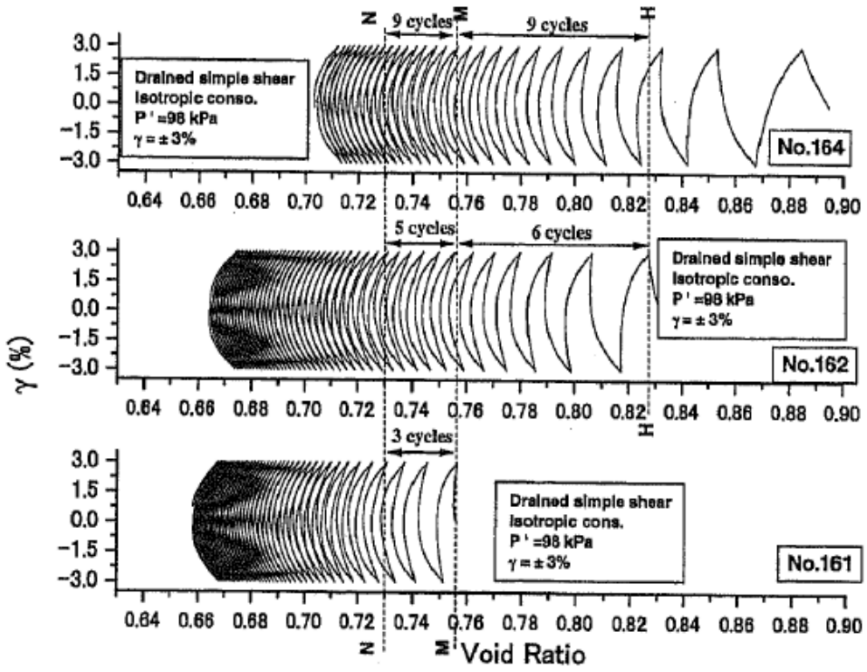

***Figure 2.10**: Drained cyclic torsional simple shear tests at a single amplitude shear strain of 3% for different initial void ratios of samples (figure after Shahnazari and Towhata, 2002)* .

One of the most crucial parameters determining the cyclic response is the applied strain level. For very small applied shear strain level ($\gamma < 10^{-4}$), plastic strain accumulation with cycles is very close to zero and shear modulus has not degraded considerably. This strain level is commonly referred as volumetric threshold shear strain in the literature (e.g. Vucetic, 1994). Models with (small) yield surfaces (e.g., Dafalias and Manzari 2004) ensure elastic response within them and the zero strain accumulation may be then achieved for a proper calibration of the yield surface size. However, this is much more difficult, or even practically impossible, to achieve for models with vanished yield surface. For intermediate strain levels ($10^{-4} < \gamma < 10^{-2}$), shear modulus degrades and plastic strains accumulate with number of cycles. This strain range corresponds to cyclic loading due to earthquake, wind, waves etc. and is the most common range where models sufficient for cyclic response apply. Finally, when it comes to undrained cyclic loading and liquefaction, exhibited shear strains abruptly increase and then gradually accumulate with cycles, reaching $\gamma > 3 \times 10^{-2}$, or even much more as the number of cycles increase. Hence, it becomes clear that, the challenge for a constitutive model to predict an accurate response

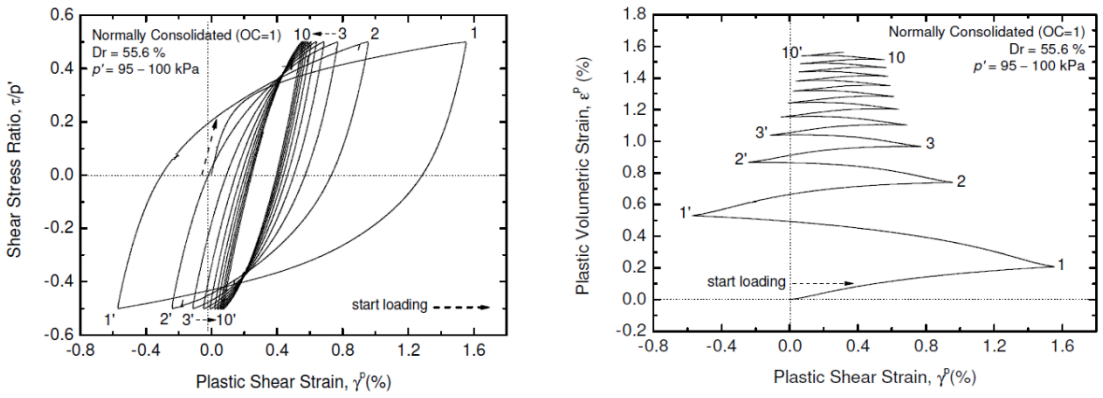

***Figure 2.11**: Drained cyclic torsional shear stress-controlled tests after Wahyudi et al. (2010) (a) increase of stiffness in stress-strain terms and (b) decreasing rate of accumulation of volumetric strains (figure after Wahyudi et al. 2010) .*

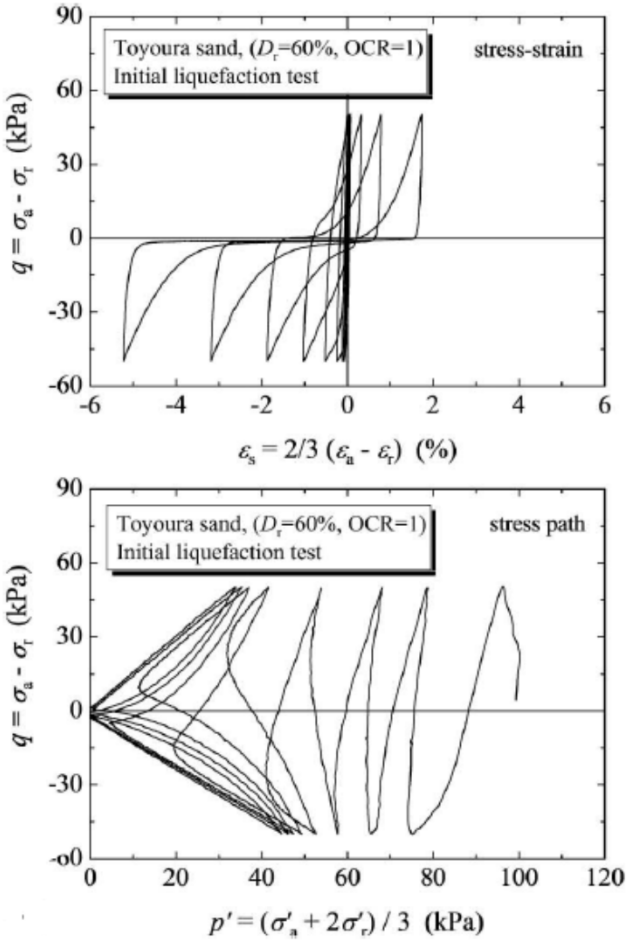

***Figure 2.12**: Undrained cyclic triaxial tests leading to liquefaction (figure after Toyota and Takada, 2017) .*

for any given strain level is significant.

Finally, the significance of drainage conditions in cyclic response (as in monotonic as well) should not be considered unimportant. Drained cyclic loading leads to densification and to a continuous increase of stiffness in stress-strain terms. Concurrently, the rate of volumetric change decreases with the number of cycles (**Figure 2.11**). On the contrary, in undrained loading volumetric change is prohibited and it leads to a decrease of effective stresses and of stiffness in stress-strain terms. At the same time, the rate of excess pore pressure build-up is not constantly decreasing, but it abruptly increases after a number of cycles and eventually liquefaction occurs (**Figure 2.12**). These complicated mechanisms act in a contradicting way in nature, and consequently in fully-coupled numerical analyses, and should be taken into account in constitutive modeling.

The previous paragraphs attempted to describe the complexity of cyclic loading of granular materials, which has thus attracted a lot of attention in the literature leading to multiple publications of constitutive models. As a whole, the key issues during cyclic loading of sands are: a) an induced densification with cycles under drained loading and b) progressive increase of pore pressures and eventual liquefaction under undrained cyclic loading. In the following, a rough categorization of various models is presented, on the basis of the basic constitutive mechanism they utilize to achieve the behavioral aspect of interest.

A. Constitutive approaches for cyclic loading

I. Cumulative functions

The fundamental two-surface model proposed by Manzari and Dafalias (1997) predicts apart from monotonic, also cyclic response under a unified framework. However, apart from the effect of the evolution of the included state parameter ψ, there is no other mechanism to contribute to the densification and cyclic hardening or compliance. Hence, while pore pressure build-up is predicted, its evolution rate is not accurate, especially for a large number of loading cycles, and liquefaction is not actually captured. This shortcoming revealed the need for a constitutive mechanism to replicate the progressive densification and hardening cycle per cycle during drained conditions or the decreasing rate of pore-

pressure build-up and the abrupt (or progressive) liquefaction. The use of functions that accumulate a quantity that evolves continuously and progressively during loading, has been proven a widely used constitutive ingredient so far, aiming to replicate macroscopically the fabric evolution effects. Their role is mainly to provoke stiffening cycle per cycle and hence a decreasing tendency for volumetric change (in drained conditions) and pore pressure build-up (in undrained conditions) and moreover, to enable increased compliance after dilation under undrained loading.

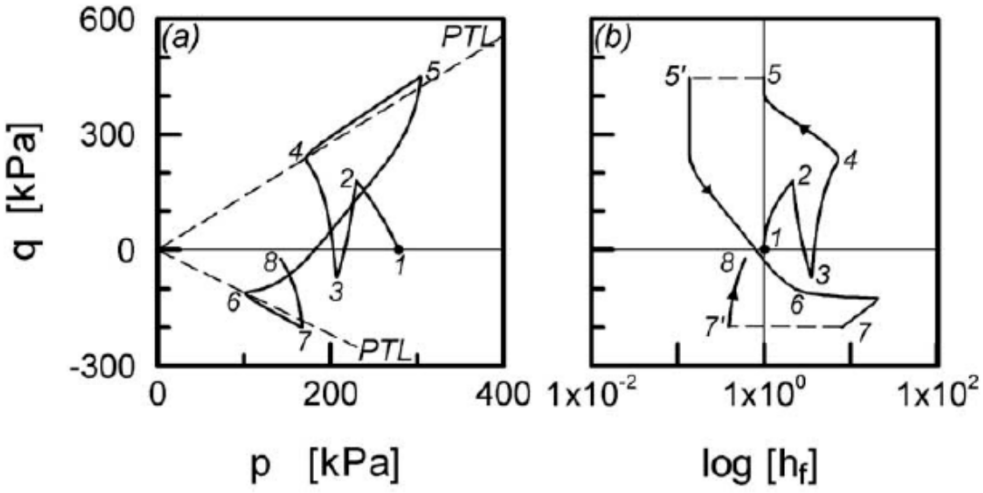

***Figure 2.13**: Evolution of a cumulative fabric function h_f during an undrained cyclic triaxial test (figure after Papadimitriou and Bouckovalas, 2002).*

In this train of thought, Papadimitriou and Bouckovalas (2002) proposed a scalar-valued fabric evolution function, to predict macroscopically the effect of fabric on cyclic response. It is a cumulative index of plastic volumetric strain, that renders stiffer response during contraction thus capturing the decreasing rates of pore-pressure build up or volumetric strain accumulation and softer response after dilation, thus leading to eventual liquefaction (**Figure 2.13**). The same concept was inherited to the NTUA-SAND model of Andrianopoulos et al. (2010a). The Dafalias and Manzari (2004) uses a similar index, which only provides the softening response following dilation. In this way, stress softening and eventual liquefaction are well-predicted, but rate of pore-pressure build up is overestimated, while the decreasing rate of densification under drained conditions is not predicted. Similarly, Ling and Yang (2006) used a cumulative function of plastic deviatoric

strains applied on the plastic modulus to increase stiffening, while modifying the aperture of the bounding surface for possible modulus degradation. Boulanger and Ziotopoulou (2013) maintained the concept of Dafalias and Manzari (2004), which serves their baseline-model, but added numerous cumulative indices related to macroscopic fabric functions to predict undrained cyclic response and liquefaction, but also a reasonable rate of pore pressure accumulation. In the same way, the model of Wang and Xie (2014) considers the influence of accumulated plastic strains on plastic modulus to improve the simulation of densification and cyclic mobility. In a similar vein, Tasiopoulou and Gerolymos (2016a) used accumulation functions of deviatoric strain in their hardening laws and equations of model surfaces to provide stiffening during drained cyclic loading and control the number of cycles to liquefaction. On the other hand, Wei et al. (2020) use an accumulation of plastic deviatoric strain to provide stiffening response on their model silty sands under cyclic loading.

II. Memory surfaces related to fabric evolution

From another point of view, fabric evolution of granular soils is not related to cumulative indices, but to an additional evolving model surface within the stress space. The so-called "memory surface" exhibits isotropic and kinematic hardening and through its expansion or shrinkage, provokes stiffening or softening, by utilizing the distance of the current stress state from it. This concept is originally proposed by Corti et al. (2016) and can be combined with any model under the framework of muti-surface or bounding surface plasticity. Specifically, Liu et al. (2019) and Liu et al. (2020) incorporated this feature to the Dafalias and Manzari (2004) model and proposed the SANISAND-MS model (**Figure 2.14**), while so did Yang et al. (2020) for the SANISAND-MSf model.

III. Fabric tensors - Anisotropy

Postulates of Anisotropic Critical State Theory (ACST), albeit more widespread and commonly applied in constitutive modeling of monotonic response, have started to extend to models for cyclic loading as well. Under this framework, neither cumulative macroscopic functions, nor memory surfaces are utilized. The response is captured by a continuously evolving real fabric tensor, which describes the geometrical properties of void

spaces of a granular assembly. Some models recently found in the literature, incorporating these features are those proposed by Yin et al. (2010), Gao and Zhao (2015) and Wang et al. (2021). Such approaches are very robust and elegant, but they are yet to provide quantitative accuracy in all aspects of cyclic loading.

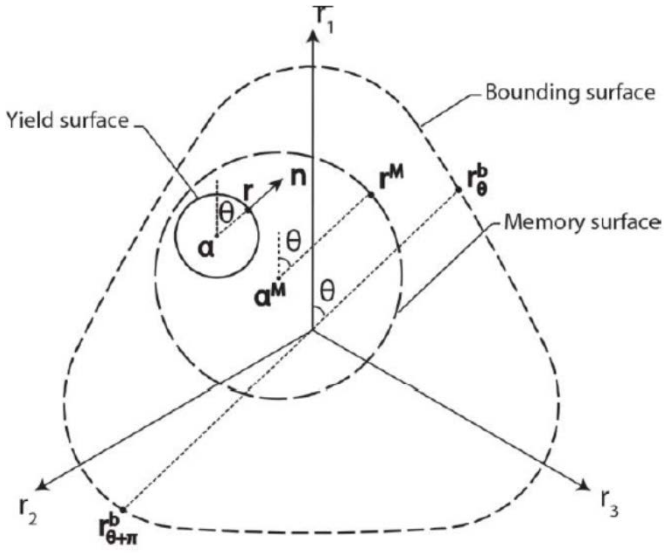

***Figure 2.14**: Memory surface of SANISAND-MS model (Liu et al., 2019) accounting for fabric evolution, incorporated in a bounding surface model (figure after Liu et al., 2019).*

IV. Degradation of elastic moduli

Some models adopt evolving mechanisms for the elastic moduli during loading apart from the change that is already taken into account via the change in density and stress level. For example, Papadimitriou and Bouckovalas (2002) and later Andrianopoulos et al. (2010a), following the example of Hueckel and Nova (1979), have incorporated small-strain non-linearity in elastic moduli by adding a Ramberg-Osgood type hysteretic degradation during shearing. This addition enables some hysteretic response to develop, with increasing stress ratio, even in small applied strains. Moreover, this has been proven a very useful tool to reconcile the drained and undrained stress-dilatancy response (especially during monotonic loading) with a unique realistic calibration of elastic moduli. In this context, this feature was also adopted by Loukidis and Salgado (2009) and Taborda et al. (2014). A dependence of elastic stiffness on stress-ratio is also present in ISA-model by Fuentes and

Triantafyllidis (2015). Finally, some models (e.g., Boulanger and Ziotopoulou, 2013 or Cheng and Detournay, 2021) adopt a degradation of elastic moduli related to cumulative functions, which start accumulating close to liquefaction and continue as the number of cycles increases.

V. "Explicit models" - for high number of loading cycles

According to Niemunis et al. (2005) the explicit method links 'explicitly' the accumulated strains to the number of applied loading cycles *N* and the strain components are only calculated at the end of each loading cycle, without the solution of the stress-strain constitutive equation. In this framework, the equivalent constitutive equation is the relationship between accumulated strains and applied number of cycles *N* (**Figure 2.15**). This correlation emerges from empirical relationships accounting for micro-structural/mechanical properties (e.g., void ratio, grain size distribution, shear strength), as well as loading parameters (e.g., stress or strain amplitude, stress level). Owing to their low computational costs, explicit formulations have been widely applied to numerical analysis of soil structure interaction problems where a high number of cycles are expected (e.g., offshore structures subjected to wave and wind loading), by reducing real cyclic loading

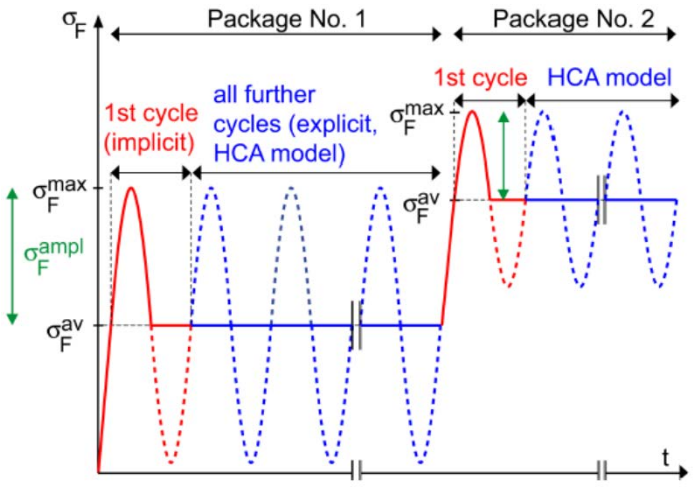

***Figure 2.15**: Cyclic loading applied during two successive packages of cycles with different average stresses and stress amplitudes using a high-cycle accumulation (HCA) explicit model (figure after Wichtmann et al. 2017).*

histories to sequences of *N* driven monotonic steps. Some examples of such models are proposed by (Niemunis et al. 2005), Wichtmann et al. (2017) and Staubach and Wichtmann (2020). However, such models are loading type specific, i.e., they cannot be used for types of loading different than the ones for which they were built (e.g., they cannot be used for monotonic loading).

2.2.3 Challenging behavioral and numerical aspects

A. Post-liquefaction strain accumulation

In recent years, within the framework of performance-based design, special research effort has been focused not only on liquefaction triggering, but also on the investigation of post-liquefaction deformations. There is a plethora of experimental evidence (e.g., Kammerer et al., 2000; Wu et al., 2004 - **Figure 2.16**; Arulmoli et al., 1992; Bastidas, 2016) exhibiting significant shear strain accumulation after initial liquefaction, i.e., the state when the sand first reaches an excess pore pressure Δu that is at least 95% of the initial mean effective stress p_o, or equivalently when the mean effective stress p is smaller or equal to 5% of p_o. Hence, a multitude of recent papers deal specifically with post-liquefaction strain accumulation.

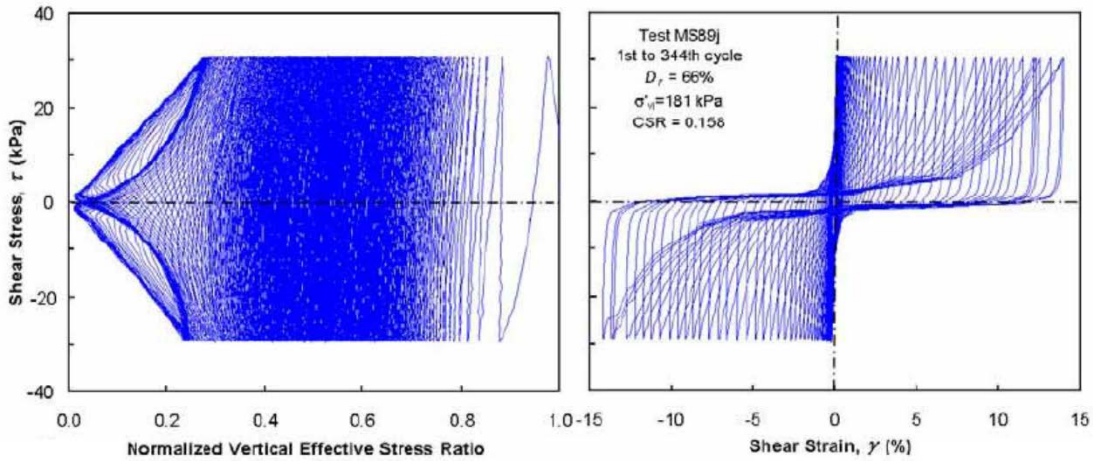

***Figure 2.16**: Post-liquefaction shear strain accumulation during undrained cyclic simple shear tests on Monderey No. 0/30 sand (figure after Wu et al., 2004).*

Elgamal et al. (2003) proposed a method to decrease the tendency for dilation upon reloading and thus leading to increased straining. Zhang and Wang (2012) continued the work of Shamoto et al. (1997) and proposed a theoretical and constitutive framework for

the modeling of post-liquefaction strain accumulation, by dividing the plastic volumetric strains into irreversible and reversible counterparts and then using an intrinsic relationship between residual volumetric strain and shear strain. This concept was implemented by Wang et al. (2014). The UBCSand model by Beaty and Byrne (2011) predicts also post-liquefaction shear strain accumulation. Boulanger and Ziotopoulou (2013) included a series of functions based on cumulative indexes in their model, targeting to decrease exhibited dilation cycle per cycle after initial liquefaction and thus enabling shear strain accumulation and prevent shear locking. For this purpose, Tasiopoulou and Gerolymos (2016a) proposed the evolution of the stress ratios of the bounding and dilatancy surfaces to be a function of the cumulative deviatoric strain increments. More recently, Barrero et al. (2020) proposed the concept of "semi-fluidized state (Sf)" and proposed a new internal state variable that evolves from 0 to 1 within the Sf range of low mean effective stresses and its constitutive role is to reduce the values of parameters controlling the plastic modulus and dilatancy. This concept was incorporated in the same way by Yang et al. (2020) in the SANISAND-MSf model, while a similar approach is followed by Cheng and Detournay (2021).

B. Effect of overburden stress level on liquefaction resistance

The effect of overburden stress on cyclic resistance ratio CRR is often expressed and quantified in terms of a correction factor, known as K_σ, and actually describes the curvature of the cyclic strength envelope with increasing consolidation stress (Montgomery et al., 2012) and for overburden stress levels above 1atm takes values less than unity. There are numerous experimental evidence in the literature that corroborate this effect (e.g., Idriss and Boulanger 2008; Youd and Idriss 2001) (**Figure 2.17**).

Based on the above, models in the literature dealing with liquefaction incorporate special components to consider this effect. Some examples are the PM4Sand model proposed by Boulanger and Ziotopoulou (2013), which was one of the first discussing this issue in the literature, the P2PSand model by Cheng and Detournay (2021), the Tager model by Tasiopoulou and Gerolymos (2016a) (in Gerolymos and Anthi, 2019) and the UBCSand model by Beaty and Byrne (2011).

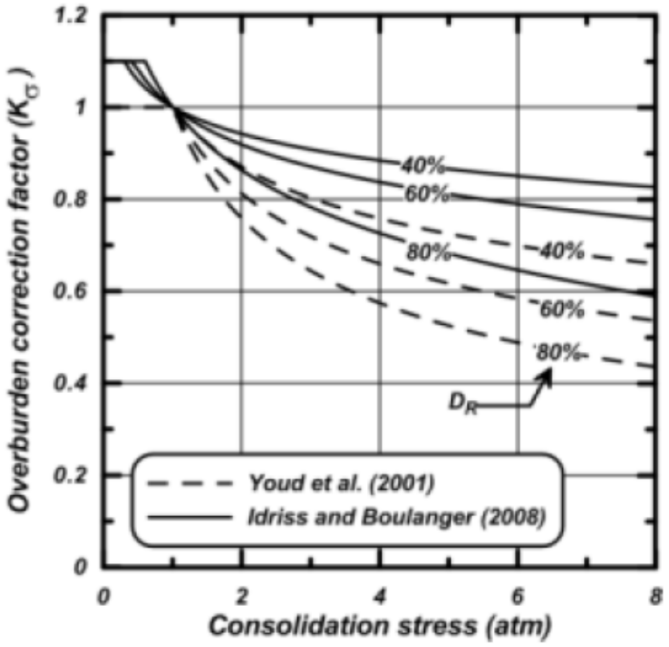

***Figure 2.17**: Relationships for K_σ factor proposed by Idriss and Boulanger (2008) and Youd et al. (2001) (figure after Montgomery et al., 2012).*

C. Strain accumulation at high number of (partially) drained loading cycles

The engineering analysis of cyclic response proves very challenging for long-lasting cyclic loading events (namely, 'high-cyclic' loading), such as those experienced by soils and foundations under operating offshore structures. Quite indicative is the case of monopile or bucket foundations for offshore wind turbines, whose design must assure full functionality of the structure during their whole operational life, while experiencing loading cycles with alternating sequences of small-amplitude vibrations and severe storms loadings. The order of magnitude of the number of cycles used for such type of analyses may be around 10^8 - 10^9 (**Figure 2.18**). The degradation of soil's stiffness with the number of cycles may lead to a change of the natural frequency of structure – soil system and to permanent non-operational displacements of the structure. Actually, during the cyclic loading history, usually partial drainage occurs and two competitive mechanisms act: a tendency for excess pore pressure development and a resultant soil's stiffness decay and an antagonistic tendency for densification and increase of soil's stiffness. In a fully coupled analysis, which of the two aforementioned mechanisms dominates the response depends, among others, on loading characteristics (intensity, duration, rate etc…) and drainage effects (permeability

coefficient of the soil, drainage paths etc..). However, even if the response is closer to the drained and volumetric straining continues with a decreasing rate for a significant part of the loading, it is possible, at very large numbers of cycles, the stiffness of foundation to decrease due to irreversible damages in soil's structure (e.g., Bhattacharya et al., 2013; Tasiopoulou et al. 2021). This topic constitutes a relatively fresh field of research in terms of constitutive modeling of sands, as the strain range, the duration and the drainage conditions of loading are far different of what earthquakes impose. Additionally, modeling becomes even more challenging when considering the limited experimental data in the literature for such loading conditions.

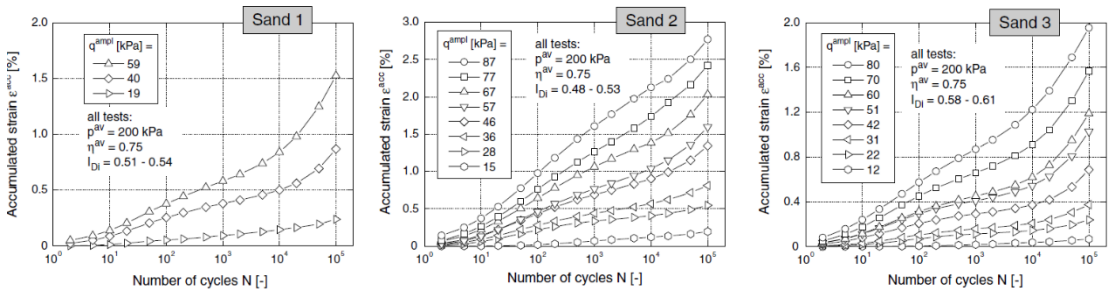

***Figure 2.18**: Strain accumulation during high-cycle (~10^5) cyclic triaxial experiments (figure after Wichtmann et al., 2009).*

Apart from the solution of "explicit" constitutive models described in a previous paragraph, there are attempts in the literature of conventional advanced constitutive models trying to replicate these mechanisms of response and some examples are given by Liu et al. (2019), Liu et al. (2020) and Tasiopoulou et al. (2021).

D. Post-liquefaction reconsolidation settlements

Volumetric strains that develop during post-liquefaction reconsolidation of sand are difficult to be predicted numerically, since they are not produced by shearing. Such a consolidation path induces very little change in stress-ratio values, and hence, stress-ratio driven models are bound to estimate very small plastic strains due to this type of loading. This result highlights a well-known limitation of stress–ratio driven constitutive models, in which a constant stress-ratio stress path leads to zero plastic straining.

To account for plastic volumetric strains developed due to such types of loading, additional mechanisms for plastic strain rate development may be considered. As discussed above, a possible solution to this problem is the incorporation of an extra bounding surface in the stress space intersecting the hydrostatic axis and acting like a “cap” to the other (stress-ratio-based) model surfaces. The model proposed by Taiebat and Dafalias (2008) with a closed yield surface, or the “cap” surface proposed by Wang et al. (1990) may prove very useful constitutive tools for such additional loading mechanisms.

On the other hand, there are models in the literature, that although do not incorporate a mechanism like those described above, bypass this inadequacy by incorporating macroscopic formulas for predicting plastic volumetric strains in post liquefaction regime. For example, the PM4Sand model (Boulanger and Ziotopoulou, 2013) approaches the estimation of realistic post-shaking volumetric strains by artificially reducing the elastic moduli. In this way, plastic volumetric strains induced during re-consolidation continue to be negligible, but the target total values are reached by the increase of the elastic components. Such an approach is obviously phenomenological and may prove difficult to handle in numerical analyses of boundary value problems.

E. Stress principal axes rotation

The significance of stress principal axes rotation during phenomena like wave loading, earthquakes, and traffic loading is well recognized in the literature (e.g., Towhata and Ishihara, 1985). During this type of loading, as only the direction and not the measure of the principal stresses change, the stress-ratio is maintained constant. Experimental studies of these loading conditions (e.g., Ishihara and Towhata, 1983; Ishihara and Yamazaki, 1984;Tong et al. 2010) show considerable strain accumulation (**Figure 2.19**), which under undrained conditions may even induce liquefaction after a sufficient number of cycles.

However, this is a response that cannot be captured by models based on the change of stress-ratio to induce plastic strains. Moreover, neither the incorporation of a closed-type “cap” mechanism would be useful, as there is not a change in the stress level – actually, the resultant stress-ratio during such a loading is maintained constant in the stress-ratio space. Recently, following the work of Gutierrez et al. (1991), (1993), Gutierrez and Vardoulakis (2007) and Gutierrez and Wang (2009), Petalas et al. (2019) proposed a constitutive scheme

to deal with this issue. They enriched the framework of the SANISAND-F model (Petalas et al., 2020), by including the effect of non-coaxiality between stress and plastic strain rate tensors due to plastic loading induced by the continuous principal axis' rotation on the plastic modulus and dilatancy terms of their model. There are also other approaches in which a second loading mechanism is introduced, or multiple dilatancy functions, but since the proposed model is not targeting this type of response no further analysis is considered useful here.

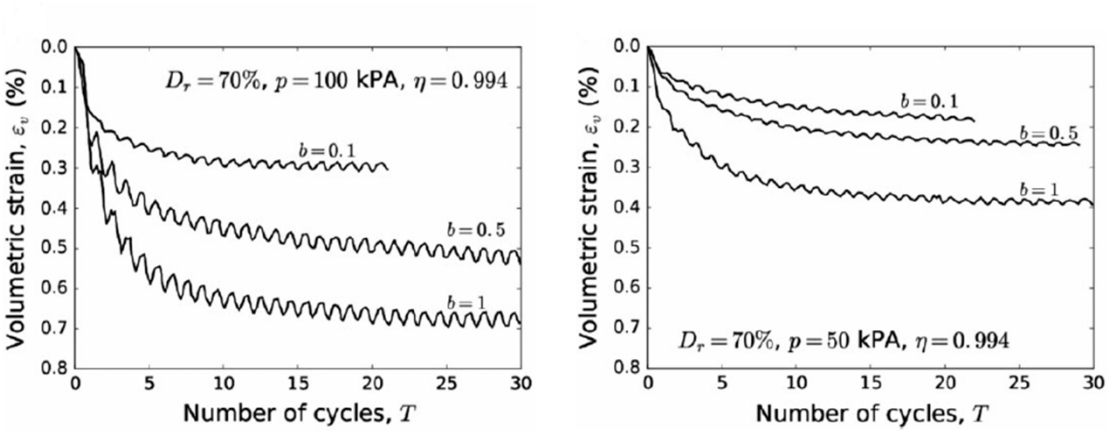

***Figure 2.19**: Volumetric strain accumulation in drained tests experiencing stress PA rotation after Tong et al. 2010 (figure after Petalas et al., 2019).*

F. Problem of stress-strain overshooting

One of the problems faced in models employing the last load reversal point, or in models employing reversal surfaces in general, is the stress-strain overshooting upon unloading and immediate reloading, i.e., the prediction of a stress-strain curve that is unrealistic since it overshoots the expected continuation that this curve would have if this unloading-reloading cycle had not occurred. The foregoing problem is related to the unnecessary updating of the retained in memory stress-ratio tensor at the last load reversal point, upon unloading and upon immediate reloading. The occurrence of these numerically "*informal*" load reversal signals affects mainly the monotonic response and the predictions in static problems (e.g., problems of static bearing capacity), where unexpected overshooting occurs. In their recent work Duque et al. (2021) underlined the high sensitivity of both advanced plasticity (e.g., bounding surface) and hypoplasticity models to this issue. In models with reversal surfaces (such as the presented in this Thesis), the problem is more

complicated, since also the loading direction tensor and the employed mapping rule may be affected. So, the issue may be not just an overshooting problem, but in terms of constitutive modeling it boils down to what is the "*accurate*" value of the load reversal point for having a realistic response in any load path that may be encountered in boundary value problems, both static and dynamic. This premise makes the inclusion of a mitigation technique necessary.

This problem has been sufficiently studied in the literature leading to several approaches for overcoming it. Dafalias and Taiebat (2016), follow the approach of Dafalias (1986) and "adjust" the value of stress-ratio tensor "retained" at the last load reversal point, depending on the "significance" - in-terms of accumulated deviatoric strain - of the intervening loading path. This concept was enriched furtherly by Cheng and Detournay (2021), who added the extra condition of a sufficiently large change in stress-ratio to occur before the aforementioned tensor to be updated according to Dawson et al. (2001) and a provision of reset of the reversal point when the stress ratio reaches once again the "*back-bone*" curve during reloading, according to Wang et al. (1990). Similar techniques and approaches have been incorporated in the constitutive framework of Boulanger and Ziotopoulou (2013), while the recent literature is increasingly concerned with this issue (e.g., Li and Liu, 2020; Zhang et al., 2021).

Chapter 3

Constitutive Formulation

3.1 Model platform

The formulation of the model is presented in the multiaxial stress space and the equations are given in tensorial form. Second-order tensors are written in bold characters, so as to be distinguished from scalars, while normal stress components are considered effective. A superposed dot over scalar or tensorial quantities implies material time derivative or rate. A symbol : between 2 tensors denotes their double inner product or equivalently the trace (tr) of their product. Specifically, the strain tensor is depicted as ε and can be decomposed into its (scalar) volumetric component $\varepsilon_{vol} = \mathrm{tr}\boldsymbol{\varepsilon}$ and the (tensorial) deviatoric component $\boldsymbol{e} = \boldsymbol{\varepsilon} - (\varepsilon_{vol}/3)\,\boldsymbol{I}$, with $\boldsymbol{I}$ standing for the second-order identity tensor. According to the theory of plasticity, the rates of these strain components are independently decomposed into an elastic and a plastic part:

$$\dot{\varepsilon}_{vol} = \dot{\varepsilon}^{e}_{vol} + \dot{\varepsilon}^{p}_{vol} \tag{3.1}$$

$$\dot{\boldsymbol{e}} = \dot{\boldsymbol{e}}^{e} + \dot{\boldsymbol{e}}^{p} \tag{3.2}$$

where superscripts *e* and *p* denote the elastic and plastic parts, respectively. The effective stress tensor is symbolized by $\boldsymbol{\sigma}$ and consists of its hydrostatic component $p = (1/3)\,\mathrm{tr}\boldsymbol{\sigma}$ (i.e., the mean effective stress) and its deviatoric component $\boldsymbol{s} = \boldsymbol{\sigma} - p\boldsymbol{I}$. Of great importance is also the deviatoric stress ratio tensor $\boldsymbol{r} = \boldsymbol{s}/p$, which is instrumental in the constitutive equations of this model.

According to isotropic elasticity, any given effective stress rate $\dot{\boldsymbol{\sigma}}$ results in an elastic strain rate $\dot{\boldsymbol{\varepsilon}}^{e}$ equal to:

$$\dot{\boldsymbol{\varepsilon}}^{e} = \dot{\boldsymbol{e}}^{e} + \frac{\dot{\varepsilon}^{e}_{vol}}{3}\boldsymbol{I} = \frac{1}{2G}\dot{\boldsymbol{s}} + \frac{1}{3K}\dot{p}\boldsymbol{I} \tag{3.3}$$

where G is the shear modulus and K the bulk modulus, respectively. The plastic strain rate $\dot{\boldsymbol{\varepsilon}}^{p}$ is defined as:

$$\dot{\boldsymbol{\varepsilon}}^{\mathrm{p}} = \dot{\boldsymbol{e}}^{\mathrm{p}} + \frac{\dot{\varepsilon}^{\mathrm{p}}_{\mathrm{vol}}}{3}\boldsymbol{I} = \langle \Lambda \rangle \boldsymbol{R} = \langle \Lambda \rangle \left(\boldsymbol{n} + \frac{D}{3}\boldsymbol{I} \right) \tag{3.4}$$

$$\boldsymbol{R} = \boldsymbol{n} + (D/3)\boldsymbol{I} \tag{3.5}$$

where $\boldsymbol{R}$ is the plastic strain rate direction, with unit-norm tensor $\boldsymbol{n}$ constituting its deviatoric part and D, the dilatancy function of the model, defining its volumetric part. The $\boldsymbol{n}$ adopts all the properties of unit-norm deviatoric tensors (i.e., $\boldsymbol{n} = \boldsymbol{n}^{\mathrm{T}}$, tr$\boldsymbol{n}$ = 0 and $\boldsymbol{n}$:$\boldsymbol{n}$ = 1**)** and is determined according to the adopted mapping rule of the model, while the dilatancy function D is explicitly defined. The scalar value Λ is the loading index, which is set in Macauley brackets, yielding $\langle \Lambda \rangle = 0$ when $\Lambda \leq 0$ and $\langle \Lambda \rangle = \Lambda$, when $\Lambda > 0$. In stress terms it is determined as:

$$\Lambda = \frac{1}{K_{\mathrm{p}}}\boldsymbol{L} : \dot{\boldsymbol{\sigma}} = \frac{1}{K_{\mathrm{p}}}\boldsymbol{n} : p\dot{\boldsymbol{r}} \tag{3.6}$$

where K_{p} is the plastic modulus of the model and $\boldsymbol{L}$ describes the loading direction in the multiaxial stress space, which equals to:

$$\boldsymbol{L} = \boldsymbol{n} - \frac{\boldsymbol{n} : \boldsymbol{r}}{3}\boldsymbol{I} \tag{3.7}$$

In Equation (3.4) the inclusion of loading index Λ in Macauley brackets implies that the plastic strain rate is zero when $\Lambda < 0$ (unloading) or $\Lambda = 0$ (neutral loading), and non-zero in cases of loading ($\Lambda > 0$). According to Equation (3.6), loading takes place either with a combination of $\boldsymbol{n} : \dot{\boldsymbol{r}} > 0$ (p is always nonnegative) and $K_{\mathrm{p}} > 0$ (hardening response) or $\boldsymbol{n} : \dot{\boldsymbol{r}} < 0$ and $K_{\mathrm{p}} < 0$ (softening response). Considering all the above, a non-zero deviatoric stress ratio rate ($\dot{\boldsymbol{r}} \neq 0$) serves as the necessary condition for non-zero plastic strain rates. This concept, while quite realistic during shearing, should be used with caution in problems where loading under constant stress ratio prevails (e.g., one-dimensional consolidation). To account for plastic strains developed due to such types of loading, additional mechanisms for plastic strain rate development may be considered (e.g., (Taiebat and Dafalias, 2008 or Wang et al., 1990). However, such complications are beyond the

scope of this model. Finally note, that a non-zero deviatoric stress ratio rate ($\dot{\boldsymbol{r}} \neq 0$) is a necessary, but not a sufficient condition for non-zero plastic strain rates. This is because the so-called neutral loading ($\Lambda = 0$) may appear for tangential loading paths where both $\boldsymbol{n} \neq 0$ and $\dot{\boldsymbol{r}} \neq 0$ continuously, but $\boldsymbol{n} : \dot{\boldsymbol{r}} = 0$ throughout the loading. In this sense, the model does not have a truly zero elastic range in stress space, as was clarified by Dafalias and Taiebat (2016) for models of this type.

In closing, Equations (3.3) and (3.4) quantify strain rates for any given stress rate. However, in numerical codes the input is usually the strain rate, hence the above equations are properly rearranged to give the effective stress rate $\dot{\boldsymbol{\sigma}}$ as a function of any given strain rate $\dot{\boldsymbol{\varepsilon}}$ as:

$$\dot{\boldsymbol{\sigma}} = 2G\dot{\boldsymbol{e}} + K\dot{\varepsilon}_{\mathrm{v}}\boldsymbol{I} - \langle \Lambda \rangle \left(2G\boldsymbol{n} + KD\boldsymbol{I}\right) \tag{3.8}$$

where the loading index Λ is now expressed in terms of applied strain $\dot{\boldsymbol{\varepsilon}}$ rate via:

$$\Lambda = \frac{2G\mathbf{n} : \dot{\boldsymbol{e}} - \left(\mathbf{n} : \mathbf{r}\right) K\dot{\varepsilon}_{\mathrm{v}}}{K_{\mathrm{p}} + 2G - \left(\mathbf{n} : \mathbf{r}\right) KD} \tag{3.9}$$

3.2 Critical state behavior

The proposed model formulation incorporates the Critical State Theory of Soil Mechanics (Schofield and Wroth, 1968) by adopting a unique Critical State Surface (CSS) in the stress $\boldsymbol{\sigma}$ - void ratio e space. In practice, it firstly employs the projection of the CSS on the mean effective p - void ratio e space, i.e., the so-called Critical State Line (CSL) in this space. A power relation is preferred for the CSL, allowing for a greater range of applicability for p values. Hence, for a given mean effective stress p, the corresponding critical value of void ratio e_{cs} on the CSL is given by (Dafalias and Manzari, 2004; Li and Wang, 1998):

$$e_{\mathrm{cs}} = e_{\mathrm{o}} - \lambda \left(\frac{p}{p_{\mathrm{atm}}} \right)^{\xi} \tag{3.10}$$

where e_{o} is the value of void ratio at $p=0$ controlling the position of CSL (a model constant),

p_{atm} the atmospheric pressure (e.g., p_{atm}=101.3 kPa) and λ and ξ nonnegative model constants forming CSL's curvature and shape in the (p – e) space.

The current state of the material is always identified with reference to the CSL through the state parameter ψ, which quantifies the difference between the current void ratio e and the corresponding critical state value e_{cs} at the current mean effective stress p via (Been and Jefferies, 1985):

$$\psi = e - e_{cs} \tag{3.11}$$

Parameter ψ determines the state of the material as a combined function of its density (through void ratio e) and its effective mean stress (through e_{cs}), expressing how far from critical is the current state. It is obvious that a state (e, p) above the CSL in the (p - e) space corresponds to $\psi > 0$ and consequently to contractive behavior, while, on the contrary, a state below the CSL in the (p - e) space corresponds to $\psi < 0$ and consequently to dilative behavior. A schematic illustration of ψ in (p,e) space is presented in **Figure 3.1** The explicit incorporation of ψ in model equations, starting from the model surfaces in the next Section, is what gives the SANISAND character to this model.

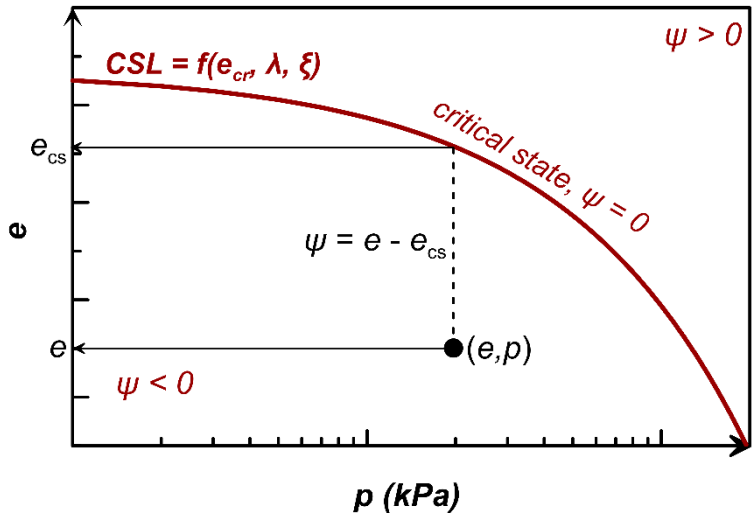

Figure 3.1: *Critical state line (CSL) as a projection of the CSS on the (p – e) space and definition of state parameter ψ for any current state (p , e).*

3.3 Model surfaces

Being of the SANISAND-type, the proposed bounding surface plasticity model is stress ratio-driven. For the common case of loading in triaxial compression (TC), the critical state M_c^c, the bounding (or peak) M_c^b and the dilatancy M_c^d stress ratios (collectively $M_c^{c,b,d}$) are related to each other via the state parameter ψ, as follows:

$$M_c^b = M_c^c \exp\left(n^b \langle -\psi \rangle\right) \tag{3.12}$$

$$M_c^d = M_c^c \exp\left(n^d \psi\right) \tag{3.13}$$

where, M_c^c, n^b and n^d are nonnegative model parameters. Note that the subscript c depicts that the loading is in triaxial compression, while superscripts c, b or d clarify which of the three stress ratios is of interest. These exponential equations are adopted from Li and Dafalias (2000) and Dafalias and Manzari (2004). Note also that here Macauley brackets appear in Equation (3.12) to make it qualitatively compatible with the linear form of this equation in Manzari and Dafalias (1997). Hence, based on Equations (3.12) and (3.13), for dilative states where $\psi < 0$, $M_c^d < M_c^c < M_c^b$ holds. This implies that the peak stress ratio is higher than the critical state ratio, while the dilatancy stress ratio is lower than both of them. Similarly, for contractive states ($\psi > 0$) $M_c^d > M_c^c = M_c^b$ holds, implying purely contractive response (since the M_c^d is not reached) and attainment of the peak stress ratio at critical state.

The generalization of these three stress ratios in multiaxial stress space takes the form of surfaces, namely the critical state, the bounding and the dilatancy surface. All three surfaces have the shape of an open cone, with their apex on the origin of stress space, are homologous and their apertures are defined by the stress ratio values M_θ^c, M_θ^b and M_θ^d respectively. The subscript θ in the foregoing stress ratio values depicts that this generalization is performed with the aid of the Lode angle θ, that is hereby defined in terms of the unit-norm deviatoric loading direction tensor $\boldsymbol{n}$, according to:

$$\cos(3\theta) = \sqrt{6}\,\mathrm{tr}\left(\boldsymbol{n}^3\right) = 3\sqrt{6}\,\det\boldsymbol{n} \tag{3.14}$$

where det is the determinant of a (second-order) tensor. Based on its definition, angle θ ranges between 0° and 60°, where 0° corresponds to loading in triaxial compression (TC) and 60° to triaxial extension (TE). All the intermediate values of θ correspond to non-triaxial loading conditions. Hence, the M stress ratio of the aforementioned surfaces can be defined as a continuous function of θ, a notion firstly proposed for soils by van Eekelen (1980). In this model, this function is depicted by g and is used as follows:

$$M_{\theta}^{c,b,d} = g(\theta,c)\, M_{c}^{c,b,d} \tag{3.15}$$

where $c = M_{e}^{c}/M_{c}^{c}$ is a nonnegative model parameter that is equal to the ratio of the critical stress ratio in triaxial extension (TE) over that in TC. In this paper, the adopted $g(\theta,c)$ function is borrowed from Loukidis and Salgado (2009),although its original form dates back to Van Eekelen (1980), and reads:

$$g(\theta,c) = \frac{2^{\mu}\, c}{\left[1 + c^{1/\mu} - \left(1 - c^{1/\mu}\right)\cos\left(3\theta\right)\right]^{\mu}} \tag{3.16}$$

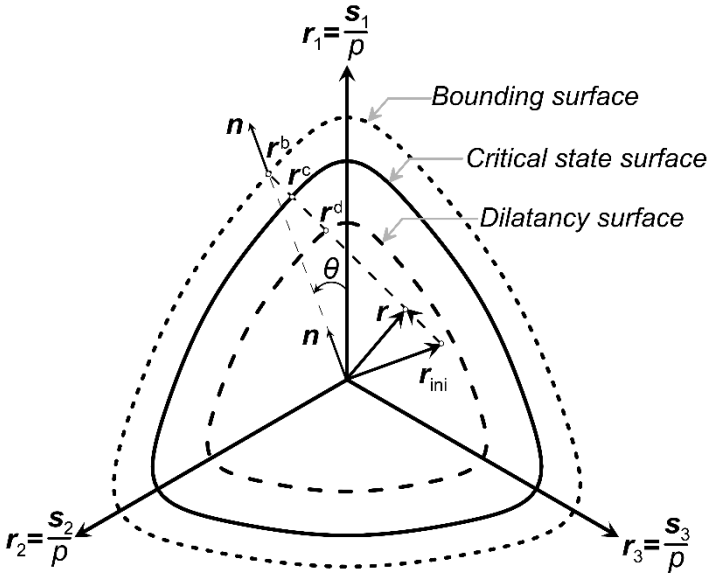

Figure 3.2: *Model surfaces on the π-plane of the deviatoric stress-ratio space and adopted mapping rule. The relative location of dilatancy and bounding surfaces corresponds to a dilative state ($\psi < 0$).*

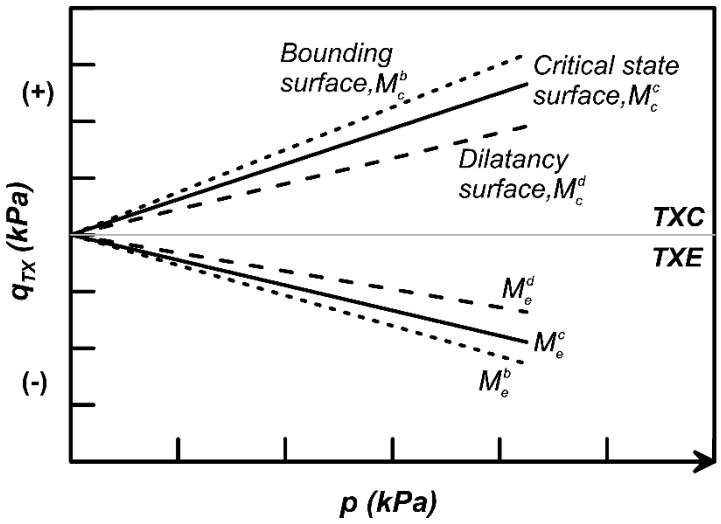

Figure 3.3: *Model surfaces on the triaxial q_{TX} - p space. The relative location of dilatancy and bounding surfaces corresponds to a dilative state ($\psi < 0$).*

where exponent μ controls the convexity of the surface on the π-plane of the deviatoric stress ratio space. This μ is set fixed to 0.16 here, which provides convexity for the usual cases of $c > 0.67$. Observe here, that $g = 1$ for $\theta = 0^o$ and $g = c$ for $\theta = 60^o$, thus rendering the pertinent values for the stress ratios in TC and TE on the basis of Equation (3.15). The procuring shape of the three model surfaces (for c =0.712) on the foregoing π-plane is shown in **Figure 3.2** for an exemplary case where $\psi < 0$, which dictates their apertures as a function of Equations (3.12) and (3.13). Moreover, **Figure 3.3** shows their projection on the triaxial *q*-*p* space, where *q* is the deviatoric stress.

3.4 Mapping rule

The distance of the current stress ratio $\boldsymbol{r}$ from these surfaces on the π-plane of the deviatoric stress ratio space is a key component of the constitutive equations. The distance from each surface is defined with the aid of the image-points $\boldsymbol{r}^c$, $\boldsymbol{r}^b$ and $\boldsymbol{r}^d$ (collectively $\boldsymbol{r}^{c,b,d}$) of $\boldsymbol{r}$ on the critical state, the bounding and the dilatancy surfaces, respectively. These image points are defined on the basis of the selected mapping rule, which is schematically illustrated in **Figure 3.2**. This radial mapping rule has been repeatedly used in the past (e.g., (Andrianopoulos et al., 2010a; Wang et al., 1990).

The all-important tensor $\boldsymbol{r}_{ini}$ refers to the tensor $\boldsymbol{r}$ when the last load reversal took place, i.e., when the loading index Λ of Equation (3.6) or (3.9) took a negative value last. For the first shearing path it is, by default, equal to the value of tensor $\boldsymbol{r}$ at the initial state

(e.g., end of consolidation). This correlation to the recent shear history via $\boldsymbol{r}_{\text{ini}}$ dates back to the concept of stress reversal surfaces by Mróz et al. (1979) and Mroz and Zienkiewicz (1984). Having determined the image point $\boldsymbol{r}^{\text{b}}$ on the bounding surface allows for the definition of the unit-norm deviatoric tensor $\boldsymbol{n}$ starting from the stress origin and depicting its direction as:

$$\boldsymbol{n} = \frac{\boldsymbol{r}^{\text{b}}}{\sqrt{\boldsymbol{r}^{\text{b}} : \boldsymbol{r}^{\text{b}}}} \tag{3.17}$$

Given the unit-norm tensor $\boldsymbol{n}$, the image points on all three model surfaces may be computed as:

$$\boldsymbol{r}^{\text{c,b,d}} = \sqrt{\frac{2}{3}} M_{\theta}^{\text{c,b,d}} \boldsymbol{n} \tag{3.18}$$

where $M_{\theta}^{\text{c,b,d}}$ is defined in Equation (3.15). Consequently, the scalar distance between the current stress ratio $\boldsymbol{r}$ and the model surfaces (collectively $d^{\text{c,b,d}}$) is computed along the $\boldsymbol{n}$ direction, as:

$$d^{\text{c,b,d}} = (\boldsymbol{r}^{\text{c,b,d}} - \boldsymbol{r}) : \boldsymbol{n} \tag{3.19}$$

According to Equation (3.19), a positive $d^{\text{c,b,d}}$ value implies a current stress ratio $\boldsymbol{r}$ located inside the corresponding surface, while a negative value of the distance $d^{\text{c,b,d}}$ depicts that it is outside.

3.5 Elastic moduli

The maximum value of the shear modulus G_{max} used herein follows a hypoelastic formulation, since it is a function of the current values of the mean effective stress p and the void ratio e. Specifically, based on Hardin (1978), it holds:

$$G_{\text{max}} = G_{\text{o}}\ p_{\text{atm}} \left(\frac{1}{0.3 + 0.7e^2} \right) \sqrt{\frac{p}{p_{\text{atm}}}} \tag{3.20}$$

where G_{o} is a model parameter and p_{atm} is the atmospheric pressure. However, the tangential value of the shear modulus G_{t} entering the calculation of the elastic strain rate (see Equation

(3)) incorporates a Ramberg-Osgood type (Ramberg and Osgood, 1943) hysteretic behavior, which provides a non-linear degradation with strain. This concept, originally proposed by Papadimitriou et al. (2001) and Papadimitriou and Bouckovalas (2002) and then used slightly modified by Andrianopoulos et al. (2010a), Loukidis and Salgado (2009) and Taborda et al. (2014), allows for a smooth decrease of the tangential shear modulus G_t, from its maximum value (equal to G_{max} from Equation (20)) and a consequent smooth increase of viscous damping with increasing shear amplitude (e.g. Vucetic and Dobry, 1991). In more detail, the non-linear hysteretic form of G_t is given as:

$$G_t = \frac{G_{max}}{T} \tag{3.21}$$

where T is a positive scalar (≥ 1) variable, defined as:

$$T = 1 + 2\left(\frac{1}{a_1} - 1\right)\left(\frac{\sqrt{\frac{1}{2}(\boldsymbol{r} - \boldsymbol{r}_{ini}) : (\boldsymbol{r} - \boldsymbol{r}_{ini})}}{a_1\left(\frac{G_{max}}{p}\right)\gamma_1}\right) \tag{3.22}$$

Respectively, the tangential bulk modulus K_t entering Equation (3.3) is interrelated to the tangential shear modulus G_t on the basis of a constant value v of the Poisson's ratio (a model parameter) according to:

$$K_t = \frac{2}{3}\frac{(1+v)}{(1-2v)}G_t \tag{3.23}$$

Note that according to Equation (3.22) variable T reduces the shear modulus G_t as the current deviatoric stress ratio $\boldsymbol{r}$ diverts from the stress ratio $\boldsymbol{r}_{ini}$ at the last stress reversal point. The first difference from Andrianopoulos et al. (2010a) is that in the denominator of variable T the current values of G_{max} and p are used and not those at the last stress reversal point. The second difference is the use of a_1 (≤ 1) and γ_1 (> 0) that were considered as model parameters in the foregoing model, but are fixed constants herein. Particularly, based on Papadimitriou et al. (2001), the decrease of both a_1 and γ_1 leads to increased non-linearity, while the γ_1 may be viewed as a characteristic threshold shear strain beyond which any further degradation to the overall soil stiffness is mainly attributed to the development and

accumulation of plastic strains. For this model, the fixed values $a_1 = 0.85$ and $\gamma_1 = 0.03\%$ are adopted, i.e., they correspond to the upper-bound of the range originally proposed by Papadimitriou et al. (2001). It has to be underlined here that without the additional nonlinearity offered by variable T it is impossible to attain accurate simulations across the whole range of shear strains, from small-strain dynamic loading to large-strain monotonic shearing using the same set of model parameters. Moreover, it is the inclusion of this variable T, in combination with the plastic modulus detailed in the sequel, that permit the calibration of G_{max} from truly small strain measurements (e.g., bender elements, geophysical measurements). Another significant contribution of this formulation was highlighted in Loukidis and Salgado (2009), where it was shown that without variable T it is impossible to obtain compatible drained and undrained stress-dilatancy response, while retaining realistic values of Poisson's ratio v and G_{max} irrespective of type of loading.

3.6 Plastic modulus

The plastic modulus K_p in Equation (3.24) is given by:

$$K_p = h_o \; h_\theta \; h_f \; h_{pp} \; h_{ep} \; p \frac{d^b}{(\boldsymbol{r}-\boldsymbol{r}_{ini}) : \boldsymbol{n}} \tag{3.24}$$

where h_θ, h_f, h_{pp}, h_{ep} are nonnegative model functions that will be discussed extensively in the sequel, and h_o a nonnegative model parameter. The formulation of plastic modulus with its dependence on d^b and $(\boldsymbol{r}-\boldsymbol{r}_{ini})$ indicates that it smoothly decreases, resulting in increased plastic strains, as shearing evolves monotonically and stress ratio $\boldsymbol{r}$ increases and moves away its value at the loading initialization $\boldsymbol{r}_{ini}$. Based on Equation (3.24), the sign of plastic modulus K_p is controlled by the sign of the distance d^b. According to Equation (3.6), and given that $\Lambda > 0$, hardening response occurs ($\boldsymbol{n} : \dot{\boldsymbol{r}} > 0$ and $K_p > 0$) when a stress ratio lies inside the bounding surface ($d^b > 0$) or on the contrary softening response occurs ($\boldsymbol{n} : \dot{\boldsymbol{r}} < 0$ and $K_p < 0$) when a stress ratio lies outside the bounding surface ($d^b < 0$). Moreover, denominator $(\boldsymbol{r}-\boldsymbol{r}_{ini}):\boldsymbol{n}$ implies that at the initialization of a load reversal (where $\boldsymbol{r}_{ini}$ has just been updated to the value of $\boldsymbol{r}$) K_p takes an infinite value, thus leading to zero plastic straining at the beginning of every new shearing process.

Function h_{pp}, given as:

$$h_{pp} = \sqrt{\frac{p_{atm}}{p}} \tag{3.25}$$

in combination with p multiplying the right part of Equation (3.24), results in a total effect of mean effective stress on K_p of an exponent of 0.5, in agreement with Equation (3.20) for the elastic modulus, where the exponent of p is the same.

The effect of void ratio is also included in plastic modulus through a decreasing function of e:

$$h_{ep} = e^{-ch} \tag{3.26}$$

where c_h is a model parameter.

An interesting experimental finding that this model targets to simulate is the differentiation in strength under cyclic undrained loading, in terms of cyclic resistance to liquefaction (Mulilis et al., 1977; Vaid and Sivathayalan, 1996), where despite the continuous change of loading direction between TC and TE, triaxial conditions show greater cyclic resistance than simple shear (SS).

Without incorporating a special constitutive framework accounting for anisotropy, an additional loading direction function is added in this model to capture this effect in a quantitative way. This loading direction effect is already taken into account through Lode angle (θ) effect on model surfaces and distances d^b and d^d, but this slight differentiation of the position of the bounding and dilatancy surfaces, specifically for the intermediate Lode angles θ between TC and TE, has been proven not sufficient enough. Attempting to treat this only through modifying function g would lead to problems of non-convexity of the bounding surfaces. Thus, the role of function h_θ (≤ 1) is to enhance this effect by incorporating it directly on plastic modulus, as follows:

$$h_\theta = \left[2g(\theta', c) - 1\right]^{5/2} \tag{3.27}$$

Function h_θ actually utilizes function g of Equation (3.16) to capture the foregoing effect, but for a modified Lode angle $\theta' = \theta + 30^o$. The idea of using in this expression ($\theta + 30^o$) instead of current θ stems from the need of a softer response in SS conditions, while

not intervening TC and TE, where the effect is quite well captured by the existing model features. In this way, for θ = 0° (TC) and θ = 60° (TE), the value of g entering Equation (3.27) is the same and h_θ attains its maximum value. For intermediate values of θ, g attains lower values, resulting in lower values also for h_θ.

3.6.1 Effect of fabric on plastic modulus

The use of fabric functions, as empirical macroscopic indicators of sand fabric evolution during cyclic shearing, is a common practice in constitutive modeling (Andrianopoulos et al., 2010a; Boulanger and Ziotopoulou, 2013; Dafalias and Manzari, 2004; Papadimitriou et al., 2001). In this model this significant effect on plastic strains is described macroscopically by the scalar-valued function h_f on plastic modulus, given as:

$$h_f = \frac{1+\left\langle f_p - c_f \right\rangle^2}{1+\left\langle \boldsymbol{f}_{ini} : \boldsymbol{n} \right\rangle} \tag{3.28}$$

According to Equation (3.28), h_f - borrowing the formulation of fabric functions introduced earlier by Papadimitriou and Bouckovalas (2002) and Andrianopoulos et al. (2010a) - is a function of the scalar-valued function f_p and fabric tensor $\boldsymbol{f}$, both of them starting from zero and evolving independently with plastic volumetric strains, as follows:

$$\dot{f}_p = (2-a)\, N\, h_{pf}\, \dot{\boldsymbol{\varepsilon}}^p_{vol} \tag{3.29}$$

$$\dot{\boldsymbol{f}} = -N\, h_{post\text{-}liq} \left(\boldsymbol{f} + f_{max}^{(1+a)}\, \boldsymbol{n} \right) \left\langle -\dot{\boldsymbol{\varepsilon}}^p_{vol} \right\rangle \tag{3.30}$$

where:

$$N = N_o \cdot h_{ef} \cdot \left\langle -\psi_o \right\rangle^{0.1} \tag{3.31}$$

$$h_{pf} = \left(\frac{p_{atm}}{p_o} \right)^{\frac{1}{2e_o^2}} \leq 1.5 \tag{3.32}$$

$$h_{ef} = e_o^{-0.5ch} \tag{3.33}$$

$$f_{max} = \max\left(f_p \right) \tag{3.34}$$

$$0 \le a = -2\left(\frac{\left| \int \dot{\varepsilon}_{vol} \right|}{\left| \int \dot{\varepsilon}_{vol}^{p} \right|} - 1 \right) \le 1 \tag{3.35}$$

Equations (3.28) – (3.35) describe a complete framework for the evolution of fabric function and are explained in detail in the following. Function $h_{post\text{-}liq}$ is not presented yet, as it accounts for cyclic mobility and accumulation of strains after liquefaction is triggered, and its formulation is analyzed in a special section below. For now, note that $h_{post\text{-}liq} = 1$ unless initial liquefaction occurs, i.e., the state when the current p becomes smaller or equal to a critical value p_l, defined as a $p_l = \min(0.05\, p_o; 10\ \text{kPa})$. As already mentioned, Equation (3.28) incorporates the effect of the current fabric state on plastic modulus K_p and in extent on plastic strains. According to Equation (3.29), function f_p on the nominator of h_f follows the whole shearing history of the sand. Therefore, when the shearing path remains under the dilatancy surface and the response is purely contractive and only positive plastic volumetric strains occur, f_p steadily increases. In subplot **3.4c** of Figure **3.4**, evolution of f_p is illustrated during shearing. Points a-f' show the aforementioned continuous increase of f_p, albeit some decreasing parts are apparent near the load reversal points as stress path slightly passes in dilation (points a-f' in subplot **3.4a**). Hence, a continuous stiffening behavior is simulated during cyclic unloading-reloading paths as the nominator of K_p always increases, too. Model constant c_f, and inclusion of f_p - c_f into Macauley brackets, implies that there is a threshold value of f_p, only beyond which stiffening starts to act on plastic modulus. This aims to prevent early stiffening during monotonic shear loadings which pass an extensive part of their loading path under contraction. The constant value of $c_f = 1$, is found to be quite appropriate for the whole simulation procedure. This is well perceived, when observing that h_f becomes larger than unity for the first time (point a' on subplot **3.4b**), since f_p firstly becomes larger than one (point a' on subplot **3.4c**). On the other hand, when loading in dilation occurs, negative value of plastic volumetric strains decreases f_p, stiffening ceases or its rate of increase falls and a slight softening starts to prevail. The decrease of f_p during dilation is shown in paths f'- j' in sublot **3.4c**, where important part of the stress paths lies into dilation (paths f'-j' in subplot **3.4a**). However,

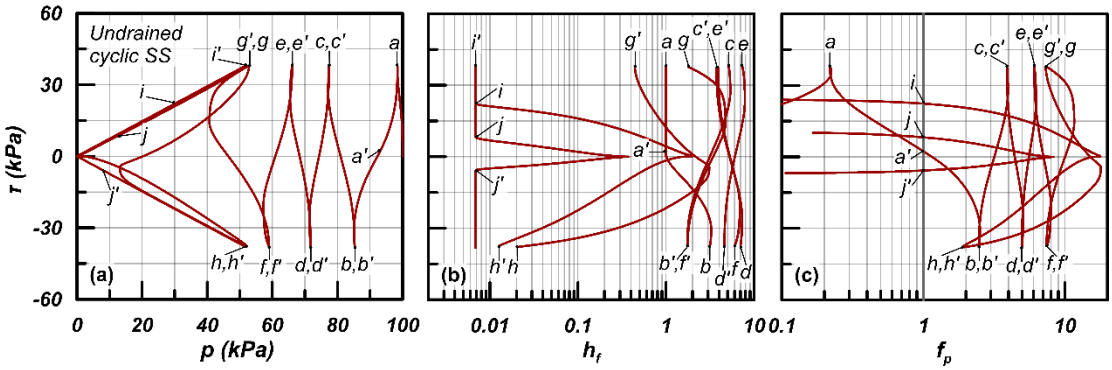

Figure 3.4: (a) *Typical stress path during undrained cyclic loading,* ***(b)*** *evolution of the fabric function* h_f *and* ***(c)*** *evolution of the fabric function component* f_p*, during shearing.*

the existence of Macauley brackets and the plus 1 ensure that the nominator of h_f cannot pass below unity, even if the whole attained f_p is erased after extensive dilation and becomes negative (points i, i' and j' on subplots **3.4b** and **3.4c**). The evolution of f_p in subplot **3.4c** is not shown for values smaller than 0.1, without this meaning that f_p does not reach negative values due to the extensive dilation of the applied shearing. In a contractive stress path, following dilation, f_p starts increasing again and since it becomes again larger than 1, it leads h_f to increase (point j on subplots **3.4b** and **3.4c**). At the same time, according to Equation (3.30), the other important component of h_f, fabric tensor $\boldsymbol{f}$, starts evolving upon dilation. However, during this dilative shear path, the denominator of h_f remains equal to 1, as $\boldsymbol{f}$ - due to sign (-) on its rate equation - develops on the opposite direction of $\boldsymbol{n}$ and thus $<\boldsymbol{f}:\boldsymbol{n}> = 0$. The denominator of h_f becomes larger than 1, only after a load reversal that follows a dilative path and maintains the value of $1 + <\boldsymbol{f}_{ini}:\boldsymbol{n}>$ until the next load reversal. It should be noted that, although between successive load reversals tensor $\boldsymbol{f}$ evolves, the denominator of h_f remains constant, maintaining the value of $\boldsymbol{f}$ caught at the moment of the load reversal ($\boldsymbol{f}_{ini}$). This increase of the denominator of h_f is of key importance for capturing the softening response and the compliant unloading paths, observed after shear unloading above dilatancy surface that eventually leads to liquefaction under undrained cyclic conditions. Apart from the decrease of f_p, the parallel increase of $\boldsymbol{f}$ during dilation leads to a more intense decrease of fabric function h_f as shown in subplot **3.4b**. According to Equations (3.29) and (3.30), the rate of both f_p and $\boldsymbol{f}$ is quantified through a common intensity of evolution, indicated as N and given in (3.31), where the value N_o is a model parameter. Apart from this, the value of N is controlled by some other variables referring

to the initial state of the sand after consolidation.

Function h_{ef}, like its similar form in plastic modulus (Equation (3.26)), indicates a decreasing void ratio dependency of N on void ratio. In other words, the denser the state of a sand, the more intense is its rate of fabric evolution. Moreover, function h_{pf} (Equation (3.32)) accompanies N in Equation (3.31) and describes the effect of initial mean effective stress on f_p evolution and subsequently on cyclic shear behavior, and specifically as it gets larger, the stiffening is less intense. The role of this function is in line with experimental results (Hynes and Olsen, 1999; Vaid and Sivathayalan, 1996) and analytical relations (Idriss and Boulanger, 2008) for K_σ overburden stress effect on the resistance to liquefaction. This also explains the upper-bound value of 1.5 in h_{pf} of Equation (3.32) in order to disallow excessive increase of liquefaction resistance for very small p_o values.

Finally, it should be discussed that for initial contractive states ($\psi_o > 0$), the Equation (3.31) becomes zero, implying that fabric evolution during shearing is taken into account into cyclic response only for initially dilative states ($\psi_o < 0$). However, the effects of initial e_o and p_o, defining ψ_o, are already considered into functions h_{ef} and h_{pf}, thus an exponent of 0.1 is selected to minimize its quantitative effect on N. The form of Equation (3.30), indicates that there is a maximum value that fabric tensor $\boldsymbol{f}$ can attain. This maximum norm, indicated as f_{max}, equals to the maximum value ever reached by f_p implying that softening is the result of fabric deconstruction during dilation, and it is directly related to the intensity of structured f_p during contraction. This maximum value is always nonnegative as f_p initiates always from zero. The functionality described above is well perceived, if observing that in subplot **3.4c** there is a minimum threshold below which h_f cannot further decrease. This is because $\boldsymbol{f}$ has attained its maximum value and h_f nominator cannot become lower than unity. Moreover, the presence of function $h_{post\text{-}liq}$ on the right-hand side of Equation (3.30) aims to increase the rate of $\boldsymbol{f}$ evolution in small p regimes, since liquefaction is reached, enhancing this way the softening of the response.

Gradual stiffening response with cycles is apparent both in drained and in early stages of undrained cyclic element tests. That is the reason why the accumulation of fabric-related components was conceptually chosen to develop with the plastic component of the volumetric strain and not its total increment (e.g., Andrianopoulos et al., 2010a; Dafalias and Manzari, 2004; Papadimitriou et al., 2001). However, this creates an inherent

quantitative differentiation of the developing fabric function during different drainage conditions. For example, in cases where (partial or full) drainage is allowed, there is a differentiation of void ratio e that directly affects the plastic modulus K_p via function h_{ep} of Equation (3.26), and hence the value of the plastic volumetric strain increment entering fabric evolution via Equations (3.29) and (3.30). To counterbalance this effect, Equations (3.29) and (3.30) continue to be directly related to the plastic volumetric strain increment (as in previous similar models of Andrianopoulos et al., 2010a and Papadimitriou et al., 2001), but the intensity of evolution is also set to depend on the correlation between plastic and total volumetric strains. Hence, the intensity of fabric evolution during loading is set to depend on the correlation between the integral of the total volumetric strain and the integral of the plastic volumetric strain during loading via factor a that is introduced in Equation (3.35) and takes values between 0.0 and 1.0. This factor scales appropriately the evolution of f_p and f in Equations (3.29) and (3.30). In particular, factor a is a function of the ratio of the integral of (accumulated) total volumetric strain during loading from the initial state over the respective integral of (accumulated) plastic volumetric strain (both in absolute terms). Based on its definition in Equation (3.35), when total volumetric strains are equal to zero (e.g., in the extreme case of fully undrained conditions), then a = 1.0. On the other hand, when the ratio of the strain integrals is greater than 1.0, i.e., when volume change is significant (e.g., in the unlikely case of fully drained conditions), then a = 0.0. For all the intermediate states, factor a attains values between 0.0 and 1.0 according to Equation (3.35). Given the above definitions, the term $(2 - a)N$ that acts as the scaling factor in Equation (3.29) takes values between N and $2N$, while the maximum norm $f_{max}^{(1+a)}$ that fabric tensor $\boldsymbol{f}$ may take in the bracketed tensor term of Equation (3.30) takes values between f_{max} and f_{max}^2.

In essence, the role of factor a is to enhance or reduce fabric evolution effects on the plastic modulus K_p depending on whether the loading induces volume change or not. Such a factor does not appear in any previous similar model (e.g., e.g., Andrianopoulos et al., 2010a; Dafalias and Manzari, 2004; Papadimitriou et al., 2001) and an example of its necessity is discussed below. Specifically, based on its original proposal in Papadimitriou et al. (2001) (and as a term enhancing the dilatancy in Dafalias and Manzari, 2004), the primary role of the denominator of function h_f is to offer softened response following

dilation, that under undrained cyclic loading may lead to liquefaction. However, it is uncertain how its formulation, while quite convenient for simulating the increased excess pore water pressure buildup upon load reversal following dilation in undrained loading, behaves under drained cyclic loading. For this purpose, **Figure 3.5** presents the estimated shear stress-strain (τ - γ_{SS}) relation and volumetric strain (ε_{vol} - γ_{SS}) accumulation within 30 cycles of a strain-controlled drained cyclic simple shear test with single amplitude cyclic shear strain equal to $\gamma_{SS,cyc}$ = 0.1%. Subplots c and d include the model estimate having factor a varying according to Equation (3.35), while subplots a and b present the same results but with a factor a = 1.0, that leads to the lowest f_p evolution rate equal to N and a highest maximum norm of $\boldsymbol{f}$ equal to f_{max}^2. According to experimental evidence (e.g., Shahnazari and Towhata, 2002), in drained cyclic loading, even for large cyclic shear strain amplitudes for which the shearing leads to dilation before the load reversal , the volumetric strain ε_{vol} accumulates with cycles, but at a steadily decreasing rate (e.g., see subplot **d**, in **Figure 3.5**), while the stress-strain relation becomes gradually stiffer (e.g., see subplot **c**, in **Figure 3.5**). In order to achieve this response, the new model (with variable a) employs f_p evolution rates higher than N, thus enhancing the numerator of h_f, concurrently with values of maximum norm of $\boldsymbol{f}$ lower than f_{max}^2, thus reducing the importance of the denominator of h_f. As a result, the estimated response is a gradual stiffening with cycles due to the effect of a gradually increasing h_f, which macroscopically is in accordance with experimental evidence (e.g., Shahnazari and Towhata, 2002).

On the contrary, using a constant value of a = 1.0, leads to a milder increase of the numerator of h_f concurrently with the potential for a more intense increase of its denominator. Such a choice may lead to the undesired response presented in subplots **3.5a, b** of **Figure 3.5**. Specifically, in the first cycles (phase A) the response becomes gradually stiffer due to the increase of f_p and consequently of h_f. As a result, the rate of ε_{vol} accumulation decreases with cycles, in qualitative agreement with experimental evidence. However, as the stress-strain loops become stiffer, the values of stress ratio $\boldsymbol{r}$ become higher and the stress point may shift outside the dilatancy surface. Due to the large maximum norm of f_{max}^2, this partly dilative loading is enough to increase the $\boldsymbol{f}$ and thus the denominator of function h_f. In fact, as cyclic loading continues (phase B), the h_f gradually decreases, which leads to a softening response with cycles, i.e., an accelerated rate of ε_{vol} accumulation and

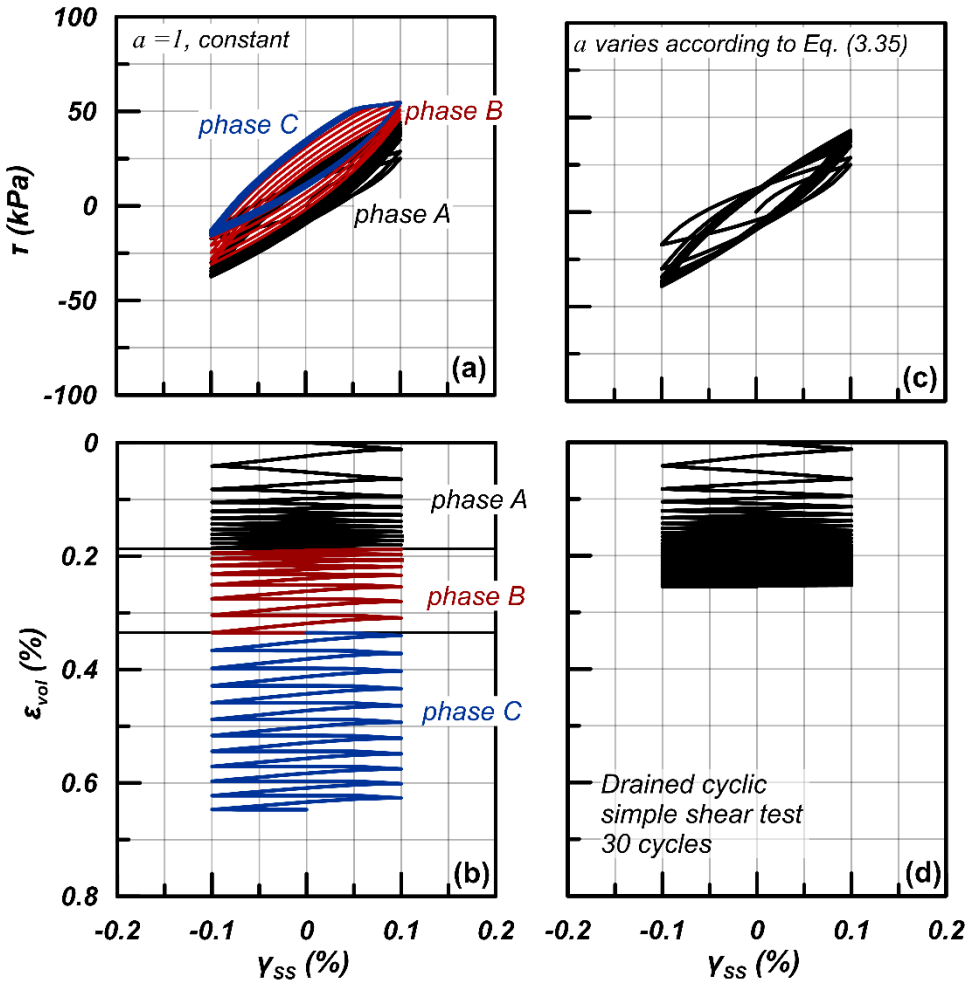

***Figure 3.5**: Effect of factor a on the shear stress-strain (τ - γ_{ss}) relation and the volumetric strain (ε_{vol} - γ_{ss}) accumulation in 30 cycles of a strain-controlled drained cyclic simple shear test: (a) and (b) a = 1; (c) and (d) variable a, according to Equation (3.35).*

an unrealistic "shift" of the stress-strain loops. Interestingly, the unrealistic softening leads to gradually larger ε_{vol} increments, which, in turn, allow for an intense evolution of the f_p and of the numerator of h_f. As a result, phase C of the loading appears, where the h_f increases and reduces equally within each cycle, thus leading to a, more or less, closed stress-strain loop and a constant rate of ε_{vol} accumulation with cycles, both of which are again unrealistic. The comparison between the desired response in subplots **3.5c, d** of **Figure 3.5**, versus the problematic response in subplots **3.5a, b** of **Figure 3.5**, respectively, shows that the role of the h_f denominator should be primary only when large plastic volumetric strains are expected (e.g., after significant excess pore pressure buildup, close to the onset of liquefaction during undrained cyclic shearing), and not when the plastic component of

volumetric strain is comparable to the total ε_{vol}. Such observations led to the proposal of a variable factor a, as per Equation (3.35), that affects inversely the numerator and the denominator of h_f.

3.7 Dilatancy

According to Equation (3.5), the definition of plastic strain rate direction $\boldsymbol{R}$ in this model implies non-associativeness only on the plastic volumetric strains with the introduction of scalar-valued dilatancy function D. The dilatancy D quantifies the incremental plastic volumetric strain (see also Equation (3.5)), as:

$$\dot{\varepsilon}_{vol}^{p} = \langle \Lambda \rangle D \tag{3.36}$$

and is explicitly defined in the following.

3.7.1 Contraction

Plastic volumetric strains during contraction (when $d^d > 0$) for the model presented herein are computed using the following expression for D:

$$D = A_o \frac{\left[(\boldsymbol{r} - \boldsymbol{r}_{ini}) : \boldsymbol{n} + \left\langle -d_{ini}^{d} \right\rangle \right]}{h_{pd,c}} d^d \tag{3.37}$$

where A_o is a nonnegative model parameter and $h_{pd,c}$ an also nonnegative function discussed in detail in the following. Equation (3.37), whilst founded on the principle of Rowe's dilatancy theory (Rowe, 1962), notably differs from it, as the addition of the multiplier $[(\boldsymbol{r} - \boldsymbol{r}_{ini}):\boldsymbol{n} + < -d_{ini}^{d} >]$ on the right-hand side modifies the proportionality between D and d^d. The inclusion of the term $(\boldsymbol{r}\text{-}\boldsymbol{r}_{ini}):\boldsymbol{n}$ in dilatancy function is crucial to improve the slope of the relation between cyclic resistance to liquefaction (CRR) and number of uniform loading cycles to reach liquefaction, as already referenced in the literature (Boulanger and Ziotopoulou, 2013; Cheng and Detournay, 2021). Alternatively, but aiming at the same target, Tsaparli et al. (2020) included in the dilatancy function the ratio of the distance from the dilatancy surface over the value of the respective distance at the last shear reversal.

In order to understand how Equation (3.37) works for cyclic loading, **Figure 3.6** presents the estimated effective stress path during an undrained cyclic simple shear test (subplot **3.6a**), concurrently with the variation of dilatancy D vs the distance d^{d} (subplot **3.6b**) and the quantity $(\boldsymbol{r} - \boldsymbol{r}_{\mathrm{ini}}):\boldsymbol{n}$ (subplot **3.6c**). Different points on the effective stress path are depicted with letters a through i in subplot **3.6a**, in order to make the correspondence with the values of D in subplot **3.6b** and subplot **3.6c**, while the dashed lines in subplot **3.6a** show the projection of the dilatancy surface in this stress space. For each of the load reversal points of the effective stress path (points b, d, f, h), there are 2 points in each of the subplots for D, presenting its values before and after the load reversal, the latter depicted by an apostrophe ′ following the letter. For the initial state (point a) and the load reversal inside the dilatancy surface (point b), the quantity in Macauley brackets is zero, and the D is analogous to $[(\boldsymbol{r} - \boldsymbol{r}_{\mathrm{ini}}):\boldsymbol{n}]\ d^{\mathrm{d}}$. Hence, at the onset of a new loading path and update of $\boldsymbol{r}_{\mathrm{ini}}$ (points a and b′), the D resets to zero, regardless that the distance d^{d} is non-zero, a significant differentiation from Rowe's theory. Then, as shearing continues, the $(\boldsymbol{r} - \boldsymbol{r}_{\mathrm{ini}}):\boldsymbol{n}$ and the d^{d} evolve in an opposite and complementary way. Here, it should be reminded that $\boldsymbol{r}$ and d^{d} are fully interrelated, as the d^{d} measures the distance (along $\boldsymbol{n}$) between the $\boldsymbol{r}$ and its conjugate image point on the dilatancy surface. Hence, as the $\boldsymbol{r}$ diverts from $\boldsymbol{r}_{\mathrm{ini}}$ and so the $(\boldsymbol{r} - \boldsymbol{r}_{\mathrm{ini}}):\boldsymbol{n}$ increases, the d^{d} decreases accordingly (see Equation (3.19)). This means that after a load reversal occurs, the D is primarily affected by the rapidly increasing $(\boldsymbol{r} - \boldsymbol{r}_{\mathrm{ini}}):\boldsymbol{n}$, before it eventually starts to decrease, as the effect of the decreasing d^{d} prevails when approaching the dilatancy surface (see paths a - b and b′- c in **Figure 3.6**). This is because when the $\boldsymbol{r}$ crosses the dilatancy surface (points c, e, g in **Figure 3.6**), the $d^{\mathrm{d}} = 0$ thus rendering $D = 0$, regardless of where the previous load reversal appeared. If loading continues further, the response becomes dilative and will be described in the next Section. Note here that the proposed Equation (3.37) for D in contraction gives positive values of D close to zero for small values of quantity $(\boldsymbol{r} - \boldsymbol{r}_{\mathrm{ini}}):\boldsymbol{n}$. This means that for cyclic loading in which this quantity remains generally small (e.g., for low amplitude cyclic loading), the D remains close to zero. This constitutive trait proves very useful for estimating minimal volume change under drained conditions, or minimal excess pore pressure buildup under undrained conditions, when low amplitude cyclic loading is at hand. Similar formulations for dilatancy (in contraction), that deviate from Rowe's theory, have been proposed already

in the literature (e.g., Boulanger and Ziotopoulou, 2013; Cheng and Detournay, 2021; Tsaparli et al., 2020), mainly aiming at relatively "flat" liquefaction resistance curves.

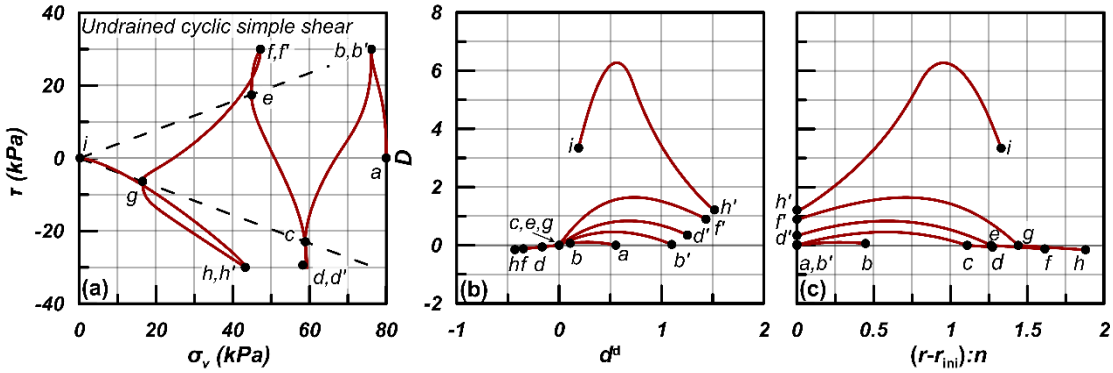

Figure 3.6: *(a) Typical stress path during undrained cyclic loading, and evolution of the dilatancy D as a function of (b) the distance d^d from the dilatancy surface and (c) quantity $(r - r_{ini}):n$ from last reversal point.*

Returning to Equation (3.37), the term $< -d^{\,d}_{\,ini} >$, implies that when a load reversal occurs above dilatancy surface then D does not start form a zero value, as $d^{\,d}_{\,ini}$ has attained a negative value before load reversal (**Figure 3.6**, points d', f', h'). Actually, this initial value increases with the stress ratio at which the last reversal occurred, and to this extent D at a loading process initialization is also increased (compare points d' and h' in **Figure 3.6**). In any other case, the Macauley brackets nullify this term and the concept described in the previous paragraph is applied. The inclusion of this term enables some volumetric strain to develop early after unloading above dilatancy surface, improving this way the volumetric strain accumulation at large strain γ amplitudes during drained cyclic loading and enhancing the pore pressure buildup at high stress ratios regime during undrained cyclic loading. Note also here that a term of similar functionality was used also by Boulanger and Ziotopoulou (2013), while reduced and non-zero initial value of D upon shear reversal is also estimated in Tsaparli et al. (2020).

The last term to be discussed, is the function $h_{pd,c}$, given as:

$$h_{pd,c} = \begin{cases} h_{pd,c}^{\,*} & \textit{default} \\ \min\left[h_{pd,c}^{\,*}; \dfrac{h_{pd,c,liq}}{h_{pl,d}} \right] & \textit{after initial liquefaction} \end{cases} \tag{3.38}$$

with:

$$h_{pd,c}{}^{*}=1-\left\langle \text{sign}\left(-\psi_{o}\right)\right\rangle \left[\left\langle 1-\left(\frac{p}{p_{o}}\right)^{0.5}\right\rangle -c_{pd,c}\right] \tag{3.39}$$

$$h_{pl,d}=exp\left(-\left(\frac{p}{16p_{l}}\right)^{4}\right) \tag{3.40}$$

Function $h_{pd,c}$ acquires a double form, depending on whether or not initial liquefaction has occurred. In its default form (before initial liquefaction), function $h_{pd,c} = h_{pd,c*}$. This $h_{pd,c*}$ function decreases from 1.0 as p decreases from its initial value p_o, thus leading to gradual increase of D as per Equation (3.37). Due to the exponent 0.5, the foregoing decrease of $h_{pd,c*}$ is notable only after a significant decrease of the p/p_o ratio (e.g., after significant excess pore pressure buildup) and appears only for initially dilative initial states, i.e., only when the sign of $-\psi_o$ is positive, and hence the $\left\langle \text{sign}\left(-\psi_{o}\right)\right\rangle =1$. The inclusion of $c_{pd,c} = 0.1$ (i.e., a small positive number) guarantees that $h_{pd,c*}$ remains positive and non-zero, when $p = 0$, while the Macauley brackets inside the bracketed term of Equation (3.39) make sure that for $p/p_o > 1$, the $h_{pd,c*}$ remains constant and does not affect the response. Once initial liquefaction occurs, the value of $h_{pd,c*}$ is stored as $h_{pd,c,liq}$. Thereafter, the value of $h_{pd,c}$ is estimated as the minimum of 2 values: the $h_{pd,c*}$ on the basis of Equation (3.39) and the ratio of the aforementioned stored $h_{pd,c,liq}$ value over the function $h_{pl,d}$ of Equation (3.40) that introduces an effect of the p/p_l ratio. As a whole, Equations (3.38) - (3.40) ensure that in contractive paths after initial liquefaction, the $h_{pd,c}$ remains lower than what the $h_{pd,c*}$ prescribes and only when $p/p_l > 20$, approximately, the $h_{pd,c}$ becomes equal to $h_{pd,c*}$ again, due to the operation of Equation (3.40). The double form of h_{pdc} function before and after initial liquefaction is depicted in **Figure 3.7** (subplots **3.7a** and **3.7b** respectively). Equation (3.40) defines $h_{pd,l}$ as a function of p/p_l. However, as p_l is a percentage of p_o equal to 5% (and no greater than 10 kPa), $h_{pd,l}$ can also be written as a function of p/p_o. This correlation is depicted in **Figure 3.7**, where in subplot **3.7a** $h_{pd,l}$ is written in terms of p/p_o, while in subplot **3.7b** p/p_l is used. Subsequently, **Figure 3.8** shows the evolution of $h_{pd,c}$ in its default form before liquefaction (subplot **3.8a**) and in its form after initial liquefaction (subplot **3.8b**). In this figure $h_{pd,l}$ is written in terms of p/p_o, so as

a direct comparison between $h_{pd,c,liq}/h_{pd,l}$ and $h_{pd,c*}$ to be made.

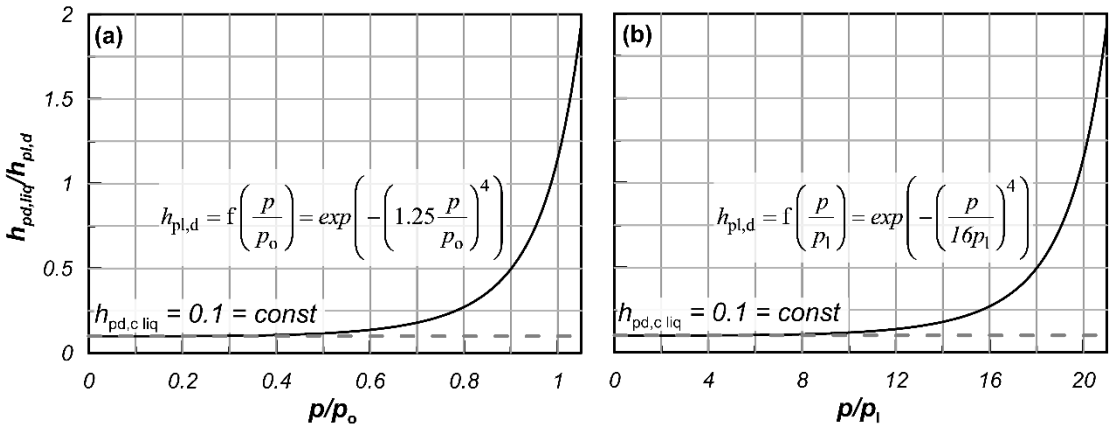

Figure 3.7: *Function $h_{pl,d}$ expressed in terms of: (a) p/p_o (b) p/p_l.*

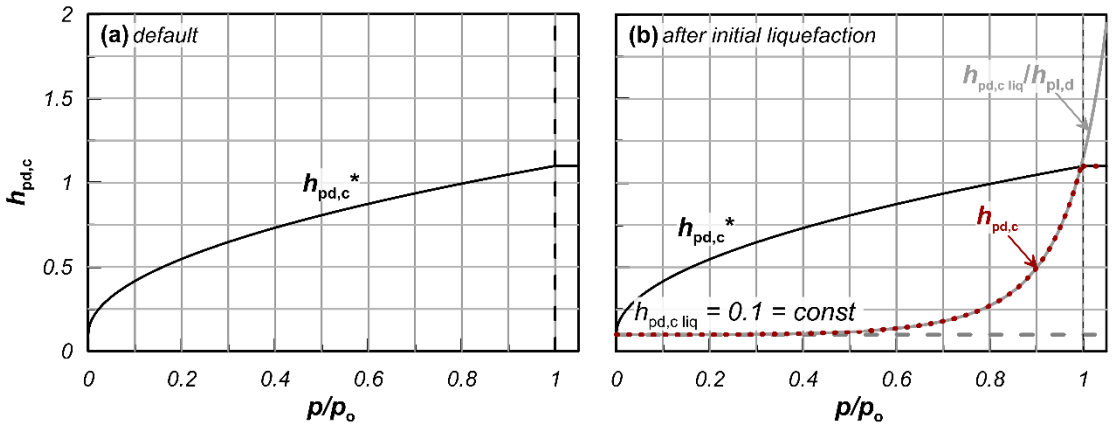

Figure 3.8: *Evolution of function $h_{pd,c}$ (a) before liquefaction (b) after initial liquefaction.*

3.7.2 Dilation

It has been made clear so far, that in this model distinct dilatancy functions are proposed for contraction ($d^d > 0$ and dilation ($d^d < 0$). However, it should be noted that during the transition from contractive to dilative stress ratio regime any discontinuity is prevented, as both functions are proportional to d^d and thus, at the crossing point with dilatancy surface $D = 0$.

During dilation, plastic volumetric strains are related to plastic deviatoric strains according to:

$$D=A_o \frac{2\,h_\theta}{h_{post\text{-}liq}\;h_{fd}}\;d^d \tag{3.41}$$

where A_o is the same model parameter as in Equation (3.37), while h_θ is the function incorporating the loading direction (Lode angle θ) that is identical to that in Equation (3.27), i.e., identical to that incorporated in the plastic modulus K_p equation, for the same reason. It is noted here that while in contraction, the inclusion of the effect of h_θ only in K_p is proven sufficient, this effect is too subtle while in dilation, something that is especially true in monotonic loading. As also mentioned in the text explaining the K_p formulation, function $h_{post\text{-}liq}$ accounts for accumulation of strains after liquefaction is triggered, and its formulation is detailed in a following dedicated section below. It suffices here to note that $h_{post\text{-}liq}$=1 unless liquefaction occurs. Focusing on the form of Equation (3.41) it is deduced that, unlike Equation (3.37), it adopts directly the essence of Rowe's dilatancy theory by defining a linear relation between D and d^d (see also paths c - d, e - f, g - h in **Figure 3.6b**). Of course, the current distance d^d and the stress ratio $\boldsymbol{r}$ are interrelated, so the D in dilation is indirectly a linear function of $(\boldsymbol{r}-\boldsymbol{r}_{ini}):\boldsymbol{n}$ as well (see paths c - d, e - f, g - h in **Figure 3.6c**).

What remains is the explanation of the effect of fabric evolution on D (in dilation only) that is introduced via function h_{fd}. Its inclusion in Equation (3.41) stems from experimental observations in cyclic loading tests with very large cyclic shear amplitudes, in which net volume reduction is observed cycle after cycle, even if the stress state remains outside the dilatancy surface for significant portions of the loading. Very indicative of this observation are the drained cyclic experiments of Shahnazari and Towhata (2002), in which medium dense ($D_r \approx 58\%$) or even dense ($D_r \approx 75\%$) Toyoura sand underwent successive cycles with very large single-amplitude shear strain amplitude of 3% and produced net contraction (e.g., $\varepsilon_{vol} \approx 5\%$ after 40 cycles for initial $D_r \approx 58\%$). This seemingly reduced tendency for dilation seems to appear gradually, i.e., it is not consistent with the dilation shown by the same sand under monotonic loading (e.g., Verdugo and Ishihara, 1996). As such, it is considered in the model only in the D in dilation in the following form:

$$h_{fd} = 1+\left\langle f_{pd} - c_{fd} \right\rangle \tag{3.42}$$

where f_{pd} is a cumulative index (initiating from $f_{pd} = 0$ at initial state), whose evolution equation is similar to that of f_p in Equation (3.29), according to:

$$\dot{f}_{pd} = (1-a)\, N\, h_{pf} \left\langle \dot{\varepsilon}_{vol}^{p} \right\rangle \tag{3.43}$$

Oppositely to scalar f_p and Equation (3.29) observe that the scalar f_{pd} evolves only when the accumulated total and plastic volumetric strains have a comparable measure (and hence $0 \leq a < 1$ holds) and its evolution is solely increasing, due to the inclusion of the plastic volumetric increment in Macauley brackets. In this way, for large intensity cyclic loading in which the stress state goes outside the dilatancy surface, the accumulation of positive plastic volumetric strain cycle after cycle progressively leads to less intense dilation within each successive cycle, due to the reduction of the D in dilation in Equation (3.42) via the increasing h_{fd}. On the other hand, for small intensity cyclic loading which retains the stress state inside the dilatancy surface, the aforementioned effect plays no role. Finally, the inclusion of the ($f_{fd} - c_{fd}$) in Macauley brackets in Equation (3.42), similarly to what appears in the numerator of h_f in Equation (3.28), implies that a sufficiently large f_{fd} quantity should be accumulated, before the h_{fd} starts reducing the D in dilation. This essentially eliminates the h_{fd} effect in monotonic loading, in accordance with experimental evidence. For this purpose, a constant value of $c_{fd} = 3$ has been found capable to serve this purpose for all sands.

3.8 Post-liquefaction response and cyclic mobility

In recent years, within the framework of performance-based design, special research effort has been focused not only on liquefaction triggering, but also on the investigation of post-liquefaction deformations. There is a plethora of experimental evidence (e.g. (Arulmoli et al., 1992; Bastidas, 2016; Kammerer et al., 2000; Wu et al., 2004) exhibiting significant shear strain accumulation after initial liquefaction, i.e., the state when the sand first reaches an excess pore pressure Δu that is at least 95% of the initial mean effective stress p_o, or equivalently when the mean effective stress p is smaller or equal to 5% of p_o. Capturing the response after initial liquefaction has proven a challenge for constitutive models. To this extent, a variety of constitutive schemes has been proposed first by Elgamal et al. (2003), then by Zhang and Wang (2012), Boulanger and Ziotopoulou (2013) and Tasiopoulou and

Gerolymos (2016), and very recently by numerous publications targeting this issue (e.g., (Barrero et al., 2020; Cheng and Detournay, 2021; Liu et al., 2020; Yang et al., 2020). In this model, the cyclic mobility response is captured with the aid of function $h_{\text{post-liq}}$, primarily in Equation (3.41) for the dilatancy D in dilation and secondarily in Equation (3.30) for the evolution equation of the deviatoric fabric $\boldsymbol{f}$ that affects the plastic modulus K_{p}. Specifically, the role of function $h_{\text{post-liq}}$ is to enable shear strain accumulation with cycles by (primarily) decreasing the dilation potential (via decreasing the D in dilation) after initial liquefaction in a progressive way. The target of this reduction of D is to avoid overlaid repeating stress strain loops during cyclic mobility. This concept is already found in the literature, where existing models (e.g., Boulanger and Ziotopoulou, 2013) utilize fabric-based cumulative functions and fabric-related criteria to control the intensity and the limit of the reduction of D. Here, this is achieved via a cumulative function varying continuously with mean effective stress p once initial liquefaction occurred, a concept originating from Barrero et al. (2020).

This function, here, is given as:

$$h_{\text{post-liq}} = 1 + \left(2^{h_{\text{l}}} - 1\right) f_{\text{l}} \tag{3.44}$$

where f_{l} is a cumulative variable (initiating from $f_{\text{l}} = 0$), whose evolution equation reads:

$$\dot{f}_{\text{l}} = S\, L\, h_{\text{pl}} \left| \dot{\varepsilon}^{\text{p}}_{\text{vol}} \right| \tag{3.45}$$

with:

$$L = L_0\, e_0^{\,0.5 c_{\text{h}}} \tag{3.46}$$

being the rate of its evolution, calibrated via L_{o} a nonnegative model parameter and the void ratio e_{o} at initial state. Equations (3.44) and (3.45) include h_{l} and h_{pl}, two nonnegative functions of p, given by:

$$h_{\text{l}} = exp\left(-\left(\frac{p}{4\, p_{\text{l}}} \right)^4 \right) \tag{3.47}$$

$$h_{pl} = exp\left(-\left(\frac{p}{10\,p_l}\right)^4\right) \tag{3.48}$$

Crucial for the evolution of f_l in Equation (3.45) is S, i.e., a flag function with a default value of zero. This S is set equal to 1 only when initial liquefaction is reached for the first-time during loading, i.e., when the current p becomes smaller or equal to a critical value p_l. Functions h_l and h_{pl} are plotted vs p/p_l according to Equations (3.47) and (3.48), on subplot **3.9a** of **Figure 3.9**. As p_l is correlated to p_o via Equation (3.49), h_l and h_{pl} are also plotted as functions of p/p_o in subplot **3.9b**.

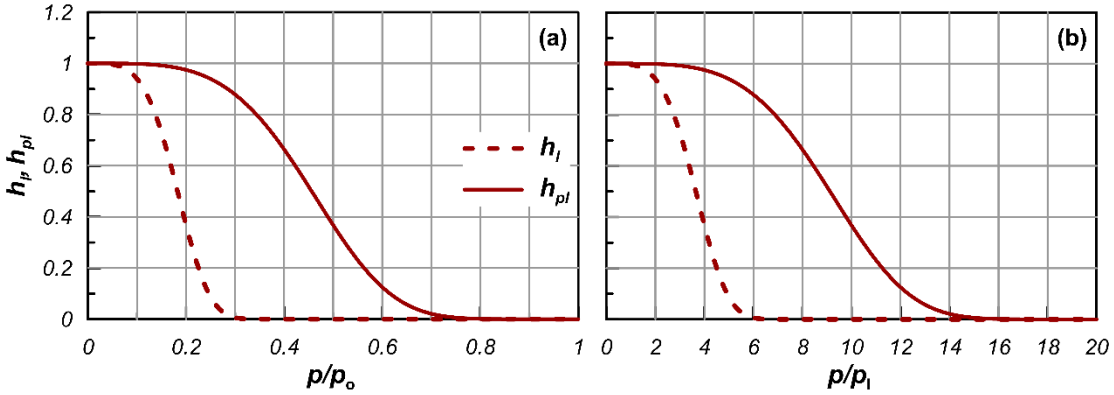

Figure 3.9: *Evolution of h_l functions h_l and h_{pl} vs (a) p/p_o and (b) p/p_l.*

Based on the above, the f_l starts to accumulate via Equation (3.45) only when the p becomes lower than p_l for the first time (due to switching to S = 1) on the basis of the absolute value of the plastic volumetric strain rate. The use of the absolute value of this strain rate ensures that the f_l after initial liquefaction does not decrease, regardless of whether the sand experiences contraction or dilation. Of major importance in this f_l accumulation is the h_{pl} function which scales the rate of evolution L in Equation (3.45). According to Equation (3.48), the h_{pl} is a continuous non-linear function of p/p_l with an upper limit equal to 1.0 (when the p approaches zero) and a lower limit of 0.0 (when the p has increased sufficiently beyond p_l). This dependence of f_l accumulation on p is fundamental in this model. In essence, function h_{pl} allows for f_l accumulation only when

the p is within a low effective stress regime and disallows it if the p becomes much larger, e.g., in the case of post-liquefaction re-consolidation. Such a p-dependence was recently introduced by Barrero et al. (2020) and in the sequel by Yang et al. (2020), who characterized every state in this small p regime as semi-fluidized and properly adjusted the plastic modulus and dilatancy functions. Then this concept was adopted in a similar way by Cheng and Detournay (2021) on the plastic modulus of their recently proposed model.

A p-dependence is also introduced on the $h_{\text{post-liq}}$ itself in Equation (3.44), via function h_{l} in Equation (3.47) that is very similar to the h_{pl} function of Equation (3.48). Again, the h_{l} is a continuous non-linear function of p/p_{l} with an upper limit equal to 1.0 (when the p approaches zero) and a lower limit of 0.0 (when the p has increased beyond p_{l}). This means that the $h_{\text{post-liq}}$ varies between 1.0 (when $h_{\text{l}} = 0.0$) and $(1 + f_{\text{l}}) > 1$ (when $h_{\text{l}} = 1.0$). The operation of function $h_{\text{post-liq}}$ is discussed in **Figure 3.10** on the basis of the estimated response during cyclic mobility (following initial liquefaction) in undrained cyclic simple shear loading. Specifically, of interest is the response during the 3 overlaid effective stress path loops of this test shown in subplot **3.10a**, which correspond to the 3 non-overlaid stress-strain loops of increasing shear strain amplitude in subplot **3.10b**. Crucial in the successful simulation of this stress-strain response is the operation of $h_{\text{post-liq}}$, whose value during these 3 loading cycles is shown in subplot **3.10c**. Emphasis on the low mean effective stress p regime is provided via the shading, that depicts a range of $p < 20$ kPa and $p/p_{\text{l}} < 4$ (since $p_{\text{l}} = 5$ kPa for this example case). Observe in subplot **3.10c**, that during the dilative phases of the loading cycles the $h_{\text{post-liq}}$ initiates from a set value (equal to $1 + f_{\text{l}}$) at $p \rightarrow 0$ (points a, c, e, g, i, k) and remains significantly larger than 1.0 only within the low stress regime, since the increase of p reduces the value of h_{l} in Equation (3.44), thus leading to $h_{\text{post-liq}} = 1.0$ asymptotically, and this regardless of the value of f_{l} in Equation (3.45). However, the value of accumulated f_{l} increases cycle after cycle (due to the accumulation of plastic volumetric strain in Equation (3.45) and so does the value of $(1 + f_{\text{l}})$ from which initiates the $h_{\text{post-liq}}$ in each successive dilative phase. The end result is increased values of $h_{\text{post-liq}}$ in each successive dilative phase, especially in the low stress regime (compare $h_{\text{post-liq}}$ values in paths a - b, c - d, e - f, g - h, i - j, k - l in subplot **3.10c**). Based on Equation (3.41), these increased values of $h_{\text{post-liq}}$ lead to similarly decreased dilatancy D in

successive dilative phases, which in turn lead to increased shear strains, especially in the low stress regime (compare range of γ_{SS} in paths a - b, c - d, e - f, g - h, i - j, k - l in subplot **3.10b**). Note here that the above describe the primary effect of $h_{post\text{-}liq}$ via the dilatancy function D in dilation.

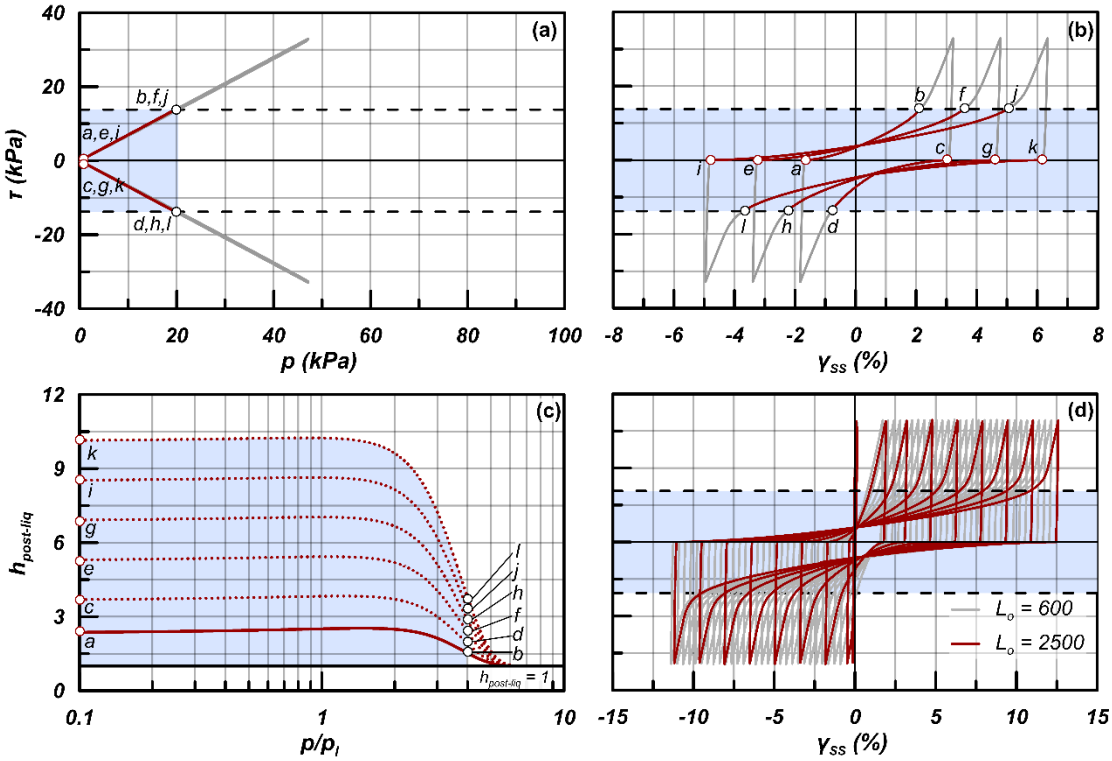

Figure 3.10: *(a) Typical overlaid effective stress path loops during cyclic mobility following initial liquefaction in undrained simple shear loading; (b) corresponding stress-strain loops with progressive shear strain accumulation with cycles; (c) evolution of function $h_{post\text{-}liq}$ as a function of p/p_l and (d) effect of model parameter L_o on post-liquefaction shear strain accumulation rate with cycles.*

There is also a secondary effect, originating from having the $h_{post\text{-}liq}$ multiplying the $\left\langle -\dot{\varepsilon}^{p}_{vol} \right\rangle$ term in the evolution of fabric tensor $\boldsymbol{f}$ in Equation (3.30). If one considers that this plastic volumetric strain rate term is reduced by $h_{post\text{-}liq}$ due to the D in dilation in Equation (3.41), its multiplication by $h_{post\text{-}liq}$ in Equation (3.30) essentially cancels out the post-liquefaction effect in the evolution of the fabric tensor $\boldsymbol{f}$, and through it, on the fabric evolution index h_f and the plastic modulus K_p. This ensures that during cyclic mobility the effective stress path loops remain essentially overlaid (see subplot **3.10a**), despite the shear

strain accumulation exhibited by the stress-strain loops cycle after cycle (see subplot **3.10b**), in accordance with experimental evidence (see also the model performance in **Chapter 5**).

Moreover, subplot **3.10d** explores the effect of model parameter L_o that controls the rate of f_l accumulation via L, as per Equations (3.45) and (3.46). It becomes obvious, that the higher the L_o value, the faster the f_l accumulation, and thus the larger the value of $h_{post\text{-}liq}$ and more intense shear strain accumulation, with the value of $L_o = 2500$ corresponding to the value that is relevant to Toyoura sand (**Table 5.1**). The value of rate L in Equation (3.46) is also made a function of the void ratio at the initial state e_o, implying lower rates of post-liquefaction strain accumulation with an increase in relative density and the opposite, in accordance to experimental evidence (e.g. Tasiopoulou et al., 2020).

In closing, the formulation described above eventually leads to $h_{post\text{-}liq} = 1$ when a future loading process leads to values of p much larger than the p_l, i.e., outside the small p value regime related to liquefaction and cyclic mobility. In addition, if this future loading process leads to value of $p \geq p_o$ (e.g., re-consolidation after liquefaction), the model sets $f_l = 0$, i.e., it erases the memory of the preceding liquefaction. This approach is simple, but has a limitation with respect to what happens if this future loading process increases the p, but to values lower than p_o. The model unavoidably retains in memory the preceding liquefaction phase and hence the accumulated $f_l > 0$, something that may be potentially erroneous. To address such issues an additional constitutive mechanism to eliminate and readjust this effect for subsequent totally different loading conditions, like in Barrero et al. (2020), should be included, but such a complication is beyond the scope of this model.

3.9 Mitigation of the stress-strain overshooting problem

The current model employs the deviatoric stress ratio tensor at the last load reversal $\boldsymbol{r}_{ini}$ for defining a number of constitutive aspects, namely the loading direction tensor $\boldsymbol{n}$ (**Figure 3.2**), the small-strain nonlinearity (Equation (3.20)), the plastic modulus (Equation (3.24)) and the dilatancy in contraction (Equation (3.37)). For example, in Equations (3.20) and (3.24), the updating of $\boldsymbol{r}_{ini}$ at load reversal allows for a smooth elasto-plastic transition, as the $T = 1$ and $K_p \rightarrow \infty$, thus leading to $G_t = G_{max}$ and a zero plastic strain rate upon unloading. One of the problems faced in models employing the last load reversal point, or in models

employing reversal surfaces in general, is the overshooting upon unloading and immediate reloading, i.e., the estimate of a stress-strain curve that is unrealistic since it overshoots the expected continuation that this curve would have if this unloading-reloading cycle had not occurred. The foregoing problem is related to the updating of $\boldsymbol{r}_{ini}$ upon unloading and upon immediate reloading. In their recent work Duque et al. (2021) underlined the sensitivity of both advanced plasticity (e.g., bounding surface) and hypoplasticity models to this issue. It has been sufficiently studied in the literature leading to several approaches for overcoming it (e.g., Boulanger and Ziotopoulou, 2013; Cheng and Detournay, 2021; Dafalias, 1986; Dafalias and Taiebat, 2016).

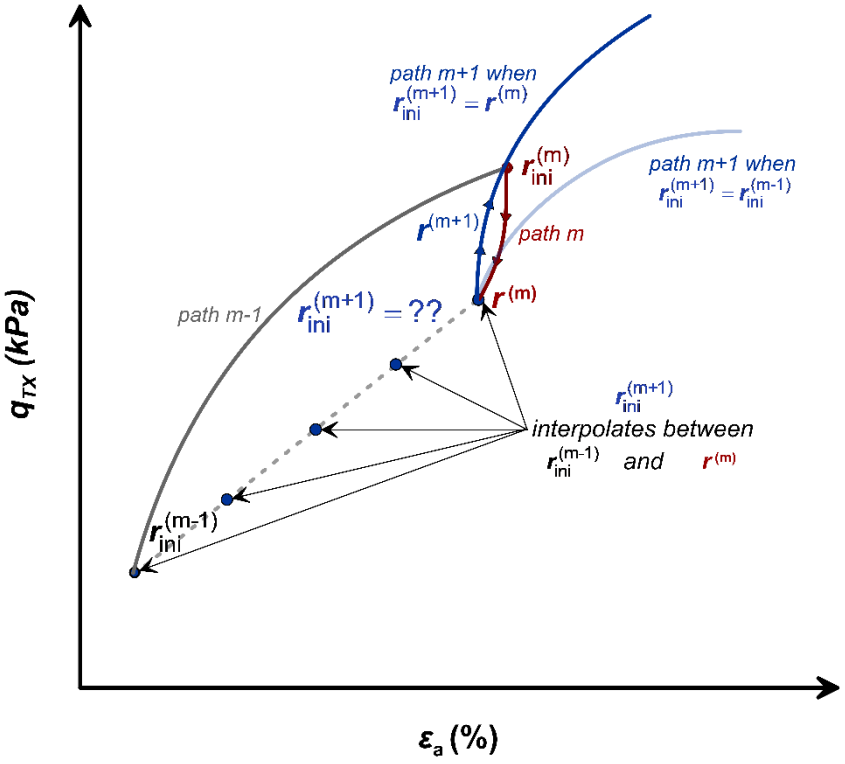

***Figure 3.11**: Schematic illustration of stress – strain overshooting problem after a small unloading path during a monotonic triaxial compression test.*

In this model, the problem is more complicated, since also the loading direction tensor $\boldsymbol{n}$ may be affected, while the dilatancy is updated as well (e.g., rendering $D = 0$ if the load reversal is inside the dilatancy surface). So, the issue here is not just an overshooting problem, and in terms of constitutive modeling it boils down to what is the "*accurate*" value of $\boldsymbol{r}_{ini}$ for having a realistic response in any load path that may be encountered in boundary value problems, both static and dynamic.

As a first step, here the approach of Dafalias and Taiebat (2016) is adopted for this purpose, i.e., a robust methodology for "*adjusting*" the value of $\boldsymbol{r}_{\text{ini}}$ depending on the load path. In order to understand their methodology, the following terms are defined: $\boldsymbol{r}^{(\text{m})}$ is the current stress-ratio tensor along the current load path (m) at the moment of load reversal (i.e., when $A < 0$ appears), $\boldsymbol{r}_{\text{ini}}^{(\text{m})}$ refers to the $\boldsymbol{r}_{\text{ini}}$ adopted at the initiation of load path (m), $\boldsymbol{r}_{\text{ini}}^{(\text{m-1})}$ is the $\boldsymbol{r}_{\text{ini}}$ of the previous load path (m-1) and $\boldsymbol{r}_{\text{ini}}^{(\text{m+1})}$ refers to the $\boldsymbol{r}_{\text{ini}}$ that is going to be adopted after the initiation of the upcoming (m+1) load path. When $A < 0$ appears during load path (m), the $\boldsymbol{r} = \boldsymbol{r}^{(\text{m})}$ and the quandary is whether $\boldsymbol{r}_{\text{ini}}^{(\text{m+1})}$ should be updated to $\boldsymbol{r}^{(\text{m})}$, thus increasing the stiffness of the stress-strain curve during the upcoming path (m+1), or whether it should take another value. The concept described above is schematically illustration in **Figure 3.11** for the exemplary case of a triaxial test.

According to Dafalias and Taiebat (2016), the answer depends on the "*magnitude*" of load path (m), that is quantified in terms of $e^{\text{p(m)}}$, the integral of plastic deviatoric strain quantity $\sqrt{(2/3)\dot{\boldsymbol{e}}^{\text{p}}:\dot{\boldsymbol{e}}^{\text{p}}}$ during this path. For example, if the plastic deviatoric strain $e^{\text{p(m)}}$ is negligible, then the value of $\boldsymbol{r}^{(\text{m})}$ should be irrelevant for the definition of $\boldsymbol{r}_{\text{ini}}^{(\text{m+1})}$, whose value should be based on the $\boldsymbol{r}_{\text{ini}}^{(\text{m-1})}$ that is kept in memory. On the contrary, if the plastic deviatoric strain $e^{\text{p(m)}}$ is very large, then the $\boldsymbol{r}_{\text{ini}}^{(\text{m-1})}$ should be irrelevant, and the definition of $\boldsymbol{r}_{\text{ini}}^{(\text{m+1})}$ should be based on the value of $\boldsymbol{r}^{(\text{m})}$. For intermediate values of $e^{\text{p(m)}}$ an interpolation function for $\boldsymbol{r}_{\text{ini}}^{(\text{m+1})}$ should be used (see **Figure 3.11**), which according to Dafalias and Taiebat (2016) reads:

$$\boldsymbol{r}_{\text{ini}}^{(\text{m+1})} = k\,\boldsymbol{r}_{\text{ini}}^{(\text{m-1})} + (1-k)\,\boldsymbol{r}^{(\text{m})} \tag{3.49}$$

$$k = \left\langle 1 - \left(\frac{e^{\text{p(m)}}}{e_1^{\text{p}}} \right)^{n} \right\rangle \tag{3.50}$$

where k is the weighting parameter of Equation (3.49), that quantifies the significance of load path (m) on the basis of the relative magnitude of plastic deviatoric strain $e^{\text{p(m)}}$ in comparison to e_1^{p}, a model constant serving as a shear strain threshold beyond which $\boldsymbol{r}_{\text{ini}}^{(\text{m+1})}$

$= \boldsymbol{r}^{(m)}$. In this model, $\boldsymbol{e}_1^p = 10^{-4}$ and n, the model constant controlling the non-linearity of Equation (3.50), is chosen to be equal to 1, following the advice of Dafalias and Taiebat (2016). Based on the above, during any load path (m), both $\boldsymbol{r}_{ini}^{(m-1)}$ and $\boldsymbol{r}_{ini}^{(m)}$ should be kept into memory, the former for use in Equation (3.49) while the latter as the $\boldsymbol{r}_{ini}$ entering all aspects of the constitutive model presented above.

According to Equations (3.49) and (3.50), if load path (m) is negligible in terms of $e^{p(m)}$, then $\boldsymbol{r}_{ini}^{(m+1)} = \boldsymbol{r}_{ini}^{(m-1)}$ (due to $k = 1$) and for loading path (m+1), only $\boldsymbol{r}_{ini}^{(m)}$ and $\boldsymbol{r}_{ini}^{(m+1)}$ are kept into memory, while the all-important $\boldsymbol{r}_{ini}^{(m-1)}$ is erased from memory. This is fine if loading path (m+1) is significant. However, one should wonder, what will happen if loading path (m+1) is again negligible in terms of $e^{p(m+1)}$, and $k = 1$ holds again. Then, ideally, the $\boldsymbol{r}_{ini}^{(m+2)}$ should be again equal to $\boldsymbol{r}_{ini}^{(m-1)}$ (thus neglecting the load reversals related to the two successive un-important load paths), only that this value has been erased from memory. This loss-of-memory problem does not only appear when $k = 1$, but also for $0 < k < 1$, only that it requires a number of successive un-important load paths to erase from memory the effect of the all-important $\boldsymbol{r}_{ini}^{(m-1)}$. Such paths with successive un-important load paths are not uncommon in boundary value problems, especially of dynamic nature. This shortcoming is hereby remedied, by supplementing the foregoing methodology with a criterion on whether a load reversal (a state where $\Lambda < 0$) is "*formal*" or "*informal*". Namely, as soon as a load reversal is detected for the initiation of load path (m+1), say at $\boldsymbol{r} = \boldsymbol{r}^{(m)}$, it is considered by default "*informal*" and no update of $\boldsymbol{r}_{ini}$ is performed ($\boldsymbol{r}_{ini} = \boldsymbol{r}_{ini}^{(m)}$ remains). This holds until the accumulated stress-ratio difference from the "*informal*" load reversal point is larger than a preset (small) tolerance level r_{tol}. If this occurs, then the load reversal point is considered "*formal*" and the estimation of the $\boldsymbol{r}_{ini}^{(m+1)}$ is performed on the basis of Equations (3.49) and (3.50). In more detail, the condition that should be satisfied for considering the last load reversal as "*formal*" reads:

$$\sqrt{(2/3)\left(\boldsymbol{r}-\boldsymbol{r}^{(m)}\right):\left(\boldsymbol{r}-\boldsymbol{r}^{(m)}\right)} \geq r_{tol} \tag{3.51}$$

where r_{tol} is a model constant selected equal to 0.01 here. Note here that during the (small) loading path following an "*informal*" load reversal that has not updated the $\boldsymbol{r}_{ini}$, the loading

index Λ usually continues to be negative, thus only elastic deformations are developed. In **Figure 3.12** the effectiveness of this enhanced methodology for mitigating overshooting is presented. To do so, an undrained triaxial test is simulated. The test is not monotonic, since when the axial strain becomes equal to ε_a = 0.5% and 1% three different cases of imposed unloading - reloading are considered, as depicted in subplots **3.12a, b, c**.

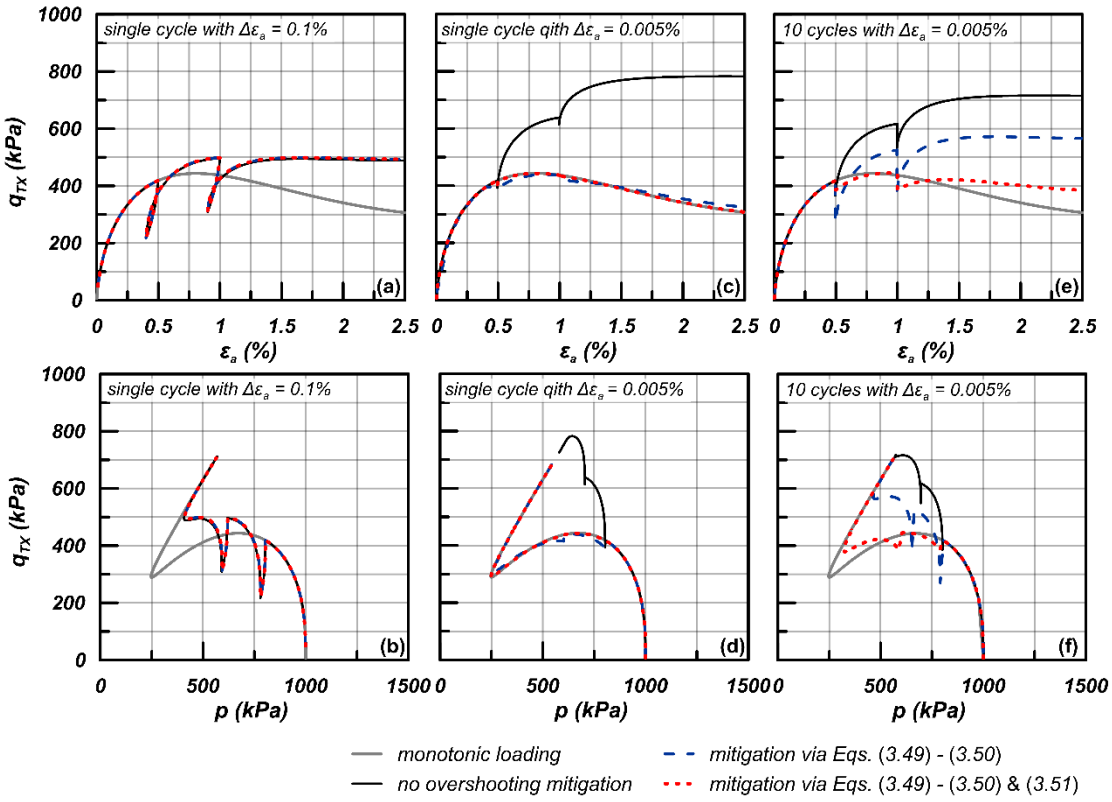

***Figure 3.12**: Performance of different schemes to treat overshooting for the stress-strain response of an undrained triaxial compression test, with three different cases of unloading-reloading cycles at ε_a = 0.5% and 1.0%: (a) single cycle with $\Delta\varepsilon_a$ = 0.1%, (b) single cycle with $\Delta\varepsilon_a$ = 0.005%, (c) 10 successive cycles with $\Delta\varepsilon_a$ = 0.005%.*

Specifically, in subplots **3.12a** and **3.12b**, a single strain-controlled cycle with a large $\Delta\varepsilon_a$ = 0.1% is applied at both levels of ε_a, while in subplots **3.12c** and **3.12d** this single cycle has a much smaller strain amplitude of $\Delta\varepsilon_a$ = 0.005%. Finally, in subplots **3.12e** and **3.12f**, at both levels of ε_a, 10 successive cycles with $\Delta\varepsilon_a$ = 0.005% are applied. In all subplots the curve of the reference monotonic test is included, but this may only be considered relevant in subplots **3.12c, d** and subplot **3.12e, f** where the applied unload-reload cycles are of very

small strain amplitude. On top of this monotonic test curve, in all subplots, three stress-strain curves and three stress paths of the actual test are compared: one without mitigating overshooting, one that employs only Equations (3.49) and (3.50), and one that employs the whole methodology (including Equation (3.51)). It is concluded that overshooting correction is not needed when the unload-reload cycles are of large amplitude (subplots **3.12a, b**). However, it is also shown that the overshooting correction of Dafalias and Taiebat (2016), Equations (3.49) and (3.50), is required when the unload-reload cycles are of small amplitude (subplots **3.12c, d**), with the addition of Equation (3.51) proving necessary for the more general case of multiple cycles of small amplitude (see subplots **3.12e, f**). In closing note that the large differences in the stress-strain response with and without overshooting mitigation shown in **Figure 3.12** (e.g., increase of q_{TX} by more than 100% for ε_a = 2% in subplots **3.12c, d** and **3.12e, f**) should be viewed as an upper bound estimate. For fully drained conditions and/or a more dilative initial state the differences would be smaller, yet they would still vouch for the need of stress-strain overshooting mitigation.

3.10 Summary

This Chapter describes the formulation of a constitutive model for monotonic and cyclic shearing of sands. It is a SANISAND-type model, that does not consider a (small) yield surface and employs the last stress reversal point for defining both the elastic and the plastic strain rates. It introduces a double formulation of the dilatancy function in contraction and in dilation, respectively. It is characterized by concepts like the small and medium strain nonlinearity and the fabric evolution index for large strain response, albeit modified from previous similar expressions in the literature. Stress reversals are appropriately updated in order to avoid the stress-strain overshooting problem, but also to establish that strain accumulation does not appear at very small-strain cyclic loading in accordance to literature. Post-liquefaction strains are in focus with an appropriate modification of the dilatancy function.

It should be clarified here that being of the SANISAND-type, the proposed model is accurate in monotonic or cyclic shearing paths where non-zero deviatoric stress ratio rates ($\dot{\boldsymbol{r}} \neq 0$) prevail, but underestimates plastic strain in problems where loading under constant

stress ratio appears (e.g., one-dimensional consolidation). Accounting for plastic strains due to such types of loading may require additional mechanisms for plastic strain rate development, but such complications are beyond the scope of this model. Similarly, this model is unable to capture the plastic strains appearing during effective stress principal axes rotation, due to the ensuing non-coaxiality between the stress and the plastic strain rate tensors. For SANISAND-type models additional plastic load mechanisms, or multiple dilatancy and plastic modulus expressions, or, in the simplest way, a reformulation of the dilatancy and plastic modulus expressions have been proposed in the literature to remedy this shortcoming. Again, such constitutive complexities are beyond the target of this model. Despite the foregoing limitations, the verification process in **Chapters 5** and **6** proves that the proposed is a useful general-purpose constitutive model for sands, since it provides the user with a convincing satisfactory performance without a need for recalibration regardless of the boundary value problem at hand.

In closing, all the constitutive equations of the model are outlined in **Table 3.1**.

Table 3.1*: Outline of equations of constitutive model.*

Description	**Equation**	**No.**	**Model Param.**
Elastic strain rate	$\dot{\boldsymbol{\varepsilon}}^{\mathrm{e}} = \dot{\boldsymbol{e}}^{\mathrm{e}} + \left(\dot{\varepsilon}^{\mathrm{e}}_{\mathrm{vol}}/3\right)\boldsymbol{I} = \left[1/(2G)\right]\dot{\boldsymbol{s}} + \left[1/(3K)\right]\dot{p}\boldsymbol{I}$	(3.3)	
Plastic strain rate	$\dot{\boldsymbol{\varepsilon}}^{\mathrm{p}} = \dot{\boldsymbol{e}}^{\mathrm{p}} + \left(\dot{\varepsilon}^{e}_{vol}/3\right)\boldsymbol{I} = \langle \Lambda \rangle \boldsymbol{R} = \langle \Lambda \rangle \left(\boldsymbol{n} + (D/3)\boldsymbol{I}\right)$	(3.4)	
Plastic strain direction	$\boldsymbol{R} = \boldsymbol{n} + (D/3)\boldsymbol{I}$	(3.5)	
Loading direction	$\boldsymbol{L} = \boldsymbol{n} - \left((\boldsymbol{n}:\boldsymbol{r})/3\right)\boldsymbol{I}$	(3.7)	
Loading index	$\Lambda = \dfrac{2G\mathbf{n}:\dot{\boldsymbol{e}} - (\mathbf{n}:\mathbf{r})K\dot{\varepsilon}_{\mathrm{v}}}{K_{\mathrm{p}} + 2G - (\mathbf{n}:\mathbf{r})KD}$	(3.9)	
Critical value of void ratio	$e_{\mathrm{cs}} = e_{\mathrm{o}} - \lambda\left(p/p_{\mathrm{atm}}\right)^{\xi}$	(3.10)	e_{cs} λ ξ
State parameter	$\psi = e - e_{\mathrm{cs}}$	(3.11)	
Deviatoric stress ratio on bounding surface in TC	$M^{\mathrm{b}}_{\mathrm{c}} = M^{\mathrm{c}}_{\mathrm{c}}\ exp\left(n^{\mathrm{b}}\langle -\psi \rangle\right)$	(3.12)	$M^{\mathrm{c}}_{\mathrm{c}}$ n^{b}
Deviatoric stress ratio on dilatancy surface in TC	$M^{\mathrm{d}}_{\mathrm{c}} = M^{\mathrm{c}}_{\mathrm{c}}\ exp\left(n^{\mathrm{d}}\psi\right)$	(3.13)	n^{d}
Lode angle	$\cos(3\theta) = \sqrt{6}\,\mathrm{tr}\left(\boldsymbol{n}^3\right) = 3\sqrt{6}\ \det\boldsymbol{n}$	(3.14)	

Generalized model surfaces in the deviatoric stress ratio space	$M_\theta^{c,b,d} = g(\theta,c)\, M_c^{c,b,d}$	(3.15)	
Shape of model surfaces on the π-plane of the deviatoric stress ratio space	$g(\theta,c) = \dfrac{2^\mu\, c}{\left[1 + c^{1/\mu} - \left(1 - c^{1/\mu}\right)\cos\left(3\theta\right)\right]^\mu}$	(3.16)	c
Unit-norm deviatoric tensor	$\boldsymbol{n} = \boldsymbol{r}^b \Big/ \sqrt{\boldsymbol{r}^b : \boldsymbol{r}^b}$	(3.17)	
Image points on model surfaces	$\boldsymbol{r}^{c,b,d} = \sqrt{2/3} M_\theta^{c,b,d} \boldsymbol{n}$	(3.18)	
Scalar distance of image point from the current stress ratio	$d^{c,b,d} = (\boldsymbol{r}^{c,b,d} - \boldsymbol{r}) : \boldsymbol{n}$	(3.19)	
Maximum shear modulus	$G_{max} = G_o\, p_{atm} \left[1 \Big/ \left(0.3 + 0.7e^2\right)\right] \sqrt{p / p_{atm}}$	(3.20)	G_o
Tangential shear modulus	$G_t = \dfrac{G_{max}}{T}$ $T = 1 + 2\left(1/a_1 - 1\right) \dfrac{\sqrt{\frac{1}{2}\left(\boldsymbol{r} - \boldsymbol{r}_{ini}\right) : \left(\boldsymbol{r} - \boldsymbol{r}_{ini}\right)}}{a_1 \left(G_{max}/p\right)^{\gamma_1}}$	(3.21) to (3.22)	
Tangential bulk modulus	$K_t = \left[2\left(1+\nu\right) \Big/ \left(3\left(1-2\nu\right)\right)\right] G_t$	(3.23)	ν
Plastic modulus	$K_p = \left(h_o\, h_\theta\, h_f\, h_{pp}\, h_{ep}\, p\, d^b\right) \Big/ \left((\boldsymbol{r} - \boldsymbol{r}_{ini}) : \boldsymbol{n}\right)$ $h_{pp} = \sqrt{p_{atm}/p}$ $h_{ep} = e^{-ch}$ $h_\theta = \left[2g(\theta', c) - 1\right]^{5/2}$	(3.24) to (3.27)	h_o c_h
Macroscopic fabric function	$h_f = \left(1 + \left\langle f_p - c_f \right\rangle^2\right) \Big/ \left(1 + \left\langle \boldsymbol{f}_{ini} : \boldsymbol{n} \right\rangle\right)$ $\dot{f}_p = \left(2 - a\right) N\, h_{pf}\, \dot{\boldsymbol{\varepsilon}}_{vol}^p$ $\dot{\boldsymbol{f}} = -N\, h_{post\text{-}liq} \left(\boldsymbol{f} + f_{max}^{(1+a)}\, \boldsymbol{n}\right) \left\langle -\dot{\boldsymbol{\varepsilon}}_{vol}^p \right\rangle$ $N = N_o h_{ef} \left\langle -\psi_o \right\rangle^{0.1}$ $h_{pf} = \left(p_{atm}/p_o\right)^{1/2e_o^2} \le 1.5$ $h_{ef} = e_o^{-0.5 c_h}$ $f_{max} = \max\left(f_p\right)$ $0 \le a = -2\left(\left\lvert \int \dot{\varepsilon}_{vol} \right\rvert \Big/ \left\lvert \int \dot{\varepsilon}_{vol}^p \right\rvert - 1\right) \le 1$	(3.28) to (3.35)	N_o

Dilatancy function for contraction	$D = A_o \left[\left((\boldsymbol{r} - \boldsymbol{r}_{ini}) : \boldsymbol{n} + \left\langle -d^d_{ini} \right\rangle \right) d^d \right] \Big/ h_{pd,c}$ $h_{pd,c} = \begin{cases} h_{pd,c}^* & \textit{default} \\ \min\left[h_{pd,c}^*; \dfrac{h_{pd,c,liq}}{h_{pl,d}} \right] & \textit{after initial liquefaction} \end{cases}$ $h_{pd,c}^* = 1 - \left\langle \text{sign}(-\psi_o) \right\rangle \left[\left\langle 1 - \left(\dfrac{p}{p_o} \right)^{0.5} \right\rangle - c_{pd,c} \right]$ $h_{pl,d} = exp\left(-\left(\dfrac{p}{16 p_l} \right)^4 \right)$	(3.37) to (3.40)	A_o
Dilatancy function for dilation	$D = A_o \left(2 h_\theta d^d \right) \Big/ \left(h_{post\text{-}liq}\ h_{fd} \right)$ $h_{fd} = 1 + \left\langle f_{pd} - c_{fd} \right\rangle$ $\dot{f}_{pd} = (1 - a)\, N\, h_{pf} \left\langle \dot{\varepsilon}^p_{vol} \right\rangle$	(3.41) to (3.43)	
Function for post-liquefaction shear strain accumulation	$h_{post\text{-}liq} = 1 + \left(2^{h_l} - 1 \right) f_l$ $\dot{f}_l = S\, L\, h_{pl} \left\lvert \dot{\varepsilon}^p_{vol} \right\rvert$ $L = L_0\, e_0^{\,0.5 c_h}$ $h_l = exp\left[-\left(p / (4 p_l) \right)^4 \right]$ $h_{pl} = exp\left[-\left(p / (10 p_l) \right)^4 \right]$	(3.44) to (3.48)	L_o
Mitigation of overshooting	$\boldsymbol{r}_{ini}^{(m+1)} = k\, \boldsymbol{r}_{ini}^{(m-1)} + (1 - k)\, \boldsymbol{r}^{(m)}$ $k = \left\langle 1 - \left(e^{p(m)} / e_1^p \right)^n \right\rangle$ $\sqrt{(2/3) \left(\boldsymbol{r} - \boldsymbol{r}^{(m)} \right) : \left(\boldsymbol{r} - \boldsymbol{r}^{(m)} \right)} \geq r_{tol}$	(3.49) to (3.51)	

Chapter 4

Implementation in Numerical codes *FLAC* and *FLAC^{3D}*

4.1 General

The new constitutive model presented in **Chapter 3** is implemented in commercial numerical codes *FLAC* (Itasca Consulting Group Inc., 2011) and *FLAC^{3D}* (Itasca Consulting Group Inc. 2012). These codes provide users the option of implementing new constitutive models as UDMs (User Defined Models) that are called during the analysis and describe the constitutive framework of the response. The integration process of the constitutive equations, so as - for given strain increments - stress increments to be estimated, is instrumental for the accuracy of numerical results especially when the response is highly non-linear. In the following, the implementation process of the new model is analyzed. All the specific implementation components are described step-by-step in the following paragraphs, focusing on the numerical code *FLAC*, while exactly the same methodology holds for the implementation in *FLAC^{3D}*.

4.2 Finite difference codes *FLAC* and *FLAC^{3D}*

A very detailed description of the theoretical background of codes *FLAC* and *FLAC^{3D}* is made in their program guides (Itasca Consulting Group Inc. 2011, 2012) and needed be repeated here. However, a brief description of the basic points of the numerical process will be discussed here, as background information for understanding the employed implementation process.

FLAC (*Fast Lagrangian Analysis of Continua*) (Itasca Consulting Group Inc. ,2011) is an explicit finite difference program, specialized in the numerical analysis of problems of geotechnical engineering. Soil is considered as a continuum and it is discretized in elements (zones in *FLAC*'s terminology), which shape the desired geometry of the model to be analyzed (grid in *FLAC*'s terminology). The forces and the motion equations are applied at the nodes of each zone (gridpoints in *FLAC*'s terminology). The stress-strain response of each element is described by the adopted constitutive law, following the

kinematic and boundary restraints. The user-defined constitutive models (UDMs) are encoded in C++ and are compiled in a dynamic link library form (DLL).

4.2.1 The explicit finite difference method

In the finite difference method, every derivative in the set of governing equations is replaced directly by an algebraic expression written in terms of the field variables (e.g., stresses or displacements) at discrete points in space, while these variables are undefined within elements (or zones). The fundamental difference between this method, and the finite element method is that the latter has a basic requirement that the field variables (e.g., stresses or displacements) vary throughout each element in a prescribed way, using specific functions. The formulation involves the adjustment of these variables to minimize error terms. Moreover, finite element programs often combine the element matrices into a large global stiffness matrix, whereas this is not normally done in finite difference programs, because it is relatively efficient to regenerate the finite difference equations at each computational step.

Based on the above, even for the solution of a static problem, the dynamic equations of motion are included in the formulation. One reason for doing this is to ensure that the numerical scheme is stable when the physical system being modeled is unstable. The general calculation sequence embodied in *FLAC* is illustrated in **Figure 4.1**. According to this procedure, given the stresses and forces applied at discrete points, motion equations are invoked to derive new velocities and displacements. Velocities and displacements result in strain rates that are inputs to the constitutive framework. Subsequently, new stresses are derived. One step is considered as a full cycle of the procedure described above. It is very crucial to understand, that in an explicit method like this applied here, in each stage in **Figure 4.1** all grid variables (stresses or displacements) are updated from known values that remain fixed during the stage in question. For example, while the computational stage is where the constitutive equation is applied (lower box in **Figure 4.1**), the velocities are already calculated and for these given values, new stresses are computed. During this stage, the velocities remain “frozen” and unchanged, i.e., they are not affected by the new stresses just calculated. Practically, the operations in each stage (or box in **Figure 4.1)** are independent of each other. This may seem unreasonable because it is expected that, a

change of stresses within a zone will influence its neighbors and change their velocities. The key to ensure numerical stability and prevent this from happening, is the choice of a "*timestep*" adequately small, so as information cannot physically pass from one zone to its neighbor within the duration of that timestep. In other words, the fundamental concept is that the "*calculational wave velocity*" always keeps ahead of the "*physical wave velocity*", so that the equations always operate on known values that are fixed for the duration of the calculation. The measure of this adequately small "*timestep*" is defined on the basis of various parameters (e.g., size of zones, velocity at which information can propagate in each material etc.). However, after several cycles of the loop, disturbances can propagate across several zones, just as they would propagate physically.

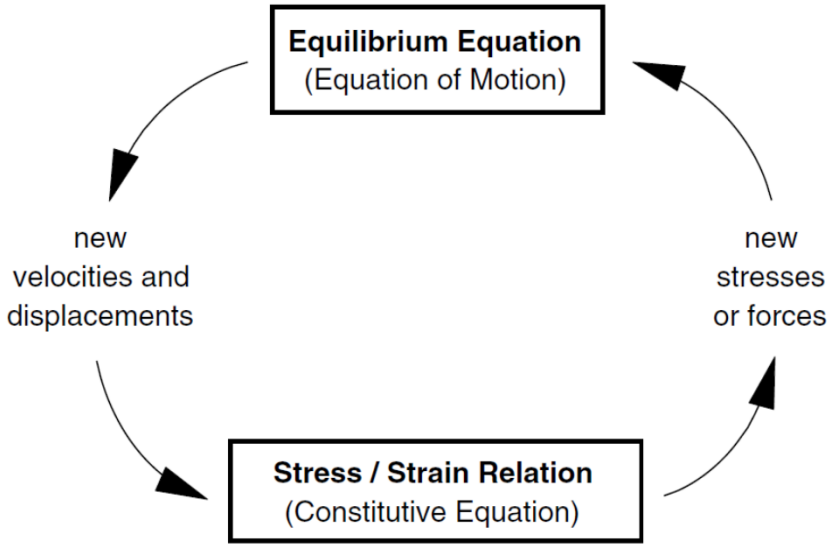

Figure 4.1: *Basic explicit calculation cycle (figure after Itasca Consulting Group Inc., 2011).*

The most important advantage of the explicit finite difference method is that no iteration process is necessary when computing stresses from strains in a zone, even if the constitutive law is intensely nonlinear. In implicit methods (which are commonly used in finite element codes), every element communicates with every other element during one solution step and as a result, several cycles of iteration are necessary before compatibility and equilibrium are obtained. However, the advantage of this explicit method comes at the price of a small "*timestep*", which means that a much large number of steps must be taken so as the computational process to be completed.

4.2.2 Mixed grid discretization

The solid body is divided by the user into a finite difference mesh composed of quadrilateral zones. For 2D analyses, *FLAC* internally subdivides each zone into two overlaid sets of constant-strain triangular sub-zones, as shown in **Figure 4.2**. Velocities and forces are concentrated and act on the nodes of these sub-zones and the equations of motions are solved at these nodes. The spatial derivatives of velocities and forces (i.e., stresses and strain rates) are maintained constant within the zones. The use of triangular sub-zones eliminates the problem of hourglass deformations that may occur with constant-strain finite difference quadrilaterals. The term "*hourglassing*" comes from the shape of the deformation pattern of elements within a mesh. For polygons with more than three nodes, there are combinations of nodal displacements which produce no strain and result in no opposing forces. The resulting effect is unopposed deformations of alternating direction. To overcome this problem, the isotropic stress and strain components are taken to be constant over the whole quadrilateral zone, while the deviatoric components are treated separately for each triangular sub-zone. This procedure, referred to as "*mixed discretization*", is described by Marti and Cundall (1982). The term mixed discretization arises from the different discretization techniques for the isotropic and deviatoric parts of the stress and stain tensors.

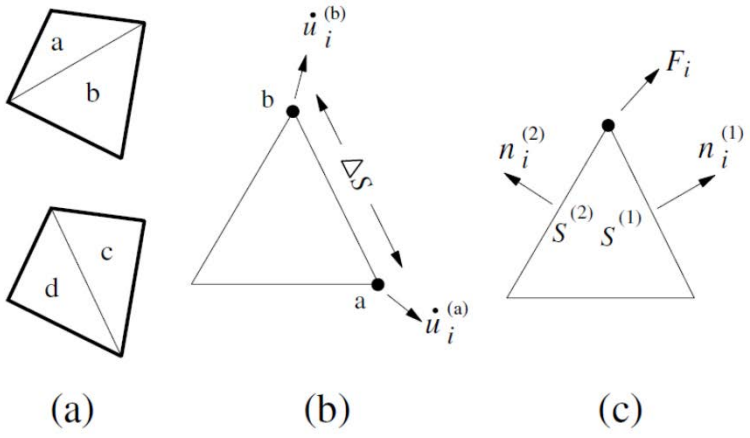

Figure 4.2: *(a) Overlaid quadrilateral zones used in FLAC, (b) typical triangular element with velocity vectors and (c) nodal force vectors (figure after Itasca Consulting Group Inc. 2011).*

The four triangular sub-zones are termed a, b, c and d. As explained above, the deviatoric stress components of each triangle are maintained independently, requiring all the stress components to be stored separately for each quadrilateral ($4 \cdot \sigma_{xx}$, σ_{yy}, σ_{zz}, σ_{xy}). The force vector exerted on each node is taken to be the mean of the two force vectors exerted by the two overlaid quadrilaterals. A similar mixed discretization technique is also used in *FLAC*^{3D}, with the difference being that the continuum is not discretized into quadrilaterals but into tetrahedra.

4.2.3 Motion equation and constitutive law

In a continuous solid body, Newton's law of motion is generalized as:

$$\rho \frac{\partial \dot{u}_i}{\partial t} = \rho \frac{\partial \sigma_{ij}}{\partial x_j} + \rho g_i \tag{4.1}$$

where:

ρ : mass density

t : time

x_i : components of coordinate vector

g_i : components of gravitational acceleration

σ_{ij} : components of stress tensor

$\dot{u}_i$: components of velocity vector

Subsequently, strain rate $\dot{e}_{ij}$ is derived from the velocity gradient:

$$\dot{e}_{ij} = \frac{1}{2}\left[\frac{\partial \dot{u}_i}{\partial x_j} + \frac{\partial \dot{u}_j}{\partial x_i}\right] \tag{4.2}$$

Finally, according to the constitutive law adopted in each subzone the stress increment $\Delta\sigma$ in each subzone is estimated as per:

$$\Delta\sigma = f(\sigma, \dot{e}, \kappa) \tag{4.3}$$

where κ stands for the sum of hardening parameters of the constitutive framework. Additionally, subscripts i and j denote the components of a vector or a tensor and can be omitted, if reference to specific components does not need to be made.

4.2.4 Finite difference equations

The difference equations for a triangle are derived from the generalized form of Gauss' divergence theorem, according to which:

$$\int_s n_i \, f \, ds = \int_A \frac{\partial f}{\partial x_i} dA \tag{4.4}$$

where:

$\int_s$: the integral around the boundary of a closed surface, S

n_i : the unit normal to the surface, S

f: a scalar, vector or tensor

x_i : position vectors

ds : an incremental length

$\int_A$: the integral over the surface area, A

Defining the average value of the gradient of f over the area A as

$$\left\langle \frac{\partial f}{\partial x_i} \right\rangle = \frac{1}{A} \int_A \frac{\partial f}{\partial x_i} dA \tag{4.5}$$

where $\langle f \rangle$ is taken to be the average over the surface, by substitution, it is deduced that:

$$\left\langle \frac{\partial f}{\partial x_i} \right\rangle = \frac{1}{A} \int_s n_i \, f \, ds \tag{4.6}$$

And for a triangular sub-element, the finite-difference form of Equation (4.6) becomes:

$$\left\langle \frac{\partial f}{\partial x_i} \right\rangle = \frac{1}{A} \sum_s \langle f \rangle \, n_i \, \Delta S = \frac{1}{2A} \sum_s \langle n_i \rangle \left(f^{(a)} + f^{(b)} \right) \Delta S \tag{4.7}$$

where ΔS is the length of a side of the triangle.

The summation occurs over the three sides of the triangular subzone and (a) and (b) are two consecutive nodes on a side.

Equation (4.7) can be used to derive all the components of the strain rate tensor based on nodal velocities, as:

$$\frac{\partial \dot{u}_i}{\partial x_j} = \frac{1}{2A} \sum_s \left(\dot{u}_i^{(a)} + \dot{u}_i^{(b)} \right) n_j \Delta s \tag{4.8}$$

4.2.5 Fluid – mechanical coupling

The formulation of coupled fluid-deformation mechanisms in *FLAC* is based on the Biot theory of consolidation. The governing differential equations corresponding to *FLAC*'s numerical implementation are discussed below. According to Darcy's law, water flow is described as:

$$q_i = -k_{ij} \hat{k}(s) \frac{\partial}{\partial x_j} \left(P - \rho_w g_k x_k \right) \tag{4.9}$$

where:

q_i : specific charge vector

k_{ij} : mobility coefficient tensor (measure of permeability, equal to the permeability coefficient $k_{H,ij}$ used in Darcy's law, divided by the fluid's unit weight, so as: $k_{ij}=k_{H,ij}/(\rho_w g)$.

P : fluid pressure

ρ_w : mass density of the fluid

g_k : gravitational acceleration vector

For saturated/unsaturated flow in *FLAC*, the air pressure is assumed to be constant and equal to zero.

The fluid pressure *P* follows the constitutive law below:

$$\frac{\partial P}{\partial t} = -M \frac{\partial \varepsilon_{\text{vol}}}{\partial t} \tag{4.10}$$

with:

ε_{vol} : volumetric strain

M : Biot's fluid modulus equal to:

$$M = \frac{K_{\text{w}}}{n + (a - n)(1 - a)\frac{K_{\text{w}}}{K}} \tag{4.11}$$

where:

a : Biot's coefficient

n : the porosity of the porous medium

K : the drained bulk modulus of the porous medium

K_{w} : the fluid bulk modulus

If the compressibility of grains is neglected - compared to that of the drained bulk material, then Biot's coefficient *a* equals to 1, so:

$$M = \frac{K_w}{n} \tag{4.12}$$

It should be noted, that when coupling between mechanical and fluid response applies, the stresses are effective and the mass density of the material is the saturated one, estimated as:

$$\rho_{\text{sat}} = \rho_{\text{d}} + n\rho_{\text{w}} \tag{4.13}$$

4.2.6 *"Timestep"* determination

As previously described, the explicit-solution procedure is not unconditionally stable: the velocity of the "*calculation front*" must be greater than the maximum velocity at which

information propagates. As such, a "*timestep*" that is smaller than some "*critical timestep*" must be chosen.

The stability condition for an elastic solid discretized into elements is:

$$\Delta t < \frac{\Delta x}{C} \tag{4.14}$$

where:

Δx : the minimum propagation distance, estimated as $A/\Delta x_{max}$ in *FLAC* and $V/\Delta A_{max}$ in *FLAC*^{3D}.

C: the maximum velocity at which information can propagate - typically, the *P*-wave velocity:

$$C_p = \sqrt{\frac{K + \frac{4}{3}G}{\rho}} \tag{4.15}$$

For a single mass-spring element, the stability condition is:

$$\Delta t < 2\sqrt{\frac{m}{k_{stiff}}} \tag{4.16}$$

where m is the mass, and k_{stiff} is the stiffness. In a general system consisting of solid material and arbitrary networks of interconnected masses and springs, the "*critical timestep*" is related to the smallest natural period of the system, T_{min}:

$$\Delta t < \frac{T_{min}}{\pi} \tag{4.17}$$

For the simple case of a rectangular zone, with area A_z, thickness T_z and diagonal length L_d, the gridpoint mass and the zone stiffness can be expressed as:

$$m = \frac{1}{4}\rho A_z T_z \tag{4.18}$$

$$k_{stiff} = \left(K + \frac{4G}{3}\right)\frac{L_d^2}{A_z}T_z \tag{4.19}$$

In the case of effective stress analyses, where groundwater is present, the bulk modulus of the fluid increases the mechanical stiffness of the saturated zone, thus reducing the selected "*timestep*".

4.2.7 User defined model (UDM) routines

Both *FLAC* and *FLAC*^{3D} provide the user with the possibility to implement User Defined Model (UDM) routines written in C++ and compiled as Dynamic Link Libraries (DLLs). The DLL files are plugged-in the code and they can used exactly as the built-in models. For example, they can be assigned to any zone and they can be given any properties.

In each numerical cycle, the input to the UDM algorithm is the total strain increment of the current step and the stress state of the previous one, while the output is the new stress state. The UDM routine is called once per subzone for every solution step, i.e., 4 times per solution step. The output stress tensor for each subzone is exported directly from the UDM routine to *FLAC* or *FLAC*^{3D}, where the averaging procedure according to the mixed discretization scheme is internally handled. This new stress tensor is then an input to the UDM routine for the next step. Concurrently, the model's hardening parameters are stored for each subzone and are manually averaged inside the UDM algorithm, when the calculation process is completed for all 4 subzones. These averaged values are common input for all 4 subzones in the next step. The foregoing general implementation procedure is described in detail in Andrianopoulos (2006) and Karamitros (2010). Moreover, in Karamitros (2010) an original description is provided of the necessary components comprising the UDM routine written in C++. The framework of the algorithm, herein, is exactly as described in Karamitros (2010), and the new constitutive equations and components of the new model were properly included following the same rationale.

Finally, it should be noted that the foregoing input and output stress tensors for the UDM routine refer to effective stress tensors. Pore pressures are used, so as effective stresses are taken for given total stresses, before the constitutive model is called in the calculation cycle. The reverse process of calculating total stresses on the basis their effective counterparts is performed after model calculations in each calculation cycle are completed.

4.3 The Integration Scheme

The numerical process during a calculation step within the UDM routine should be structured, so as a stress increment to be computed, for any given stress state and any given strain increment. Hence, the constitutive stress-strain relationship (Equation (3.8)) needs to be integrated. In general, explicit integration schemes can be easily applied for the numerical integration of complex and highly non-linear constitutive laws, as they are straightforward to implement in explicit finite difference codes like *FLAC* and *FLAC*^{3D}.

For the integration of the constitutive equations and the calculation of stress increments and hardening parameters for any given strain increment, the explicit scheme of Andrianopoulos et al. (2010a) was hereby used. Specifically, the integration of the constitutive equations at each subzone is performed via a second order modified forward Euler method and is accomplished by dividing the given strain increment in one or more sub-increments (or sub-steps in *FLAC*'s terminology), in order for the local error at each step to be maintained below a desired tolerance level. This integration scheme in combination with an automatic error control and a sub-stepping technique, was originally introduced by Sloan (1987) and Sloan et al. (2001) and the scheme adopted in this model is presented in detail in Andrianopoulos et al. (2010b) and in Andrianopoulos (2006), with appropriate modifications to comply with the specific constitutive form of the proposed model. It is reminded here that for each step the integration is performed for all 4 sub-zones that form a zone of the grid. However, at the end of each step the resultant stress tensor is returned to *FLAC* (or *FLAC*^{3D}) and handled appropriately according to the adopted mixed discretization scheme. It is noted here that the hardening parameters are averaged manually for the whole zone, as part of the UDM routine procedure.

4.3.1 Modified Euler integration scheme with automatic sub-stepping and error control

Following the work of Andrianopoulos (2006) and Andrianopoulos et al. (2010a), the modified Euler integration scheme with automatic substepping and error control is used herein. In the following, the integration process will be discussed.

Specifically, for each step a pseudo-time T ($0 \le T \le 1$) parameter is defined, so as to divide given strain increments in smaller fractions (sub-increments or sub-steps) to

facilitate the error control process. State $T = 0$ refers to the beginning of the sub-stepping, and it incrementally increases up to $T = 1$, when the total strain increment has been applied. The step of pseudo-time is depicted by ΔT_n and obviously $0 \le \Delta T_n \le 1$ holds. Subscripts n and n-1 refer to the pseudo-time instances T_{n-1} and $T_n = T_{n-1} + \Delta T_n$, and denote the start and the end of the sub-step respectively. ΔT_n controls the measure of the fraction of the currently applied strain sub-increment, as per:

$$\dot{\boldsymbol{\varepsilon}}_n = \Delta T_n \dot{\boldsymbol{\varepsilon}} \tag{4.20}$$

where:

$\dot{\boldsymbol{\varepsilon}}_n$: the fraction of strain increment applied during a sub-step

$\dot{\boldsymbol{\varepsilon}}$: the total strain increment for the full step

The size of ΔT_n progressively decreases down to a minimum value, if the local error insists on exceeding a prescribed threshold, or it may also increase after an accepted error control, in an effort to reduce the total computational cost. The integration process follows the flow described below.

Step 1

Reading from the code the total strain increment, $\dot{\boldsymbol{\varepsilon}}_\zeta$, for the step ζ, for each one of the 4 subzones. For each subzone, the value of the effective stress tensor $\boldsymbol{\sigma}_{\zeta-1}$ from the previous step ζ-1 is available, after been implicitly processed by the code according to the mixed discretization scheme (at the end of the previous step). Moreover, for each zone, the set of hardening parameters of the model is available, as a result of an averaging process over the 4 subzones at the end of the previous step.

Initialization also of $T = 0$ and $\Delta T_n = 1$.

Step 2

While $T<1$, follow steps 3 - 11.

Step 3

Given a strain sub-increment $\dot{\boldsymbol{\varepsilon}}_n = \Delta T_n \dot{\boldsymbol{\varepsilon}}_\zeta$, a first order prediction (i = 1) of the effective stress increment $\dot{\boldsymbol{\sigma}}_i$ is made according to the constitutive equations of the model. The necessary stress tensor components entering the equations refer to the current state ($\boldsymbol{\sigma}$)

when the step initiates and are derived at the end of the previous step. Moreover, a first order prediction (i = 1) is also made for the hardening parameters of the model included in the error control procedure, which for the proposed model are the 4 cumulative indices f_p (Eq. (3.29)), $\boldsymbol{f}$ (Eq. (3.30)), f_{pd} (Eq. (3.43)) and f_l (Eq. (3.45)). In the following the set of these hardening parameters is denoted as κ. An updated value is also calculated for the void ratio e. Then, a temporary update of the effective stress state is made based on this first prediction and the current (temporary) value is $\boldsymbol{\sigma} + \dot{\boldsymbol{\sigma}}_1$. The same temporary update is made for all the hardening parameters of the model and their current (temporary) value is $\kappa + \dot{\kappa}_1$

.

Step 4

Initiating from this temporarily updated state and given the same strain sub-increment $\dot{\boldsymbol{\varepsilon}}_n$, a second approximation (i = 2) of the effective stress increment $\dot{\boldsymbol{\sigma}}_2$ and of the hardening parameters $\dot{\kappa}_2$ of the model is made according to the constitutive equations. The necessary stress tensor components and hardening parameters entering the constitutive equations refer to the (temporary) updated values derived during the previous first prediction.

Step 5

The actual increment of $\boldsymbol{\sigma}$ and κ is the average value of $\dot{\boldsymbol{\sigma}}_1$ and $\dot{\boldsymbol{\sigma}}_2$ and $\dot{\kappa}_1$ and $\dot{\kappa}_2$, respectively. In other words, the final estimate of the sub-step is the state $\boldsymbol{\sigma}_n = \boldsymbol{\sigma}_{n-1} + 0.5(\dot{\boldsymbol{\sigma}}_1 + \dot{\boldsymbol{\sigma}}_2)$ and $\kappa_n = \kappa_{n-1} + 0.5(\dot{\kappa}_1 + \dot{\kappa}_2)$.

Step 6

Subsequently, based on the two estimated increment predictions and the temporary estimated values of each parameter, the local error is computed for each parameter as:

$$R_\sigma = 0.5\frac{\left\|\dot{\boldsymbol{\sigma}}_2 - \dot{\boldsymbol{\sigma}}_1\right\|}{\left\|\boldsymbol{\sigma}_n\right\|} \tag{4.21}$$

$$R_\kappa = 0.5\frac{\left\|\dot{\kappa}_2 - \dot{\kappa}_1\right\|}{\left\|\dot{\kappa}_n\right\|} \tag{4.22}$$

It is underlined here that Eq. (4.22) is considered 4 times, separately for each of the 4 hardening parameters of this model. The relative error of the integration sub-step is denoted by R and is defined as the maximum of the calculated local errors, as:

$$R = \max\left[R_{\sigma}; R_{\kappa}\right] \tag{4.23}$$

Step 7

The relative error R is compared to a predefined tolerance level of relative error, S_{tol}. According to Sloan et al. (2001), a good range for S_{tol} is between 10^{-1} and 10^{-4}, with an optimal value equal to 10^{-3}. The smaller the tolerance level, the stricter the criteria for the acceptance of the integration during the sub-step. A value of $S_{tol} = 10^{-3}$ was selected in this model, as the default one.

If $R > S_{tol}$, then the sub-step is rejected and steps 3 -7 are repeated, this time with a smaller sub-increment of strain. For this purpose, a smaller value of ΔT_n is adopted as per:

$$\Delta T_n = \max\left[q\Delta T_n; \Delta T_{min}\right] \tag{4.24}$$

where:

$$q = \max\left[0.9\sqrt{\frac{S_{tol}}{R}}; 0.1\right] \tag{4.25}$$

and $\Delta T_{min} = 10^{-3}$, a fixed value, that leads to a division of the step into 1000 sub-steps. This value was introduced by Sloan et al. (2001) for reasons of code robustness. This iterative procedure is repeated until the local relative error falls below the tolerance level.

If $R \leq S_{tol}$ or $\Delta T_n = \Delta T_{min,}$ the sub-step is accepted, all the temporary values of $\boldsymbol{\sigma}_n$ and κ_n are accepted and the integration proceeds to the next sub-step.

Pseudo-time moment T_{n+1} denoting the beginning of the next sub-step is equal to:

$$T_{n+1} = T_n + \Delta T_n \tag{4.26}$$

Step 8

The new value of the new sub-step is defined as:

$$\Delta T_n = q\Delta T_n \tag{4.27}$$

where:

$$q = \min\left[0.9\sqrt{\frac{S_{\text{tol}}}{R_{\text{n}}}};1.1\right] \tag{4.28}$$

However, if the last sub-step had been accepted because $\Delta T_{\text{n}} = \Delta T_{\text{min}}$, albeit $R_{\text{n}} > S_{\text{tol}}$, then:

$$q = \min\left[q;1.0\right] \tag{4.29}$$

Step 9

The new ΔT_{n} must be checked, so as not to be smaller than ΔT_{min}, and not to lead to a total time T greater than 1.0.

$$\Delta T_{\text{n}} = \max\left[\Delta T_{\text{n}};\Delta T_{\text{min}}\right] \tag{4.30}$$

$$\Delta T_{\text{n}} = \min\left[\Delta T_{\text{n}};1-T\right] \tag{4.31}$$

Go to ***Step 2***.

Step 10

After all the sub-steps have been completed, the total increment has been applied. The final values of stress tensor $\boldsymbol{\sigma}_{\zeta}$ for each subzone, for the given strain increment, are returned to *FLAC* (or *FLAC*^{3D}) and handled further internally, while the hardening parameters κ_{ζ} are kept in memory so as to be averaged for the whole zone, after the integration for all the 4 subzones is completed. The next step starts.

The integration algorithm described above is an integral part of the model. Specifically, **Figure 4.3** shows a simplified flowchart of the integration algorithm from the beginning to the end of a calculation step, including the procedures of error control and sub-stepping that were previously described step-by-step. Subsequently, **Figure 4.4** aids in the presentation of the second order modified forward Euler method for the integration of stresses and of the hardening parameters governing the error control procedure.

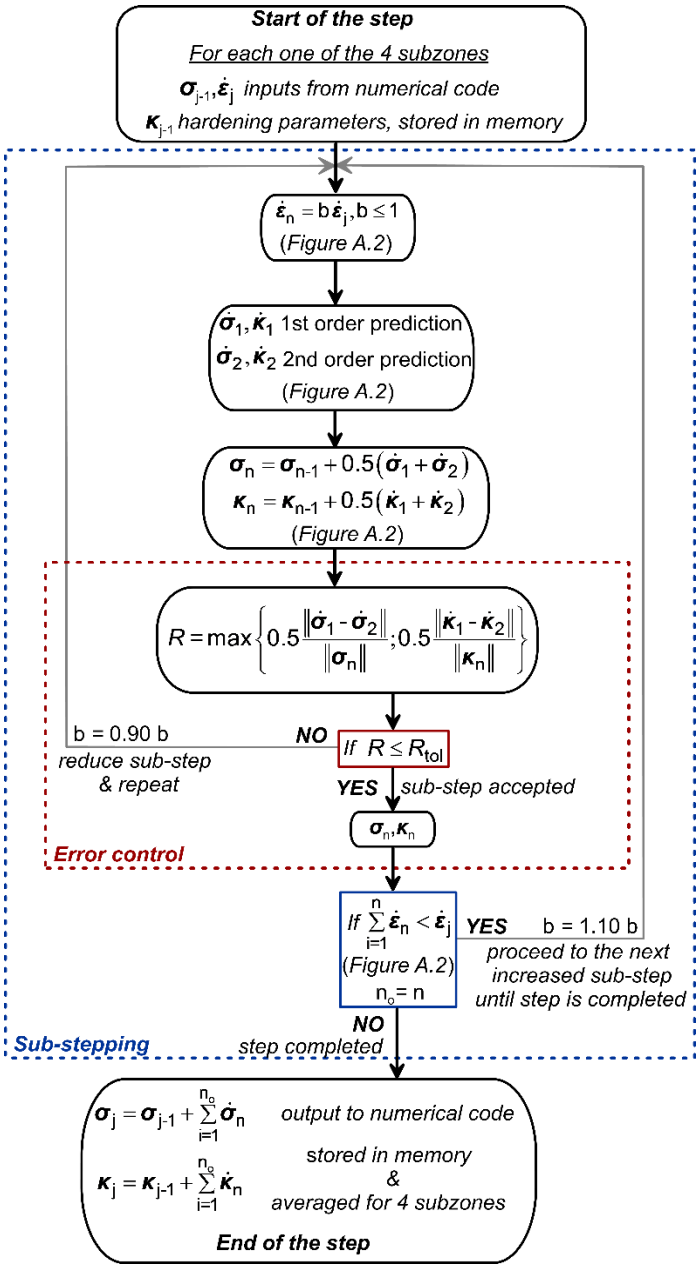

***Figure 4.3**: Flowchart of the integration process of effective stress and hardening parameters including sub-stepping.*

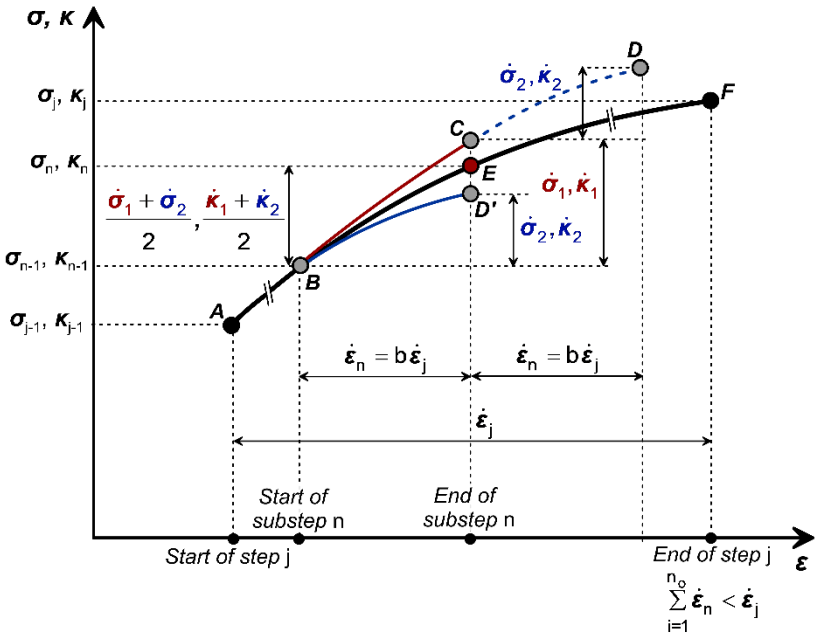

***Figure 4.4**: Schematic illustration of the second order modified forward Euler integration method.*

4.3.2 Correction of stress state when outside the bounding surface

This subroutine performs a possible correction of the stress whenever it is outside the bounding surface. It targets to decrease the distance of the current stress state from the bounding surface, only when the stress state lies outside it by an unrealistically large amount. The resultant stress state, after the execution of the function, remains outside the bounding surface, but it is transferred to a closer distance. The basic premise of this routine is that by-design, whenever the stress is outside the bounding surface in SANISAND-type models this appears by a very small amount sufficient to predict softening, while larger amounts are possibly related to numerical instabilities mostly in the very small stress liquefaction regime. Hence, a correction is required to bring the stress state closer to the bounding surface, yet still outside from it.

The methodology was adopted by the implementation of the NTUA-SAND model, according to Andrianopoulos (2006), Andrianopoulos et al. (2010b) and Karamitros (2010). The tolerance level of this distance is named $F_{bs,tol,1}$ and is equal to 10^{-2}. Respectively, $F_{bs,1}$ denotes the distance of the current deviatoric stress ratio $\boldsymbol{r}$ from the bounding surface, along the direction of $\boldsymbol{r}$, as:

$$F_{\mathrm{bs},1} = \|\boldsymbol{r}\| - \sqrt{\frac{2}{3}} M_{\omega}^{\mathrm{b}} \tag{4.32}$$

where $\|\boldsymbol{r}\|$ denotes the norm of tensor $\boldsymbol{r}$ and $M_{\omega}^{\mathrm{b}} = g(\omega, c) M_{\mathrm{c}}^{\mathrm{b}}$ the aperture of the bounding surface along the direction of $\boldsymbol{r}$. The aperture across this direction is defined with the aid of function g (see Equation (3.16)), only here the variable Lode angle ω (see Equation (3.14)) entering the function is defined in terms of the unit-norm tensor $\boldsymbol{m}$, which denotes the direction of $\boldsymbol{r}$:

$$\boldsymbol{m} = \frac{\boldsymbol{r}}{\|\boldsymbol{r}\|} \tag{4.33}$$

According to Equation (4.32), negative values of $F_{\mathrm{bs},1}$ mean that $\boldsymbol{r}$ lies within the bounding surface, while positive values mean that it is outside.

Step 1

Reading the new stress tensor and check if it lies outside the bounding surface. If $F_{\mathrm{bs},1} \leq 0$ then the stress state is inside the bounding surface, and no correction is needed. Otherwise, if $F_{\mathrm{bs},1} > 0$, i.e., the stress state is outside the bounding surface, go to *Step 2*.

Step 2

Check how much is the stress state outside from the bounding surface. Specifically, if $F_{\mathrm{bs},1} < F_{\mathrm{bs,tol},1} = 10^{-2}$, then the stress state is quite close to the bounding surface and no further modification of the distance is needed. Otherwise, the stress state is far from the bounding surface and it should come closer to it, so proceed to *Step 3*.

Step 3

The current stress tensor is kept into the memory. Moreover, the utilized correction parameter for the downscaling of $\boldsymbol{\sigma}$, named as a_{corr}, is set equal to 1. Hence, the measure of downscaling is defined, via the correction factor F_{corr} as per:

$$F_{\mathrm{corr}} = \frac{a_{\mathrm{corr}} F_{\mathrm{bs},1}}{\|\boldsymbol{L}\|} = \frac{a_{\mathrm{corr}} F_{\mathrm{bs},1}}{\sqrt{\boldsymbol{L} : \boldsymbol{L}}} \tag{4.34}$$

where $\boldsymbol{L}$, is the direction of the downscaling of $\boldsymbol{\sigma}$, equal to:

$$\boldsymbol{L} = \boldsymbol{m} - \left(\frac{V}{3}\right)\boldsymbol{I} \tag{4.35}$$

$$V = \boldsymbol{m} : \boldsymbol{r} \tag{4.36}$$

The new (downscaled) stress state $\boldsymbol{\sigma}_{\text{down}}$ is:

$$\boldsymbol{\sigma}_{\text{down}} = \boldsymbol{\sigma} - F_{\text{corr}}\,\boldsymbol{L} \tag{4.37}$$

Step 4

Check if the stress point came closer to the bounding surface, but without getting inside it. So, if $F_{\text{bs,1}}$ became lower than zero ($F_{\text{bs,1}} < 0$), it means that the correction was larger than needed. In this case, the previous *Step 3* is neglected and it is repeated again, but with a smaller correction parameter a_{corr}:

$$a_{\text{corr,new}} = 0.9\, a_{\text{corr}} \tag{4.38}$$

Otherwise, if $0 < F_{\text{bs,1}} \leq 10^{-2}$, the correction was appropriate and the new stress tensor is:

$$\boldsymbol{\sigma} = \boldsymbol{\sigma}_{\text{down}} \tag{4.39}$$

4.4 Mapping rule - Determination of image point on the bounding surface

The application of the mapping rule essentially refers to the determination of the image point of the current stress ratio on the bounding surface. The employed methodology is borrowed from the implementation of the NTUA-SAND model, according to Andrianopoulos (2006), Andrianopoulos et al. (2010b) and Karamitros (2010). This image point is defined as $\boldsymbol{r}^{\text{b}}$ in **Chapter 3** (see Equation (3.18)). This point lies on the bounding surface, and simultaneously on the projection of the vector defined by the current deviatoric stress ratio $\boldsymbol{r}$ and the $\boldsymbol{r}_{\text{ini}}$, which refers to the tensor $\boldsymbol{r}$ when the last load reversal took place. The location of the image point may be expressed as a function of $\boldsymbol{r}$ and $\boldsymbol{r}_{\text{ini}}$, with the aid of variable β as (see also **Figure 3.2**):

$$\boldsymbol{r}^{\text{b}} = \boldsymbol{r}_{\text{ini}} + \beta\left(\boldsymbol{r} - \boldsymbol{r}_{\text{ini}}\right) \tag{4.40}$$

Then, adopting the same nomenclature like in the previous section, respectively, $F_{bs,2}$ denotes the distance of the image stress ratio $\boldsymbol{r}^b$ from the bounding surface, from the bounding surface, along the direction of $\boldsymbol{r}^b$, as:

$$F_{bs,2} = \left\| \boldsymbol{r}^b \right\| - \sqrt{\frac{2}{3}} M_\theta^b \tag{4.41}$$

According to Equation (4.41) negative values of $F_{bs,2}$ mean that $\boldsymbol{r}^b$ lies within the bounding surface, while positive values mean that it lies outside. In order for $\boldsymbol{r}^b$ to stand for the required image point the condition $F_{bs,2} = 0$ should be satisfied. Hence, an iterative procedure is necessary, so as to pinpoint an adequate value of β to satisfy this condition.

Step 1

Initialization of parameters β_o and β_1, which will be utilized as multipliers of the vector ($\boldsymbol{r}$-$\boldsymbol{r}_{ini}$). Parameter β will be determined as a linear interpolation between β_o and β_1. Parameter β_o defines a deviatoric stress ratio inside the bounding surface, while β_1 defines a deviatoric stress ratio outside from it.

$\beta_o = 0$ and $\beta_1 = 1$ (4.42)

By substituting in Equation (4.40) the temporary image points $\boldsymbol{r}^b$ defined with the use of β_o and β_1 are:

$$\boldsymbol{r}^b(\beta_o) = \boldsymbol{r}_{ini} + \beta_o(\boldsymbol{r} - \boldsymbol{r}_{ini}) \tag{4.43}$$

$$\boldsymbol{r}^b(\beta_1) = \boldsymbol{r}_{ini} + \beta_1(\boldsymbol{r} - \boldsymbol{r}_{ini}) \tag{4.44}$$

and the corresponding distances from the bounding surface $F_{bs,2}[\boldsymbol{r}^b(\beta_o)]$ and $F_{bs,2}[\boldsymbol{r}^b(\beta_1)]$ are computed.

Step 2

Check if the stress point $\boldsymbol{r}^b(\beta_1)$ is outside the bounding surface, i.e., if $F_{bs,2}[\boldsymbol{r}^b(\beta_1)] > 0$. If this condition is satisfied, then go to *Step 3*.

Otherwise, iterations should be made to eventually τo bring $\boldsymbol{r}^{b}(\beta_1)$ outside the bounding surface. Hence,

$$\beta_o = \beta_1 \text{ and } \beta_1 = 2\,\beta_1 \tag{4.45}$$

and the new distances $F_{bs,2}[\boldsymbol{r}^{b}(\beta_o)]$ and $F_{bs,2}[\boldsymbol{r}^{b}(\beta_1)]$ are calculated.

This procedure continues until $F_{bs,2}[\boldsymbol{r}^{b}(\beta_o)]$ becomes larger than zero. Moreover, it should be noted that in order for this step to be successful the condition, according to which $F_{bs,2}[\boldsymbol{r}^{b}(\beta_o)] \cdot F_{bs,2}[\boldsymbol{r}^{b}(\beta_1)] \leq 0$ should be satisfied, i.e., $\boldsymbol{r}^{b}(\beta_o)$ and $\boldsymbol{r}^{b}(\beta_1)$ to lie on either sides of the bounding surface.

Step 3

An iterative procedure to determine the precise value of β, which ensures that the image deviatoric stress ratio practically lies on the bounding surface, starts. This is achieved by using a linear interpolation between β_o and β_1. Specifically:

$$\beta = \frac{(\beta_1 - \beta_o)\,F_{bs,2}\left[\boldsymbol{r}^{b}(\beta_1)\right]}{F_{bs,2}\left[\boldsymbol{r}^{b}(\beta_1)\right] - F_{bs,2}\left[\boldsymbol{r}^{b}(\beta_o)\right]} \tag{4.46}$$

$$\boldsymbol{r}^{b}(\beta) = \boldsymbol{r}_{ini} + \beta\left(\boldsymbol{r} - \boldsymbol{r}_{ini}\right) \tag{4.47}$$

Then, if the image point is sufficiently close to the bounding surface, i.e., according to Equation (4.41), $F_{bs,2}[\boldsymbol{r}^{b}(\beta_o)] < 10^{-5}$, the iterative procedure comes to an end.

Otherwise, an effort to bring the image point closer to the bounding surface is made. If the β has the same sign as β_o, this means that the estimated image point is inside the bounding surface, and in order to be brought closer to the bounding surface, β_o should be increased. On the other hand, if the β has the same sign as β_1, this means that the estimated image point is outside the bounding surface, and to be brought closer to the bounding surface, β_1 should be decreased. Then, the new β and the new distance of the image point from the bounding surface are calculated. This rationale is efficient as the β interpolates linearly between β_o and β_1.

4.5 Formulation to mitigate stress-strain overshooting

As described in detail in **Chapter 3**, two criteria are included in the formulation to remedy the shortcoming of a stress-strain curve that is "*overshooted*" as a result of an "*informal*" unloading-reloading cycle during the numerical analysis. The foregoing problem is related to the unnecessary updating of $\boldsymbol{r}_{\text{ini}}$ upon unloading and immediate reloading. The first criterion, among the two that constitute the mitigation methodology, determines whether a load reversal (i.e., a state where $\Lambda < 0$) is "*formal*" or "*informal*", while the second one incorporates the methodology of Dafalias and Taiebat (2016) and adjusts the value of $\boldsymbol{r}_{\text{ini}}$ depending on the significance of the intervening loading path, but only when the load reversal has been approved as "*formal*".

In order to understand the methodology, the following terms are defined: $\boldsymbol{r}^{(\text{m})}$ is the current stress-ratio tensor along the current load path (m) at the moment of load reversal (i.e., when $\Lambda < 0$ appears), $\boldsymbol{r}_{\text{ini}}^{(\text{m})}$ refers to the $\boldsymbol{r}_{\text{ini}}$ adopted at the initiation of load path (m), $\boldsymbol{r}_{\text{ini}}^{(\text{m-1})}$is the $\boldsymbol{r}_{\text{ini}}$ of the previous load path (m-1) and $\boldsymbol{r}_{\text{ini}}^{(\text{m+1})}$refers to the $\boldsymbol{r}_{\text{ini}}$ that is going to be adopted after the initiation of the upcoming (m+1) load path. When $\Lambda < 0$ appears during load path (m), the $\boldsymbol{r} = \boldsymbol{r}^{(\text{m})}$ and the quandary is whether $\boldsymbol{r}_{\text{ini}}^{(\text{m+1})}$ should be updated to $\boldsymbol{r}^{(\text{m})}$, thus increasing the stiffness of the stress-strain curve during the upcoming path (m+1), or whether it should take another value. The implementation of this procedure is described step-by-step below.

Step 1

Use of an index, namely I_{LR}, which records during a step whether a load reversal signal occurs for each subzone. This means that if all 4 subzones are given a load reversal signal during a step, the value of this index will be equal to 4. If a load reversal signal occurs for a subzone, then the tensor $\boldsymbol{r}_{\text{subzone}}^{(\text{m})}$ of the subzone at that moment on path (m) is stored in memory. This procedure continues for all 4 subzones, and after the completion of the step an average of all the $\boldsymbol{r}_{\text{subzone}}^{(\text{m})}$tensors kept in memory is calculated and denoted as $\boldsymbol{r}^{(\text{m})}$. This is a "*candidate*" $\boldsymbol{r}_{\text{ini}}$ tensor, for the upcoming load path (m+1).

In the interval between the moment when the signal for load reversal was detected on path (m) and until the main constitutive calculations for one subzone to be completed,

all the computations and functions for each subzone are performed using the $\boldsymbol{r}_{\text{ini}}^{(\text{m})}$ tensor, which is not updated yet, and still holds, even for the new load path (m+1). Specifically, as soon as a load reversal is detected, it is considered by default "*informal*" and no update of $\boldsymbol{r}_{\text{ini}}$ is performed immediately. As such, all the computations continue with a non-updated $\boldsymbol{r}_{\text{ini}} = \boldsymbol{r}_{\text{ini}}^{(\text{m})}$, until it is verified if the load reversal is "*formal*" or not. In the meantime, plastic deviatoric strain and stress ratio increments are calculated.

Step 2

All the main computations have been completed for all the subzones. Now, it is checked if any of them has received a signal for load reversal. If even one subzone has received a signal, then $I_{\text{LR}} > 0$ and the option to update the $\boldsymbol{r}_{\text{ini}}$ should be checked.

The criterion for deciding if the signal was "*formal*" is to check how much the stress ratio $\boldsymbol{r}$ has changed during loading on path (m+1), from the moment when the signal was detected. In other words, of importance is the distance of the current stress-ratio $\boldsymbol{r}$ from the tensor $\boldsymbol{r}$ at the beginning of the step, which is equal to the tensor $\boldsymbol{r}^{(\text{m})}$, given all the subzones where subjected to a signal for load reversal. If this distance is larger than a preset (small) tolerance level r_{tol} then the load reversal is considered "*formal*" and the estimation of $\boldsymbol{r}_{\text{ini}}^{(\text{m+1})}$ is made according to the methodology of Dafalias and Taiebat (2016). The value of r_{tol} is selected equal to 10^{-2} here and the check has the form:

$$\sqrt{(2/3)\left(\boldsymbol{r}-\boldsymbol{r}^{(\text{m})}\right):\left(\boldsymbol{r}-\boldsymbol{r}^{(\text{m})}\right)} \geq r_{\text{tol}} \tag{4.48}$$

In the case where the criterion above is satisfied, then go to *Step 3*.

However, it should be noted that the tensor $\boldsymbol{r}$ may not increase adequately in only one step, and as such the criterion of Equation (4.48) may not be satisfied in the first step of path (m+1), immediately after the load reversal signal is detected. In that case, the next step is proceeded without any update of $\boldsymbol{r}_{\text{ini}}$ yet and the procedure is continued until the distance between $\boldsymbol{r}$ - $\boldsymbol{r}^{(\text{m})}$ to become sufficiently large and $\boldsymbol{r}_{\text{ini}}$ to be updated. During these steps, where $\boldsymbol{r}_{\text{ini}}$ has not been updated yet, the loading index Λ usually continues to be negative (see Equation (3.9)), so special attention is given so as the $\boldsymbol{r}^{(\text{m})}$ to be caught only at the first time

when $\Lambda < 0$ (at the end of path (m) and at the beginning of path (m+1)), and not be continuously updated in the following steps.

It is worth mentioning that if during this sequence of steps, where $\boldsymbol{r}_{\text{ini}}$ has not yet been updated, a new load reversal signal is detected, then the previous load reversal is considered "*informal*" by result, the $\boldsymbol{r}^{(\text{m})}$ in memory is neglected as a candidate $\boldsymbol{r}_{\text{ini}}$ and now, the procedure of characterizing the current load reversal starts from scratch from *Step 1* for the new (m+1) path.

Step 3

This *Step 3* is proceeded given the criterion described by the Equation (4.48) is satisfied. Since loading reversal has been accepted as "*formal*", the updated $\boldsymbol{r}_{\text{ini}}$ for the upcoming (m+1) path (denoted as $\boldsymbol{r}_{\text{ini}}^{(\text{m}+1)}$) is not necessarily equal to $\boldsymbol{r}^{(\text{m})}$, but it is estimated according to Dafalias and Taiebat (2016). Specifically, it depends on the "*magnitude*" of the load path (m) and is quantified in terms of the integral of plastic deviatoric strain developed during path (m), as:

$$\boldsymbol{r}_{\text{ini}}^{(\text{m})} = k\,\boldsymbol{r}_{\text{ini}}^{(\text{m}-1)} + \left(1 - k\right)\boldsymbol{r}^{(\text{m})} \tag{4.49}$$

where:

$$k = \left\langle 1 - \left(\frac{e^{\text{p}}}{e_1^{\text{p}}} \right)^n \right\rangle \tag{4.50}$$

where k is a weighting parameter, that quantifies the significance of the load path (m) on the basis of the relative magnitude of accumulated plastic deviatoric strain e^{p} in comparison to e_1^{p}, a model constant serving as a shear strain threshold.

The e^{p} is given as:

$$e^{\text{p}} = \sqrt{\left(2/3\right)\dot{\boldsymbol{e}}^{\text{p}} : \dot{\boldsymbol{e}}^{\text{p}}} \tag{4.51}$$

which accumulates during load path (m). In this model, $e_1^p=10^{-4}$, and n, the model constant controlling the non-linearity is set equal to 1, following the advice of Dafalias and Taiebat (2016) for both. Since a load reversal is accepted as "*formal*", the quantity e^p nullifies and starts accumulating from scratch for the ongoing path, so as to be utilized at the determination of the $\boldsymbol{r}_{ini}$ of the following load path and so on.

4.6 Summary

In this Chapter the implementation of the proposed model in numerical codes *FLAC* and *FLAC*^{3D} is presented. The methodology is described with emphasis mainly on numerical code *FLAC*, but it extends unchanged in *FLAC*^{3D}. A brief description of the theoretical background of the codes is provided. Then, the integration scheme of the stress-strain constitutive equation is described. Specifically, a modified Euler integration scheme is used for this model, in conjunction with a sub-stepping technique and an automatic error-control, which target the reduction of the local error derived at the application of strain increment. Subsequently, supplementary routines are described that account for: a) the correction of the stress state when it is located (far) outside the bounding surface, b) the determination of the image point on the bounding surface (as part of the mapping rule) and c) the formulation to mitigate stress-strain overshooting. All these components serve as an integral part of the UDM model routine and ensure its robust response in element, but also in system level numerical analyses.

Chapter 5

Model Performance in Element tests

5.1 Calibration procedure

The proposed model requires in total the calibration of 14 parameters. All of them are dimensionless, non-negative material-specific model constants and their role in the constitutive equations is described in detail in **Chapter 3**. The constitutive role and the relevant constitutive equation, where each one appears, are summarized on columns 2 and 3 of **Table 5.1**. The procedure of determining their values will be discussed in this Section using experimental data of Toyoura sand, as merely an example case.

Table 5.1: *Constitutive role, relevant constitutive equation and suggested calibration procedure of model parameters.*

Model Parameter	Constitutive role	Relevant Constitutive Eq.	Calibration
G_o	Elasticity	(3.20)	directly calibratable
ν		(3.23)	
e_{ref}	CSL	(3.10)	directly calibratable
λ			
ξ			
M_c^c		(3.12), (3.13)	
c		(3.16)	
n^b	Plastic modulus	(3.12)	directly calibratable
h_o		(3.24)	indirectly calibratable
c_h		(3.26)	
n^d	Dilatancy	(3.13)	directly calibratable
A_o		(3.37), (3.41)	indirectly calibratable
N_o	Fabric	(3.31)	indirectly calibratable
L_o	Post-liquefaction	(3.46)	

Having deeply understood their constitutive role, it is deduced that the model parameters, for each sand, can be divided in two separate categories, as mentioned on the last column of **Table 5.1**: a) those directly evaluated on the basis of experimental data, and b) those indirectly estimated through a trial- and-error procedure. The parameters classified in the first category constitute the majority (9 out of 14), and their estimation is suggested to precede that (5 out of 14) of the second category.

5.1.1 Directly calibrated model parameters

A. Parameters related to Critical State

The 5 critical state parameters comprise the critical stress ratio in triaxial compression (M_c^c), the ratio of critical stress ratio in extension over compression (c), and the parameters e_{cs}, λ, and ξ of Equation (3.10) that define the position of the CSL on the (p - e) space. To calibrate these parameters, monotonic tests that have reached (or approach asymptotically) the critical state are necessary.

The parameters e_{cs}, λ, and ξ, are estimated by fitting Equation (3.10) to pairs of (p, e) obtained after monotonic shearing, when critical state has been approached. Based on the monotonic triaxial compression drained and undrained experiments of Verdugo and Ishihara (1996), Li and Wang (1998) proposed for Toyoura sand a CSL with e_{cs} = 0.934, λ = 0.019, and ξ = 0.70, values that are adopted also here (**Figure 5.1**).

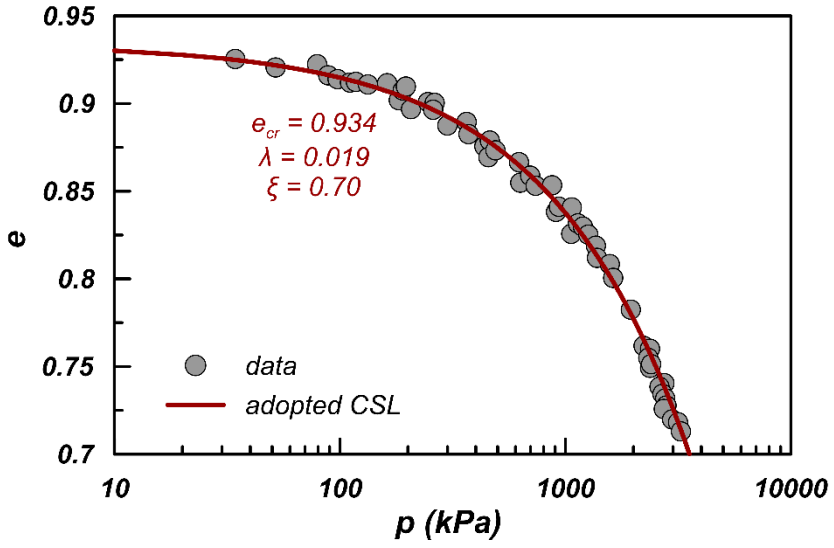

***Figure 5.1**: Calibration of CSL constants on (p - e) space for Toyoura sand. Data after Verdugo and Ishihara (1996).*

Values of M_c^c can be obtained by plotting monotonic triaxial compression stress paths on the (q_{TX} - p) space, and pointing the critical stress ratio. The obtained pairs of q_{TX}^c and p^c - with superscript c denoting the values are at critical state - can be plotted as in **Figure 5.2**.

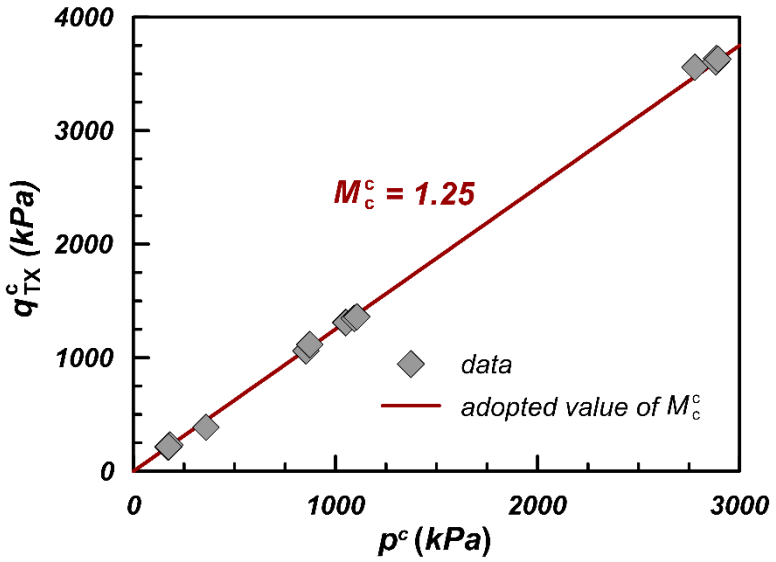

***Figure 5.2**: Calibration of model parameter M^c_c on q_{TX} - p space for Toyoura sand. Data after Verdugo and Ishihara (1996).*

As shown, for Toyoura sand, a quite good approximation is the value M^c_c = 1.25. A similar approach can be followed for triaxial extension stress paths to estimate the value of *c*, however, here the value of *c* = 0.712 is adopted for Toyoura sand according to Dafalias and Manzari (2004), Dafalias and Taiebat (2016) and Papadimitriou et al. (2019).

B. Parameters related to Elasticity

Based on Equations (3.20) and (3.23), the elasticity formulation requires the calibration of 2 model parameters. The G_o parameter that defines the elastic shear modulus of sand (G_{max}) should be calibrated against small strain tests (e.g., bender elements, resonant column tests), wave propagation tests in the field or laboratory or in the absence of specific measurements from empirical relations of the literature. According to McAllister et al. (2015), the use of conventional triaxial data for this purpose (as is usually performed in the literature) may lead to underestimation of its value. Here, the data of Wicaksono and Kuwano (2009) for Toyoura sand are used for this purpose. As shear modulus was measured through different dynamic methods (e.g., trigger accelerometer, bender element, plate transducer), an average value is considered for the calibration of G_o. In **Figure 5.3**, the comparison between the measured and estimated (by Equation (3.20)) elastic small strain shear modulus, G_{max}, is presented, for the estimated value of G_o = 650. The comparison is made in terms of G_{max}

versus mean effective stress p, for three different values of void ratio (e = 0.811 - $D_r \approx 45\%$, e = 0.756 - $D_r \approx 60$ % and e = 0.700 - $D_r \approx 75$ %). Based on the good fitting of the data in **Figure 5.3**, apart from the appropriate G_o value, the calibrated Equation (3.20) estimates quite well the correlation of G_{max} with relative density and applied stress level.

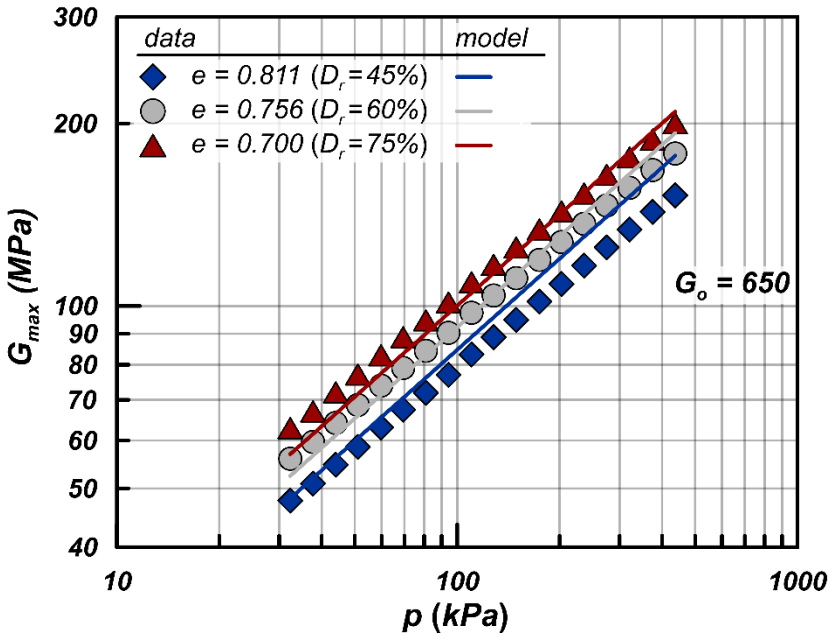

***Figure 5.3**: Comparison of estimated G_{max} values as a function of void ratio e and mean effective stress p, after calibration of parameter G_o for Toyoura sand. Data after Wicaksono and Kuwano (2009).*

The second elastic parameter, Poisson's ratio v, is considered constant in the current model. The determination of Poisson's ratio requires the use of local-strain transducers, which are rarely available on laboratory experiments. Alternatively, for dry soil only it can be estimated by using the measured wave velocities from wave propagation tests of P and S waves (e.g. Crosshole or Downhole tests), as per:

$$v = \frac{\left(\frac{V_p}{V_s}\right)^2 - 2}{2\left[\left(\frac{V_p}{V_s}\right)^2 - 1\right]} \qquad (5.1)$$

Herein, a value of 0.15 is adopted for Toyoura sand in accordance with Shibuya et al. (1994) and Tatsuoka et al. (1994). As this parameter shows a small variation in the literature (0.05-0.33), it is believed that the selected value can be assumed as quite representative for sands in general, in absence of more specific experimental measurements (Loukidis and Salgado, 2009).

C. Parameters related to Model Surfaces

The next two parameters, n^b and n^d, correlate the aperture of model's surfaces on the deviatoric stress ratio space with the current state parameter ψ. The parameter n^b, referring to the bounding surface of the model, can be determined by fitting Equation (3.12) at experimental peak stress ratio values from monotonic, drained and undrained tests plotted against the corresponding ψ value. Here, the monotonic drained and undrained triaxial compression tests of Verdugo and Ishihara (1996) are used for this purpose, so the utilized stress ratios refer to triaxial conditions. Specifically, if properly manipulating Equation (3.12) and replacing M_c^b and M_c^c by the peak ($(q_{TX}/p)^b$) and critical ($(q_{TX}/p)^c$) stress ratios measured during the experiment at hand, where the deviatoric stress $q_{TX} = \sigma_a - \sigma_r$, with σ_a denoting the axial effective stress and σ_r the radial. Hence, n^b can be derived as per:

$$n^b = \frac{1}{\psi^b} \cdot \ln\left[\frac{(q_{TX}/p)^c}{(q_{TX}/p)^b}\right] \tag{5.2}$$

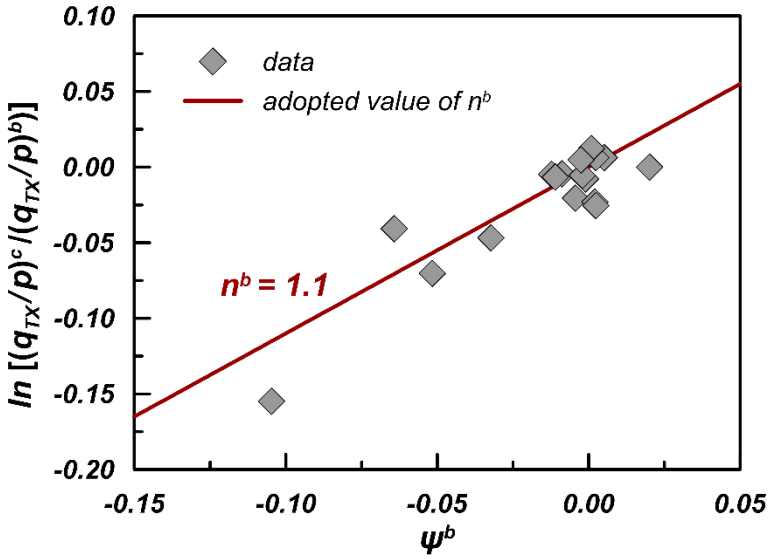

***Figure 5.4**: Calibration of model parameter n^b for Toyoura sand. Data after Verdugo and Ishihara (1996).*

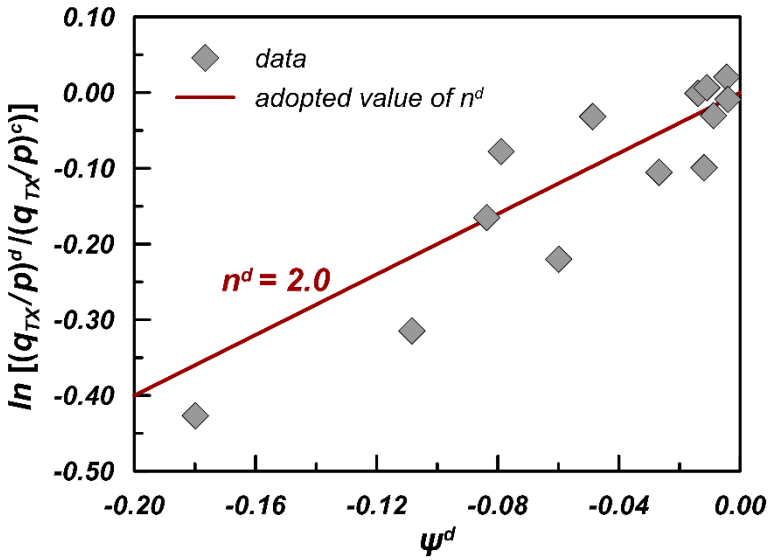

***Figure 5.5**: Calibration of model parameter n^d for Toyoura sand. Data after Verdugo and Ishihara (1996).*

As shown in **Figure 5.4**, a value of n^b equal to 1.1 can be considered quite appropriate for Toyoura sand, as typically referenced in the literature (Dafalias and Manzari, 2004; Loukidis and Salgado, 2009).

Similarly, the parameter n^d, controlling the aperture of the dilatancy surface of the model, can be estimated by fitting Equation (3.13) at experimental stress ratios from monotonic, drained and undrained, tests at the phase transformation state plotted against the respective ψ value. The same dataset of Verdugo and Ishihara (1996) is used for this purpose, so in triaxial conditions, Equation (3.13) can be transformed to:

$$n^d = \frac{1}{\psi^d} \cdot \ln\left[\frac{(q_{TX}/p)^d}{(q_{TX}/p)^c}\right] \tag{5.3}$$

After interpretation of the experimental monotonic data, according to **Figure 5.5**, a value equal to 2.0 is adopted, which is very close to 2.1 proposed also by Taiebat and Dafalias (2008) for Toyoura sand.

5.1.2 Indirectly calibrated model parameters

Trial-and-error repetitive tests are necessary to be performed to estimate the value of these parameters. At this calibration step, the values of the aforementioned directly calibrated model parameters are kept fixed throughout the process according to the procedure

described above, while values of the parameters under estimation are arbitrarily initialized for the first iteration. Although the model is able to estimate satisfactorily the response regardless the applied stress level and density, it is suggested that during this process, emphasis to be given to comparison with experimental data of initial conditions (stress level and void ratio) and shearing conditions (drained/undrained, monotonic/cyclic) indicative of each specific application. Moreover, it is recommended that the calibration procedure to be holistic and not case specific, so as all the aspects of the response to be explored. This approach is also followed herein.

A. Parameters related to Plastic Modulus

Apart from n^b, controlling the aperture of bounding surface according to state parameter ψ and hence the hardening response, parameters h_o and c_h entering plastic modulus function of the model (Equations (3.24) and (3.26)) need to be calibrated. The plastic modulus multiplier h_o is determined through a trial-and-error process, so that in drained monotonic tests there is an adequate match between the estimated and the actual stress-strain curve up to peak stress state. To illustrate the sensitivity of the simulated response on parameter h_o, **Figure 5.6** compares reference simulations to the data of monotonic drained triaxial compression tests of Verdugo and Ishihara (1996) for the indicative cases of e_o = 0.831 ($D_r \approx 43\%$), 0.917 ($D_r \approx 23\%$) and 0.996 ($D_r < 3\%$), where p_o = 100 kPa. In subplots **5.6a** and **5.6b** h_o is considered equal to 20, in subplots **5.6e** and **5.6f** equal to 180, while subplots **5.6c** and **5.6d** refer to the finally calibrated value of h_o which is equal to 60. For these etsimates, apart from the continuously changing h_o, all the other parameters are kept fixed.

This figure shows that an increase in h_o leads to a stiffer response in terms of stress-strain curves at the part before peak-strength (subplot **5.6e)**, but also limits the shear induced volumetric strain, especially when it comes to contraction (subplot **5.6f)**. The opposite observations hold, if the adopted value of h_o is smaller than that implied by the data (subplots **5.6a** and **5.6b)**. The best match is achieved for the finally calibrated value of h_o= 60 (subplots **5.6c** and **5.6d).**

On the other hand, in undrained monotonic tests, h_o should be determined so as an adequate match of stress paths until phase transformation to be achieved. As in **Figure 5.6**, **Figure 5.7** similarly compares reference simulations to the data of monotonic undrained

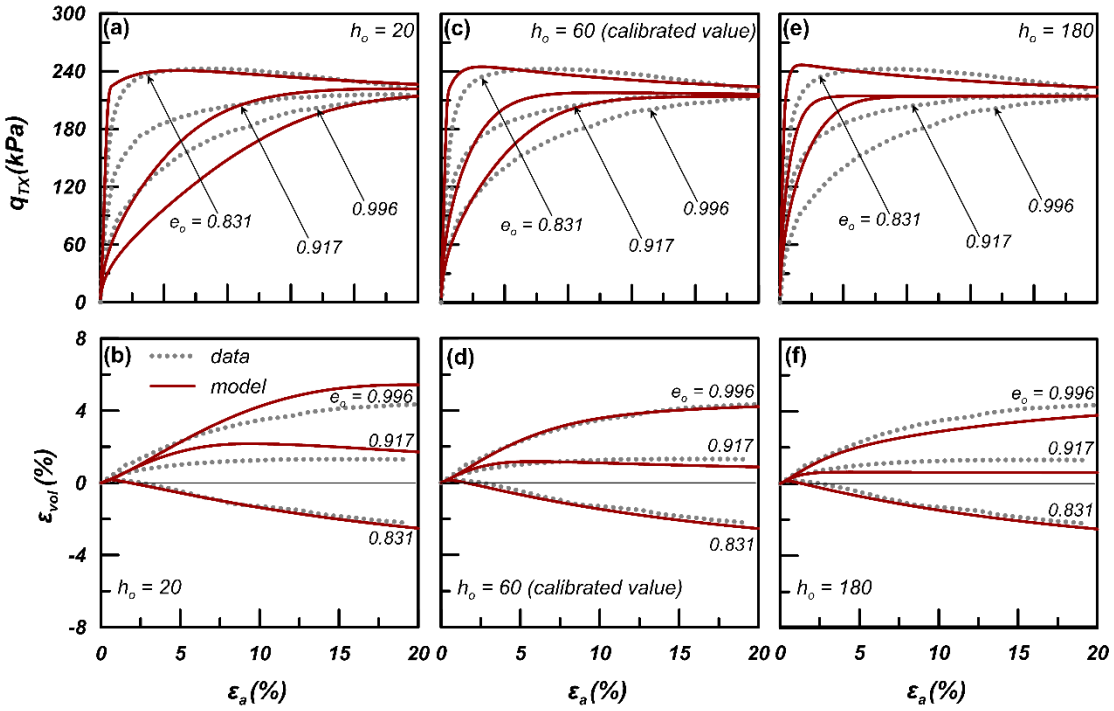

***Figure 5.6**: Sensitivity of simulated monotonic drained triaxial response to model parameter h_o: (a,b) h_o = 20, (c,d) h_o = 60 - (calibrated value) and (e,f) h_o =180. Data after Verdugo and Ishihara (1996).*

triaxial compression tests of Verdugo and Ishihara (1996) for the indicative cases of e = 0.833 ($D_r \approx 37\%$) and p_o = 100, 1000 and 2000 kPa. In subplots **5.7a** and **5.7b,** h_o is considered equal to 20, in subplots **5.7e** and **5.7f** equal to 180, while subplots **5.7c** and **5.7d** refer to the finally calibrated value of h_o which is equal to 60, while keeping again the values of all other parameters fixed. The effect of h_o in the simulated undrained response is the same as in drained conditions, although possibly more intense. Specifically, an increase of h_o leads to a stiffer response in terms of stress-strain curves (subplot **5.7e**) and concurrently to a limited tendency for pore pressure buildup and subsequent decrease of p in terms of q_{TX} - p stress paths (subplot **5.7f**) and vice versa.

A trial-and-error process is also necessary to estimate the proper value of parameter c_h, so as the correct void ratio effect is captured on the hardening response. This is achieved by fitting the response of samples with very different initial void ratio e_o values. To illustrate the sensitivity of the simulated response to parameter c_h, **Figure 5.8** compares reference simulations to the already shown data of monotonic drained triaxial compression tests of Verdugo and Ishihara (1996). The significant variation of e_o in these tests, between

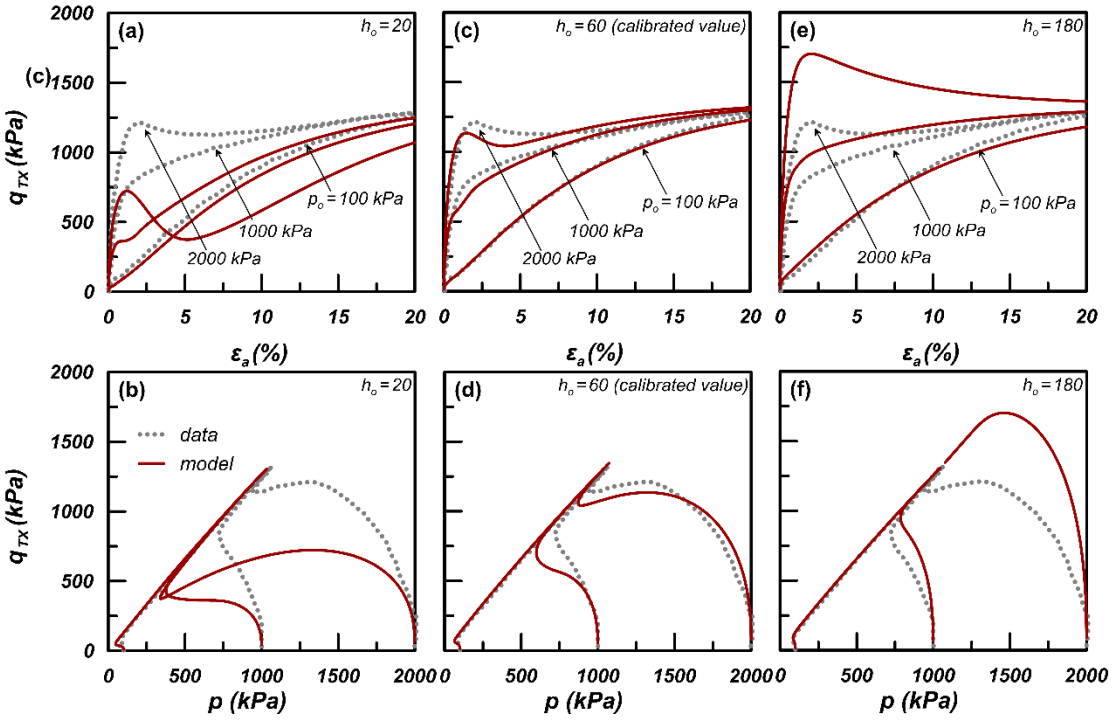

***Figure 5.7**: Sensitivity of simulated monotonic undrained triaxial response to model parameter h_o: (a,b) h_o = 20, (c,d) h_o = 60 - (calibrated value) and (e,f) h_o =180. Data after Verdugo and Ishihara (1996).*

0.831 ($D_r \approx 43\%$) and 0.996 ($D_r < 3\%$), proves very useful for the proper calibration of c_h. It should be noted that while trying different values of c_h, the values of h_o, N_o and L_o should also be appropriately readjusted. According to Equations (3.24) and (3.26), (3.31) and (3.33) and (3.45) and (3.46) it is implied that any change of c_h modifies not only the effect of void ratio on the respective functions, but also their measure for a given value of void ratio e. Hence, in order to keep the value of K_p - for a reference value of void ratio – at a desired level, regardless of any change of c_h, the value of h_o should also be properly adapted. By adopting practically unaffected the response for a reference void ratio, the effect of e will be relatively illustrated to this reference response. For comparisons of **Figure 5.8**, the test with a value of e equal to 0.831 is selected as reference, and so, h_o is modified in parallel with c_h, so as that corresponding response of this test to remain unaffected despite any change of c_h. In subplots **5.8a** and **5.8b**, c_h is considered equal to 3, in subplots **5.8e** and **5.8f** equal to 20, while subplots **5.8b** and **5.8c** refer to the finally calibrated value of c_h, which is equal to 12. The respective values of h_o are estimated according to the rationale previously described and are noted on the respective figures. It is observed that the lower

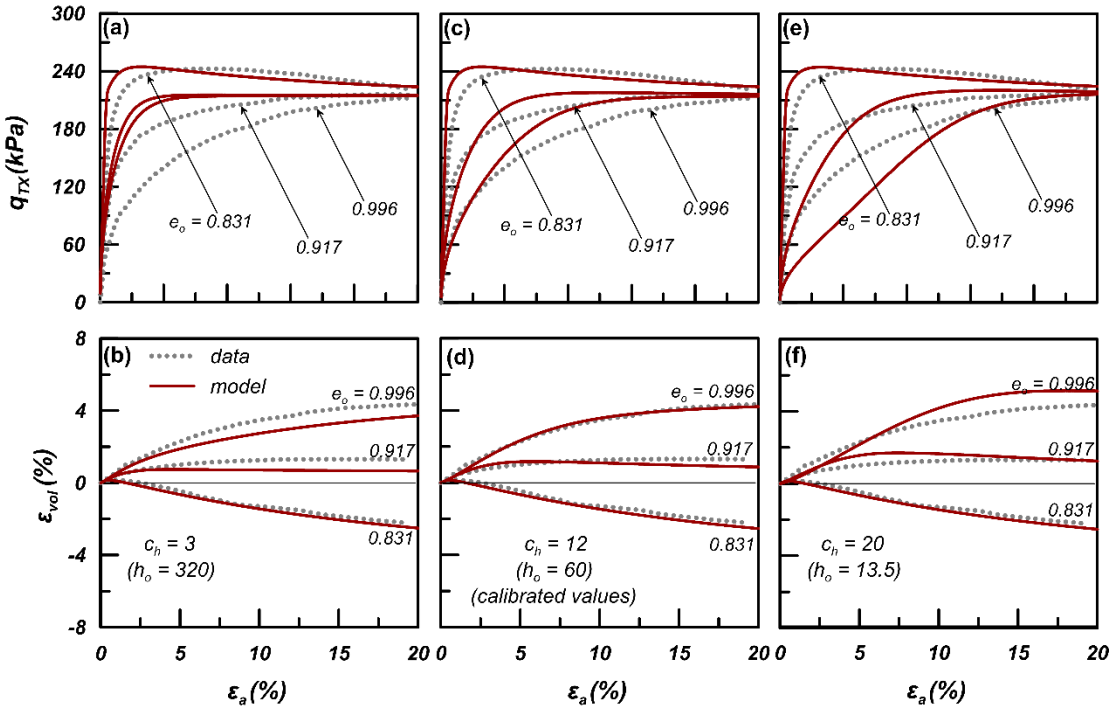

***Figure 5.8**: Sensitivity of simulated monotonic drained triaxial response to value of model parameter c_h: (a,b) c_h = 3, (c,d) c_h = 12 - (calibrated value) and (e,f) c_h = 20. Data after Verdugo and Ishihara (1996).*

the value of c_h, the smaller the effect of void ratio on stress-strain response, as all the simulated curves plot close one to another (subplot **5.8a**). Smaller than the experimentally measured is also the effect of void ratio on accumulation of volumetric strain (subplot **5.8b**). The opposite observations are made when the value of c_h is greater than what the data indicate (subplots **5.8e** and **5.8f**).

Here it should be noted that the effect of void ratio, via model parameter c_h, enters also the intensity functions of fabric accumulation (Equation (3.31)) and post-liquefaction shear strain accumulation (Equation (3.46)), acting during cyclic loading - the latter only during undrained conditions after liquefaction. The effect is similar, as an increase of c_h leads to a more pronounced effect of D_r on these intensity functions and hence, on the accumulation of the relative hardening parameters. Moreover, it is similarly implied that any change of c_h modifies not only the effect of void ratio on the respective functions, but also their measure, for a given value of void ratio e. Hence, as in the case of plastic modulus, in order to keep the values of N and L - for a reference value of void ratio - at a desired level, regardless of any change of c_h, the values of N_o and L_o should also be properly

adapted.

B. Parameter related to Dilatancy

The estimation of dilatancy parameter A_o requires stress-dilatancy data and can be calibrated against volumetric strain vs deviatoric strain curves from derived drained monotonic tests, so as the volumetric strain accumulation during shearing is properly quantified. **Figure 5.9** presents comparisons between sensitivity simulations and the drained monotonic data of Verdugo and Ishihara (1996). In subplots **5.9a** and **5.9b**, A_o is considered equal to 0.5, in subplots **5.9e** and **5.9f** equal to 3.0, while subplots **5.9b** and **5.9c** refer to the finally calibrated value of A_o which is equal to 1.5. Observe that the appropriate calibration of A_o proves very important for the correct simulation of volumetric strain accumulation and dilatancy response. A small value of A_o leads to lower accumulation of ε_{vol} (subplot **5.9b**) than the measured and vice versa (subplot **5.9f**). Observe, also, that the effect of A_o on stress-strain response is less important and it mainly affects the response after peak stress is reached, resulting in a more softening response as A_o increases.

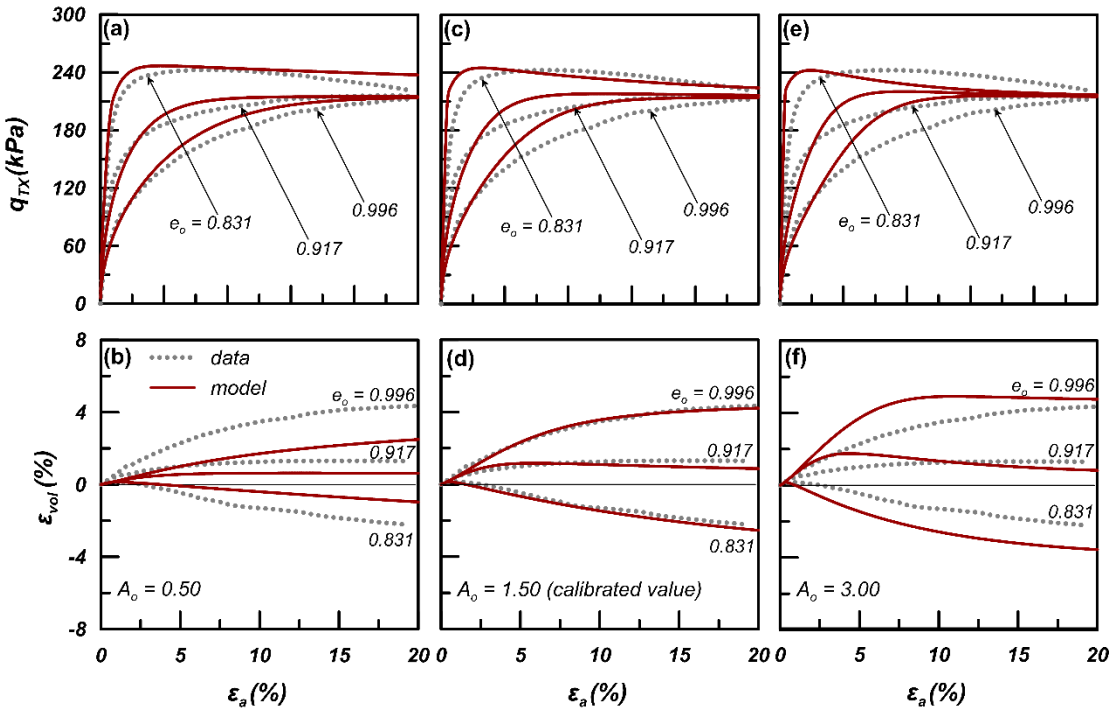

***Figure 5.9**: Sensitivity of simulated monotonic drained triaxial response to value of model parameter A_o: (a,b) A_o = 0.5, (c,d) A_o = 1.5 - (calibrated value) and (e,f) A_o = 3.0. Data after Verdugo and Ishihara (1996).*

C. Parameter related to fabric evolution intensity

In paragraphs A and B above, the parameters h_o, c_h and A_o are calibrated, as they suffice for monotonic loading. In the current paragraph C, and in the next paragraph D, the remaining two parameters N_o and L_o are calibrated, respectively. Specifically, The fabric evolution intensity constant N_o determines the cyclic response and may be estimated after all the 12 preceding parameters only on the basis of cyclic tests. It is calibrated by a trial-and-error process by targeting either the accumulated volumetric strains during cyclic drained tests, or the number of cycles to reach initial liquefaction during cyclic undrained tests. The selection of type of cyclic tests to be used depends on availability, or the task at hand, but both can be used equally well. **Figure 5.10** illustrates the key role of N_o that con-

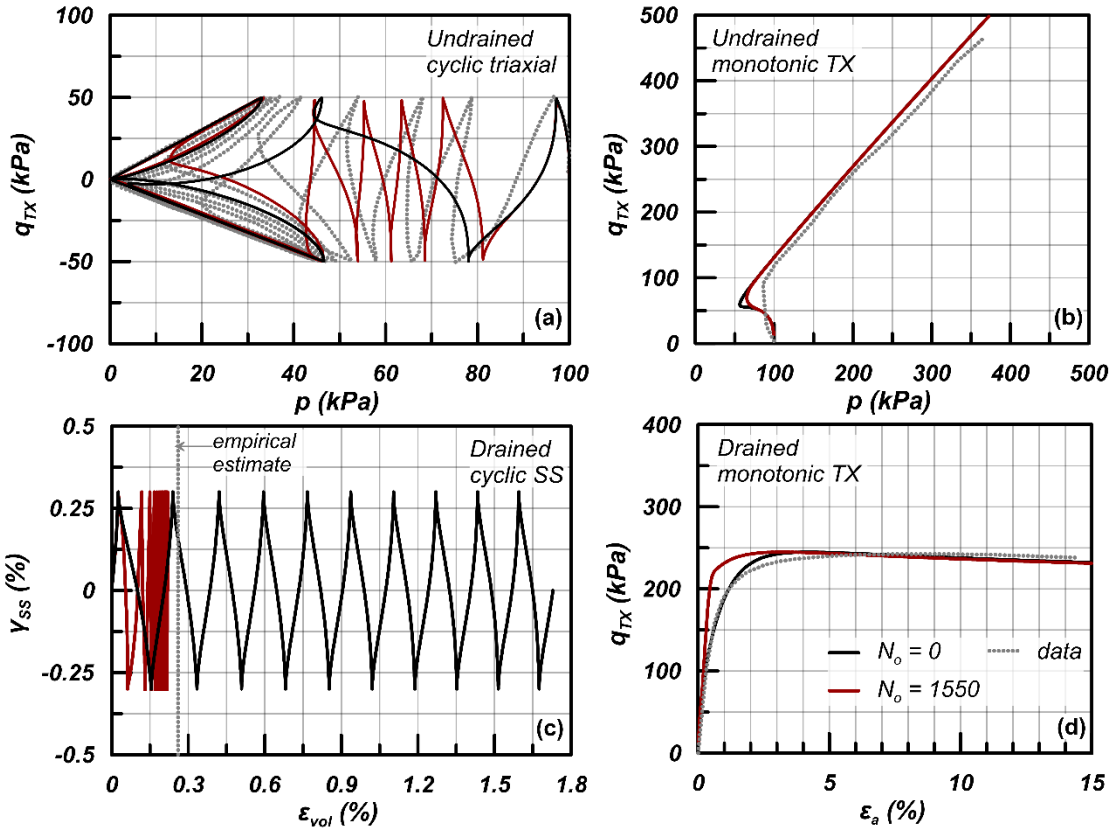

Figure 5.10: *Effect of fabric evolution function and its scaling parameter N_o on: (a) effective stress path during an undrained cyclic triaxial test; (b) rate of accumulation of volumetric strain during a drained cyclic simple shear test; (c) effective stress path during an undrained monotonic triaxial compression test; (d) stress-strain response during a drained monotonic triaxial compression test.*

trols the intensity of fabric evolution function h_f (Equation (3.31)) in four indicative loading conditions: two under cyclic (subplots **5.10a** and **5.10c**) and two under monotonic conditions (subplots **5.10b** and **5.10d**). In subplot **5.10a**, the effective stress path of a cyclic undrained triaxial test shows how the parameter N_o can be used to adjust the estimated rate of excess pore-pressure buildup and the number of cycles until initial liquefaction is triggered. Model results are compared with an undrained cyclic triaxial test performed by Toyota and Takada (2017) (e = 0.756 - $D_r \approx 60\%$, p_o = 98.1 kPa). In the same way, in subplot **5.10c** the effect of N_o on the rate of accumulation of volumetric strains during a drained cyclic simple shear test - with the same initial conditions as the undrained one - is explored. For this type of loading, experimental data for Toyoura sand are not available, but at least the accumulation of volumetric strains is validated against the empirical realtionship of Duku et al. (2008).

Moreover, subplots **5.10b** and **5.10d** compare model results to monotonic triaxial compression tests of Verdugo and Ishihara (1996) (subplot **5.10b**: undrained test with e = 0.831 - $D_r \approx 40\%$, p_o = 100 kPa and subplot **5.10d**: drained test with e = 0.833 - $D_r \approx 40\%$, p_o = 100 kPa). These comparisons with monotonic test data show that the fabric evolution function affects marginally the monotonic response, but is crucial for a satisfactory cyclic loading estimate.

D. Parameter related to post-liquefaction shear strain accumulation

The last model parameter L_o requiring calibration is linked to the post-liquefaction shear strain accumulation and is quantified also by a trial-and-error procedure. It controls the intensity of the decrease of dilation after initial liquefaction occurs, and thus the rate of strain accumulation (Equations (3.41) and (3.44) - (3.48)). Note that it has no effect on the pre-liquefaction phase and this is why it can be calibrated last. Supplementarily to **Figure 3.9**, **Figure 5.11** depicts the effect of L_o on post-liquefaction shear strain accumulation through sensitivity analyses for the indicative cases of L_o = 0 (shear strain accumulation locking) (subplot **5.11b**), L_o = 2500 - (calibrated value) (subplot **5.11c**) and L_o = 5000 (subplot **5.11d**). Model results are compared with an undrained cyclic torsional shear test performed by Zhang (1997) ($D_r \approx 70\%$, p_o = 100 kPa). The calibration of L_o requires good quality cyclic undrained tests reaching well beyond initial liquefaction, thus allowing the

estimation of the rate of strain accumulation thereafter. In absence of specific experimental data, the semi-empirical framework of post-liquefaction shear deformation accumulation in sands, recently proposed by Tasiopoulou et al. (2020), can prove a very useful tool for this purpose.

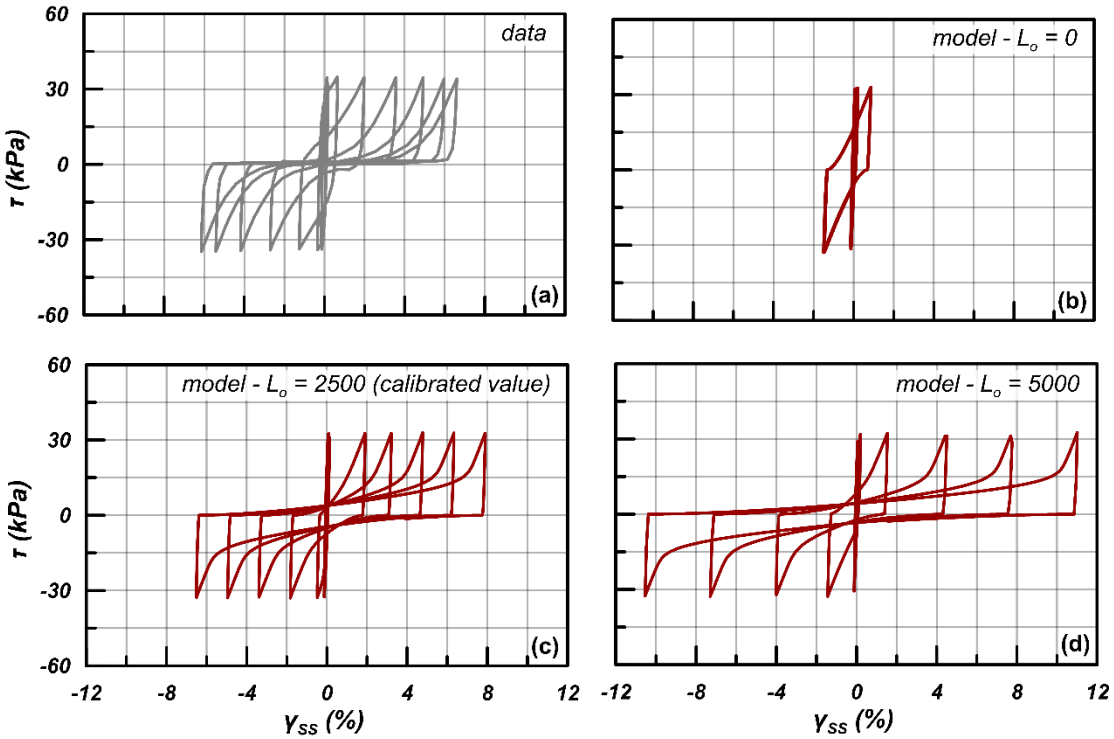

***Figure 5.11**: Sensitivity of post-liquefaction shear strain accumulation to value of model parameter L_o: (a) Data after Toyota and Takada (2017), (b) model estimate for L_o = 0, (c) L_o = 2500 - (calibrated value) and (c) L_o = 5000.*

5.2 Model Verification

In this Section, the performance of the new model is verified through element level comparisons between simulations and experimental data on Toyoura sand, i.e., a fine subangular-to-angular silica sand with $D_{50} \approx 0.16$ mm, for which a large amount of experimental data can be found in the literature. Its gradation curve, according to Ishihara and Watanabe (1976) is presented in **Figure 5.12**, although some small variations of this gradation curve have appeared in the literature. The most commonly referenced values for e_{min} and e_{max} are 0.597 and 0.970 respectively, but as a significant variation occurs in the literature, in the following it will be clarified if they are considered different, according to the specific data and information at hand.

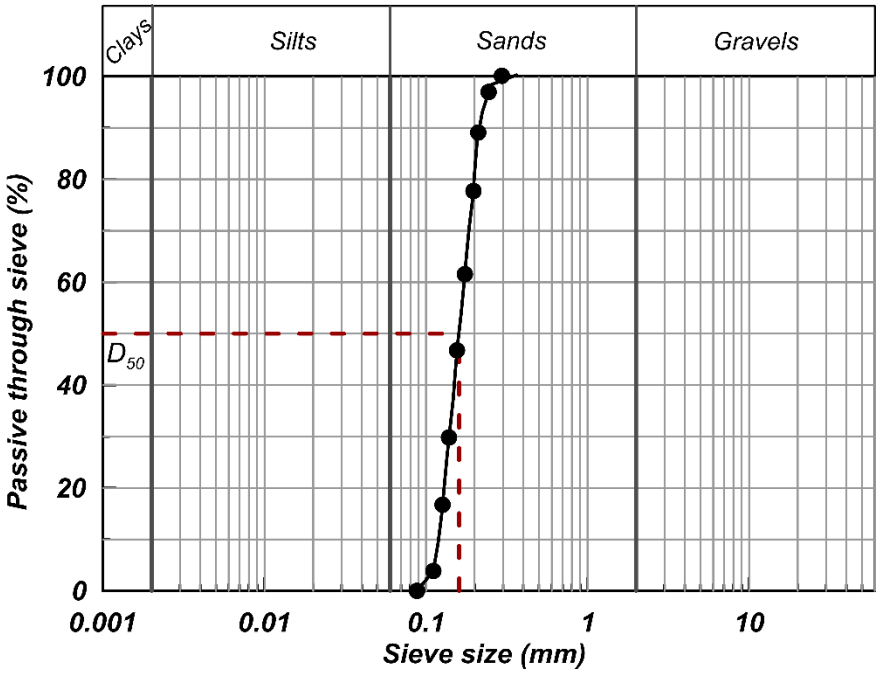

Figure 5.12: *Gradation curve of Toyoura sand. Data after Ishihara and Watanabe (1976).*

The values of all 14 model parameters for Toyoura sand, as they were estimated according to the calibration procedure described in detail above, are presented in **Table 5.2**. The validation includes simulations of both monotonic and cyclic shearing tests on Toyoura sand, that were performed with these values of model parameters. In order to present a thorough evaluation of model performance that addresses all important aspects of monotonic and cyclic response, wherever sand-specific data are lacking, the model performance is validated against empirical relations from the literature, especially for cyclic loading. All the information regarding the characteristics of the element tests employed for Toyoura sand is summarized in **Tables A1** and **A2** in the **Appendix**.

5.2.1 Drained and undrained monotonic loading

The new model is used to simulate drained triaxial compression tests (TC) on Toyoura sand, performed by Verdugo and Ishihara (1996) on isotropically consolidated samples prepared using the moisture placement or wet tamping method. **Figure 5.13** compares numerical simulations to experimental data in the (triaxial) deviatoric stress $q_{TX} = \sigma_a - \sigma_r$ versus axial strain, ε_a (subplots **5.13a** and **5.13c**) and ε_a (equal to ε_1 for TC) versus volumetric strain, ε_{vol} (subplots **5.13b** and **5.13d**) spaces. Subscripts a and r denote the axial and radial directions of the triaxial sample, respectively. Subplots **5.13a** and **5.13b** pertain to

tests with p_o = 100 kPa, while subplots **5.13c** and **5.13d** to tests with p_o = 500 kPa, with p_o denoting the initial mean effective stress of the sample. The model simulates quite accurately the three distinct behaviors of the sand, as they emerge from the tests based on the initial value of void ratio, e_o, of the samples after consolidation. More specifically, stress - strain response and volumetric strain are properly estimated both in the cases of the dilative response of the medium dense (e_o = 0.810 - 0.830, with D_r = 38% - 43%) and the slightly (e_o = 0.886 - 0.917, with D_r = 23% - 14%) or intensively (e_o = 0.960 -0.996, with D_r < 3%) contractive specimens, for both stress levels.

Table 5.2: *Values of model parameters for Toyoura sand.*

Constitutive part	Parameter	Values
		Toyoura sand
Elasticity	G_o	650
	ν	0.15
CSL	e_{ref}	0.934
	λ	0.019
	ξ	0.70
	M_c^c	1.25
	c	0.712
Plastic modulus	n^b	1.1
	h_o	60
	c_h	12
Dilatancy	n^d	2.0
	A_o	1.5
Fabric	N_o	1550
Post-liquefaction	L_o	2500

In the sequel, the model performance is evaluated against the drained torsional shear tests (TS) of Pradhan et al. (1988). These torsional shear tests were performed after K_o - consolidation of the samples to an initial axial stress $\sigma_{a,o}$, and then, shear deformation is applied producing shear stress τ in the torsional shear apparatus, while retaining the effective axial stress constant ($\sigma_a = \sigma_{a,o}$). At the same time, radial and circumferential strain increments were kept equal to zero throughout the test, ensuring simple shear loading conditions. Three different combinations of initial axial stress $\sigma_{a,o}$ and initial void ratios e_o are presented. In **Figure 5.14**, the comparison of data to simulations is presented in terms

of the stress ratio τ/σ_a versus shear strain $\gamma = \varepsilon_1 - \varepsilon_3$ (subplot **5.14a**) and ε_{vol} versus γ (subplot **5.14b**), where subscripts 1 and 3 denote the maximum and minimum principal values of the tensor, irrespective of its direction. The overall response is simulated with fair accuracy, besides the slight stiffer stress-strain response, mainly for the very dense sample with e_o = 0.674 (D_r = 81%).

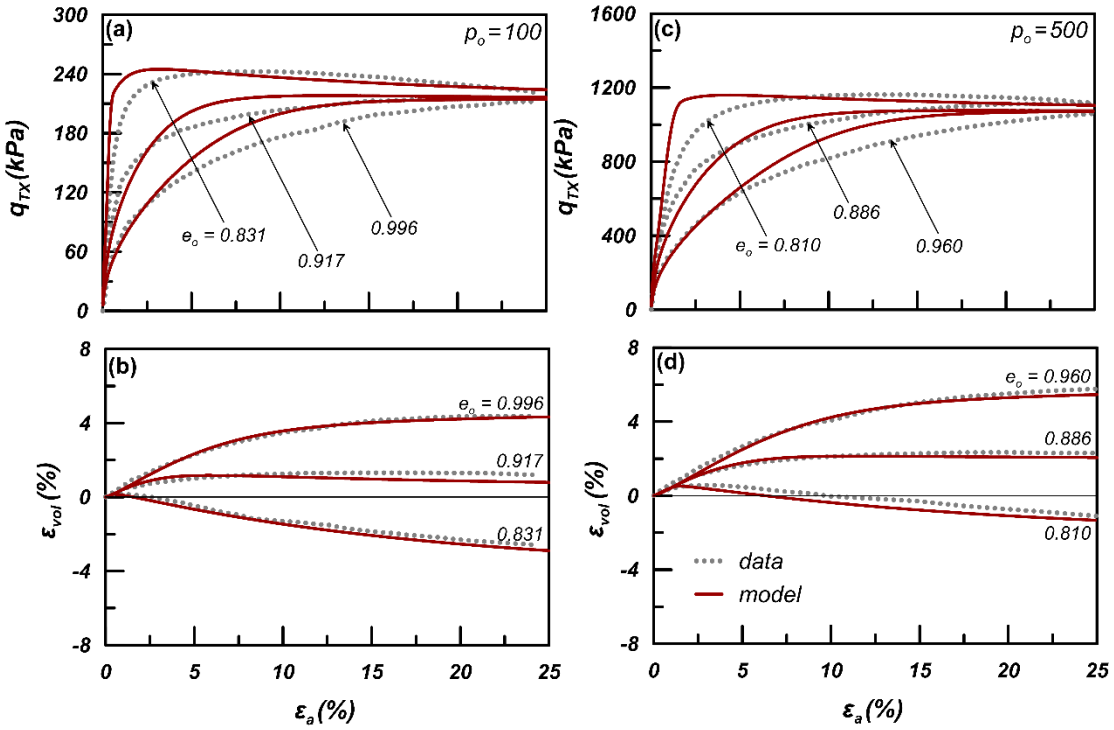

Figure 5.13: *Experimental results and model estimates of drained monotonic triaxial compression tests. Data on Toyoura sand after Verdugo and Ishihara (1996).*

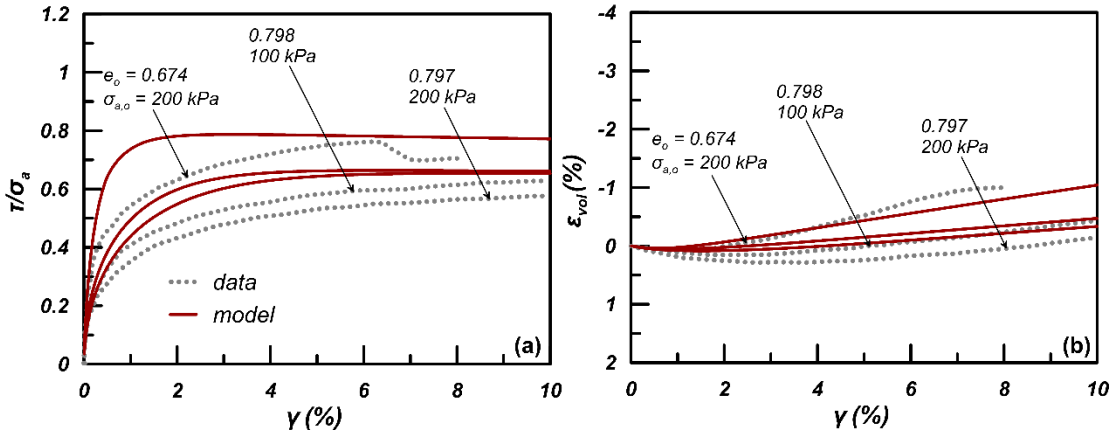

Figure 5.14: *Experimental results and model estimates of drained monotonic torsional shear tests. Data on Toyoura sand after Pradhan et al. (1988).*

Subsequently, in **Figure 5.15**, the model is evaluated against the undrained TC tests of Verdugo and Ishihara (1996). The comparison of data versus simulations is shown in the spaces of q_{TX} versus p (subplots **5.15a** and **5.15c**) and q_{TX} versus ε_a (subplots **5.15b** and **5.15d**). The simulations concern two relative densities (e = 0.735 and 0.833, with D_r = 63% - 37%) and a great range of initial mean effective stresses, from p_o = 100 kPa to the extremely high value of p_o = 2000 kPa. Hence, the versatility of the model to estimate both contractive or dilative response for this wide range of initial conditions, depending on the combination of e - p_o, is depicted.

Then, **Figure 5.16** compares experimental data to numerical simulations for undrained simple shear tests (SS), performed by Yoshimine et al. (1998), on isotropically consolidated samples of Toyoura sand. The initial mean effective stress p_o has a common value of 100 kPa for all samples, and the examined relative densities cover a range between loose and medium dense conditions (e = 0.804 – 0.888, with D_r = 22% - 45%). In all cases, the comparison is made in terms of effective stress paths $q = \sigma_1 - \sigma_3$ versus p (subplot **5.16a**) and stress-strain relations q vs γ (subplot **5.16b**). The simulations are fair for the most dilative of the examined densities and show a gradually increasing contractive response as the void ratio e increases. However, an underestimation of the effect of void ratio e may be observed, as well as an inability to estimate the intense contraction presented by the data for the looser states. It is underlined here that this is not necessarily a limitation of the model, but of the selected calibration, whose emphasis is to provide satisfactory simulations for a huge range of void ratio values of Toyoura sand, from e = 0.674 (D_r = 81% in **Figure 5.14**) to e = 0.994 (D_r < 0% in **Figure 5.13**).

5.2.2 Undrained cyclic loading

With the same set of model parameters, as listed in **Table 5.2** and used for the simulations of the monotonic drained and undrained tests of the previous Section, undrained cyclic loading tests are simulated here. **Figure 5.17** shows the model capability in simulating an undrained cyclic torsional shear test conducted by Zhang (1997) on Toyoura sand and presented by Zhang and Wang (2012). It was isotropically consolidated at p_o = 100 kPa and a relative density D_r = 70%, which according to the given values of e_{max} = 0.973 and e_{min} = 0.635 corresponds to a void ratio e equal to 0.736. The single amplitude of the cyclically

applied shear stress for this test is τ_{cyc} = 33 kPa. The comparison is made in the spaces of shear stress τ versus mean effective stress p (subplots **5.17a** and **5.17c**) and τ vs shear strainγ_{SS} (subplots **5.17b** and **5.17d**), where γ_{SS} is the directly measured shear strain during a torsional shear test. The comparison is quite satisfactory as the model successfully

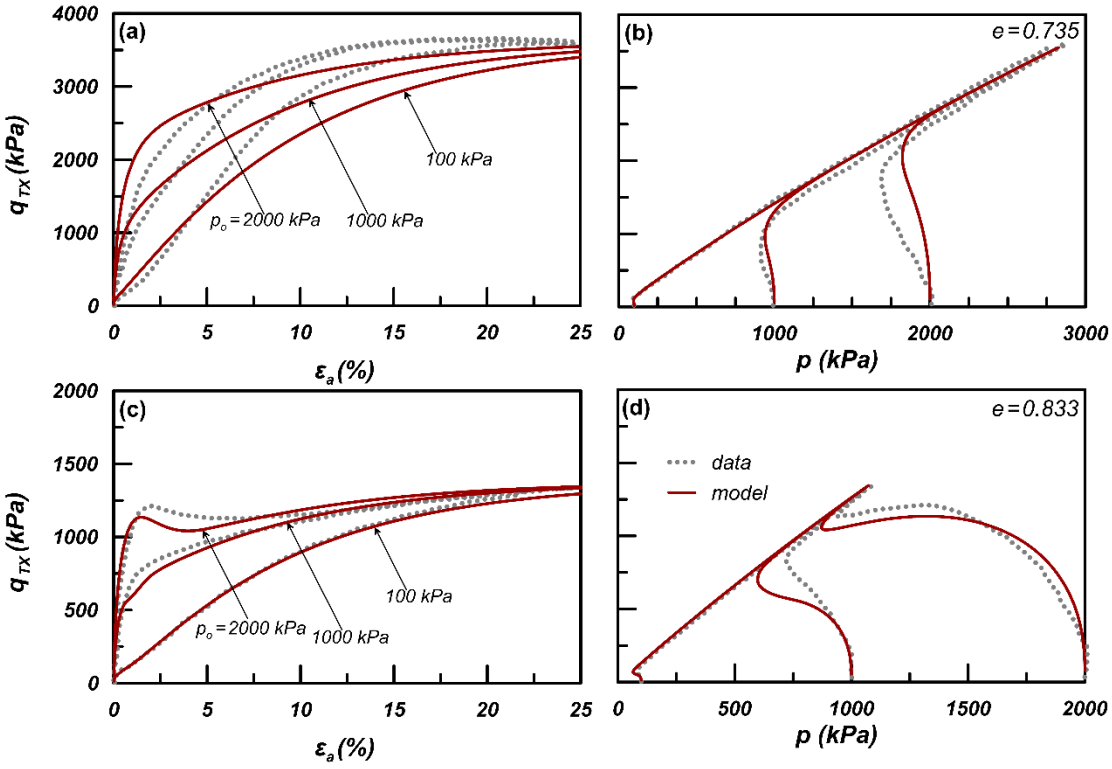

***Figure 5.15**: Experimental results and model estimates of undrained monotonic triaxial compression tests. Data on Toyoura sand after Verdugo and Ishihara (1996).*

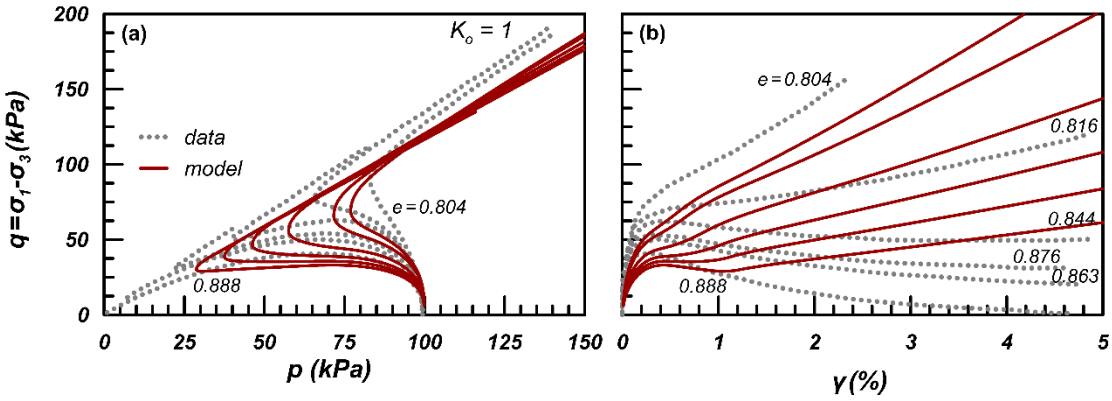

***Figure 5.16:** Experimental results and model estimates of undrained monotonic simple shear tests (K_o = 1). Data on Toyoura sand after Yoshimine et al. (1998).*

captures the cyclic mobility between loading-unloading paths and illustrates "butterfly-shaped" stress-strain (τ versus γ_{SS}) loops when approaching p = 0 (initial liquefaction). Moreover, shear strain continuously increases during the cyclic shearing after liquefaction triggering in good agreement with the experimental data.

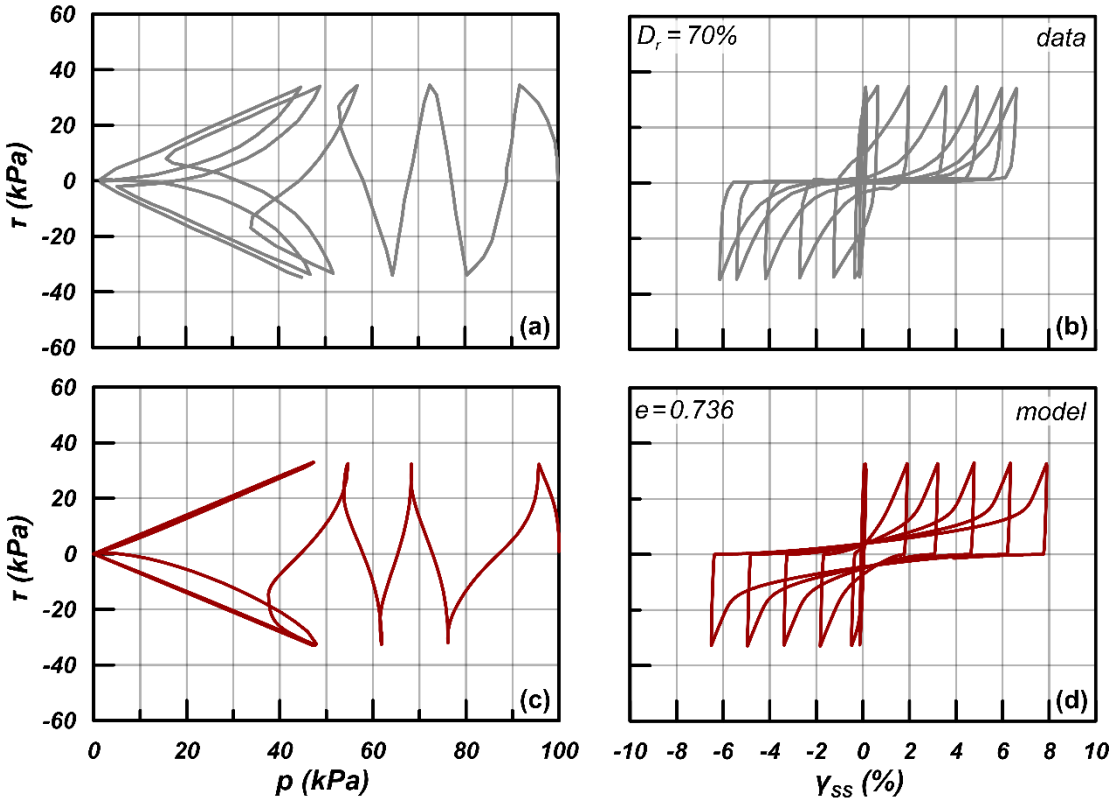

***Figure 5.17**: Experimental results and model estimates of undrained cyclic torsional shear test. Data on Toyoura sand after Zhang (1997).*

Then, in **Figure 5.18** the simulation of an undrained cyclic triaxial test performed on Toyoura sand by Toyota and Takada (2017) is presented. Here, the sample was isotropically consolidated at an initial mean effective pressure p_o = 100 kPa and a relative density D_r = 60% which, according to the given values of e_{max} = 0.990 and e_{min} = 0.597, corresponds to a void ratio e = 0.754. The single amplitude of the cyclically applied triaxial deviatoric stress $q_{TX,cyc}$ equals to 50 kPa. The model response is in good agreement with the experimental curves and fully captures the decrease of mean effective stress, as a result of excess pore pressure buildup, at the phase before initial liquefaction. Moreover, at the phase after initial liquefaction the expected accumulation of axial strain is acceptable, although the model shows small bias in strain accumulation in the stress-strain relation (q_{TX}

versus ε_a) towards the extension side. This is attributed to the different shear strengths in triaxial compression and extension, which lead to different strain accumulation rates. This bias is a common shortcoming of constitutive models aiming at liquefaction response and has been reduced, yet not alleviated, due to the introduction of the post-liquefaction constitutive ingredient $h_{\text{post-liq}}$ of Equation (3.44). Note here that this bias is not evidenced in cyclic loading in simple shear or torsional shear (e.g., in **Figure 5.17**) where the Lode angle θ change within a loading cyclic is very small in comparison to the "*jump*" between $\theta = 0^o$ and $\theta = 60^o$ in cyclic triaxial loadings. This is why any model aiming at successful liquefaction estimates should always be verified in both triaxial and simple shear or torsional cyclic loading.

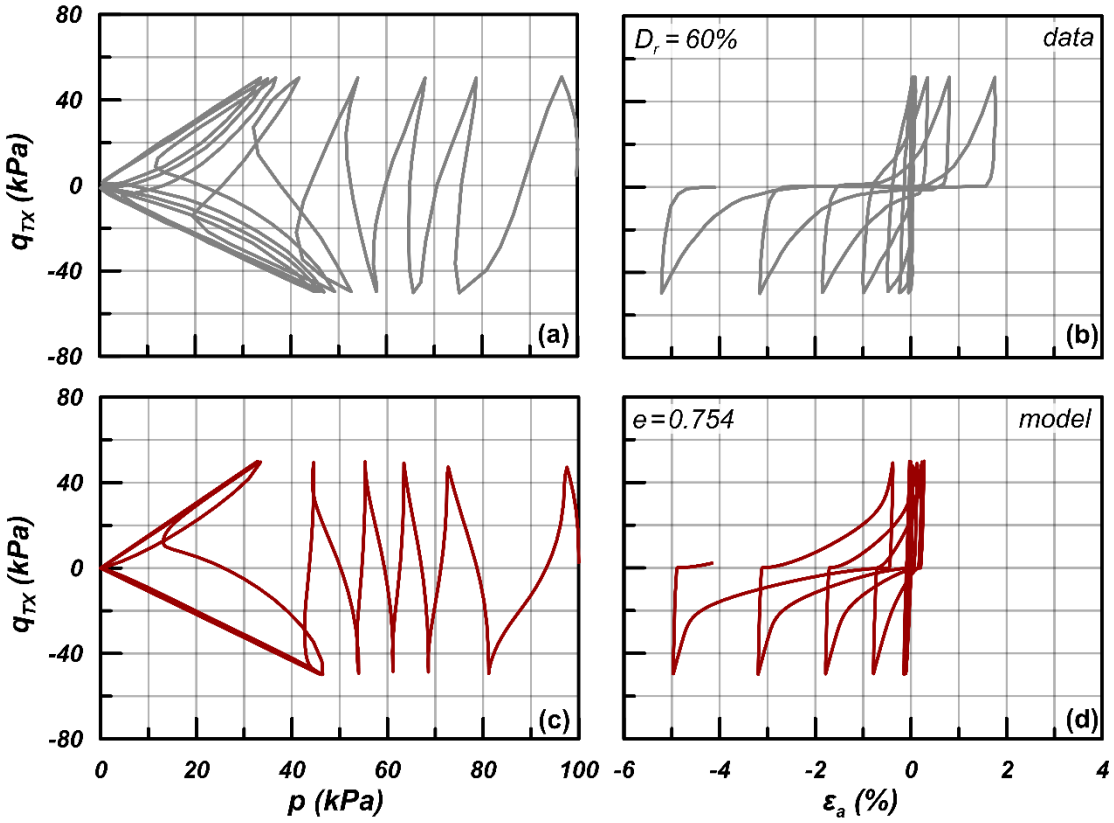

***Figure 5.18**: Experimental results and model estimates of undrained cyclic triaxial test. Data on Toyoura sand after (Toyota and Takada (2017).*

A. Liquefaction resistance curves for different relative densities

Liquefaction resistance curves is a practical tool for assessing the simulation success for undrained cyclic loading, since it provides a grouping of many element tests for different

cyclic stress ratio amplitudes, relative densities and stress levels, and even different loading conditions. Toyoura sand is one of the most widely used sands for the study of liquefaction, so there is a plethora of experimental liquefaction resistance curves published by different researchers worldwide. Given the use of different Toyoura sand batches, there is significant scatter in the pertinent data, even when pertaining to the same values of relative density, initial stress level, as well as the same preparation method or loading type. Hence, it was deemed fairer to evaluate the model's accuracy in estimating liquefaction resistance through comparison with a group of liquefaction resistance curves of Toyoura sand from the literature (Ishihara and Tsukamoto, 2004; Lombardi et al., 2014; Toyota and Takada, 2017; Wang et al., 2014; Yamashita and Toki, 1993) instead of a single set of curves. In this perspective, in **Figure 5.19** a wide range of liquefaction resistance curves from cyclic triaxial tests is presented. The grouping of the experimental data was based on the relative density D_r of the sand, in groups of test data with D_r = 45% (subplot **5.19a**), 60% (subplot **5.19b**) and 75-80% (subplot **5.19c**). Notice that, there is a large deviation between the referenced values of e_{min} (0.597 - 0.635) and e_{max} (0.970 - 0.990) in the employed studies. Since the model requires values of void ratio e and not D_r, their calculation is based on the average values of e_{min} = 0.609 and e_{max} = 0.976 that were estimated on the basis of the employed studies. So, the simulated void ratio for D_r = 45% is 0.811, for D_r = 60% is 0.756 and for D_r = 77.5% (a mean value between 75% and 80%) is 0.691. To reduce the scatter of the literature results, all selected literature resistance curves refer to isotropically consolidated samples at initial mean effective stress p_o = 100 kPa which are prepared with the method of air-pluviation, except for the data of Yamashita and Toki (1993) at D_r = 80%, where the vibration method was used. The comparison is made in terms of cyclic stress ratio $CSR = q_{TX,cyc}/(2p_o)$ versus N_l, the number of cycles required so as the liquefaction criterion to be achieved. Here, the criterion requires a double amplitude axial strain equal to 5% to be developed. Observe that the liquefaction resistance curves procuring from the simulations generally plot within the range of the experimental data, albeit showing a slightly steeper inclination. However, it should be acknowledged that the typical experimental observation of no liquefaction ($N_l \rightarrow \infty$) at small CSR values is well captured by the model, i.e., the model remedies a common shortcoming of liquefaction models (e.g. Andrianopoulos et al., 2010a; Dafalias and Manzari 2004). On the other hand, the model

simulates well the experimentally established increase in liquefaction resistance with relative density.

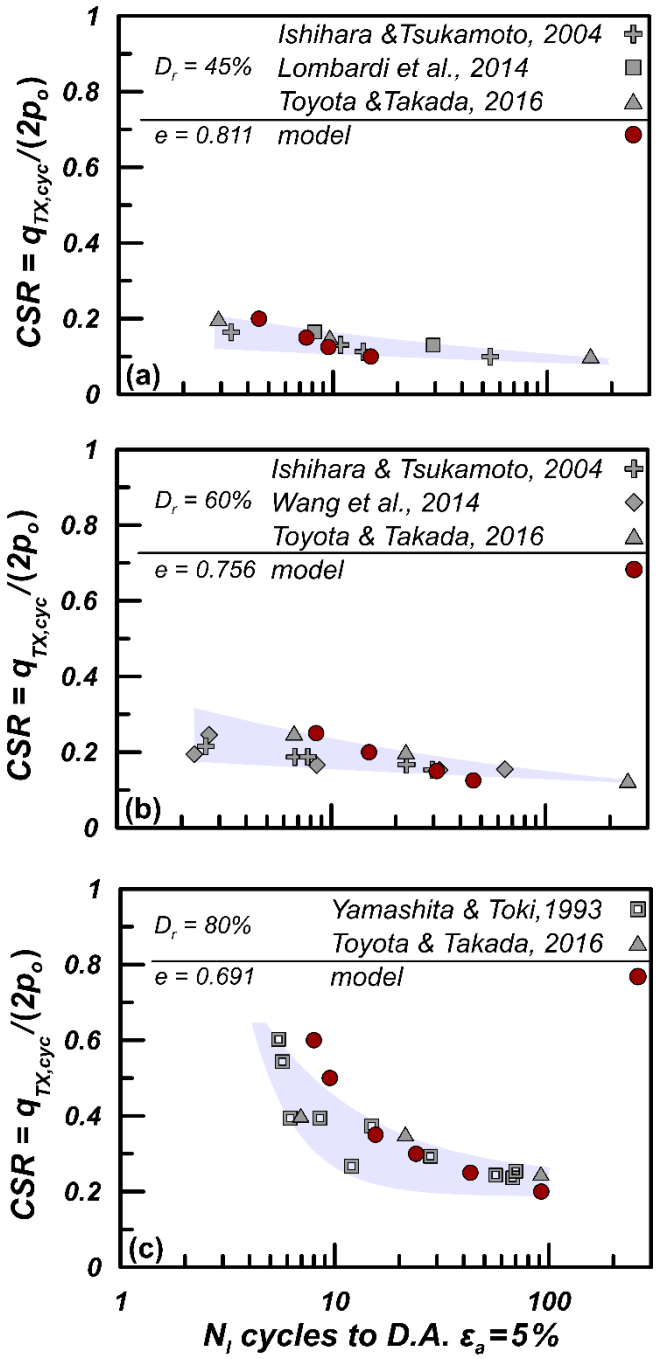

***Figure 5.19**: Experimental results and model estimates of liquefaction resistance curves on the basis of undrained cyclic triaxial tests: (a) D_r = 45%, (b) D_r = 60% and (c) D_r = 80%. Data on Toyoura sand after (Ishihara and Tsukamoto, 2004; Lombardi et al., 2014; Toyota and Takada, 2017; Wang et al., 2014; Yamashita and Toki, 1993).*

B. Effect of confining stress on liquefaction resistance

As already discussed in a previous Section, the effect of overburden stress on cyclic resistance ratio *CRR* is often expressed and quantified in terms of a correction factor, known as K_σ, which is defined as:

$$K_\sigma = \frac{CRR_{\sigma_{a,o}}}{CRR_{\sigma_{a,o}=100\text{kPa}}} \tag{5.4}$$

In order to assess the ability of the model in estimating the K_σ factor, the undrained cyclic triaxial test simulations for Toyoura sand that were presented in **Figure 5.19** and referred to $p_o = \sigma_{a,o} = 100$kPa are now repeated for higher levels of initial mean effective stress, namely $p_o = 200$ kPa and 400 kPa, without changing the void ratio values. By comparing the *CRR* values obtained at 15 uniform loading cycles (in compliance with other studies, e.g., Boulanger and Ziotopoulou, 2013; Cheng and Detournay, 2021) the values of K_σ are thus estimated for different $\sigma_{a,o}$ and D_r values. The same procedure is then followed for estimating K_σ values for undrained cyclic simple shear tests of Toyoura sand, for the same initial states ($\sigma_{a,o}$ and e). These values are compared to the well-established empirical curves of Idriss and Boulanger (2008) and Hynes and Olsen (1999) in **Figure 5.20**, According to Idriss and Boulanger (2008):

$$K_\sigma = 1 - C_\sigma \ln\left(\frac{\sigma_{a,o}}{p_{atm}}\right) \leq 1.1 \tag{5.5}$$

$$C_\sigma = \frac{1}{18.9 - 17.3 D_r} \leq 0.3 \tag{5.6}$$

while according to Hynes and Olsen (1999):

$$K_\sigma = \left(\frac{\sigma_{a,o}}{p_{atm}}\right)^{-(1-f)} \leq 1.0 \tag{5.7}$$

with f values suggested by Youd et al. (2001) as:

$$f = 1 - \frac{D_r}{2}, 0.6 \le f \le 0.8 \tag{5.8}$$

The comparison is in good agreement with the literature and especially with the empirical relationship of Idriss and Boulanger (2008). The model estimates accurately that liquefaction resistance decreases with increasing confining stresses and that the rate of decrease is nonlinear. Moreover, the model also estimates that the cyclic strengths for dense sands are comparatively more affected by confining stress than what is observed for loose sands.

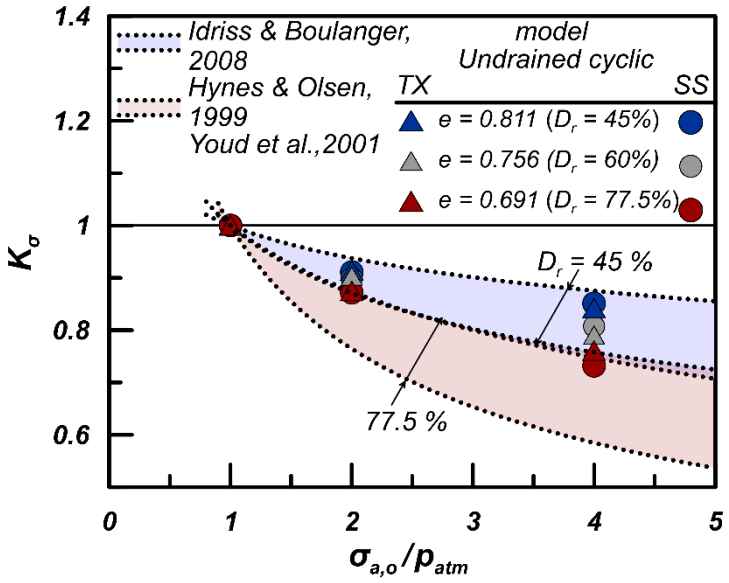

Figure 5.20: *Comparison of K_σ values for different loading types and different relative density D_r values estimated by the model for Toyoura sand versus the empirical relation of Idriss and Boulanger (2008) and Hynes and Olsen (1999).*

5.2.3 Drained cyclic loading

A. Shear modulus degradation and damping ratio increase curves

Figure 5.21 shows the normalized secant shear modulus G/G_{max} degradation curves (subplot **5.21a**) and the damping ratio ξ increase curves (subplot **5.21b**) derived from simulations of strain-controlled cyclic simple shear loading. The horizontal axis of both diagrams $\gamma_{SS,cyc}$ depicts the single amplitude cyclic shear strain of the performed numerical simulations, which covers a range from 0.0001% to 1%. The secant shear modulus G and

the corresponding damping ratio ξ refer to the 1st cycle of loading, while the initial void ratio e_o is selected to correspond to an initial D_r almost equal to 60% for Toyoura sand (e = 0.756). Two extreme levels of initial effective axial stress $\sigma_{a,o}$ are examined, namely 100 and 1000 kPa. In terms of shear modulus degradation, the results estimated by the model are consistent with the empirical relation proposed by Darendeli (2001), while they exhibit a less pronounced non-linearity with respect to the Vucetic and Dobry (1991) curve. Moreover, the simulated G/G_{max} reduction shows a dependency on stress level consistent with the empirical correlations. In terms of damping ratio ξ, the results of the new model up to the strain level of 0.1% are compared satisfactorily with the empirical relations. However, for larger strain levels, there is an overestimation of ξ values, especially at the lower stress level. As explained by Taborda et al. (2014), this is a well-known problem of constitutive models that comply with original Masing rules (Masing, 1926), and this model is no exception. At least, significant overestimation appears only for very large cyclic shear strains that are not very common in boundary value problems of practice, and only for low vertical stresses (e.g., in free-field conditions, or under light structures). It should be underlined here that evaluating model accuracy in terms of G/G_{max} versus $\gamma_{SS,cyc}$ curves makes sense, only if the G_{max} value is accurately estimated. In the proposed model, the G_{max} is calibrated directly on the basis of small strain measurements (e.g., see **Figure 5.3** for Toyoura sand) and thus satisfies this requirement, but this is unfortunately rarely the case in papers presenting constitutive models in the literature, where the G_{max} is seldom validated, thus undermining the reliability of the G/G_{max} versus $\gamma_{SS,cyc}$ relation.

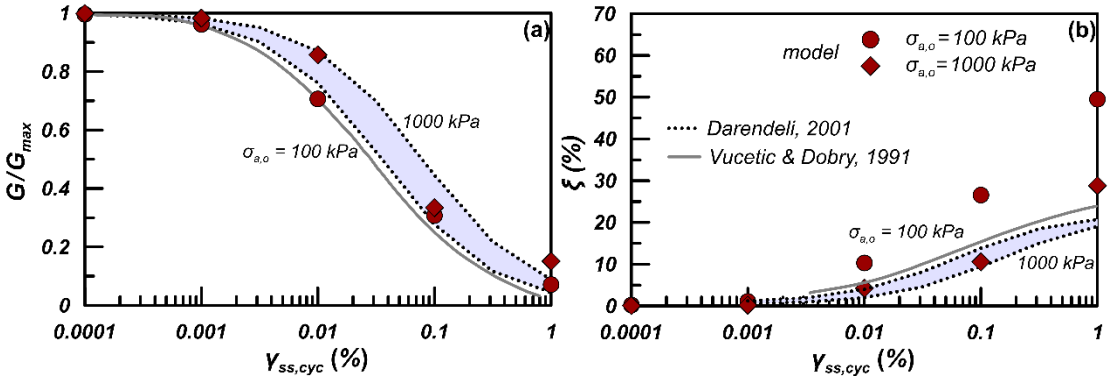

Figure 5.21: *Comparison of shear modulus degradation curves and damping ratio increase curves estimated by the model for Toyoura sand versus the empirical relations of Darendeli (2001) and Vucetic and Dobry (1991).*

B. Accumulation of strains with cycles

Figure 5.22 presents a summary of estimated values of accumulated volumetric strains ε_{vol} after 10 cycles of strain controlled drained simple shear loading, at various levels of single amplitude cyclic shear strains $\gamma_{SS,cyc}$ ranging from 0.01% to 0.5% The initial relative densities of 40% and 80%, which correspond to initial void ratios of e_o = 0.829 and e_o = 0.683, for Toyoura sand, are examined. The samples are consolidated at an initial effective axial stress $\sigma_{a,o}$ = 100 kPa. The estimated values are compared with the empirical relations of Duku et al. (2008), according to which:

$$\varepsilon_{vol}\left(N_d\right) = C_N \varepsilon_{vol}\left(15\right) \tag{5.9}$$

with:

$$C_N = R\ln\left(N_d\right) + 1 - R\ln\left(15\right) \tag{5.10}$$

$$\varepsilon_{vol}\left(15\right) = a\left(\gamma_{SS,cyc} - \gamma_{tv}\right)^b \tag{5.11}$$

where N_d stands for the applied number of cycles, $\varepsilon_{vol}(15)$ is the ε_{vol} at the end of 15th cycle, R is a parameter related to D_r with a median value equal to 0.3 adopted herein and γ_{tv} the volumetric strain threshold ranging between 0.01-0.03% - the value of 0.01% was selected here. Parameters a and b were estimated by the authors from experimental data for each examined sand and after statistical analysis, Duku et al. (2008) proposed a constant value for b equal to 1.2, while a is given as per:

$$a = 5.38\exp\left(-0.023D_r\right) \tag{5.12}$$

Supplementarily to the semi-empirical methodology described above, experimental data of Silver and Seed (1971) were also used for validation. The data refer to simple shear tests conducted on samples of Crystal silica sand of relative density ranging between 40% to 80%, consolidated at a vertical stress between 25 kPa to 100 kPa. As in the study of Silver and Seed (1971) semi-empirical relationships, correlating shear strain amplitude and induced volumetric strains, were not proposed, their experimental results for the stress level

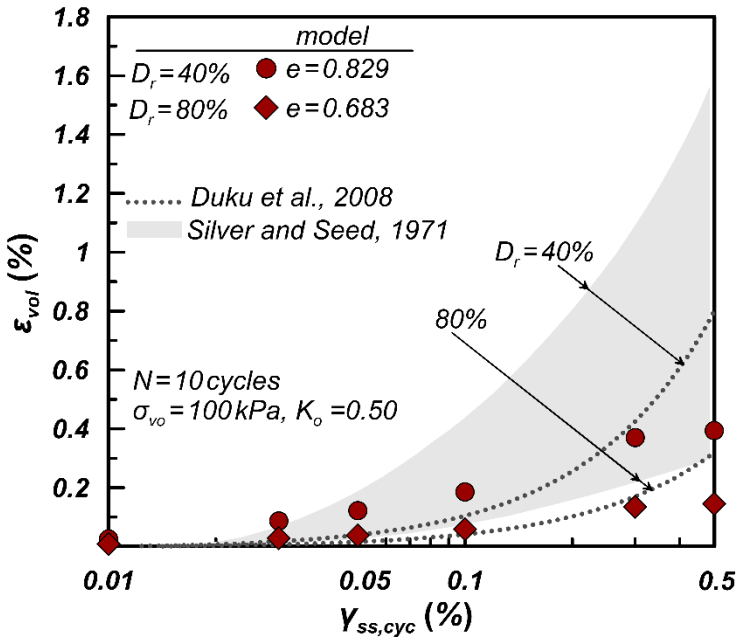

Figure 5.22: *Comparison of accumulated volumetric strains from drained cyclic simple shear tests estimated by the model for Toyoura sand versus the empirical relations of Duku et al. (2008) and the range of experimental data of Silver and Seed (1971).*

of 100 kPa, after 10 applied cycles are presented here as a shade covering the range of relative densities mentioned above. The lower bound of the shading refers to the density of 80%, while the upper bound refers to the density of 40%. It is observed that, on the whole, the comparison is acceptable. Specifically, at small and intermediate $\gamma_{SS,cyc}$ strain levels, the estimated volumetric strains by the model are closer to the range of experimental data of Silver and Seed (1971), while at larger $\gamma_{SS,cyc}$ strain levels, the accumulation of volumetric strains is in accordance to the empirical relations of Duku et al. (2008). Moreover, the qualitative dependency of accumulated volumetric strains on relative density D_r is reasonably consistent with the empirical data. Finally, note that the form given to the dilatancy function in contraction, as well as the inclusion of the enhanced formulation for addressing the overshooting problem reduces significantly strain accumulation at very small $\gamma_{SS,cyc}$ strains. As such, the ε_{vol} accumulated in cyclic shearing with $\gamma_{SS,cyc}$ lower than a volumetric strain threshold γ_{tv} (e.g., smaller than 0.01% on average for sands) is insignificant.

Figure 5.23 presents a summary comparison of accumulated volumetric strains ε_{vol} (subplot **5.23a**) and accumulated shear strains $\gamma_{TX} = \varepsilon_a - \varepsilon_r$ (subplot **5.23b**) in cyclic drained

triaxial tests as estimated by the new model versus the pertinent values from the empirical relations of Bouckovalas et al. (1984) and Stamatopoulos et al. (1991), according to which:

$$\varepsilon_{\mathrm{vol}}\left(N_{\mathrm{d}}\right)=\varepsilon_{\mathrm{vol}}\left(1\right)N_{\mathrm{d}}{}^{0.40} \tag{5.13}$$

$$\gamma_{\mathrm{TX}}\left(N_{\mathrm{d}}\right)=\gamma_{\mathrm{TX}}\left(1\right)N_{\mathrm{d}}{}^{0.40} \tag{5.14}$$

where:

$$\varepsilon_{\mathrm{vol}}\left(1\right)=0.00685\left[1-\left(\frac{\left(q_{\mathrm{TX}}/p\right)}{M_{\mathrm{c}}^{\mathrm{d}}}\right)^{11}\right]\gamma_{TX,c}{}^{1.26} \tag{5.15}$$

$$\gamma_{\mathrm{TX}}\left(1\right)=0.0349\left(\frac{q_{\mathrm{TX}}}{p}\right)^{2}\gamma_{\mathrm{TX},c}{}^{1.26} \tag{5.16}$$

where N_{d} stands for the applied number of cycles, $\varepsilon_{\mathrm{vol}}(1)$ and $\gamma_{\mathrm{TX}}(1)$ are the $\varepsilon_{\mathrm{vol}}$ and γ_{TX} at the end of 1st cycle, $\gamma_{\mathrm{TX,c}}$ is the double amplitude shear strain as a percentage (%) and $M_{\mathrm{c}}^{\mathrm{d}}$ the position of dilatancy surface on the stress-ratio space.

Strain accumulation is measured after N_{d} = 1, 30, 100 and 300 cycles, which means that the model is hereby verified for boundary value problems that include many more cycles than what earthquakes produce. Specifically, the initial relative densities of D_{r} = 40%, 60% and 80%, with initial void rations e_{o} = 0.829, 0.756 and 0.683 are examined. All simulated tests were anisotropically consolidated at a mean effective stress p_{o} = 200 kPa, with an appropriate combination of initial axial and radial stresses, so as initial stress ratios $q_{\mathrm{TX,o}}/p_{\mathrm{o}}$ = 0.35 and 0.75 to be attained after consolidation. The anisotropic consolidation permits, in addition to accumulation of volumetric strain $\varepsilon_{\mathrm{vol}}$ with cycles (e.g., see **Figure 5.22**), to also study the concurrent accumulation of shear strains γ_{TX}. Moreover, depending on the applied deviatoric stress increment $q_{\mathrm{TX,cyc}}$, the simulations corresponded to both one-way (when q_{TX} remains non-negative) and two-way cyclic tests (when q_{TX} alternates between positive and negative values). Hence, in both subplots of **Figure 5.23** different symbols depict the different number of cycles, while the solid diagonal line is the locus of points of perfect agreement between estimates by the model and estimates by the empirical relations. Similarly, the two dashed lines define the loci of overestimation and underestimation by the denoted factor. In terms of accumulated volumetric strains $\varepsilon_{\mathrm{vol}}$

(subplot **5.23a**), a quite good overall agreement is observed, as the ratio of numerical over empirical values ranges between 0.5 to 2.0. On the other hand, in terms of accumulated shear strains γ_{TX} (subplot **5.23b**), the comparison is less impressive, but remains satisfactory.

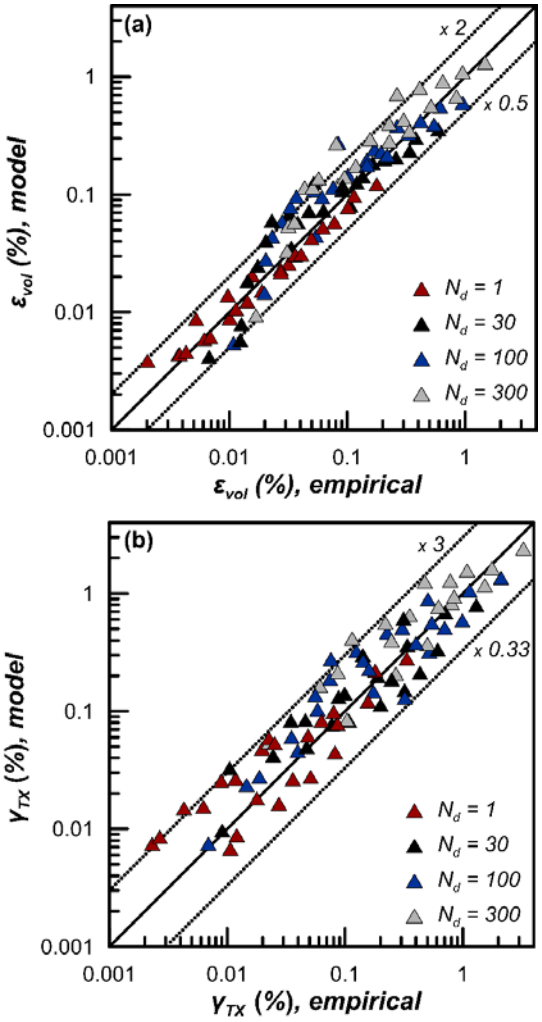

Figure 5.23: *Comparison of accumulated volumetric strains and shear strains from drained cyclic triaxial tests estimated by the model for Toyoura sand and by the empirical relations of Bouckovalas et al. (1984) and Stamatopoulos et al. (1991).*

5.3 Model Verification for Ottawa-F65 sand

In this Section, the performance of the new model is verified through element level comparisons between simulations and experimental data on Ottawa F-65 sand. Ottawa F-65 sand is a fine subrounded-to-subangular silica sand with $D_{50} \approx 0.20$ mm and is the mainly used sand in LEAP Project (El Ghoraiby et al. 2017, 2018; Vasko et al. 2018). Its gradation curve according to El Ghoraiby et al. (2017, 2018) is presented in **Figure 5.24**. All the information regarding the characteristics of the element tests employed for Ottawa-F65 sand is summarized in **Tables A3** and **A4** in the **Appendix**.

A range of e_{max} and e_{min} values have previously been reported for Ottawa F-65 sand. In the following, if there is no specific information about the exact void ratio of a test, the e_{min} and e_{max} values reported and measured by Vasko (2015) will be used. These values are equal to $e_{min} = 0.492$ and $e_{max}=0.739$.

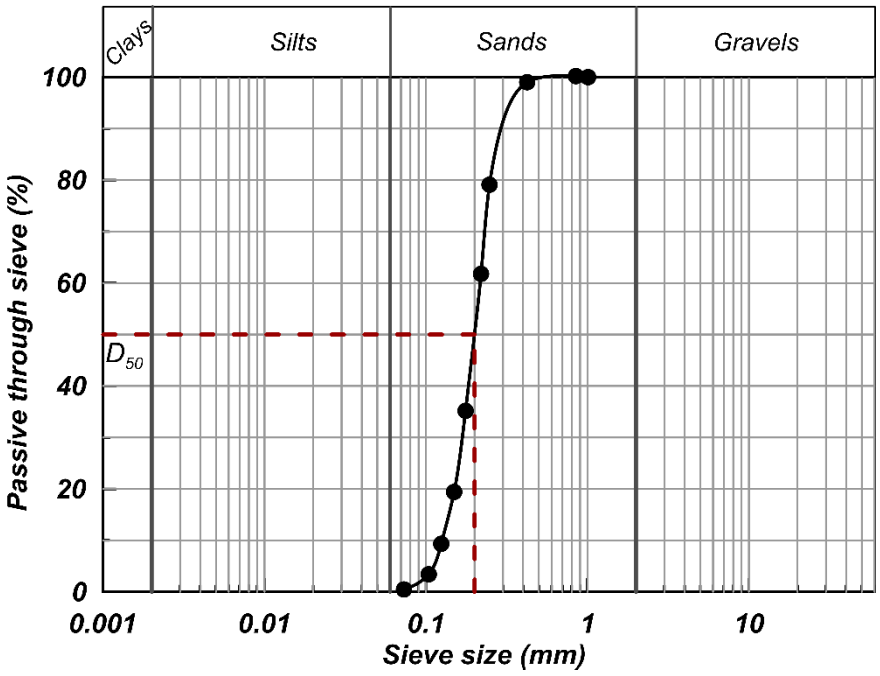

Figure 5.24: *Gradation curve of Ottawa sand. Data after El Ghoraiby et al. (2017, 2018).*

The values of all 14 model parameters for Ottawa F-65 sand, as they were estimated according to the calibration procedure described in detail in **Section 5.1**, are presented in **Table 5.3**. The validation includes simulations of both monotonic and cyclic shearing tests on Ottawa F-65 sand, that were performed with the foregoing values of model parameters.

The presentation is structured like for Toyoura sand. In order to present a thorough evaluation of model performance that addresses all important aspects of monotonic and cyclic response, wherever sand-specific data are lacking, the model performance is validated against empirical relations from the literature, especially for cyclic loading.

Table 5.3: *Values of model parameters for Ottawa F-65 sand.*

Constitutive part	Parameter	Values
		Ottawa F-65 sand
Elasticity	G_o	400
	ν	0.15
CSL	e_{ref}	0.81
	λ	0.02
	ξ	0.75
	M_c^c	1.38
	c	0.74
Plastic modulus	n^b	0.7
	h_o	29
	c_h	8
Dilatancy	n^d	2.0
	A_o	2.4
Fabric	N_o	600
Post-liquefaction	L_o	5000

5.3.1 Drained monotonic loading

Figure 5.25 shows model's performance for drained TC tests on Ottawa F-65 sand conducted by Vasko (2015) and Vasko et al. (2018) for medium dense (e_o = 0.604, D_r = 55%) and denser (e_o = 0.585, D_r = 62%) sand specimens. The adopted sample preparation technique was dry pluviation with minor tapping on the mold. The comparison is presented in terms of q_{TX} versus ε_a (subplots **5.25a** and **Figure 5.25c**) and ε_{vol} versus ε_a (subplots **5.25b** and **5.25d**) curves. Three stress levels, between 100 kPa and 300 kPa, are examined for each density. The comparison for e_o = 0.604 is quite satisfactory, while that for e_o = 0.585 is considered fair, with a slight underestimation of the peak strength of these denser samples and an expected variation in dilation in terms of ε_{vol} with stress level, which is not apparent in the experiments.

5.3.2 Undrained cyclic loading

With the same set of model parameters, as listed in **Table 5.3** and used for the simulations of the monotonic tests of the previous section, undrained cyclic loading tests are simulated here. In **Figure 5.26** the model is evaluated against a cyclic undrained triaxial test on Ottawa F-65 sand, performed by El Ghoraiby et al. (2018). The soil is prepared using dry pluviation where a constant drop height is maintained. The test is performed on a void ratio of 0.585 and the sample was initially consolidated at a mean effective stress of 100 kPa. The comparison is made in the spaces of q_{TX} versus radial effective stress σ_r (subplots **5.26a** and **5.26c**) and q_{TX} vs axial strain ε_a (subplots **5.26b** and **5.26d**). The test is performed as stress controlled with a single amplitude of $q_{TX,cyc}$ equal to 34 kPa. Both stress and stress-strain response are captured quite well by the model, while strain accumulation bias is observed also in this cyclic triaxial simulation. Model simulations are in good agreement with the experimental data when stress path heads towards liquefaction, but also at the post -liquefaction stage when strain continues to accumulate with number of cycles.

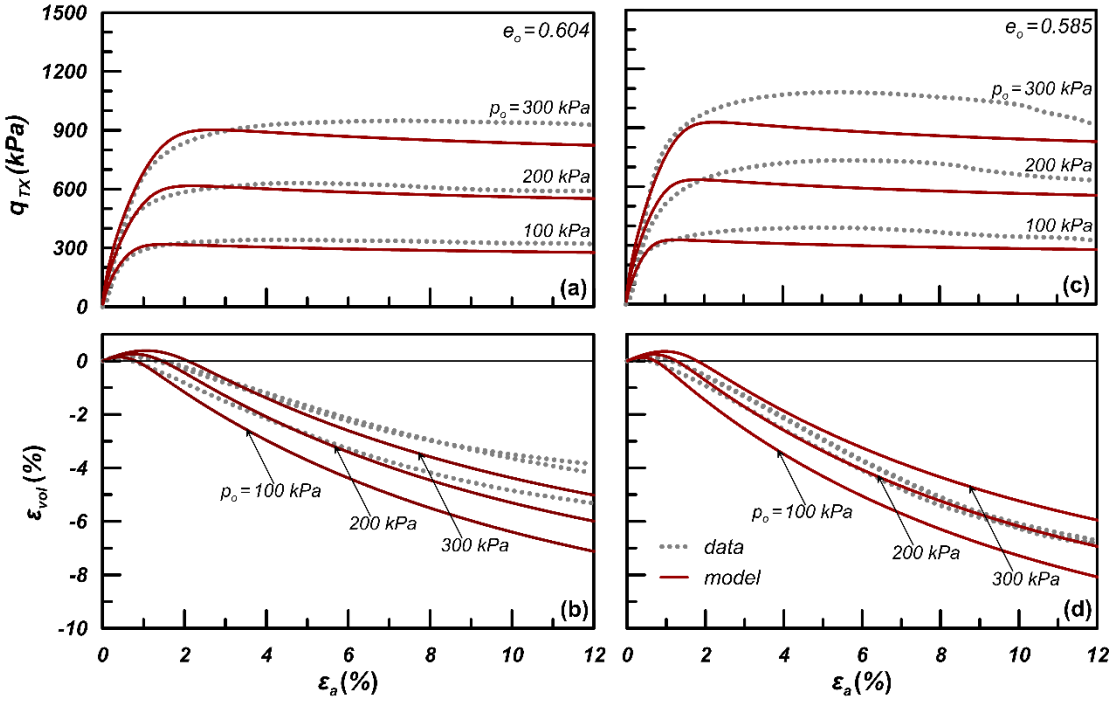

***Figure 5.25**: Experimental results and model estimates of drained monotonic triaxial compression tests. Data on Ottawa F-65 sand after Vasko et al. (2018).*

Figure 5.27 shows model's performance for an undrained torsional shear test of Ueda et al. (2018), which was performed on Ottawa F-65 sand. The sample was isotropically consolidated at a mean effective stress of 104 kPa with a measured relative density D_r = 60% after consolidation. As there is no information about the exact void ratio, considering the e_{min} and e_{max} values reported and measured by Vasko (2015) equal to 0.492 and 0.739, the aforementioned density corresponds to a void ratio almost equal to 0.590.

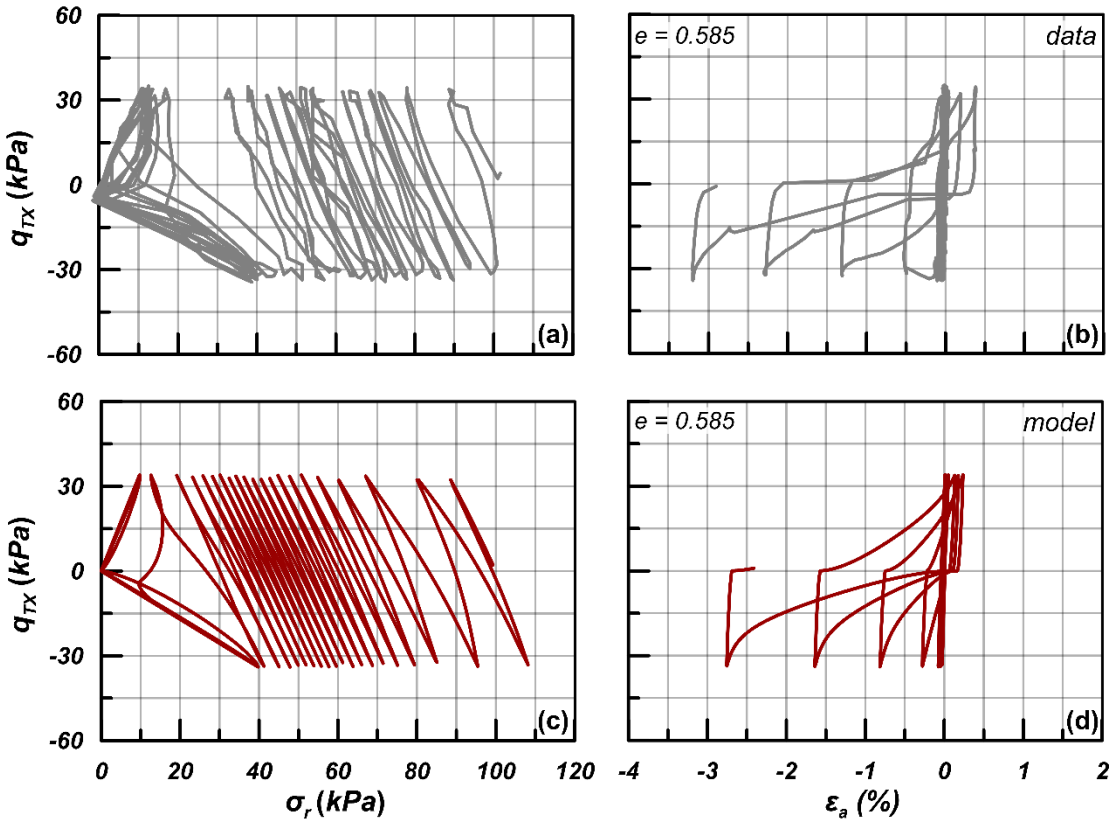

***Figure 5.26**: Experimental results and model estimates of undrained cyclic triaxial test. Data on Ottawa F-65 sand after El Ghoraiby et al. (2018).*

The comparison is presented in terms of shear stress τ versus p (subplots **5.27a** and **5.27c**) and τ vs shear strain γ_{SS} (subplots **5.27b** and **5.27d**). The single amplitude of the cyclically applied shear stress τ_{cyc} = 18.1 kPa. The simulation shows that the model estimates well the initially decreasing rate of excess pore pressure buildup with cycles and then how this rate increases to bring the sand to initial liquefaction. This non-constant rate of excess pore pressure buildup is typical of sand response (see also **Figure 5.26**). However, it is rarely commented on in the literature of constitutive models for liquefaction, despite its importance for accurate simulations of boundary value problems. Finally, observe how

the model estimates very well the intense shear strain accumulation following initial liquefaction, without any bias since it is a torsional shear test.

A. Liquefaction resistance curves

Subsequently, **Figure 5.28** presents the liquefaction resistance curves for the undrained cyclic triaxial tests on Ottawa F-65 conducted by El Ghoraiby et al. (2018). The

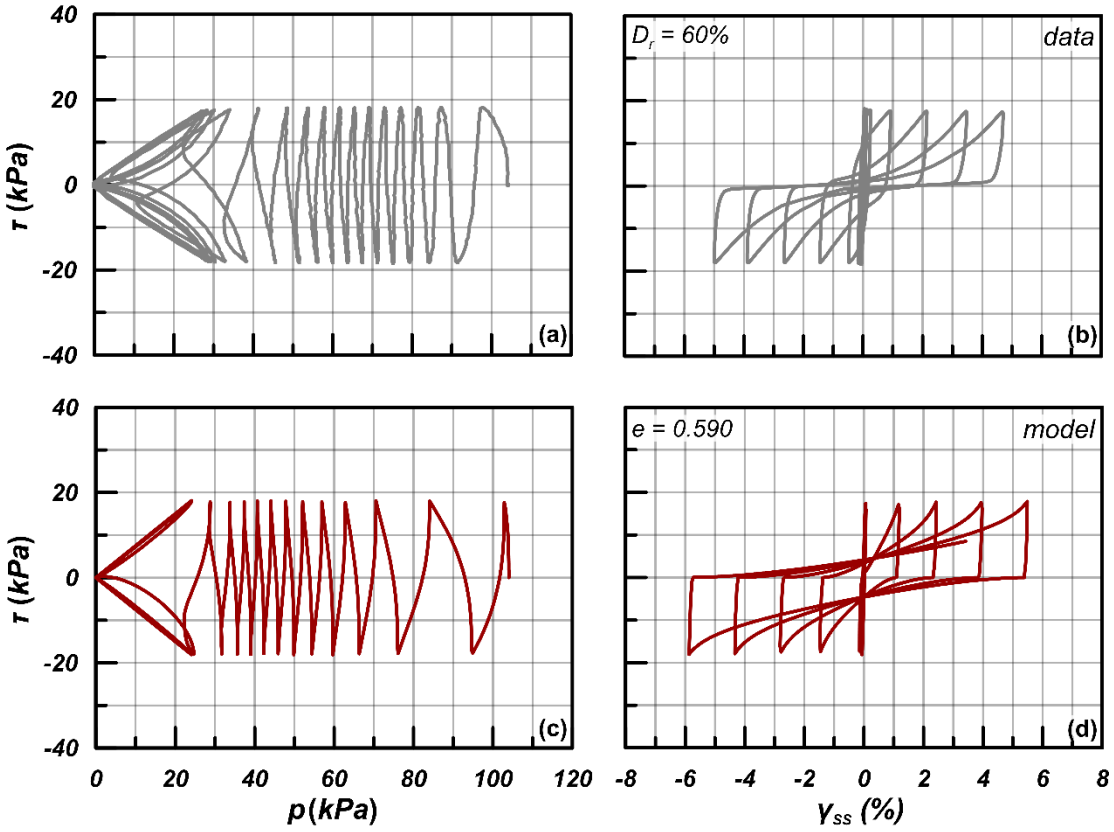

***Figure 5.27**: Experimental results and model estimates of an undrained cyclic torsional shear test. Data on Ottawa F-65 sand after Ueda et al. (2018).*

comparison is made for two void ratios, e = 0.585 and e = 0.542, corresponding to $D_r \approx$ 60% and 80% according to the values of e_{min} and e_{max} presented earlier for Ottawa F-65. The consolidation stress level and preparation method are described above in **Figure 5.26**, as the element test presented there is included to the liquefaction curve of e = 0.585. The experimental data and the simulations are compared in terms of *CSR* vs cycles N_l, to reach axial strain of single amplitude equal to 2.5%. The simulations are in good agreement with

the model results, with a slightly steeper inclination for the case of e = 0.585 estimated by the model. Notice, again that the tendency of the model, in accordance with the data, is to estimate non liquefaction when a small *CSR* ratio is applied.

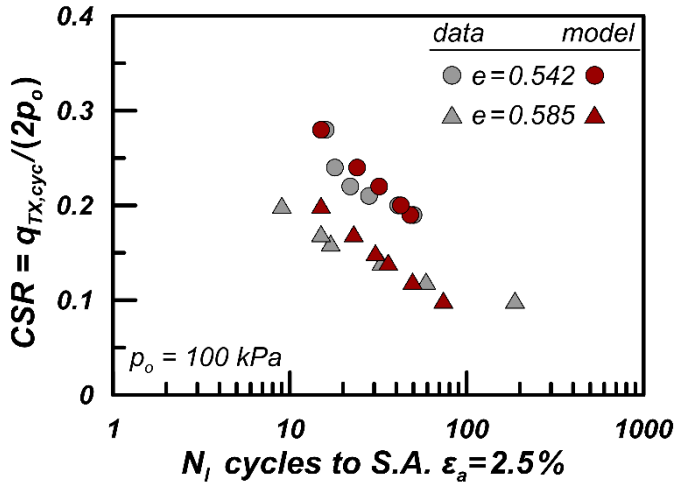

***Figure 5.28**: Experimental results and model estimates of liquefaction resistance curves on the basis of undrained cyclic triaxial tests. Data on Ottawa F-65 sand after El Ghoraiby et al. (2018).*

B. Effect of confining stress on liquefaction resistance

The same procedure as for Toyoura sand is followed for estimating K_σ values for undrained cyclic triaxial tests of Ottawa sand for a range of initial axial stresses $\sigma_{a,o}$ and D_r = 40% - 80%. These values are compared to the well-established empirical curves of Idriss and Boulanger (2008) and Hynes and Olsen (1999) in **Figure 5.29**. The K_σ values estimated by Hynes and Olsen (1999) are lower than that estimated by Idriss and Boulanger (2008). The comparison shows very good agreement with the relationship of Hynes and Olsen (1999), i.e., the model estimates quite accurately that liquefaction resistance decreases with increasing confining stresses and that the rate of decrease is nonlinear. As according to Equations (3.31) and (3.32) the effect of confining stress level on cyclic resistance depends on initial void ratio, it is expected the lower values of initial void ratios corresponding to Ottawa sand, lead to lower values of K_σ values.

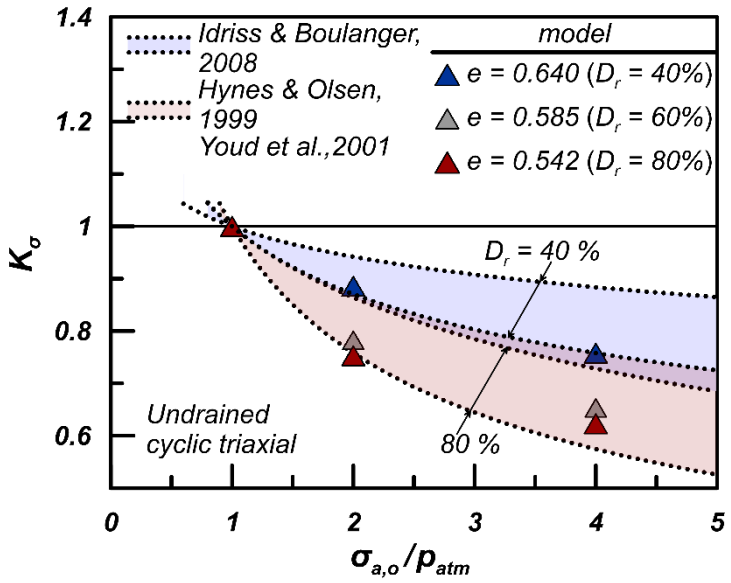

Figure 5.29: *Comparison of K_σ values for different relative density D_r values estimated by the model for Ottawa sand versus the empirical relations of Idriss and Boulanger (2008) and Hynes and Olsen (1999).*

5.3.3 Drained cyclic loading

A. Shear modulus degradation and damping ratio increase curves

Figure 5.30 shows the normalized secant shear modulus G/G_{max} degradation curves (subplot **5.30a**) and the damping ratio ξ increase curves (subplot **5.30b**) derived from simulations of strain-controlled cyclic simple shear loading. The horizontal axis of both diagrams $\gamma_{SS,cyc}$ depicts the single amplitude cyclic shear strain of the performed numerical simulations, which covers a range from 0.0001% to 1%. The secant shear modulus G and the corresponding damping ratio ξ refer to the 1st cycle of loading, while the initial void ratio e_o is selected to correspond to an initial D_r almost equal to 60% for Ottawa F-65 sand (e = 0.585). Two extreme levels of initial effective axial stress $\sigma_{a,o}$ are examined, namely 100 and 1000 kPa. In terms of shear modulus degradation, the results estimated by the model are consistent with the empirical relation proposed by Darendeli (2001), while they exhibit a less pronounced non-linearity with respect to the Vucetic and Dobry (1991) curve. Moreover, the simulated G/G_{max} reduction show a dependency on stress level consistent with the empirical correlations. In terms of damping ratio ξ, the results of the new model up to the strain level of 0.1% are compared satisfactorily with the empirical relations.

However, for larger strain levels, there is an overestimation of ξ values, especially at the lower stress level.

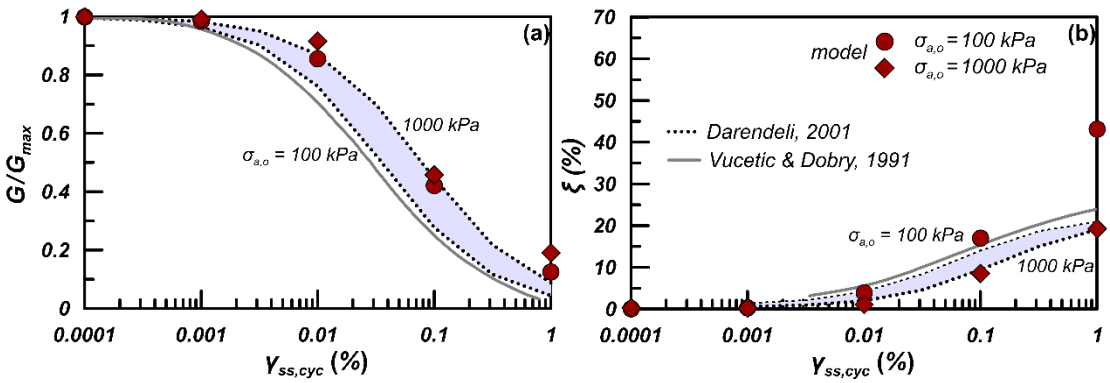

Figure 5.30: *Comparison of shear modulus degradation curves and damping ratio increase curves estimated by the model for Ottawa sand versus the empirical relations of Darendeli (2001) and Vucetic and Dobry (1991).*

B. Accumulation of strains with cycles

Figure 5.31 presents a summary of estimated values of accumulated volumetric strains ε_{vol} after 10 cycles of strain controlled drained simple shear loading, at various levels of single amplitude cyclic shear strains $\gamma_{SS,cyc}$ ranging from 0.01% to 0.5% The initial relative densities of 40% and 80%, which correspond to initial void ratios of e_o = 0.640 and e_o = 0.542, for Ottawa F-65 sand, are examined. The samples are consolidated at an initial effective axial stress $\sigma_{a,o}$ = 100 kPa. The numerical values are compared with the empirical relations of Duku et al. (2008). Supplementarily, experimental data of Silver and Seed (1971) was also used for validation. It is observed that, on the whole, the comparison is acceptable. Specifically, at small and intermediate $\gamma_{SS,cyc}$ strain levels, the numerical volumetric strains by the model are closer to the range of experimental data of Silver and Seed (1971), while at larger $\gamma_{SS,cyc}$ strain levels, the accumulation of volumetric strains is in accordance to the empirical relations of Duku et al. (2008). Moreover, the qualitative dependency of accumulated volumetric strains on relative density D_r is reasonably consistent with the empirical data.

Figure 5.32 presents a summary comparison of accumulated volumetric strains ε_{vol} (subplot **5.32a**) and accumulated shear strains $\gamma_{TX} = \varepsilon_a - \varepsilon_r$ (subplot **5.32b**) in cyclic drained triaxial tests as estimated by the new model versus the pertinent values from the empirical

relations of Bouckovalas et al. (1984) and Stamatopoulos et al. (1991). Strain accumulation is measured after N_d = 1, 30, 100 and 300 cycles. Specifically, the initial relative densities of D_r = 40%, 60% and 80%, with initial void rations e_o = 0.640, 0.585 and 0.542 are examined. All simulated tests were anisotropically consolidated at a mean effective stress p_o = 200 kPa, with an appropriate combination of initial axial and radial stresses, so as initial stress ratios $q_{TX,o}/p_o$ = 0.35 and 0.75 to be attained after consolidation. In both subplots of **Figure 5.32** different symbols depict the different number of cycles, while the solid diagonal line is the locus of points of perfect agreement between estimates by the model and estimates by the empirical relations. Similarly, the two dashed lines define the loci of overestimation and underestimation by the denoted factor. In terms of accumulated volumetric strains ε_{vol} (subplot **5.32a**), a quite good overall agreement is observed, as the ratio of numerical over empirical values ranges between 0.5 to 2.0. On the other hand, in terms of accumulated shear strains γ_{TX} (subplot **5.32b**), the comparison is less impressive, but remains satisfactory.

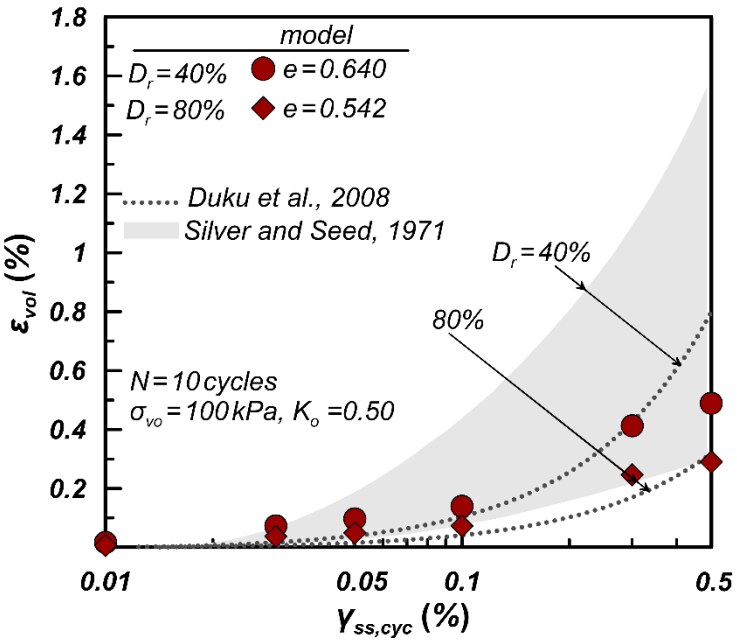

Figure 5.31: *Comparison of accumulated volumetric strains from drained cyclic simple shear tests estimated by the model for Ottawa F-65 sand versus the empirical relations of Duku et al. (2008) and the range of experimental data of Silver and Seed (1971).*

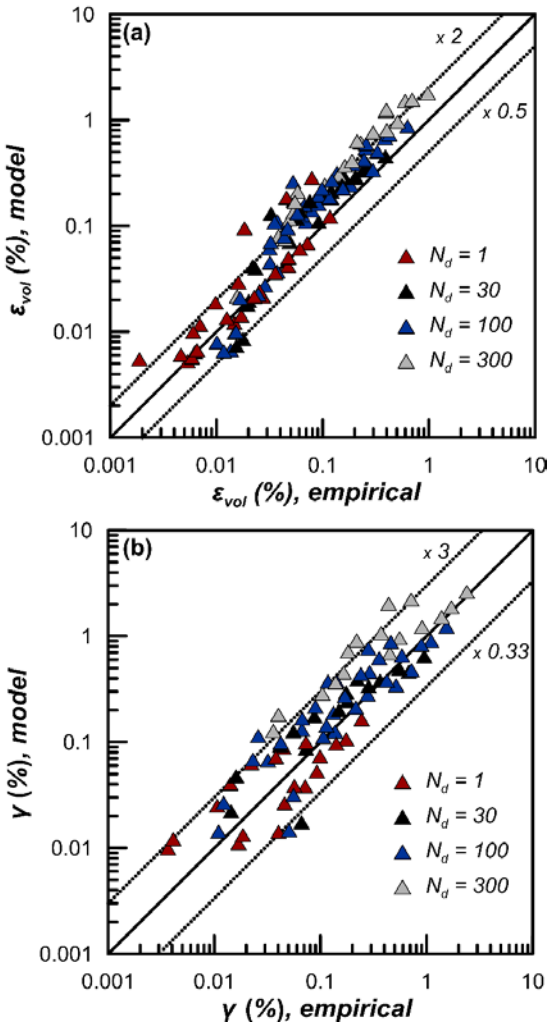

Figure 5.32: *Comparison of accumulated volumetric strains and shear strains from drained cyclic triaxial tests estimated by the model for Ottawa F-65 sand and by the empirical relations of Bouckovalas et al. (1984) and Stamatopoulos et al. (1991).*

5.4 Model Verification for Nevada sand

In this Section, the performance of the new model is verified through element level for Nevada fine silica sand with $D_{50} \approx 0.10$ mm, which is the sand material used in VELACS Project (Arulmoli et al., 1992). Its gradation curve according to Arulmoli et al. (1992) is presented in **Figure 5.33**. The measured values of e_{min} and e_{max} are equal to 0.511 and 0.887 respectively. The values of all 14 model parameters for Nevada sand, as they were estimated according to the calibration procedure described in detail above, are presented in **Table 5.4**. All the information regarding the characteristics of the element tests employed for Nevada sand is summarized in **Tables A5** and **A6** in the **Appendix**.

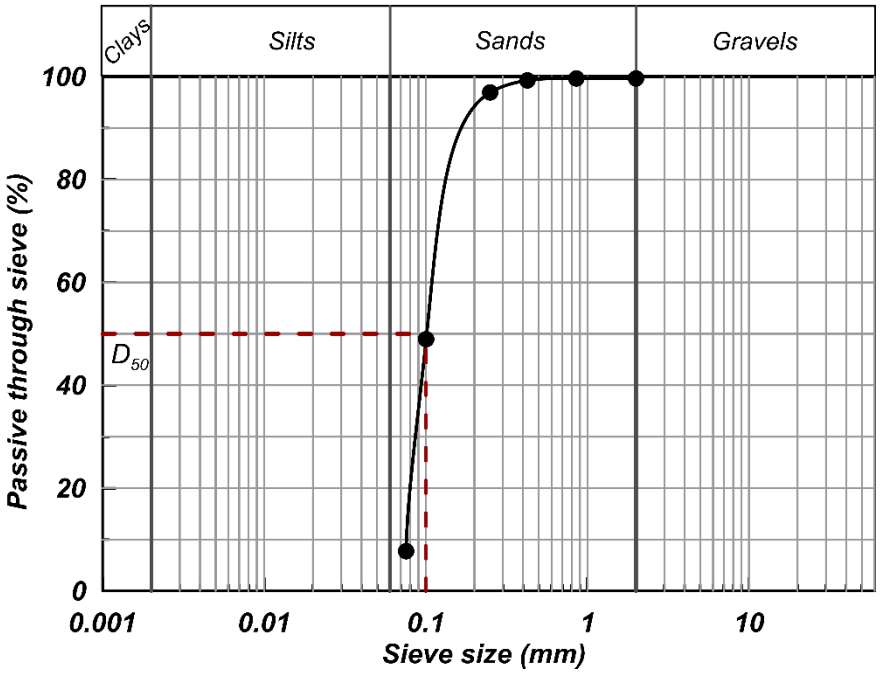

Figure 5.33: *Gradation curve of Nevada sand. Data after Arulmoli et al. (1992).*

Table 5.4: *Values of model parameters for Nevada sand.*

Constitutive part	Parameter	Values
		Nevada sand
Elasticity	G_o	500
	ν	0.15
CSL	e_{ref}	0.875
	λ	0.079
	ξ	0.19
	M_c^c	1.25
	c	0.74
Plastic modulus	n^b	1.1
	h_o	235
	c_h	4
Dilatancy	n^d	1.2
	A_o	2.6
Fabric	N_o	4400
Post-liquefaction	L_o	750

5.4.1 Undrained monotonic loading

Figure 5.34 presents one-to-one comparisons of the model simulations to the respective experimental data for undrained monotonic triaxial compression tests (TC), performed by

Arulmoli et al. (1992) on isotropically consolidated specimens of Nevada sand. The comparison of data versus simulations is shown in the spaces of q_{TX} versus p (subplots **5.34a** and **5.34c**) and q_{TX} versus ε_a (subplots **5.34b** and **5.34d**). The simulations are performed for two relative densities of D_r = 40% and 60%, and a range of initial mean effective stresses, from p_o = 40 kPa to 160 kPa.

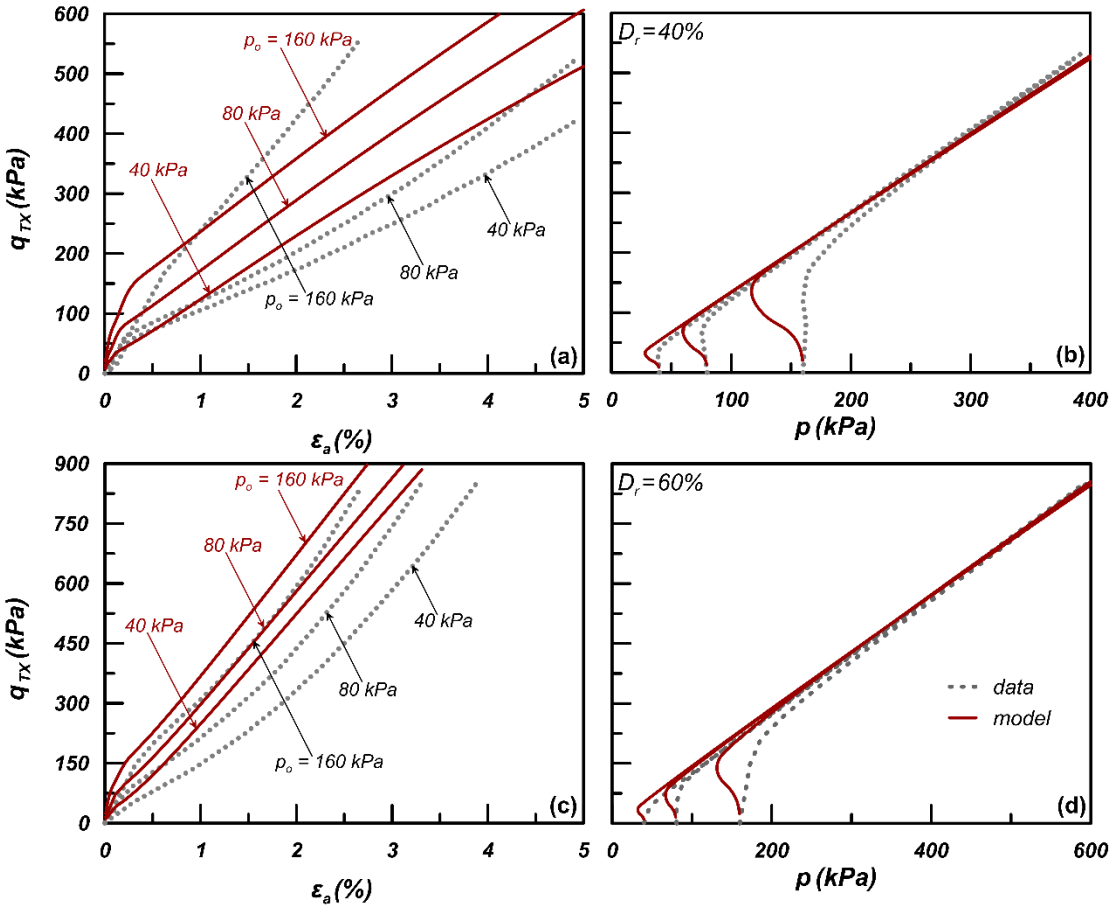

***Figure 5.34**: Experimental results and model estimates of undrained monotonic triaxial compression tests. Data on Nevada sand after Arulmoli et al. (1992).*

5.4.2 Undrained cyclic loading

Then, **Figure 5.35** shows model's simulations of two indicative cases of undrained cyclic simple shear tests performed on Nevada sand by Arulmoli et al. (1992). Subplots **5.35a - 5.35d** refer to a sample of relative density equal to 40%, while subplots **5.35e - 5.35h** refer to a sample of relative density equal to 60%. Both of them were consolidated at an initial axial effective pressure $\sigma_{a,o}$ = 160 kPa. The single amplitude of the cyclically applied shear stress τ equals to 21.5 kPa for the sample with D_r = 40% and 26 kPa for the sample with D_r

= 60%. The comparison is made in the spaces of shear stress τ versus axial effective confining stress σ_a (subplots **5.35a** and **5.35c** and subplots **5.35e** and **5.35g**) and τ vs shear strain γ_{SS} (subplots **5.35b** and **5.35d** and subplots **5.35f** and **5.35h**). Special attention was given to capture both liquefaction triggering response and post-liquefaction shear strain accumulation.

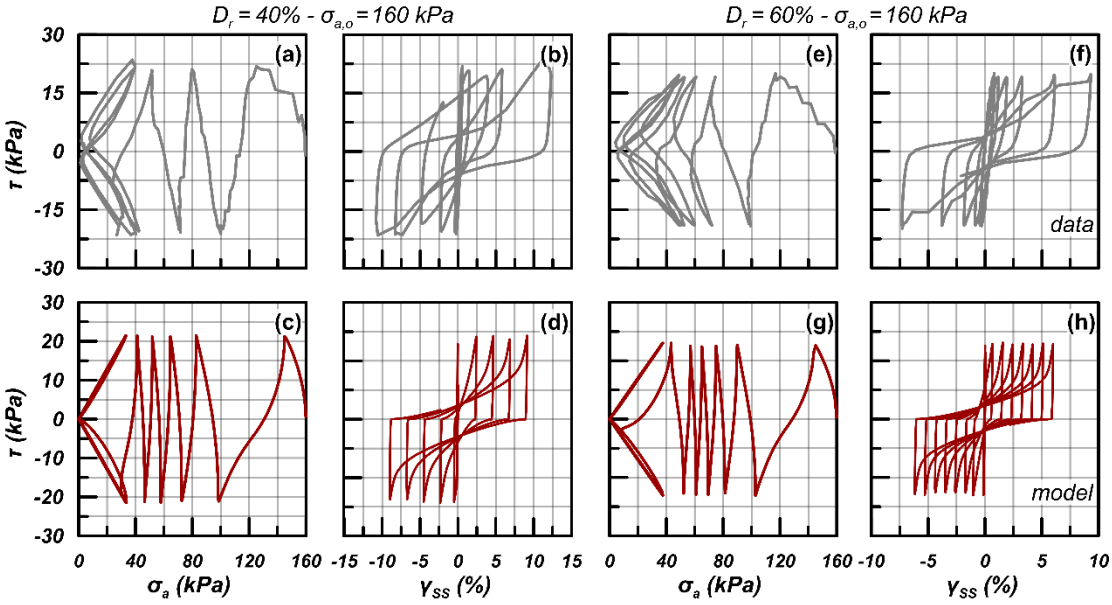

***Figure 5.35**: Experimental results and model estimates of undrained cyclic simple shear tests. Data on Nevada sand after Arulmoli et al. (1992).*

A. Liquefaction resistance curves

Figure 5.36 compares the liquefaction resistance curves derived from the available element tests and the respective model results. The available data for the examined relative densities of D_r = 40% and 60% refer to the experimental work of Arulmoli et al. (1992), while the data for D_r = 90% refer to the experimental work of Kammerer et al. (2000). The points refer to the specific element tests at hand, obeying to the various implied initial conditions, while the dashed ruby-red lines are model's numerical liquefaction curves of the various D_r, with an average initial effective axial stress between these reported in the element tests, i.e., 100 kPa. Moreover, it should be noted that the data points for D_r = 40% and 60% refer to the triggering of initial liquefaction, while the data point for D_r =90% refers to the liquefaction criterion of accumulation of single amplitude shear strain equal to 3%.

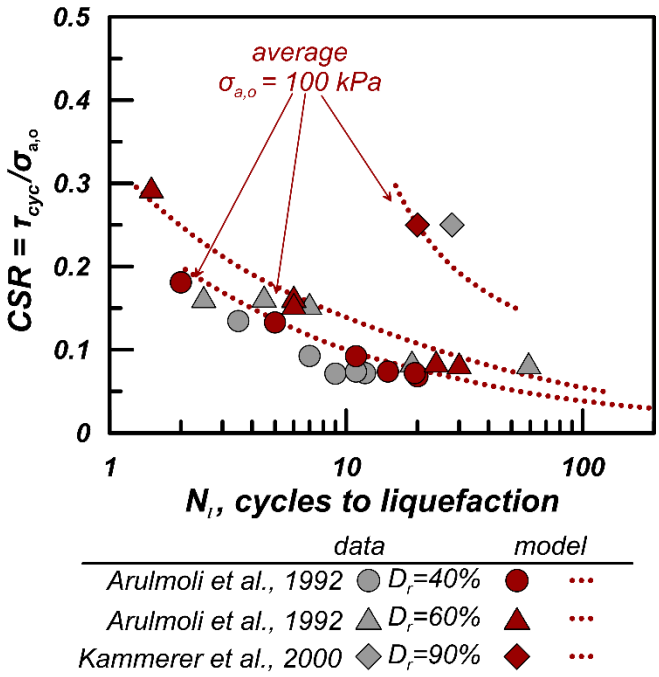

***Figure 5.36**: Liquefaction resistance curves. Experimental results and model estimates of undrained cyclic simple shear tests. Data on Nevada sand after Arulmoli et al. (1992) and Kammerer et al. (2000).*

B. Effect of confining stress on cyclic resistance

The same procedure as for Toyoura and Ottawa sands is followed for estimating K_σ values for undrained cyclic triaxial tests of Nevada sand for a range of initial axial stresses $\sigma_{a,o}$ and D_r = 40% - 80%. These values are compared to the well-established empirical curves of Idriss and Boulanger (2008) and Hynes and Olsen (1999) in **Figure 5.37**. The estimated values of K_σ fall int the range defined by the two groups of empirical relationships.

5.4.3 Drained cyclic loading

A. Shear modulus degradation and damping ratio increase curves

Figure 5.38 shows comparison of the elastic shear modulus of Nevada sand at small strain level, i.e., G_{max} (subplot **5.38a**), of the normalized secant shear modulus G/G_{max} and of the equivalent damping ratio ξ curves (combined in subplot **5.38b**), between experimental results of Arulmoli et al. (1992), empirical relations of Darendeli (2001) and model estimates. Subplot **5.38a** shows an one-to-one comparison of the measured G_{max} values according to the data and those estimated by the model, for densities D_r = 40% and 60%

and initial mean effective stresses equal to p_o = 40 kPa, 80 kPa and 160 kPa. The solid diagonal line is the locus of points of perfect agreement between estimates by the model and experimental data. The comparison is quite fair, indicating a realistic calibration of G_{max} and a correct estimate of shear modulus at the small level of strain. Then, subplot **5.38b** presents the reduction of G (left vertical axis) and the simultaneous increase of damping ratio, ξ (right vertical axis), with strain level. Results for relative densities D_r = 40% and 60% for the indicative stress level of p_o = 80 kPa are compared to the experimental

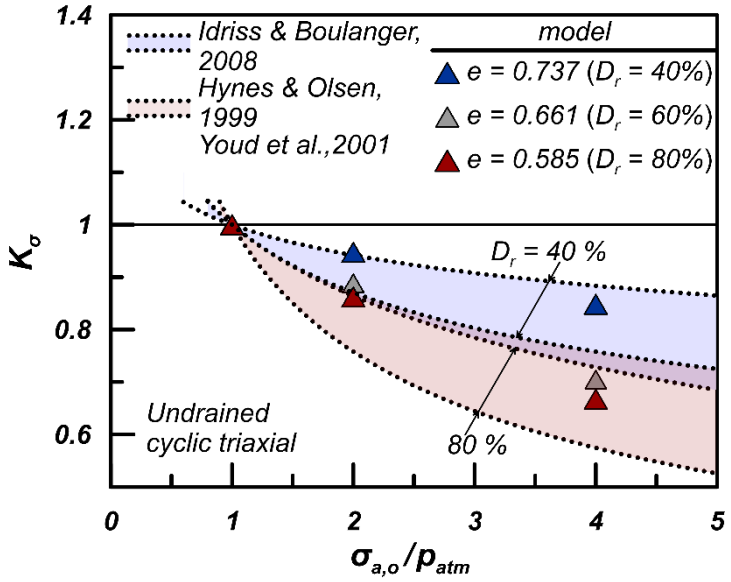

Figure 5.37: *Comparison of K_σ values for different relative density D_r values estimated by the model for Nevada sand versus the empirical relations of Idriss and Boulanger (2008) and Hynes and Olsen (1999).*

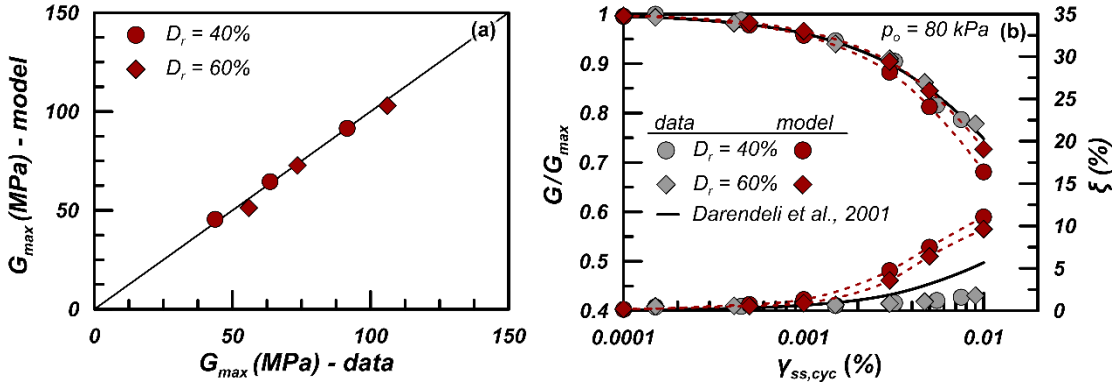

Figure 5.38*: Comparison of (a) G_{max} values and (b) shear modulus reduction curve and damping ratio curve estimated by the model and measured experimentally. Data on Nevada sand after Arulmoli et al. (1992) and empirical relation after Darendeli (2001).*

data of Arulmoli et al. (1992). The comparisons refer to element tests depicted with symbols, while the dashed line is added for reasons of visual continuity. In terms of G/G_{max} the comparison is quite fair primarily against the experimental data, but also against the empirical relation. On the other hand, in terms of damping ratio, ξ, the comparison is not so satisfactory, with the model here overestimating the ξ value compared to that shown by the data, which, however, is quite low. The numerical curve approaches more the damping curve of Darendeli (2001), but again the estimated values are higher.

B. Accumulation of strains with cycles

Figure 5.39 presents a summary of numerical values of accumulated volumetric strains ε_{vol} after 10 cycles of strain controlled drained simple shear loading, at various levels of single amplitude cyclic shear strains $\gamma_{SS,cyc}$ ranging from 0.01% to 0.5% The initial relative densities of 40% and 80%, which correspond to initial void ratios of e_o = 0.737 and e_o = 0.585, for Nevada sand, are examined. The samples are consolidated at an initial effective axial stress $\sigma_{a,o}$ = 100 kPa. The numerical values are compared with the empirical relations of Duku et al. (2008). Supplementarily, experimental data of Silver and Seed (1971) was also used for validation. It is observed that, on the whole, the comparison is acceptable. Specifically, at small and intermediate $\gamma_{SS,cyc}$ strain levels, the estimated volumetric strains by the model are closer to the range of experimental data of Silver and Seed (1971), while at larger $\gamma_{SS,cyc}$ strain levels, the accumulation of volumetric strains is in accordance to the empirical relations of Duku et al. (2008). Moreover, the qualitative dependency of accumulated volumetric strains on relative density D_r is reasonably consistent with the empirical data.

Figure 5.40 presents a summary comparison of accumulated volumetric strains ε_{vol} (subplot **5.40a**) and accumulated shear strains $\gamma_{TX} = \varepsilon_a - \varepsilon_r$ (subplot **5.40b**) in cyclic drained triaxial tests as estimated by the new model versus the pertinent values from the empirical relations of of Bouckovalas et al. (1984) and Stamatopoulos et al. (1991). Strain accumulation is measured after N_d = 1, 30, 100 and 300 cycles. Specifically, the initial relative densities of D_r = 40%, 60% and 80%, with initial void rations e_o = 0.640, 0.585 and 0.542 are examined. All the simulated tests were anisotropically consolidated at a mean effective stress p_o = 200 kPa, with an appropriate combination of initial axial and radial

stresses, so as initial stress ratios $q_{TX,o}/p_o$ = 0.35 and 0.75 to be attained after consolidation. In both subplots of **Figure 5.40** different symbols depict the different number of cycles, while the solid diagonal line is the locus of points of perfect agreement between numerical results and values given by the empirical relations. Similarly, the two dashed lines define the loci of overestimation and underestimation by the denoted factor. In terms of accumulated volumetric strains ε_{vol} (subplot **5.40a**), a quite good overall agreement is observed, as the ratio of numerical over empirical values ranges between 0.5 to 2.0. On the other hand, in terms of accumulated shear strains γ_{TX} (subplot **5.40b**), the comparison is less impressive, but remains satisfactory.

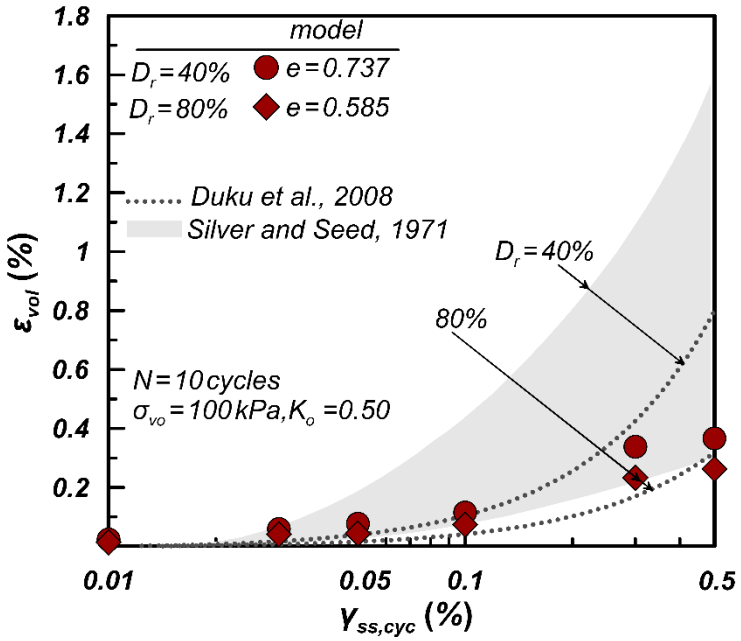

Figure 5.39: *Comparison of accumulated volumetric strains from drained cyclic simple shear tests estimated by the model for Nevada sand versus the empirical relations of Duku et al. (2008) and the range of experimental data of Silver and Seed (1971).*

5.5 Model Verification for M31 sand

In this section, the performance of the new model is verified through element – level comparisons between simulations and experimental data on M31 sand. M31 sand is a medium-fine sub-angular quartz sand with $D_{50} \approx 0.30$ mm and is the sand material mainly

studied experimentally in the Laboratory of Soil Mechanics in NTUA. Its gradation curve according to Pavlopoulou and Georgiannou (2021) is presented in **Figure 5.41**. Its measured values of e_{min} and e_{max} are equal to 0.528 and 0.870 respectively. The values of all 14 model parameters for M31 sand, as they were estimated according to the calibration procedure described in detail above, are presented in **Table 5.5**. All the information regarding the characteristics of the element tests employed for M31 sand is summarized in **Table A7** in the **Appendix**.

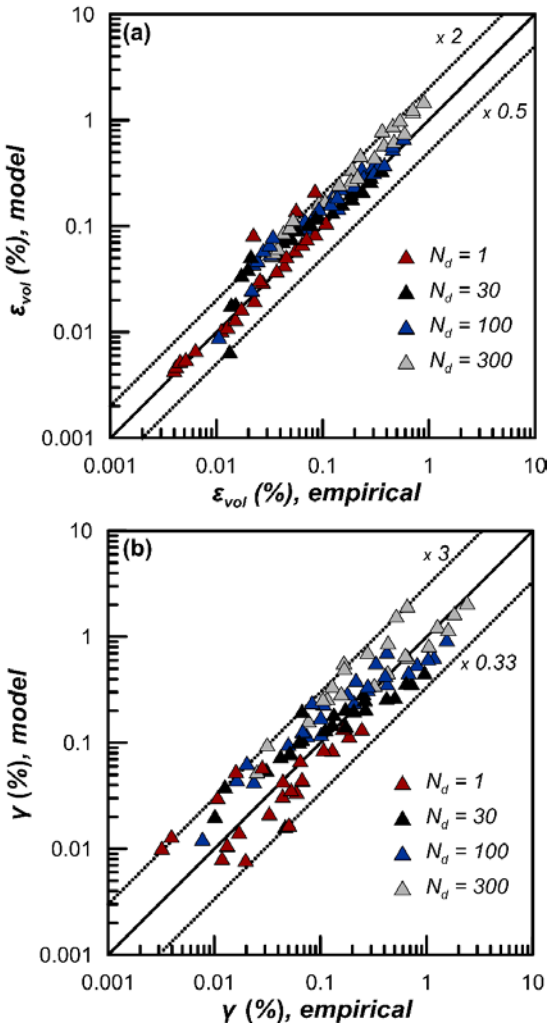

Figure 5.40: *Comparison of accumulated volumetric strains and shear strains from drained cyclic triaxial tests estimated by the model for Nevada sand and by the empirical relations of Bouckovalas et al. (1984) and Stamatopoulos et al. (1991).*

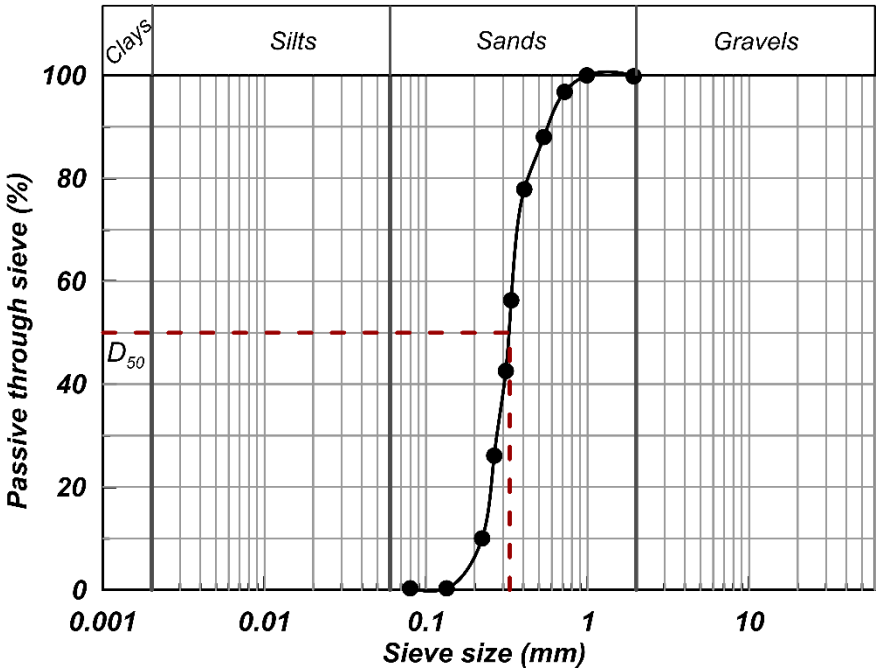

Figure 5.41: *Gradation curve of M31 sand. Data after Pavlopoulou and Georgiannou 2021).*

Table 5.5: *Values of model parameters for M31 sand.*

Constitutive part	Parameter	Values
		M31 sand
Elasticity	G_o	450
	ν	0.05
CSL	e_{ref}	0.786
	λ	0.013
	ξ	0.61
	M_c^c	1.25
	c	0.712
Plastic modulus	n^b	1
	h_o	200
	c_h	4
Dilatancy	n^d	2.6
	A_o	1.3
Fabric	N_o	3400
Post-liquefaction	L_o	200

5.5.1 Drained and undrained monotonic loading

Figure 5.42 shows model's performance for drained (TC) tests on M31 sand conducted by Pavlopoulou and Georgiannou (2021) for medium dense (e_o = 0.717, D_r = 45% and e_o = 0.710, D_r = 47%) and denser (e_o = 0.691, D_r = 52% and e_o = 0.676, D_r = 57%) sand specimens. The adopted sample preparation technique was water sedimentation. The comparison is presented in terms of q_{TX} versus ε_a (subplot **5.42a**) and ε_{vol} versus ε_a (subplot **5.42b**) curves. Three stress levels, between 200 kPa and 700 kPa, are examined. The comparison in terms of peak stress is satisfactory, while a stiffer initial stress-strain response is captured for all the examined cases. In terms of volumetric strain accumulation through shearing, model estimates are very close to the final ε_{vol} according to the experimental results, albeit more dilation than that indicated by the data is shown, especially for the lowest stress level of 200 kPa.

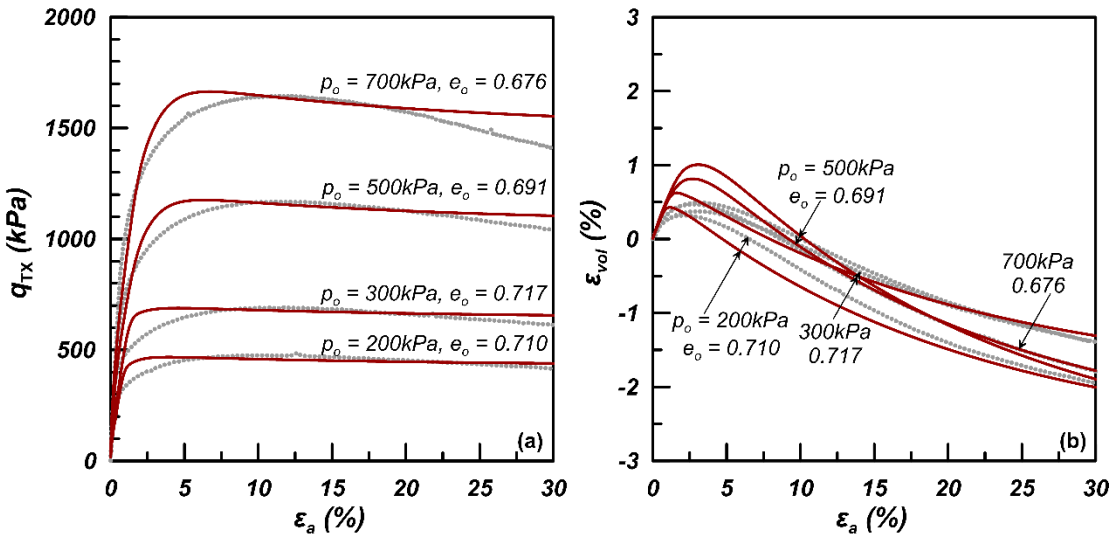

***Figure 5.42**: Experimental results and model estimates of drained monotonic triaxial compression tests. Data on M31 sand after Pavlopoulou and Georgiannou (2021).*

Subsequently, **Figure 5.43** presents one-to-one comparisons of the model simulations to the respective experimental data for undrained monotonic triaxial compression tests (TC), performed by Pavlopoulou and Georgiannou (2021) on isotropically consolidated medium - dense (e = 0.708, D_r = 47%) and denser (e = 0.681, D_r = 55% and e = 0.661, D_r = 61%) specimens of M31 sand. The comparison of data versus

simulations is shown in the spaces of q_{TX} versus ε_a (subplot **5.43a)** and q_{TX} versus p (subplot **5.43b**). The simulations refer to three levels of initial mean effective stresses, from p_o = 300 kPa to 2000 kPa. The comparisons are quite fair, especially in terms of peak strength, with model exhibiting a less contractive response up to the strain level of 10%.

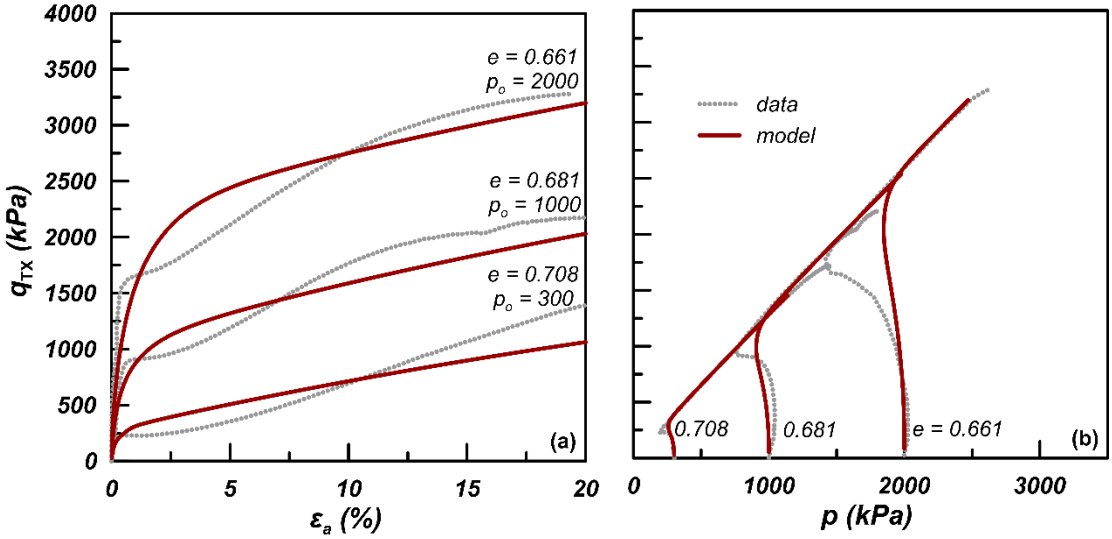

***Figure 5.43**: Experimental results and model estimates of undrained monotonic triaxial compression tests. Data on M31 sand after Pavlopoulou and Georgiannou (2021).*

5.5.2 Undrained cyclic loading

Then, **Figure 5.44** and **Figure 5.45** shows model's simulations for two indicative cases of undrained cyclic triaxial tests performed on Nevada sand by Pavlopoulou and Georgiannou (2021). **Figure 5.44** refers to a sample of initial void ratio equal to 0.633 with relative density equal to 69%, while **Figure 5.45** refer to a sample of initial void ratio equal to 0.742 and with relative density equal to 37%. Both of them were consolidated at an initial axial effective pressure $\sigma_{a,o}$ = 200 kPa. The single amplitude of the cyclically applied deviatoric stress q_{TX} equals to 76 kPa for the sample with D_r = 69% and 78 kPa for the sample with D_r = 37%. The comparison is made in the spaces of shear stress q_{TX} versus mean effective confining stress p (subplots **5.44a, 5.44c** and subplots **5.44a, 5.44c**) and q_{TX} vs axial strain ε_a (subplots **5.45b, 5.45d** and subplots **5.45b, 5.45d**). Special attention was given to capture both liquefaction triggering response and post-liquefaction shear strain accumulation.

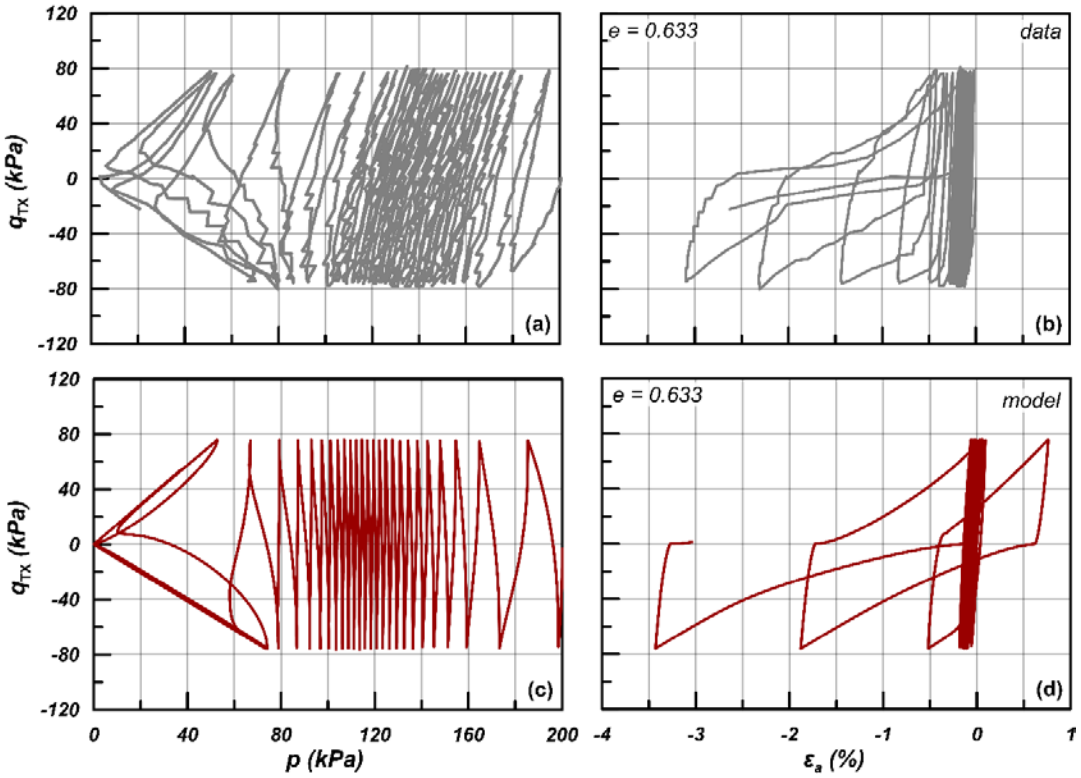

***Figure 5.44**: Experimental results and model estimates of undrained cyclic triaxial tests. Data on M31 sand after Pavlopoulou and Georgiannou (2021).*

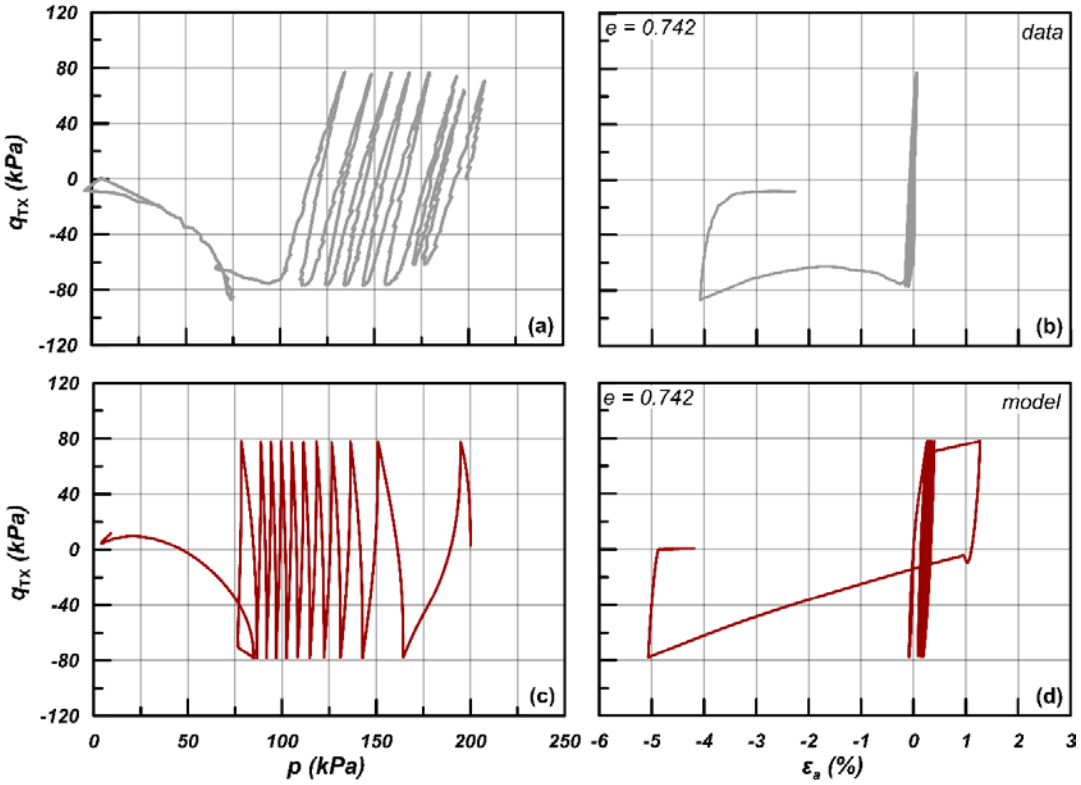

***Figure 5.45**: Experimental results and model estimates of undrained cyclic triaxial tests. Data on M31 sand after Pavlopoulou and Georgiannou (2021).*

A. Liquefaction resistance

Figure 5.46 shows a comparison of estimated response and experimental data of M31 in *CSR* vs N_l space. The available data are collected by the available dataset of Soil Mechanics' Laboratory of NTUA (personal communication with Pavlopoulou E-M.) and refer to samples with density $D_r \approx 65\%$ (e = 0.653 - 0.633), which are initially isotropically consolidated at 100 kPa and 200 kPa. All the data points correspond to the triggering of initial liquefaction.

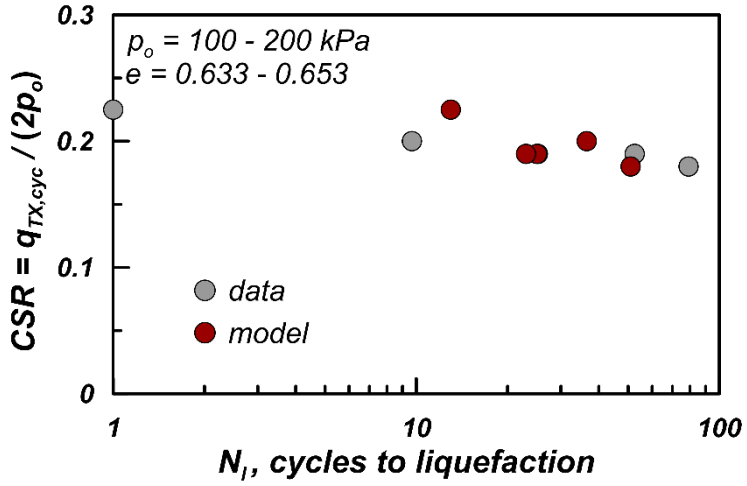

***Figure 5.46**: Experimental results and model estimates of undrained cyclic triaxial tests, in terms of liquefaction resistance. Data on M31 sand collected by the available dataset of Soil Mechanics' Laboratory of NTUA (personal communication with Pavlopoulou E-M.).*

5.6 Model Verification for Monterey sand

In this section, the performance of the new model is verified through element - level comparisons between simulations and experimental data on Monterey sand. Monterey sand is a medium-sized sub-angular to sub-rounded quartz sand with $D_{50} \approx 0.37$ mm. Its gradation curve according to Kammerer et al. (2000) is presented in **Figure 5.47**. Its measured values of e_{min} and e_{max} are equal to 0.541 and 0.885 respectively. The values of all 14 model parameters for Monterey sand, as they were estimated according to the calibration procedure described in detail above, are presented in **Table 5.6**. All the information regarding the characteristics of the element tests employed for Monterey sand is summarized in **Table A8** in the **Appendix**.

5.6.1 Undrained cyclic loading

A. Liquefaction resistance

This sand material is used, together with Nevada sand calibrated in a previous section, to the centrifuge testing series conducted by Dashti et al. (2010) to evaluate the response of different structures on liquefiable sand profiles. These centrifuge tests, among others, are utilized in **Chapter 6** for the validation of the present model against boundary value problems at system level. Hence, the model is initially calibrated against the undrained cyclic response of this sand, at element level here.

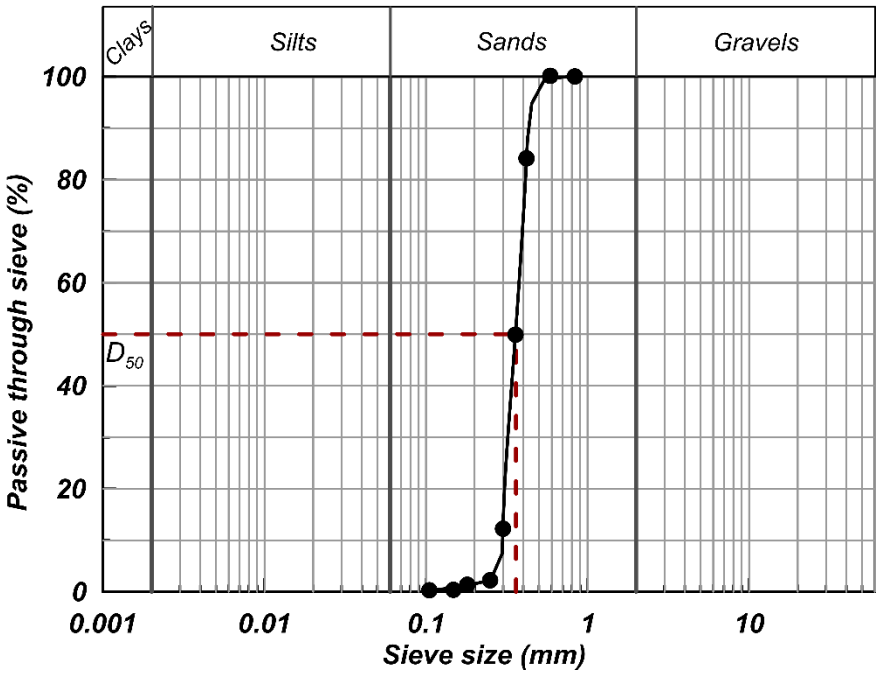

Figure 5.47: *Gradation curve of Monterey sand. Data after Kammerer et al. (2000).*

The calibration of the model parameters to simulate the cyclic response of Monterey sand with $D_r \approx 85\%$ was based on the cyclic undrained simple shear tests performed by Wu et al. (2004). This relative density was chosen, as it rspresents that used in the centrifuge testing series of Dashti et al. (2010). **Figure 5.48** shows the liquefaction resistance curve derived from the available experimental data with initial conditions referring to a relative density of $D_r = 85\%$ and an initial effective axial stress equal to 80 kPa applied to samples

prepared by wet tamping. As the data show a scatter, the ruby red line is an average numerically derived liquefaction resistance curve by the model, adopting the same initial conditions. Both the experimental and the numerical results adopt the criterion of induced strain of double amplitude equal to 6%, so as the liquefaction resistance to be reached.

Table 5.6: *Values of model parameters for Monterey sand.*

Constitutive part	Parameter	Values
		Monterey sand
Elasticity	G_o	400
	ν	0.15
CSL	e_{ref}	0.934
	λ	0.019
	ξ	0.70
	M_c^c	1.25
	c	0.72
Plastic modulus	n^b	1.1
	h_o	200
	c_h	7
Dilatancy	n^d	0.5
	A_o	2
Fabric	N_o	1800
Post-liquefaction	L_o	200

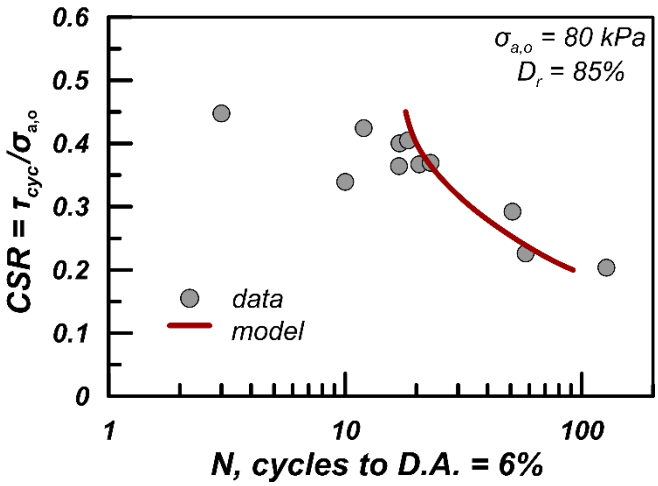

Figure 5.48*: Experimental results and model estimates of undrained cyclic simple shear tests, in terms of liquefaction resistance. Data on Monterey sand after Wu et al. (2004).*

5.7 Model Verification for Pea gravels

Model's results are here validated against experimental data of coarser granular soils. Specifically, experimental data are acquired after the work of Hubler (2017) and Hubler et al. (2017) and two gravel soils are examined. Pea gravels consist of rounded-to-subrounded particles, with a $D_{50} \approx 9$ mm and the grain distribution curve of the material is presented on **Figure 5.49**. The measured values of e_{min} and e_{max} are equal to 0.574 and 0.772 respectively. The values of all 14 model parameters for Pea gravels, as they were estimated according to the calibration procedure described in detail above, are presented in **Table 5.7**. For this more coarse - grained material, the monotonic and cyclic response could not be coupled equally well as in the previously examined sand materials, using exactly the same set of model parameters. However, the de-activation of functions related to fabric accumulation

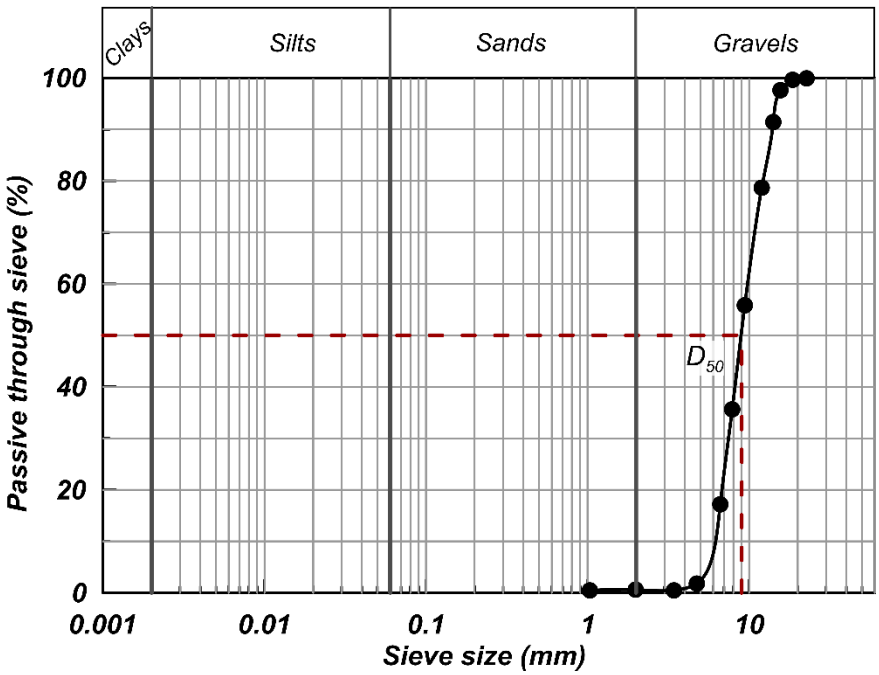

Figure 5.49: *Gradation curve of Pea gravels. Data after Hubler (2017) and Hubler et al. (2017).*

during monotonic loading, through nullifying the model parameter N_o, has proven sufficient enough to permit capturing the monotonic and the cyclic response without intervening to the rest set of uniquely calibrated parameters. An alternative calibration, would be based on the increase of the parameter h_o, that scales the plastic modulus, during cyclic loading, compared to its adopted monotonic value, to capture the induced ratio of pore pressure

buildup according to the data, while keeping the values of all the other parameters (and N_o) common between monotonic and cyclic loading. However, this scheme was deemed more complicated for the users, and hence is not adopted as the proposed one in the following comparisons. All the information regarding the characteristics of the element tests employed for Pea gravels is summarized in **Table A9** in the **Appendix**.

Table 5.7: *Values of model parameters for Pea gravels.*

Constitutive part	Parameter	Values
		Pea gravels
Elasticity	G_o	580
	ν	0.05
CSL	e_{ref}	0.72
	λ	0.019
	ξ	2
	M_c^c	1.1
	c	0.74
Plastic modulus	n^b	0.05
	h_o	300
	c_h	0.5
Dilatancy	n^d	1.25
	A_o	1.5
Fabric	N_o	0 (monotonic) 7250 (cyclic)
Post-liquefaction	L_o	50

5.7.1 Undrained monotonic loading

Figure 5.50 presents one-to-one comparisons of the model simulations to the respective experimental data for undrained monotonic simple shear (SS) tests, performed by Hubler (2017) on medium dense (e = 0.674 - 0.685, $D_r \approx$ 43% - 49%) and very dense (e = 0.592 – 0.598, $D_r \approx$ 87% - 90%) specimens of Pea gravels. The comparison of data versus simulations is shown in the spaces of τ versus γ_{SS} (subplots **5.50a** and **5.50c)** and τ versus σ_a (subplots **5.50b** and **5.50d)**. The simulations refer to three levels of initial axial effective stresses, from σ_a = 100 kPa to 400 kPa. The model results can be evaluated as generally fair, especially for the denser gravel samples, while for the medium dense samples

contractive response is slightly underestimated. It should be noted here that the experimental results show relatively very small effect of void ratio on the response and an effort is made while calibrating, this trend to be captured also by the model.

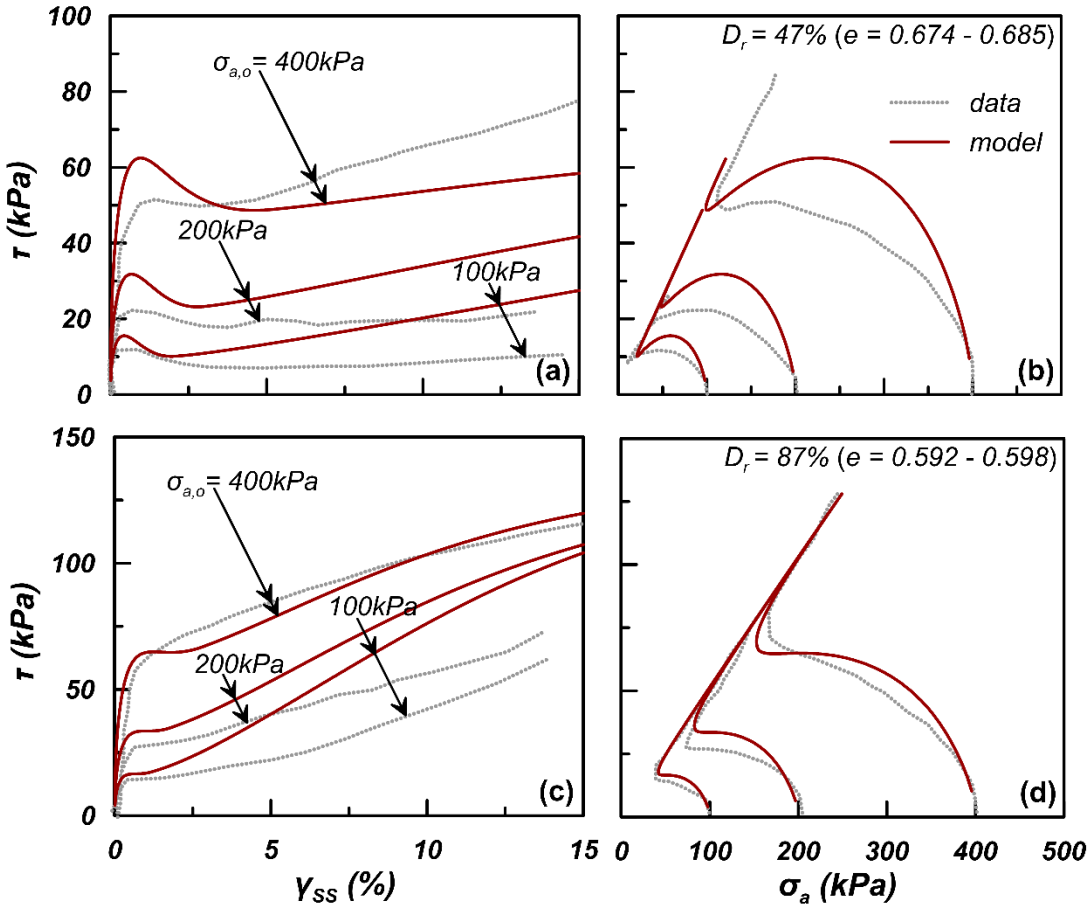

***Figure 5.50**: Experimental results and model estimates of undrained monotonic simple shear tests. Data on Pea gravels after Hubler (2017).*

5.7.2 Undrained cyclic loading

Then, **Figure 5.51** shows model's simulation of an indicative case of undrained cyclic simple test performed on Pea gravel material by Hubler (2017). **Figure 5.51** refers to a sample of initial void ratio equal to 0.686 with relative density equal to 43%, consolidated at an initial axial effective pressure $\sigma_{a,o}$ = 100 kPa. The single amplitude of the cyclically applied deviatoric stress τ equals to 9.4 kPa. The comparison is made in the spaces of shear stress τ versus axial effective confining stress σ_a (subplots **5.51a** and **5.51c**) and τ vs shear

strain γ_{SS} (subplots **5.51b** and **5.51d)**. The data and numerical results are compared satisfactorily, with model estimating higher decrease of axial effective stress during the first cycle, but reaching the accurate number of cycles until initial liquefaction, as the experiment indicates.

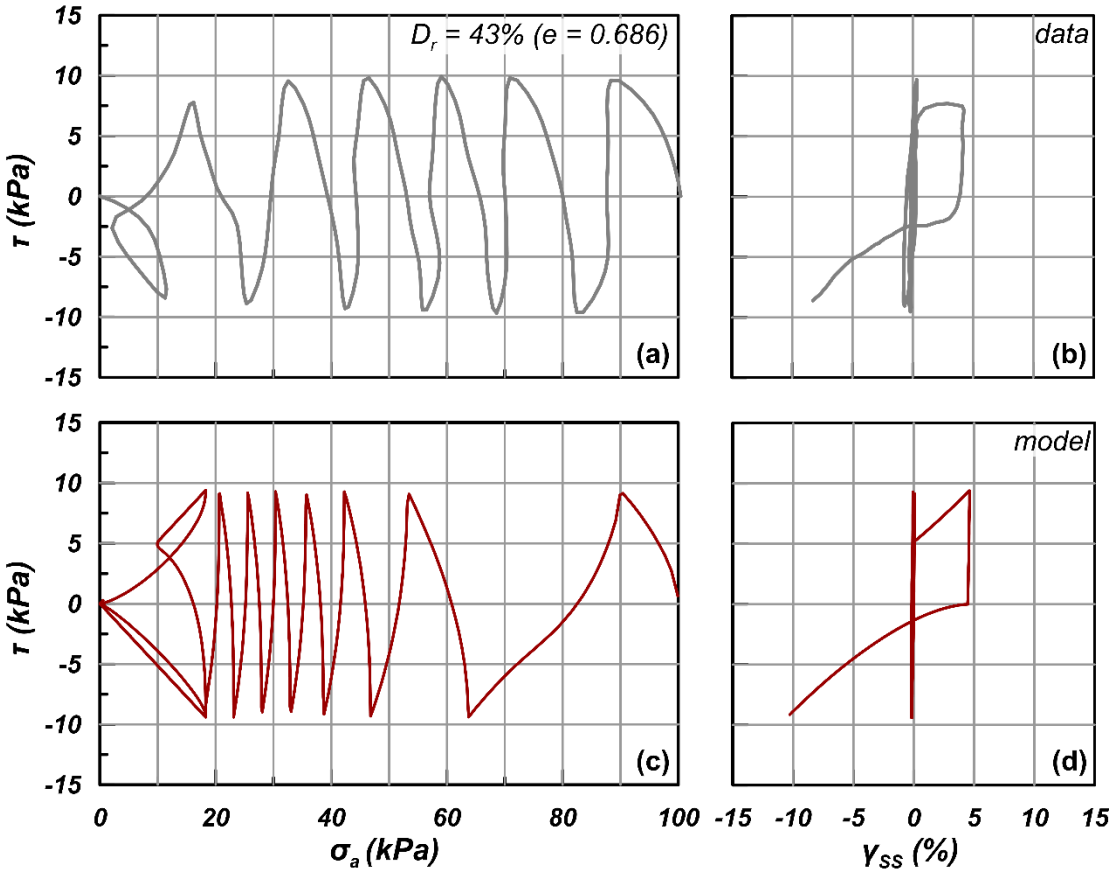

***Figure 5.51**: Experimental results and model estimates of undrained cyclic triaxial tests. Data on Pea gravels after Hubler (2017).*

A. Liquefaction resistance

Figure 5.52 shows a comparison of estimated response and experimental data of Pea gravels in *CSR* vs N_l space. The available data are presented by Hubler (2017) and refer to samples of Pea gravels with density $D_r \approx 43$ - 49 % (e = 0.680 - 0.686) and $D_r \approx 87$ - 92 % (e = 0.589 - 0.602). In subplot **5.52a** the examined axial effective stress levels range from 50 to 100 kPa, while subplot **5.52b** focuses only on the stress level of 100 kPa. The adopted liquefaction criterion corresponds to the triggering of initial liquefaction. The comparison is quite satisfactory.

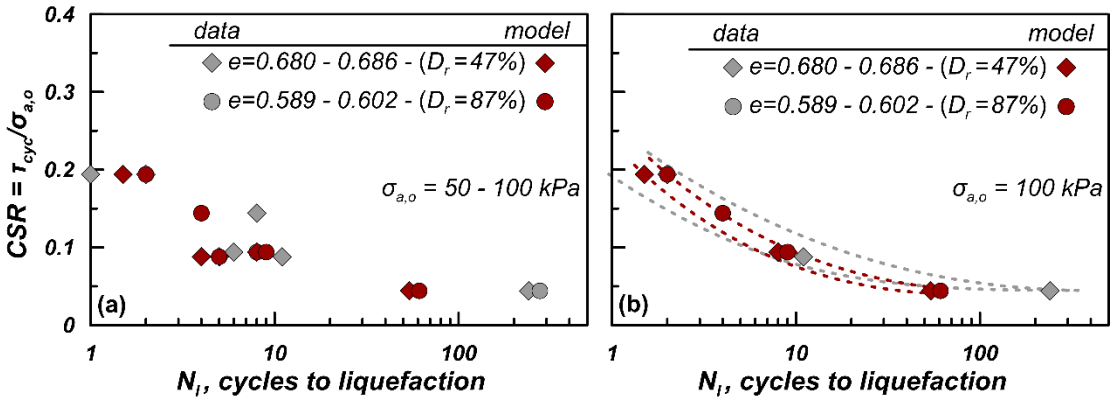

***Figure 5.52**: Experimental results and model estimates of undrained simple shear tests, in terms of liquefaction resistance. Data on Pea gravels after Hubler (2017).*

5.8 Model Verification for 8-mm Crushed Limestone (CLS8) gravels

The response of the second gravel material, examined in this study, is also introduced by Hubler (2017) and Hubler et al. (2017) and refers to Crushed Limestone gravels with relatively uniform gradation and particle size around 8mm. The grain size distribution curve of this material is presented on **Figure 5.53.** The measured values of e_{min} and e_{max} are equal to 0.513 and 0.953 respectively. The values of all 14 model parameters for CSL8 gravels, as they were estimated according to the calibration procedure described in detail above, are presented in **Table 5.8**. Also for this gravel material, the de-activation of functions related to fabric accumulation during monotonic loading, through nullifying the model parameter N_o, has proven sufficient enough to permit capturing the monotonic and the cyclic response without intervening to the rest set of uniquely calibrated parameters. Again, n alternative calibration, would be based on the increase of the parameter h_o, that scales the plastic modulus, during cyclic loading, compared to its adopted monotonic value, to capture the induced ratio of pore pressure buildup according to the data, while keeping the values of all the other parameters (and N_o) common between monotonic and cyclic loading. However, this scheme was deemed more complicated for the users, and hence is not adopted as the proposed one in the following comparisons. All the information regarding the characteristics of the element tests employed for Pea gravels is summarized in **Table A10** in the **Appendix**.

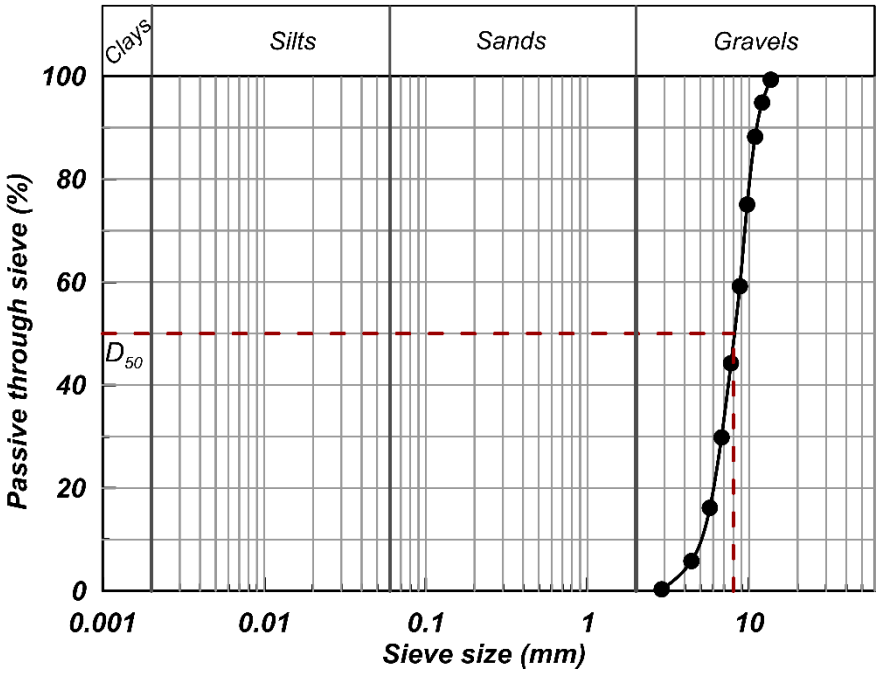

Figure 5.53: *Gradation curve of CSL8 gravels. Data after Hubler (2017) and Hubler et al. (2017).*

Table 5.8: *Values of model parameters for CSL8 gravels.*

Constitutive part	Parameter	Values
		CSL8 gravels
Elasticity	G_o	660
	ν	0.05
CSL	e_{ref}	0.825
	λ	0.003
	ξ	1.5
	M_c^c	1.3
	c	0.712
Plastic modulus	n^b	0.01
	h_o	200
	c_h	0.5
Dilatancy	n^d	1.3
	A_o	0.6
Fabric	N_o	0 (monotonic) 11700 (cyclic)
Post-liquefaction	L_o	50

5.8.1 Undrained monotonic loading

Figure 5.54 presents one-to-one comparisons of the model simulations to the respective experimental data for undrained monotonic simple shear (SS) tests, performed by Hubler (2017) on medium dense (e = 0.738 - 0.755, $D_r \approx$ 45% - 48%) and very dense (e = 0.581 - 0.563, $D_r \approx$ 85% - 88%) specimens of CSL8 gravels. The comparison of data versus simulations is shown in the spaces of τ versus γ_{SS} (**Figures 5.54a** and **5.54c)** and τ versus σ_a (**Figures 5.54b** and **5.54d)**. The simulations refer to four levels of initial axial effective stresses, from σ_a = 50 kPa to 400 kPa. The model results can be evaluated as generally fair, especially for the denser gravel samples. It should be noted here that, as for Pea gravels, experimental results show a relatively small effect of void ratio on the response and while calibrating, an effort is made in the calibration, so as this effect to be also captured by the model.

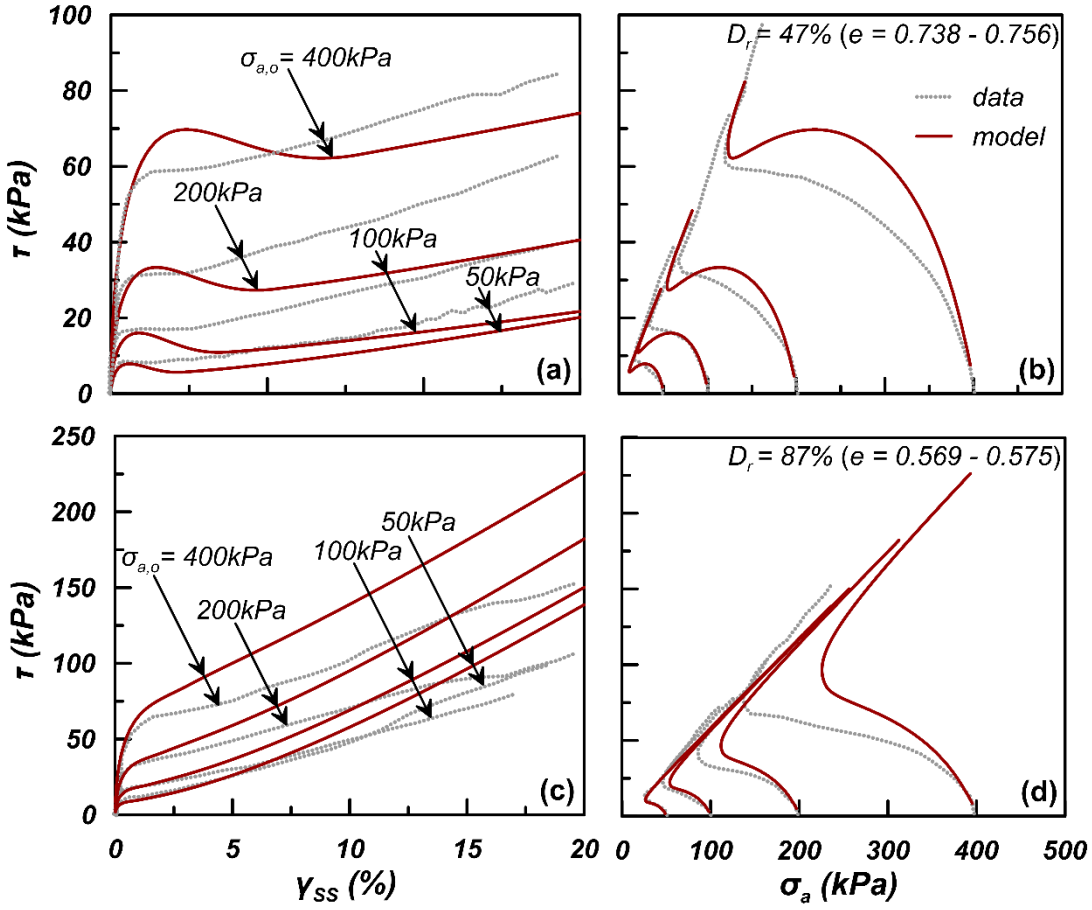

***Figure 5.54**: Experimental results and model estimates of undrained monotonic simple shear tests. Data on CSL8 gravels after Hubler (2017).*

5.8.2 Undrained cyclic loading

Then, **Figure 5.55** shows model's simulation of an indicative case of undrained cyclic simple test performed on CSL8 material by Hubler (2017). **Figure 5.55** refers to a sample of initial void ratio equal to 0.755 with relative density equal to 45%, consolidated at an initial axial effective pressure $\sigma_{a,o}$ = 100 kPa. The single amplitude of the cyclically applied shear stress τ equals to 9.4 kPa. The comparison is made in the spaces of shear stress τ versus axial effective confining stress σ_a (subplots **5.55a** and **5.55c**) and τ vs shear strain γ_{SS} (subplots **5.55b** and **5.55d)**. The data and model results are compared satisfactorily, with model estimating higher decrease of axial effective stress during the first cycle, but reaching the accurate number of cycles until initial liquefaction, as in the experiment.

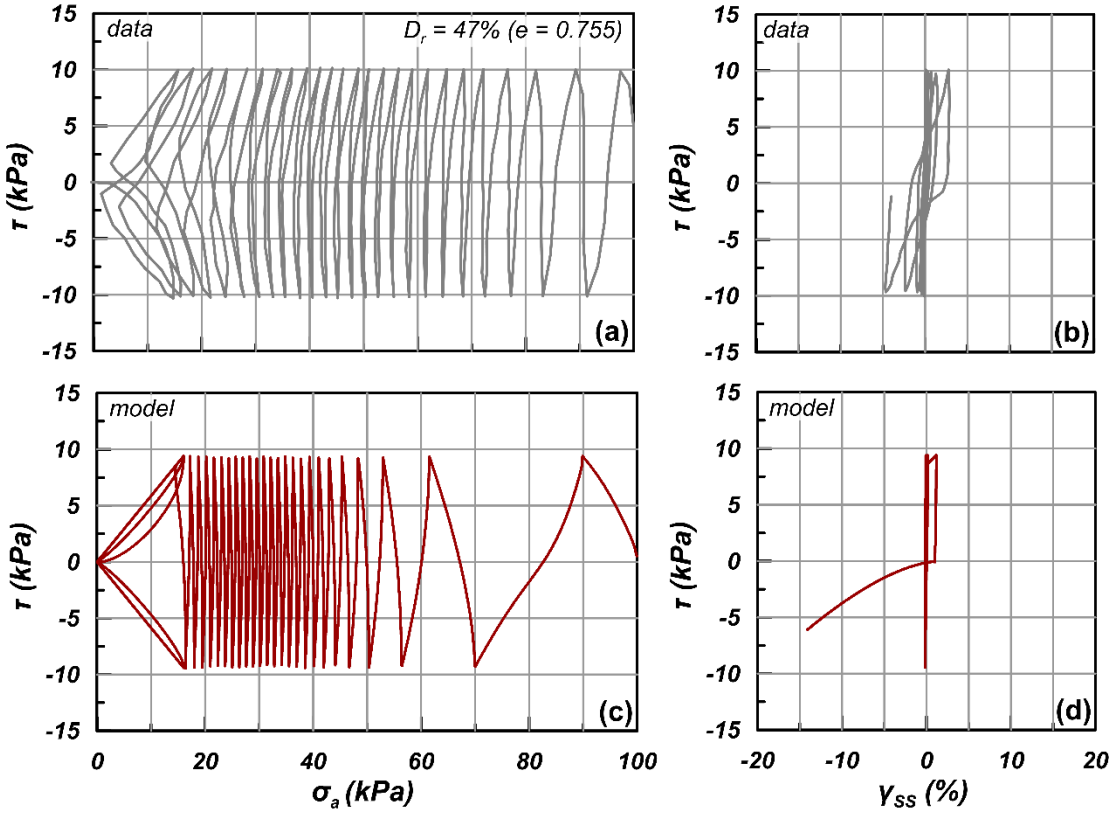

***Figure 5.55**: Experimental results and model estimates of undrained cyclic triaxial tests. Data on CSL8 gravels after Hubler (2017).*

A. Liquefaction resistance

Figure 5.56 shows a comparison of the numerical response and experimental data of CSL8 gravels in *CSR* vs N_l space. The available data are presented by Hubler (2017) and refer to

samples of CSL8 gravels with density $D_r \approx 45$ - 49 % (e = 0.738 – 0.755) and $D_r \approx 85$ - 89% (e = 0.563 – 0.581). In subplot **5.56a** all the examined axial effective stress levels are compared, ranging from 50 to 400 kPa, while subplot **5.56b** focuses only on the stress level of 100 kPa. The adopted liquefaction criterion corresponds to an axial strain accumulation of single amplitude equal to 3.75%. The comparison is again quite satisfactory.

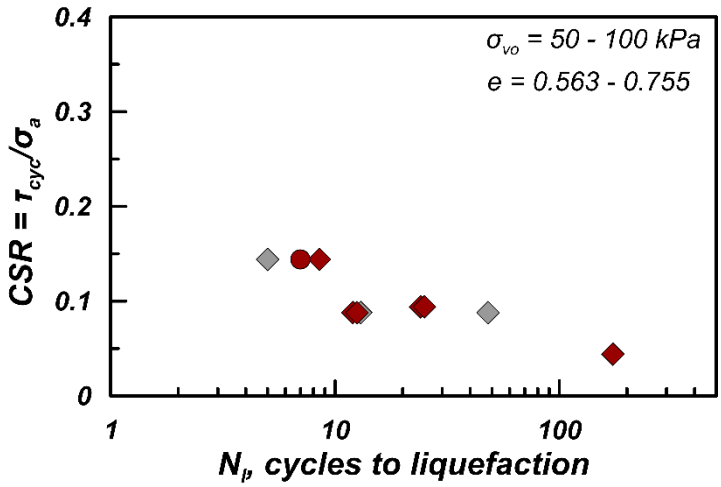

***Figure 5.56**: Experimental results and model estimates of undrained simple shear tests, in terms of liquefaction resistance. Data on CSL8 gravels after Hubler (2017).*

5.9 Summary

The Chapter presents the model formulation and the step-by-step calibration process of its 14 constants, first of the 12 constants required for monotonic loading and then the 2 additional constants related to cyclic loading. Being a SANISAND-type model, its calibration process includes trial-and-error runs, however these have been clearly identified and explained. Model performance is verified against a large database of monotonic and cyclic shearing tests, both drained and undrained, on samples of 4 sands: Toyoura, Ottawa-F65, Nevada and M31 and 2 gravels: Pea and CSL8 gravels. Wherever material-specific data are lacking, empirical relations are also used for validating specific aspects of the response, thus targeting a thorough and complete model verification.

The validation of the model at element level covers the whole range of cyclic response, in terms of straining. It starts from the small strain regime and the “quasi-elastic” response, where the calibration of its model parameters is based on actual dynamic measurements. Then, it continues to the medium strain regime, where a well verified

accumulation of strains with cycles is exhibited. Finally, the large strains related to liquefaction are well captured.

The monotonic response is captured effectively until the critical state, using the same model parameters as in the cyclic loading conditions, at least when it comes to sands. On the other hand, when it comes to gravels, the de-activation of functions related to fabric accumulation during monotonic loading, through nullifying the model parameter N_o, has proven sufficient enough to permit capturing the monotonic and the cyclic response without intervening to the rest set of uniquely calibrated parameters.

Chapter 6

Model Performance in Centrifuge tests

6.1 General

Apart from the meticulous validation against element tests, the model verification may be considered successful after supplementary extensive use and comparisons of numerical and experimental results from boundary value problems (BVPs) (e.g., Manzari and El Ghoraiby, 2021). Recent advances in geotechnical earthquake engineering and the well-established need for performance-based design of the structures make increasingly necessary the proper simulation of the non-linear dynamic response of the soil. Hence, non-linear dynamic analyses of BVPs of geotechnical structures have become a routine in research, and more and more in practice as well. This has been historically using a series of constitutive models (e.g., Andrianopoulos et al., 2010a; Beaty and Byrne, 2011; Boulanger and Ziotopoulou, 2013; Cheng and Detournay, 2021; Dafalias and Manzari, 2004; Taiebat and Dafalias, 2008; Tasiopoulou and Gerolymos, 2016; Zhang and Wang, 2012) and the results vary depending on the selected model, its calibration and the type of problem. More specifically, given the complexity of the dynamic response of geostructures, especially in a liquefaction regime, the results often show a significant deviation and require deep understanding of the activated failure mechanisms of geostructures. Based on the above, in this Chapter, the validation process of the new plasticity model is complemented by verifying its simulative potential through comparisons with experimental data from dynamic centrifuge tests related to liquefaction. Aiming to build even greater confidence in the new model, the same numerical methodology and modeling procedure, as well as a unique set of sand-specific model parameters are maintained, regardless of the specific conditions of the problem at hand (arrangement of soil layers of different density, different excitation characteristics, different deformation mechanisms, etc.). This validation is performed by beginning from a systematic validation of the presented model against experimental data at element level performed for Nevada sand. Then, comparisons between results from centrifuge experiments on the same sand and model estimates are made for a variety of liquefaction related BVPs. The validation process includes:

- the simulation of the free field response of a level-ground liquefiable sand layer (Taboada and Dobry, 1994),
- the simulation of an inclined liquefiable sand layer producing lateral spreading phenomena (Taboada and Dobry, 1994b),
- the simulation of shallow foundations' seismic response on level liquefiable soil (Carnevale and Elgamal, 1994; Dashti et al., 2010a; b; Farrel and Kutter, 1994; Krstelj and Prevost, 1994),
- the simulation of a pile group response in an inclined liquefiable soil profile (Pamuk et al., 2007).

As already described in **Chapter 4**, the new model has been implemented in *FLAC* (Itasca Consulting Group Inc., 2011) and *FLAC*^{3D} (Itasca Consulting Group Inc. 2012), hence all the simulations below are performed with the explicit finite-difference method of these numerical codes. All the examined cases in the following adopt a unique set of sand-specific model parameters and follow the same modeling procedure. Small variations may appear according to the specifications and restrictions of each experiment, as explained wherever necessary. The primary goal was to demonstrate the model's ability to simulate satisfactorily the response of the same sand in a variety of boundary value problems without case specific changes, in model parameters or modeling procedure.

6.2 Case 1: Seismic response of horizontal liquefiable layer – VELACS 1

Results from centrifuge Model test No. 1 of the VELACS project (Taboada and Dobry, 1994a) have been used to validate the new model's ability to simulate the one-dimensional (1D) seismic response of a liquefiable soil layer under level ground conditions. In prototype scale, a 10 m deep Nevada sand layer of approximately 40% relative density is examined. The model was built into a laminar box of internal dimensions equal to 22.86 m x 12.70 m x 13.2 m and the water table was set 1 m above the ground surface. The configuration of the model is illustrated in **Figure 6.1**.

The input motion applied at the base of the box consisted of approximately 20 cycles with a duration of almost 13.5 sec, with a peak horizontal acceleration of 0.235g and a predominant frequency of 2Hz, the time-history of which is plotted in **Figure 6.2**. It should be noted that the motion was baseline corrected, so as to result in a practically zero

displacement of the base at the end of shaking. The response of the horizontal liquefiable ground was monitored along the axis of symmetry of the box, as well as closer to the boundaries, with a number of accelerometers, pore pressure transducers and LVDTs measuring displacements. The model was spun up to a 50g centrifugal acceleration and water was used as a pore fluid.

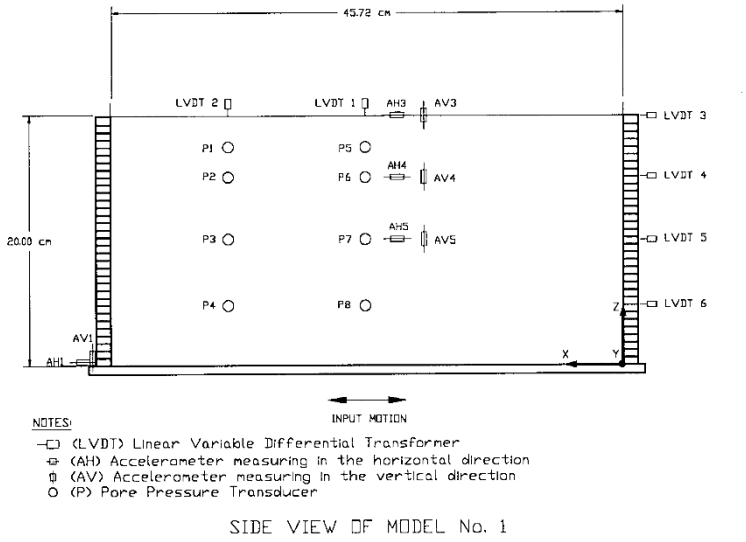

***Figure 6.1**: Experimental setup of Model test No. 1 of the VELACS project (figure after Taboada and Dobry, 1994a).*

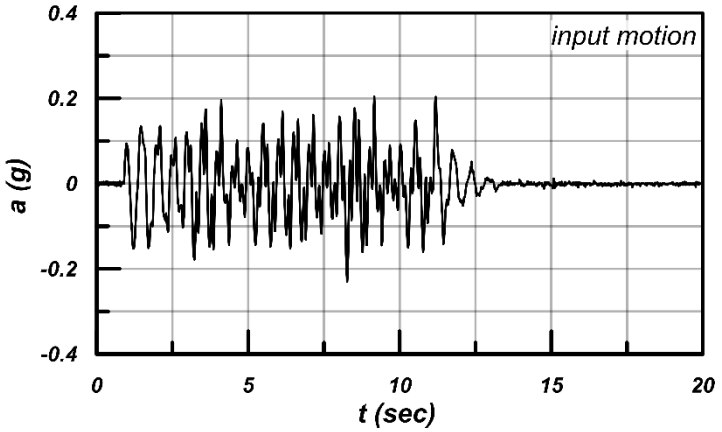

***Figure 6.2**: Baseline corrected applied motion at the base of the model (data after Taboada and Dobry, 1994a).*

The modeling procedure follows the rationale described by Andrianopoulos et al. (2010a) and Andrianopoulos, (2006). The finite-difference grid used for the numerical analysis was uniform with 0.994m×1m square elements, as it is discretized in **Figure 6.3**, which illustrates the test layout as modeled numerically and the positioning of selected instruments, the measurements of which are utilized for the validation process. A uniform sand layer was assumed, with an initial void ratio equal to 0.736, corresponding to a D_r = 40%. The bottom boundary of the grid was forced to follow the time-history of the input horizontal acceleration, while the vertical acceleration during the experiments was assumed as parasitic and was not taken account into the numerical simulation. At the vertical edges of the mesh, the boundary condition of tied nodes was adopted. This boundary condition imposes the same horizontal and vertical velocity at the nodes of the same elevation, so as

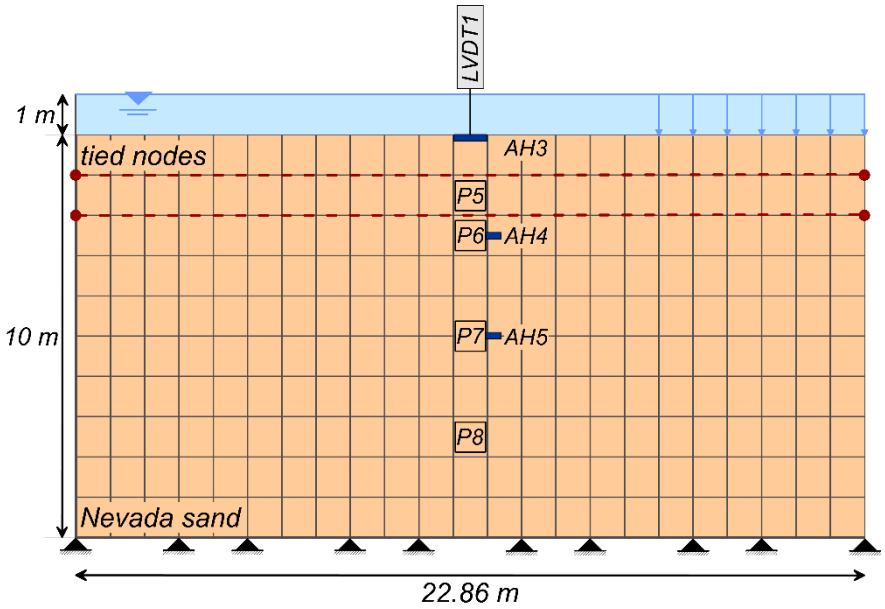

***Figure 6.3**: Layout of the numerical model - Model test No. 1 of the VELACS project.*

they are forced to move as attached to one-another. As the horizontal and the vertical displacements of the two vertical boundaries are common, the kinematic restraints of the laminar box were simulated. The existence of a 1m water above the ground surface was simulated by applying a uniform normal stress and a respective pore pressure equal to 9.81 kPa. Lateral and bottom boundaries were assumed impermeable, so water flow is permitted only towards the free surface of the model. Initially, the geostatic stress field is achieved assuming elastic response with a K_o value equal to 0.50, under static equilibrium. Then,

fluid-mechanical coupled dynamic analysis was performed. The permeability coefficient of Nevada sand was measured to range with relative density according to constant-head permeability tests with water as pore fluid under a 1g field, conducted by Arulmoli et al. (1992). For a relative density of approximately 40%, a permeability coefficient equal to $k = 6.5 \cdot 10^{-5}$ - $6.6 \cdot 10^{-5}$ m/sec is documented. To allow for an accurate replication of the experiment performed at a 50 g centrifugal acceleration with water as a pore fluid, the adopted permeability coefficient value in the analysis was firstly scaled up by 50. However, as described by Tan and Scott (1985), there is a conflict between the timescales of dynamic pore pressure generation and diffusion during centrifuge experiments. Hence, many researchers (e.g., Dashti and Bray, 2013; Liu and Dobry, 1997; Popescu and Prevost, 1993) have indicated the necessity of using a lower permeability coefficient during the dynamic excitation in the numerical simulation. Specifically, Popescu and Prevost (1993) proposed a division by 4 and this is also adopted by Dashti and Bray (2013). In this simulation, the rationale described above is followed and the adopted value for permeability coefficient is derived by scaling up by 50 the k value measured at 1g, and then decreasing it by a factor of 4. So, if denoting as k' the final permeability coefficient used in the numerical analysis, it equals to $k' = (50/4)\, k = 8.25 \cdot 10^{-4}$ m/sec.

Additionally, concerning the compressibility of water, the excess pore pressure buildup is slightly overestimated when adopting a fluid bulk modulus of de-aired water equal to $2 \cdot 10^6$ kPa, which corresponds to a saturation ratio $S_r \approx 100\%$, given that full saturation is practically unlikely to be achieved in centrifuge tests (e.g., Dashti and Bray, 2013; Shahir and Pak, 2010). On this basis, a fluid bulk modulus of water equal to $4 \cdot 10^5$ kPa was adopted here, which corresponds to an average saturation ratio $S_r \approx 99\%$ (Dashti and Bray, 2013). Finally, additional local damping of 2% was considered in the dynamic analyses in order to account for the approximately zero hysteretic damping simulated by any constitutive model at the very small strains.

Figure 6.4 compares the time-histories of generated excess pore pressure ratio $r_u = \Delta u/\sigma_{v,o}$ between the measured values with pore pressure transducers of the experiment and the numerical results. The quantity Δu refers to the generated excess pore pressure, while $\sigma_{v,o}$ to the vertical effective stress of the initial geostatic stress field before shaking. It should be noted that for all cases presented in this Thesis, as the experimental data are given in

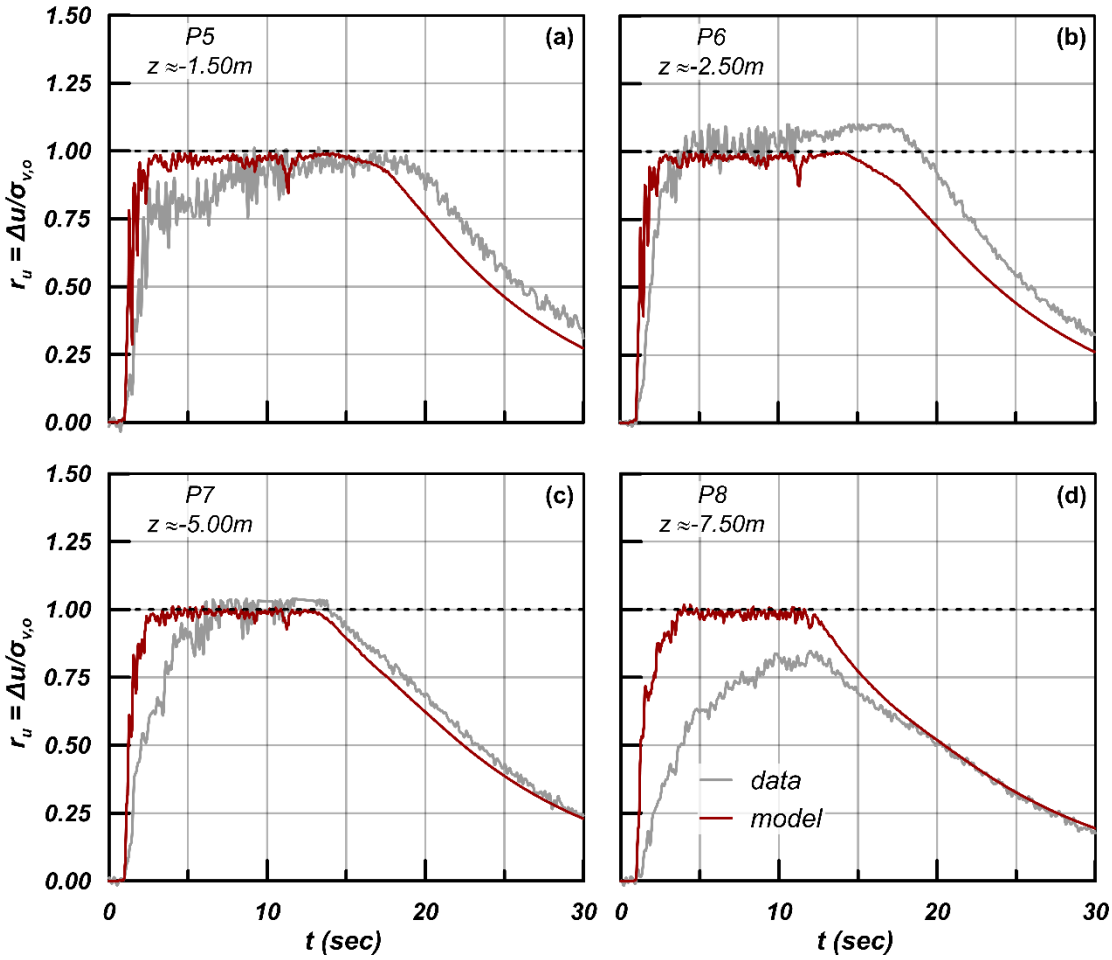

***Figure 6.4**: Experimental results and model estimates of excess pore pressure ratios, r_u, at various depths along the axis of VELACS Model test No.1. Data after Taboada and Dobry (1994a).*

terms of generated excess pore pressures, the same $\sigma_{v,o}$ - derived from the numerical analysis - is used for expressing both experimental and numerical results in terms of r_u. Comparisons are presented for the three indicative locations of transducers P5 (subplot **6.4a**), P6 (subplot **6.4b**), P7 (subplot **6.4c**) and P8 (subplot **6.4d**), which are installed at depths $z \approx$ -1.5 m, -2.5 m, -5.0 m along the axis of the model, with z counting from the ground surface. The ruby-red lines refer to the results derived numerically, while the gray lines refer to the experimental results. In general, the comparison is satisfactory. Though numerical results exhibit a faster pore-pressure buildup, both recordings and simulations reach $r_u \approx 1$, for shallow depths z, in the first few seconds and remain in this liquefied state until the end of shaking. However, it should be noted that the model estimates liquefaction even for the deepest position (P8), in contrast to the experiment where this depth does not

seem to liquefy (maximum $r_u \approx 0.8$). Moreover, the rates of pore-pressure dissipation are quite well captured by the model for all depths, although the draining process initiates earlier in the numerical simulations.

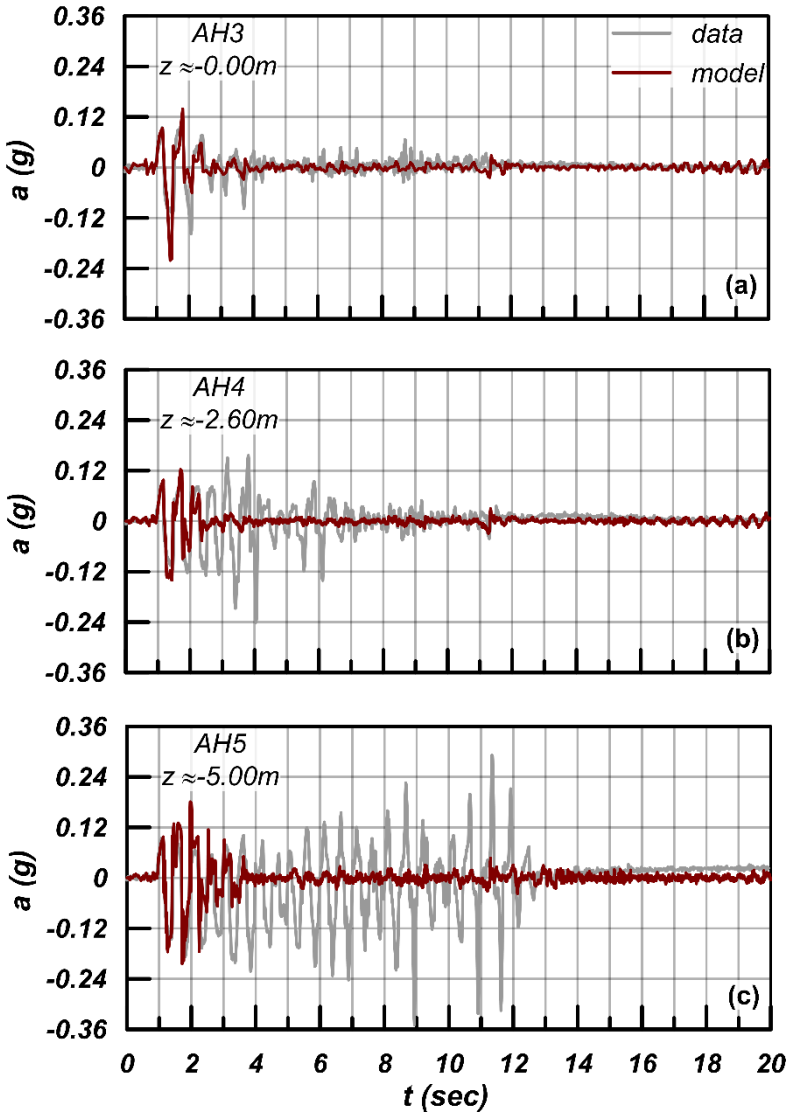

***Figure 6.5**: Experimental results and model estimates of the horizontal acceleration at various depths at the axis of VELACS Model test No.1. Data after Taboada and Dobry (1994a).*

Subsequently, **Figure 6.5** shows a comparison between the recorded (gray lines) and the numerical (ruby-red lines) horizontal acceleration time-histories at the locations of accelerometers AH3, AH4 and AH5 at the center of the mesh. The depths of the accelerometers are $z \approx 0.0$ m, -2.6 m and -5.0 m respectively. Here, the numerical results after $t = 2$ sec, show a more intense and faster attenuation of the motion. This is a

consequence of the higher r_u values already obtained in the first seconds of the shaking in the numerical analysis. This attenuation due to liquefaction is a well-established finding in the literature (e.g., Bouckovalas et al., 2016; Kokusho, 2014; Taiebat et al., 2010). However, once liquefaction is reached according to recordings, experimental and numerical results are in a good agreement. The comparison becomes less accurate as the depth z increases, as the model estimates generally higher r_u values for depths z greater than 5.0 m.

Finally, **Figure 6.6** compares the value of the free-field settlement recorded during the experiment with LVDT1 and that estimated by the model. Here, the numerical results are far from the data, with numerical results underestimating the measured settlement by approximately one order of magnitude. This is a well- known limitation of stress-ratio driven constitutive models, in which a constant stress-ratio stress path leads to zero plastic straining. In this test, the large settlement of ground surface in free-field conditions is not induced by shearing, but is due to the development of intense plastic volumetric strains caused by post-liquefaction consolidation. To account for plastic volumetric strains developed due to such types of loading, additional mechanisms for plastic strain rate development may be considered (e.g., Taiebat and Dafalias, 2008 or Wang et al., 1990). However, such formulations were beyond the scope of the constitutive model presented here, as discussed already in **Chapter 3**, and were not adopted in its formulation.

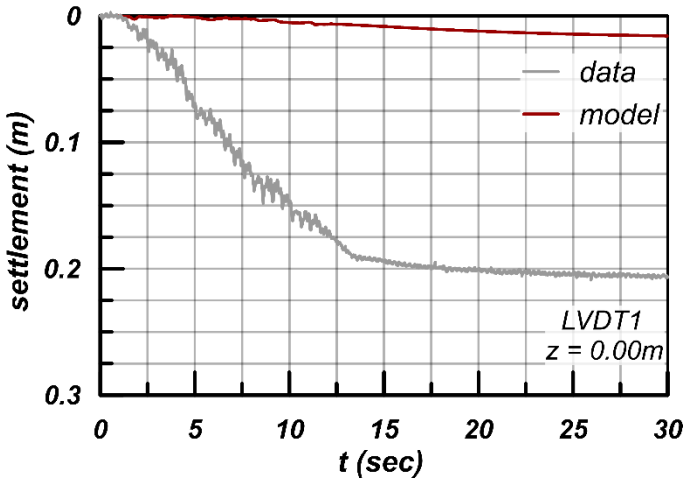

Figure 6.6: *Experimental measurement and numerical estimate of the ground surface free-field settlement at the axis of VELACS Model test No.1. Data after Taboada and Dobry (1994a).*

6.2.1 Effect of varying permeability coefficient with time

So far, the applied methodology - which is considered as the default methodology for this problem - adopts the permeability coefficient value *k*' as described above and maintains it constant with time. Now, a second scenario is analyzed here, according to which a variation of the permeability coefficient occurs with time, as this is a common assumption in the literature for the numerical analysis of Model test No. 1 of the VELACS project. In the literature, it has been shown that the permeability coefficient of sand increases during

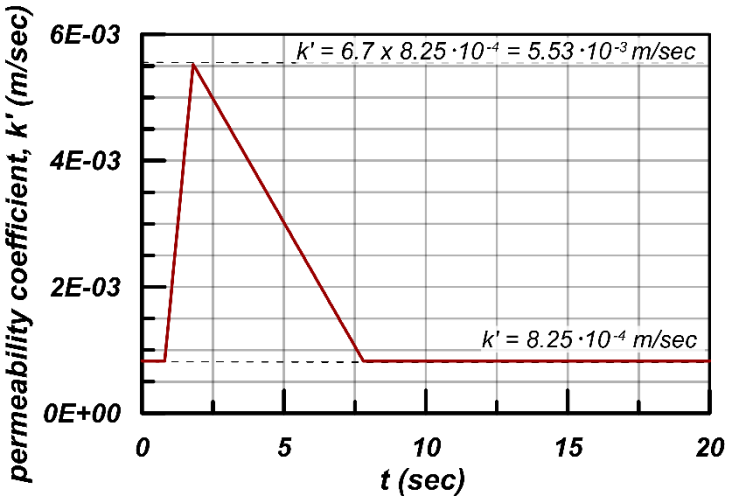

Figure 6.7: *Time-history of varying permeability coefficient with time.*

liquefaction (e.g., Arulanandan and Sybico, 1992; Jafarzadeh and Yanagisawa, 1995; Shahir and Pak, 2010; Taiebat et al., 2007). Arulanandan and Sybico (1992) investigated the change of sand fabric during liquefaction and correlated the maximum increase of permeability coefficient with the occurrence of initial liquefaction, when the soil particles lose their contacts and hence, flow paths increase. These findings were incorporated by Manzari and Arulanandan (1994) in the numerical analysis of Model test No. 1 of the VELACS project, where the initial permeability coefficient increases rapidly, as the soil approaches initial liquefaction, and then it decreases more smoothly to its initial value. This concept was also adopted by Andrianopoulos et al. (2010a) for Model test No. 1 and is examined also here in a similar way. Specifically, the value *k*' of permeability coefficient was increased up to 6.7 times, as the soil approaches initial liquefaction (at t = 1.8 sec in

this problem) and then it decreases again to k' (at t = 7.8 sec). The time-history of k' is presented in **Figure 6.7**.

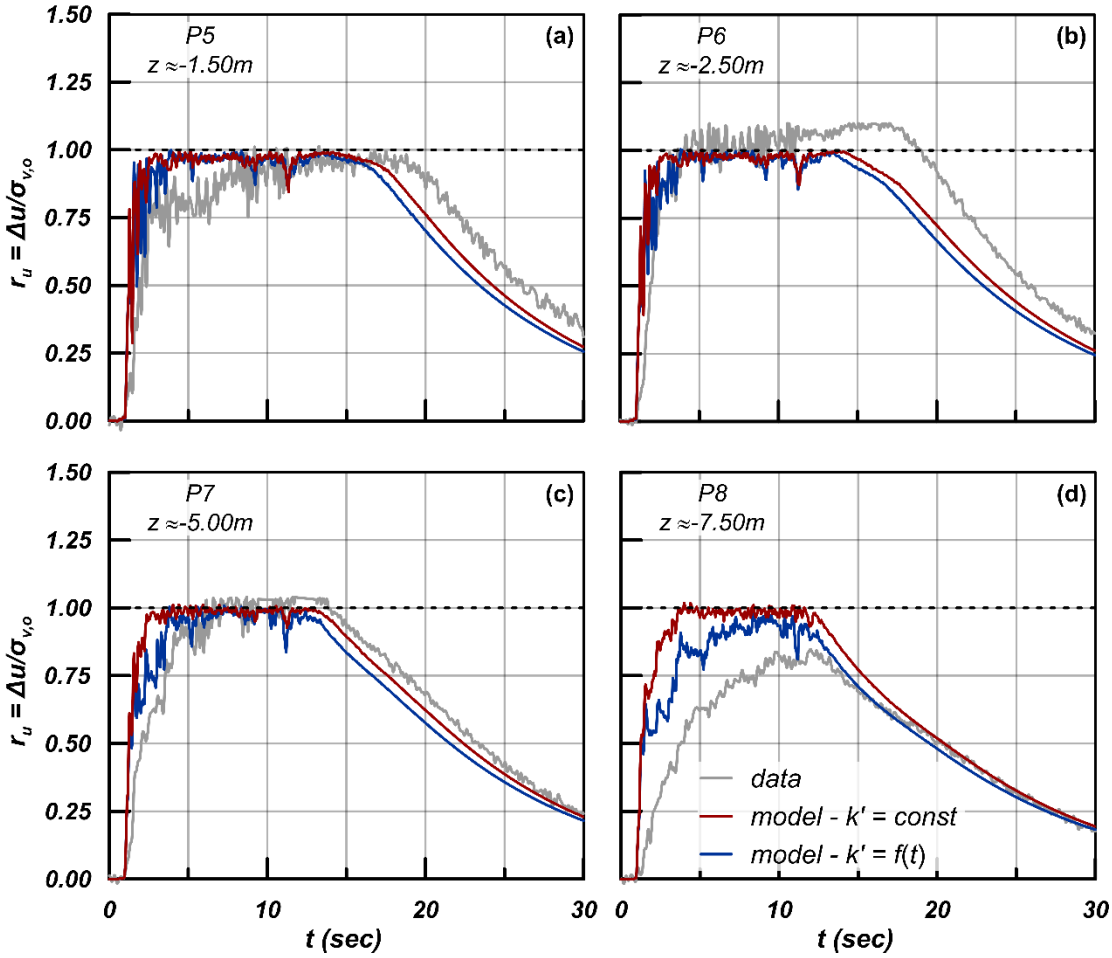

***Figure 6.8**: Experimental results and model estimates of excess pore pressure ratios, r_u, for two examined permeability coefficient scenarios, at various depths along the axis of VELACS Model test No.1. Data after Taboada and Dobry (1994a).*

In **Figure 6.8, Figure 6.4** is repeated with a comparison between the two examined scenarios of k'. The ruby-red lines refer to the results derived assuming constant permeability coefficient (k') with time, while the navy-blue lines refer to the scenario with varying permeability coefficient with time (k' = $f(t)$ – according to time-history of **Figure 6.7**). In the case where k' varies with time, there is a delay at the pore-pressure buildup, especially at the larger depths. Specifically, for greater absolute values of z the numerical results with varying permeability coefficient are closer to the data, as the higher permeability coefficient prevents full liquefaction. Moreover, it is shown that after shaking the rate of dissipation is slightly higher when k' varies with time.

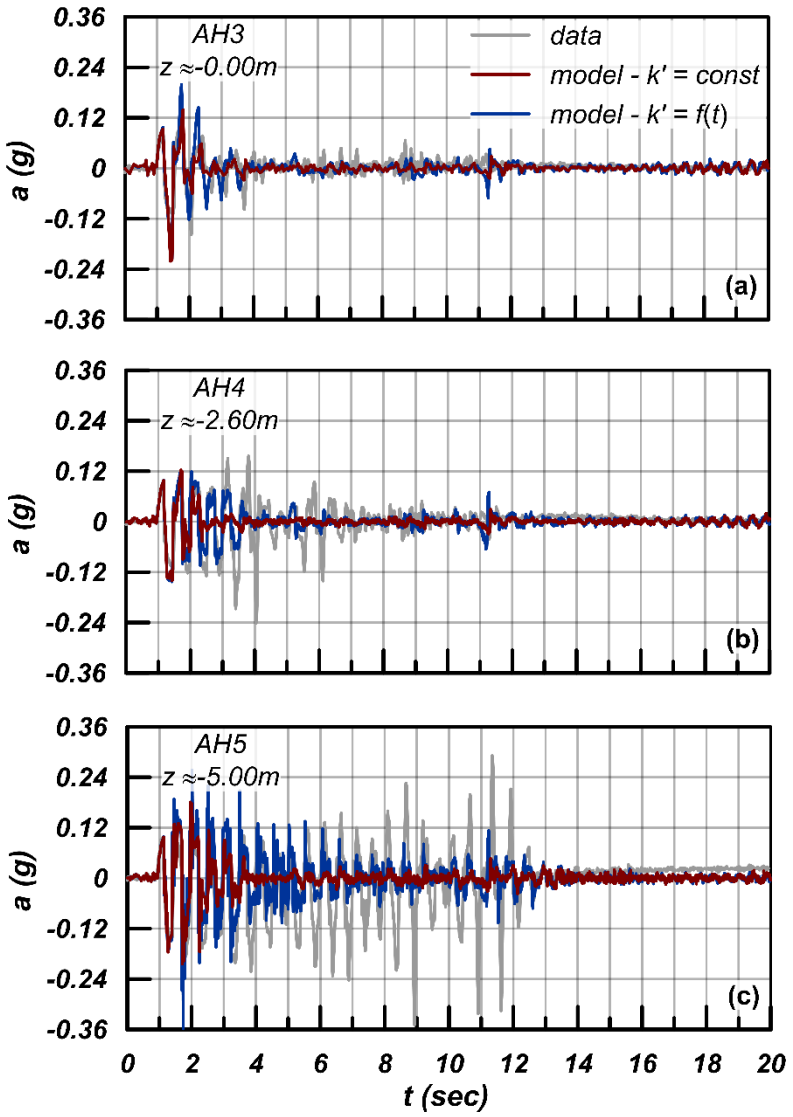

***Figure 6.9**: Experimental results and model estimates of the horizontal acceleration, for two examined permeability coefficient scenarios, at various depths at the axis of VELACS Model test No.1. Data after Taboada and Dobry (1994a).*

Subsequently, in **Figure 6.9** a comparison is made between the effects of two permeability coefficient scenarios on the acceleration time-histories. Again, the ruby-red lines refer to a constant *k*' with time, while the navy-blue to a varying *k*'. In case of a varying *k*', the attenuation observed in **Figure 6.5** is not so intense, as the r_u values are generally smaller for this case. This is better depicted at greater depths, e.g., at *z* = -7.50 m, where the liquefaction is not attained by adopting a varying permeability coefficient, which also leads to a time-history of horizontal acceleration very close to the experimental.

Finally, **Figure 6.10** compares the value of the free-field settlement recorded during

the experiment with LVDT1 and that estimated by the model for the two permeability coefficient scenarios. In case of $k' = f(t)$, the estimated settlement is slightly larger due to the contribution of enhanced drainage. However, the estimates still significantly remain far from the data due to the limitation of the employed constitutive model.

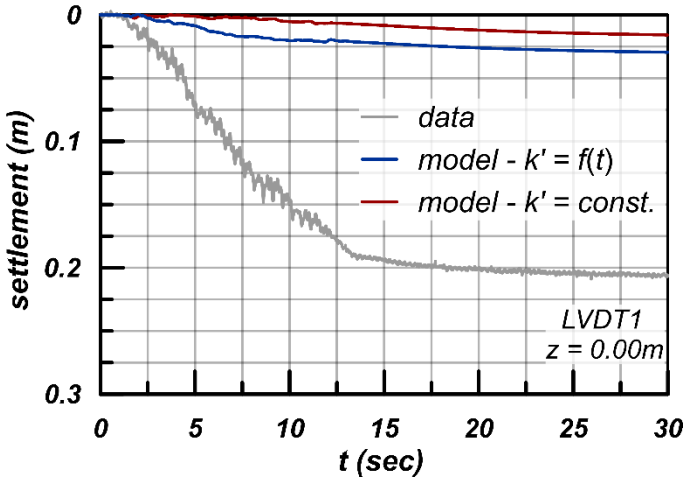

Figure 6.10: *Experimental results and model estimates of the ground surface free-field settlement, for two examined permeability coefficient scenarios, at the axis of VELACS Model test No.1. Data after Taboada and Dobry (1994a).*

6.3 Case 2: Seismic response of mildly-sloping liquefiable layer – VELACS 2

The model's ability to simulate the seismic response of a mildly-sloping liquefiable soil layer undergoing lateral spreading is verified against the experimental data of centrifuge Model test No. 2 of the VELACS project (Taboada and Dobry, 1994b). The layout is quite similar to that of Model test No.1. In prototype scale, a 10 m deep Nevada sand layer of approximately 40% relative density is examined and the model was built into a laminar box, where the water table was set 1 m above the ground surface. The only difference is that, in this test, the box was tilted by 2^o towards the clockwise direction thus inducing an equal mild inclination of the ground surface. This enables the investigation of the response of a laterally spreading liquefied soil layer (**Figure 6.11**). The input motion was applied at the base of the box and consisted of approximately 20 cycles with a duration of almost 13.5 sec, with a peak horizontal acceleration of almost 0.23g and a predominant frequency of 2Hz, whose time-history is plotted in **Figure 6.12**. It should be noted that the motion was baseline corrected, so as to result in a practically zero displacement of the base at the end of shaking. The response of the inclined liquefiable ground was monitored along the axis

of symmetry of the box, as well as closer to the boundaries, with the installation of accelerometers, pore pressure transducers and LVDTs measuring displacements. The model was spun up to a 50g centrifugal acceleration and water was used as a pore fluid.

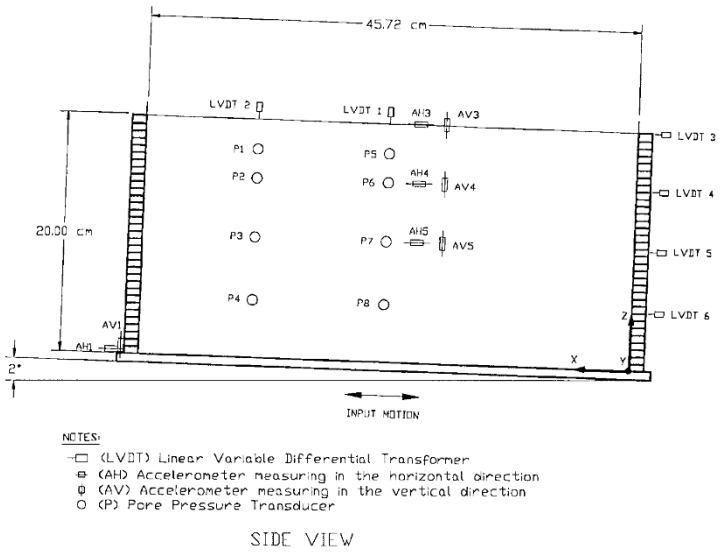

Figure 6.11*: Experimental setup of Model test No. 2 of the VELACS project (figure after Taboada and Dobry, 1994b).*

The finite-difference grid used for the numerical analysis has the same discretization as in Model test No.1 in Figure 6.13, along and with the location of a number of selected instruments is plotted on **Figure 6.13**. Given the overall similarities, the modeling procedure for this test in termsof dynamic boundary conditions (tied nodes), pore fluid modulus (4 x 105 kPa), local damping (2%) are identical to those for Model test No.1 and needn't be repeated here. The actual inclined stress field in this test was induced by applying an extra horizontal gravitational component, which in combination with the vertical one, reproduce the inclined stress field. Hence, the resultant vector of gravity is rotated towards the counterclockwise direction by 2^{o}. Moreover, a slightly smaller initial value of void ratio is adopted, as there was a variance of the relative density of the sand into the box after consolidation (Taboada and Dobry, 1994b). The finally selected value of void ratio e = 0.724 refers to the average between the referenced values of D_r = 40 % and 45% (Arulmoli et al., 1992; Taboada and Dobry, 1994b). For the permeability coefficient the default scenario of constant k' with time is only investigated.

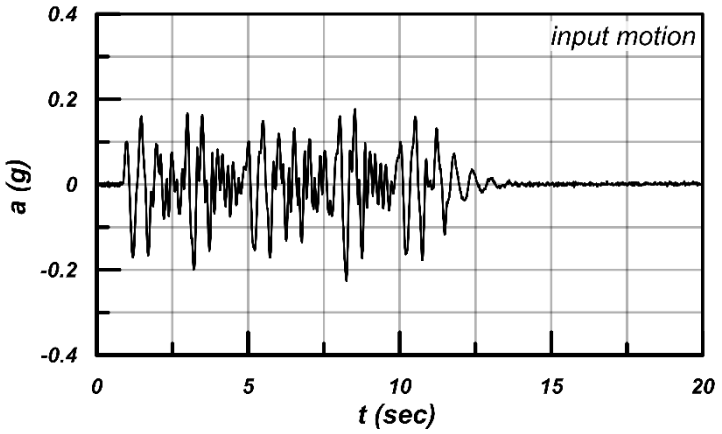

***Figure 6.12**: Baseline corrected applied motion at the base of the model (data after Taboada and Dobry, 1994b).*

Figure 6.14 presents a comparison of the time-histories of excess pore pressure ratio r_u between the measured values and the estimated numerical results. Comparisons are presented for the four indicative locations of pore pressure transducers P5, P6, P7 and P8 at the axis of the grid, which correspond to the depths $z \approx$ -1.5 m, -2.5 m, -5.0 m and -7.5 m, with z counting from the ground surface. The ruby-red lines refer to the results derived numerically, while the gray lines refer to the experimental results. The numerical results are again, in general, satisfactory. Though numerical estimates exhibit a faster pore-pressure buildup, both recordings and simulations reach values of $r_u \geq 0.95$ in the first few seconds and maintain this state up to 13.5 sec. However, the model results experience more intense dilation spikes throughout the shaking, which eventually result in an earlier drop of r_u with time. Unlike what was observed for the horizontal ground of Model test No.1, even a very mild ground inclination - like in in this test - in combination with the generated excess pore pressures and potential liquefaction cause significant non-symmetrical shear strain accumulation and an eventual lateral displacement of the soil layer. As a result, soil experiences dilative response, especially at the lower depths of the layer. Moreover, the post-shaking rates of pore-pressure dissipation are quite well captured for all depths by the model, with the draining process initiating a little bit earlier in the numerical simulations, as in Model test No.1.

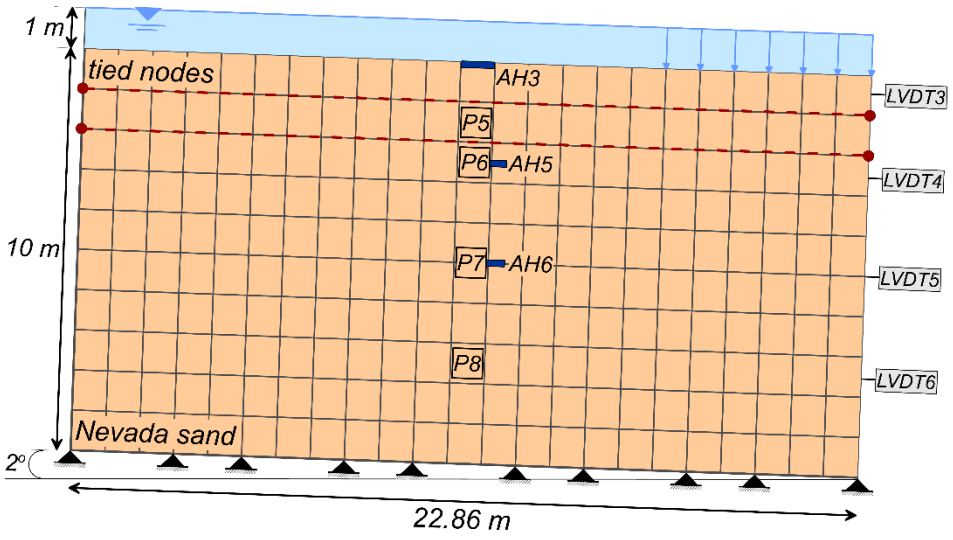

***Figure 6.13**: Layout of the numerical model - Model test No. 2 of the VELACS project.*

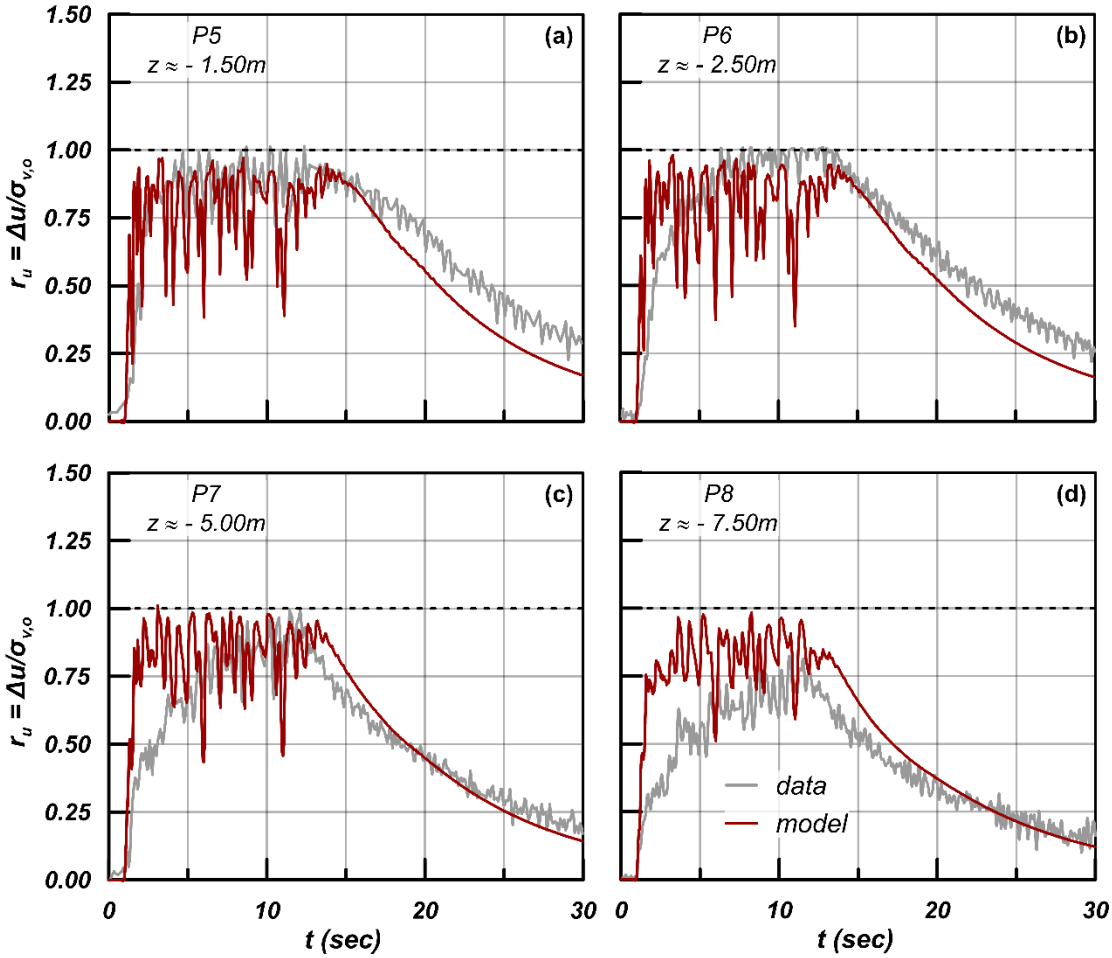

***Figure 6.14**: Experimental results and model estimates of excess pore pressure ratios, r_u, at various depths along the axis of VELACS Model test No.2. Data after (Taboada and Dobry 1994b).*

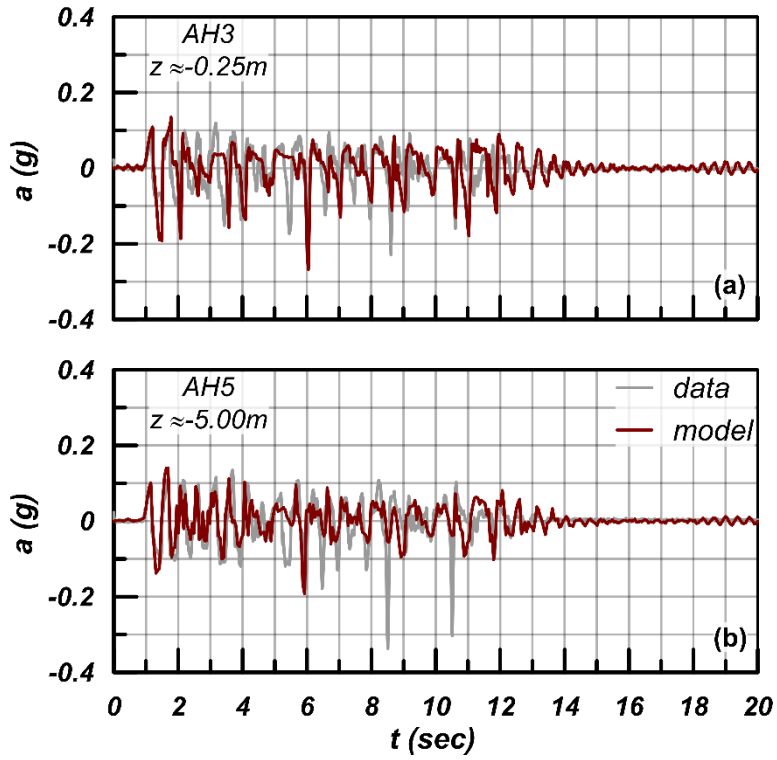

***Figure 6.15**: Experimental results and model estimates of the horizontal acceleration at various depths at the axis of VELACS Model test No.2. Data after (Taboada and Dobry, 1994b).*

In the sequel, **Figure 6.15** shows a comparison between the recorded (gray lines) and the measured (ruby-red lines) horizontal acceleration time-histories at the locations of accelerometers AH3 and AH5 at the axis of symmetry of the grid. The depths of the accelerometers are $z \approx$ -0.25 m and -5.0 m respectively. Generally, there is a satisfactory agreement, as both the experimentally recorded accelerations and those estimated by the model show a comparable de-amplification, in relation to the applied acceleration time-history at the bottom of the mesh. This de-amplification is due to the generated excess pore pressures and is observed in both examined depths. Moreover, it should be noticed that, in this test, the motion has not totally nullified, unlike in Model test No.1, despite that liquefaction has occurred. The intense dilation in this test, is attributed to the tendency of the soil to spread laterally towards the downslope side, since high excess pore pressures have been generated and the soil's shearing resistance has diminished. This intense dilative response prevents the total attenuation of the motion and is fairly well captured by the model. Finally, the numerical time-histories maintain a small value after the time of 13.5 seconds, in contrast to the recording, as the estimated r_u values start dissipating earlier than

in the test. This small residual vibration in the analysis gradually fades with time as the input motion has already ceased.

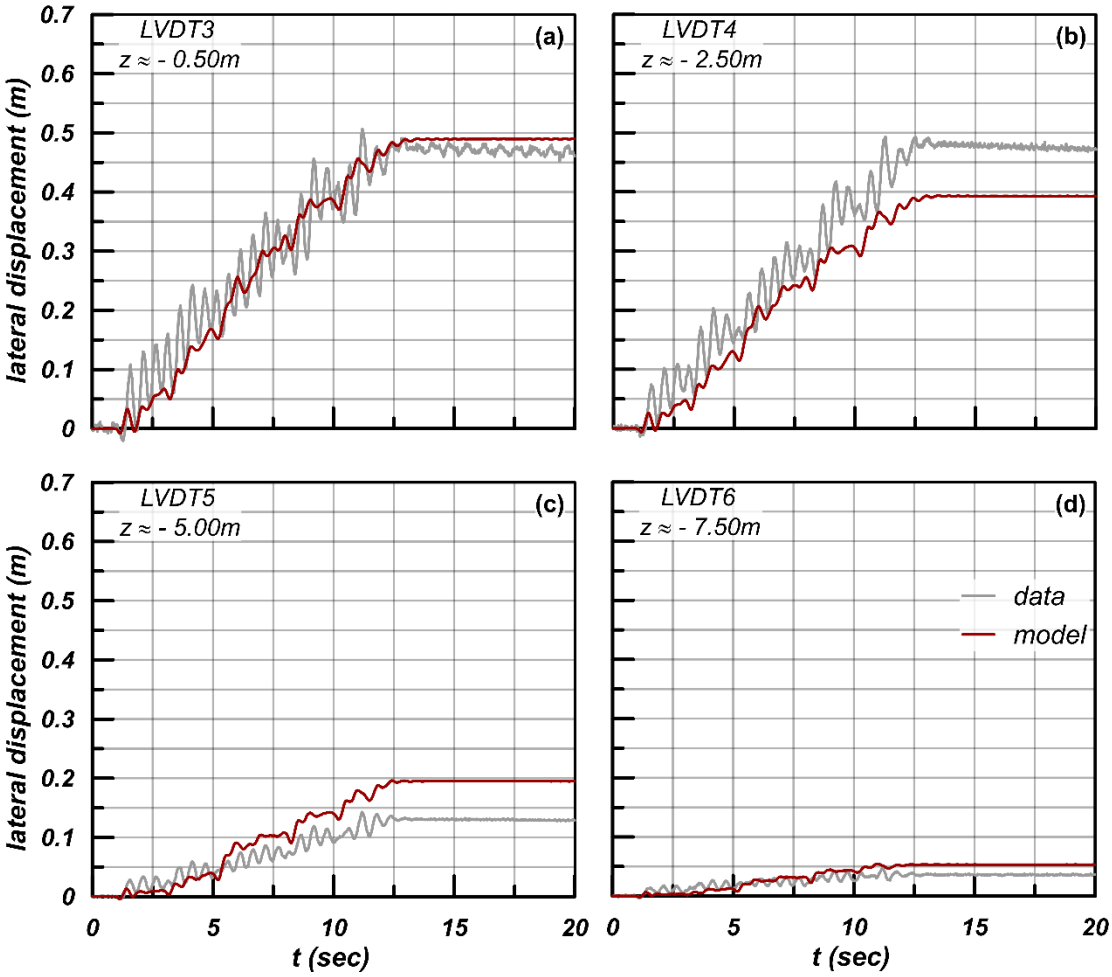

***Figure 6.16**: Experimental results and model estimates of the lateral displacement of soil layer at various depths along the right edge of VELACS Model test No.2. Data after (Taboada and Dobry, 1994b).*

Subsequently, **Figure 6.16** compares the time-histories of induced lateral displacements measured during test with those estimated by the numerical analysis. The results refer to the locations of transducers LVDT3 (subplot **6.16a**), LVDT4 (subplot **6.16b**), LVDT5 (subplot **6.16c**) and LVDT6 (subplot **6.16d**). Again, the gray lines refer to the experimental data, while the ruby-red lines refer to model results. According to the experimental results, the lateral displacement accumulates practically linearly with time, and this is well captured also by the model. Exception is the depth z = -2.50 m, where the the measured lateral displacement is practically equal to that of *z* = 0.00 m, while the model

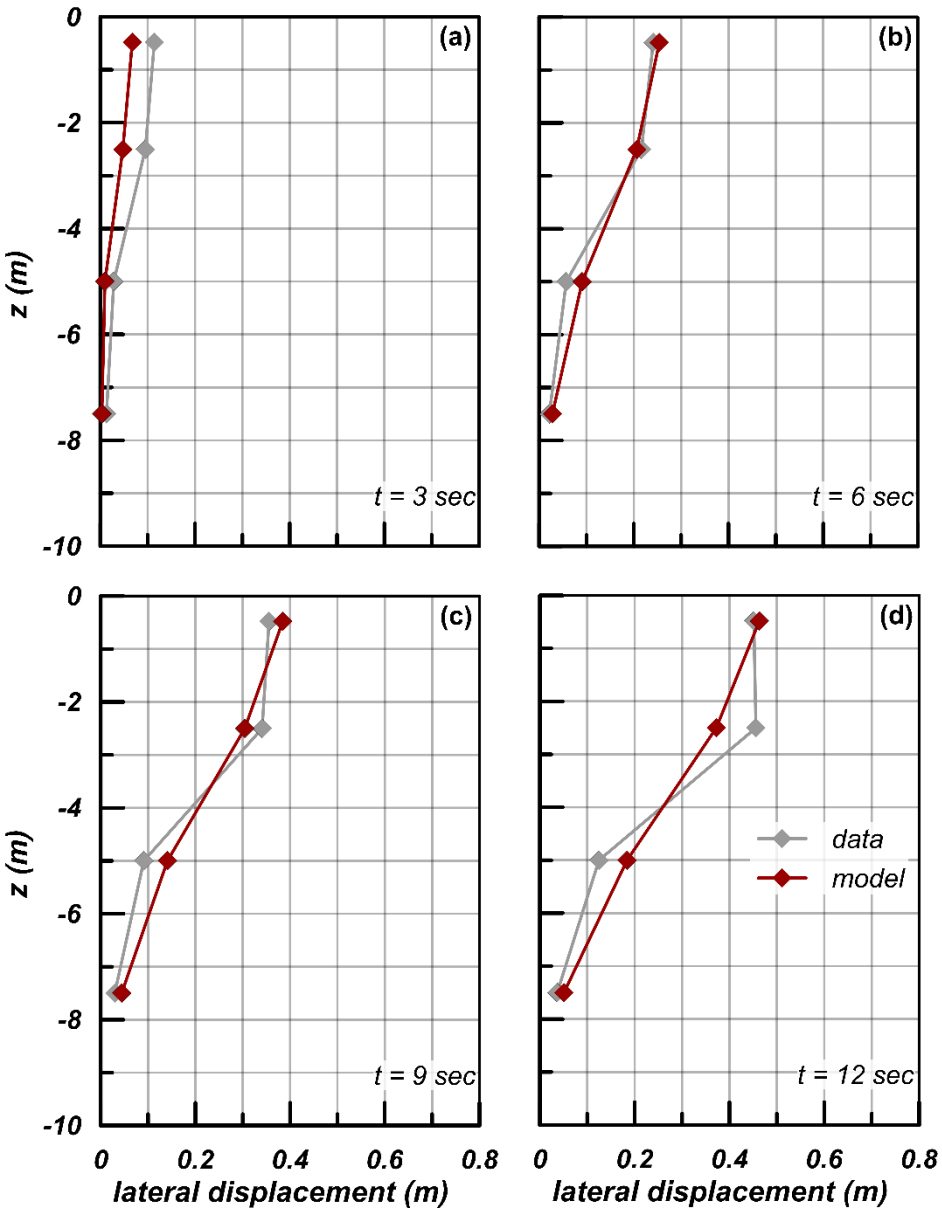

Figure 6.17: *Experimental results and model estimates of snapshots of the lateral displacement of the soil layer along the right edge of VELACS Model test No.2 at various time moments. Data after (Taboada and Dobry, 1994b).*

estimates decreasing displacement with depth and hence, a lower displacement for z = -2.50 m. Moreover, as the depth of the examined locations increases, numerical results slightly overestimate the displacement, but the comparison is quite fair at the surface of the laterally spreading layer, where experimental and numerical results plot very close.

Figure 6.17 presents a comparison of the displacement data and the pertinent numerical results from a different perspective. Here, the lateral displacements are compared as snapshots along the axis of the whole liquefied layer at the specific time moments of t =

3 sec (subplot **6.17a**), 6 sec (subplot **6.17b**), 9 sec (subplot **6.17c**) and 12 sec (subplot **6.17d**). The comparison is generally satisfactory, with numerical results sightly overestimating the displacements at the lower depths (as already shown in **Figure 6.16**) and approaching them at the shallower locations.

Finally, **Figure 6.18** depicts a snapshot of contours of accumulated shear strains at the end of shaking, in order to gain insight on the deformation mechanism of the liquefied layer. The layer has been sheared, experiencing downslope lateral permanent displacement. Moreover, it is shown that the lateral deformation does not decrease linearly with depth, as the region at the middle of the layer has been sheared more intensively.

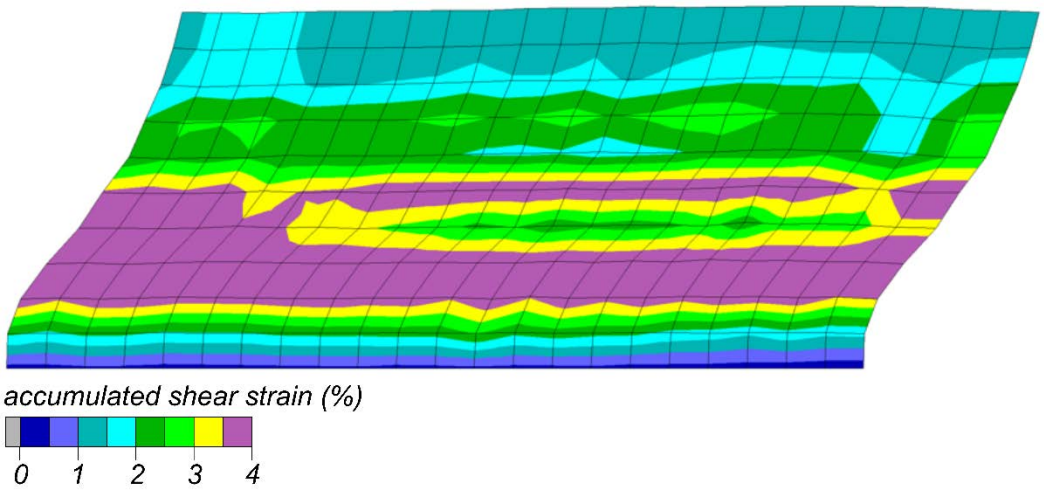

***Figure 6.18**: Contours of shear strain increment and deformed mesh at the end of shaking of VELACS Model test No.2.*

6.3.1 Effect of intensity of post-liquefaction shear strain accumulation

For this boundary value problem, a different scenario is also examined, this time in terms of the intensity of shear strain accumulation during the post-liquefaction phase. In the first scenario, which is considered as the default one, the value of the model parameter L_o – controlling the intensity of post-liquefaction shear strain accumulation (Equations (3.44) – (3.46)) – is the one calibrated against the experimental data for Nevada sand and is equal to 750. In the second scenario, a significantly higher value was selected for L_o (= 75000), so as the role of post-liquefaction strain accumulation feature and its intensity to be demonstrated.

In **Figure 6.19, Figure 6.14** is repeated with a comparison between the two examined scenarios for the value of model parameter L_o. The ruby-red lines refer to the use of the default calibrated value of L_o, while the navy-blue lines refer to the much higher value of L_o. In general, the results for the different values of L_o do not differ significantly. However, the response for L_o = 75000 exhibits more intense dilation spikes and the draining process initiates earlier in this case. This is justified by **Figure 6.20** in the sequel, where a comparison of the induced lateral displacements according the both examined scenarios of L_o is shown. As expected, the value of L_o = 75000 results in larger lateral displacements of the soil layer and this demonstrates the effect of post-liquefaction shear-strain accumulation intensity on the response. Namely, the higher the L_o, the larger the shear strain accumulation. Of particular inte rest is that the time - histories of displacements for both

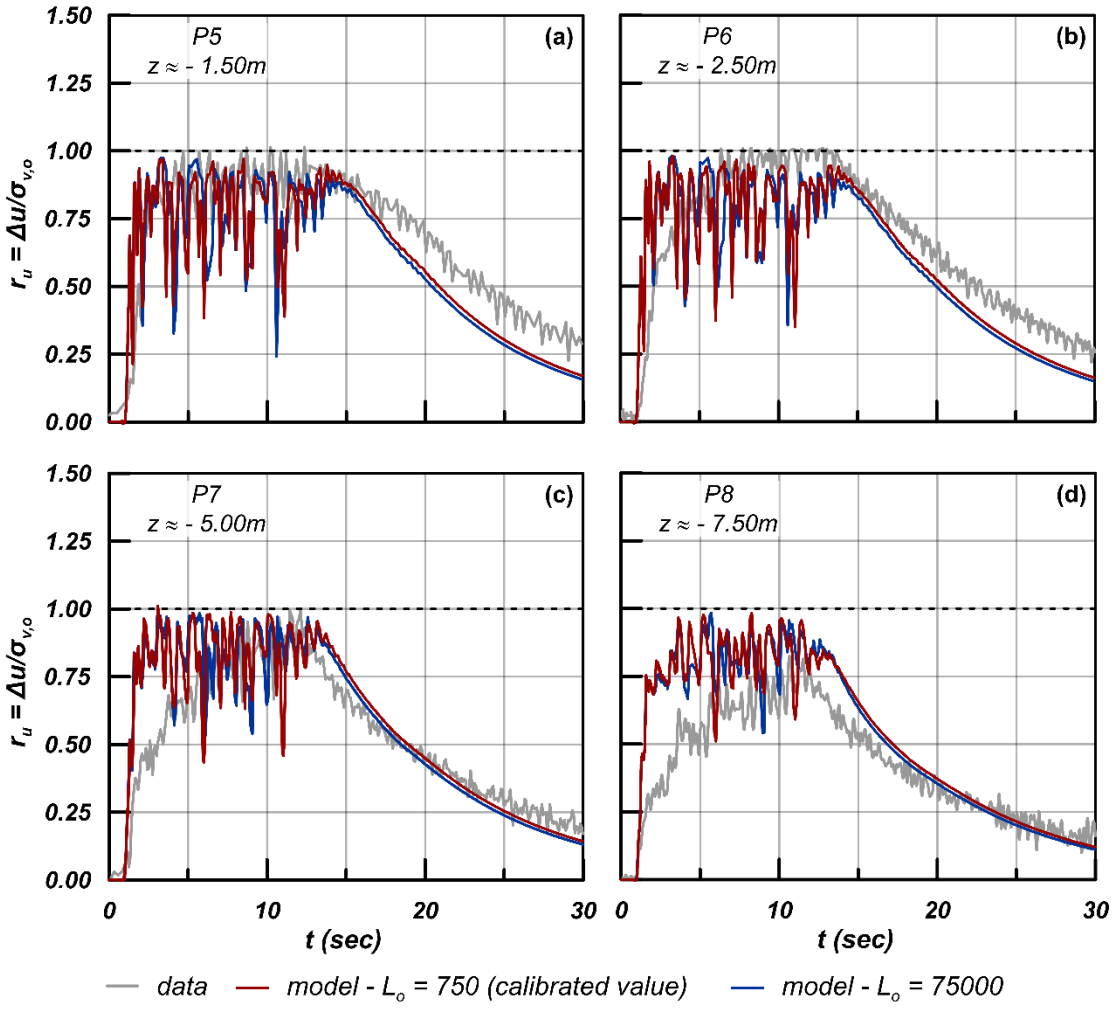

***Figure 6.19**: Experimental results and model estimates of excess pore pressure ratios, r_u, for two examined scenarios of model parameter L_o, at various depths along the axis of VELACS Model test No.2. Data after Taboada and Dobry (1994b).*

L_o = 750 and 75000 practically coincide until the moment of $t \approx 2$ sec, where r_u values obtain a value larger than 0.95 for the first time and initial liquefaction occurs. After that point, significant differentiation initiates. However, it should be noted that the increase of displacement – up to 100% difference if one considers all depths and all time instances – is not proportional to the increase of the value of L_o, thus indicating that this parameter is significant, but not crucial for the numerical modeling of the response.

Figure 6.21, illustrates the snapshots of lateral displacements of the liquefied soil layer vs depth for distinct time moments. Here, it is also clear that as the value of L_o increases the soil layer experiences more intense lateral displacement. This is also reflected on the contours of shear strain accumulation at the end of shaking in **Figure 6.22**.

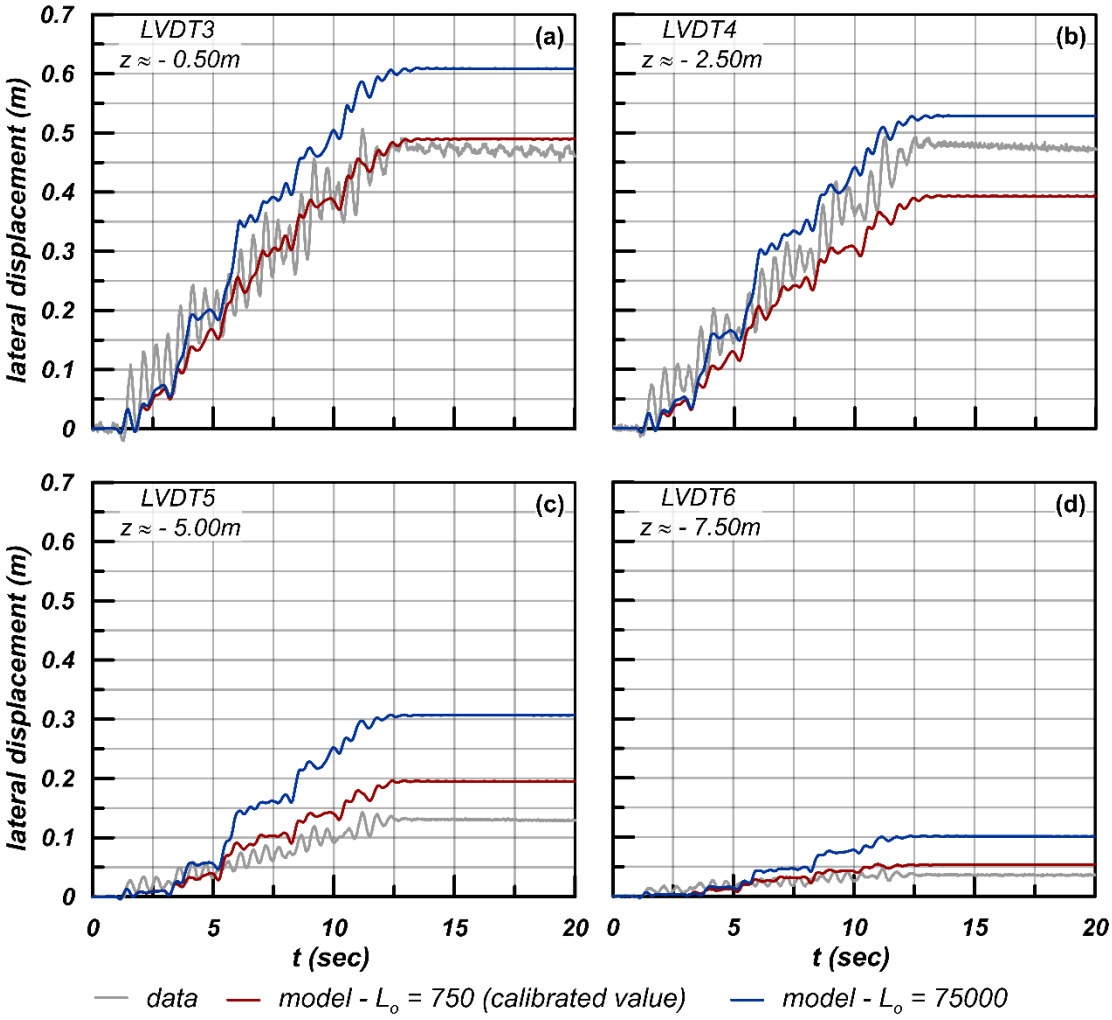

***Figure 6.20**: Experimental results and model estimates of lateral displacements for two examined scenarios of model parameter L_o, at various depths along the axis of VELACS Model test No.2. Data after Taboada and Dobry (1994b).*

Specifically, the strain accumulation is greater here with a maximum value close to 6% in the middle of the mesh, by comparing it to **Figure 6.18** where the calibrated, lower value of L_o was adopted and the maximum value was approximately 4%.

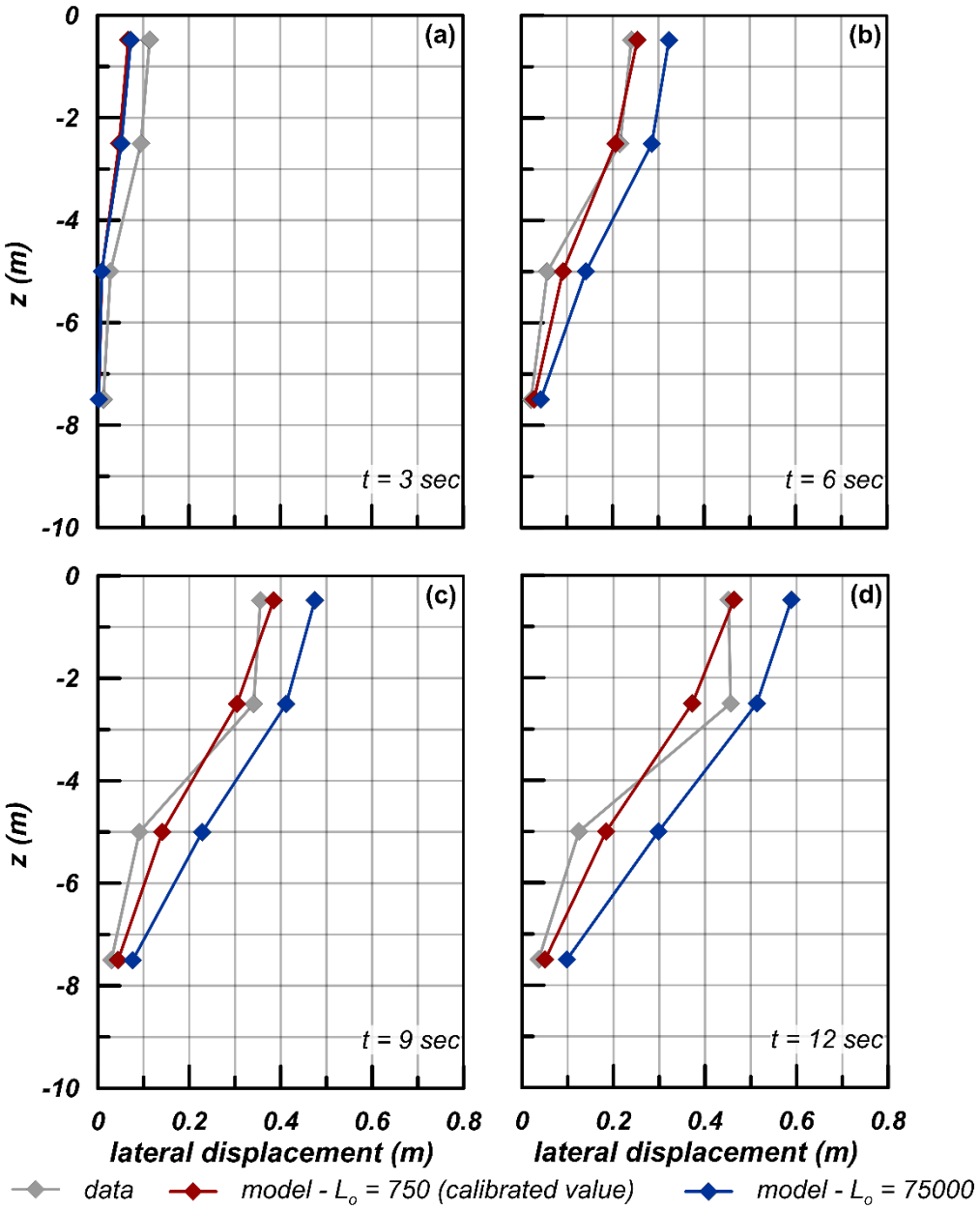

***Figure 6.21**: Experimental results and model estimates of lateral snapshots of displacements for two examined scenarios of model parameter L_o, at various depths along the axis of VELACS Model test No.2. Data after Taboada and Dobry (1994b).*

Finally, in **Figure 6.23** a comparison is made for the effects of the two scenarios of L_o in terms of acceleration time-histories. Again, the ruby-red lines refer to L_o = 750, while the navy-blue to L_o = 75000. The numerical results for the two different values of L_o are

generally close one to another, with the results with L_o = 75000 giving few more intense (unrealistic) spikes for the reasons already discussed above.

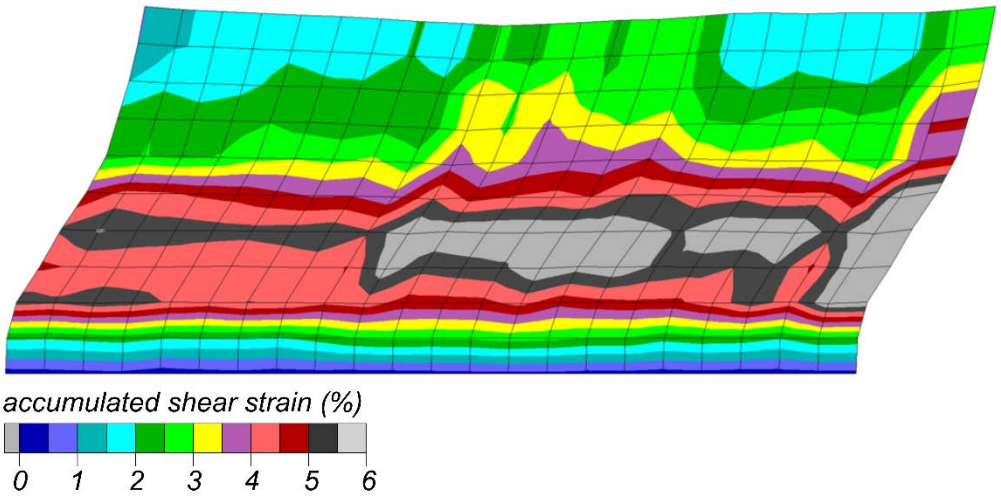

***Figure 6.22**: Contours of shear strain increment and deformed mesh at the end of shaking of VELACS Model test No.2 for the scenario of L_o = 50000.*

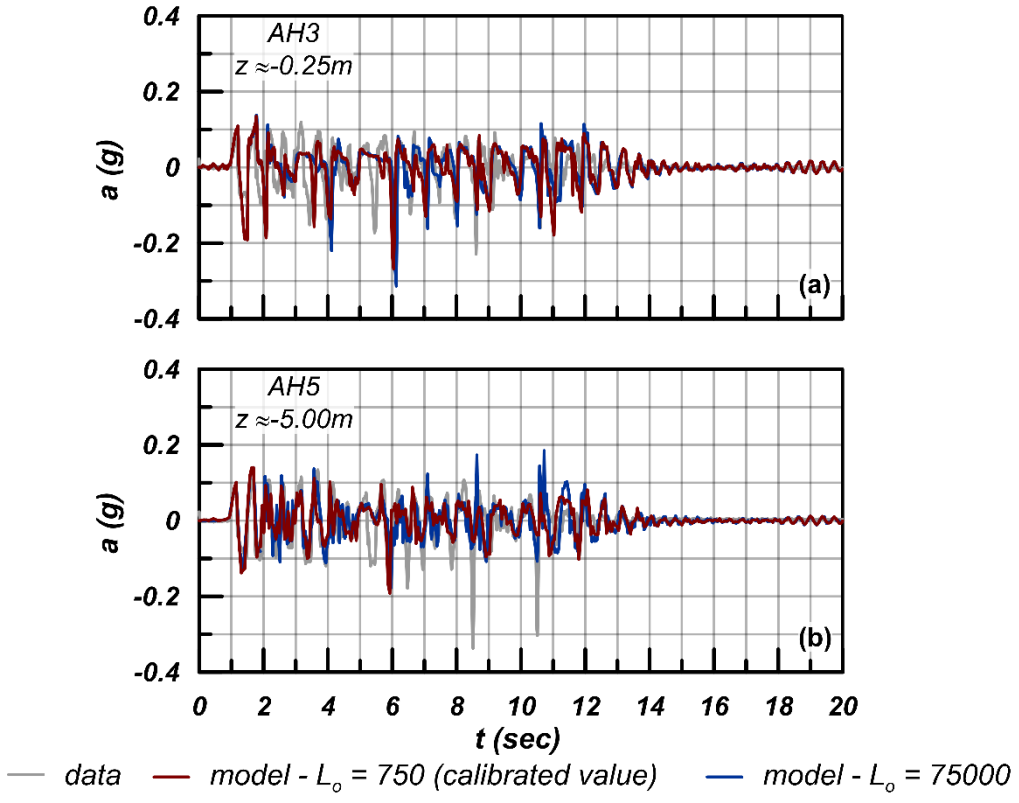

***Figure 6.23**: Experimental results and model estimates of the lateral acceleration for two examined scenarios of model parameter L_o, at various depths at the axis of VELACS Model test No.2Data after (Taboada and Dobry, 1994b).*

6.4 Case 3: Seismic response of shallow foundations on liquefiable layer

In the following paragraphs the ability of the model to simulate the typical structural response of a shallow footing founded on a liquefiable layer is validated through comparisons with experimental data from VELACS Model test No.12 (Carnevale and Elgamal, 1994; Farrel and Kutter, 1994; Krstelj and Prevost, 1994), as well as centrifuge experiments performed by Dashti et al. (2010a; b). For reasons of clarity, the pertinent simulations are presented in different paragraphs.

6.4.1 Validation against VELACS Model test No. 12

Firstly, the numerical analysis of VELACS Model test No.12 is presented. In prototype scale, a 6 m deep Nevada sand layer of approximately 60% relative density is examined. This liquefiable soil layer is overlaid by a 1m thick Bonnie silt layer, and the water table was set 1m above the surface of the silt. A rigid structure of square plan, with height equal to 4 m and width 3 m was founded 0.50 m below the interface of silt and sand. It was made out of aluminum and filled with lead shot, so as a bearing pressure of 150 kPa to be achieved. The model was built into a rigid box with internal dimensions of 28.2 m × 12.8 m (**Figure 6.24**) and was spun up to a 100 g centrifugal acceleration. The pore fluid used during test was water. The response of the soil-structure system was monitored with accelerometers located at different depths below the footing, pore pressure transducers,

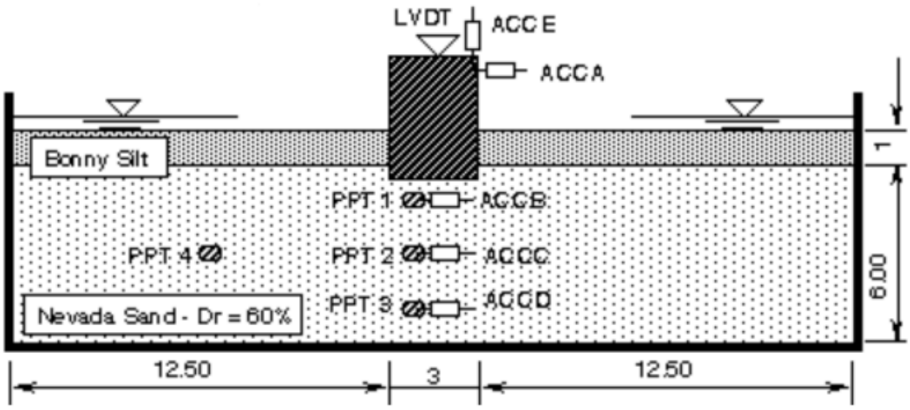

***Figure 6.24**: Experimental setup of Model test No. 12 of the VELACS project (Source: www.princeton.edu).*

placed both below the footing and at free field, and 1 LVDT placed on the top of the structure to measure its settlement. The original specifications defined a base input motion of almost 10 uniform cycles of 0.25g peak horizontal acceleration with a frequency of 2Hz. However, as this test was performed by 3 different research teams at 3 different universities (Carnevale and Elgamal, 1994; Farrel and Kutter, 1994; Krstelj and Prevost, 1994), a deviation from the target input motion was finally observed. Specifically, the applied peak ground acceleration, a_{max}, ranged from 0.21 g to 0.40 g and the average ground acceleration, a_{ave}, from 0.18 g to 0.34 g.

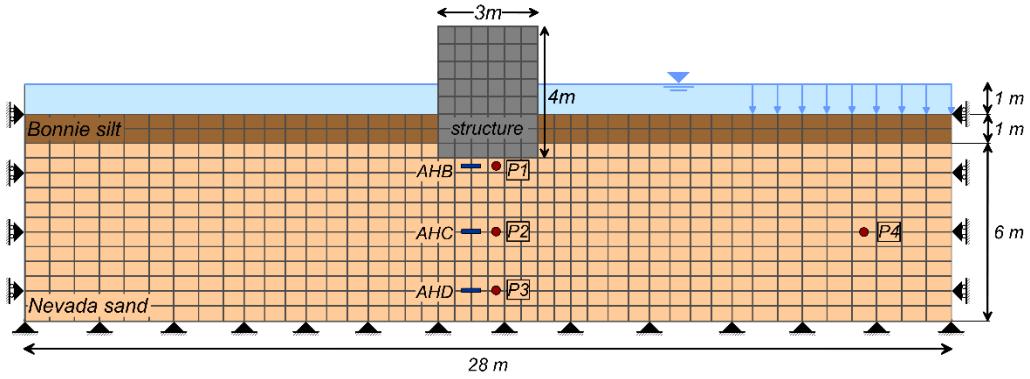

***Figure 6.25**: Layout of the numerical model - Model test No. 12 of the VELACS project.*

The modeling methodology follows also here the logic described by Andrianopoulos et al. (2010a). The numerical layout of the test and the arrangement of the measuring instruments selected to be used for the validation process are shown in **Figure 6.25**. The finite-difference grid used for the numerical analysis was not uniform, with the zone size varying from 0.75 m × 0.50 m far from the footing to 0.50 m × 0.50 m at the vicinity of the footing. A uniform sand layer was assumed with an initial void ratio equal to 0.668, corresponding to a $D_r \approx 60\%$. Both bottom and lateral boundaries of the mesh were forced to follow the time-history of the input ground acceleration, so as the kinematic constraints of the rigid box to be simulated. The vertical acceleration during the experiments was assumed as parasitic and was not taken account into the numerical simulation. At the lateral boundaries of the mesh, no restraint was considered in the vertical direction, thus not disallowing settlements. The input motion used for the simulation approaches the input motion of Test No.1 of RPI (Carnevale and Elgamal, 1994) and consists of 1 transitional cycle at the beginning of the motion, 10 main cycles with a peak ground acceleration of

0.26 g and a frequency of 2 Hz, and 7 transitional cycles at the end, as depicted in **Figure 6.26**. The existence of a 1m water above the ground surface was simulated by applying a uniform normal stress and a respective pore pressure equal to 9.81 kPa at the free ground surface, like in the previous cases. Lateral and bottom boundaries, but also the structure, were assumed impermeable, so water flow is permitted only towards the free surface of the soil in the model.

The simpler Ramberg and Osgood (1943) constitutive model was used to simulate the nonlinear hysteretic response of the Bonnie silt layer. As the Bonnie silt covers only a 1 m layer at the top of the soil profile, a low shear wave velocity equal to 60 m/sec was assumed for the calibration of elastic shear modulus, while the other parameters of the model were calibrated against the experimental shear modulus reduction and damping ratio curves of Vucetic and Dobry (1991) for a plasticity index equal to *PI* = 15%. However, it should be noted that this simplified approach for the simulation of this material is not expected to affect significantly the response of the structure, as the silt layer is placed at the top of the sand profile, it covers a small amount of the total height of the soil layer, the structure is not founded on it and given the generated excess pore pressure regime developed in Nevada sand layer, the resulting failure mechanism is not practically affected by this thin silt crust on its sides.

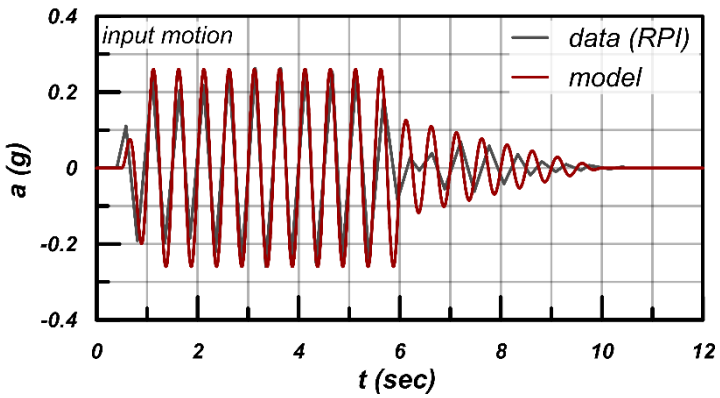

***Figure 6.26**: Applied motion at the base of the model (Carnevale and Elgamal, 1994).*

The structure was simulated as a rigid elastic block and the elastic parameters of aluminum (shear modulus equal to 29 GPa and bulk modulus equal to 39 GPa) were adopted. The unit weight of the superstructure was adjusted appropriately to reproduce the

target contact pressure. Since the performed analysis is two-dimensional (2D), assuming plane strain conditions, a possible reduction of the contact pressure induced by the structure should be examined to properly take into account the three-dimensional (3D) conditions under which the prototype test was carried out. Popescu and Prevost (1993) suggested that for the equivalent strip foundation a reduced value of the contact pressure should be considered, so as this pressure produces the same elastic static settlements in 2D plane strain conditions, as that produced by 150 kPa in 3D conditions. This was also adopted by Andrianopoulos et al. (2010a). In this study, this effect was taken into account in a similar way, by applying empirical relations from the literature for the calculation of elastic settlements of footings (e.g., Janbu et al., 1956). Specifically, the relation proposed by Janbu et al. (1956) was adopted, where the correlation between 2D and 3D geometry is expressed via the correction factors of Christian and Carrier (1978), where the dimensions and the depth of the compressible soil layer below the footing are considered. If L is the length of the footing and B its width, the comparison between the case of $L/B = 1$ (actual 3D conditions) and the case of $L/B \rightarrow \infty$, which corresponds to the applied 2D conditions of a strip footing, gives that the applied contact pressure should be reduced to the value of 120 kPa, so as the resulting settlements to be common in both cases. This result is taken by considering that the depth of the compressible soil layer below the footing, hereafter indicated as D, is approximately twice the width of the footing, as in the layout of the test (D = 5.5m versus B = 3m). Moreover, according to Itasca Consulting Group Inc. (2011), the real footing width in the numerical analysis is something larger than the designed footing width on the mesh, as the vertical component of the velocity vector developing, while the footing is settling, varies linearly from the value developed at the last gridpoint of the designed footing to zero at the next neighboring gridpoint of the mesh. This means that the "real" footing width may be considered equal to the designed width plus half the width of the zones on either side of the footing. In other words, the "real" footing width is 3.0 + 2x0.5/2 = 3.6 m. Hence, in order for the bearing load not to be overestimated, the applied pressure was appropriately reduced for this reason. The finally applied pressure was 102.85 kPa. Initially, the geostatic stress field is achieved assuming elastic response with a K_o value equal to 0.50, under static equilibrium, while the superstructure was constructed gradually in multiple steps. Then, coupled dynamic analysis was performed.

For a relative density of Nevada sand approximately equal to 60%, a permeability coefficient equal to $k = 5 \cdot 10^{-5}$ - $5.5 \cdot 10^{-5}$ m/sec is documented (Arulmoli et al., 1992). As in previous cases, to allow for an accurate simulation of the experiment performed at a 100 g centrifugal acceleration with water as a pore fluid, the adopted permeability coefficient was firstly scaled up by 100 and then decreased by a factor of 4 to account for the conflict between dynamic and diffusion times. The permeability coefficient of Bonnie silt was assumed equal to $2 \cdot 10^{-8}$ m/sec, while the structure was presumed practically impermeable. Similarly in this case, a fluid bulk modulus of water equal to $4 \cdot 10^{5}$ kPa was adopted, which corresponds to an average saturation ratio $S_r \approx 99\%$ (Dashti and Bray, 2013) and a local damping value of 2% was used.

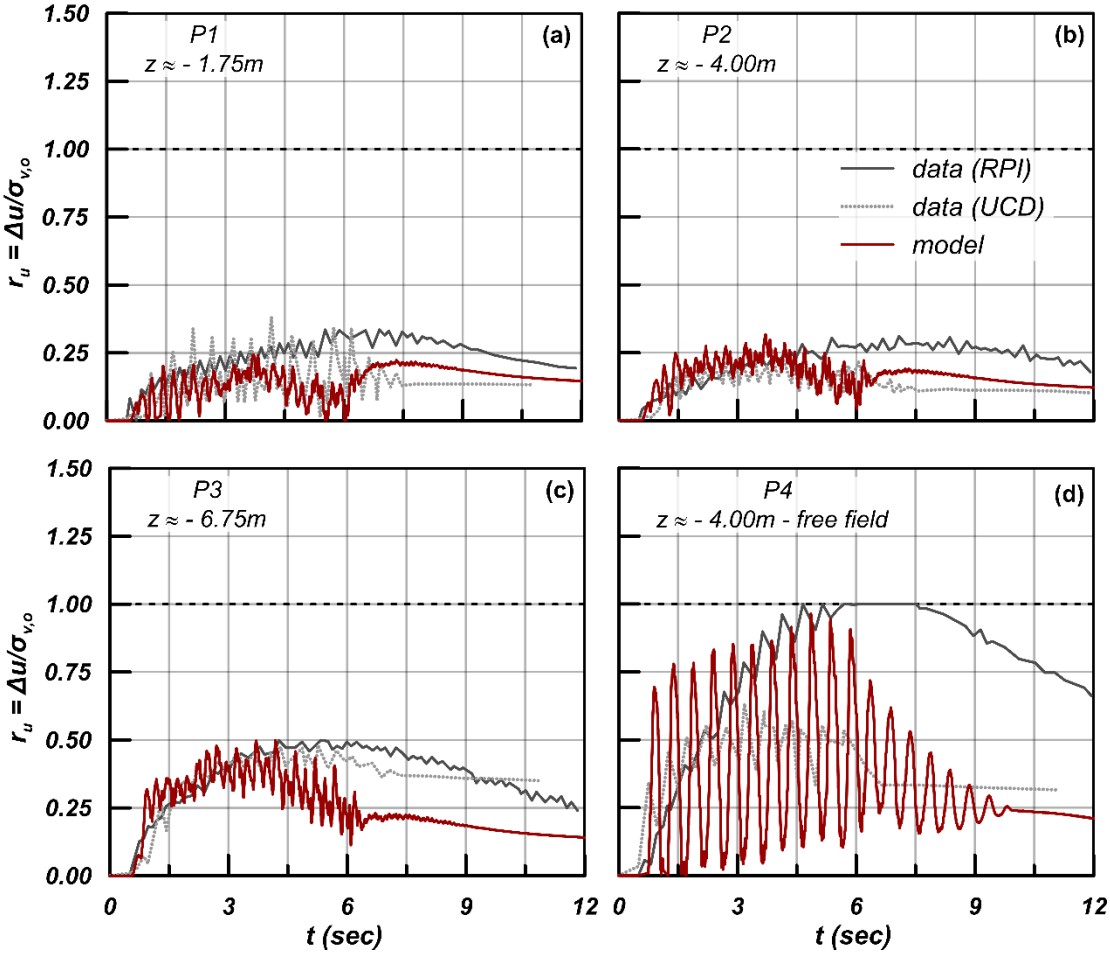

***Figure 6.27**: Experimental results and model estimates of excess pore pressure ratios, r_u, at various locations of VELACS Model test No.12. Data after Krstelj and Prevost (1994) and Carnevale and Elgamal (1994).*

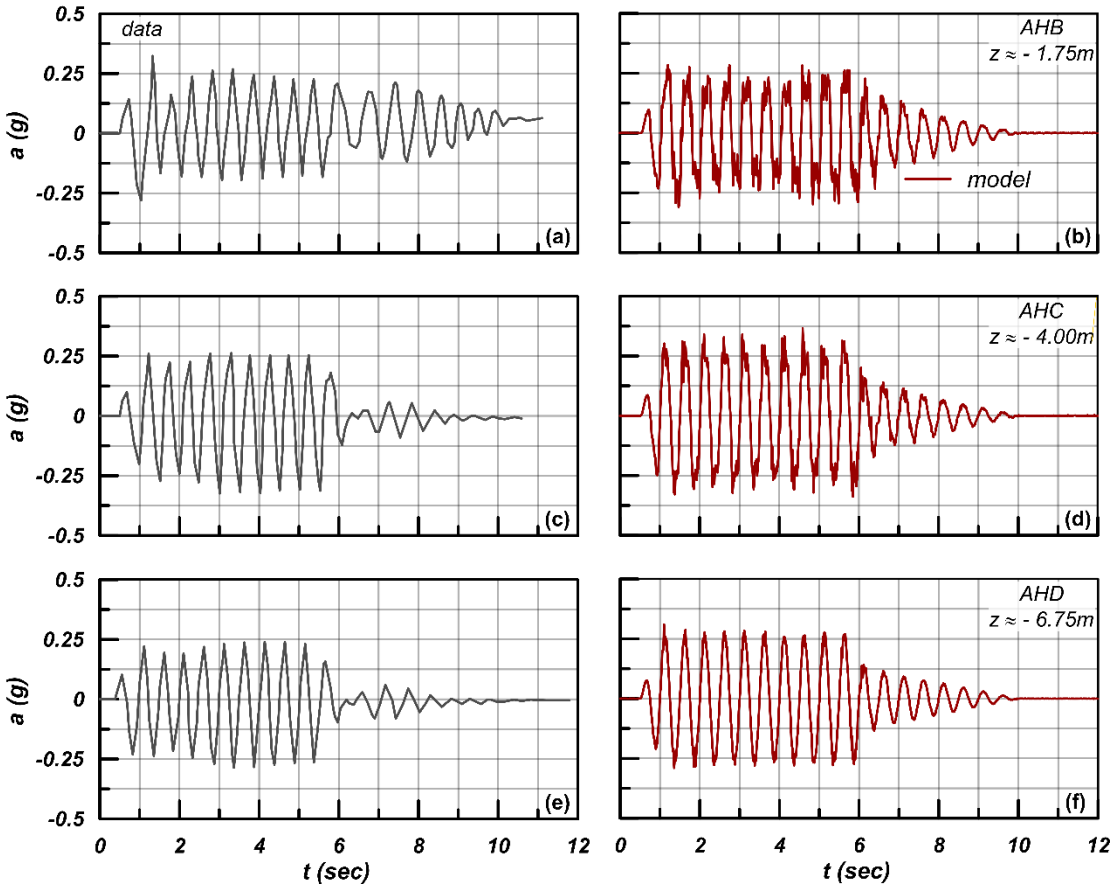

Figure 6.28: *Experimental results and model estimates of the horizontal acceleration below the structure at the axis of VELACS Model test No.12. Data after Carnevale and Elgamal (1994).*

Figure 6.27 presents a comparison of the time-histories of excess pore pressure ratio r_u between the measured values with pore pressure transducers during the experiment and the numerical results. Comparisons are presented for the four indicative locations of P1 (subplot **6.27a**), P2 (subplot **6.27b**), P3 (subplot **6.27c**) and P4 (subplot **6.27d**), which correspond to the depths $z \approx$ -1.75 m, - 4.00 m (under footing and in free-field) and -6.75 m, with z counting from the ground surface. Pore pressure transducers P1, P2 and P3 are placed below the footing, while P4 is placed at the same elevation as P2 at the free field. The comparison includes experimental data only from the tests which were excited with similar base input motions like the applied in the numerical analysis. Namely, RPI test and UCD test No.3 are included. By comparing the experimental data and the numerical results, it is shown that the model results are quite satisfactory. The measurements of excess pore pressure generation at the locations of transducers P1, P2 and P3 below the footing, show

that liquefaction has not occurred at this area and the peak observed value of r_u ranges between 0.25 - 0.30. This is well captured by the model, thus its ability of estimating accurately intermediate phases before liquefaction is proved. On the contrary, in free-filed location of transducer P4, excess pore pressure ratio attains larger values and specifically in RPI test liquefaction occurs gradually, while in test UCD r_u does not exceed the value of 0.50. The numerical results, in accordance with the data, give higher r_u values at this location with an average r_u around 0.75 and full liquefaction is not actually predicted. The intense, almost harmonic fluctuation of r_u with time at this location, apart from the induced dilative response due to the settlement of the building, is directly related also to the selected boundary conditions of the lateral edge of the grid. As already discussed, the same acceleration time-history is applied at the bottom and lateral boundaries to simulate the kinematic conditions of the rigid box. Hence, the response at the location of transducer P4 is highly affected by the applied motion, since it is very close to the vertical boundary of the rigid (and not flexible or laminar) box.

In the sequel, **Figure 6.28** shows a comparison between the recorded (subplots **6.28a**, **6.28c** and **6.28e**) and the estimated (subplots **6.28b**, **6.28d** and **6.28f**) horizontal acceleration time-histories at the locations of accelerometers AHB, AHC and AHD placed at the depth of $z \approx$ - 1.75 m, -3.75m and -6.75 m at the axis of symmetry of the grid. The experimental data refer to the RPI test, as they provide the only available acceleration recordings. In the case of the numerical analysis (ruby-red line) the results plot very close to the data. The slight amplification of the motion in AHB is similar in the numerical and the experimental results and implies that the soil layer has not fully liquefied, in good agreement with the r_u time-histories depicted in **Figure 6.27**.

Subsequently, **Figure 6.29** compares the time-history of the induced settlement of the structure during the test and that estimated by the numerical analysis. As before, the comparison includes experimental data only from the tests which were excited with similar base input motions like the applied one in the numerical analysis. Namely, RPI test and UCD test No.3 are presented. Actually, a deviation between the experimental results is observed due to the differences in the applied motion and the induced excess pore pressure field, with the numerical results falling closer to the experimental results of UCD test No.3. This is explained by observing that the model predictions agree more with the results of the

UCD test No.3 also in terms of r_u (**Figure 6.27**), while the larger values of r_u exhibited in the RPI test are expected to result in larger settlements. Moreover, by comparing the experimental and the numerical results in Figure 6.29 one finds qualitative agreement, i.e., the settlements accumulate linearly with time, and they stop accumulating when the base motion ceases.

In order to examine the model's ability to estimate the increase of settlement of the superstructure due to a stronger shaking event, two supplementary numerical analyses with peak ground acceleration a_{max} = 0.32 g and 0.375 g and 12 main cycles instead of 10 were carried out, keeping the frequency of the motion unchanged. The analysis with a_{max} = 0.375 g approaches the excitation characteristics of UDC test No.2. The results, in terms of the final settlement of the structure, are included in **Figure 6.30**, where the vertical axis refers to the induced settlements at the end of shaking and the horizontal axis refers to the peak ground acceleration of the applied input motion. The numerical results are satisfactorily compared, both qualitatively and quantitatively, to the experimental data of UCD and RPI, with the trend of the settlement to increase with increasing a_{max} being correctly captured, though the model predicts a smaller effect of the intensity of the applied motion than the experiments.

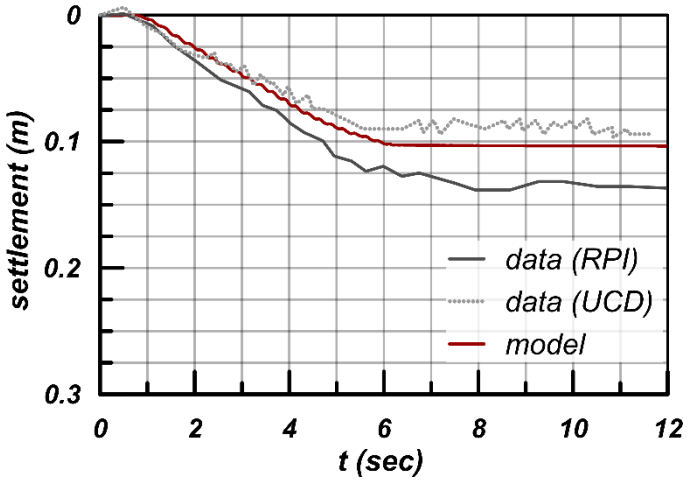

Figure 6.29: *Experimental results and model estimate of the time-history of the induced settlement of the structure of VELACS Model test No.12. Data after Carnevale and Elgamal (1994).*

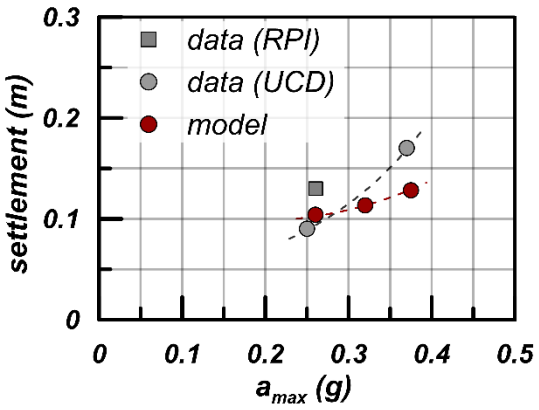

Figure 6.30: *Experimental results and model estimates of the induced settlement of the structure of VELACS Model test No.12 for different applied maximum accelerations. Data after Krstelj and Prevost (1994) and Carnevale and Elgamal (1994).*

Figure 6.31 depicts a snapshot of contours of accumulated shear strains at the end of shaking, in order to gain insight into the soil deformation mechanisms that contribute to the induced settlement of the structure, and whether they are realistically captured by the model. The primary mechanism is of deviatoric type, as the structure tends to punch into the soil during shaking. The area of the soil under the structure may not have liquefied, but to its right and left side the shearing resistance of the soil has significantly diminished, due to the generated excess pore pressures, and the footing is not prevented from settling (e.g., Karamitros et al., 2013). Quite characteristic are also the horizontal shear bands at the bottom of the failure mechanism, but also the areas with high shear strain accumulation below the edges of the footing. With a ratio $B/D \approx 0.55$, the deformation mechanism adopts characteristics also from the bearing capacity type of failure, hence being flatter and extending horizontally, in contrast to a pure punching failure mechanism as will be formed for very low values of B/D (e.g. Adamidis and Madabhushi, 2017). Moreover, due to the rigidity of the structure and the imposed cyclic loading, rocking response and ratcheting are induced leading to symmetrically localized straining areas on both sides of the structure (e.g. Adamidis and Madabhushi, 2017; Dashti et al., 2010a).

Figure 6.32 shows a snapshot of displacement vectors at the time of $t = 6$ sec and the shape of the deformation mechanism that resembles that of failure in bearing capacity, with flatter shear bands at its bottom.

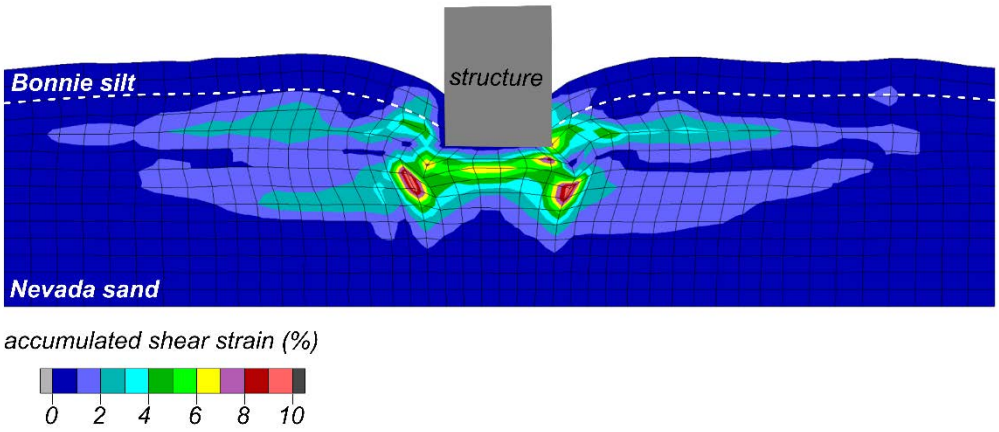

Figure 6.31: *Contours of accumulated shear strain (ssi in FLAC's terminology) and deformed mesh at the end of shaking of VELACS Model test No.12.*

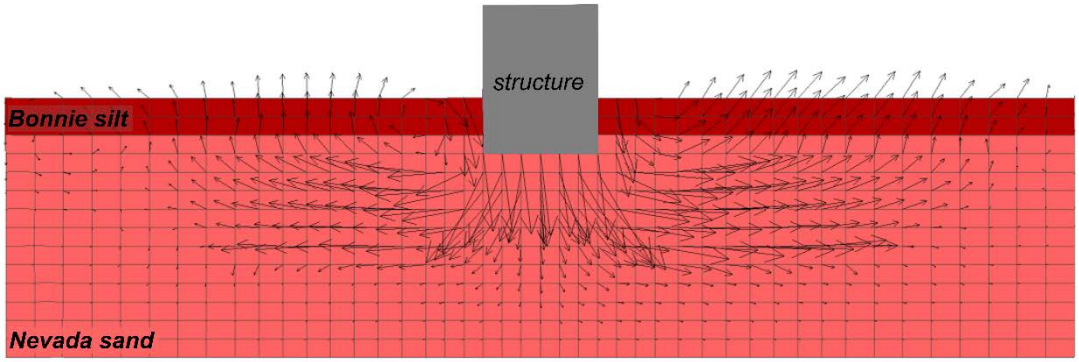

Figure 6.32: *Displacement vectors derived from the numerical analysis at t = 6 sec.*

A. Effect of mitigation of stress-strain overshooting

As already discussed in **Chapter 3**, a routine mitigating the effect of stress-strain overshooting throughout the numerical analysis is incorporated in the model formulation. In that Chapter the significance of this routine is demonstrated at element level. As already clarified, the occurrence of these numerically "*informal*" load reversal signals affects mainly the monotonic response and the numerical results in static problems (e.g., problems of bearing capacity), for which the inclusion of such a mitigation technique is considered necessary. However, as this mitigation scheme constitutes an integral part of the model acting both in monotonic and cyclic problems, it was considered quite interesting to examine its effect in a cyclic problem like that presented here. So, for this test, another numerical scenario was performed, where the formulation for mitigation of stress-strain

overshooting according to the methodology described in **Chapter 3** is deactivated. It should be noted that the default scenario examined so far, refers to the inclusion of the formulation for mitigating stress-strain overshooting.

Figure 6.33 presents a comparison of the time-histories of generated excess pore pressure ratio r_u between the experimentally measured values and the two numerical scenarios with and without including the formulation for the mitigation of stress-strain overshooting. The ruby-red lines refer to numerical results incorporating the routine for overshooting, while the navy-blue lines refer to numerical results where this routine is

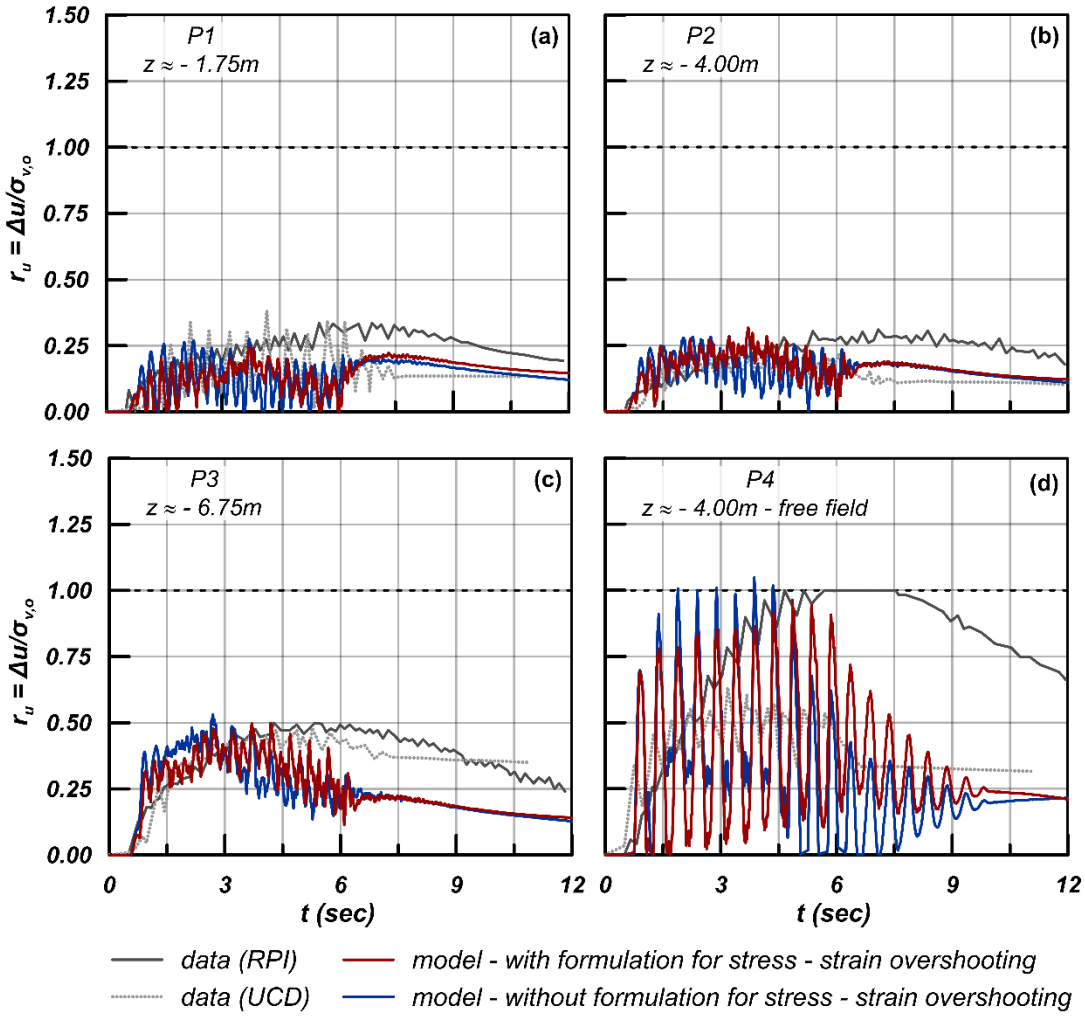

Figure 6.33: *Experimental results and numerical estimates of excess pore pressure ratios, ru at various locations of VELACS Model test No.12, with and without including the routine for overshooting mitigation. Data after Krstelj and Prevost (1994) and Carnevale and Elgamal (1994).*

deactivated, as discussed above. Overall, the differences are not big, e.g., in both cases the lower r_u values below the footing are captured, in comparison to the higher values at the free field, but the analysis with the formulation being active seems more in accordance with the data. Looking at this comparison in more detail, one observes that in the first seconds of the excitation (e.g., up to t = 3 sec) the model without mitigation of stress-strain overshooting estimates higher values of r_u at all locations, something that may be considered counter-intuitive. However, in this model, also the elastic moduli employ the $\boldsymbol{r}_{ini}$ for predicting their nonlinearity via a Ramberg-Osgood type formulation, and not only the plastic strain rate. Hence, "*informal*" load reversals appearing at the early stages of shaking seem to disallow the nonlinear degradation of the elastic moduli, thus leading (via the non-degraded elastic bulk modulus) to more intense excess pore pressure buildup in the analysis without mitigation of overshooting. Thereafter (for t > 3 sec), the r_u values are reduced and become lower than in the analysis with mitigation of overshooting. This will be related to enhanced dilation in the figures that follow.

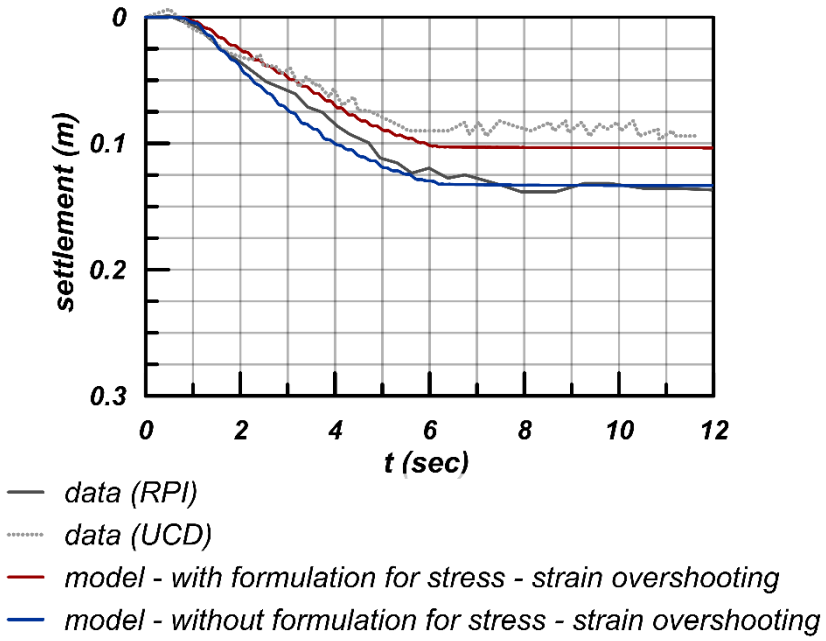

Figure 6.34: *Experimental results and numerical estimates of the time-history of the induced settlement of the structure of VELACS Model test No.12, with and without including the formulation for stress- strain overshooting mitigation. Data after Carnevale and Elgamal (1994).*

Additionally **Figure 6.34** shows a comparison between the numerically estimated footing settlements with and without the aforementioned formulation for stress-strain overshooting mitigation (ruby-red and navy-blue lines), compared with the experimentally measured. Here, it is illustrated that by omitting the inclusion of this routine, the numerical displacements are slightly increased by 15 - 20% and that this result is more in tune with the measurements. On the other hand, the analysis without the foregoing formulation seems to overestimate the rate of settlement accumulation during the strong shaking. This increased rate is intense only in the initial stages of loading (for $t < 3$ sec), while the accumulation rates become similar for $t > 3$ sec, with the structure ceasing its settlement after the end of strong shaking (for $t > 6$ sec) in both analyses. This comparatively increased

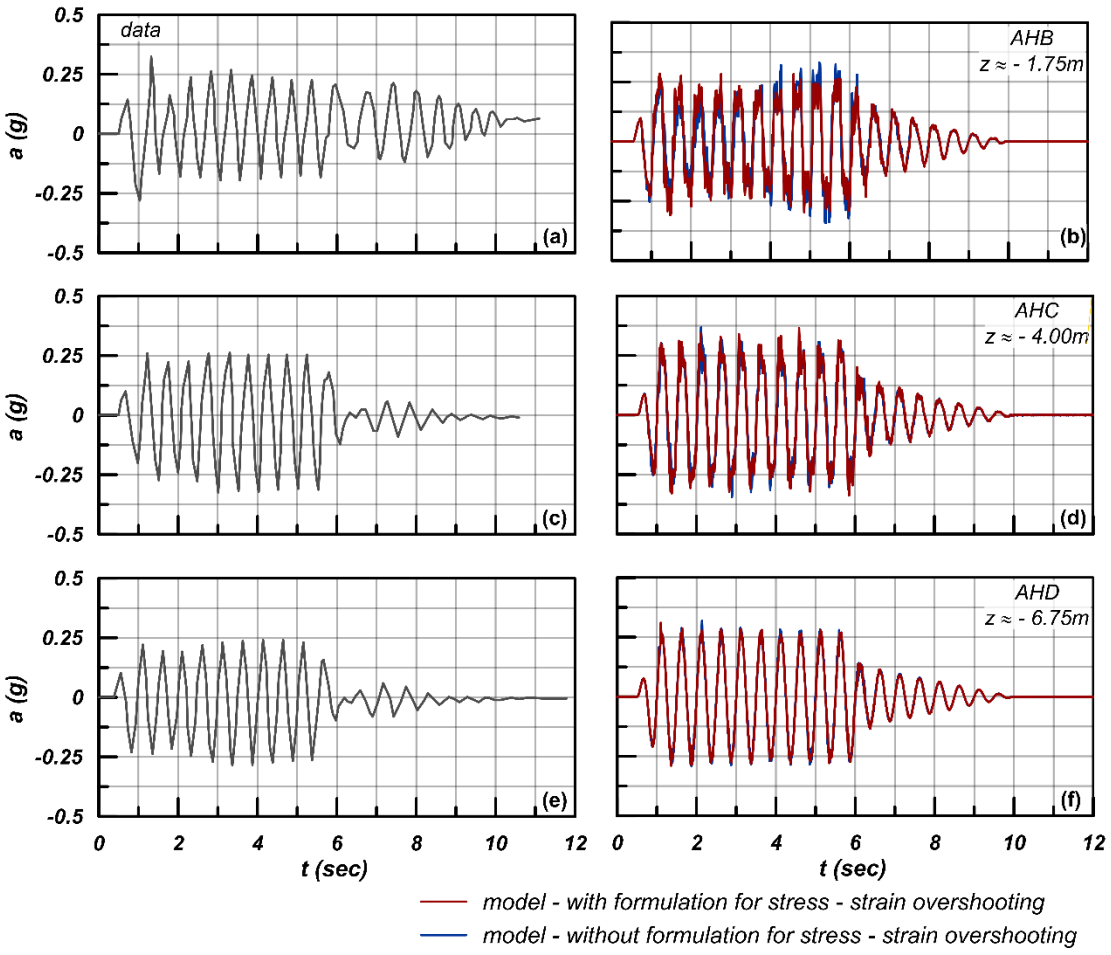

***Figure 6.35**: Experimental results and numerical estimates of the horizontal acceleration below the structure at the axis of VELACS Model test No.12, with and without including the routine for overshooting mitigation. Data after Carnevale and Elgamal (1994).*

settlement rate for $t < 3$ sec is consistent with the larger r_u values estimated by this analysis (**Figure 6.33**). For $t > 3$ sec, the structure has comparatively larger settlement in the analysis without the foregoing formulation, thus increased shearing and consequently enhanced dilative response in the foundation soil. Hence, the r_u becomes eventually smaller (**Figure 6.33**). Despite these notable differences, the overall effect of this formulation cannot be considered crucial for the accuracy of the numerical results. This conclusion is considered valid for liquefaction-related dynamic BVPs, but cannot be necessarily generalized for other types of BVPs (e.g., static analyses).

Finally, **Figure 6.35** shows a comparison of the two scenarios in terms of horizontal acceleration time-histories. The numerical results without the inclusion of the formulation mitigating the stress-strain overshooting show slightly lower values of acceleration at the first seconds of the excitation especially for the lower depths, as a result of the higher induced r_u values. On the other hand, this is inversed for $t > 3$ sec, when the r_u values for the analysis not including the formulation drop. For the larger depth, the difference is practically negligible. Hence, overall the differences between the two examined scenarios are significant, but not crucial for the predicted accuracy, at least for this type of liquefaction-related BVPs..

6.4.2 Validation against the T3-50 Moderate P.I. test performed by Dashti et al. (2010a; b)

Dashti et al. (2010a; b) performed a set of centrifuge experiments to explore both quantitatively and qualitatively the liquefaction-related settlements and deformation mechanisms of buildings founded on shallow footings. The series of centrifuge models included three types of steel and aluminum structures with varying dimensions and bearing pressures, placed on 1 m thick rigid mat foundations. Different soil profiles were examined with varying density and thickness of the liquefiable soil layer and different materials at the ground surface are placed. The models were subjected to a sequence of shaking events with increasing intensity, consisting of scaled versions of the north-south, fault-normal component of the 1995 Kobe Port Island (P.I.) recording.

The experiment utilized here for the validation of the model is the T3-50 Moderate P.I. test. In prototype scale, the stratigraphy includes a 3 m thick medium dense Nevada

sand layer with a relative density of approximately 50%, underlain by a 21 m thick layer of dense Nevada sand with a relative density of 85% - 90 %. The medium dense Nevada sand layer is overlain by a 2 m thick dense Monterey sand layer with a relative density equal to approximately 85%, and the water table was set 1 m below the ground surface. Each experiment includes all three examined structures, arranged next to each other, with a sufficiently large distance between them so as their response to be completely independent (Dashti et al. 2010a; b; Dashti and Bray 2013). The layout of the experiment is illustrated in **Figure 6.36.**

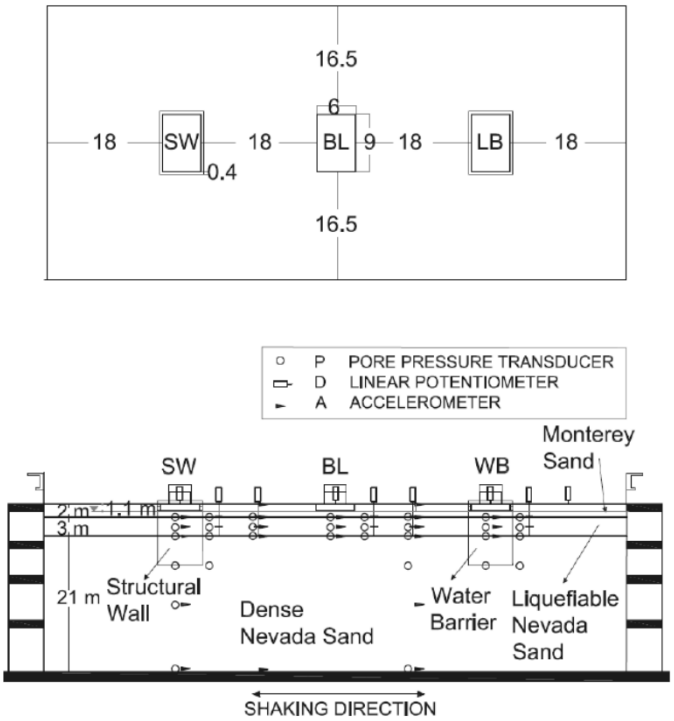

Figure 6.36: *Centrifuge model layout in experiment T3-50 with most of the approximately 120 transducers omitted for clarity: (a) plan view; (b) cross section view. (source: Dashti et al., 2009).*

The analyzed case in this Section focuses on Structure A (or BL) of the experiment, which refers to a 5 m high single-degree-of-freedom structure, founded on a rigid mat with a width equal to 6 m and a length equal to 9 m, carrying a bearing pressure equal to 80 kPa. The embedment depth of the foundation mat was 1 m. The model was built into a flexible container and was spun up to a 55 g centrifugal acceleration. The pore fluid used during test had a viscosity 22 times larger than that of water. The response of the soil-structure system was monitored with numerous accelerometers and pore pressure transducers placed

at different locations in the vicinity of the structure, but also in the free-field and linear potentiometers placed on the corners of the structure to measure its displacement. The input motion applied horizontally at the base of the container was a scaled version of the fault-normal component (north-south) of ground motion recordings at the depth of 83 m at Kobe Port Island (P.I.) during Kobe earthquake in 1995. The input motion was scaled, so as a peak ground acceleration of 0.15 g to be achieved and the predominant frequency was about 1.2 Hz (Dashti et al. 2010a; b; Dashti and Bray 2013). The finite-difference grid used for the numerical analysis was not uniform, with the zone size varying from 0.80 m × 1.00 m

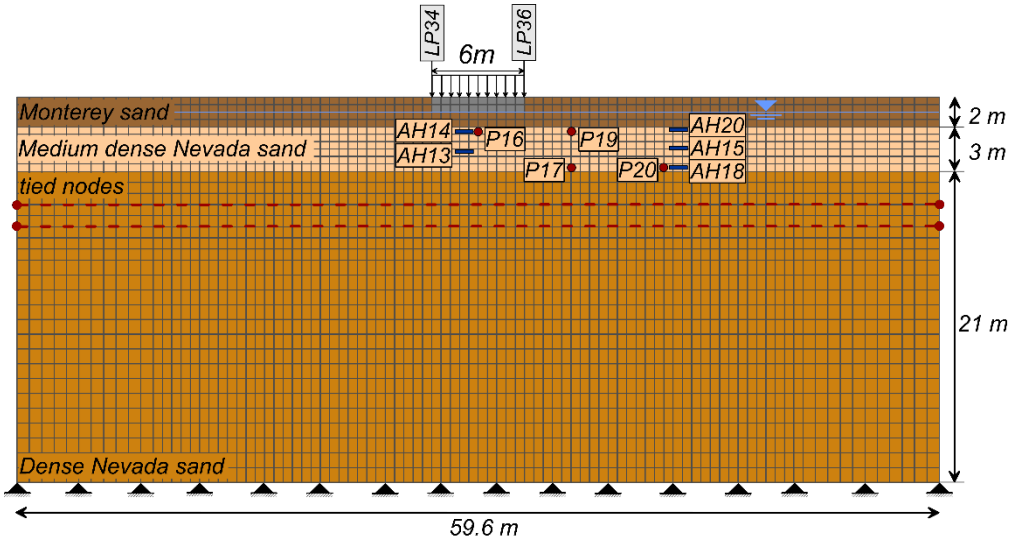

Figure 6.37: *Numerical model layout for analysis of Structure BL of T3-50 test performed by Dashti et al. (2010b).*

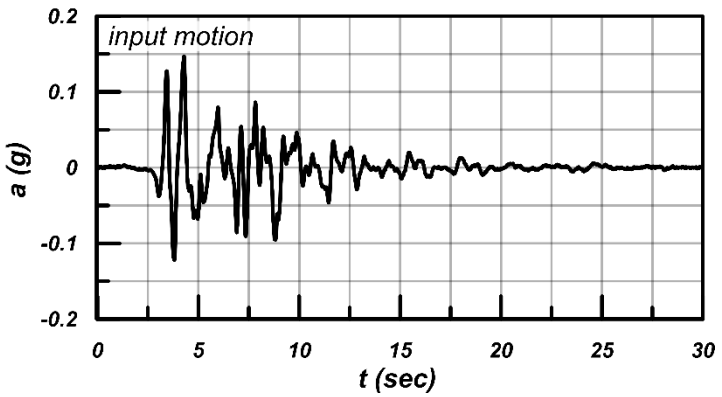

Figure 6.38: *Time-history of the applied horizontal base acceleration. Scaled version of Kobe Port Island (P.I.) earthquake in 1995 (Dashti and Bray 2013).*

far from the footing to 0.60 m × 0.50 m at the vicinity of the footing, as presented in the **Figure 6.37**. The bottom boundary of the grid was forced to follow the time-history of the input horizontal acceleration of **Figure 6.38**, while the vertical acceleration during the experiments was considered zero. At the vertical edges of the mesh, the boundary condition of tied nodes was adopted, so the kinematic restraints of the flexible container to be simulated.

The foundation mat was simulated as a rigid elastic block of 1 m high, embedded 1 m below the ground surface, and the elastic parameters of aluminum (shear modulus equal to 29 GPa and bulk modulus equal to 39 GPa) were adopted. The bearing pressure due to the superstructure was modeled as a constant stress applied on the foundation. This simulation, while quite simplified, is not expected to affect significantly the induced building settlements, since the specific structure selected to be analyzed is not of high slenderness ($H/(B/2) \approx 1.67$ – where H denotes the height of the structure and B its width) – with a fixed-base period, T_{str}, equal to 0.21 sec (Dashti et al., 2009a), thus indicating a relatively rigid system (Dashti et al. 2010a; b). More specifically, previous studies have shown that a rigid structure settles approximately the same with a shallow foundation of equal total weight in a liquefied regime, with Soil Structure Interaction (SSI) effects being minimal in this case (e.g., (Karamitros et al., 2013). Additionally, Karimi et al. (2018) and Bullock et al. (2019) have shown that the lower the slenderness ratio of the structure, the lower also the applied rocking-induced structural moments, thus rendering SSI effects less important. Hence, the target final bearing pressure of 80 kPa was reproduced by the sum of the pressure induced by the unit weight of the foundation mat and the applied constant stress. Additionally, following the same course of thought as in the simulation of VELACS Model test No. 12 for the probably necessary reduction of the applied pressure due to 2D conditions, the methodology of Janbu et al. (1956) - combined with the factors of Christian and Carrier (1978) - was followed also in this analysis. The difference here is that the ratio D/B, where D stands for the thickness of the compressible soil layer below the footing, is only 0.50. This value is deduced by taking into account that the medium dense Nevada sand layer is the only one prone to liquefaction, thus almost the total settlement of the structure is expected to occur within this layer (e.g., Bertalot and Brennan, 2015), leaving the dense Nevada sand layer below practically unaffected. So, in this case, for $D/B = 0.50$ and L/B

=1.5, it is calculated that the applied contact pressure does not need to be reduced. A similar choice, of not reducing the contact pressure in the 2D plane-strain numerical simulation of this test, was also made by Dashti and Bray (2013), but there it was on the basis of a more accurate simulation of the dynamic properties of the SDOF structures they have modeled. Moreover, as in Model test No. 12 of VELACS project, according to Itasca Consulting Group Inc. (2011), the real footing width in the numerical analysis is something larger than the designed footing width on the mesh, as the vertical component of the velocity vector developing, while the footing is settling, varies linearly from the value developed at the last gridpoint of the designed footing to zero at the next neighboring gridpoint of the mesh. This means that the "real" footing width may be considered equal to the designed width plus half the width of the zones on either side of the footing. In other words, the "real" footing width is 6.0 + 2x0.6/2 = 6.6 m. Hence, in order for the bearing load not to be overestimated, the applied pressure was appropriately reduced for this reason. The finally applied pressure was 72.72 kPa.

The calibration of the model parameters to simulate the cyclic response of Monterey sand with $D_r \approx 85\%$ was based on the cyclic undrained simple shear tests performed by Wu et al. (2004), as detailed in **Chapter 5**. **Figure 6.39** compares the liquefaction resistance curves derived from the available element tests and the respective numerical results for

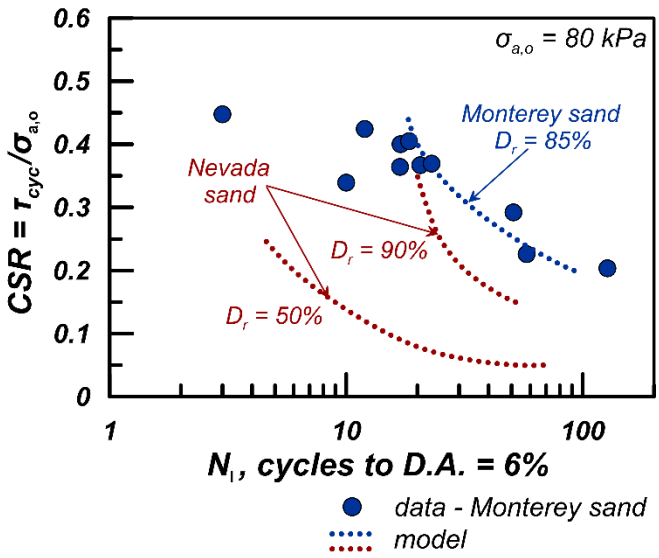

Figure 6.39: *Liquefaction resistance curves. Experimental results and model estimates of undrained cyclic simple shear tests. Data on Monterey sand after Wu et al. (2004).*

initial conditions referring to a relative density of D_r = 85% and an initial effective axial stress equal to 80 kPa. To give a sense of the comparative resistance to liquefaction of all the sand materials used in the model, the liquefaction resistance curves of D_r = 50% and 90% Nevada sand at stress level of 80 kPa were also added in **Figure 6.39**.

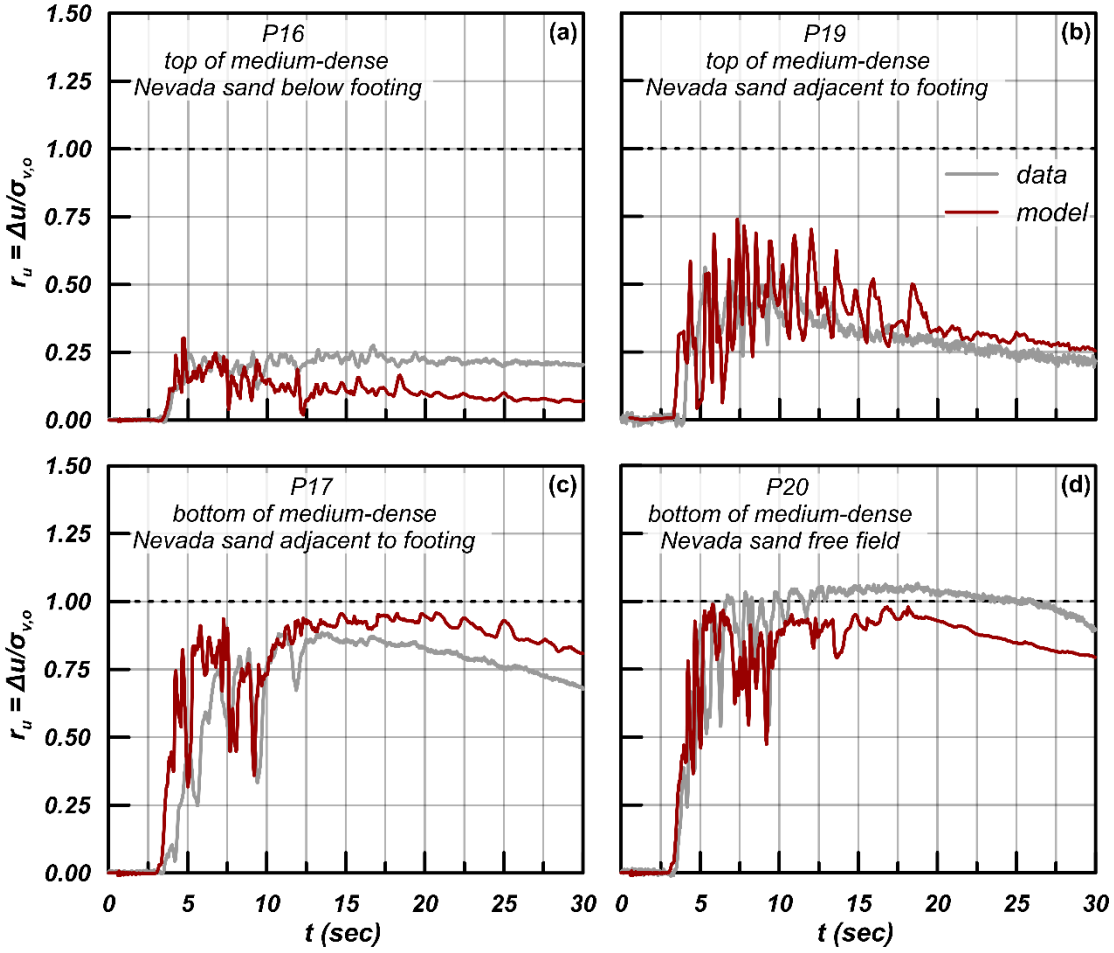

Figure 6.40: *Experimental results and numerical estimates of excess pore pressure ratios, r_u, at various locations of T3-50 test. Data after (Dashti et al. 2010a; b).*

Initially, the geostatic stress field is achieved assuming elastic response with a K_o value equal to 0.50, under static equilibrium and then, coupled dynamic analysis was performed. For a relative density of approximately 50%, a permeability coefficient equal to $k = 6 \cdot 10^{-5}$ m/sec is documented (Arulmoli et al., 1992; Dashti and Bray, 2013) for Nevada sand, while for the denser layer of D_r = 85% - 90% a lower permeability coefficient equal to $k = 2.25 \cdot 10^{-5}$ m/sec is adopted (Arulmoli et al., 1992; Dashti and Bray, 2013). For Monterey sand with D_r = 85%, k is measured equal to $5.29 \cdot 10^{-4}$ m/sec (Dashti and Bray, 2013; McCartney et al., 2005). In this test, as the used pore fluid has a viscosity 22 times

higher than that of water's, the adopted permeability coefficient was firstly scaled up by 55/22 and then decreased by a factor of 4 to account for the time-scale gap between dynamic and diffusion times. Similarly in this case, a fluid bulk modulus of water equal to $4 \cdot 10^5$ kPa was adopted, which corresponds to an average saturation ratio $S_r \approx 99\%$ (Dashti and Bray, 2013) and a local damping value of 2% was used.

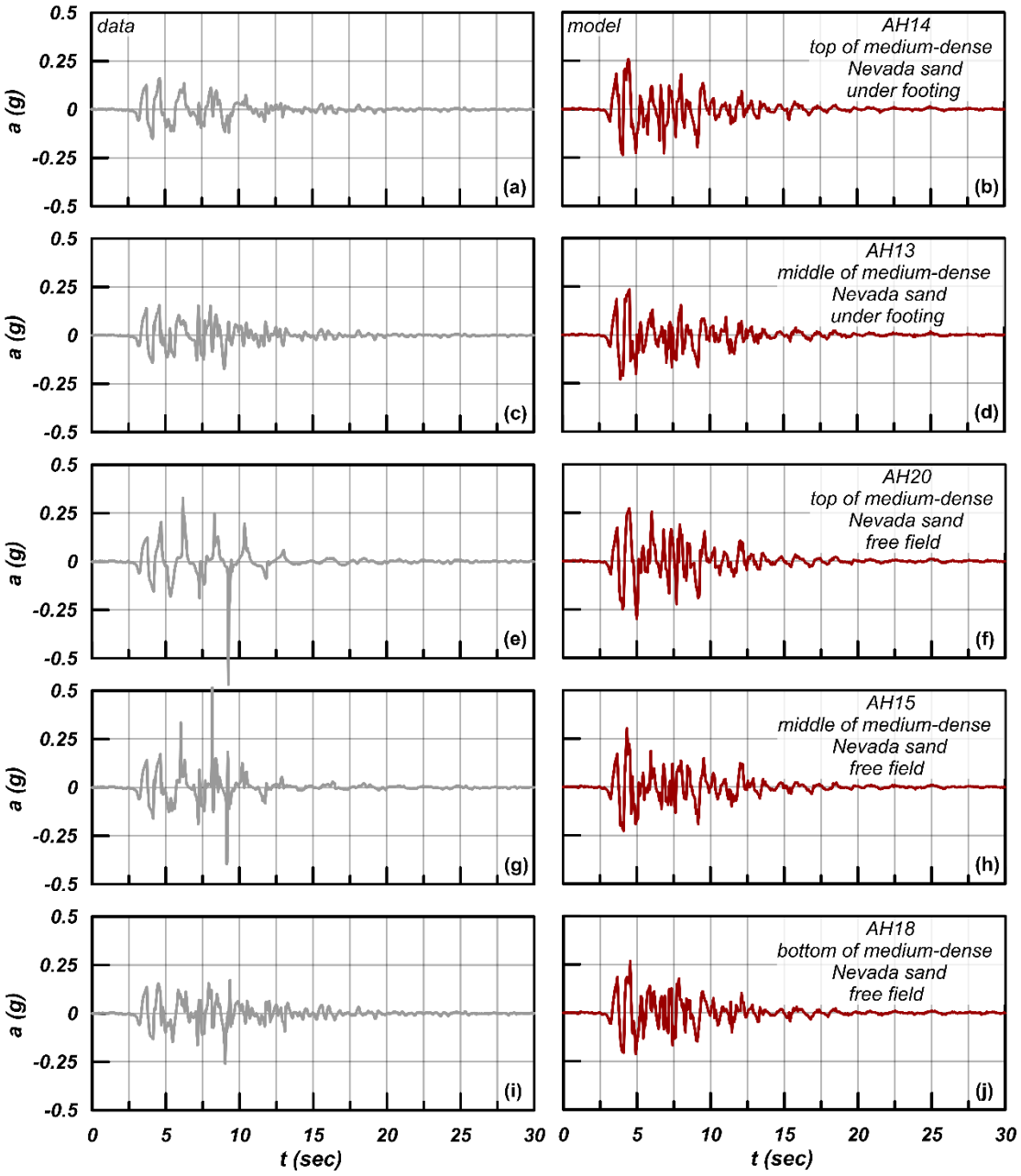

Figure 6.41: *Experimental results and numerical estimates of the horizontal acceleration at various locations in medium dense Nevada sand of T3-50 test. Data after (Dashti et al. 2010a; b).*

Figure 6.40 presents a comparison of the time-histories of generated excess pore pressure ratio r_u between the measured values with pore pressure transducers of the experiment and the numerical results. Comparisons are presented for the 3 indicative locations of P16 (subplot **6.40a**), P19 (subplot **6.40b**), P17 (subplot **6.40c**) and P20 (subplot **6.40d**) which correspond to depths at the top and the bottom of the medium dense Nevada sand. Pore pressure transducer P16 is located at the axis beneath the footing, transducers P17 and P19 are placed at a 3m distance adjacently to the footing, while P20 is located at a 9m distance in the free field. The comparison of data to the numerical results are in general quite satisfactory. The measurement of excess pore pressure at the location of transducer P16 below the footing shows that liquefaction has not occurred in this area and the peak observed r_u reaches the value of 0.25. This same low peak r_u value is also captured by the analysis. However, then the analysis shows r_u value to decrease until the end of shaking, in contrast to the experimental results where the r_u value remains practically constant with time. It is mentioned here that the tendency of excess pore pressures underneath and close to the footing to initially increase and then decrease is commonly referenced in the literature, both from experimental (e.g., Adalier et al., 2003) and numerical (e.g., Karamitros et al., 2013). The same pattern holds for the location of transducer P19, placed adjacently to the right edge of the footing at the top of medium dense Nevada sand. Here, the peak r_u value is higher but again it does not exceed the value of 0.50 - 0.75 and this is captured by the analysis. At a larger depth, where the transducer P17 is located, larger values of r_u have been measured and the numerical results, albeit with a faster rate of pore pressure buildup, estimate satisfactorily the time history of the generated r_u. Finally, at free field where the transducer P20 is located, larger values of r_u have been measured and this is also satisfactorily captured also by the analysis.

In the sequel, **Figure 6.41** shows a comparison between the recorded and the numerical horizontal acceleration time-histories at the locations of accelerometers AH14, AH13, AH20, AH15 and AH18. Specifically, accelerometers AH14 and AH13 are located below the footing at the top and middle of the medium dense sand layer respectively, while accelerometers AH20, AH15 and AH18 are located at the free field at the top, middle and bottom of the medium dense sand layer respectively. The numerical results compare similarly to the recordings at all locations, with the analysis estimating a small

amplification of the motion in the first 7 sec of shaking, especially at the locations below the footing and at the top of the liquefiable sand at free field. For t > 7 sec the numerical results plot quite close one to another. In this case, like in VELACS Model test No. 12, the motion is not totally attenuated as full liquefaction has not occurred under the footing and this is reflected on the non-nullified acceleration time-histories.

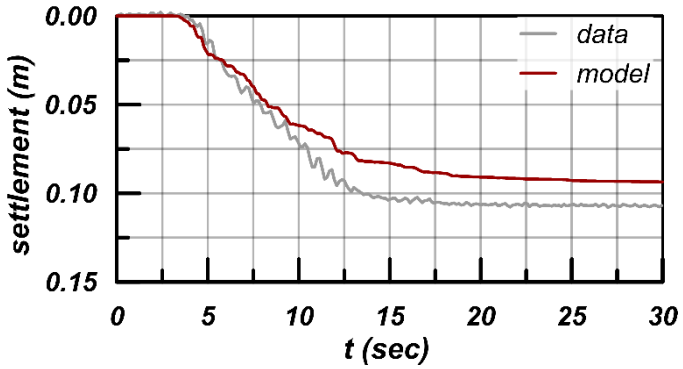

Figure 6.42: *Experimental measurement and model estimate of the time-history of the induced settlement of the structure of T3-50 test. Data after Dashti et al. (2010a; b).*

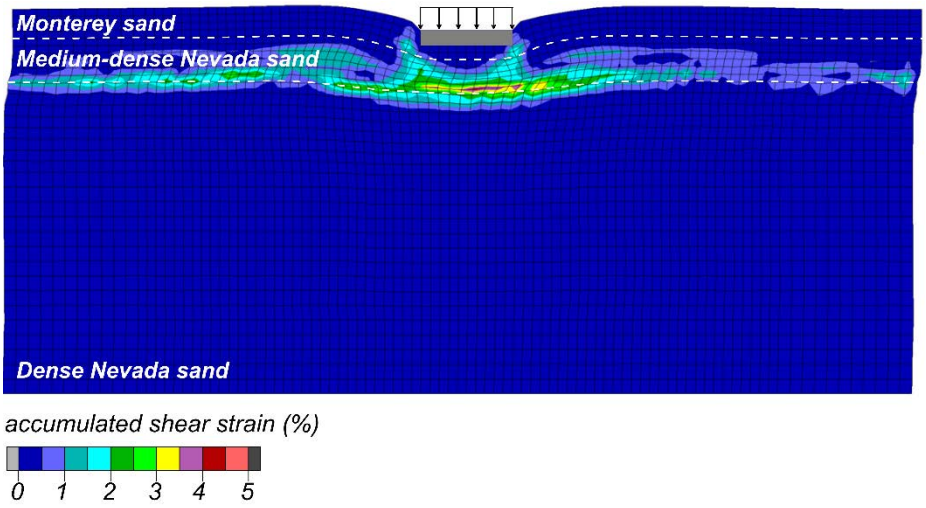

Figure 6.43: *Contours of accumulated shear strain (ssi in FLAC's terminology) and deformed mesh at the end of shaking of T3-50 test.*

Subsequently, **Figure 6.42** compares the time-histories of the induced settlement of the structure during the centrifuge test and that estimated by the numerical analysis. The numerical results refer to the axis of the footing, while for the comparison the average value between the measurements of linear potentiometers LP34 and LP36 was considered in the

figure. Qualitatively, the nearly linear with time accumulation of the settlement with time is similar in experimental data and the numerical results, while settlement stops accumulating when the base motion fades. Quantitatively, the results are comparable, with the numerical analysis slightly underestimating the final settlement of the footing.

Figure 6.43 depicts a snapshot of contours of accumulated shear strains at the end of shaking of test T3-50 Moderate P.I. The primary soil mechanism is of the deviatoric type and the structure tends to punch into the soil during shaking. However, as the liquefiable medium dense sand is underlain by a non-liquefiable dense layer of Nevada sand, the deformation mechanism remains within the medium dense layer. This confirms that the settlement practically occurs in total due to the medium dense Nevada sand layer (e.g., Bertalot and Brennan, 2015), as the lower dense sand layer practically acts as an incompressible barrier limiting the settlement. As a result, the footing width over compliant layer thickness ratio B/D has a value of 2, indicating a shallow deformation mechanism more similar to that of bearing capacity failure, with horizontal outwards displacements and shear bands that is limited by the underlain stiffer layer (e.g. Adamidis and Madabhushi, 2017; Bertalot and Brennan 2015). This result also confirms the assumption for not reducing the bearing pressure of the footing for performing a 2D, rather than a more accurate 3D analysis.

In order to examine the model's ability to estimate the settlements of the superstructure due to different shaking events and different thicknesses of liquefiable layer, two supplementary numerical analyses were carried out. That for the T3-50 Large P.I. 1 and that for the T6-40 Moderate P.I. tests performed by Dashti et al. (2010a; b) were numerically simulated. The T3-50 Large P.I. 1 test adopts the same geometry and soil layering like the test presented meticulously in the previous paragraphs, but it the laminar box is excited by a stronger shaking event. Namely, the same component of the Kobe Port Island recording is used, but now it is scaled to a larger value, so as a peak ground acceleration of 0.38 g to be achieved. On the other hand, in the T6-40 Moderate P.I. test, the excitation is the scaled version of 0.15 g of the P.I. recording, but the liquefiable medium sand layer has a thickness of 6 m, instead of the 3 m in T3-50 test, and its relative density is now equal to 40% instead of 50%. In this way, the ability of the model to capture the effects of the applied peak ground acceleration, the relative density of the liquefiable

soil layer and its thickness, is roughly examined. Here, it should be noted that for the case of T6-40 test, where the ratio of the thickness of the compressible liquefiable soil layer over the width of the footing is unity (D/B = 1), the applied bearing pressure on the footing was reduced appropriately, in order to be consistent with the methodology described earlier for the transition from 3D to 2D conditions (Janbu et al. 1956). Specifically, according, to the aforementioned methodology of common elastic settlements in 2D and 3D, the adopted contact pressure was set equal to 65kPa. The comparison between the experimental and numerical results is made in terms of induced settlements and is concluded in **Figure 6.44**, where the horizontal axis refers to the experimental measurements for these aforementioned tests, while the vertical axis refers to the numerical values. The solid diagonal line is the locus of points of perfect agreement between results by the analyses and the experimental data. The results are generally well compared, , showing that the analyses capture quite satisfactorily the effects of relative density and thickness of the liquefiable sand and peak ground acceleration in a range of +/- 25%.

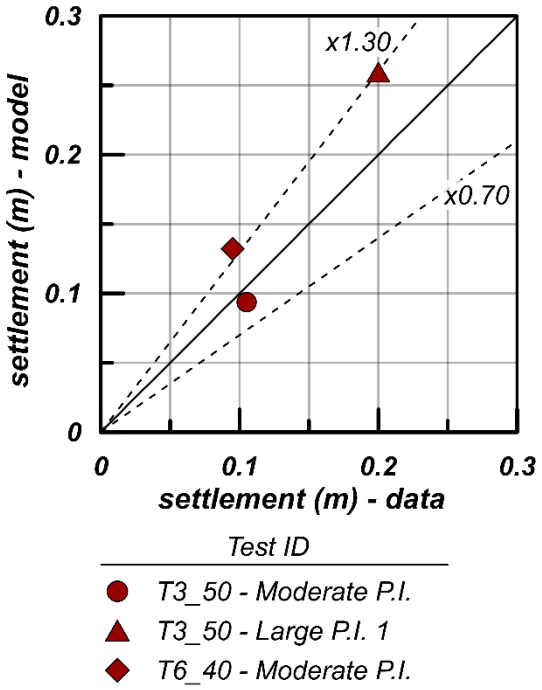

Figure 6.44: *One to one comparison of experimental results and model estimates of induced settlements of the structure of T3-50 Moderate P.I., T3-60 Large P.I.1 and T6-40 Moderate P.I. tests. Data after Dashti et al. (2010a; b).*

6.4.3 Summarized numerical results in terms of settlements

In the previous paragraphs the ability of the model to simulate the typical structural response of shallow footings founded on soil profiles including liquefiable layers is validated through comparisons with experimental data from VELACS Model test No.12 (Carnevale and Elgamal, 1994; Farrel and Kutter, 1994; Krstelj and Prevost, 1994), as well as centrifuge experiments performed by Dashti et al. (2010a; b). **Figure 6.45** shows a summarized comparison of the numerical results in terms of settlements against their respective experimental values from all the 6 centrifuge tests, which are used for the validation of the model. Collectively, 2 widths of foundations, B, equal to 3m and 6m are examined. The structures are founded on soil profiles with different stratigraphies, including always liquefiable Nevada sand layers with average relative densities, D_r, ranging between 40% and 85%, while the thickness of these liquefiable layers, H_{liq}, are 3 m and 6 m. The applied peak ground acceleration, a_{max}, ranges between 0.15 and 0.38 g. The comparison shows satisfactory accuracy (± 30%) in the estimation of shallow structures' settlement in liquefaction regime.

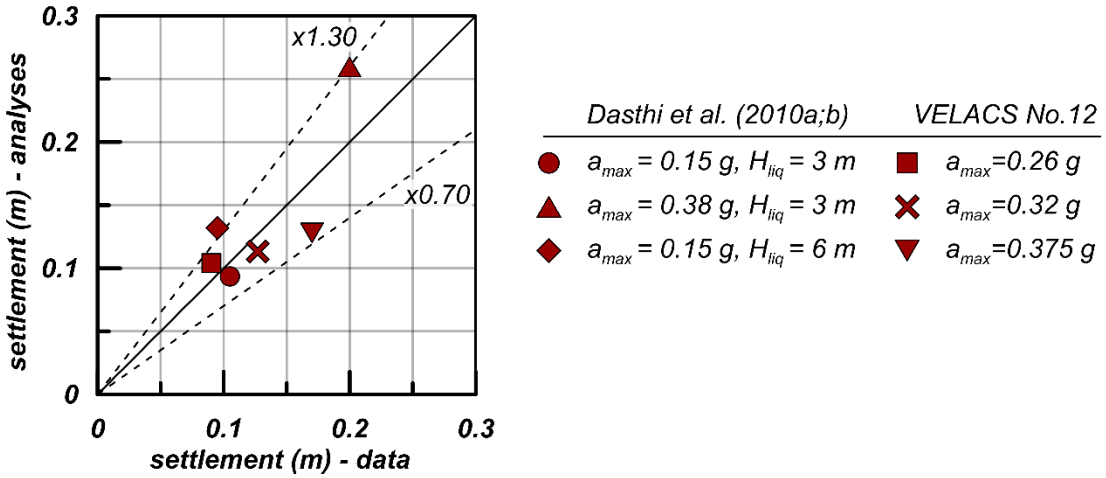

***Figure 6.45**: Comparison of experimental data from centrifuge tests and numerical results in terms of settlements of shallow foundations.*

s

6.5 Case 4: Seismic response of deep pile foundation in a mildly-sloping liquefiable layer

In this final paragraph, the model is validated in a 3D boundary value problem, including a deep pile foundation placed in a mildly-sloping liquefiable sand layer. For this purpose, the centrifuge experiment of Pamuk et al. (2007) is simulated numerically by using the finite difference code *FLAC*^{3D} (Itasca Consulting Group Inc., 2012), where the model is implemented via the UDM option as described in **Chapter 4**.

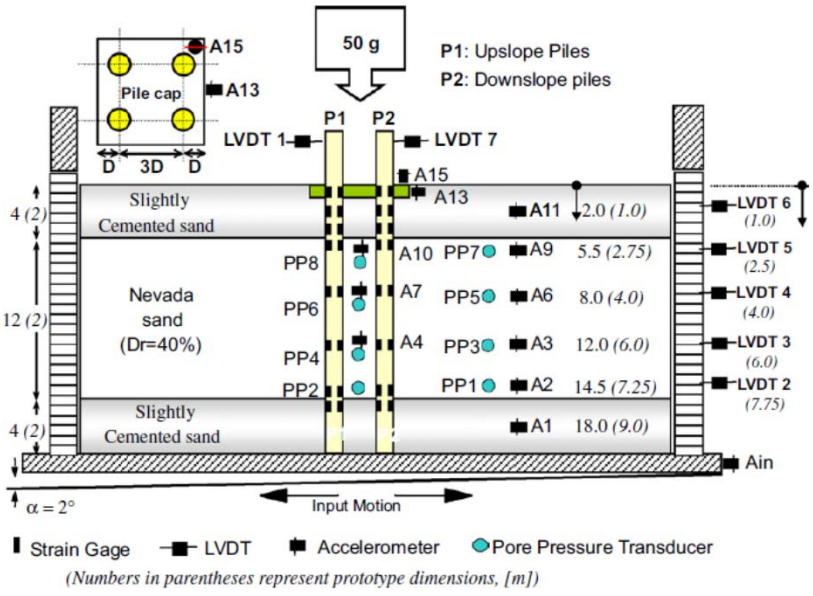

***Figure 6.46**: Experimental setup of centrifuge experiment of Pamuk et al. (2007) (Source: Pamuk et al., 2007).*

Pamuk et al. (2007) performed a set of centrifuge experiments to explore the effect of passive stabilization with colloidal silica on the seismic response of a soil-structure system consisting of a pile group installed in a three-layered, mildly-sloping soil profile including a liquefiable sand layer as the middle layer. The same layout was examined with and without passive stabilization of the liquefiable sand layer, so as the potential benefits of the applied mitigation measure to be evaluated. For the validation of the model presented in this Thesis, the default experiment without passive stabilization is numerically analyzed. The layout consisted of a 10 m-deep three-layered soil system with a 2 x 2 end-bearing pile group and a pile top-cap. In prototype scale, the stratigraphy included a bottom layer of 2

m-thick cemented, non-liquefiable sand, followed by a 6 m-thick uniform liquefiable Nevada sand layer of relative density close to 40%, topped by a 2 m-thick cemented, non-liquefiable sand layer. As in the free-field test of VELACS Model test No. 2, the soil profile had a clockwise inclination of 2^{o} to the horizontal, so as a mild slope to be created. Similarly to VELACS Model test No. 2, the actual inclined stress field in this test was induced by applying an extra horizontal gravitational component, which in combination with the vertical one, reproduce the inclined stress field. Hence, the resultant vector of gravity is rotated towards the counterclockwise direction by 2^{o}. The pile top-cap had dimensions equal to 3 m (width) x 3 m (length) x 0.7 m (height) in prototype units and was embedded in the top cemented sand layer at the center of the box. The piles had a diameter of D = 0.6 m in prototype scale and were spaced at a distance of 3D. Their bending stiffness (EI) was

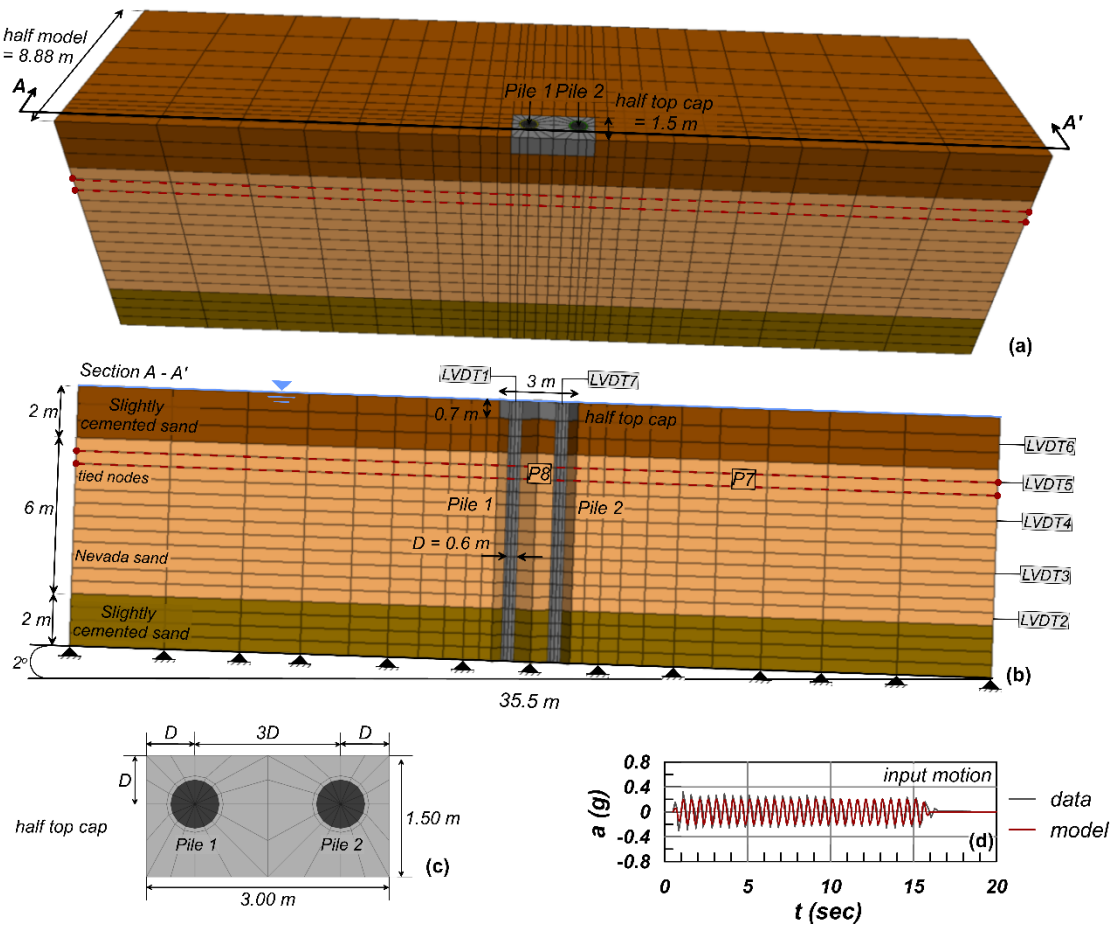

Figure 6.47: *(a) Numerical model layout of analysis of centrifuge test performed by Pamuk et al. (2007), (b) cross- section A-A' of numerical layout, (c) top-cap plan view and (d) time-history of input base motion.*

measured 8000 kNm^2. The model was built into a 35.5 m (length) x 17.5 m (width) laminar box and was spun up to a 50 g centrifugal acceleration. The experimental setup is showed in **Figure 6.47**. A sinusoidal input motion was applied horizontally at the base of the laminar box and it consisted of 29 main cycles of frequency equal to 2 Hz and peak acceleration equal to 0.25 g and 2 transitional cycles before and after the main event (**Figure 6.47d**). Given that the experimental setup is totally symmetrical (four piles of common geometry, connected with a top-cap placed centrally in the laminar box and a uni-directional applied seismic motion), it was chosen to simulate the half of the numerical problem, as depicted in **Figure 6.47**.

In general, the applied numerical methodology at this boundary value problem follows exactly the same rationale as in the 2D numerical problems described in the previous paragraphs, while for its specific characteristics the assumptions of Tiptiris (2017) and Pavlopoulou (2021) were mainly adopted. Here, it should be noted that since in Pamuk et al. (2007) the information about the cemented sand layers and the structural elements is rather limited, rational assumptions about their properties and their proper simulation were made, on the basis of the experimental results and the observed system response. Specifically, both the base and the surface cemented sand layers were simulated as elastic. After a sequence of sensitivity analyses for the cemented sand layer of the base, values for elastic shear modulus equal to 4350 kPa and a bulk modulus equal to 11300 kPa were adopted, by observing its lateral displacement at the end of the shaking. As the same cemented material is used also for the surficial sand layer, reduced values of the elastic moduli of the base were adopted, so as the effect of the mean effective stress p to be taken into account. Specifically, the values of 1450 kPa and 3782 kPa for the elastic shear and bulk moduli were respectively considered. For the saturation of the soil profile, water was used as pore fluid and water table was set at ground surface. For both of these layers, the permeability coefficient k' was considered equal to 10^{-8} m/sec, indicating practically impermeable sand layers due to cementation. On the contrary, for the middle liquefiable loose Nevada sand layer a value of k' equal to $8.25 \cdot 10^{-4}$ m/sec was adopted, following the same rationale of previous paragraphs, (i.e., the 1g permeability coefficient $k = 6.6 \cdot 10^{-5}$ m/sec was multiplied by a scalar of 50 and then divided by 4). As in all numerical analyses in this Thesis, the calibration of model parameters for this layer follows the values reported

for Nevada sand in **Table 5.3.** Finally, additional local damping of 2% was considered in the dynamic analyses in order to account for the approximately zero hysteretic damping simulated by any constitutive model at the very small strains.

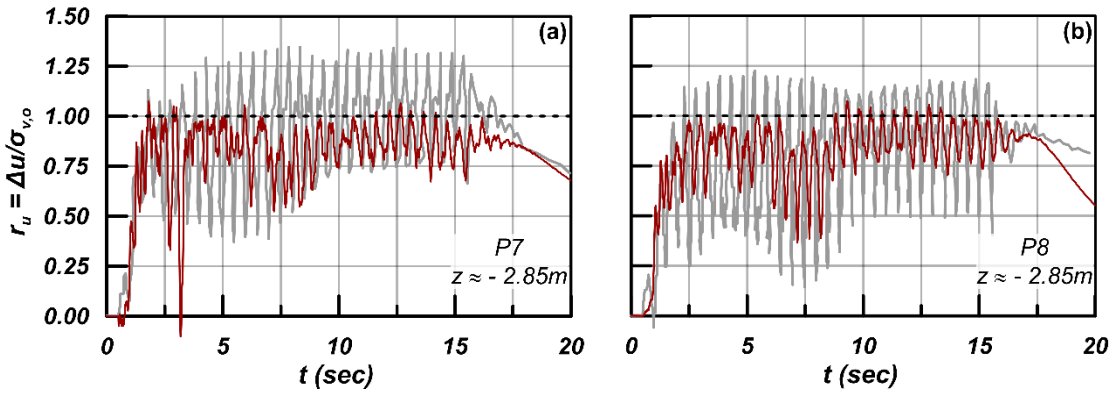

Figure 6.48: *Experimental results and model estimates of excess pore pressure ratios, r_u, at locations of pore pressure transducers P7 and P8. Data after Pamuk et al. (2007).*

The structural elements, including the piles and the top-cap, were simulated also as elastic, while their elastic moduli were chosen to be in accordance with the values of stiffness reported by Pamuk et al. (2007). Here, it should be noted that the simulation of piles with solid elements, as is done here, is not equivalent to their simulation with beam elements in terms of bending stiffness. Thus, the elastic moduli of the piles were properly adjusted, so as - for the same imposed horizontal force at their top - a common horizontal displacement to be derived, either piles are simulated with solid or beam elements with EI = 8000 kN/m^2. Specifically for the piles, $G = 23.56 \cdot 10^4$ kPa and $K = 31.31. 10^4$ kPa were adopted via the foregoing procedure. Moreover, an elasto-plastic interface with friction angle equal to 36^o was considered between the piles and the surrounding soil. Finally, for the elastic simulation of the top-cap the values of $G = 70.68 \cdot 10^4$ kPa and $K = 93.93. 10^4$ kPa were adopted, which are 3 times larger than the respective values for the piles. Given the lack of information for the top-cap material used in the experiment, these specific properties were selected sufficiently large to ensure the rigidity of the connection between pile and top-cap, without sacrificing the runtime of the analysis. Both piles and the top-cap were simulated as practically impermeable, adopting a value of k' equal to 10^{-8} m/sec. At this point, it should be recognized that the numerical analysis has significant uncertainty,

regarding all the materials utilized in this centrifuge test except from the liquefiable Nevada sand. However, in this analysis, emphasis is given on the liquefiable sand layer and on the response of piles' system in it during lateral spreading, which is not expected to be significantly affected by the uncertainties mentioned above.

Figure 6.48 presents a comparison of the time-histories of excess pore pressure ratios, r_u, between the measured values with pore pressure transducers during the experiment and those given by the numerical analysis. Comparisons are presented for the indicative locations of P7 (subplot **6.48**a) and P8 (subplot **6.48**b), which correspond to the depth of z = - 2.85 m at the free field and between piles P1 and P2 respectively (see location in **Figure 6.46)**. In comparison to the experimental data, the numerical results show good agreement, albeit the analysis estimates less intense dilation spikes than the experiment. The measurements of excess pore pressure generation at both locations show that liquefaction has occurred not only in the free field, but also in between the piles and this is accurately captured by the numerical analysis. On the other hand, the r_u values above 1.0 which are instantly recorded during the experiment are not captured by the model. These recorded high r_u values are probably attributed to an increase of the total stress field during the experiment, compared to the geostatic, due to the displacement of the pile group, thus increasing the potential for excess - pore pressure. However, while the numerical r_u may instantly acquire values slightly higher than 1.0 due to transient increase of total vertical stresses during shaking, these values do not reach a 25% increase as shown by the data.

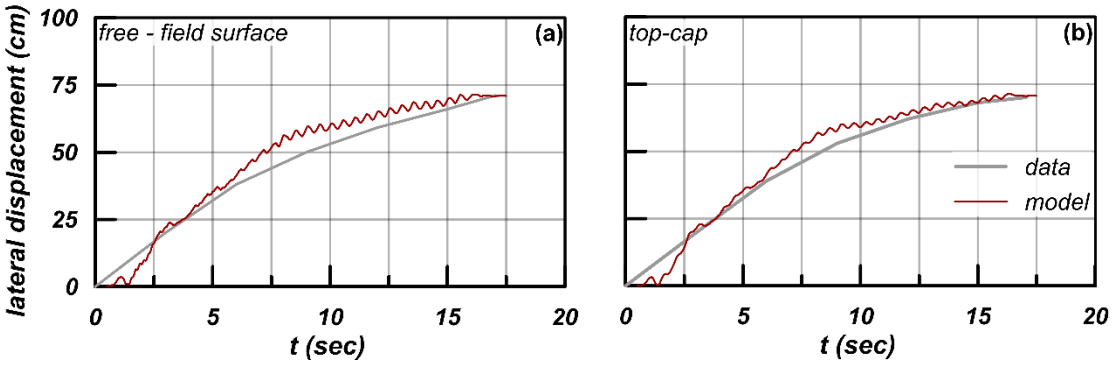

***Figure 6.49**: Experimental results and model estimates of lateral displacements of free-field surface and top-cap. Data after Pamuk et al. (2007).*

Subsequently, **Figure 6.49** compares the time-histories of the induced lateral displacement of the surface at the free-field (subplot **6.49a**) and of the top-cap (subplot **6.49b**) measured during the experiment and those given by the numerical analysis. The lateral displacement is the result of the lateral spreading of the liquefied loose Nevada sand layer, as already discussed in **Section 6.4.1**. The comparison is very satisfactory in terms of lateral displacements in both locations throughout the shaking.

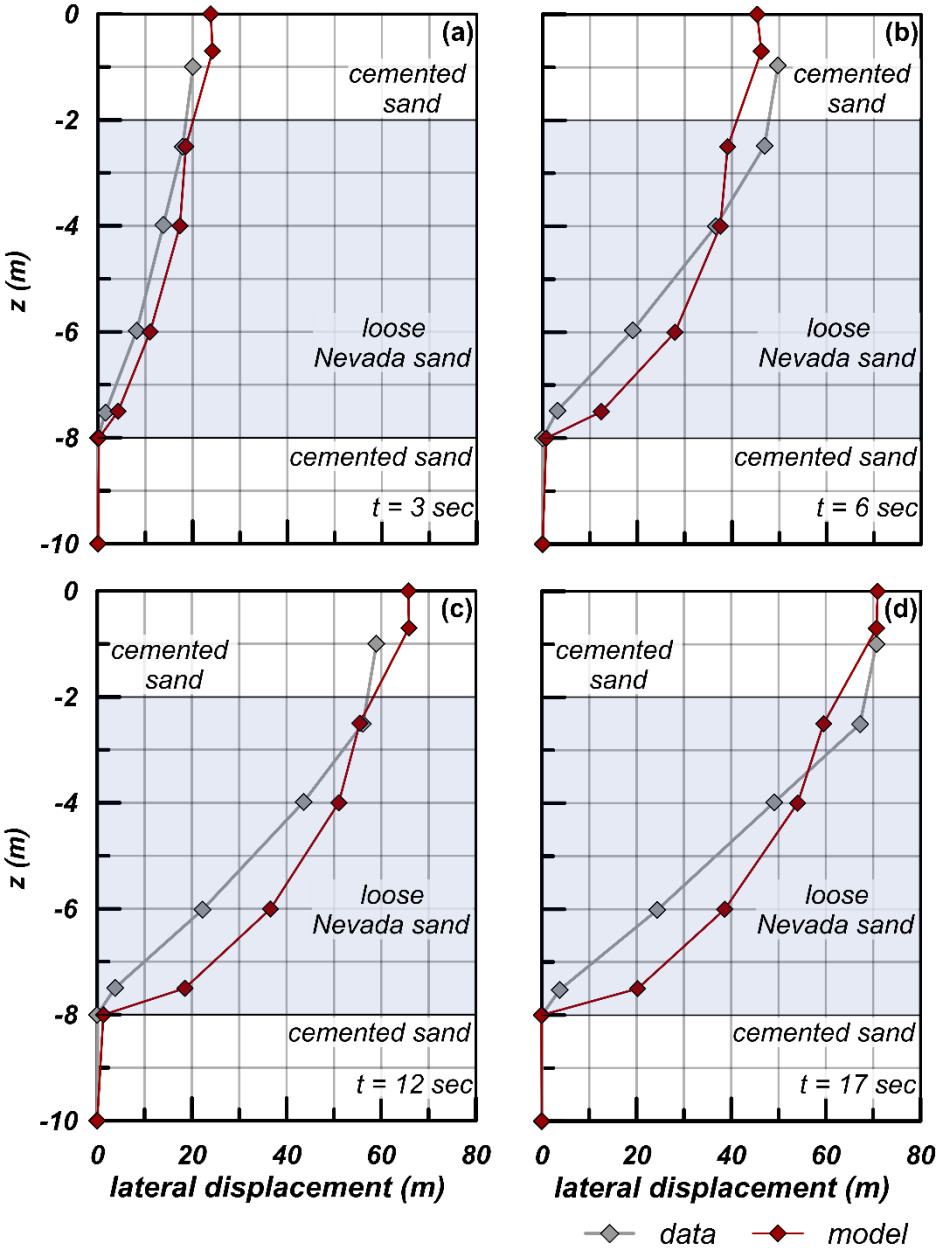

***Figure 6.50**: Experimental results and model estimates of snapshots of lateral displacements at various depths along right side of the layout. Data after Pamuk et al. (2007).*

Figure 6.50 presents a comparison of the data and the numerical results of lateral displacements of the free-field as snapshots along the whole soil profile depth at the locations of LVDTs 2 - 6 at the specific time moments of t = 3 sec (subplot **6.50a**), 6 sec (subplot **6.50b**), 12 sec (subplot **6.50c**) and 17 sec (subplot **6.50d**). The comparison is generally satisfactory, with numerical results sightly overestimating the displacements at the lower depths and approaching them at the shallower locations, and thus showing a more curved distribution of lateral displacement with depth.

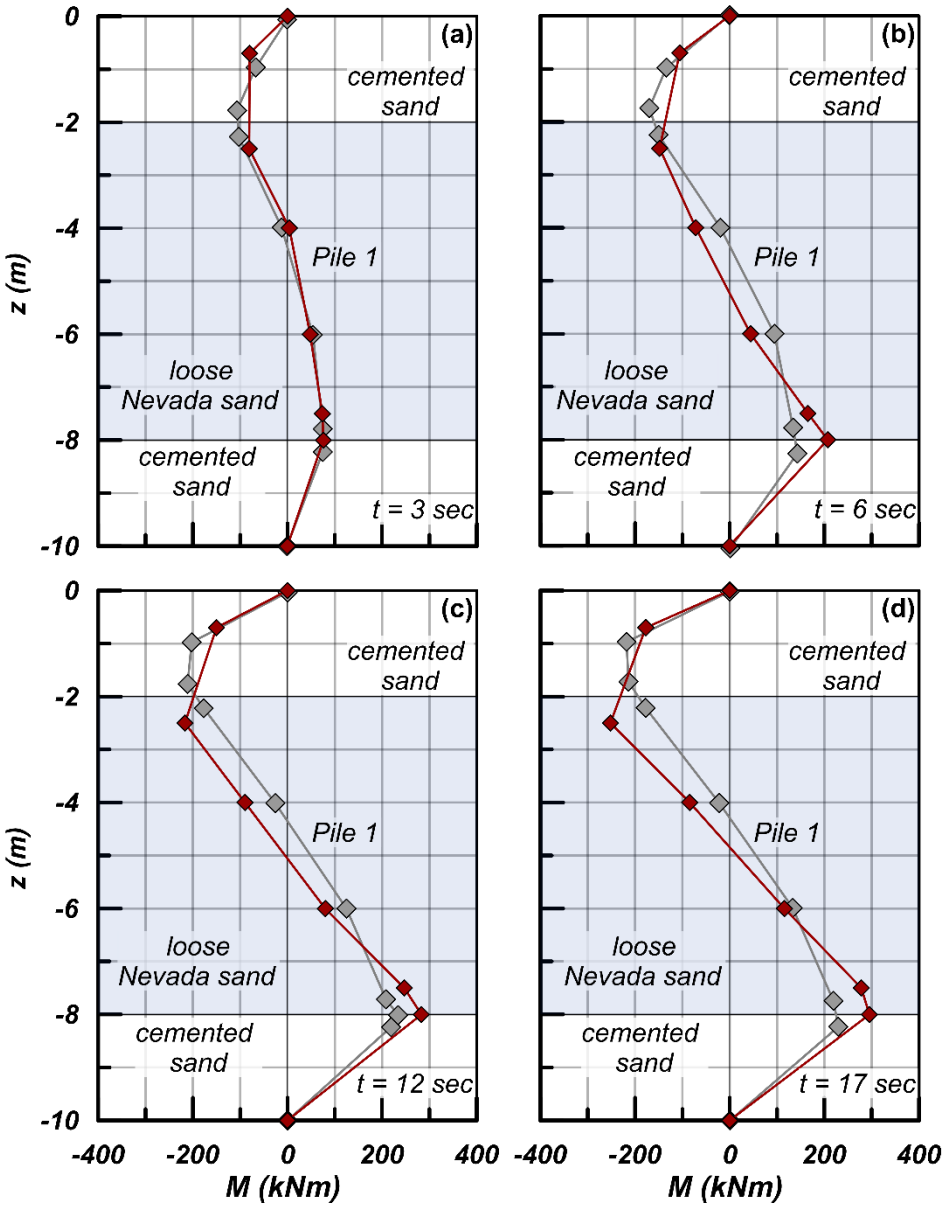

***Figure 6.51**: Experimental results and model estimates of snapshots of bending moments along Pile 1. Data after Pamuk et al. (2007).*

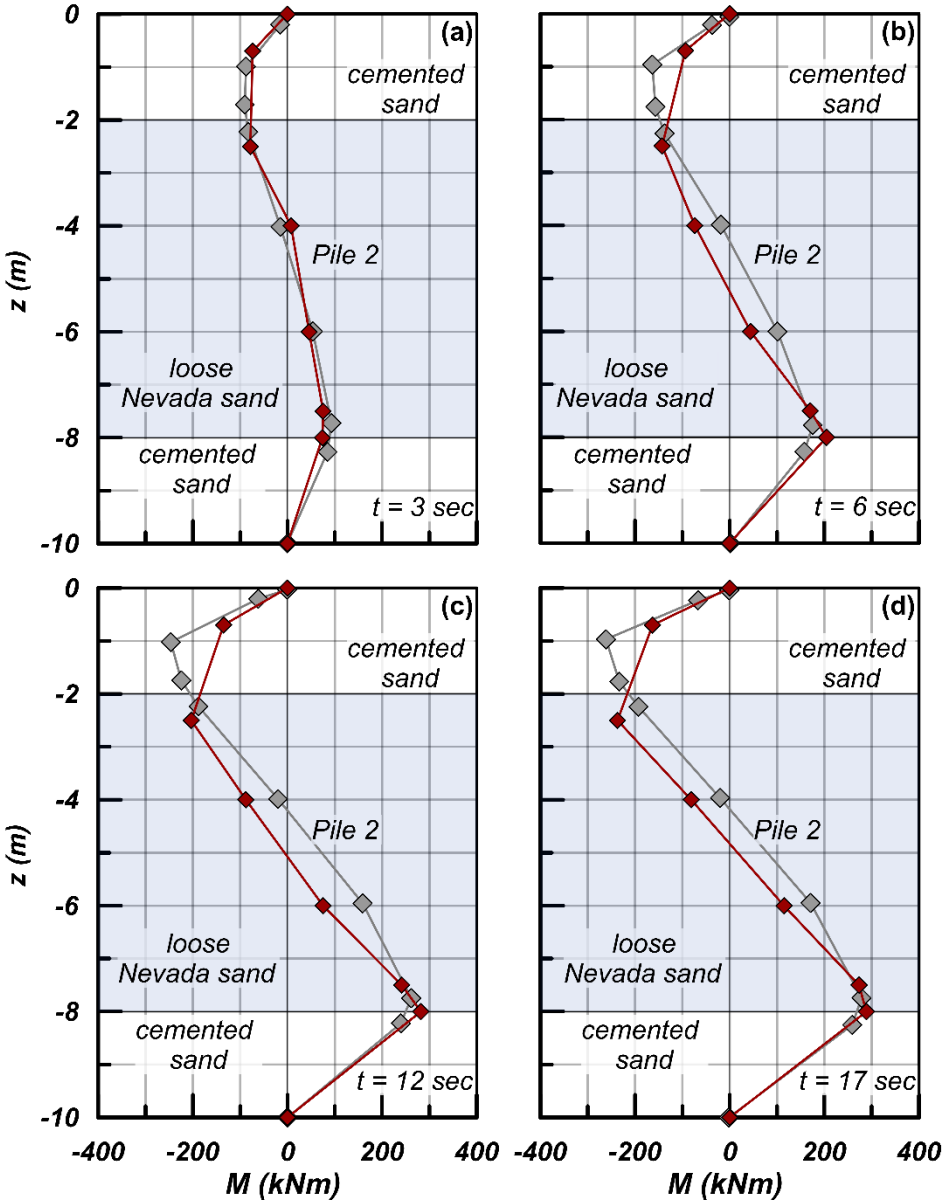

***Figure 6.52**: Experimental results and model estimates of snapshots of bending moments along Pile 2. Data after Pamuk et al. (2007).*

Additionally, **Figures 6.51** and **6.52** compare the recorded and the numerically predicted bending moments that developed along Pile 1 (**Figure 6.51**) and Pile 2 (**Figure 6.52**) at the specific time moments of t = 3 sec (subplots **6.51a** and **6.52a**), 6 sec (subplots **6.51b** and **6.52b**), 12 sec (subplots **6.51c** and **6.52c**) and 17 sec (subplots **6.51d** and **6.52d**). The numerical results are derived analytically utilizing the induced lateral displacement of the piles. The comparison is in general quite satisfactory, with numerical results estimating both quantitatively and qualitatively well the developed moments on the piles at all depths

and at all times. The "S" shaped distribution of the moments with depth and their high values at the interfaces between the loose liquefied Nevada sand layer and the cemented upper and lower sand layers are consistently captured by the analysis.

Finally, **Figure 6.53** depicts a snapshot of contours of accumulated shear strains within the soil medium at the moment of t = 17 sec and provides insight into the deformation mechanism of the system. The soil profile has been sheared, experiencing downslope lateral permanent displacement due to the liquefaction of the middle loose Nevada sand layer. The upper cemented sand layer actually follows its underlain layer and their relative displacement is rather limited. On the contrary, significant relative displacement is induced between the cemented non-liquefied base sand layer which practically has not displaced and its overlain liquefied layer that has experienced lateral spreading. This justifies the intense shear strain accumulation at their interface. Shear strain has also accumulated on both sides and between the piles, as a result of their movement during shaking. The deformed mesh follows the shape of the distribution of lateral displacement through depth, as already shown in **Figure 6.50.**

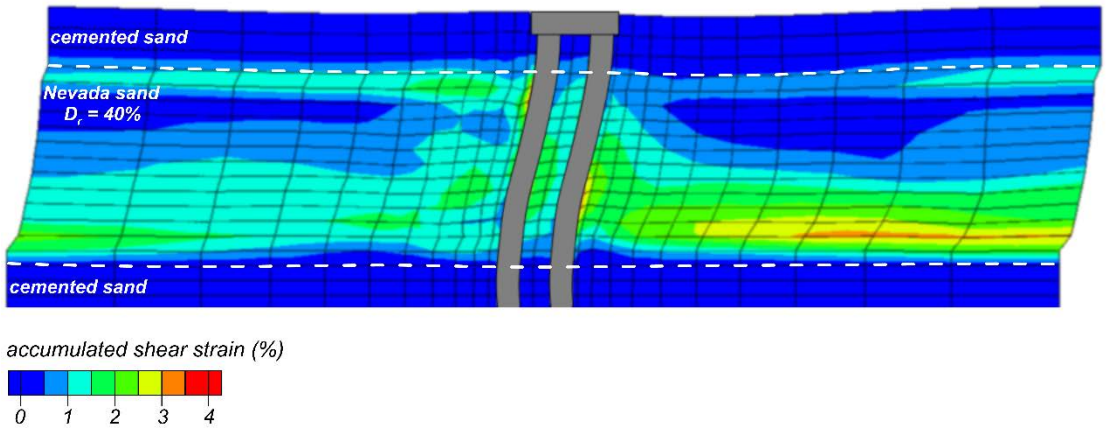

Figure 6.53: *Contours of accumulated shear strain (ssi in FLAC's terminology) and deformed mesh at the end of shaking, for the simulation of the centrifuge experiment of Pamuk et al. (2007)*

6.6 Summary

This Chapter employs the same set of values of model parameters (derived in **Chapter 5)** for Nevada sand and verifies model's simulative potential at the system level, via comparisons with data from 9 dynamic centrifuge tests performed on the same sand. These

tests refer to: a) the free-field response of a horizontal liquefiable layer (Model test No. 1 of VELACS Project), b) the lateral spreading response of a gently sloping liquefiable layer (Model test No. 2 of VELACS Project), c) the seismic response of rigid foundations on a single-layered liquefiable ground (3 tests for Model test No. 12 of VELACS Project), as well as on a two-layered horizontal liquefiable ground (3 tests of Dashti et al., 2010b) and d) the piles' system response in an inclined liquefiable soil profile (Pamuk et al., 2007). The caterories a) - c) are simulated in 2D (plane strain) conditions, while the category d) is simulated in 3D conditions.

The model is proven to provide satisfactory accuracy in simulating accelerations, excess pore pressures and (vertical and horizontal) displacements of geostructures in a liquefaction regime, without the need of case-specific re-calibration, despite that in the analyzed BVPs the peak acceleration varied from 0.15 g to 0.38 g, while the relative density D_r of Nevada sand varied from 40% to 90%. Note that this accuracy is achieved with a sand permeability value that only depends on the D_r of the sand, without resorting to approximations of time-dependent (or possibly excess pore pressure ratio, r_u -dependent) permeability coefficient due to liquefaction, as often performed in the literature.

Additional analyses of these same BVPs show that incorporating a post-liquefaction strain accumulation formulation leads to larger accumulated displacements of geostructures, without this increase of displacements being overly significant. This means that such formulations, that have started to appear in different forms in sand constitutive models lately, are useful, but their accuracy relies on proper calibration. To be frank, their properly-calibrated use seems not to be critical for BVPs involving liquefaction, which means that the reliability of existing and widely used liquefaction models in the literature without such a formulation (e.g., (Andrianopoulos et al. 2010a; Dafalias and Manzari 2004)) is not significantly undermined on the basis of this finding (e.g., (Reyes et al. 2021)). Similarly, additional analyses of these same BVPs show that the formulation for the appropriate updating of the $\boldsymbol{r}_{ini}$ in order to avoid stress-strain overshooting is a useful tool, especially in the employed model in which both the elastic and the plastic strain rates are affected by its definition. Specifically, the analyses show a differentiation of up to 20% on

displacements, which means that the overall effect of this formulation cannot be considered crucial for the accuracy of the numerical estimates. This conclusion is considered valid for liquefaction-related dynamic BVPs, but cannot be generalized for other types of BVPs (e.g., static analyses) without further study.

Given the depicted underestimation of free-field ground settlements in 1D liquefied ground response, it should be clarified here that being of the SANISAND-type, the proposed model is accurate in monotonic or cyclic shearing paths where non-zero deviatoric stress ratio rates ($\dot{\boldsymbol{r}} \neq 0$) prevail, but under-estimates plastic strain in problems where loading under constant stress ratio is significant (e.g., one-dimensional consolidation). This is a limitation shared by many similar stress-ratio driven models in the literature, that do not incorporate a double-yield mechanism, either via a closed (convex) yield surface shape (e.g., (Taiebat and Dafalias 2008)) or via a cap (e.g., (Wang et al. 1990)). Such constitutive formulations were beyond the scope of the new constitutive model. Despite the foregoing limitation, the verification process in this paper proves that the proposed model is a reliable numerical tool for user-friendly performance-based design of geostructures in a liquefaction regime.

Chapter 7

Summary, Conclusions and Future Research Directions

7.1 Summary

In this Thesis, a new constitutive model for the simulation of the monotonic and cyclic response of granular soils is formulated, calibrated and validated at the element and system levels. Specifically, this research effort has two major parts: (a) the formulation of the new constitutive model, its calibration and validation at the element level, against a large database of experimental data and empirical relationships from the literature and (b) its implementation in numerical codes *FLAC* and *FLAC*^{3D} and its validation at system level, against results from numerous dynamic centrifuge tests related to liquefaction.

The first part of the Thesis proposes a new bounding surface plasticity model developed in conjunction with the concept of stress reversal surfaces. It is a member of the SANISAND family of models and builds on the NTUA-SAND model, from which it inherits constitutive concepts, like the small and medium strain nonlinearity via a Ramberg-Osgood type formulation and a fabric evolution index for large strain response, albeit modified. Being of the SANISAND-type, the model employs three surfaces, the bounding, the dilatancy and the critical state surface, that take the form of homologous open cone surfaces with apex at the stress origin, without a (small) yield surface. The aperture of these surfaces depends on the Lode angle θ and the state parameter ψ. The model incorporates different formulations for dilatancy in contraction and dilation. The concept of reversal surfaces is incorporated via the updating of $\boldsymbol{r}_{\text{ini}}$, i.e., the deviatoric stress ratio tensor value at the last load reversal, which enters the calculations of the mapping rule and the loading direction, the elastic moduli, the plastic modulus and the dilatancy (in contraction). As such, the model incorporates a robust formulation for the appropriate updating of the $\boldsymbol{r}_{\text{ini}}$ in order to avoid stress-strain overshooting, but also to establish that strain accumulation is insignificant at very small-strain cyclic loading in accordance to the literature. Fabric-related cumulative functions are used to scale the plastic modulus and the dilatancy (in dilation), targeting strain accumulation with cycles. Moreover, post-liquefaction strains are in focus, with an appropriate modification of the dilatancy function (in dilation) in the small

mean effective stress regime. The calibration procedure of its 14 model parameters, as well as its verification at the element level is performed for 7 granular materials from the literature, including 5 sands and 2 gravels.

The second part of the Thesis includes the new model's implementation in the finite-difference codes *FLAC* and *FLAC*^{3D}. Its implementation as a UDM (User-Defined-Model) routine inherits the methodology and the concepts that were used for the same implementation of the NTUA-SAND model in the past, after proper modifications. For this purpose, an explicit stress integration algorithm with automatic error control and a sub-stepping technique were used. Then, the model is validated at the system level, against dynamic problems related to seismic liquefaction. The validation is performed on the basis of experimental results from centrifuge tests of geostructures on Nevada sand. In total, 9 different boundary value problems were examined, that fall into 4 different categories. Specifically, the validation included the 2D seismic response of: a) a horizontal liquefiable sand layer, b) a mildly sloping liquefiable sand layer and c) systems of shallow foundations on different soil profiles including liquefiable sand layers and excited by different seismic motions and finally, the 3D seismic response of a pile group in a mildly sloping soil profile including a liquefiable sand layer. Since the utilized liquefiable sand is the same in all 9 boundary value problems, the model calibration is unique in all the examined cases, as it was derived on the basis of laboratory data and comparisons at the element level. In addition, the same numerical methodology (e.g., permeability coefficient, numerical damping) is adopted in all centrifuge test simulations for a clearer model verification.

7.2 Conclusions

The main conclusions, that arise from this work, can be summarized in the following:

a) The proposed SANISAND-type constitutive model serves as an effective numerical tool for simulating both the monotonic and the cyclic response of granular soils, with a unique (per soil) set of 14 model parameters irrespective of stress level, density or loading conditions. Of these parameters, 12 are related to monotonic loading and the last 2 are required for cyclic. Overall, 9 parameters may be directly calibrated, while the last 5 require trial-and-error runs in a well-defined procedure.

b) The simulative potential of the new model at element level was based on comparisons with experimental data and empirical relations from the literature for 7 different granular soils, that in terms of mean particle diameter D_{50} cover a range between 0.10-9 mm. This process included 5 sands and 2 gravels and the total number of simulated element tests is 450. These tests cover a huge range of initial conditions, namely: the initial mean effective stress p_o ranges from 33.33 to 2000 kPa, while the initial relative density D_r from <2% to 90%.

c) For cyclic loading in particular, its validation at element level covers the whole range of possible cyclic shear strains and serves as a paradigm for such procedures. Namely, it starts from the *small strain regime* and the "quasi-elastic" response, for which the calibration of elastic moduli is based on dynamic measurements, and not the initial part of monotonic tests which underestimate their values. Then, it continues to the *medium strain regime,* where an accurate accumulation of (volumetric and shear) strains with cycles is exhibited, along with a satisfactory estimate of shear modulus degradation and hysteretic damping increase, with the latter being overestimated at large cyclic strains (e.g., 0.5%) as in all Masing-type models. Finally, it concludes with the *large strain regime*, for which liquefaction strength and post-liquefaction strain accumulation are well captured.

d) The monotonic response is captured effectively until the critical state, using the same model parameters as in the cyclic loading conditions, at least when it comes to sands. On the other hand, when it comes to gravels, the de-activation of fabric-related functions (via nullifying the model parameter N_o) in monotonic simulations has proven sufficient, without changing any other model parameter. Yet, further study for gravels is required, since there are few laboratory databases in the literature that include both monotonic and cyclic tests for the same gravel material.

e) The validation at system level was performed after the model implementation in *FLAC* and *FLAC*^{3D} using an explicit stress integration algorithm, that proved efficient for problems involving liquefaction. Specifically, the validation was performed via 2D and 3D simulations against data from 9 dynamic centrifuge tests (from the literature) involving liquefaction of the same (Nevada) sand, but different soil-structure systems. It revealed the potential of the new model in providing satisfactory

accuracy in simulating ground accelerations, excess pore pressures and (vertical and horizontal) displacements of geostructures in a liquefaction regime, without the need of problem-specific model recalibration. This accuracy is achieved despite that in the analyzed boundary value problems the peak ground acceleration varied from 0.15 g to 0.38 g, while the relative density D_r of the liquefiable sand varied from 40% to 90%. It should be underlined here that this unique set of model parameters was derived on the basis of element tests on the utilized sand and not back-estimated on the basis of the centrifuge test results. More importantly, all centrifuge test simulations were performed without altering the numerical methodology per test (e.g., sand permeability coefficient was a function of D_r, numerical damping of 2%).

f) Additional sensitivity analyses of these same boundary value problems focusing on specific novel constitutive ingredients show that incorporating the post-liquefaction strain accumulation formulation leads to larger accumulated displacements of geostructures, without this increase of displacements being overly significant. Similar analyses also show that the formulation for the appropriate updating of the $\boldsymbol{r}_{ini}$ in order to avoid stress-strain overshooting is a useful tool, especially in the employed model in which both the elastic and the plastic strain rates are based on its proper updating.

g) As any other model, the proposed one has limitations. For example, the model is accurate in shearing paths where non-zero deviatoric stress ratio rates prevail, but predicts only elastic strains in problems where loading under constant stress ratio appears (e.g., one-dimensional consolidation). This shortcoming is based on the definition of the loading index, is common in all SANISAND-type models and its importance was shown in the underprediction of the free-field settlement of a horizontal liquefiable soil layer (in 1 of the 9 centrifuge tests). Accounting for plastic strains due to such types of loading may require additional mechanisms for plastic strain rate development (e.g., Wang et al., 1990).

h) Similarly, this model is, by design, unable to capture the plastic strains appearing during effective stress principal axes rotation, due to the ensuing non-coaxiality between the stress and the plastic strain rate tensors. Such paths may appear in seabeds due to wave action, and for SANISAND-type models additional plastic load

mechanisms, or multiple dilatancy and plastic modulus expressions must be considered for this purpose, if necessary (e.g., Petalas et al., 2019)

i) In closing, note that the proposed model is, by design, a general-purpose constitutive model for granular soils. Hence, its accuracy may not always be equal to that of problem-dedicated models. For example, the accuracy of a fabric-based anisotropic model (e.g. Papadimitriou et al., 2019) may be superior for monotonic loading, or, similarly, the plastic strain accumulation under thousands of small-amplitude cycles (e.g., during storm loading of offshore structures) may be better captured by dedicated "*high-cycle*" models (e.g., Niemunis et al., 2005). However, the proposed model enables the user to have satisfactory accuracy regardless of the problem at hand and without a need for problem-specific calibration.

7.3 Future Research Directions

It has been concluded that the new constitutive model achieves quite satisfactorily its primary purpose of serving as a general-purpose constitutive model of granular soils. However, there is still a need for improvement. In the following, future research directions involving the proposed model are outlined:

a) Until now, the model has been verified against fine and medium sands (D_{50} = 0.10 – 0.37 mm) and medium gravels (D_{50} = 8 - 9 mm). Hence, in the future, emphasis should be put on verifying the model for other granular soils, like coarse grained sands (D_{50} = 0.5 - 2 mm) and fine gravels (D_{50} = 2 - 6 mm), but also for non-plastic silts. Additionally, emphasis should be put on sand-silt and sand-gravel mixtures, i.e., on granular soils that are not uniform, as those already studied herein. This task will not be easy, since published laboratory test databases are not as rich as the ones employed herein, which include many different types of tests on each soil.

b) The model has 14 model parameters, whose calibration is described in detail. However, for practical applications their calibration is not the easiest task. The fact that the model has already been calibrated for 7 granular soils, highlights the sensitivity of model parameters to different soil types and may act as a guideline for fixing some of them. Calibrating the model, as is, to more granular soils will also add reliability to this process.

c) Until now, the model has been verified against dynamic centrifuge tests involving seismic liquefaction. Hence, in the future, emphasis should be put on verifying the model for other types of boundary value problems, not necessarily seismic and not necessarily involving liquefaction. For example, such tests could focus on drained response, either under static loading, or under low-frequency cyclic loading. This task will not be easy, since published physical modeling test results on granular soils have mostly focused historically on the problem of seismic liquefaction, but also because the published physical tests are not accompanied by element tests allowing proper model calibration.

d) Research may focus on alleviating the depicted constitutive limitations of the new model. Possibly the most important limitation is that the model is stress-ratio driven (as all SANISAND models). To account for plastic strains developed due constant stress-ratio loading paths, additional mechanisms for plastic strain rate development may be considered. The incorporation of model surfaces with a modified closed form in multiaxial stress space, or more simply of a "*cap*" in addition to the existing model surfaces may significantly contribute towards this direction (e.g., as in the models of Wang et al., 1990).

e) In the same train of thought, and aiming at more accurate monotonic shear paths, the model could consider inherent and evolving anisotropy until the unique Critical State condition. The more robust manner in performing this task is the incorporation of the Anisotropic Critical State Theory (ACST) of Li and Dafalias (2012). For example, Papadimitriou et al. (2019) proposed the fabric-based anisotropic SANISAND-FR model, but showed the pros and cons of reducing their model to an "*isotropic*" SANISAND-R variant (with fewer model parameters). This juxtaposition of model formulations may be used as a guideline for incorporating the ACST in this model. Similarly, if principal stress axes (PSA) rotation is of importance, then additional plastic load mechanisms, or multiple dilatancy and plastic modulus expressions must be considered. The work of Petalas et al. (2019) in proposing the SANISAND-FN model that accounts for PSA rotation, in juxtaposition to the simpler SANISAND-F model Petalas et al. (2020) that does not include a PSA rotation formulation, may be used as a guideline for this purpose.

Bibliography

Adalier, K., Elgamal, A., Meneses, J., and Baez, J. . (2003). “Stone columns as liquefaction countermeasure in non-plastic silty soils.” *Soil Dynamics and Earthquake Engineering*, 23(7), 571–584.

Adamidis, O., and Madabhushi, S. P. G. (2017). “Deformation mechanisms under shallow foundations on liquefiable layers of varying thickness.” *Géotechnique*, 1–12.

Andrianopoulos, K. I. (2006). “Numerical Modeling of static and dynamic behavior of elastoplastic soils (in Greek).” School of Civil Engineering, National Technical University of Athens.

Andrianopoulos, K. I., Papadimitriou, A. G., and Bouckovalas, G. D. (2010a). “Bounding surface plasticity model for the seismic liquefaction analysis of geostructures.” *Soil Dynamics and Earthquake Engineering*, Elsevier, 30(10), 895–911.

Andrianopoulos, K. I., Papadimitriou, A. G., and Bouckovalas, G. D. (2010b). “Explicit integration of bounding surface model for the analysis of earthquake soil liquefaction.” *International Journal for Numerical and Analytical Methods in Geomechanics*, 34(15), 1586–1614.

Arulanandan, K., and Sybico, Jj. (1992). “Post liquefaction settlement of sands.” *Proc. of the Wroth Memorial Symposium*, Oxford University, England.

Arulmoli, K., Muraleetharan, K. K., Hossain, M. M., and Fruth, L. S. (1992). *VELACS: Verification of liquefaction analysis by centrifuge studies, laboratory testing program. Soil Data Report*. Irvine,CA.

Askarinejad, F., Halabian, A. M., and Hashemalhosseini, S. H. (2021). “New Viscoplastic Bounding Surface Subloading Model for Time-Dependent Behavior of Sands.” *International Journal of Geomechanics*, 21(4), 04021034.

Bardet, J. P. (1986). “Bounding Surface Plasticity Model for Sands.” *Journal of*

Engineering Mechanics, 112(11), 1198–1217.

Barrero, A. R., Taiebat, M., and Dafalias, Y. F. (2020). "Modeling cyclic shearing of sands in the semifluidized state." *International Journal for Numerical and Analytical Methods in Geomechanics*, 44(3), 371–388.

Bastidas, A. M. P. (2016). "Ottawa F-65 Sand Characterization." University of California,Davis.

Bauer, E., and Wu, W. (1993). "A Hypoplastic Model for Granular Soils under Cyclic Loading." *Modern Approaches to Plasticity*, Elsevier, 247–258.

Beaty, M. H., and Byrne, P. M. (2011). *"UBCSAND constitutive model version 904aR." Documentation Rep.,UBCSAND Constitutive Model on Itasca UDM Website*.

Been, K., and Jefferies, M. G. (1985). "A state parameter for sands." *Géotechnique*, 35(2), 99–112.

Bertalot, D., and Brennan, A. J. (2015). "Influence of initial stress distribution on liquefaction-induced settlement of shallow foundations." *Géotechnique*, 65(5), 418–428.

Bhattacharya, S., Cox, J. A., Lombardi, D., and Muir Wood, D. (2013). "Dynamics of offshore wind turbines supported on two foundations." *Proceedings of the Institution of Civil Engineers - Geotechnical Engineering*, 166(2), 159–169.

Bouckovalas, G. D., Tsiapas, Y. Z., Theocharis, A. I., and Chaloulos, Y. K. (2016). "Ground response at liquefied sites: seismic isolation or amplification?" *Soil Dynamics and Earthquake Engineering*, 91, 329–339.

Bouckovalas, G., Whitman, R. V., and Marr, W. A. (1984). "Permanent Displacement of Sand With Cyclic Loading." *Journal of Geotechnical Engineering*, 110(11), 1606–1623.

Boulanger, R. W., and Ziotopoulou, K. (2013). "Formulation of a sand plasticity plane-strain model for earthquake engineering applications." *Soil Dynamics and*

Earthquake Engineering, Elsevier, 53, 254–267.

Bullock, Z., Karimi, Z., Dashti, S., Porter, K., Liel, A. B., and Franke, K. W. (2019). "A physics-informed semi-empirical probabilistic model for the settlement of shallow-founded structures on liquefiable ground." *Géotechnique*, 69(5), 406–419.

Carnevale, R., and Elgamal, A. (1994). "Experimental results of RPI centrifuge Model No. 12." *Proceedings of Int. Conf. on Verification of numerical procedures for the analysis of soil liquefaction problems*, Davis, CA, 17-10, October, 1019–1026, Vol. I.

Cheng, Z., and Detournay, C. (2021). "Formulation, validation and application of a practice-oriented two-surface plasticity sand model." *Computers and Geotechnics*, 132.

Christian, J. T., and David Carrier III, W. (1978). "Janbu, Bjerrum and Kjaernsli's chart reinterpreted." *Canadian Geotechnical Journal*, 15(1), 123–128.

Corti, R., Diambra, A., Wood, D. M., Escribano, D. E., and Nash, D. F. T. (2016). "Memory Surface Hardening Model for Granular Soils under Repeated Loading Conditions." *Journal of Engineering Mechanics*, 142(12), 04016102.

Cubrinovski, M., and Ishihara, K. (1998). "Modelling of Sand Behaviour Based on State Concept." *Soils and Foundations*, 38(3), 115–127.

Dafalias, Y. F. (1986). "Bounding Surface Plasticity. I: Mathematical Foundation and Hypoplasticity." *Journal of Engineering Mechanics*, 112(9), 966–987.

Dafalias, Y. F., and Manzari, M. T. (2004). "Simple Plasticity Sand Model Accounting for Fabric Change Effects." *Journal of Engineering Mechanics*, 130(6), 622–634.

Dafalias, Y. F., Papadimitriou, A. G., and Li, X. S. (2004). "Sand Plasticity Model Accounting for Inherent Fabric Anisotropy." *Journal of Engineering Mechanics*, 130(11), 1319–1333.

Dafalias, Y. F., and Popov, E. P. (1975). “A model of nonlinearly hardening materials for complex loading.” *Acta Mechanica*, 21(3), 173–192.

Dafalias, Y. F., and Taiebat, M. (2016). “SANISAND-Z: zero elastic range sand plasticity model.” *Géotechnique*, 66(12), 999–1013.

Darendeli, M. (2001). “Development of a new family of normalized modulus reduction and material damping curves.” The University of Texas at Austin.

Dashti, S., and Bray, J. D. (2013). “Numerical Simulation of Building Response on Liquefiable Sand.” *Journal of Geotechnical and Geoenvironmental Engineering*, 139(8), 1235–1249.

Dashti, S., Bray, J. D., Pestana, J. M., Riemer, M., and Wilson, D. (2010a). “Mechanisms of Seismically Induced Settlement of Buildings with Shallow Foundations on Liquefiable Soil.” *Journal of Geotechnical and Geoenvironmental Engineering*, 136(1), 151–164.

Dashti, S., Bray, J. D., Pestana, J. M., Riemer, M., and Wilson, D. (2010b). “Centrifuge Testing to Evaluate and Mitigate Liquefaction-Induced Building Settlement Mechanisms.” *Journal of Geotechnical and Geoenvironmental Engineering*, 136(7), 918–929.

Dashti, S., Bray, J., Pestana, J., Riemer, M., and Wilson, D. (2009a). *Towards Developing an Engineering Procedure for Evaluating Building Performance on Softened Ground, REPORT NO. UCB/CGMDR-09/07*. Berkeley, CA.

Dashti, S., Bray, J., Pestana, J., Riemer, M., and Wilson, D. (2009b). *NEESR-II Project: “Towards Developing an Engineering Procedure for Evaluating Building Performance on Softened Ground” Centrifuge Test Plan for Test Series SHD04*. Berkeley, CA.

Dawson, E. M., Roth, W. H., Nesarajah, S., Bureau, G., and Davis, C. A. (2001). “A practice oriented pore-pressure generation model.” *FLAC and Numerical Modeling in Geomechanics*, CRC Press, 47–54.

DorMohammadi, H., and Khoei, A. R. (2008). “A three-invariant cap model with isotropic–kinematic hardening rule and associated plasticity for granular materials.” *International Journal of Solids and Structures*, 45(2), 631–656.

Duku, P. M., Stewart, J. P., Whang, D. H., and Yee, E. (2008). “Volumetric Strains of Clean Sands Subject to Cyclic Loads.” *Journal of Geotechnical and Geoenvironmental Engineering*, 134(8), 1073–1085.

Duque, J., Yang, M., Fuentes, W., Mašín, D., and Taiebat, M. (2021). “Characteristic limitations of advanced plasticity and hypoplasticity models for cyclic loading of sands.” *Acta Geotechnica*.

Van Eekelen, H. A. M. (1980). “Isotropic yield surfaces in three dimensions for use in soil mechanics.” *International Journal for Numerical and Analytical Methods in Geomechanics*, 4(1), 89–101.

Elgamal, A., Yang, Z., Parra, E., and Ragheb, A. (2003). “Modeling of cyclic mobility in saturated cohesionless soils.” *International Journal of Plasticity*, 19(6), 883–905.

Farrel, T., and Kutter, B. (1994). “Experimental results of model No. 12.” *Proceedings of Int. Conf. on Verification of numerical procedures for the analysis of soil liquefaction problems*, Davis, CA, 17-10, October, 1027–1034, Vol. I.

Fuentes, W., and Triantafyllidis, T. (2015). “ISA: A constitutive model for deposited sand.” *Aktuelle Forschung in der Bodenmechanik 2015*, Springer Berlin Heidelberg, Berlin, Heidelberg, 169–187.

Gajo, A., and Muir Wood, D. (1999). “A kinematic hardening constitutive model for sands: the multiaxial formulation.” *International Journal for Numerical and Analytical Methods in Geomechanics*, 23(9), 925–965.

Gao, Z., and Zhao, J. (2015). “Constitutive Modeling of Anisotropic Sand Behavior in Monotonic and Cyclic Loading.” *Journal of Engineering Mechanics*, 141(8), 04015017.

Gao, Z., Zhao, J., Li, X.-S., and Dafalias, Y. F. (2014). “A critical state sand plasticity model accounting for fabric evolution.” *International Journal for Numerical and Analytical Methods in Geomechanics*, 38(4), 370–390.

Gerolymos, N., and Anthi, M. (2019). “A calibration procedure for sand plasticity modeling in earthquake engineering: Application to TA-GER, UBCSAND and PM4SAND.” *7th International Conference on Earthquake Geotechnical Engineering (ICEGE)*, F. Silvestri and Moraci M, eds., Rome, Italy, 1138–1145.

El Ghoraiby, M. A., Park, H., and Manzari, M. T. (2017). *LEAP 2017: Soil Characterization and Element Tests for Ottawa F65 Sand*. Washington, DC.

El Ghoraiby, M., Park, H., and Manzari, M. (2018). *LEAP-2017 GWU Laboratory Tests*.

Hardin, B. O. (1978). “The nature of stress-strain behavior for soils.” *Volume I :Earthquake Engineering and Soil Dynamics--Proceedings of the ASCE Geotechnical Engineering Division Specialty Conference*, New York, NY United States, 3–90.

Houlsby, G., and Puzrin, A. (2006). *Principles of Hyperplasticity*. Springer London, London.

Hubler, J. F. (2017). “Laboratory and In-Situ Assessment of Liquefaction of Gravelly Soils.” The University of Michigan.

Hubler, J. F., Athanasopoulos-Zekkos, A., and Zekkos, D. (2017). “Monotonic, Cyclic, and Postcyclic Simple Shear Response of Three Uniform Gravels in Constant Volume Conditions.” *Journal of Geotechnical and Geoenvironmental Engineering*, 143(9), 04017043.

Hueckel, T., and Nova, R. (1979). “Some hysteresis effects of the behaviour of geologic media.” *International Journal of Solids and Structures*, 15(8), 625–642.

Hynes, M. E., and Olsen, R. (1999). “Influence of confining stress on liquefaction resistance.” *Physics and Mechanics of Soil Liquefaction*, Lade P.V. and

Yamamuro J.A., eds., Balkema, Rotterdam, Netherlands, 145–152.

Idriss, I. M., and Boulanger, R. W. (2008). *Soil liquefaction during earthquakes*. Earthquake Engineering Research Institute, Oakland, CA.

Ishihara, K. (1993). "Liquefaction and flow failure during earthquakes." *Géotechnique*, 43(3), 351–451.

Ishihara, K., and Towhata, I. (1983). "Sand Response to Cyclic Rotation of Principal Stress Directions as Induced by Wave Loads." *Soils and Foundations*, 23(4), 11–26.

Ishihara, K., and Tsukamoto, Y. (2004). "Cyclic strength of imperfectly saturated sands and analysis of liquefaction." *Proceedings of the Japan Academy, Series B*, 80(8), 372–391.

Ishihara, K., and Watanabe, T. (1976). "Sand Liquefaction Through Volume Decrease Potential." *Soils and Foundations*, 16(4), 61–70.

Ishihara, K., and Yamazaki, A. (1984). "Analysis of Wave-Induced Liquefaction in Seabed Deposits of Sand." *Soils and Foundations*, 24(3), 85–100.

Itasca Consulting Group Inc. (2011). "*FLAC*—Fast Lagrangian Analysis of Continua, version 7.0." Itasca, Minneapolis.

Itasca Consulting Group Inc. (2012). "*FLAC*^{3D} v.5."

Iwan, W. D., and Yoder, P. J. (1983). "Computational Aspects of Strain-Space Plasticity." *Journal of Engineering Mechanics*, 109(1), 231–243.

Jafarzadeh, F., and Yanagisawa, E. (1995). "Settlement of sand models under unidirectional shaking." *Proc. of 1st Int. Conference on Earthquake Geotechnical Engineering*, K. Ishihara, ed., A. A. Balkema, Rotterdam, Netherlands, 693–698, Vol.2.

Janbu, N., Bjerrum, L., and Kjaernsli, B. (1956). *Stabilitetsberegning for fyllinger skjaeringer og naturlige skraninger*. Norwegian Geotechnical Institute, Publication No. 16, Oslo, Norway.

Kammerer, A. M., Wu, J., Pestana, J. M., Riemer, M., and Seed, R. B. (2000). *Kammerer, A. M., Wu, J., Pestana, J. M., Riemer, M., and Seed, R. B. (2000). Cyclic simple shear testing of Nevada sand for PEER center project 2051999*. Berkeley, CA.

Karamitros, D. K. (2010). "Development of a numerical algorithm for the dynamic elastoplastic analysis of geotechnical structures in two (2) and three (3) dimensions." National Technical University of Athens.

Karamitros, D. K., Bouckovalas, G. D., and Chaloulos, Y. K. (2013a). "Insight into the Seismic Liquefaction Performance of Shallow Foundations." *Journal of Geotechnical and Geoenvironmental Engineering*, 139(4), 599–607.

Karamitros, D. K., Bouckovalas, G. D., Chaloulos, Y. K., and Andrianopoulos, K. I. (2013b). "Numerical analysis of liquefaction-induced bearing capacity degradation of shallow foundations on a two-layered soil profile." *Soil Dynamics and Earthquake Engineering*, 44, 90–101.

Karimi, Z., Dashti, S., Bullock, Z., Porter, K., and Liel, A. (2018). "Key predictors of structure settlement on liquefiable ground: a numerical parametric study." *Soil Dynamics and Earthquake Engineering*, 113, 286–308.

Kokusho, T. (2014). "Seismic base-isolation mechanism in liquefied sand in terms of energy." *Soil Dynamics and Earthquake Engineering*, 63, 92–97.

Kolymbas, D. (2012). "Barodesy: a new hypoplastic approach." *International Journal for Numerical and Analytical Methods in Geomechanics*, 36(9), 1220–1240.

Krieg, R. D. (1975). "A Practical Two Surface Plasticity Theory." *Journal of Applied Mechanics*, 42(3), 641–646.

Krstelj, I., and Prevost, J. (1994). "Experimental results of Model No. 12." *Proceedings of Int. Conf. on Verification of numerical procedures for the analysis of soil liquefaction problems*, Davis, CA, 17-10, October, 1007–1017, Vol. I.

Li, X.-S., Dafalias, Y. F., and Wang, Z.-L. (1999). “State-dependant dilatancy in critical-state constitutive modelling of sand.” *Canadian Geotechnical Journal*, 36(4), 599–611.

Li, X. S., and Dafalias, Y. F. (2000). “Dilatancy for cohesionless soils.” *Geotechnique*, 50(4), 449–460.

Li, X. S., and Dafalias, Y. F. (2002). “Constitutive Modeling of Inherently Anisotropic Sand Behavior.” *Journal of Geotechnical and Geoenvironmental Engineering*, 128(10), 868–880.

Li, X. S., and Dafalias, Y. F. (2012). “Anisotropic Critical State Theory: Role of Fabric.” *Journal of Engineering Mechanics*, 138(3), 263–275.

Li, X. S., and Wang, Y. (1998). “Linear Representation of Steady-State Line for Sand.” *Journal of Geotechnical and Geoenvironmental Engineering*, 124(12), 1215–1217.

Li, Z., and Liu, H. (2020). “An isotropic-kinematic hardening model for cyclic shakedown and ratcheting of sand.” *Soil Dynamics and Earthquake Engineering*, 138, 106329.

Ling, H. I., and Yang, S. (2006). “Unified Sand Model Based on the Critical State and Generalized Plasticity.” *Journal of Engineering Mechanics*, 132(12), 1380–1391.

Liu, H., Diambra, A., Abell, J. A., and Pisanò, F. (2020). “Memory-Enhanced Plasticity Modeling of Sand Behavior under Undrained Cyclic Loading.” *Journal of Geotechnical and Geoenvironmental Engineering*, 146(11), 04020122.

Liu, H. Y., Abell, J. A., Diambra, A., and Pisanò, F. (2019). “Modelling the cyclic ratcheting of sands through memory-enhanced bounding surface plasticity.” *Géotechnique*, 69(9), 783–800.

Liu, L., and Dobry, R. (1997). “Seismic Response of Shallow Foundation on Liquefiable Sand.” *Journal of Geotechnical and Geoenvironmental Engineering*, 123(6), 557–567.

Lombardi, D., Bhattacharya, S., Hyodo, M., and Kaneko, T. (2014). “Undrained behaviour of two silica sands and practical implications for modelling SSI in liquefiable soils.” *Soil Dynamics and Earthquake Engineering*, 66, 293–304.

Loukidis, D., and Salgado, R. (2009). “Modeling sand response using two-surface plasticity.” *Computers and Geotechnics*, Elsevier Ltd, 36(1–2), 166–186.

Manzari, M., and Arulanandan, K. (1994). “Numerical predictions for Model No. 1.” *Proc. of Int. Conf. on Verification of numerical procedures for the analysis of soil liquefaction problems*, Davis, CA, 17-10, October, 179–185, Vol. 1.

Manzari, M. T., and Dafalias, Y. F. (1997). “A critical state two-surface plasticity model for sands.” *Géotechnique*, 47(2), 255–272.

Manzari, M. T., and El Ghoraiby, M. A. (2021). “On Validation of a Two-Surface Plasticity Model for Soil Liquefaction Analysis.” 723–730.

Masing, G. (1926). “Eigenspannungen und verfestigung beim messing (Self stretching and hardening for brass) (in German).” *Second International Congress of Applied Mechanics*, Zurich, Switzerland, 332–335.

McAllister, G., Taiebat, M., Ghofrani, A., Chen, L., and Arduino, P. (2015). “Nonlinear Site Response Analyses and High Frequency Dilation Pulses.” *68e Conférence Canadienne de Géotechnique et 7e Conférence Canadienne sur le Pergélisol, 20 au 23 septembre 2015, Québec, Québec.*, (1997).

McCartney, J., Kuhn, J., and Zornberg, J. (2005). “Geosynthetic drainage layers in contact with unsaturated soils.” *Proc., 16th ISSMGE Conf. on Geotechnical Engineering in Harmony with the Global Environment*, Ministry of Land, Infrastructure and Transport and the Ministry of the Environment, Tokyo.

Montgomery, J., Boulanger, R., and Harder, L. (2012). *Examination of the Kσ overburden correction factor on liquefaction resistance, Report No. UCD/CGM-12/02*.

Mróz, Z. (1967). “On the description of anisotropic workhardening.” *Journal of the*

Mechanics and Physics of Solids, 15(3), 163–175.

Mróz, Z., Norris, V. A., and Zienkiewicz, O. C. (1979). "Application of an anisotropic hardening model in the analysis of elasto–plastic deformation of soils." *Géotechnique*, 29(1), 1–34.

Mroz, Z., and Zienkiewicz, O. (1984a). "Uniform formulation of constitutive equations for clays and sand." *Mechanics of Engineering Materials*, C. Desai and R. Gallagher, eds., Wiley, New York, NY United States, 415–450.

Mroz, Z., and Zienkiewicz, O. C. (1984b). "Uniform formulation of constitutive equations for clays and sands." *Mechanics of engineering materials. Wiley*, C. Desai and R. Gallagher, eds., John Wiley & Sons Ltd, 415–449.

Mulilis, P., Arulanandan, K., Mitchell, J. K., Chan, C. K., and Seed, H. B. (1977). "Effects of Sample Preparation on Sand Liquefaction." *Journal of the Geotechnical Engineering Division*, 103(2), 91–108.

Niemunis, A., Wichtmann, T., and Triantafyllidis, T. (2005). "A high-cycle accumulation model for sand." *Computers and Geotechnics*, 32(4), 245–263.

Oda, M., Koishikawa, I., and Higuchi, T. (1978). "Experimental Study of Anisotropic Shear Strength of Sand by Plane Strain Test." *Soils and Foundations*, 18(1), 25–38.

Pamuk, A., Gallagher, P. M., and Zimmie, T. F. (2007). "Remediation of piled foundations against lateral spreading by passive site stabilization technique." *Soil Dynamics and Earthquake Engineering*, 27(9), 864–874.

Papadimitriou, A. G., and Bouckovalas, G. D. (2002). "Plasticity model for sand under small and large cyclic strains: A multiaxial formulation." *Soil Dynamics and Earthquake Engineering*, 22(3), 191–204.

Papadimitriou, A. G., Bouckovalas, G. D., and Dafalias, Y. F. (2001). "Plasticity Model for Sand under Small and Large Cyclic Strains." *Journal of Geotechnical and Geoenvironmental Engineering*, 127(11), 973–983.

Papadimitriou, A. G., Chaloulos, Y. K., and Dafalias, Y. F. (2019). “A fabric-based sand plasticity model with reversal surfaces within anisotropic critical state theory.” *Acta Geotechnica*, 14(2), 253–277.

Pastor, M., Zienkiewicz, O. C., and Chan, A. H. C. (1990). “Generalized plasticity and the modelling of soil behaviour.” *International Journal for Numerical and Analytical Methods in Geomechanics*, 14(3), 151–190.

Pavlopoulou, A. (2021). “Numerical simulation of seismic response of soil and foundations after passive stabilization with colloidal silica against liquefaction. Diploma thesis in Greek.” National Technical University of Athens.

Pavlopoulou, E.-M. E., and Georgiannou, V. N. (2021). “Effect of Colloidal Silica Aqueous Gel on the Monotonic and Cyclic Response of Sands.” *Journal of Geotechnical and Geoenvironmental Engineering*, 147(11), 04021122.

Petalas, A. L., Dafalias, Y. F., and Papadimitriou, A. G. (2019). “SANISAND-FN: An evolving fabric-based sand model accounting for stress principal axes rotation.” *International Journal for Numerical and Analytical Methods in Geomechanics*, 43(1), 97–123.

Petalas, A. L., Dafalias, Y. F., and Papadimitriou, A. G. (2020). “SANISAND-F: Sand constitutive model with evolving fabric anisotropy.” *International Journal of Solids and Structures*, Pergamon, 188–189, 12–31.

Popescu, R., and Prevost, J. H. (1993). “Centrifuge validation of a numerical model for dynamic soil liquefaction.” *Soil Dynamics and Earthquake Engineering*, 12(2), 73–90.

Pradhan, T. B. S., Tatsuoka, F., and Horii, N. (1988). “Strength and deformation characteristics of sand in torsional simple shear.” *Soils and Foundations*, Elsevier, 28(3), 131–148.

Ramberg, W., and Osgood, W. R. (1943). *Description of stress-strain curve by three parameters*. Washington, D.C.

Reyes, A., Yang, M., Barrero, A. R., and Taiebat, M. (2021). “Numerical modeling of soil liquefaction and lateral spreading using the SANISAND-Sf model in the LEAP experiments.” *Soil Dynamics and Earthquake Engineering*, 143, 106613.

Roscoe, K. H., Schofield, A. N., and Wroth, C. P. (1958). “On The Yielding of Soils.” *Géotechnique*, 8(1), 22–53.

Rowe, P. W. (1962). “The stress-dilatancy relation for static equilibrium of an assembly of particles in contact.” *Proceedings of the Royal Society of London. Series A. Mathematical and Physical Sciences*, 269(1339), 500–527.

Schofield, A., and Wroth, P. (1968). *Critical State Soil Mechanics*. McGraw-Hill.

Shahir, H., and Pak, A. (2010). “Estimating liquefaction-induced settlement of shallow foundations by numerical approach.” *Computers and Geotechnics*, 37(3), 267–279.

Shahnazari, H., and Towhata, I. (2002). “Torsion Shear Tests on Cyclic Stress-Dilatancy Relationship of Sand.” *Soils and Foundations*, 42(1), 105–119.

Shamoto, Y., Zhang, J.-M., and Goto, S. (1997). “Mechanism of Large Post-Liquefaction Deformation in Saturated Sand.” *Soils and Foundations*, 37(2), 71–80.

Shibuya, S., Park, C.-S., Tatsuoka, F., Abe, F., Teachavorasinskun, S., Kohata, Y., and Sato, T. (1994). “The Significance of Local Lateral-Strain Measurement of Soil Specimens for a Wide Range of Strain.” *Soils and Foundations*, 34(2), 95–105.

Silver, M., and Seed, B. (1971). “Volume Changes in Sands during Cyclic Loading.” *Journal of the Soil Mechanics and Foundations Division*, 97(9), 1171–1182.

Sloan, S. W. (1987). “Substepping schemes for the numerical integration of elastoplastic stress-strain relations.” *International Journal for Numerical Methods in Engineering*, 24(5), 893–911.

Sloan, S. W., Abbo, A. J., and Sheng, D. (2001). “Refined explicit integration of

elastoplastic models with automatic error control.” *Engineering Computations*, 18(1/2), 121–194.

Stamatopoulos, C. A., Bouckovalas, G., and Whitman, R. V. (1991). “Analytical Prediction of Earthquake-Induced Permanent Deformations.” *Journal of Geotechnical Engineering*, 117(10), 1471–1491.

Staubach, P., and Wichtmann, T. (2020). “Long-term deformations of monopile foundations for offshore wind turbines studied with a high-cycle accumulation model.” *Computers and Geotechnics*, 124, 103553.

Taboada, V., and Dobry, R. (1994a). “Experimental results of Model No. 1 at RPI.” *Proceedings of Int. Conf. on Verification of numerical procedures for the analysis of soil liquefaction problems*, Davis, CA, 17-10, October, 3–17, Vol.1.

Taboada, V., and Dobry, R. (1994b). “Experimental results of Model No. 2 at RPI.” *Proceedings of Int. Conf. on Verification of numerical procedures for the analysis of soil liquefaction problems*, Davis, CA, 17-10, October, 277–294, Vol. 1.

Taborda, D. M. G., Zdravković, L., Kontoe, S., and Potts, D. M. (2014). “Computational study on the modification of a bounding surface plasticity model for sands.” *Computers and Geotechnics*, 59, 145–160.

Taiebat, M., and Dafalias, Y. F. (2008). “SANISAND: Simple anisotropic sand plasticity model.” *International Journal for Numerical and Analytical Methods in Geomechanics*, 32(8), 915–948.

Taiebat, M., Jeremić, B., Dafalias, Y. F., Kaynia, A. M., and Cheng, Z. (2010). “Propagation of seismic waves through liquefied soils.” *Soil Dynamics and Earthquake Engineering*, 30(4), 236–257.

Taiebat, M., Shahir, H., and Pak, A. (2007). “Study of pore pressure variation during liquefaction using two constitutive models for sand.” *Soil Dynamics and Earthquake Engineering*, 27(1), 60–72.

Tan, T.-S., and Scott, R. F. (1985). “Centrifuge scaling considerations for fluid-particle systems.” *Géotechnique*, 35(4), 461–470.

Tasiopoulou, P., Chaloulos, Y., Gerolymos, N., Giannakou, A., and Chacko, J. (2021). “Cyclic lateral response of OWT bucket foundations in sand: 3D coupled effective stress analysis with Ta-Ger model.” *Soils and Foundations*, 61(2), 371–385.

Tasiopoulou, P., and Gerolymos, N. (2016). “Constitutive modeling of sand: Formulation of a new plasticity approach.” *Soil Dynamics and Earthquake Engineering*, Elsevier, 82, 205–221.

Tasiopoulou, P., Ziotopoulou, K., Humire, F., Giannakou, A., Chacko, J., and Travasarou, T. (2020). “Development and Implementation of Semiempirical Framework for Modeling Postliquefaction Shear Deformation Accumulation in Sands.” *Journal of Geotechnical and Geoenvironmental Engineering*, 146(1), 04019120.

Tatsuoka, F., Ochi, K., Fujii, S., and Okamoto, M. (1986). “Cyclic Undrained Triaxial and Torsional Shear Strength of Sands for Different Sample Preparation Methods.” *Soils and Foundations*, 26(3), 23–41.

Tatsuoka, F., Teachavorasinskun, S., Dong, J., Kohata, Y., and Sato, T. (1994). “Importance of Measuring Local Strains in Cyclic Triaxial Tests on Granular Materials.” *Dynamic Geotechnical Testing II*, ASTM International, 100 Barr Harbor Drive, PO Box C700, West Conshohocken, PA 19428-2959, 288-288–15.

Theocharis, A. I., Vairaktaris, E., Dafalias, Y. F., and Papadimitriou, A. G. (2017). “Proof of Incompleteness of Critical State Theory in Granular Mechanics and Its Remedy.” *Journal of Engineering Mechanics*, 143(2), 04016117.

Tiptiris, I. (2017). “Numerical simulation of the seismic response of soil and deep foundations after passive stabilization with colloidal silica. Diploma thesis in Greek.” National Technical University of Athens.

Tong, Z.-X., Zhang, J.-M., Yu, Y.-L., and Zhang, G. (2010). “Drained Deformation Behavior of Anisotropic Sands during Cyclic Rotation of Principal Stress Axes.” *Journal of Geotechnical and Geoenvironmental Engineering*, 136(11), 1509–1518.

Towhata, I., and Ishihara, K. (1985). “Undrained Strength of Sand Undergoing Cyclic Rotation of Principal Stress Axes.” *Soils and Foundations*, 25(2), 135–147.

Toyota, H., and Takada, S. (2017). “Variation of Liquefaction Strength Induced by Monotonic and Cyclic Loading Histories.” *Journal of Geotechnical and Geoenvironmental Engineering*, 143(4), 04016120.

Tsaparli, V. (vasia), Kontoe, S., Taborda, D. M. G., and Potts, D. M. (2020). “A case study of liquefaction: demonstrating the application of an advanced model and understanding the pitfalls of the simplified procedure.” *Géotechnique*, 70(6), 538–558.

Ueda, K., Vargas, R., and Uemura, K. (2018). *LEAP-Asia-2018: stress–strain response of Ottawa sand in cyclic torsional shear tests*.

Vaid, Y. P., and Chern, J. C. (1985). “Cyclic and monotonic undrained response of saturated sands.” *Proc., Advances in the Art of Testing Soils Under Cyclic Loading*, ASCE, New York, 120–147.

Vaid, Y. P., and Sivathayalan, S. (1996). “Static and cyclic liquefaction potential of Fraser Delta sand in simple shear and triaxial tests.” *Canadian Geotechnical Journal*, 33(2), 281–289.

Vasko, A. (2015). “An Investigation into the Behavior of Ottawa Sand through Monotonic and Cyclic Shear Tests.” The George Washington University.

Vasko, A., El Ghoraiby, M., and Manzari, M. (2018). *LEAP-GWU-2015 Laboratory Tests*.

Verdugo, R. (1992). “Characterization of sandy soil behaviour under large deformation.” University of Tokyo.

Verdugo, R., and Ishihara, K. (1996). “The Steady State of Sandy Soils.” *Soils and Foundations*, Elsevier BV, 36(2), 81–91.

Vucetic, M. (1994). “Cyclic Threshold Shear Strains in Soils.” *Journal of Geotechnical Engineering*, 120(12), 2208–2228.

Vucetic, M., and Dobry, R. (1991). “Effect of Soil Plasticity on Cyclic Response.” *Journal of Geotechnical Engineering*, 117(1), 89–107.

Wahyudi, S., Chiaro, G., De Silva, L., and Koseki, J. (2010). “Stress dilatancy behavior of loose sand during drained cyclic torsional shear loading.” *12th JSCE International Summer Symposium*, Funabashi, Chiba.

Wan, R. G., and Guo, P. J. (1998). “A simple constitutive model for granular soils: Modified stress-dilatancy approach.” *Computers and Geotechnics*, 22(2), 109–133.

Wang, G., and Xie, Y. (2014). “Modified Bounding Surface Hypoplasticity Model for Sands under Cyclic Loading.” *Journal of Engineering Mechanics*, 140(1), 91–101.

Wang, H., Koseki, J., and Sato, T. (2014a). “Resistance against liquefaction of unsaturated Toyoura sand and Inagi sand.” *Bulletin of ERS, No. 47*, University of Tokyo.

Wang, R., Cao, W., Xue, L., and Zhang, J.-M. (2021). “An anisotropic plasticity model incorporating fabric evolution for monotonic and cyclic behavior of sand.” *Acta Geotechnica*, 16(1), 43–65.

Wang, R., Zhang, J.-M., and Wang, G. (2014b). “A unified plasticity model for large post-liquefaction shear deformation of sand.” *Computers and Geotechnics*, 59, 54–66.

Wang, Z.-L., Dafalias, Y. F., Li, X.-S., and Makdisi, F. I. (2002). “State Pressure Index for Modeling Sand Behavior.” *Journal of Geotechnical and Geoenvironmental Engineering*, 128(6), 511–519.

Wang, Z., Dafalias, Y. F., and Shen, C. (1990). “Bounding Surface Hypoplasticity Model for Sand.” *Journal of Engineering Mechanics*, 116(5), 983–1001.

Wei, X., Chen, Y., and Yang, J. (2020). “A unified critical state constitutive model for cyclic behavior of silty sands.” *Computers and Geotechnics*, 127, 103760.

Wicaksono, R. I., and Kuwano, R. (2009). “Small strain shear stiffness of Toyoura sand obtained from various wave measurement techniques.” *Bulletin of ERS*, 42(42), 107–120.

Wichtmann, T., Niemunis, A., and Triantafyllidis, T. H. (2009). “Validation and Calibration of a High-Cycle Accumulation Model Based on Cyclic Triaxial Tests on Eight Sands.” *Soils and Foundations*, 49(5), 711–728.

Wichtmann, T., Triantafyllidis, T., Chrisopoulos, S., and Zachert, H. (2017). “Prediction of Long-Term Deformations of Offshore Wind Power Plant Foundations Using HCA-Based Engineer-Oriented Models.” *International Journal of Offshore and Polar Engineering*, 27(4), 346–356.

Wood, D. M., and Belkheir, K. (1994). “Strain softening and state parameter for sand modelling.” *Géotechnique*, 44(2), 335–339.

Wu, J., Kammerer, A., Riemer, M., Seed, R., and Pestana, J. (2004). “Laboratory study of liquefaction triggering criteria.” *13th World Conference on Earthquake Engineering Vancouver, B .C., Canada*, Vancouver, B.C., Canada, August 1-6.

Yamashita, S., and Toki, S. (1993). “Effects of Fabric Anisotropy of Sand on Cyclic Undrained Triaxial and Torsional Strengths.” *Soils and Foundations*, 33(3), 92–104.

Yang, M., Taiebat, M., and Dafalias, Y. F. (2020). “SANISAND-MSf: a sand plasticity model with memory surface and semifluidised state.” *Géotechnique*, 1–20.

Yang, Z., and Elgamal, A. (2008). “Multi-surface Cyclic Plasticity Sand Model with Lode Angle Effect.” *Geotechnical and Geological Engineering*, 26(3), 335–348.

Yin, Z.-Y., Chang, C. S., and Hicher, P.-Y. (2010). “Micromechanical modelling for effect of inherent anisotropy on cyclic behaviour of sand.” *International Journal of Solids and Structures*, 47(14–15), 1933–1951.

Yoshimine, M., Ishihara, K., and Vargas, W. (1998). “Effects of principal stress direction and intermediate principal stress on undrained shear behavior of sand.” *Soils and Foundations*, Japanese Geotechnical Society, 38(3), 179–188.

Youd, T. L., and Idriss, I. M. (2001). “Liquefaction Resistance of Soils: Summary Report from the 1996 NCEER and 1998 NCEER/NSF Workshops on Evaluation of Liquefaction Resistance of Soils.” *Journal of Geotechnical and Geoenvironmental Engineering*, 127(4), 297–313.

Zhang, J. M., and Wang, G. (2012). “Large post-liquefaction deformation of sand, part I: Physical mechanism, constitutive description and numerical algorithm.” *Acta Geotechnica*, 7(2), 69–113.

Zhang, J., Rao, Q., and Yi, W. (2020). “Viscoelastic Parameter Prediction of Multi-Layered Coarse-Grained Soil with Consideration of Interface-Layer Effect.” *Applied Sciences*, 10(24), 8879.

Zhang JM. (1997). “Cyclic critical stress state theory of sand with its application to geotechnical problems. PhD Thesis.” Tokyo Institute of Technology.

Zhang, W., Lim, K., Ghahari, S. F., Arduino, P., and Taciroglu, E. (2021). “On the implementation and validation of a three-dimensional pressure-dependent bounding surface plasticity model for soil nonlinear wave propagation and soil-structure interaction analyses.” *International Journal for Numerical and Analytical Methods in Geomechanics*, 45(8), 1091–1119.

Zienkiewicz, O., and Mroz, Z. (1984). “Generalized plasticity formulation and applications to geomechanics.” *Mechanics of Engineering Materials*, D. CS and G. RH, eds., Wiley, New York, 655–679.

Appendix

This Appendix presents **Tables A1 – A9** that summarize the information about the laboratory tests employed in the model validation process in **Chapter 5**. This information includes the sand name, the type of test and its initial conditions in terms of void ratio e_o, axial effective stress $\sigma_{a,o}$, mean effective stress p_o and state parameter ψ_o.

Table A1: *Initial conditions of tests used in model validation process for* ***Toyoura sand*** *against experimental data.*

Figure No.	Sand	Test*	Initial void ratio, e_o	Initial axial effective stress, $\sigma_{a,o}$	Initial mean effective stress, p_o	Initial state parameter, ψ_o
5.13	Toyoura	DM/TC	0.831	100	100 (K_o =1)	-0.084
5.13	Toyoura	DM/TC	0.917	100	100 (K_o =1)	0.002
5.13	Toyoura	DM/TC	0.996	100	100 (K_o =1)	0.081
5.13	Toyoura	DM/TC	0.810	500	500 (K_o =1)	-0.066
5.13	Toyoura	DM/TC	0.886	500	500 (K_o =1)	0.010
5.13	Toyoura	DM/TC	0.960	500	500 (K_o =1)	0.084
5.14	Toyoura	DM/TS	0.674	200	113.33 (K_o = 0.350**)	-0.239
5.14	Toyoura	DM/TS	0.798	100	61 (K_o = 0.415**)	-0.123
5.14	Toyoura	DM/TS	0.797	200	121.87 (K_o = 0.414**)	-0.115
5.15	Toyoura	UM/TC	0.735	100	100 (K_o =1)	-0.180
5.15	Toyoura	UM/TC	0.735	1000	1000 (K_o =1)	-0.105
5.15	Toyoura	UM/TC	0.735	2000	2000 (K_o =1)	-0.046
5.15	Toyoura	UM/TC	0.833	100	100 (K_o =1)	-0.082
5.15	Toyoura	UM/TC	0.833	1000	1000 (K_o =1)	-0.007
5.15	Toyoura	UM/TC	0.833	2000	2000 (K_o =1)	0.052
5.16	Toyoura	UM/SS	0.804	100	100 (K_o =1)	-0.111
5.16	Toyoura	UM/SS	0.816	100	100 (K_o =1)	-0.099
5.16	Toyoura	UM/SS	0.844	100	100 (K_o =1)	-0.071
5.16	Toyoura	UM/SS	0.876	100	100 (K_o =1)	-0.039
5.16	Toyoura	UM/SS	0.863	100	100 (K_o =1)	-0.052
5.16	Toyoura	UM/SS	0.888	100	100 (K_o =1)	-0.027
5.17	Toyoura	UCyc/TS	0.736	100	100 (K_o =1)	-0.179
5.18	Toyoura	UCyc/TX	0.754	100	100 (K_o =1)	-0.161
5.19	Toyoura	UCyc/TX	0.811	100	100 (K_o =1)	-0.104
5.19	Toyoura	UCyc/TX	0.756	100	100 (K_o =1)	-0.159
5.19	Toyoura	UCyc/TX	0.691	100	100 (K_o =1)	-0.224

*DM: Drained monotonic, UM: Undrained monotonic, DCyc: Drained cyclic, UCyc: Undrained cyclic

TC: Triaxial compression, TX: Triaxial, TS: Torsional shear, SS: Simple shear

** $K_o = 0.52e_o$ according to Pradhan et al. (1988)

***Table A2**: Initial conditions of tests used in model validation process for **Toyoura sand** against empirical relations.*

Figure No.	Sand	Test*	Initial void ratio, e_o	Initial axial effective stress, $\sigma_{a,o}$	Initial mean effective stress, p_o	Initial state parameter, ψ_o
5.20	Toyoura	UCyc/TX	0.811	100	100 (K_o =1)	-0.104
5.20	Toyoura	UCyc/TX	0.811	200	200 (K_o =1)	-0.092
5.20	Toyoura	UCyc/TX	0.811	400	400 (K_o =1)	-0.073
5.20	Toyoura	UCyc/TX	0.756	100	100 (K_o =1)	-0.159
5.20	Toyoura	UCyc/TX	0.756	200	200 (K_o =1)	-0.147
5.20	Toyoura	UCyc/TX	0.756	400	400 (K_o =1)	-0.128
5.20	Toyoura	UCyc/TX	0.691	100	100 (K_o =1)	-0.224
5.20	Toyoura	UCyc/TX	0.691	200	200 (K_o =1)	-0.212
5.20	Toyoura	UCyc/TX	0.691	400	400 (K_o =1)	-0.193
5.20	Toyoura	UCyc/SS	0.811	100	100 (K_o =1)	-0.104
5.20	Toyoura	UCyc/SS	0.811	200	200 (K_o =1)	-0.092
5.20	Toyoura	UCyc/SS	0.811	400	400 (K_o =1)	-0.073
5.20	Toyoura	UCyc/SS	0.756	100	100 (K_o =1)	-0.159
5.20	Toyoura	UCyc/SS	0.756	200	200 (K_o =1)	-0.147
5.20	Toyoura	UCyc/SS	0.756	400	400 (K_o =1)	-0.128
5.20	Toyoura	UCyc/SS	0.691	100	100 (K_o =1)	-0.224
5.20	Toyoura	UCyc/SS	0.691	200	200 (K_o =1)	-0.212
5.20	Toyoura	UCyc/SS	0.691	400	400 (K_o =1)	-0.193
5.21	Toyoura	DCyc/SS	0.756	100	100 (K_o =1)	-0.159
5.21	Toyoura	DCyc/SS	0.756	1000	1000 (K_o =1)	-0.084
5.22	Toyoura	DCyc/SS	0.829	100	66.67 (K_o =0.50)	-0.091
5.22	Toyoura	DCyc/SS	0.683	100	66.67 (K_o =0.50)	-0.237
5.23	Toyoura	DCyc/TX	0.829	246.67	200 ($q_{TX,o}/p_o$ =0.35)	-0.074
5.23	Toyoura	DCyc/TX	0.756	246.67	200 ($q_{TX,o}/p_o$ =0.35)	-0.147
5.23	Toyoura	DCyc/TX	0.683	246.67	200 ($q_{TX,o}/p_o$ =0.35)	-0.220
5.23	Toyoura	DCyc/TX	0.829	300	200 ($q_{TX,o}/p_o$ =0.75)	-0.074
5.23	Toyoura	DCyc/TX	0.756	300	200 ($q_{TX,o}/p_o$ =0.75)	-0.147
5.23	Toyoura	DCyc/TX	0.683	300	200 ($q_{TX,o}/p_o$ =0.75)	-0.220

*DCyc: Drained cyclic; UCyc: Undrained cyclic; TX: Triaxial; SS: Simple shear

Table A3: *Initial conditions of tests used in model validation process for* ***Ottawa-F65*** *sand against experimental data.*

Figure No.	Sand	Test*	Initial void ratio, e_o	Initial axial effective stress, $\sigma_{a,o}$	Initial mean effective stress, p_o	Initial state parameter, ψ_o
5.25	Ottawa-F65	DM/TC	0.585	100	100 (K_o =1)	-0.205
5.25	Ottawa-F65	DM/TC	0.585	200	200 (K_o =1)	-0.192
5.25	Ottawa-F65	DM/TC	0.585	300	300 (K_o =1)	-0.180
5.25	Ottawa-F65	DM/TC	0.604	100	100 (K_o =1)	-0.186
5.25	Ottawa-F65	DM/TC	0.604	200	200 (K_o =1)	-0.173
5.25	Ottawa-F65	DM/TC	0.604	300	300 (K_o =1)	-0.161
5.26	Ottawa-F65	UCyc/TX	0.585	100	100 (K_o =1)	-0.205
5.27	Ottawa-F65	UCyc/TS	0.590	100	100 (K_o =1)	-0.200
5.28	Ottawa-F65	UCyc/TX	0.585	100	100 (K_o =1)	-0.205
5.28	Ottawa-F65	UCyc/TX	0.542	100	100 (K_o =1)	-0.248

Table A4*: Initial conditions of tests used in model validation process for* ***Ottawa-F65*** *sand against empirical relations.*

Figure No.	Sand	Test*	Initial void ratio, e_o	Initial axial effective stress, $\sigma_{a,o}$	Initial mean effective stress, p_o	Initial state parameter, ψ_o
5.29	Ottawa-F65	UCyc/TX	0.640	100	100 (K_o =1)	-0.150
5.29	Ottawa-F65	UCyc/TX	0.640	200	200 (K_o =1)	-0.137
5.29	Ottawa-F65	UCyc/TX	0.640	400	400 (K_o =1)	-0.114
5.29	Ottawa-F65	UCyc/TX	0.585	100	100 (K_o =1)	-0.205
5.29	Ottawa-F65	UCyc/TX	0.585	200	200 (K_o =1)	-0.192
5.29	Ottawa-F65	UCyc/TX	0.585	400	400 (K_o =1)	-0.169
5.29	Ottawa-F65	UCyc/TX	0.542	100	100 (K_o =1)	-0.248
5.29	Ottawa-F65	UCyc/TX	0.542	200	200 (K_o =1)	-0.235
5.29	Ottawa-F65	UCyc/TX	0.542	400	400 (K_o =1)	-0.212
5.30	Ottawa-F65	DCyc/SS	0.590	100	100 (K_o =1)	-0.200
5.30	Ottawa-F65	DCyc/SS	0.590	1000	1000 (K_o =1)	-0.109
5.31	Ottawa-F65	DCyc/SS	0.640	100	66.67 (K_o =0.50)	-0.155
5.31	Ottawa-F65	DCyc/SS	0.542	100	66.67 (K_o =0.50)	-0.253
5.32	Ottawa-F65	DCyc/TX	0.640	246.67	200 ($q_{TX,o}/p_o$ =0.35)	-0.137
5.32	Ottawa-F65	DCyc/TX	0.585	246.67	200 ($q_{TX,o}/p_o$ =0.35)	-0.192
5.32	Ottawa-F65	DCyc/TX	0.542	246.67	200 ($q_{TX,o}/p_o$ =0.35)	-0.235
5.32	Ottawa-F65	DCyc/TX	0.640	300	200 ($q_{TX,o}/p_o$ =0.75)	-0.137
5.32	Ottawa-F65	DCyc/TX	0.585	300	200 ($q_{TX,o}/p_o$ =0.75)	-0.192
5.32	Ottawa-F65	DCyc/TX	0.542	300	200 ($q_{TX,o}/p_o$ =0.75)	-0.235

Table A5: *Initial conditions of tests used in model validation process for* ***Nevada sand*** *against experimental data.*

Figure No.	Sand	Test*	Initial void ratio, e_o	Initial axial effective stress, $\sigma_{a,o}$	Initial mean effective stress, p_o	Initial state parameter, ψ_o
5.34	Nevada	UM/TC	0.736	40	40 (K_o =1)	-0.073
5.34	Nevada	UM /TC	0.729	80	80 (K_o =1)	-0.070
5.34	Nevada	UM TC	0.725	160	160 (K_o =1)	-0.064
5.34	Nevada	UM /TC	0.660	40	40(K_o =1)	-0.149
5.34	Nevada	UM /TC	0.657	80	80 (K_o =1)	-0.142
5.34	Nevada	UM /TC	0.649	160	160 (K_o =1)	-0.140
5.35	Nevada	UCyc/SS	0.727	160	96 (K_o =0.40)	-0.070
5.35	Nevada	UCyc/SS	0.655	160	96 (K_o =0.40)	-0.142
5.36	Nevada	UCyc/SS	0.724	100	60 (K_o =0.40)	-0.079
5.36	Nevada	UCyc/SS	0.655	100	60 (K_o =0.40)	-0.148
5.36	Nevada	UCyc/SS	0.549	100	60 (K_o =0.40)	-0.254
5.36	Nevada	UCyc/SS	0.727	160	96 (K_o =0.40)	-0.070
5.36	Nevada	UCyc/SS	0.725	160	96 (K_o =0.40)	-0.072
5.36	Nevada	UCyc/SS	0.719	80	48 (K_o =0.40)	-0.087
5.36	Nevada	UCyc/SS	0.715	80	48 (K_o =0.40)	-0.091
5.36	Nevada	UCyc/SS	0.723	160	96 (K_o =0.40)	-0.074
5.36	Nevada	UCyc/SS	0.732	160	96 (K_o =0.40)	-0.065
5.36	Nevada	UCyc/SS	0.727	160	96 (K_o =0.40)	-0.070
5.36	Nevada	UCyc/SS	0.650	80	48 (K_o =0.40)	-0.156
5.36	Nevada	UCyc/SS	0.652	80	48 (K_o =0.40)	-0.154
5.36	Nevada	UCyc/SS	0.656	160	96 (K_o =0.40)	-0.141
5.36	Nevada	UCyc/SS	0.661	160	96 (K_o =0.40)	-0.136
5.36	Nevada	UCyc/SS	0.655	160	96 (K_o =0.40)	-0.142
5.36	Nevada	UCyc/SS	0.654	160	96 (K_o =0.40)	-0.143
5.36	Nevada	UCyc/SS	0.655	160	96 (K_o =0.40)	-0.142

***Table A6**: Initial conditions of tests used in model validation process for **Nevada sand** against empirical relations.*

Figure No.	Sand	Test*	Initial void ratio, e_o	Initial axial effective stress, $\sigma_{a,o}$	Initial mean effective stress, p_o	Initial state parameter, ψ_o
5.37	Nevada	UCyc/TX	0.737	100	100 (K_o =1)	-0.059
5.37	Nevada	UCyc/TX	0.737	200	200 (K_o =1)	-0.048
5.37	Nevada	UCyc/TX	0.737	400	400 (K_o =1)	-0.035
5.37	Nevada	UCyc/TX	0.661	100	100 (K_o =1)	-0.135
5.37	Nevada	UCyc/TX	0.661	200	200 (K_o =1)	-0.124
5.37	Nevada	UCyc/TX	0.661	400	400 (K_o =1)	-0.111
5.37	Nevada	UCyc/TX	0.585	100	100 (K_o =1)	-0.211
5.37	Nevada	UCyc/TX	0.585	200	200 (K_o =1)	-0.200
5.37	Nevada	UCyc/TX	0.585	400	400 (K_o =1)	-0.184
5.38	Nevada	DCyc/SS	0.737	80	80(K_o =1)	-0.063
5.38	Nevada	DCyc/SS	0.664	80	80 (K_o =1)	-0.138
5.39	Nevada	DCyc/SS	0.737	100	66.67 (K_o =0.50)	-0.065
5.39	Nevada	DCyc/SS	0.585	100	66.67 (K_o =0.50)	-0.217
5.40	Nevada	DCyc/TX	0.737	246.67	200 ($q_{TX,o}/p_o$ =0.35)	-0.048
5.40	Nevada	DCyc/TX	0.661	246.67	200 ($q_{TX,o}/p_o$ =0.35)	-0.124
5.40	Nevada	DCyc/TX	0.585	246.67	200 ($q_{TX,o}/p_o$ =0.35)	-0.200
5.40	Nevada	DCyc/TX	0.737	300	200 ($q_{TX,o}/p_o$ =0.75)	-0.048
5.40	Nevada	DCyc/TX	0.661	300	200 ($q_{TX,o}/p_o$ =0.75)	-0.124
5.40	Nevada	DCyc/TX	0.585	300	200 ($q_{TX,o}/p_o$ =0.75)	-0.200

***Table A7:** Initial conditions of tests used in model validation process for **M31 sand** against experimental data.*

Figure No.	Sand	Test*	Initial void ratio, e_o	Initial axial effective stress, $\sigma_{a,o}$	Initial mean effective stress, p_o	Initial state parameter, ψ_o
5.42	M31	DM/TC	0.710	200	200 (K_o =1)	-0.042
5.42	M31	DM/TC	0.717	300	300 (K_o =1)	-0.028
5.42	M31	DM/TC	0.691	500	500 (K_o =1)	-0.044
5.42	M31	DM/TC	0.676	700	700 (K_o =1)	-0.050
5.43	M31	UM/TC	0.708	300	300 (K_o =1)	-0.037
5.43	M31	UM/TC	0.681	1000	1000 (K_o =1)	-0.033
5.43	M31	UM/TC	0.661	2000	2000 (K_o =1)	-0.020
5.44	M31	UCyc/TX	0.633	200	200 (K_o =1)	-0.119
5.45	M31	UCyc/TX	0.742	200	200 (K_o =1)	-0.010
5.46	M31	UCyc/TX	0.653	100	100 (K_o =1)	-0.106
5.46	M31	UCyc/TX	0.650	100	100 (K_o =1)	-0.109
5.46	M31	UCyc/TX	0.633	200	200 (K_o =1)	-0.119
5.46	M31	UCyc/TX	0.653	200	200 (K_o =1)	-0.099
5.46	M31	UCyc/TX	0.649	200	200 (K_o =1)	-0.103

Table A8: *Initial conditions of tests used in model validation process for* ***Monterey sand*** *against experimental data.*

Figure No.	Sand	Test*	Initial void ratio, e_o	Initial axial effective stress, $\sigma_{a,o}$	Initial mean effective stress, p_o	Initial state parameter, ψ_o
5.48	Monterey	UCyc/SS	0.610	80	53.33 (K_o =0.50)	-0.312

Table A9: *Initial conditions of tests used in model validation process for Pea gravels against experimental data.*

Figure No.	Sand	Test*	Initial void ratio, e_o	Initial axial effective stress, $\sigma_{a,o}$	Initial mean effective stress, p_o	Initial state parameter, ψ_o
5.50	Pea gravels	UM/SS	0.685	100	66.67 (K_o =0.50)	-0.027
5.50	Pea gravels	UM/SS	0.681	200	133.33 (K_o =0.50)	-0.006
5.50	Pea gravels	UM/SS	0.682	400	267.67 (K_o =0.50)	0.095
5.50	Pea gravels	UM/SS	0.592	100	66.67 (K_o =0.50)	-0.120
5.50	Pea gravels	UM/SS	0.598	200	133.33 (K_o =0.50)	-0.089
5.50	Pea gravels	UM/SS	0.593	400	267.67 (K_o =0.50)	0.006
5.51	Pea gravels	UCyc//SS	0.686	100	66.67 (K_o =0.50)	-0.026
5.52	Pea gravels	UCyc//SS	0.680	50	33.33 (K_o =0.50)	-0.038
5.52	Pea gravels	UCyc//SS	0.680	100	66.67 (K_o =0.50)	-0.032
5.52	Pea gravels	UCyc//SS	0.681	100	66.67 (K_o =0.50)	-0.031
5.52	Pea gravels	UCyc//SS	0.684	100	66.67 (K_o =0.50)	-0.028
5.52	Pea gravels	UCyc//SS	0.589	50	33.33 (K_o =0.50)	-0.129
5.52	Pea gravels	UCyc//SS	0.589	100	66.67 (K_o =0.50)	-0.123
5.52	Pea gravels	UCyc//SS	0.590	100	66.67 (K_o =0.50)	-0.122
5.52	Pea gravels	UCyc//SS	0.599	100	66.67 (K_o =0.50)	-0.113
5.52	Pea gravels	UCyc//SS	0.602	100	66.67 (K_o =0.50)	-0.110

Table A10: *Initial conditions of tests used in model validation process for CSL8 gravels against experimental data.*

Figure No.	Sand	Test*	Initial void ratio, e_o	Initial axial effective stress, $\sigma_{a,o}$	Initial mean effective stress, p_o	Initial state parameter, ψ_o
5.54	CSL8 gravels	UM/SS	0.738	50	33.33 (K_o =0.50)	-0.086
5.54	CSL8 gravels	UM/SS	0.756	100	66.67 (K_o =0.50)	-0.065
5.54	CSL8 gravels	UM/SS	0.747	200	133.33 (K_o =0.50)	-0.062
5.54	CSL8 gravels	UM/SS	0.748	400	267.67 (K_o =0.50)	-0.014
5.54	CSL8 gravels	UM/SS	0.572	50	33.33 (K_o =0.50)	-0.252
5.54	CSL8 gravels	UM/SS	0.575	100	66.67 (K_o =0.50)	-0.246
5.54	CSL8 gravels	UM/SS	0.569	200	133.33 (K_o =0.50)	-0.240
5.54	CSL8 gravels	UM/SS	0.574	400	267.67 (K_o =0.50)	-0.188
5.55	CSL8 gravels	UCyc//SS	0.755	100	66.67 (K_o =0.50)	-0.066
5.55	CSL8 gravels	UCyc//SS	0.755	100	66.67 (K_o =0.50)	-0.066
5.55	CSL8 gravels	UCyc//SS	0.755	50	33.33 (K_o =0.50)	-0.066
5.55	CSL8 gravels	UCyc//SS	0.751	100	66.67 (K_o =0.50)	-0.070
.55	CSL8 gravels	UCyc//SS	0.581	100	66.67 (K_o =0.50)	-0.240